Springer Series in Reliability Engineering

Paolo Gardoni *Editor*

Risk and Reliability Analysis: Theory and Applications

In Honor of Prof. Armen Der Kiureghian

Springer

Springer Series in Reliability Engineering

Series editor

Hoang Pham, Piscataway, USA

More information about this series at http://www.springer.com/series/6917

Paolo Gardoni
Editor

Risk and Reliability Analysis: Theory and Applications

In Honor of Prof. Armen Der Kiureghian

Springer

Editor
Paolo Gardoni
Civil and Environmental Engineering,
3118 Newmark Civil Engineering
Laboratory
University of Illinois at Urbana-Champaign
Urbana, IL
USA

ISSN 1614-7839 ISSN 2196-999X (electronic)
Springer Series in Reliability Engineering
ISBN 978-3-319-52424-5 ISBN 978-3-319-52425-2 (eBook)
DOI 10.1007/978-3-319-52425-2

Library of Congress Control Number: 2016963335

Printed on acid-free paper

This Springer imprint is published by Springer Nature
The registered company is Springer International Publishing AG
The registered company address is: Gewerbestrasse 11, 6330 Cham, Switzerland

This book is dedicated to Professor Armen Der Kiureghian

Preface

Communities face a number of risks from natural and anthropogenic hazards. Risk and reliability analysis provide essential information for risk determination (the quantification of the probabilities of potential consequences in various hazardous scenarios), evaluation (the decision of whether actions are necessary, under conditions of uncertainty), and mitigation (the decision of how to act).

Over the past few decades, risk and reliability analysis have gone from a specialty topic to a mainstream subject in engineering, becoming essential tools for informed decision-making, hazard mitigation and planning. This book presents the state of the art in risk and reliability with a unique collection of contributions from some of the foremost scholars in the field. Combining the most advanced analysis techniques with practical applications, this book is one of the most comprehensive and up-to-date references available on this subject, makes the state of the art in risk and reliability analysis accessible to a large audience, and helps make risk and reliability analysis the rigorous foundation of engineering decision-making. The fundamental concepts needed to conduct risk and reliability assessments are covered in detail, providing readers with a sound understanding of the field and making the book a powerful tool for students and researchers alike.

The book is a tribute to one of the fathers of modern risk and reliability analysis, Prof. Armen Der Kiureghian. During his career, Prof. Der Kiureghian has made fundamental and revolutionary research contributions. He has pioneered methods for safety and reliability assessment of complex structures and for stochastic seismic analysis of buildings, bridges and critical equipment. He has more than 300 publications, including more than 100 journal articles and book chapters. Many of his publications have become mandatory reading for the current and future generations of students, researchers and practitioners.

The book is organized into six parts. Part I gives a general introduction of the book including a discussion of its goal and contributions, presents an overview of the field of risk and reliability analysis, and discusses the role of Armen Der Kiureghian in modern risk and reliability analysis. Part II focuses specifically on reliability analysis, and includes a description of computational methods and applications to some of the most complex real-life problems. Part III covers the

subject of stochastic dynamics. As in Part II, Part III also includes both theoretical formulations and applications. Part IV discusses methods for sensitivity analysis and optimization in the context of risk and reliability analysis. Part V focuses on statistical analysis and the development of probabilistic models. Finally, Part VI covers life-cycle and resilience analysis as well as financial tools for risk mitigation. While each part has a specific and distinct focus, many of the chapters draw from methods and techniques covered in some of the other parts of the book. Such links among chapters help understand the relations among the different subjects.

Urbana, IL, USA Paolo Gardoni

Armen Der Kiureghian

Acknowledgements

This book builds upon the presentations, discussions, and related outcomes from the *Risk and Reliability Symposium in Honor of Professor Armen Der Kiureghian* that took place at the University of Illinois at Urbana-Champaign, during October 4–5, 2015. Funding for the symposium was provided by the MAE Center: Creating a Multi-hazard Approach to Engineering (http://mae.cee.illinois.edu/), and the Structural Engineering and the Societal Risk Management (SRM) programs of the Department of Civil and Environmental Engineering at the University of Illinois at Urbana-Champaign.

Contents

Part VI Life-cycle and Resilience Analysis and Financial Tools

Part I
Introduction

Risk and Reliability Analysis

Paolo Gardoni

Abstract Natural and anthropogenic hazards pose significant risks to individuals and communities. Over the past few decades, risk and reliability analysis have gone from a specialty topic to a mainstream subject in engineering, becoming essential tools for informed decision making, hazard mitigation, and planning. This book presents the state-of-the-art in risk and reliability analysis with a unique collection of contributions from some of the foremost scholars in the field. Combining the most advanced analysis techniques with practical applications, this book is one of the most comprehensive and up-to-date references available on this subject, makes the state-of-the-art in risk and reliability analysis accessible to a large audience, and helps make risk and reliability analysis the rigorous foundation of engineering decision-making. The fundamental concepts needed to conduct risk and reliability analysis are covered in detail, providing readers with a sound understanding of the field and making the book a powerful tool for students, researchers and practitioners (engineering professionals and risk analysts) alike. The book is a tribute to Professor Armen Der Kiureghian, one of the fathers of modern risk and reliability analysis. During his career, Professor Der Kiureghian has made fundamental and revolutionary research contributions to this field. He has pioneered methods for safety and reliability assessment of complex structures and for stochastic seismic analysis of buildings, bridges and critical equipment. Many of his publications have become mandatory readings for the current and future generations of students, researchers and practitioners. The book is organized into six parts. Part I gives a general introduction of the book including a discussion of its goal and contributions, presents an overview of the field of risk and reliability analysis, and discusses the role of Armen Der Kiureghian in modern risk and reliability analysis. Part II focuses specifically on reliability analysis, and includes a description of efficient computational methods and their applications to some of the most complex real-life problems. Part III covers the subject of stochastic dynamics, presenting both

P. Gardoni (✉)
Civil and Environmental Engineering, 3118 Newmark Civil Engineering Laboratory, University of Illinois at Urbana-Champaign, 205 North Mathews Avenue, Urbana, IL 61801, USA
e-mail: gardoni@illinois.edu

P. Gardoni (ed.), *Risk and Reliability Analysis: Theory and Applications*,
Springer Series in Reliability Engineering, DOI 10.1007/978-3-319-52425-2_1

methods and applications. Part IV discusses methods for sensitivity analysis and optimization in the context of risk and reliability analysis. Part V focuses on statistical analysis and the development of probabilistic models. Finally, Part VI covers life-cycle and resilience analysis as well as different financial tools for risk mitigation. While each part has a specific focus, many of the chapters build on and use the methods and techniques covered in some of the other parts of the book. Such links help understand the relation between the different subjects, which is needed for a thorough understanding of the topic of risk and reliability analysis.

1 Introduction

Communities face a number of risks from natural and anthropogenic hazards (Gardoni and LaFave 2016; Gardoni et al. 2016a, b). Engineers, risk analysts, decision-makers and community leaders need to work collaboratively to develop sustainable solution strategies. "Managing such risks requires communities to make comparative judgments about the relative gravity of diverse risks. Such judgments are reflected in the priorities that communities set in terms of the risks that they will address through mitigation policy, and so the kinds of risks to which limited resources will be devoted." (Gardoni and Murphy 2014).

Risk analysis is an important tool for informed decision making (Rowe 1980; Vose 2000; Bedford and Cooke 2001; Haimes 2004; Murphy and Gardoni 2011; Gardoni and Murphy 2008, 2014). In this context, risk is typically defined in terms of the probabilities of occurrence and the associated consequences of hazardous scenarios (Kaplan and Gerrick 1981; Murphy and Gardoni 2006, 2007). Reliability analysis can be used to quantify the safety of engineering assets and to estimate the probabilities related to structural performance that are needed in risk analysis (e.g., Benjamin and Cornell 1970; Ditlevsen 1981; Hart 1982; Thoft-Christense and Baker 1982; Augusti et al. 1984; Thoft-Christense and Murotsu 1986; Ayyub and McCuen 2011; Madsen et al. 1986; Wen 1990; Ditlevsen and Madsen 1996; Melchers 1999; Ang and Tang 2007).

Modern reliability analysis dates back to the beginning of the 20th Century, with significant contributions made in the second half of that century. Over the past few decades, reliability analysis has gone from a specialty topic to a mainstream subject in engineering. Currently it is being used in the development of design codes (e.g., Ellingwood 1980; Vrouwenvelder 1997; Rosowsky and Ellingwood 2002; Nowak and Collins 2012; Briaud et al. 2013) and the assessment of a number of assets ranging from bridges (e.g., Stewart and Rosowsky 1998; Choi et al. 2004; Choe et al. 2008, 2009, 2010; Pillai et al. 2010, 2014; Zhong et al. 2012) to buildings (e.g., Rossetto and Elnashai 2003; van de Lindt and Walz 2003; van de Lindt 2004; Kwon and Elnashai 2006; Ramamoorthy et al. 2006, 2008; Williams et al. 2009; Bai et al. 2009, 2011, 2015; Xu and Gardoni 2016; Elhami Khorasani et al. 2016), and from nuclear power plants (e.g., Swain and Guttmann 1983; Ellingwood and More 1993; Gardoni et al. 2007) to offshore structures (e.g., Wirsching 1984; Melchers 2005;

Moan 2005; Mousavi et al. 2013; Mousavi and Gardoni 2014a, b; Mardfekri and Gardoni 2015). More broadly and going beyond the traditional engineering disciplinary lines, risk and reliability analysis are the rigorous foundation of the prediction of the societal impact of natural and anthropogenic hazards (Corotis 2009; Lind and Nathwani 2012; Gardoni et al. 2016a, b; Stewart and Reid 2016).

This book presents the state-of-the-art in risk and reliability with a unique collection of contributions from some of the foremost scholars in the field. Combining the most advanced analysis techniques with practical applications, it is one of the most comprehensive and up-to-date books available on risk- and reliability-based engineering. All of the fundamental concepts needed to conduct risk and reliability analysis are covered in detail, providing readers with a sound understanding of the field and making the book a powerful tool for students, researchers and practitioners alike.

The book is written in honor of Professor Armen Der Kiureghian, one of the fathers of modern risk and reliability analysis.

2 Armen Der Kiureghian and His Role in Modern Risk and Reliability Analysis

2.1 Biography

Professor Der Kiureghian is the former Taisei Professor of Civil Engineering in the Department of Civil and Environmental Engineering at the University of California, Berkeley and current President of the American University of Armenia (AUA). He was born in Isfahan, Iran. His father was prominent Armenian painter Sumbat Der Kiureghian, particularly known for his watercolors and innovative art forms (Der Kiureghian 2009). Professor Der Kiureghian later received his B.S. and M.S. in Civil Engineering from the University of Tehran, Iran and his Ph.D. in Structural Engineering in 1975 from the University of Illinois at Urbana-Champaign. In 1978, Professor Der Kiureghian joined the faculty at the University of California, Berkeley after three years as a faculty at the University of Southern California. In 1983, Professor Der Kiureghian married Nelly Ouzounian with whom he had two children, Naira and Sebouh. A few years later, after the devastating Spitak earthquake of 1988 in Armenia, he was instrumental in establishing AUA in Yerevan as an affiliate of the University of California. Before becoming President of AUA, he served as the founding Dean of Engineering (1991–2007), the Director of the Engineering Research Center (1991–2004), and as Interim Provost (2011–2012) of AUA concurrently with his position at Berkeley.

In recognition of his achievements, he is a member of a number of societies and associations. Professor Der Kiureghian is an

- Elected Member of the US National Academy of Engineering, 2011;
- Elected Foreign Member of the National Academy of Sciences of Armenia, 1998; and

- Elected Foreign Member of the National Academy of Engineering of Armenia, 1994.

In addition, he is the recipient of several awards, including the

- George Winter Medal from the Structural Engineering Institute of ASCE, 2014;
- Distinguished Research Award from the International Association for Structural Safety and Reliability, 2013;
- Alfred M. Freudenthal Medal from the Engineering Mechanics Division of ASCE, 2006;
- Thomas A. Middlebrooks Award from the Goe-Institute of ASCE, 2006;
- CERRA Award from the Civil Engineering Risk and Reliability Association, 1999; and
- Walter L. Huber Civil Engineering Research Prize from ASCE, 1989.

In 2006, Professor Der Kiureghian also became a Distinguished Alumnus of the Department of Civil and Environmental Engineering at the University of Illinois at Urbana-Champaign.

In addition to his scholarly achievements, Professor Der Kiureghian has also made contributions to the worlds of fine arts. In particular, his watercolors of landscapes and still life have been appreciated worldwide through a number of expositions. Professor Der Kiureghian is carrying forward painting techniques that he learned from his father.

2.2 *Role in Modern Risk and Reliability Analysis*

Professor Der Kiureghian is one of the fathers of modern risk and reliability analysis. During his career, he has made fundamental and groundbreaking research contributions. He has pioneered methods for safety and reliability assessment of complex structures and for stochastic seismic analysis of buildings, bridges and critical equipment. He has more than 300 publications, including more than 100 journal articles and book chapters. Many of his publications have become mandatory readings for the current and future generations of students, researchers and practitioners.

Professor Der Kiureghian scholarly contributions started with a seminal paper written with his Ph.D. advisor, Professor Alfredo H.-S. Ang, on seismic risk analysis (Der Kiureghian and Ang 1977). He then continued to make contributions to the field of risk and reliability analysis throughout his career. He pioneered novel methods for ***Reliability Analysis***[1] and made a number of significant contributions to

[1]References include (Moghtaderi-Zadeh et al. 1982; Der Kiureghian and Moghtaderi-Zadeh 1982; Der Kiureghian 1983, 1996a, b; Moghtaderi-Zadeh and Der Kiureghian 1983; Der Kiureghian and Liu 1986; Liu and Der Kiureghian 1986, 1991a; Der Kiureghian et al. 1987, 1994; Der Kiureghian and Ke 1988; Der Kiureghian 1996a, b; Der Kiureghian and DeStefano 1991; Jang et al. 1994; Der Kiureghian and Dakessian 1998; Ambartzumian et al. 1998; Der Kiureghian and Zhang 1999; Corr et al. 2001; Der Kiureghian 2001a; Gardoni et al. 2002; Sudret and Der Kiureghian 2002; Song and

Stochastic Dynamics[2] with particular focus on earthquake engineering. Starting in the 1990s his work expanded to the fields of ***Sensitivity Analysis and Optimization,***[3] alongside with making new contributions to ***Statistical Analysis and Probabilistic Models.***[4] His contributions and careful formulations also laid the ground for a rigorous ***Life-Cycle and Resilience Analysis*** and the development of ***Financial Tools*** for risk mitigation. A few examples of his seminal contributions include his work on the Nataf transformation, search algorithms in First Order Reliability Method (FORM), curvature computations in Second Order Reliability Method (SORM), system reliability, ground motion modeling and combination rules, linearization techniques and Bayesian analysis. These are milestones in the discipline of risk and reliability analysis that have advanced the field and made risk and reliability methods accessible to a broad spectrum of academics and practitioners.

Professor Der Kiureghian's scholarly contributions are known for their mathematical elegance, precision and meticulous attention to detail. Possibly, this was an influence of his background and passion for painting real subjects. Through his

(Footnote 1 continued)

Der Kiureghian 2003; Der Kiureghian et al. 2006, 2007; Haukaas and Der Kiureghian 2006, 2007; Der Kiureghian and Song 2008; Yang et al. 2009; Straub and Der Kiureghian 2011) (These references are taken from http://faculty.ce.berkeley.edu/adk/ accessed at the time of writing this introduction).

[2]References include (Der Kiureghian 1978; Der Kiureghian 1980a, b, 1981, 1989a, b; Wilson et al. 1981; Sackman et al. 1983; Der Kiureghian et al. 1983; Nour-Omid et al. 1983; Igusa et al. 1984; Igusa and Der Kiureghian 1985a, b, c, 1988a, b, 1992; Smeby and Der Kiureghian 1985; Asfura and Der Kiureghian 1986; Lin et al. 1986; Sitar et al. 1987; Der Kiureghian and Crempien 1989; Der Kiureghian and Neuenhofer 1992; Der Kiureghian and Wung 1992; Chua et al. 1992; Der Kiureghian and Nakamura 1993; Zhang and Der Kiureghian 1994; Der Kiureghian 1996a, b; Ambartzumian et al. 1996; Casciati et al. 1997; Menun and Der Kiureghian 1998; Khachian et al. 1998; Der Kiureghian 2000; Menun and Der Kiureghian 2000a, b; Der Kiureghian et al. 2001; Hong et al. 2001, 2005; Franchin et al. 2002; Der Kiureghian and Sackman 2005; Koo et al. 2005; Der Kiureghian 2005, 2007; Song and Der Kiureghian 2006a, b; Song et al. 2007; Fujimura and Der Kiureghian 2007; Rezaeian and Der Kiureghian 2008; Taniguchi et al. 2008; Der Kiureghian and Fujimura 2009; Rezaeian and Der Kiureghian 2010; Garrè and Der Kiureghian 2010; Konakli and Der Kiureghian 2011, 2012, 2014; Rezaeian and Der Kiureghian 2012; Alibrandi and Der Kiureghian 2012; Konakli et al. 2014) (These references are taken from http://faculty.ce.berkeley.edu/adk/ accessed at the time of writing this introduction).

[3]References include (Liu and Der Kiureghian 1991b, 1993; Zhang and Der Kiureghian 1993; Kirjner-Neto et al. 1998; Royset et al. 2001a, b, 2003, 2006; Haukaas and Der Kiureghian 2005, 2007) (These references are taken from http://faculty.ce.berkeley.edu/adk/ accessed at the time of writing this introduction).

[4]References include (Der Kiureghian et al. 1997; Geyskens et al. 1998; Der Kiureghian 2001b; Sasani and Der Kiureghian 2001; Cetin et al. 2002, 2004; Sasani et al. 2002; Gardoni et al. 2002; Gardoni et al. 2003; Takahashi et al. 2004, Moss et al. 2006; Straub and Der Kiureghian 2008, 2010a, b; Der Kiureghian 2008; Der Kiureghian and Ditlevsen 2009; Bensi et al. 2011, 2013; Kayen et al. 2013) (These references are taken from http://faculty.ce.berkeley.edu/adk/ accessed at the time of writing this introduction).

advising, he also created a legacy of scholars that will be future leaders in risk and reliability analysis.

2.3 Overall Goal and Contributions of the Book

Risk and reliability analysis have gone over the past few decades from a highly theoretical niche topic of research to a widespread, ubiquitous set of concepts and tools. Either implicitly or, more and more, explicitly, risk and reliability analysis are the foundation of engineering decisions and designs. They have permeated into all engineering disciplines and they are becoming (risk analysis in particular) a natural bridge to other disciplines outside of engineering, creating new opportunities for interdisciplinary research that help address some of the most pressing societal needs. Today, the state-of-the-art in risk and reliability analysis is fragmented and presented in a multitude of papers published in different journals, conference articles and reports. There is a need for a dedicated book that features the latest methods and models in a unified, coherent and complete fashion.

Some subjects within risk and reliability analysis are more mature and other ones are emerging, prime for and in need of further developments. For the more mature subjects, there is a need to put all of the literature into proper perspective, to critically examine and compare the many methodologies and techniques available, to recommend the most appropriate ones for each case, and to identify remaining research needs. For the subjects that are less mature, there is a need to clearly define the current state-of-the-art, to identify the critical directions going forward, and to start the development of rigorous formulations.

The goal of this book is to present the state-of-the-art in risk and reliability analysis in a clear, complete and coherent way. The book puts forward detailed theoretical and mathematical treatments of the classical topics as well as of the emerging ones. To make highly mathematical formulations accessible to students, researchers, engineers and risk analysts, most chapters include real, complex examples from actual engineering cases that have either motivated the development of the new theories presented in this book or are cases ideally suited for the use and illustration of the theory.

The book is intended for all audiences. Readers already familiar with concepts of risk and reliability will appreciate the clarity, elegance and mathematical rigor of the formulations. Novices to risk and reliability analysis will value the coherent treatment of the different topics, gaining a clear overall picture of the discipline and quickly learning from the real engineering examples. The book is designed to serve as mandatory reading for scholars and practitioners working in and with risk and reliability analysis.

Advancements in risk and reliability analysis can have a direct and tangible impact on the well-being of society, specifically on the management and mitigation

of hazards, as well as on disaster response and recovery. As a result, this book aims at making a tangible contribution toward the well-being of society.

3 Structure and Overview of the Volume

The book is organized into six sections. After Part I with this introduction, Part II focuses on reliability analysis, which includes a description of computational methods and their applications to some of the most complex real-life problems. Part III covers the subject of stochastic dynamics. As in Part II, Part III also includes both theoretical formulations as well as applications. Part IV discusses methods for sensitivity analysis and optimization in the context of risk and reliability analysis. Part V focuses on statistical analysis and the development of probabilistic models. Finally, Part VI covers life-cycle and resilience analysis as well as financial tools for risk mitigation. While each part has a specific and distinct focus, many of the chapters draw from methods and techniques covered in some of the other parts of the book. Such links among chapters help understand the relations among the different subjects.

Part II Reliability Analysis: Methods and Applications

Monte Carlo simulation has been widely used to accurately estimate the reliability of engineering components and systems (Shinozuka 1971; Bucher 1988; Bucher and Bourgund 1990; Ditlevsen and Madsen 1996, Au and Beck 2001). However, for highly reliable systems the computational cost might be prohibitive (Kostandyan and Sørensen 2014). Chapter 2 titled "Structural System Reliability, Reloaded" by Jieun Byun and Junho Song provides a review of methods for structural system reliability that are generally more efficient than Monte Carlo simulation including: linear programming bounds, matrix-based system reliability method, sequential compounding method, cross-entropy-based adaptive importance sampling, selective recursive decomposition algorithm, branch-and-bound employing system reliability bounds, and genetic-algorithm-based selective search for dominant system failure modes. The mathematical formulation of each method is presented along with specific applications and a discussion on its merits and the remaining research needs.

Chapter 3 titled "Global Buckling Reliability Analysis of Slender Network Arch Bridges: An Application of Monte Carlo-based Estimation by Optimized Fitting" by Anders Rønnquist and Arvid Naess presents a novel Monte Carlo-based Estimation by Optimized Fitting as an efficient alternative to plain Monte Carlo simulations for the reliability analysis of complex engineering systems. Rønnquist and Naess illustrate their proposed approach considering the reliability analysis of network arch bridges. Network arch bridges are slender bridge structures capable of carrying the loads more efficiently than traditional bridges. However, given then slenderness, they are vulnerable to global system buckling.

The reliability analysis of spatially distributed systems such as road networks, electric power networks, water and wastewater networks, and oil and gas networks require additional considerations beyond those of component and system reliability analysis (Kiremidjian et al. 2007; Kang et al. 2008; Guikema and Gardoni 2009; Lee et al. 2011; Guidotti et al. 2016, 2017). Chap. 4 titled "Review of Quantitative Reliability Methods for Onshore Oil and Gas Pipelines" by Smitha D. Koduru and Maher A. Nessim provides a review the state-of-the-art reliability methods applicable to spatially distributed systems. The authors specifically consider onshore oil and gas pipelines. The chapter discusses common threats to pipeline integrity as well as probabilistic models and the formulation of limit-state functions for reliability analysis.

Part III Stochastic Dynamics: Methods and Applications

Estimating small probabilities of, for example, failure or first passage of random vibration systems is one of the fundamental and computationally most challenging tasks in risk and reliability analysis (e.g., Corotis et al. 1972; Shinozuka and Deodatis 1991; Deodatis 1996; Gurley et al. 1996; Roberts and Spanos 2003; Lutes and Sarkani 2004; Li and Chen 2004; Vanmarcke 2010; Mardfekri et al. 2015; Kumar et al. 2015). Some methods have been developed for estimating these small probabilities, but their computational efficiency is often not high enough for analyzing complex, real-life systems. Alfredo H.-S. Ang in Chap. 5 titled "An Intuitive Basis of the Probability Density Evolution Method (PDEM) for Stochastic Dynamics" presents a recently developed Probability Density Evolution Method (PDEM) which is ideally suited for the stochastic dynamics analysis of large and complex engineering systems. The chapter provides a clear theoretical explanation of the method, its wide applicability, and its computational efficiency.

Chapter 6 titled "The Tail Equivalent Linearization Method for Nonlinear Stochastic Processes, Genesis and Developments" by Marco Broccardo, Umberto Alibrandi, Ziqi Wang and Luca Garrè offers a detailed review of the Tail Equivalent Linearization Method (TELM) along with a discussion of some of the most recent and advanced developments. TELM is a linearization method that defines a tail-equivalent linear system (TELS) using the first-order reliability method (FORM) and then estimates the tail of the response distribution for nonlinear systems under stochastic inputs. The chapter discusses the advantages of TELM in comparison with other linearization methods.

Chapter 7 titled "Estimate of Small First Passage Probabilities of Nonlinear Random Vibration Systems" by Jun He presents a new method to efficiently estimate small probabilities in random vibration problems. The proposed method breaks down the estimation into two decoupled procedures. First, the first passage probabilities of the scalar response processes are computed by modeling the distribution tails of the extreme values of the responses of nonlinear random vibration systems. Then, the first passage probabilities of the vector responses are computed using the Copula of the extreme values. After the theoretical description of the method, the chapter presents some numerical examples that demonstrate its accuracy and efficiency.

In case of a seismic event, the signals at different points of the foundation of long structures, such as bridges, and of distributed systems, like lifelines, have different characteristics (Somerville et al. 1991; Der Kiureghian 1996a, b; Jayaram and Baker 2010; Bocchini et al. 2016). The variation is due to a time lag in the seismic wave propagation and in the change in the frequency content of the signals. Chapter 8 titled "Generation of Non-synchronous Earthquake Signals" by Davide Lavorato, Ivo Vanzi, Camillo Nuti and Giorgio Monti presents two procedures to generate asynchronous earthquake signals at different locations for a common seismic event. One procedure uses signals recorded at a few surface points. The second procedure generates the signals by a bedrock propagation process. The chapter includes a comparison and evaluation of the two procedures.

Also in relation to seismic events, Chap. 9 titled "Seismic Response Analysis with Spatially Varying Stochastic Excitation" by Katerina Konakli describes methods for the modeling of ground-motion spatial variability, the simulation of spatially varying ground-motion arrays and the evaluation of the response of multiply-supported structures to differential support excitations. Methods and concepts from stochastic time-series analysis (like coherency function, auto-power spectral densities, response-spectrum method densities) are introduced and used to account for the relevant uncertainties in the spatially varying characteristics of the ground motions.

Part IV Sensitivity Analysis and Optimization

Reliability and risk information have been increasingly used in the development of optimal design solutions (Royset et al. 2001a, b; Mathakari et al. 2007; Phoon 2008; Schüeller and Jensen 2008; Taflanidis and Beck 2008; Mahmoud and Chulahwat 2016) including topology optimization (Schevenels et al. 2011; Zhao and Wang 2014; Liu et al. 2016a, b). Chapter 10 titled "Application of CQC Method to Seismic Response Control with Viscoelastic Dampers" by Yutaka Nakamura introduces the complete quadratic combination (CQC) modal combination rule for non-classically damped structures to optimize the story-wise distribution of viscoelastic dampers in buildings subject to seismic excitations. The chapter includes specific design examples of the optimal distribution of viscoelastic dampers in high-rise buildings. The examples clearly demonstrate the effectiveness of the propose procedure.

In Chap. 11 titled "Optimal Design of Reinforced Concrete Section under Combined Dynamic Action", Michel Kahan describes a reliability-based technique for the optimization of reinforced concrete sections subject to dynamic loading. First, the technique transforms the cross-sectional forces from their original space into the standard normal space. Then, it takes advantage of the properties of the standard normal space to generate a simple expression of the safety margin of the section that has a clear geometric interpretation and can be quantified by reliability analysis.

Gradient-based solution strategies for reliability-based design optimization problems require accurate estimates of the parameter sensitivity to convergence to an optimal solution (Haukaas and Der Kiureghian 2007; Liu et al. 2016b). Chapter

12 titled "FORM Sensitivities to Distribution Parameters with the Nataf Transformation" by Jean-Marc Bourinet describes the sensitivity of the solution of a reliability problem by the First Order Reliability Method (FORM) with respect to the distribution parameters of the random inputs. The chapter also proposes an accurate formulation to estimate such sensitivities where approximations are only made in the numerical integration. Following the description of the theoretical formulation, the chapter illustrates the formulation considering the problem of stochastic crack growth.

Chapter 13 titled "Using FORM for Minimizing the Uncertain Cost of Structural Designs" by Terje Haukaas and Stevan Gavrilovic shows how the first-order reliability method (FROM) can be used to minimize the expected costs under the assumption that the cost is a continuously differentiable function. The minimization process uses exact derivatives of response quantities and costs with respect to random variables (variables that describe the geometrical and loading characteristics of the structure of interest) and design variables (variables defined by the minimization of the cost). The chapter includes both a theoretical presentation of the minimization process and a detailed example.

Part V Statistical Analysis and Probabilistic Models

The development of accurate and efficient probabilistic models is an integral part of risk and reliability analysis. Models are needed in risk and reliability analysis to predict quantities of interest accounting for the relevant uncertainties (Kareem and Gurley 1996; Gardoni et al. 2002; Der Kiureghian and Ditlevsen 2009; Bayraktarli et al. 2011; Murphy et al. 2011). Statistical analysis, in particular Bayesian inference, has been an invaluable tool to develop models based on the available information (Gardoni et al. 2002, 2003, 2009; Choe et al. 2007, 2008; Bolduc et al. 2008; Tabandeh and Gardoni 2015). Chapter 14 titled "Model Checking After Bayesian Inference" by Matteo Pozzi and Daniele Zonta discusses how to assess the accuracy of the assumptions under which a model is developed by statistical inference. The chapter puts forward a novel Bayesian model comparison and compares it with alternative approaches typical of a frequentist approach to statistical analysis. The chapter starts with a theoretical discussion of the methods and then gives specific examples that illustrate the benefits of Bayesian model comparison.

Bayesian inference has been used in the identification of structural systems and damage detection using field measurements (Beck and Katafygiotis, 1998; Huang et al. 2012, 2015a). The calibrated properties can then be used to develop accurate estimates of the system reliability (Huang et al. 2009, 2015b). Chapter 15 titled "Batch and Recursive Bayesian Estimation Methods for Nonlinear Structural System Identification" by Rodrigo Astroza, Hamed Ebrahimian and Joel P. Conte presents a Bayesian probabilistic framework for the calibration of finite element (FE) models of structural systems. The framework uses batch and recursive methods to estimate inertia, geometric, and constraint properties as well as properties in the material constitutive models based on input-output dynamic data recorded during earthquake events. Following a damaging event, the updated FE

model can be used to detect the damage in the structure. After the detailed presentation of the theory, the chapter includes an example considering a five-story, two-by-one bay, reinforced concrete frame building subject to seismic excitation.

During the construction and operation of engineering systems, information on their properties and performance becomes available through monitoring (You et al. 2014) and other means of observation (Gardoni et al. 2007). Such information can be used to update predictions of the system's reliability through a Bayesian analysis (Huang et al. 2015a, b). Chapter 16 titled "Reliability Updating in the Presence of Spatial Variability" by Daniel Straub, Iason Papaioannou and Wolfgang Betz presents a Bayesian framework to update the reliability of engineering systems that depend on spatially varying quantities treated as random fields. The chapter uses the Expansion Optimal Linear Estimation (EOLE) method to discretize the random fields. The chapter includes both a rigorous description of the general probabilistic formulation as well as a detailed illustrative example on the reliability of foundations resting on spatially varying soil.

Bayesian Network methods have gained significant importance in the modeling of infrastructure systems. However, their computational cost rapidly increases as network become realistic. Chapters 17 and 18 propose alternative solutions that significantly reduce the computational costs. Chapter 17 titled "Bayesian Networks and Infrastructure Systems: Computational and Methodological Challenges" by Francesco Cavalieri, Paolo Franchin, Pierre Gehl and Dina D'Ayala considers Bayesian Network methods for the seismic assessment of large and complex infrastructure systems. In addition to proposing a strategy to reduce the computational costs, the chapter also tackles the need for assessment measures that includes flow-based performance indicators (which are typically not included Bayesian Network methods). The chapter includes an application to a realistic water-supply network.

Chapter 18 titled "Bayesian Network Methods for Modeling and Reliability Assessment of Infrastructure Systems" by Iris Tien presents novel compression and inference algorithms the can be used to address the need for memory storage which increases exponentially as the size and complexity of the system increases. The chapter also introduces several heuristics which, combined with the compression and inference algorithms, are shown to significantly reduce the memory storage needs and computation time cost.

Kriging interpolation has been increasingly used to generated probabilistic models in several fields (e.g., Taflanidis et al. 2016). Chapter 19 titled "Kriging Interpolation Strategy for Finite Element-based Surrogate Responses of DCB Delamination Tests" by Salvatore Sessa and Nunziante Valoroso presents a Kriging interpolation technique for computing the response of Finite Element models. The chapter describes the theoretical formulation of Kriging techniques and gives a clear example of their accuracy and computational efficiency by analyzing the bending behavior of a cantilever beam.

Part VI Life-Cycle and Resilience Analysis and Financial Tools

Life-cycle and resilience analysis can be used for informed decision making, hazard mitigation, and planning (Val et al. 2000; Kong and Frangopol 2003; Van Noortwijk

and Frangopol 2004; Pachakis and Kiremidjian 2004; Streicher and Rackwitz 2004; Biondini et al. 2006; Maes and Faber 2007; Corotis 2009; Williams et al. 2009; Kumar et al. 2009; Cha and Ellingwood 2012; Kumar and Gardoni 2014; Gardoni et al. 2016a, b; Giuliani et al. 2016; Lin et al. 2016; Narasimhan et al. 2016; Padgett and Kameshwar 2016; Pilkington and Mahmoud 2016). Chapter 20 titled "Life-cycle Analysis of Engineering Systems: Modeling Deterioration, Instantaneous Reliability, and Resilience" by Gaofeng Jia, Armin Tabandeh and Paolo Gardoni proposes a rigorous stochastic formulation for the Life-Cycle Analysis (LCA) of engineering systems. The formulation includes the modeling of both deterioration processes and repair/recovery processes that define the life-cycle of engineering systems. The chapter introduces methods to compute performance measures like instantaneous reliability, resilience, availability, operation cost and benefits. An illustration of the proposed formulation is presented considering the modeling of the life-cycle of an example bridge structure.

Chapter 21 titled "Fragility Curves of Restoration Processes for Resilience Analysis" by Gian Paolo Cimellaro presents a novel formulation for the evaluation of restoration fragility functions. Restoration fragility functions are defined as the conditional probability that a restoration process will exceed a specified state for a given extent of damage. The chapter includes a theoretical discussion of the proposed method as well as an example in which restoration fragility functions are developed for a critical facility following an earthquake. The example considers two cases, one when an emergency plan is in place and one when there is no emergency plan.

Chapter 22 titled "A Decision Support Tool for Sustainable and Resilient Building Design" by Umberto Alibrandi and Khalid M. Mosalam presents an integrated approach for building design that brings together safety, resilience and sustainability. A multi-attribute decision tool is combined with the Performance-Based Engineering (PBE) approach to create rankings of different design alternatives. In the integrated approach, a Bayesian analysis is used to incorporate new information as it becomes available. The chapter includes a comprehensive presentation of the proposed integrated approach along with a specific example that considers an office space.

Building on the results of risk and reliability analysis, Chapter 23 titled "Innovative Derivatives to Drive Investment in Earthquake Protection Technologies" by Yuji Takahashi presents new financial derivatives (i.e., contracts that derive their values from the performance of the underlying financial entity) that promote investments in earthquake mitigation strategies. The chapter presents a rigorous formulation to price derivatives that uses state-of-the-art seismological models. The chapter includes a clear description of the structure of the proposed security as well as a specific example of pricing based on credit default swap (CDS) pricing.

References

Alibrandi U, Der Kiureghian A (2012) A gradient-free method for determining the design point in nonlinear stochastic dynamic analysis. Probab Eng Mech 28:2–10

Ambartzumian RV, Der Kiureghian A, Oganian VK, Sukiasian HS, Aramian RH (1996) Poisson random planes model in tunnel building. J Contemp Math Anal Armen (Academy of Sciences, (Izvestiya Nationalnoi Akademmi Nauk Armenii, Matematika), Allerton Press, New York, NY, 31(2): 1–20)

Ambartzumian RV, Der Kiureghian A, Ohanian VK, Sukiasian HS (1998) Multinormal probability by sequential conditioned importance sampling: theory and application. Probab Eng Mech 13(4):299–308

Ang AH-S, Tang W-H (2007) Probability concepts in engineering: emphasis on applications to civil and environmental engineering. Wiley, New York

Asfura A, Der Kiureghian A (1986) Floor response spectrum method for seismic analysis of multiply supported secondary systems. Earthq Engrg Struct Dyn 14(2):245–265

Au SK, Beck JL (2001) Estimation of small failure probabilities in high dimensions by subset simulation. Probab Eng Mech 16(4):263–277

Augusti G, Baratta A, Casciati F (1984) Probabilistic methods in structural mechanics. Chapman and Hall, London

Ayyub BM, McCuen RH (2011) Probability, statistics, and reliability for engineers and scientists. CRC Press

Bai J-W, Hueste MBD, Gardoni P (2009) Probabilistic assessment of structural damage due earthquakes for buildings in Mid-America. ASCE J Struct Eng 135(10):1155–1163

Bai J-W, Gardoni P, Hueste MBD (2011) Story-specific demand models and seismic fragility estimates for multi-story buildings. Struct Saf 33(1):96–107

Bai J-W, Hueste MBD, Gardoni P (2015) Seismic vulnerability assessment of tilt-up concrete structures. Struct Infrastruct Eng 11(9):1131–1146

Bayraktarli YY, Baker JW, Faber MH (2011) Uncertainty treatment in earthquake modeling using Bayesian probabilistic networks. GeoRisk 5(1):44–58

Beck JL, Katafygiotis LS (1998) Updating models and their uncertainties. I: Bayesian statistical framework. J Eng Mech 124(4):455–461

Bedford T, Cooke R (2001) Probabilistic risk analysis: foundations and methods. Cambridge University Press, Cambridge

Benjamin JR, Cornell CA (1970) Probability, statistics and decision for civil engineers. McGraw-Hill, New York

Bensi M, Der Kiureghian A, Straub D (2011) Bayesian network modeling of correlated random variables drawn from a Gaussian random field. Struct Saf 33:317–332

Bensi M, Der Kiureghian A, Straub D (2013) Efficient Bayesian network modeling of systems. Reliab Eng Syst Saf 112:200–213

Biondini F, Bontempi F, Frangopol DM, Malerba PG (2006) Probabilistic service life assessment and maintenance planning of concrete structures. J Struct Eng 132(5):810–825

Bocchini P, Christou V, Miranda MJ (2016) Correlated maps for regional multi-hazard analysis: ideas for a novel approach. In: Gardoni P, LaFave J (eds) Multi-hazard approaches to civil infrastructure engineering. Springer International Publishing, pp 15–39

Bolduc L, Gardoni P, Briaud J-L (2008) Probability of exceedance estimates for scour depth around bridge piers. J Geo Geoenviron Eng ASCE 134(2):145–265

Briaud J-L, Gardoni P, Yao C. (2013) Statistical, risk, and reliability analyses of bridge scour. J Geo Geoenviron Eng ASCE 140(2):04013011

Bucher CG (1988) Adaptive sampling—an iterative fast Monte Carlo procedure. Struct Saf 5 (2):119–126

Bucher CG, Bourgund U (1990) A fast and efficient response surface approach for structural reliability problems. Struct Saf 7(1):57–66

Casciati F, Grigoriu M, Der Kiureghian A, Wen Y-K, Vrouwenvelder T (1997) Report of the working group on dynamics. Struct Saf 19(3):271–282
Cetin KO, Der Kiureghian A, Seed RB (2002) Probabilistic models for the initiation of seismic soil liquefaction. Struct Saf 24(1):67–82
Cetin KO, Seed RB, Der Kiureghian A, Tokimatsu K, Harder LF, Kayen Jr RE, Moss RES (2004) SPT-based probabilistic and deterministic assessment of seismic soil liquefaction potential. J Geotech Geoenviron Eng ASCE 130(12):1314–1340 (Recipient of the ASCE Thomas A. Middlebrooks Award)
Cha EJ, Ellingwood BR (2012) Risk-averse decision-making for civil infrastructure exposed to low-probability, high-consequence events. Reliab Eng Syst Saf 104:27–35
Choe D, Gardoni P, Rosowsky D (2007) Closed-form fragility estimates, parameter sensitivity and Bayesian updating for RC columns. ASCE J Eng Mech 133(7):833–843
Choe D, Gardoni P, Rosowsky D, Haukaas T (2008) Probabilistic capacity models and seismic fragility estimates for RC columns subject to corrosion. Reliab Eng Syst Saf 93(3):383–393
Choe D, Gardoni P, Rosowsky D, Haukaas T (2009) Seismic fragility estimates for reinforced concrete bridges subject to corrosion. Struct Saf 31:275–283
Choe D, Gardoni P, Rosowsky D (2010) Fragility increment functions for deteriorating reinforced concrete bridge columns. ASCE J Eng Mech 136(8):969–978
Choi E, DesRoches R, Nielson B (2004) Seismic fragility of typical bridges in moderate seismic zones. Eng Struct 26(2):187–199
Chua KH, Der Kiureghian A, Monismith CL (1992) Stochastic model for pavement design. J Transp Eng ASCE 118(6):769–786
Corotis RB (2009) Societal issues in adopting life-cycle concepts within the political system. Struct Infrastruct Eng 5(1):59–65
Corotis RB, Vanmarcke EH, Cornell AC (1972) First passage of nonstationary random processes. J Eng Mech Div 98(2):401–414
Corr DJ, Monteiro PJM, Kurtis KE, Der Kiureghian A (2001) Sulfate attack of concrete: reliability analysis. ACI Mater J 98(2):99–104
Deodatis G (1996) Simulation of ergodic multivariate stochastic processes. J Eng Mech 122 (8):778–787
Der Kiureghian A (1978) Second-moment combination of stochastic loads. J Struct Div ASCE 104 (10):1551–1567
Der Kiureghian A (1980a) Reliability analysis under stochastic loads. J Struct Div ASCE 106 (2):411–429
Der Kiureghian A (1980b) Structural response to stationary excitation. J Eng Mech Div ASCE 106 (6):1195–1213
Der Kiureghian A (1981) A response spectrum method for random vibration analysis of MDF systems. Earthq Eng Struct Dyn 9(5):419–435
Der Kiureghian A (1983) Seismic risk analysis of structural systems. J Eng Mech Div ASCE 107 (6):1133–1153 (Summary translation into Japanese in Proceedings of Japan Society of Civil Engineers, 1983, p 85)
Der Kiureghian A (1989a) Measures of structural safety under imperfect states of knowledge. J Struct Engrg ASCE 115(5):1119–1140
Der Kiureghian A (1989b) Strong motion records. Earthq Spectra (special supplement on Armenian Earthquake of December 7, 1988, 43–53)
Der Kiureghian A (1996a) A coherency model for spatially varying ground motions. Earthq Eng Struct Dyn 25(1):99–111
Der Kiureghian A (1996b) Structural reliability methods in seismic safety assessment: a review. J Eng Struct 18(6):412–424
Der Kiureghian A (2000) The geometry of random vibrations and solutions by FORM and SORM. Probab Eng Mech 15(1):81–90
Der Kiureghian A (2001a) Risk assessment of satellite launch with reusable launch vehicle. J Reliab Eng Syst Saf 74(3):353–360

Der Kiureghian A (2001b) Analysis of structural reliability under model and statistical uncertainties: a Bayesian approach. Comput Struct Eng 1(2):81–87
Der Kiureghian A (2005) Non-ergodicity and PEER's framework formula. Earthq Eng Struct Dyn 34:1643–1652
Der Kiureghian A (2007) Preface to special issue on earthquake engineering for electric power equipment and lifeline systems. Earthq Eng Struct Dyn 36:163–165
Der Kiureghian A (2008) Analysis of structural reliability under parameter uncertainties. Probab Eng Mech 23:351–358
Der Kiureghian A (2009) The life and art of Sumbat. ADK & Associates Publishers, San Francisco
Der Kiureghian A, Ang AH-S (1977) A fault-rupture model for seismic risk analysis. Bull Seism Soc Am 67(4):1173–1194 (Translated into Chinese in Earthquake Engineering Abroad, 4, 1981, Institute of Engineering Mechanics, Chinese Academy of Sciences, Harbin, China, 20–34)
Der Kiureghian A, Crempien J (1989) An evolutionary model for earthquake ground motion. Struct Saf 6(2–4):235–246
Der Kiureghian A, Dakessian T (1998) Multiple design points in first and second-order reliability. Struct Saf 20(1):37–49
Der Kiureghian A, DeStefano M (1991) Efficient algorithm for second-order reliability analysis. J Engrg Mech ASCE 117(12):2904–2923
Der Kiureghian A, Ditlevsen O (2009) Aleatory or epistemic? Does it matter? Struct Saf 31:105–112
Der Kiureghian A, Fujimura K (2009) Nonlinear stochastic dynamic analysis for performance-based earthquake engineering. Earthq Eng Struct Dyn 38:719–738
Der Kiureghian A, Ke J-B (1988) The stochastic finite element method in structural reliability. Probab Eng Mech 3(2):83–91
Der Kiureghian A, Liu P-L (1986) Structural reliability under incomplete probability information. J Eng Mech ASCE 112(1):85–104
Der Kiureghian A, Moghtaderi-Zadeh M (1982) An integrated approach to the reliability of engineering systems. Nucl Engrg Des 71:349–354
Der Kiureghian A, Nakamura Y (1993) CQC modal combination rule for high-frequency modes. Earthq Eng Struct Dyn 22(11):943–956
Der Kiureghian A, Neuenhofer A (1992) Response spectrum method for multiple-support seismic excitation. Earthq Engrg Struct Dyn 21(8):713–740
Der Kiureghian A, Sackman JL (2005) Tangent geometric stiffness of inclined cables under self weight. J Struct Eng ASCE 131(6):941–945
Der Kiureghian A, Song J (2008) Multi-scale reliability analysis and updating of complex systems by use of linear programming. Reliab Eng Syst Saf 93:288–297
Der Kiureghian A, Wung C-D (1992) A computer-assisted learning system for random vibrations. Comput Struct 43(5):975–993
Der Kiureghian A, Zhang Y (1999) Space-variant finite element reliability analysis. Comput Methods Appl Mech Engrg 168(1–4):173–183
Der Kiureghian A, Sackman JL, Nour-Omid B (1983) Dynamic analysis of light equipment in structures: response to stochastic input. J Eng Mech ASCE 109(1):90–110
Der Kiureghian A, Lin H-Z, Hwang S-J (1987) Second-order reliability approximations. J Engrg Mech ASCE 113(8):1208–1225
Der Kiureghian A, Zhang Y, Li C-C (1994) Inverse reliability problem. J Eng Mech ASCE 120 (5):1154–1159
Der Kiureghian A, Geyskens PV, Khalessi M (1997) Probabilistic assessment of debris impact damage on orbital structures. Int J Impact Eng 19(7):571–588
Der Kiureghian A, Sackman JL, Hong K-J (2001) Seismic interaction in linearly connected electrical substation equipment. Earthq Eng Struct Dyn 30:327–347
Der Kiureghian A, Haukaas T, Fujimura K (2006) Structural reliability software at the University of California, Berkeley. Struct Saf 28(1–2):44–67
Der Kiureghian A, Ditlevsen O, Song J (2007) Availability, reliability and downtime of systems with repairable components. Reliab Eng Syst Saf 92:231–242

Ditlevsen O (1981) Uncertainty modeling. McGraw-Hill, New York
Ditlevsen O, Madsen HO (1996) Structural reliability methods. Wiley, New York
Elhami Khorasani N, Garlock M, Gardoni P (2016) Probabilistic performance-based evaluation of a tall steel moment resisting frame under post-earthquake fires. J Struct Fire Eng 7(3):193–216
Ellingwood B (1980) Development of a probability based load criterion for American National Standard A58: building code requirements for minimum design loads in buildings and other structures, vol 13. US Department of Commerce, National Bureau of Standards
Ellingwood BR, Mori Y (1993) Probabilistic methods for condition assessment and life prediction of concrete structures in nuclear power plants. Nucl Eng Des 142(2–3):155–166
Franchin P, Ditlevsen O, Der Kiureghian A (2002) Model correction factor method for reliability problems involving integrals of non-Gaussian random fields. Probab Eng Mech 17(2):109–122
Fujimura K, Der Kiureghian A (2007) Tail-equivalent linearization method for nonlinear random vibration. Probab Eng Mech 22:63–76
Gardoni P, LaFave J (2016) Multi-hazard approaches to civil infrastructure engineering. Springer
Gardoni P, Murphy C (2008) Recovery from natural and man-made disasters as capabilities restoration and enhancement. Int J Sustain Dev Plan 3(4):1–17
Gardoni P, Murphy C (2014) A scale of risk. Risk Analysis 34(7):1208–1227
Gardoni P, Der Kiureghian A, Mosalam K (2002) Probabilistic capacity models and fragility estimates for RC columns based on experimental observations. J Eng Mech ASCE 128 (10):1024–1038
Gardoni P, Mosalam K, Der Kiureghian A (2003) Probabilistic seismic demand models and fragility estimates for RC bridges. J Earthq Eng 7(S1):79–106
Gardoni P, Reinschmidt KF, Kumar R (2007) A probabilistic framework for Bayesian adaptive forecasting of project progress. Comput-Aided Civil Infrastruct Eng 22(3):182–196
Gardoni P, Trejo D, Vannucci M, Bhattacharjee C (2009) Probabilistic models for modulus of elasticity of self-consolidated concrete: a Bayesian approach. ASCE J Eng Mech 135 (4):295–306
Gardoni P, Murphy M, Rowell A (2016) Risk analysis of natural hazards. Springer
Gardoni P, Guevara-Lopez F, Contento A (2016b) The Life Profitability Method (LPM): a financial approach to engineering decisions. Struct Saf 63:11–20
Garrè L, Der Kiureghian A (2010) Tail-equivalent linearization method in frequency domain and application to marine structures. Marine Struct 23:322–338
Geyskens PhV, Der Kiureghian A, Monteiro P (1998) Bayesian prediction of elastic modulus of concrete. J Struct Eng ASCE 124(1):89–95
Giuliani L, Revez A, Sparf J, Jayasena S, Havbro Faber M (2016) Social and technological aspects of disaster resilience. Int J Strat Property Manag 20(3):277–290
Guidotti R, Chmielewski H, Unnikrishnan V, Gardoni P, McAllister T, van de Lindt JW (2016) modeling the resilience of critical infrastructure: the role of network dependencies. Sustain Resil Infrastruct 1(3–4):153–168
Guidotti R, Gardoni P, Chen Y (2017) Network reliability analysis with link and nodal weights and auxiliary nodes. Struct Saf 65:12–26
Guikema S, Gardoni P (2009) Reliability estimation for networks of reinforced concrete bridges. ASCE J Infrastruct Syst 15(2):61–69
Gurley KR, Kareem A, Tognarelli MA (1996) Simulation of a class of non-normal random processes. Int J Non-Linear Mech 31(5):601–617
Haimes YY (2004) Risk modeling, assessment, and management, 2nd edn. Wiley Series in Systems Engineering and Management, Hoboken
Hart GC (1982) Uncertainty analysis, loads, and safety in structural engineering. Prentice-Hall, Englewood Cliffs
Haukaas T, Der Kiureghian A (2005) Parameter sensitivity and importance measures in nonlinear finite element reliability analysis. J Eng Mech ASCE 131(10):1013–1026
Haukaas T, Der Kiureghian A (2006) Strategies for finding the design point in nonlinear finite element reliability analysis. Probab Eng Mech 21:133–147

Haukaas T, Der Kiureghian A (2007) Methods and object-oriented software for FE reliability and sensitivity analysis with application to a bridge structure. J Comput Civil Eng ASCE 21 (3):151–163

Hong K-J, Der Kiureghian A, Sackman JL (2001) Seismic interaction in cable-connected equipment items. J Eng Mech ASCE 127(11):1096–1105

Hong K-J, Der Kiureghian A, Sackman JL (2005) Bending behavior of hellically wrapped cables. J Eng Mech ASCE 131(5):500–511 (Discussion and Closure, 132(7): 790–792)

Huang Q, Gardoni P, Hurlebaus S (2009) Probabilistic capacity models and fragility estimates for reinforced concrete columns Incorporating NDT data. ASCE J Eng Mech 135(12):1384–1392

Huang Q, Gardoni P, Hurlebaus S (2012) A probabilistic damage detection approach using vibration-based nondestructive testing. Struct Saf 38(2012):11–21

Huang Q, Gardoni P, Hurlebaus S (2015a) Assessment of modal parameters considering measurement and modeling errors. J Smart Struct Syst 15(3):717–733

Huang Q, Gardoni P, Hurlebaus S (2015b) Adaptive reliability analysis of reinforced concrete bridges subject to seismic loading using nondestructive testing. ASCE-ASME J Risk Uncertain Eng Syst Part A: Civil Eng 1(4):04015014

Igusa T, Der Kiureghian A (1985a) Dynamic characterization of two degree-of-freedom equipment-structure systems. J Eng Mech ASCE 111(1):1–19

Igusa T, Der Kiureghian A (1985b) Dynamic response of multiply supported secondary systems. J Eng Mech ASCE 111(1):20–41

Igusa T, Der Kiureghian A (1985c) Generation of floor response spectra including oscillator-structure interaction. Earthq Eng Struct Dyn 13(5):661–676

Igusa T, Der Kiureghian A (1988a) Response of uncertain systems to stochastic excitation. J Engrg Mech ASCE 114(5):812–832

Igusa T, Der Kiureghian A (1988b) Dynamic response of tertiary subsystems. J Engrg Mech ASCE 114(8):1375–1395

Igusa T, Der Kiureghian A (1992) Interaction in primary-secondary systems. J Press Vessel Tech ASME 114(1):53–59

Igusa T, Der Kiureghian A, Sackman JL (1984) Modal decomposition method for stationary response of non-classically damped systems. Earthq Engrg Struct Dyn 12(1):121–136

Jang Y-S, Sitar N, Der Kiureghian A (1994) Reliability analysis of contaminant transport in saturated porous media. Water Resour Res 30(8):2435–2448

Jayaram N, Baker JW (2010) Considering spatial correlation in mixed-effects regression, and impact on ground-motion models. Bull Seismol Soc Am 100(6):3295–3303

Kang W-H, Song J, Gardoni P (2008) Matrix-based system reliability method and applications to bridge networks. Reliab Eng Syst Saf 93:1584–1593

Kaplan S, Gerrick BJ (1981) On the quantitative definition of risk. Risk Analysis 1:11–27

Kareem A, Gurley K (1996) Damping in structures: its evaluation and treatment of uncertainty. J Wind Eng Ind Aerodyn 59(2):131–157

Kayen R, Moss R, Thompson EM, Seed R, Cetin OK, Der Kiureghian A, Tanaka Y, Tokimatsu K (2013) Shear wave velocity-based probabilistic and deterministic assessment of seismic soil liquefaction potential. J Geotechn Geoenviron Eng ASCE 139(3):407–419

Khachian E, Der Kiureghian A, Tonoyan A (1998) Dynamic properties of primary-secondary systems. J Struct Eng Assoc Yerevan Armen 7(24):1–4 (in Armenian)

Kiremidjian AS, Stergiou E, Lee R (2007) Issues in seismic risk assessment of transportation networks. In: Earthquake geotechnical engineering. Springer, The Netherlands, pp 461–480

Kirjner-Neto C, Polak E, Der Kiureghian A (1998) An outer approximations approach to reliability-based optimal design of structures. J Optim Theory Appl 98(1):1–17

Konakli K, Der Kiureghian A (2011) Extended MSRS rule for seismic analysis of bridges subjected to differential support motions. Earthq Eng Struct Dyn 40(12):1315–1335

Konakli K, Der Kiureghian A (2012) Simulation of spatially varying ground motions including incoherence, wave-passage and differential site-response effects. Earthq Eng Struct Dyn 41:495–513

Konakli K, Der Kiureghian A (2014) The 'equal displacement' approximation for bridges subjected to differential support motions. Earthq Eng Struct Dyn 43(1):23–39
Konakli K, Der Kiureghian A, Dreger D (2014) Coherency analysis of accelerograms recorded by the UPSAR array during the 2004 Parkfield Earthquake. Earthq Eng Struct Dyn 43(5):641–659
Kong S, Fragopol DM (2003) Evaluation of expected life-cycle maintenance cost of deteriorating structures. J Struct Eng 129(5):682–691
Koo H, Der Kiureghian A, Fujimura K (2005) Design-point excitation for nonlinear random vibrations. Probab Eng Mech 20:136–147
Kostandyan E, Sørensen J (2014) Dependent systems reliability estimation by structural reliability approach. Int J Perform Eng 10(6):605–614
Kumar R, Gardoni P (2014) Renewal theory-based life-cycle analysis of deteriorating engineering systems. Struct Saf 50:94–102
Kumar R, Gardoni P, Sanchez-Silva M (2009) Effect of cumulative seismic damage and corrosion on life-cycle cost of reinforced concrete bridges. Earthq Eng Struct Dyn 38(7):887–905
Kumar R, Cline D, Gardoni P (2015) A stochastic framework to model deterioration in engineering systems. Struct Saf 53:36–43
Kwon OS, Elnashai A (2006) The effect of material and ground motion uncertainty on the seismic vulnerability curves of RC structure. Eng Struct 28(2):289–303
Lee Y-J, Song J, Gardoni P, Lim H-W (2011) Post-hazard flow capacity of bridge transportation networks considering structural deterioration of bridges. Struct Infrastruct Eng 7(7):509–521
Li J, Chen JB (2004) Probability density evolution method for dynamic response analysis of structures with uncertain parameters. Comput Mech 34(5):400–409
Li C-C, Der Kiureghian A (1993) Optimal discretization of random fields. J Eng Mech ASCE 119 (6):1136–1154
Lin YK, Kozin F, Wen YK, Casciati F, Schueller GI, Der Kiureghian A, Ditlevsen O, Vanmarcke EH (1986) Methods of stochastic structural dynamics. Struct Saf 3(3+4):167–194
Lin P, Wang N, Ellingwood BR (2016) A risk de-aggregation framework that relates community resilience goals to building performance objectives. Sustain Resil Infrastruct 1(1–2):1–13
Lind N, Nathwani J (2012) LQI bibliography and abstracts. LQI symposium in Kgs. Lyngby, Denmark August 21–23
Liu P-L, Der Kiureghian A (1986) Multivariate distribution models with prescribed marginals and covariances. Probab Eng Mech 1(2):105–112
Liu P-L, Der Kiureghian A (1991a) Finite element reliability of geometrically nonlinear uncertain structures. J Engrg Mech ASCE 117(8):1806–1825
Liu P-L, Der Kiureghian A (1991b) Optimization algorithms for structural reliability. Struct Saf 9 (3):161–177
Liu K, Paulino G, Gardoni P (2016a) Reliability-based topology optimization using a new method for sensitivity approximation—application to ground structures. J Struct Multidiscip Optim 54 (3):553–571
Liu K, Paulino G, Gardoni P (2016b) Segmental multi-point linearization for parameter sensitivity approximation in reliability analysis. Struct Saf 62:101–115
Lutes L, Sarkani S (2004) Random vibrations: analysis of structural and mechanical systems. Elsevier Butterworth-Heinemann, Burlington, Mass
Madsen HO, Krenk S, Lind NC (1986) Methods of structural theory and its applications. Prentice-Hall, Englewood Cliffs, NJ
Maes MA, Faber MH (2007) Preferences, utility and risk perception in engineering decision making. Int J Risk Assess Manag 7(6/7):813–827
Mahmoud H, Chulahwat A (2016) Multi-hazard multi-objective optimization of building systems with isolated floors under seismic and wind demands. In: Gardoni P, LaFave J (eds) Multi-hazard approaches to civil infrastructure engineering. Springer International Publishing, pp 141–164
Mardfekri M, Gardoni P (2015) Multi-hazard reliability assessment of offshore wind turbines. Wind Energy 18(8):1433–1450

Mardfekri M, Gardoni P, Bisadi V (2015) Service reliability of offshore wind turbines. Int J Sustain Energ 34(7):468–484
Mathakari S, Gardoni P, Agarwal P, Raich A, Haukaas T (2007) Reliability-based optimal design of electrical transmission towers using multi-objective genetic algorithms. Comput-Aided Civil Infrastruct Eng 22(4):282–292
Melchers RE (1999) Structural reliability: analysis and prediction, 2nd edn. Wiley, New York
Melchers RE (2005) The effect of corrosion on the structural reliability of steel offshore structures. Corros Sci 47(10):2391–2410
Menun C, Der Kiureghian A (1998) A replacement for the 30%, 40% and SRSS rules for multi-component seismic analysis. Earthq Spectra 14(1):153–163
Menun C, Der Kiureghian A (2000a) Envelopes for seismic response interaction part I: theory. J Struct Eng ASCE 126(4):467–473
Menun C, Der Kiureghian A (2000b) Envelopes for seismic response interaction part II: application. J Struct Eng ASCE 126(4):474–481
Moan T (2005) Reliability-based management of inspection, maintenance and repair of offshore structures. Struct Infrastruct Eng 1(1):33–62
Moghtaderi-Zadeh M, Der Kiureghian A (1983) Reliability upgrading of lifeline networks for post-earthquake serviceability. Earthq Engrg Struct Dyn 11(4):557–566
Moghtaderi-Zadeh M, Wood K, Der Kiureghian A, Barlow RE (1982) Seismic reliability of lifeline networks. J Tech Councils ASCE 108(1): 60–78
Moss RES, Seed RB, Kayen RE, Stewart JP, Der Kiureghian A, Cetin KO (2006) CPT-based probabilistic and deterministic assessment of in situ seismic soil liquefaction potential. J Geotech Geoenviron Eng ASCE 132:1032–1051
Mousavi ME, Gardoni P (2014a) Integrity index and integrity-based optimal design of structural systems. Eng Struct 60(2014):206–213
Mousavi ME, Gardoni P (2014b) A simplified method for reliability- and integrity-based design of engineering systems and its application to offshore mooring systems. Marine Struct 36:88–104
Mousavi ME, Gardoni P, Maadooliat M (2013) Progressive reliability method and its application to offshore mooring systems. Eng Struct 56:2131–2138
Murphy C, Gardoni P (2006) The role of society in engineering risk analysis: a capabilities-based approach. Risk Analysis 26(4):1073–1083
Murphy C, Gardoni P (2007) Determining public policy and resource allocation priorities for mitigating natural hazards: a capabilities-based approach. Sci Eng Ethics 13(4):489–504
Murphy C, Gardoni P (2011) Evaluating the source of the risks associated with natural events. Res Publica 17(2):125–140
Murphy C, Gardoni P, Harris CE (2011) Classification and moral evaluation of uncertainties in engineering modeling. Sci Eng Ethics 17(3):553–570
Narasimhan H, Ferlisi S, Cascini L, De Chiara G, Faber MH (2016) A cost-benefit analysis of mitigation options for optimal management of risks posed by flow-like phenomena. Nat Hazards 81(1):117–144
Nour-Omid B, Sackman JL, Der Kiureghian A (1983) Modal characterization of equipment-continuous structure systems. J. Sound Vib 88(4):459–472
Nowak AS, Collins KR (2012) Reliability of structures. CRC Press
Pachakis D, Kiremidjian AS (2004) Estimation of downtime-related revenue losses in seaports following scenario earthquakes. Earthq Spectra 20(2):427–449
Padgett JE, Kameshwar S (2016) Supporting life cycle management of bridges through multi-hazard reliability and risk assessment. In: Gardoni P, LaFave J (eds) Multi-hazard approaches to civil infrastructure engineering. Springer International Publishing, pp 41–58
Phoon KK (ed) (2008) Reliability-based design in geotechnical engineering: computations and applications. CRC Press
Pilkington SF, Mahmoud HN (2016) Using artificial neural networks to forecast economic impact of multi-hazard hurricane-based events. Sustain Resil Infrastruct 1(1–2):63–83

Pillai RG, Hueste MD, Gardoni P, Trejo D, Reinschmidt KF (2010) Time-variant service reliability of post-tensioned, segmental, concrete bridges exposed to corrosive environments. Eng Struct 32(9):2596–2605

Pillai RG, Trejo D, Gardoni P, Hueste MB, Reinschmidt KF (2014) Time-variant flexural reliability of post-tensioned, segmental concrete bridges exposed to corrosive environments. ASCE J Struct Eng 140(8):A4014018

Ramamoorthy KS, Gardoni P, Bracci MJ (2006) Probabilistic demand models and fragility curves for reinforced concrete frames. ASCE J Struct Eng 132(10):1563–1572

Ramamoorthy KS, Gardoni P, Bracci MJ (2008) Seismic fragility and confidence bounds for gravity load designed reinforced concrete frames of varying height. ASCE J Struct Eng 134 (4):639–650

Rezaeian S, Der Kiureghian A (2008) A stochastic ground motion model with separable temporal and spectral nonstationarities. Earthq Eng Struct Dyn 37:1565–1584

Rezaeian S, Der Kiureghian A (2010) Simulation of synthetic ground motions for specified earthquake and site characteristics. Earthq Eng Struct Dyn 39:1155–1180. doi:10.1002/eqe.997

Rezaeian S, Der Kiureghian A (2012) Simulation of orthogonal horizontal ground motion components for specified earthquake and site characteristics. Earthq Eng Struct Dyn 41:335–353

Roberts JB, Spanos PD (2003) Random vibration and statistical linearization. Courier Corporation

Rosowsky DV, Ellingwood BR (2002) Performance-based engineering of wood frame housing: fragility analysis methodology. J Struct Eng 128(1):32–38

Rossetto T, Elnashai A (2003) Derivation of vulnerability functions for European-type RC structures based on observational data. Eng Struct 25(10):1241–1263

Rowe WD (1980) Risk assessment: theoretical approaches and methodological problems. In: Conrad J (ed) Society, technology, and risk assessment. Academic Press, New York, pp 3–29

Royset J, Der Kiureghian A, Polak E (2001a) Reliability-based optimal design of series structural systems. J Eng Mech ASCE 127(6):607–614

Royset J, Der Kiureghian A, Polak E (2001b) Reliability-based optimal structural design by the decoupling approach. Reliab Eng Syst Safty 73(3):213–221

Royset JO, Polak E, Der Kiureghian A (2003) Adaptive approximations and exact penalization for the solution of generalized semi-infinite min-max problems. SIAM J Optim 14(1):1–34

Royset JO, Der Kiureghian A, Polak E (2006) Optimal design with probabilistic objective and constraints. J Eng Mech ASCE 132(1):107–118

Sackman JL, Der Kiureghian A, Nour-Omid B (1983) Dynamic analysis of light equipment in structures: modal properties of the combined system. J Eng Mech ASCE 109(1): 73–89

Sasani M, Der Kiureghian A (2001) Seismic fragility of reinforced concrete structural walls: a displacement approach. J Struct Eng ASCE 127(2):219–228

Sasani M, Der Kiureghian A, Bertero VV (2002) Seismic fragility of short period reinforced concrete structural walls under near-source ground motions. Struct Saf 24(2–4):123–138

Schevenels M, Lazarov B, Sigmund O (2011) Robust topology optimization accounting for spatially varying manufacturing errors. Comput Methods Appl Mech Eng 200(4952):3613–3627

Schüeller G, Jensen H (2008) Computational methods in optimization considering uncertainties: an overview. Comput Methods Appl Mech Eng 198(1):2–13

Shinozuka M (1971) Simulation of multivariate and multidimensional random processes. J Acoust Soc Am 49(1B):357–368

Shinozuka M, Deodatis G (1991) Simulation of stochastic processes by spectral representation. Appl Mech Rev 44(4):191–204

Sitar N, Cawlfield JD, Der Kiureghian A (1987) First-order reliability approach to stochastic analysis of subsurface flow and contaminant transport. Water Resour Res 23(5):794–804

Smeby W, Der Kiureghian A (1985) Modal combination rules for multi-component earthquake excitation. Earthq Engrg Struct Dyn 13(1):1–12

Somerville PG, McLaran JP, Sen MK, Helmberge DV (1991) The influence of site conditions on the spatial in coherence of ground motions. Struct Saf 10(1):1–14

Song J, Der Kiureghian A (2003) Bounds on system reliability by linear programming. J Eng Mech ASCE 129(6):627–636
Song J, Der Kiureghian A (2006a) Joint first-passage probability and reliability of systems under stochastic excitation. J Eng Mech ASCE 132(1):65–77
Song J, Der Kiureghian A (2006b) Generalized Bouc-Wen model for highly asymmetric hysteresis. J Eng Mech ASCE 132:610–618 (Discussion and closure, 134:438–439, May 2008)
Song J, Der Kiureghian A, Sackman JL (2007) Seismic interaction in electrical substation equipment connected by nonlinear rigid bus conductors. Earthq Eng Struct Dyn 36:167–190
Stewart MG, Reid S (2016) Decision-making in a changing climate. Struct Infrastruct Eng 12 (4):431
Stewart MG, Rosowsky DV (1998) Time-dependent reliability of deteriorating reinforced concrete bridge decks. Struct Saf 20(1):91–109
Straub D, Der Kiureghian A (2008) Improved seismic fragility modeling from empirical data. Struct Saf 30:320–336
Straub D, Der Kiureghian A (2010a) Bayesian network enhanced with structural reliability methods: methodology. J Eng Mech ASCE 136(10):1248–1258
Straub D, Der Kiureghian A (2010b) Bayesian network enhanced with structural reliability methods: application. J Eng Mech ASCE 136(10):1259–1270
Straub D, Der Kiureghian A (2011) Reliability acceptance criteria for deteriorating elements of structural systems. J Struct Eng ASCE 137:1573–1582
Streicher H, Rackwitz R (2004) Time-variant reliability-oriented structural optimization and a renewal model for life-cycle costing. Probab Eng Mech 19(1–2):171–183
Sudret B, Der Kiureghian A (2002) Comparison of finite element reliability methods. Probab Eng Mech 17(4):337–348
Swain AD, Guttmann HE (1983) Handbook of human-reliability analysis with emphasis on nuclear power plant applications. Final report (No. NUREG/CR-1278; SAND-80–0200). Sandia National Labs, Albuquerque, NM (USA)
Tabandeh A, Gardoni P (2015) "Empirical Bayes approach for developing hierarchical probabilistic predictive models and its application to the seismic reliability analysis of FRP-retrofitted RC bridges. ASCE-ASME J Risk Uncertain Eng Syst Part A: Civil Eng 1 (2):04015002
Taflanidis AA, Beck JL (2008) An efficient framework for optimal robust stochastic system design using stochastic simulation. Comput Methods Appl Mech Eng 198(1):88–101
Taflanidis AA, Jia G, Gidaris I (2016) Natural hazard probabilistic risk assessment through surrogate modeling. In: Gardoni P, LaFave J (eds) Multi-hazard approaches to civil infrastructure engineering. Springer International Publishing, pp 59–86
Takahashi Y, Der Kiureghian A, Ang AH-S (2004) Life-cycle cost analysis based on a renewal model of earthquake occurrences. Earthq Eng Struct Dyn 33(7):859–880
Taniguchi T, Der Kiureghian A, Melkumyan M (2008) Effect of tuned mass damper on displacement demand of base-isolated structures. Eng Struct 30:3478–3488
Thoft-Christense P, Baker M (1982) Structural reliability theory and its applications. Springer, Berlin
Thoft-Christense P, Murotsu Y (1986) Applications of structural system reliability theory. Springer, Berlin
Val DV, Stewart MG, Melchers RE (2000) Life-cycle performance of RC bridges: probabilistic approach. Comput Aided Civil Infrastruct Eng 15(1):14–25
van de Lindt JW (2004) Evolution of wood shear wall testing, modeling, and reliability analysis: bibliography. Pract Period Struct Des Constr 9(1):44–53
van de Lindt JW, Walz MA (2003) Development and application of wood shear wall reliability model. J Struct Eng 129(3):405–413
Van Noortwijk JM, Frangopol DM (2004) Two probabilistic life-cycle maintenance models for deteriorating civil infrastructures. Probab Eng Mech 19(4):345–359
Vanmarcke E (2010) Random fields: analysis and synthesis (1st Edition: The MIT Press, 1983). Second (Revised and Expanded) Edition. World Scientific Publishing Company

Vose D (2000) Risk analysis: a quantitative guide. Wiley, New York
Vrouwenvelder T (1997) The JCSS probabilistic model code. Struct Saf 19(3):245–251
Wen YK (1990) Structural load modeling and combination for performance and safety evaluation. Elsevier, Amsterdam, The Netherlands
Williams RJ, Gardoni P, Bracci JM (2009) Decision analysis for seismic retrofit of structures. Struct Saf 31:188–196
Wilson EL, Der Kiureghian A, Bayo EP (1981) A replacement for the SRSS method in seismic analysis. Earthq Engrg Struct Dyn 9(2):187–194 (Summary translation into Japanese in Proceedings of Japan Society of Civil Engineers, 1983, p 69)
Wirsching PH (1984) Fatigue reliability for offshore structures. J Struct Eng 110(10):2340–2356
Xu H, Gardoni P (2016) Probabilistic capacity and seismic demand models and fragility estimates for reinforced concrete buildings based on three-dimensional analyses. Eng Struct 112:200–214
Yang TY, Moehle J, Stojadinovic B, Der Kiureghian A (2009) Seismic performance evaluation of facilities: methodology and implementation. J Struct Eng 135(10):1146–1154
You T, Gardoni P, Hurlebaus S (2014) Iterative damage index method for structural health monitoring. Strct Mon Maint 1(1):89–110
Zhang Y, Der Kiureghian A (1993) Dynamic response sensitivity of inelastic structures. Comp Methods Appl Mech Engrg 108(1):23–36
Zhang Y, Der Kiureghian A (1994) First-excursion probability of uncertain structures. Probab Eng Mech 9(1–2):135–143
Zhao J, Wang C (2014) Robust topology optimization under loading uncertainty based on linear elastic theory and orthogonal diagonalization of symmetric matrices. Comput Methods Appl Mech Eng 273(1):204–218
Zhong J, Gardoni P, Rosowsky D (2012) Seismic fragility estimates for corroding reinforced concrete bridges. Struct Infrastruct Eng 8(1):55–69

Part II
Reliability Analysis: Methods and Applications

Structural System Reliability, Reloaded

Jieun Byun and Junho Song

Abstract Over the last four decades, structural system reliability (SSR) has been an active research topic as engineering systems including structures and infrastructure networks become more complex, and the computational power has been remarkably advanced. Among many efforts to advance SSR technologies, the research by Prof. Armen Der Kiureghian in the early 2000s is considered to have built critical pathways to the development of next-generation SSR methods by *revisiting* the topic of SSR. As demonstrated in Der Kiureghian (Structural system reliability, revisited. Proceedings, 3rd ASRANet International Colloquium, Glasgow, UK, July 10-12, 2006), his research efforts led to new insights and perspectives on critical topics of structural system reliability. This has encouraged researchers to perform a variety of research activities to develop new SSR technologies that can address challenges and needs in risk management of real-world systems. This chapter provides a review on such efforts to *reload* the research community with SSR technologies, which were made possible by the *revisit*. The chapter reviews the following SSR methods: linear programming bounds, matrix-based system reliability method, sequential compounding method, cross-entropy-based adaptive importance sampling, selective recursive decomposition algorithm, branch-and-bound employing system reliability bounds, and genetic-algorithm-based selective search for dominant system failure modes. For each of the reviewed methods, their main concepts, applications and follow-up research activities are presented along with discussions on merits, remaining challenges, and future research needs.

Keywords Structural reliability · System reliability · Complex systems · Network reliability · Reliability method · Adaptive importance sampling · Branch-and-bound method · Reliability bounds · Genetic algorithm

J. Byun · J. Song (✉)
Department of Civil and Environmental Engineering, Seoul National University, Seoul 08826, Republic of Korea
e-mail: junhosong@snu.ac.kr

J. Byun
e-mail: lamoncokiy@snu.ac.kr

P. Gardoni (ed.), *Risk and Reliability Analysis: Theory and Applications*,
Springer Series in Reliability Engineering, DOI 10.1007/978-3-319-52425-2_2

1 Introduction

System reliability is defined as the probability that a system remains available or functional despite the likelihood of component failures (Der Kiureghian 2006). There is a pressing research need for formal and accurate treatment of system reliability as the concept and importance of safety have been highlighted throughout the world. However, there are innumerable roadblocks for effective system reliability analysis especially because systems are becoming more complex and larger as the technological demands from the societies increase rapidly. Moreover, in such complex systems, there exist significant statistical dependence between component failure events characterized in terms of physical members, failure modes, failure locations, and time points of failure occurrences. These technical challenges make system reliability analysis more difficult than that of a component event.

For the last four decades, there have been active research efforts to overcome the aforementioned challenges in structural system reliability (SSR) analysis. One of the most noteworthy efforts was made by Prof. Armen Der Kiureghian, who built critical pathways to next-generation SSR methods by *revisiting* the topic of SSR in the early 2000s via his research (Der Kiureghian 2006). As demonstrated in his paper, his efforts led to new insights and perspectives on the crucial topic of structural system reliability especially with regard to system reliability formulations, system reliability updating, component importance measures, parameter sensitivities of system reliability, and reliability of systems in which component failures are described by stochastic processes or show significant level of statistical dependence. This motivation has encouraged researchers to perform a variety of new research activities, which eventually *reloaded* the research community with new SSR technologies to address challenges and needs in risk management of real-world systems.

New SSR methods and the recent growth of computational power greatly advanced the capabilities of SSR analysis. However, the advent of highly complex structures and infrastructure systems demanded by today's society still hampers accurate and rapid assessment of reliability, which introduces new challenges in SSR. This chapter aims to summarize challenges addressed by new SSR methods since the *revisit*, and identify future challenges and needs based on today's SSR technological demands and capabilities.

In Sect. 2, four SSR methods developed to address essential technological needs in SSR are discussed—the linear programming bounds, the matrix-based system reliability method, the sequential compounding method, and cross-entropy-based adaptive importance sampling. In Sect. 3, three SSR methods developed to satisfy technological needs arising for complex systems are presented—selective recursive decomposition algorithm, branch-and-bound method employing system reliability bounds, and genetic-algorithm-based selective search scheme for dominant failure modes. Lastly, Sect. 4 provides a summary of the technological needs for SSR discussed in this chapter and how the reviewed SSR methods have satisfied the needs. This chapter is concluded by discussing future reloading needs.

2 Methods Developed to Address Essential Needs in SSR

There are myriad types of systems for which SSR analysis needs to be performed. In performing SSR analysis for those general systems, the followings are identified as essential needs for SSR methods: (1) Generality: SSR methods applicable to general systems are desired; (2) Flexibility: SSR methods capable of incorporating inequality or incomplete information about components are needed; (3) Inference: Through SSR analysis, it is desirable to compute conditional probabilities and to identify important components in a system; (4) Sensitivity: To facilitate decision-making process regarding system reliability, one may wish to compute parameter sensitivities of system reliability through an SSR analysis; (5) Efficiency: SSR methods should be computationally efficient enough; and (6) Scalability: As structures and infrastructure networks become larger, it is desirable to have SSR methods that can handle a large number of components. Various SSR methods have been developed for last decades to meet these needs using the available computational resources. Although remarkable developments in computational power has greatly enhanced the capability of SSR analysis, practical systems are often too complex and large to be analytically examined.

To overcome these challenges, SSR methods need to be developed based on suitable strategies that can consider limited information on hand, employ efficient analysis schemes, and introduce proper approximation schemes. Four of recently developed SSR methods are reviewed in this chapter in terms of their strengths and limitations in addressing the six essential needs described above. The evaluation results are summarized in Table 1. In the table, "O" indicates fulfillment of the corresponding need by the SSR method while "*" indicates an indirect fulfillment is possible.

2.1 Bounds on System Reliability by Linear Programming (LP Bounds)

In general, system reliability is estimated based on information of component events such as their marginal failure probabilities and statistical dependence between component events. However, complete information is rarely available in

Table 1 Evaluation of SSR methods discussed in Sect. 2 in terms of six essential needs

	Generality	Flexibility	Inference	Sensitivity	Efficiency	Scalability
LP bounds	O	O	O	O		
MSR	O		O	O	O	
SCM	O		*	O	O	O
CE-AIS	O		*		O	O

practical SSR problems. To maximize the use of available information, Song and Der Kiureghian (2003a) proposed a methodology to obtain lower and upper bounds of system failure probability using linear programming, termed "LP bounds" method.

Figure 1 illustrates the main idea of the LP bounds method. If the system failure event is divided into basic mutually exclusive and collectively exhaustive (MECE) events, the system failure probability can be calculated by summing up the probabilities of the basic MECE events belonging to the system event of interest. If each of n component events has 2 possible states, e.g. "failure" and "functioning," there exist a total of 2^n basic MECE events. For example, when there are three component events, the sample space is decomposed to $2^3(= 8)$ basic MECE events as illustrated by a Venn diagram in Fig. 1. The probability of a general system event then can be described as a linear function of the probabilities of the basic MECE events. For example, the probability of the system event $E_{sys} = (E_1 \cap E_2) \cup E_3$, represented by the shaded area in Fig. 1, can be calculated by summing up the corresponding five basic MECE events in the Venn diagram.

This linear relationship between the probabilities of the basic MECE events and the system probability is described by the equation $\mathbf{c}^{\mathrm{T}}\mathbf{p}$ where the elements in "event vector" $\mathbf{c}$ are 1 when the corresponding MECE event is included in the system event and 0 otherwise. Meanwhile p_i, the ith element in the "probability vector" $\mathbf{p}$, denotes the probability of the ith MECE event. To obtain the bounds of system reliability, the objective function of LP is defined by the function $\mathbf{c}^{\mathrm{T}}\mathbf{p}$ as written in the lower box of Fig. 1. There are two types of constraints on the LP: one set is from the probability axioms while the other represents available information on component events and their statistical dependence, given either in the form of equality or inequality equations. Once the objective function and appropriate constraints are defined, one can obtain the bounds of the system-level probability of interest using an LP algorithm.

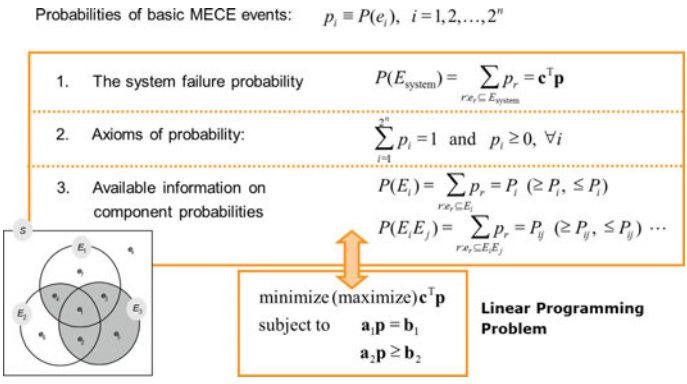

Fig. 1 Illustration of LP bounds method and a system example with three components

The LP bounds method can deal with any type of system events, e.g. parallel or series systems, general systems consisting of cut sets and link sets (Song and Der Kiureghian 2003a, 2003b, 2005; Jimenez-Rodriguez et al. 2006), and can incorporate various types of available information, e.g. an incomplete set of component probabilities or inequality constraints on component probabilities. Therefore, the essential needs for Generality and Flexibility of SSR are satisfied as noted in Table 1. Using the LP bounds method, the bounds on various quantities such as component importance measures (Song and Der Kiureghian 2005), conditional probabilities given observed events and parameter sensitivities of the system failure probability (Der Kiureghian and Song 2008) can be calculated as well. Therefore, although the results are given as bounds, the LP bounds method is considered to meet Inference and Sensitivity criteria as indicated in Table 1.

The LP bounds method has proved to be superior to existing bounding formulas (Boole 1916; Ditlevsen 1979; Hunter 1976; Kounias 1968; Zhang 1993) since the obtained bounds are guaranteed to be the narrowest ones under the available information regardless of the ordering of the components, and can use inequality information and incomplete set of probabilities to narrow the bounds. However, numerical problems may occur in running LP algorithms in the case that the bounds are too narrow or the number of components is large. Due to these current limits, the Efficiency and Scalability criteria are shown as blank in Table 1.

It is noted that there have been research efforts to overcome the scalability issue of the LP bounds method. A multi-scale analysis approach was combined with the LP bounds method to reduce the size of LP problems (Der Kiureghian and Song 2008). Chang and Mori (2013) proposed a relaxed linear programming (RLP) bounds method to overcome the scalability issue by introducing an universal generating function. An alternative strategy to reduce the number of constraints in the RLP bounds was later proposed, and a decomposition scheme of a system based on failure modes has been developed so that the LP bounds approach is applicable to large systems (Chang and Mori 2014). A small-scale LP (SSLP) approach was also developed to reduce the scale of LP problems formulated for parallel and series systems (Wei et al. 2013). The SSLP approach uses a new boundary theory so that the LP model increase linearly with respect to the number of components. This approach was applied to a structural system with multiple failure modes where both random and fuzzy inputs are present.

2.2 *Matrix-Based System Reliability (MSR) Method*

There are various types of systems such as parallel, series, cut set, and link set systems. Since there are generally multiple failure events in a system and their configurations are all different, system probability assessment using a direct Boolean formulation is usually impractical. The MSR method provides a systematic framework to facilitate analytical evaluation of general system reliability (Kang et al. 2008; Song and Kang 2009). By adopting simple matrix calculations, the

probability of a system event consisting of multiple component events can be estimated in a straightforward manner. Such simplification is obtained by separating two main parts of system reliability assessment, i.e. system event description and probabilities of events.

Figure 2 illustrates the main calculation procedures and outputs of the MSR method. By decomposing the system event into basic MECE events (as done for the LP bounds method), the probability of a system event is calculated by summation of the probabilities of the basic MECE events belonging to the system event. The *event vector* $\mathbf{c}$ is a vector that describes the system event. When the system state is determined by the binary states of its components, the vector $\mathbf{c}$ contains binary terms, i.e. 0 and 1. The *probability vector* $\mathbf{p}$ is a column vector where each element is the probability of corresponding MECE event. The probability of the system event then can be calculated by simply the inner product of the two vectors, i.e. $\mathbf{c}^{\mathrm{T}}\mathbf{p}$.

When there exists statistical dependence between component events, the probability can be estimated by the integral in the bottom box of Fig. 2 by use of the total probability theorem. In this case, common source random variables (CSRV) $\mathbf{x}$ and their joint probability density function (PDF) $f_X(\mathbf{x})$ need to be identified such that the component failures are conditionally independent given the outcomes of $\mathbf{x}$, and thus the probability vector $\mathbf{p}$ can be constructed by use of the conditional failure probabilities given $\mathbf{x}$ through the procedure originally developed for independent components. Component reliability analysis methods such as the first- or second-order reliability methods (See a comprehensive review in Der Kiureghian 2005) can be used to compute the failure probabilities of the components and their parameter sensitivities (Kang et al. 2012). Since the MSR method does not require running an additional algorithm as the LP bounds method, and can provide a straightforward reliability analysis formulation given any types of systems, Efficiency criterion in Table 1 is fulfilled.

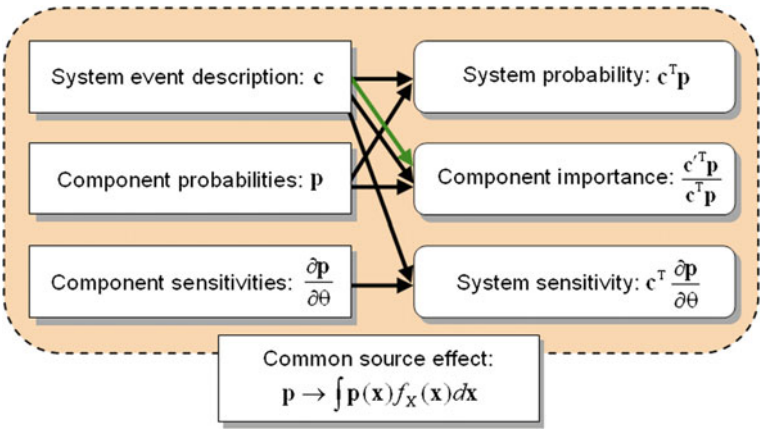

Fig. 2 Main calculation procedures and outputs of the MSR method

The MSR method is applicable to a wide range of system types, i.e. series, parallel, cut set, and link set systems, which satisfies the needs for Generality. This general applicability has been demonstrated by many examples of (1) structural systems, e.g. truss systems, a bridge pylon system, a combustion engine, a hardware system of train and Daniels systems, and (2) infrastructure networks, e.g. bridge networks, a gas distribution system, complex slopes (Xie et al. 2013). To extend the usage of the MSR method to systems whose performance is evaluated in terms of a continuous measure, i.e. non-discrete states, Lee et al. (2011) introduced the concept of a *quantity vector* $\mathbf{q}$ to replace the event vector $\mathbf{c}$. The elements of the quantity vector are defined as the value of the continuous measure of the system performance for the corresponding combination of the component states (Lee et al. 2011). Meanwhile, Byun and Song (2016) proposed to modify the elements of the event vector $\mathbf{c}$ into binomial terms to deal with k out of N systems (Byun and Song 2016).

The MSR method is able to compute conditional probability given observed or assumed events, component importance measure (Song and Ok 2010) and parameter sensitivity of system failure probability (Song and Kang 2009). These useful by-products can be obtained through simple matrix calculations. As illustrated in Fig. 2, to calculate the component importance measure, the new event vector $\mathbf{c}'$ is introduced without modifying the probability vector $\mathbf{p}$. On the other hand, parameter sensitivity of system failure probability can be obtained by replacing $\mathbf{p}$ with the sensitivity of the component failure probabilities without modifying the vector $\mathbf{c}$. Inference and Sensitivity criteria, therefore, are satisfied by the MSR method as shown in Table 1.

The MSR method requires exhaustive description of the likelihood and statistical dependence of component failure events, and thus cannot utilize inequality type information or an incomplete set. Therefore, the Flexibility criterion in Table 1 is not marked. However, in such cases, the LP bounds method can be used instead since the two methods share the same mathematical model (Kang et al. 2008; Huang and Zhang 2012). The criterion of Scalability is not marked either in Table 1 because the size of the vectors increases exponentially as the number of the components increases. The size issue can be alleviated though by adopting a multi-scale approach. For example, Song and Ok (2010) decomposed a large system into several subsystems to introduce multiple scales. At the lower-scale, the failure probabilities of the subsystems and their statistical dependence are evaluated. Using the results of the lower-scale analysis, the failure probability and parameter sensitivities of the whole system are computed at the upper-scale analysis. An important merit of the MSR method is its straightforward evaluation of the parameter sensitivity. Since this feature facilitates the use of gradient-based optimizer for reliability based design optimization, the MSR method has been applied to develop efficient system reliability based design optimization algorithms (Nguyen et al. 2009).

2.3 Sequential Compounding Method (SCM)

Although computation of multivariate normal integrals is often needed in SSR, no closed form solution is available. Accordingly, it is challenging to estimate the system reliability when such integrals are present in the formulation, particularly in the cases that components have strong statistical dependence; the size of the system is large; or the definition of the system event is complex. To properly approximate the integrals and to enhance the computational efficiency, a sequential compounding method (SCM) was proposed (Kang and Song 2010).

The SCM sequentially compounds a pair of component events in the system until the system is merged into one super-component as illustrated by an example in Fig. 3. At each compounding step, the probability of the new compound event, e.g. the super-component "A" during the first step in the example, and the correlation coefficients between the new compound event and the other remaining events, e.g. the correlation coefficients for the pairs (A, 3), (A, 4), and (A, 5), are identified for the next compounding sequences. To facilitate the calculation of correlation coefficients, an efficient numerical method was also developed (Kang and Song 2010). The SCM is applicable to any type of systems since it simply compounds a pair of adjacent components coupled by intersection or union.

The SCM shows superior accuracy and efficiency for a wide range of system types as demonstrated by numerous series, parallel and cut-set system examples with various sizes and correlation coefficients (Kang and Song 2010), topology optimization of lateral bracings of a building (Chun et al. 2013a), and system reliability analysis of rock wedge stability (Johari 2016). Hence, the SCM method seems to satisfy the Generality as indicated in Table 1. An alternative approach was later proposed to adopt a recursive approach to the SCM in order to rapidly estimate the connectivity between two nodes (Kang and Kliese 2014). Efficiency and accuracy of the proposed approach were demonstrated by applications to real-world power and water networks. On the other hand, the Flexibility criterion is not satisfied since the SCM cannot incorporate inequality information or incomplete sets. In Table 1, the Inference criterion is not marked because conditional probabilities cannot be directly evaluated by SCM. However, one could estimate conditional probabilities by evaluating the system event probabilities that appear in the numerator and denominator of the conditional probability separately by use of the SCM.

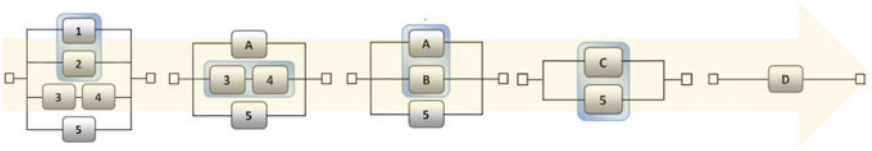

Fig. 3 Example of sequential compounding by SCM

The SCM has been further developed to evaluate the parameter sensitivity of system reliability as well (Chun et al. 2015a, b). The method can analytically compute the parameter sensitivity of the probabilities of series, parallel and general systems. The method was successfully applied to topology optimization of structures under system reliability constraints including first passage probability (Chun et al. 2015b) for which parameter sensitivities of a large-size series system is required. It is noted that the SCM also satisfies the criteria of Efficiency and Scalability since the proposed sequential compounding processes are straightforward and computationally efficient even for large-scale systems.

2.4 *Cross-Entropy-Based Adaptive Importance Sampling (CE-AIS)*

When the failure domain in the random variable space is so complex that the analytical estimation of the probability is infeasible, sampling-based methods can be used as good alternatives for component and system reliability analysis. Although the Monte Carlo simulation (MCS) is the most straightforward approach applicable to all system problems, the computational cost is sometimes overwhelming especially when the probability of the event is low. Importance sampling (IS) has been developed to alleviate the computational cost of simulation by using a more efficient sampling density located at relatively important regions, which are usually identified by additional reliability analysis. To find a near-optimal importance sampling density without such additional computational efforts, cross-entropy-based adaptive importance sampling (CE-AIS) (Rubinstein and Kroese 2013) minimizes Kullback-Leibler cross entropy, which measures the difference between the true optimal sampling density and a sampling density model being updated by pre-samplings.

Kurtz and Song (2013) proposed to adopt a Gaussian mixture as a sampling density model in the CE-AIS approach, and developed closed-form updating rules to find the near-optimal sampling density by a few rounds of small pre-sampling. CE-AIS employing a Gaussian mixture (CE-AIS-GM) has proved to be efficient and accurate, i.e. requiring far less samples to achieve the target coefficient of variation than crude MCS or CE-AIS using a unimodal distribution model (Rubinstein and Kroese 2013). Figure 4 demonstrates how Gaussian mixture models converge to near-optimal sampling densities by the CE-AIS-GM algorithm. The black lines in the figures represent the limit-state surface of a series system problem. The contours in the far left figures represent the initial GM sampling densities, and after few rounds of pre-sampling, the sampling densities converge into critical regions as noted in the far right figures in Fig. 4. It is noteworthy that even when an excessive number of sampling densities are originally employed in the Gaussian mixture model, densities tend to merge to form a Gaussian mixture model concentrating only on the important areas.

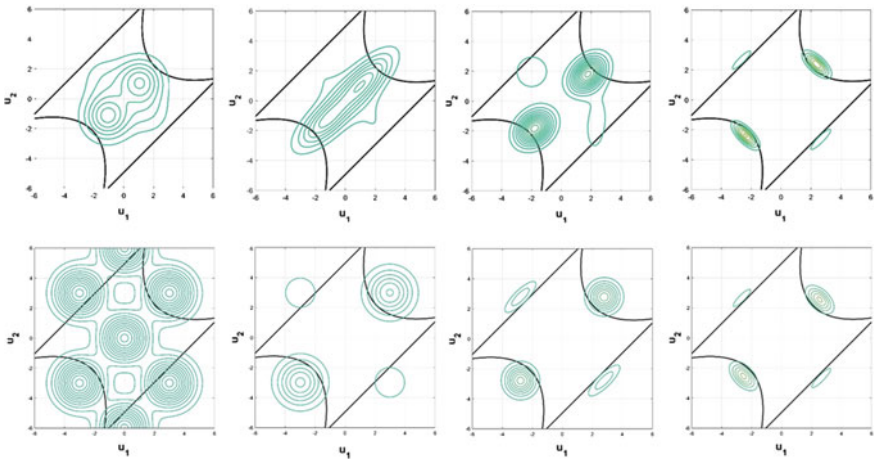

Fig. 4 Convergence (from *left* to *right*) of Gaussian mixture models with four (*top*) and seven (*bottom*) densities into near-optimal importance sampling densities by cross-entropy-based adaptive importance sampling for a series system example

As noted in Table 1, CE-AIS-GM is applicable to general systems, and its computational performance is not affected by the level of probability and the shape of limit-state functions (Kurtz and Song 2013). Efficiency and Scalability criteria are also accomplished. The method's wide applicability was demonstrated by numerical examples including a parabola limit-state function and reliability analyses of systems such as parallel, series and general systems. CE-AIS-GM was also applied to practical issues such as seismic reliability analysis (Choi and Song 2016) and time-dependent reliability of structural system (Yang et al. 2015). Although CE-AIS-GM is not able to directly estimate conditional probabilities, the criterion of Inference is considered to have been partially fulfilled in a sense that the GM model parameters obtained during pre-sampling process are helpful in identifying important areas in random variable space. The method is yet able to incorporate available information in a flexible manner or evaluate parameter sensitivities.

While CE-AIS-GM shows good performance for systems including up to about 50 random variables, the method does not work well in the random variable spaces with higher dimensions. This is because most of the probability volume is highly concentrated around the surface of the hypersphere with a certain radius in a high dimension random variable space. To be able to sample in the so-called "important ring" region, a CE-AIS method employing a von Mises-Fisher mixture model (CE-AIS-vMFM) was proposed (Wang and Song 2016). The performance of CE-AIS-vMFM was successfully demonstrated by reliability analyses of both component and system events which included up to 300 random variables. There has been another effort to resolve the difficulty in high-dimensional systems by integrating CE-AIS with Markov chain Monte Carlo methods (Chan and Kroese 2012).

3 Methods Developed to Address Needs in SSR Analysis of Complex Systems

For systems whose system-level performance or state are determined mainly by the *complex* relationship and arrangement of their components, it is crucial to identify the combinations of component states leading to system failure or survival, and interaction between the states of components. While the system failure may not be observed even after preceding failures of several component events for a redundant system, sometimes a small number of critical components would cause the system to fail promptly. In this sense, for effective SSR analysis of complex systems, proper considerations need to be made to (1) handle cascading failures in systems: the sequence of multiple component failure events leading to the system-level failure; (2) identify critical failure modes: cut sets and link sets with dominant contributions to the system failure; and (3) obtain updated or conditional probabilities for inference. Satisfying these needs would not only make the estimation of reliability of complex systems possible, but also provide a deep insight for the system, which is useful for the purpose of maintenance planning or design of structural systems.

In this regard, this section introduces three SSR methods, i.e. selective recursive decomposition algorithm, branch-and-bound method employing system reliability bounds, and genetic-algorithm-based selective searching technique. Their applications, further developments, strengths, and limitations are also discussed. Table 2 summarizes needs regarding SSR analysis of complex systems, satisfied by the reviewed methods.

3.1 Selective Recursive Decomposition Algorithm (S-RDA)

While the LP bounds method aims to overcome the difficulty aroused from incomplete information, another prevalent difficulty in SSR analysis of complex and large systems is caused by the infeasible computational cost of reliability calculations needed for numerous system failure scenarios. Therefore, identifying only a fraction of failure or survival events with dominant contributions to the

Table 2 Evaluation of SSR methods discussed in Sect. 3 in terms of needs regarding SSR analysis of complex systems

	Cascading failure	Critical failure modes	Updating/inference
S-RDA		O	O
B^3 method	O	O	O
GA-based selective Search	O	O	

system failure probability or reliability is a crucial scheme which analytical reliability methods should pursue to alleviate the computational effort.

Based on graph theories, the recursive decomposition algorithm (RDA) was developed as a non-simulation-based method for SSR analysis of networks. RDA sequentially identifies disjoint link sets and cut sets until the desired width of bound is attained (Liu and Li 2009; Li and He 2002). Searching for *disjoint* link sets and cut sets is advantageous because the upper and lower bounds of probability can be obtained by simply summing up the probabilities of identified sets. The bounds of system reliability R and system failure probability F are then obtained by

$$\sum_{i=1}^{n_L} P(L_i) \le R \le 1 - \sum_{i=1}^{n_C} P(C_i) \tag{1a}$$

$$\sum_{i=1}^{n_C} P(C_i) \le F \le 1 - \sum_{i=1}^{n_L} P(L_i) \tag{1b}$$

where $P(L_i)$ and $P(C_i)$ are the probabilities of ith link set L_i and cut set C_i, and n_L and n_C are the numbers of identified link sets and cut sets. RDA terminates the search of new link sets and cut sets when the bounds become narrow enough.

Lim and Song (2012) proposed a selective RDA (S-RDA), which greatly improves the performance of the original RDA by preferentially identifying *critical* disjoint link sets and cut sets whose probabilities are higher than others (Lim and Song 2012). Figure 5 illustrates the searching scheme of the RDA using a simple network example and compares the original RDA and S-RDA. For a given network or subnetwork, a link set is searched first. For the example in Fig. 5, there are three possible link sets, and suppose the second one (yellow box) is selected to be decomposed at the next step. As mentioned above, S-RDA selects the link set with the highest probability, i.e. critical link set while the original RDA selects the ones with the shortest path. The probabilities of such selected link sets are summed up to update the lower bound of the system reliability (Eq. 1a) or the upper bound of the system failure probability (Eq. 1b). Among the subgraphs generated by the decomposition of the selected link set (three in the example), a subgraph indicating the failure of system is classified as a cut set and its probability is added to update the upper bound of the system reliability (Eq. 1a) or the lower bound of the system failure probability (Eq. 1b). Then one of the subgraphs that are not cut sets is selected for the next decomposition. For this subgraph selection, S-RDA aims to identify a subgraph with the most likelihood of occurrence while the original RDA relies on the preset numbering choice of nodes or links. The identification of link sets and cut sets continues until the desired width is achieved for the bounds in Eqs. (1a) and (1b). The table in Fig. 5 compares two different searching strategies. Because S-RDA takes into account the probabilities of the sets during the decomposing scheme, the number of sets required to achieve the convergence of the bounds is drastically reduced. The efficiency of S-RDA was demonstrated by applications to large and complex systems such as a gas transmission network (17 nodes and 20 links) and water distribution network (50 nodes and 78 links) (Lim and Song 2012).

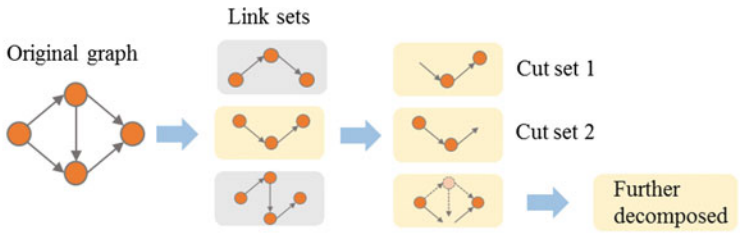

	Identifying link set	Selecting subgraph to decompose
Original RDA	Shortest path algorithm	Arbitrarily based on the preset numbering
S-RDA	Most reliable path algorithm	Decompose subgraph with higher likelihood

Fig. 5 Searching scheme of RDA and comparison between the original RDA and S-RDA

Although S-RDA considerably alleviates the computational cost of probability estimation, the algorithm still has an intrinsic limitation as the number of sets to identify increases exponentially as the number of components increases. To extend the use of S-RDA to even larger systems, Lim et al. (2015b) proposed a clustering-based multi-scale approach using S-RDA. This approach divides a system into several clusters by use of a spectral clustering algorithm. The number of clusters is determined by monitoring the variation of the eigenvalues of the graph Laplacian matrix, and components are grouped in a way that the number of links connecting nodes in different clusters is minimized while the number of nodes in each cluster is well distributed. The accuracy of this multi-scale approach is not deteriorated by considering the statistical dependence between the generated clusters termed as "super-components." If the number of clusters is still too large for S-RDA, the system can be additionally clustered to have more than two scales. By using such a hierarchical clustering approach, S-RDA can be applied to systems with even larger number of components. The proposed methodology was adopted to several practical systems with up to 257 components: 59 nodes and 99 bi-directional links.

SSR analysis employing S-RDA can deal with networks whose failure is defined in terms of the connectivity between two nodes, e.g. source and terminal nodes in gas distribution network. However, the approach does not consider cascading failures. However, conditional-probability-based importance measures and conditional probabilities given observed or assumed events can be readily computed using S-RDA. The bounds of the measures are obtained as a by-product based on the probability of critical disjoint sets identified for reliability analysis. The bounds are proved to be narrow enough to observe the relative importance of components in numerical examples. Recently, a lifeline network retrofitting prioritization scheme was developed based on multi-criteria optimization, in which the

conditional-probability-based importance measure of the network components is adopted as one of the decision-making criteria (Lim et al. 2015a).

3.2 Branch-and-Bound Method Employing System Reliability Bounds (B^3 Method)

When a series of component failures are observed, their sequence is generally an important factor that characterizes the system failure. Particularly for an indeterminate structure, the failures of certain members cause re-distribution of forces in the structural system, which affects the likelihood and sequence of the cascading failures. Different contributions of preceding failed members affect whether the structure would be able to withstand more external impacts or would collapse. There is a need for a reliability analysis method to reflect the importance of the sequence of events. For such a reliability analysis concerning fatigue-induced cascading failures, a branch-and-bound method employing system reliability bounds, termed B^3 method was developed (Lee and Song 2011). The method sequentially sorts out the most probable sequences leading to the system-level failure. The method was designed such that the identified sequences are disjoint to each other, and thus the lower and upper bounds are updated simply by adding up the probabilities of the sequences. This method is categorized as a bounding method just as LP bounds (Sect. 2.1) and S-RDA (Sect. 3.1), and in the same manner as S-RDA, the bounds can be rapidly converged by identifying the sequences with higher probabilities preferentially and be narrowed by summation of the sequences due to their disjoint relationship (Lee and Song 2011).

Figure 6 illustrates the search scheme of the B^3 method and how the system reliability bounds are narrowed as the search process proceeds. The search scheme starts from the initial node that contains all possibilities, and thus the node contains the probability of the sample space, i.e. 1. To "branch out" the node, a structural analysis is first performed to find the probabilities of the failure of each component based on the force distribution represented by the current node. Once a node is branched-out, the node becomes inactive, i.e. the probability of the node is distributed to its child nodes, and is marked by a dotted edge. The scheme generates one more branch than the remaining unbroken components. This additional node is the white circle including 0 shown in Fig. 6. This node implies that no additional failures are observed within the inspection period T_s and the upper bound is thus decreased by the probability of the white node. Next, among all active nodes, the node with the highest probability is selected for the next branching-out. If the structural analysis of the selected node indicates a system failure, the node is marked black and listed as one of the failure sequences leading to the system failure. The lower bound of the system failure probability is increased by the probability of the black node. This search scheme continues until sufficiently narrow bounds are obtained.

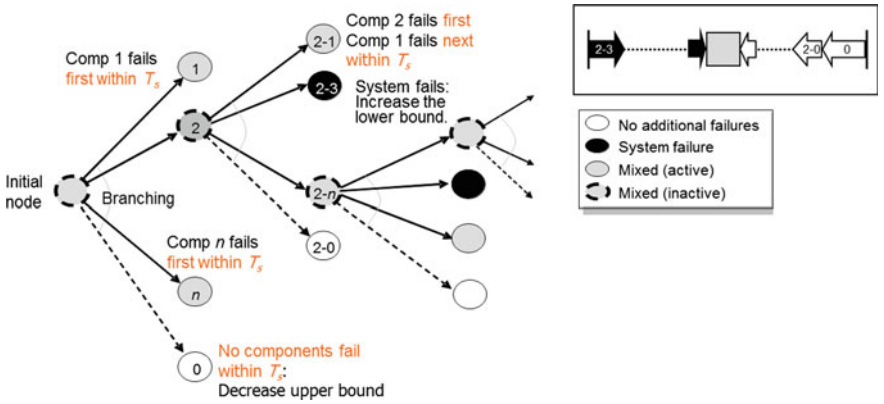

Fig. 6 Procedure for identifying critical failure sequences and narrowing bounds in B^3 method

The B^3 method showed superb performance compared to existing branch-and-bound methods (Murotsu et al. 1982; Guenard 1984) since the probabilities of identified sequences tend to decrease monotonically and the upper bound can be also obtained along with the lower bound which was not available in existing methods. There is another advantage that each structural analysis contributes to narrowing the bounds, which is especially beneficial when the computational cost is dominated by high-fidelity structural analyses than reliability assessment. The superiority of B^3 method was demonstrated by a three-dimensional truss structure (Lee and Song 2011).

The B^3 method was later combined with finite-element-based reliability analysis for applications to continuum structures (Lee and Song 2012). To this end, the limit-state formulations are modified to incorporate crack-growth analysis using an external software package, and an additional search-termination criterion is introduced. Lee and Song (2013) also proposed an inspection-based reliability updating scheme using B^3 method for both discrete and continuum structures. Quintana et al. (2014) employed the B^3 method to combine system reliability analysis, and "failure mode effects and criticality analysis" (FMECA) for quantitative classification of structural hot spots.

Since the B^3 method tends to identify sequences of component failure events in the decreasing order of the probabilities, Table 2 indicates that the method can consider cascading failures and identify dominant failure modes. The method is considered to have inference capability as well since the updating method (Lee and Song 2013) can compute conditional probabilities given information obtained from the inspections, both equality and inequality-type events. Although the B^3 method was originally developed for fatigue-induced failures in a system, the search scheme can be extended to other types of cascading failure phenomena by re-formulating the reliability calculations of the failure sequences.

3.3 Genetic-Algorithm-Based Selective Search for Dominate Failure Modes

The B^3 method (Sect. 3.2) analytically tracks down dominant failure modes in an event-tree setting. Therefore, the approach may become computationally intractable as the number of failure sequences increases exponentially as the number of components increases. By contrast, the genetic-algorithm-based search scheme (Kim et al. 2013) identifies dominant failure sequences in the random variable space through computational simulations of cascading failures. This method improves the efficiency of SSR analysis of systems subject to cascading failures by decoupling the two steps: the identification of dominant failure modes using a genetic algorithm (GA) and the estimation of the system reliability using the MSR method (Sect. 2.2). This separation is to avoid repeating unnecessary reliability analysis for components and system.

As adopting the searching feature of GA, the initial samples are randomly generated in standard normal random variable space, especially on the surface of a hypersphere with a small radius R_0. The radius is increased as the searching continues, as illustrated in Fig. 7. After transforming the generated samples into the original random variable space, structural analyses are performed for each sample point to sort out the ones that result in cascading failures leading to the system-level failure, e.g. structural collapse. For example, in Fig. 7, the system failure domain is determined by the intersection of limit-state functions. For the five samples derived from the hypersphere with radius $\mathbf{d}_i$, the structure analyses would confirm that the red-star sample is a failure mode while the other black-circle samples are not. The next generation is then produced from the failure mode samples using the two main operations of GA, *crossover* and *mutation*. The identification of new samples for a certain radius is terminated when no additional failure mode is detected after a certain number of operations. Then, another searching begins with a slightly increased radius. This outward searching scheme was proposed so that one can identify the dominant failure modes by priority based on the fact that points nearer to the origin tend to have higher probabilities in the standard normal random variable space. The overall searching process is terminated when the searching radius reaches the prescribed upper bound, e.g. R_1 in Fig. 7, or the probabilities of newly found failure modes are lower than the predefined limit. The MSR method (or a proper SSR analysis method) is then adopted to estimate the probabilities of the identified failure modes and their correlation coefficients, i.e. lower-scale analysis, and to find the probability of system failure based on the result of lower-scale analysis, i.e. higher-scale analysis (Kim et al. 2013).

The GA-based selective searching scheme has been applied to several practical problems. Kurtz (2011) applied the search scheme to a planar truss model constructed for a real bridge that has 97 elements and 50 nodes. The method was also applied to offshore structural systems under extreme loads from sea waves (Coccon 2016).

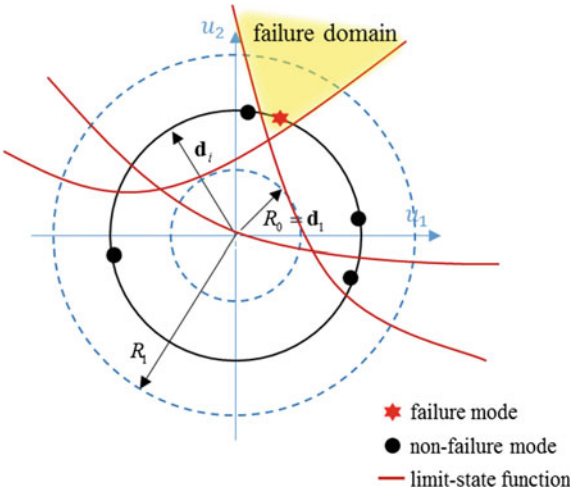

Fig. 7 GA-based selective search for dominant failure modes

Since the events generated by GA-based selective search represent the potential failure modes and the probability of each of them is identified during the analysis, criteria related to cascading failures and critical failure modes in Table 2 are dealt with by this methodology. Since the method is a sampling-based approach, it is applicable to a wide class of structures and failure phenomena as long as a proper computational simulation is feasible for the cascading failure of interest. Compared to event-tree-based search approaches such as the B^3 method, the GA-based search method is more scalable to systems with a large number of components.

4 Summary and Conclusions

This chapter provides a critical review of seven state-of-the-art structural system reliability (SSR) methods that were developed to address essential needs in SSR analysis, and new challenges in SSR analysis of complex systems. Six essential needs aroused from the innate properties of SSR, i.e. general applicability, flexibility in incorporating input information, inference capability, parameter sensitivity calculations, efficiency, and scalability to large systems were effectively addressed by linear programming bounds, matrix-based system reliability method, sequential compounding method, and cross-entropy-based adaptive importance sampling. Meanwhile, three emerging needs aroused from complex systems, i.e. considering cascading failures of multiple components, identifying critical failure modes effectively, and obtaining updated or conditional probabilities for the purpose of inference, were addressed effectively by selective recursive decomposition algorithm, branch-and-bound method employing system reliability bounds, and genetic-algorithm-based selective search for dominant failure modes. These review

results were summarized in Tables 1 and 2, respectively. Throughout the review, main concepts, merits, current limitations and future research needs of each method were presented.

Through recent research efforts including those reviewed in the chapter, the SSR technologies were significantly *reloaded* against current and future needs in risk management of structural systems. This technological *reload* was made possible by Prof. Armen Der Kiureghian's *revisit* of this important topic in the early 2000s, which has led to new insights and perspectives on the topic of SSR, especially in terms of SSR formulations, system reliability updating, component importance measures, parameter sensitivities of system reliability, and reliability of systems in which component failures are described by stochastic processes or show significant level of statistical dependence. The technological reload has relieved significant computational cost, broadened the application areas of SSR analysis, provided new insights regarding SSR, and enhanced the basis of decision-making related to structural systems. The review also reveals that there are still many technological needs for SSR analysis, e.g. bridging the gap between the results of SSR analysis and critical information needed for risk-based decision-making in practice. Meanwhile, technological demands from the societies are expected to continue growing as the complexity of structures and infrastructure networks will be increased in the future. Future *reloading* of SSR technologies need to take advantage of rapid growths of computational power, unprecedented amount of available data and statistical learning algorithms to support (near) real-time inference using monitoring and sensor data, and systematic decision-making scheme on complex systems and networks based on SSR.

Acknowledgements The second author of this chapter, Junho Song, would like to express his sincere gratitude to Prof. Armen Der Kiureghian for the valuable knowledge, insight and vision he shared as a research advisor, mentor and role model. The authors are also grateful to Won Hee Kang, Tam H. Nguyen, Young Joo Lee, Hyun-Woo Lim, Nolan Kurtz, Junho Chun, Raphael Stern, Byeong-Seong Choi, Seung-Yong Ok, Dong-Seok Kim, and Marco Coccon for their valuable contributions to the development of new structural system reliability technologies including those reviewed in this chapter. The support by the National Research Foundation of Korea (NRF) Grant (No. 2015R1A5A7037372), funded by the Korean Government (MSIP) is also acknowledged. Any opinions, findings, and conclusions expressed in this chapter are those of the authors, and do not necessarily reflect the views of the sponsors.

References

Boole G (1916) The laws of thought, vol 2. Open Court Publishing Company, Illinois

Byun J, Song J (2016) Application of Matrix-based System Reliability method to *k-out-of-N* systems described by reliability growth models. 2016 Conference of the IFIP Working Group 75 on Reliability and Optimization of Structural Systems, May 18–20, Carnegie Mellon University in Pittsburgh, Pennsylvania

Chan JC, Kroese DP (2012) Improved cross-entropy method for estimation. Stat Comput 22 (5):1031–1040

Chang Y, Mori Y (2014) A study of system reliability analysis using linear programming. J Asian Archit Build Eng 13(1):179–186
Choi B-S, Song J (2016) Seismic risk assessment for traffic network using adaptive sampling. In: 2016 Conference of the Earthquake Engineering Society of Korea, March 18, Sungnam, Korea
Chun J, Song J (2013a) Paulino GH System reliability based topology optimization of structures under stochastic excitations. In: Proceedings of 2013 Engineering Mechanics Institute Conference (EMI2013), Evanston, USA
Chun J, Song J, Paulino GH (2013b) System reliability based topology optimization of structures under stochastic excitations. In: Proceedings of 10th International Conference on Structural Safety and Reliability (ICOSSAR2013), June 16–20, New York, USA
Chun J, Song J, Paulino GH (2015a) Parameter sensitivity of system reliability using sequential compounding method. Struct Saf 55:26–36
Chun J, Song J, Paulino GH (2015b) Topology optimization of structures under constraints on first passage probability. 12th International Conference on Applications of Statistics and Probability in Civil Engineering, ICASP12Vancouver, Canada, July 12–15
Coccon MN, Song J, Ok SY, et al. (2016) KSCE J Civ Eng. doi:10.1007/s12205-016-1192-z
Der Kiureghian A (2005) First- and second-order reliability methods. In: Nikolaidis E, Ghiocel DM, Singhal S (eds), Engineering design reliability handbook Boca Raton (FL): CRC Press; 2005, chapter 14
Der Kiureghian A (2006) Structural system reliability, revisited. Proceedings, 3rd ASRANet International Colloquium, Glasgow, UK, July 10–12, 2006 (CD-ROM)
Der Kiureghian A, Song J (2008) Multi-scale reliability analysis and updating of complex systems by use of linear programming. Reliab Eng Syst Saf 93(2):288–297
Ditlevsen O (1979) Narrow reliability bounds for structural systems. J Struct Mech 7(4):453–472
Guenard Y-F (1984) Application of system reliability analysis to offshore structures. John A. Blume Earthquake Engineering Center, Standford
Huang X, Zhang Y (2012) Probabilistic approach to system reliability of mechanism with correlated failure models. Math Probl Eng 2012, Article ID 465853
Hunter D (1976) An upper bound for the probability of a union. J Appl Probab 597–603
Jimenez-Rodriguez R, Sitar N, Chacón J (2006) System reliability approach to rock slope stability. Int J Rock Mech Min Sci 43(6):847–859
Johari A (2016) System reliability analysis of rock wedge stability considering correlated failure modes using sequential compounding method. Int J Rock Mech Min Sci 82:61–70
Kang W-H, Kliese A (2014) A rapid reliability estimation method for directed acyclic lifeline networks with statistically dependent components. Reliab Eng Syst Saf 124:81–91
Kang W-H, Lee Y-J, Song J, Gencturk B (2012) Further development of matrix-based system reliability method and applications to structural systems. Struct Infrastruct Eng 8(5):441–457
Kang W-H, Song J (2010) Evaluation of multivariate normal integrals for general systems by sequential compounding. Struct Saf 32(1):35–41
Kang W-H, Song J, Gardoni P (2008) Matrix-based system reliability method and applications to bridge networks. Reliab Eng Syst Saf 93(11):1584–1593
Kim D-S, Ok S-Y, Song J, Koh H-M (2013) System reliability analysis using dominant failure modes identified by selective searching technique. Reliab Eng Syst Saf 119:316–331
Kounias E-G (1968) Bounds for the probability of a union, with applications. Ann Math Stat 39 (6):2154–2158
Kurtz NS (2011) System reliability analysis of structures subjected to fatigue induced sequential failures using evolutionary algorithms. MS Thesis. University of Illinois at Urbana-Champaign
Kurtz N, Song J (2013) Cross-entropy-based adaptive importance sampling using Gaussian mixture. Struct Saf 42:35–44
Lee Y-J, Song J (2011) Risk analysis of fatigue-induced sequential failures by branch-and-bound method employing system reliability bounds. J Eng Mech 137(12):807–821
Lee Y-J, Song J (2012) Finite-element-based system reliability analysis of fatigue-induced sequential failures. Reliab Eng Syst Saf 108:131–141

Lee Y-J, Song J (2013) System reliability updating of fatigue-induced sequential failures. J Struct Eng 140(3):1–16

Lee Y-J, Song J, Gardoni P, Lim H-W (2011) Post-hazard flow capacity of bridge transportation network considering structural deterioration of bridges. Struct Infrastruct Eng 7(7–8):509–521

Li J, He J (2002) A recursive decomposition algorithm for network seismic reliability evaluation. Earthq Eng Struct Dyn 31(8):1525–1539

Lim H-W, Song J (2012) Efficient risk assessment of lifeline networks under spatially correlated ground motions using selective recursive decomposition algorithm. Earthq Eng Struct Dyn 41 (13):1861–1882

Lim H-W, Song J, Byun JE (2015a) Multi-scale, multi-criteria decision-making for retrofitting prioritization of lifeline networks. In: 8th International Forum on Engineering Decision Making, May 6–9, Shiga, Japan

Lim H-W, Song J, Kurtz N (2015b) Seismic reliability assessment of lifeline networks using clustering-based multi-scale approach. Earthq Eng Struct Dyn 44(3):355–369

Liu W, Li J (2009) An improved recursive decomposition algorithm for reliability evaluation of lifeline networks. Earthq Eng Eng Vib 8(3):409–419

Murotsu Y, Okada H, Yonezawa M, Martin G, Taguchi K (1982) Automatic generation of stochastically dominant modes of structural failure in frame structure

Nguyen TH, Song J, Paulino GH (2009) Single-loop system reliability-based design optimization using matrix-based system reliability method: theory and applications. J Mech Des 132 (1):011005-011001-011011

Quintana C, Millwater HR, Penmetsa RC (2014) Integration of system reliability analysis and FMECA to efficiently identify structural hot spots. In: Proceedings of 16th AIAA Non-Deterministic Approaches Conference, pp 1–10

Rubinstein RY, Kroese DP (2013) The cross-entropy method: a unified approach to combinatorial optimization. Monte-Carlo simulation and machine learning. Springer Science & Business Media, Dordrecht

Song J, Der Kiureghian A (2003a) Bounds on system reliability by linear programming. J Eng Mech 129(6):627–636

Song J, Der Kiureghian A (2003b) Bounds on system reliability by linear programming and applications of electrical substations. In: Application of Statistics and Probability in Civil Engineering; Proceedings of the 9th ICASP, CA, USA, July 6–9, 2003:111–118

Song J, Der Kiureghian A (2005) Component importance measures by linear programming bounds on system reliability. In: Proceedings of the 9th International Conference on Structural Safety and Reliability ICOSSAR9, June, 2005. pp 19–23

Song J, Kang W-H (2009) System reliability and sensitivity under statistical dependence by matrix-based system reliability method. Struct Saf 31(2):148–156

Song J, Ok S-Y (2010) Multi-scale system reliability analysis of lifeline networks under earthquake hazards. Earthq Eng Struct Dyn 39(3):259–279

Wang Z, Song J (2016) Cross-entropy-based adaptive importance sampling using von Mises-Fisher mixture for high dimensional reliability analysis. Struct Saf 59:42–52

Wei P, Lu Z, Tian L (2013) Addition laws of failure probability and their applications in reliability analysis of structural system with multiple failure modes. Proc Inst Mech Eng, Part C: J Mech Eng Sci 227(1):120–136

Xie G-H, Zhang J-S, Liu R-G (2013) Application of matrix-based system reliability method in complex slopes. J Cent South Univ 20:812–820

Yang DY, Teng JG, Frangopol DM (2015) Efficient adaptive importance sampling for time-dependent reliability analysis of structures. Second International Conference on Performance-based and Lifecycle Structural Engineering (PLSE 2015), December 9–11, Brisbane, Australia

Zhang YC (1993) High-order reliability bounds for series systems and application to structural systems. Comput Struct 46(2):381–386

Global Buckling Reliability Analysis of Slender Network Arch Bridges: An Application of Monte Carlo-Based Estimation by Optimized Fitting

Anders Rønnquist and Arvid Naess

Abstract Network arch bridges are extremely slender bridge structures with a very efficient load-carrying structure. This configuration can carry loads that are several times greater than traditional tied-arch bridges with vertical hangers. These bridges are seen as an attractive structure due to their slenderness, which potentially also make them vulnerable to global system buckling. Thus, the buckling reliability of network arch bridges is here further investigated with emphasis on geometric and load uncertainties. In principle, the reliability of structural systems can be accurately predicted by standard Monte Carlo simulation. This method has several attractive features for structural system reliability. One is that the system failure criterion is easy to control, almost irrespective of the complexity of the system. However, the computational cost involved may be prohibitive for highly reliable structural systems if standard Monte Carlo simulation is used. In this chapter a recently developed enhanced Monte Carlo method has been applied for calculating the reliability. This method drastically reduced the computational burden of the standard Monte Carlo approach and thereby made it practically feasible to estimate the reliability of the bridge against buckling.

1 Introduction

The concept of network arch bridges has been continuously developed for almost 60 years and has been used for road bridges (Larsen 2012), as well as train crossings (Brunn et al. 2004). By optimizing the hanger slope configuration of the

A. Rønnquist
Department of Structural Engineering, Norwegian University of Science and Technology, 7491 Trondheim, Norway
e-mail: anders.ronnquist@ntnu.no

A. Naess (✉)
Centre for Ships and Ocean Structures & Department of Mathematical Sciences, Norwegian University of Science and Technology, 7491 Trondheim, Norway
e-mail: arvid.naess@ntnu.no

P. Gardoni (ed.), *Risk and Reliability Analysis: Theory and Applications*,
Springer Series in Reliability Engineering, DOI 10.1007/978-3-319-52425-2_3

network, the structure can be designed with a significantly lower steel weight; 50% reduction compared to other similar tied-arch bridges with vertical hanger is reported by Tveit (1987, 2006).

Network arch bridges are tied-arch bridges with inclined hangers having multiple intersections. The tie configuration follows the arch but with a much larger radius of curvature. This type of arch bridge design is thoroughly described and investigated in several papers by Tveit (1987, 2006, 2011). The inclined hangers are well suited to distribute bending moments and shear forces to the upper and lower chord, similar to a truss. This can be compared to tied-arches with vertical hangers, where the bending moment and shear forces are relatively large and decisive in the design. Thus, for network arch bridges bending moments in the transverse direction are more important than in the longitudinal direction. This property is one of the main conditions in designing some of the world's most slender bridges.

In recent years, the structural assessments of new and existing structures have included probabilistic methods to get a broader insight into the structural behavior over time. Reliability tools have been shown to be a valuable contribution in the decision-making process. For all structures, either already existing or yet to be built, and perhaps especially for large civil engineering structures, these tools can be used to evaluate different alternative methods and scenarios, as discussed by Faber (2001).

The improvement of our ability to assess the structural condition of large infrastructure systems during their life span has become an important issue to be addressed at the present time. This importance is partly due to the ever-increasing number of infrastructures reaching their final stage of design life and partly due to changing loads and nonfulfillment of maintenance, rendering physical signs of wear and tear. Results from these observations will ultimately necessitate major decisions regarding our existing and future infrastructure. Questions about whether to invest in upgrading existing structures to extend service life, or rather to replace dilapidated old structures with new, will have to be answered. Regardless of the alternative selected, major investments must be made in the immediate future to uphold today's standard and to cover future demands.

The solution to realistic structural system reliability problems is generally exceedingly difficult to obtain through conventional reliability methods, such as the first order reliability method or second order reliability method (FORM or SORM), (Madsen et al. 1986; Melchers 1999). The main reason is the high number of limit state functions and basic random variables that may be required to define the problem. The system failure event in a realistic case may be defined by a complex combination of failure modes; in general, as a combination of series and parallel systems. The failure criteria are also very often associated with nonlinear structural behavior, requiring computationally demanding numerical approaches, such as the nonlinear Finite Element (FE) analysis, to accurately assess the structural capacity, which is the situation for the example bridge in this chapter.

At least in principle, the reliability of complex structural systems can be accurately predicted by standard Monte Carlo simulation (Shinozuka 1972). If the failure criterion can be represented explicitly in terms of the basic random variables,

then it is relatively easy to evaluate the system failure criterion for each outcome of these random variables, almost irrespective of the complexity of the system and the number of variables. However, the system failure probabilities are typically of rather small magnitude, and the computational cost involved in the Monte Carlo simulation may therefore be prohibitive due to the large sample needed for robust estimation. If numerical approaches have to be used to assess the structural capacity, as mentioned above, the reliability problem might become intractable if efficient techniques, such as the response surface mthod (RSM), were not used (Bucher and Most 2008).

A new Monte Carlo based method for system reliability estimation aimed at reducing the computational cost was recently proposed by Naess et al. (2009). It exploits the regularity of tail probabilities to set up an approximation procedure for the prediction of the far tail failure probabilities, based on the estimates obtained by Monte Carlo simulations at more moderate probability levels. The method was first applied to small structural systems (Naess et al. 2009) and later to complex systems involving several thousand limit state functions and basic random variables (Naess et al. 2011). It was shown that the method provides good estimates for system failure probability with low to moderate computational cost. In this study the method is used to estimate the failure probability of global system buckling of a network arch bridge represented by a finite element (FE) structural model. Of particular interest has been to test the method for sudden failure modes which demands very low probability of failure magnitudes. The combination of low probabilities of failure together with a structural model including several numerical steps in the structural analysis will give noticeable calculation times, which then easily becomes a major issue. An important goal is therefore to show that the method offers a uniquely attractive approach to structural reliability analysis of realistic and complex engineering reliability problems.

2 Network Arch Bridge

In the present investigation an enhanced Monte Carlo simulation method is introduced to assess the system buckling reliability of a slender network arch bridge due to traffic loads. For all slender structures geometric imperfections are of special interest and their effect on the global system must be thoroughly investigated. Thus, for the presented case study four global geometric imperfections are introduced as basic random variables, width, length, height and the arch out of plumbness, see (a–d) in Fig. 1.

Furthermore, the arch tube member geometric cross-section properties are also introduced as random variables. These are the four main steel arch members' outer radii together with corresponding thicknesses, which leads to eight more basic variables. The four arch members are the wind portal frame columns, given as the

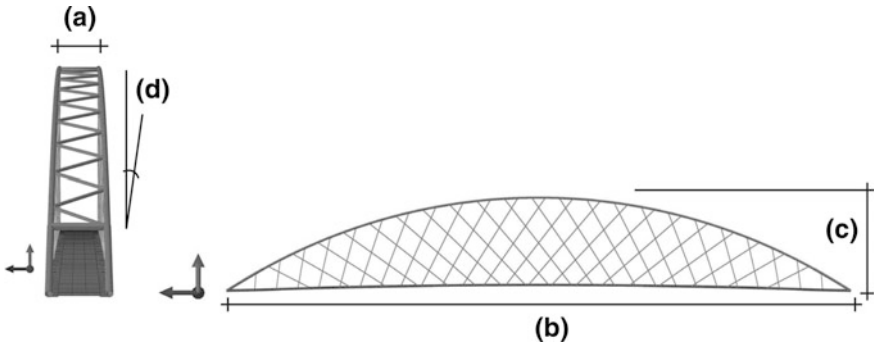

Fig. 1 Geometric imperfections introduced as basic random variables; **a** width, **b** length, **c** height and **d** out of plumbness

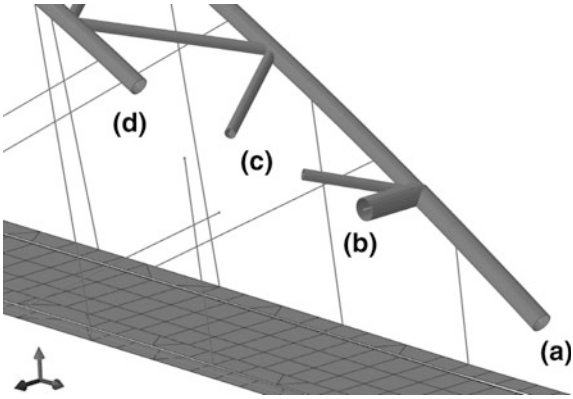

Fig. 2 Network arch steel members; **a** main arch below wind portal frame girder, **b** wind portal frame girder, **c** diagonal wind bracing and **d** main arch above wind portal frame girder

lower part of the arch (a in Fig. 2), wind portal frame girder (b in Fig. 2), wind bracing (c in Fig. 2) and the remaining arch members above the wind portal frame (d in Fig. 2). Hence, the variables shown in Figs. 1 and 2 constitute the 12 basic random variables of the system buckling reliability analysis.

All geometric random variables are assumed to be uncorrelated and normally distributed with the mean values as nominal values (i.e., the dimensions given on drawings). The coefficients of variation (CoV) given in Table 1 are chosen from the guidelines given by JCSS (2001) for arch parameters, within acceptable production tolerances (commonly given as fractions), and from Li and Sun (2011) for steel member parameters. Even though the CoVs are seemingly small their contribution cannot be neglected due to the high desired global buckling reliability. Note that due to small CoVs, it is not necessary in practice to truncate the random variables to avoid negative values.

Table 1 Coefficients of variation (CoV) for basic random variables

Random variables	CoV
Tube outer radius, r	2.5%
Tube thickness, t	2.5%
Arch length, L	1/10000
Arch height, H	1/1000
Arch width, W	1/1000
Arch out of plumbness, θ	$1.5^{o}/_{oo}$

2.1 Model Uncertainty

Most civil engineering models are based on a hypothesis regarding the physical understanding supported by empirical relations between different variables. The chosen models will introduce uncertainties due to lack of knowledge as well as inherent physical uncertainties. This lack of precision, combined with deliberate simplifications, will give model predictions differing from the real output. To account for this in the present analysis, a model parameter, I, is introduced, representing the model uncertainties for the load and structural capacity. This parameter is then treated as an additional random variable in the system.

A systematic method for choosing and quantifying the material and load model uncertainties can be found in the Reliability-Based Classification publication by the Road Directorate, Ministry of Transportation in Denmark (Scholten et al. 2004). The structural capacity model uncertainty is accounted for by the random variable I_m, introduced as a multiplicative factor in the limit state function. This variable is assumed to be lognormally distributed with a mean value of 1.0 and a coefficient of variation V_{Im}, given by:

$$V_{I_m} = \sqrt{V_{I_1}^2 + V_{I_2}^2 + V_{I_3}^2 + 2(\rho_1 V_{I_1} + \rho_2 V_{I_2} + \rho_3 V_{I_3})} \tag{1}$$

cf. Scholten et al. (2004). The coefficients of variation, V_{Ii}, and the correlation coefficients, ρ_i, are determined, based on the assumption of three main contributions ($i = 1, 2, 3$). These represent the accuracy of the computational model, uncertainty in determining material parameters and the precise identity of materials. For the present example, selections are made for the structure as a whole. To be able to select values as described by Scholten et al. (2004), the three uncertainty levels must be assessed. The following three choices are made: the uncertainty of the computational model accuracy is set to normal; the uncertainty in determining material parameters is set to medium, and the uncertainty related to the identity of materials used in construction is set to normal. These assumptions are used in accordance with Scholten et al. (2004). The coefficients of variation and correlation coefficients are found to be $V_i = 0.06$ and $\rho_i = 0.0$ for all three uncertainties.

To quantify the load model uncertainty, a model is used similar to that described by Scholten et al. (2004). The uncertainty in the computational model for loads is

then accounted for by introducing a normally distributed stochastic variable, I_f, by adding it to the limit state function. Thus, the model uncertainty for traffic loading is found by assuming a medium uncertainty in accordance with Scholten et al. (2004), rendering a zero mean value and a coefficient of variation $V_{If} = 0.15$.

2.2 Traffic Load

The traffic load represents one of the most significant contributions to the total value of the external actions to be considered in the ultimate limit state analysis. For the reliability analysis we need a traffic load model of a given return period that will represent one of several possible load cases. The traffic loads on bridges are, by their nature, of great complexity due to the high randomness covering a large range of structures and traffic situations. Hence, traffic loads are often modeled conservatively. This is a natural consequence of the significant variation of the loads, also due to their site dependency, especially for long spanning bridges (Getachew 2003).

The uncertainty in the traffic load depends on several statistical variables involved in describing the problem. Typical variables considered are type of vehicle, interval between vehicles, gross weight of each vehicle, gross weight distribution to axles, spacing between extreme axles and between any pair of axles, total external length of the vehicle, velocity, daily intensity of vehicles per lane, and the density of vehicles over the road, as described by Bez and Bailey (1993), see also Nowak et al. (2010). In most cases there is no common analytical expression for the total load distribution and the correlation coefficients between all these variables.

Bez and Bailey (1993) showed that the traffic load is highly dependent on the type of vehicles as well as their individual load situations. They identified relations between characteristic load and maximum load effects, and they showed that the axle load distributions for both loaded and unloaded vehicles are skew distributions. Thus, under the assumption that these distributions represent extreme events, they may be assumed to be Gumbel distributed. Furthermore, if a complete description of the different cases is sought, then a multimodal distribution must be used. Several similar studies are also reported by Getachew (2003), which show that a detailed description of the traffic load can be modeled by the sum of several assumed independent contributions.

The extreme values of the traffic load are assumed to be Gumbel distributed, where the described load case is assumed to represent a uniformly distributed line load. The design rules given by the Norwegian Public Road Administration (NPRA) do not clearly state what the return period of the characteristic traffic load is. However, the Eurocode NS-EN 1991–1992 (2010) is based on a return period of 1000 years.

To establish the load distribution for the present network arch bridge, the characteristic design load given in Norway by the NPRA is used. This is done to determine the necessary site-specific probabilistic load model for the reliability

analysis. The characteristic load is also compared with the expected distribution of the weight of a 250 m queue that is registered and thoroughly described by Getachew (2003). For the load model, a Gumbel distribution and a return period equal to 1000 years are assumed. To find the Gumbel parameters the estimates of the mean and standard deviation for the extreme traffic load are needed. This is obtained by fitting the available data from the two load distribution assumptions above, giving a mean and standard deviation equal to $m_q = 3.5$ N/m and $\sigma_q = 1.1$ N/m. Finally, the Gumbel distribution, *F(x),* given by Eq. (2) can be established by the location parameter α and the scale parameter δ from their relation to the above mean μ and standard deviation σ:

$$F(x) = \exp\{-\exp[-\delta(x-\alpha)]\} \tag{2}$$

where $\delta = \pi/\sigma\sqrt{6}$ and $\alpha = \mu - 0.57722/\delta$, rendering the scale parameter $\delta = 1.17$ and the location parameter $\alpha = 3.0$ (relations as used by Xiangyang and Guanghui 2010).

2.3 Buckling Analysis of Network Arch Bridges

Buckling occurs when a small increase in the axial compressive force in the structure causes a sudden outwards displacement as the loading reaches a certain critical level. Buckling does not depend solely on the applied stress reaching a critical level, but rather it depends on variations of component dimensions and the overall geometry of the structure. This may lead to sudden collapse of the structure without any initial warning.

Shallow arches are more likely to have non-linear pre-buckling behavior, with substantial deformation prior to the buckling. This effect needs to be considered and allowed for. If a classic buckling analysis is used without including these effects, the predicted critical load may be erroneous. Thus, it is important to include a pre-loading step in the analysis to allow for possible non-linear response. In the present case study bi-linear material strength is included, as well as geometric stiffness. This will allow for the correct pre-buckling deformation to occur and the correct stiffness to be established. Hence, this is to ensure a correct elastic buckling load, which is used in the structural reliability analysis. Such effects are investigated for in-plane buckling and have been shown to be of significance (Pi and Bradford 2002; Romeijn and Bouras 2008). Therefore, they are also assumed to be significant for the out-of-plane buckling. It is shown by Pi and Bradford (2002) that significant pre-buckling deformations may, especially for shallow arches, introduce a significant decrease in the buckling resistance and thus lead to overestimation of the buckling load.

For buckling of network arches, the stiffness due to the hangers will be of special importance and significantly influence the estimated buckling capacity. The hanger configuration will be much more favorable for network arches than tied-arches with

vertical hangers. If the network arch tie remains straight, the arch will have in-plane buckling modes that can be found from simple columns supported by flexural springs, as pointed out by Schanack (2009). Simplified solutions may then be found from in-plane arch calculation methods as used by Moen et al. (2011), Pi and Bradford (2002) and Schanack (2009). However, it can be seen in the present investigation that the out-of-plane buckling modes can also be expected. Here, in the case of a large network arch bridge with great slenderness, the symmetric as well as the asymmetric out-of-plane buckling modes may appear.

In-plane buckling modes for network arches were further investigated by Schanack (2009). It showed that buckling load for network arches will depend on the arch bending stiffness, the number of hangers as well as the arch to hanger angle. However, the bending stiffness and deflection of the tie were shown to have less effect on the global buckling load.

3 Efficient System Reliability Estimation

Consider a structural system for which several failure modes may be defined, and assume that each failure mode is represented by a safety margin,

$$M_i = G_i(X_1, \cdots, X_n) \tag{3}$$

where G_i, $i = 1, \ldots, m$, is the limit state function defining the safety margin M_i as a function of a vector $\boldsymbol{X} = [X_1, \ldots, X_n]^{\mathrm{T}}$ of n basic random variables. The limit state function G_i can be a rather complicated function of the random vector $\boldsymbol{X}$. In many cases a closed-form equation is not known, and the evaluation of G_i requires computationally demanding numerical models, e.g., non-linear FE models. Failure in mode i of the system is assumed to occur when $M_i = G_i(\boldsymbol{X}) \leq 0$. For a basic system of m failure modes in series, the system failure probability is defined by:

$$p_f = P\left[\bigcup_{i=1}^{m} (M_i \leq 0)\right] \tag{4}$$

To overcome the computational cost typically involved in the estimation of the failure probability of a system of several failure modes, the method proposed by Naess et al. (2009) formulates the system safety margins in the following way:

$$M_i(\lambda) = M_i - \mu_i(1 - \lambda) \tag{5}$$

where M_i is a system safety margin, given by Eq. (1), and $\mu_i = E[M_i]$ is the mean value of M_i. In general, the true mean value μ_i is unknown and therefore a sample mean estimate $\hat{\mu}_i$ is used, which is typically very accurate due to the size of the sample. The parameter λ assumes values in the interval $0 \leq \lambda \leq 1$, and its effect on the system failure probability may be interpreted as a scale factor. The original

system in Eq. (3) is obtained for $\lambda = 1$, and for $\lambda = 0$ the system is highly prone to failure, as the mean value of the system safety margins is $E[M_i(0)] = 0$. For small to intermediate values of λ, the increase in the system failure probability is sufficiently high to obtain accurate estimates of the failure probability by standard Monte Carlo simulation at moderate computational cost.

As proposed by Naess et al. (2009), for practical applications it is assumed that the failure probability is a function of λ that can be written as:

$$p_f(\lambda) \approx q \exp\{-a(\lambda - b)^c\} \text{ for } \lambda_0 \leq \lambda \leq 1 \tag{6}$$

for a suitable choice of the parameters *a, b, c, q,* and a suitable value of the tail marker λ_0. A practical aspect of the method is therefore to identify a value for λ_0 so that Eq. (6) represents a good approximation of $p_f(\lambda)$ for $\lambda \in [\lambda_0, 1]$. This is briefly discussed in the next section.

The specific class of parametric functions adopted in Eq. (6) is, strictly speaking, based on an underlying assumption that the reliability problem has been transferred to normalized Gaussian space where a FORM or SORM (or similar) type of approximation would work for the transformed limit state functions. However, when the basic random variables have "exponential" type of distributions, like Weibull, normal, lognormal, Gumbel, there is no need to make a transformation to normalized Gaussian space. Instead, the failure probability can be estimated by using the proposed method in the original space and adopt Eq. (6) there. This is the procedure adopted in this chapter.

The practical importance of the approximation provided by Eq. (6) is that the desired failure probability $p_f = p_f(1)$ can be obtained from values of $p_f(\lambda)$ for $\lambda < 1$. This is the main concept of the estimation method proposed by Naess et al. (2009). It is easier to estimate the failure probabilities $p_f(\lambda)$ for $\lambda < 1$ accurately than for the target value $\lambda = 1$. This is because $p_f(\lambda)$ for $\lambda < 1$ are larger and hence require fewer simulations and therefore incur less computational cost. Fitting the approximating function for $p_f(\lambda)$ given by Eq. (6) to the estimated values of the failure probability obtained by Monte Carlo simulation with $\lambda < 1$ will then allow us to estimate the desired failure probability by extrapolation.

It may be noted that the method described above is, in fact, very different from an importance sampling method. While importance sampling is vulnerable to the dimension of the space of basic random variables, this is not at all the case with the method described here, cf. Naess et al. (2011).

3.1 Monte Carlo-Based Reliability Estimation by Optimized Fitting

To find the four parameters q, a, b and c in Eq. (6), which defines an optimal fit between the parametric function and the estimated values of the failure probability

obtained by Monte Carlo simulation, an optimized fitting procedure was suggested by Naess et al. (2009).

A sample of size N of the basic random variable vector $\boldsymbol{X} = [X_1, \ldots, X_n]^T$ is assumed. Now, let $N_f(\lambda)$ denote the number of outcomes for which failure of the system is verified. Then an empirical estimate of the failure probability is given by:

$$\hat{p}_f(\lambda) = \frac{N_f(\lambda)}{N} \cdot \tag{7}$$

The coefficient of variation of this estimator is approximately

$$C_v\left(\hat{p}_f(\lambda)\right) \approx \frac{1}{\sqrt{p_f(\lambda)N}} \cdot \tag{8}$$

A fair approximation of the 95% confidence interval for the value $p_f(\lambda)$ can be obtained as $\mathrm{CI}_{0.95}(\lambda) = [C^-(\lambda), C^+(\lambda)]$, where,

$$C^{\pm}(\lambda) = \hat{p}_f(\lambda)\left[1 \pm 1.96 C_v\left(\hat{p}_f(\lambda)\right)\right] \cdot \tag{9}$$

As proposed by Naess et al. (2009), the optimal fit between the empirical estimates of the failure probability and the parametric function in Eq. (6) can be carried out by minimizing the following mean square error function with respect to the four parameters q, a, b and c in Eq. (6) at the log level:

$$F(q,a,b,c) = \sum_{j=1}^{M} w_j\left[\log \hat{p}_f\left(\lambda_j\right) - \log q + a\left(\lambda_j - b\right)^c\right]^2 \tag{10}$$

where $0 < \lambda_0 < \lambda_1 < \cdots < \lambda_M < 1$ denotes the set of λ values, where the failure probability is empirically estimated, and w_j denotes a weight factor putting more emphasis on the more reliable data points (Naess et al. 2009). A Levenberg-Marquardt least squares optimization method is then used.

For a simple estimation of the 95% confidence interval for the predicted value of the desired failure probability provided by the optimal curve, the empirical confidence band is reanchored to the optimal curve. Further, the optimal curve-fitting procedure is applied to the reanchored confidence band boundaries. The fitted curves, extrapolated to the level of interest, will determine an optimized confidence interval of the estimated desired failure probability. This procedure seems to give confidence intervals that are consistent with the results obtained by a nonparametric bootstrapping method (Karpa and Naess 2013). As a final point, it was verified that the predicted value is not very sensitive to the choice of λ_0, provided that it is chosen with some care. In practice this can be done by comparing the predicted values for a range of λ_0 values.

4 The Brandanger Network Arch Bridge—A Case Study

The above formulation is used to study the Brandanger Bridge (shown in Fig. 3) situated in the western part of Norway and claimed to be the world's most slender arch bridge (Tveit 2011).

The design of the bridge was suggested to the Norwegian Public Road Administration in 2004 and was finally opened on the 4th of November 2010. In the present case study an earlier-suggested version of the bridge design is used with some further modifications.

The bridge, as shown in Fig. 4, consists of a main span length of 220 meters with two parallel upper chord steel arches (max height of 33 meters) and a lower chord concrete slab tie suspended by 44 hangers on each side. Between the arches there is a simple wind portal frame and diagonal wind bracing. The arch as well as the wind bracing consists of steel tube elements, while the inclined hangers are made of high-strength steel cables. The bridge deck is constructed of pre-stressed concrete with a total width of just 7.6 m, creating an extremely light and slender structure.

The steel tube elements of the arch have two different cross sectional dimensions along their length, separated by the wind portal frame girder, as previously shown in Fig. 2. The cross sections on either side of the arch from the bridge deck up to the

Fig. 3 The brandanger bridge

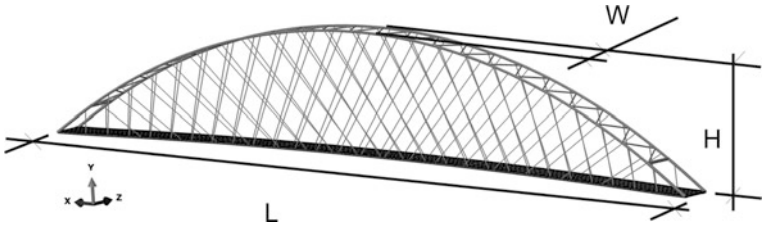

Fig. 4 Overall dimensions of the network arch bridge: width W = 7.6 m, height H = 33 m and span length L = 220 m

Table 2 Material properties used in the finite element analysis

Component	Density (kg/m^3)	Young's modulus (GPa)	Yield stress (MPa)
Structural steel	7850	210	355
Steel hangers	7850	170	1550
Concrete bridge deck	2200	28.7	35

wind bracing has an outer diameter to thickness $D/t = 711/40$. The remaining cross sections from the wind bracing to the top of the arch has an outer diameter to thickness $D/t = 711/35$. A typical dimension of the concrete slabs is 250 mm center thickness, while the first outer 1.1 m on each side has a thickness of 400 mm. The main material parameters are listed below in Table 2.

4.1 Structural Response by Finite Element Analysis

The Brandanger Bridge was subjected to extensive numerical analyses during the preliminary design phase. These included linear and non-linear static analyses, buckling analyses, as well as dynamic time domain analyses. The FE model for the present analyses is built up of beam elements with tubular cross sections for the arch and solid circular cross sections for the hangers, as well as shell elements for the lower chord bridge deck.

To model the steel network arch in the FE model, a 3-node quadratic Timoshenko beam formulation was used within Abaqus/Standard for all arch tube members, wind bracing and wind portal frame girder. For the network hangers the 2-node linear Timoshenko beam formulation was chosen. These beam formulations allow for transverse shear deformation, and the beam may be subjected to large axial strains. The lower chord bridge deck is represented with a simple first order 4-node, general purpose, conventional shell element with reduced integration formulation within Abaqus/Standard. This element includes thickness changes and transverse shear deformations, allowing for large rotations and finite membrane strains.

The FE analysis procedure distinguishes between general non-linear steps and linear perturbation steps. The general non-linear analysis is defined as sequential events, where one state of the model at the end of the step will provide the initial state for the start of the next. The linear perturbation analysis provides the linearized response of the model about the state reached at the end of the last non-linear step. At each general step in the analysis the procedure accounts for the nonlinear effects from large displacements and deformations. These effects are of special interest in the present buckling investigation, where it is important to account for the pre-buckling deformation as geometric imperfections.

4.2 Global System Buckling Reliability Estimation

The present study evaluates the system buckling limit state of the Brandanger Bridge. The analysis includes the derived simplified ultimate traffic load model and the FE linear perturbation eigenvalue solutions of the pre-loaded structure. In structural design, the system failure is defined by the buckling load exceedance of the lowest estimated structural buckling capacity. In addition to the first buckling mode, the system reliability is also considered for the two following higher modes, to investigate changes in the predicted failure probabilities as well as the uncertainty of the estimated values. It will be of special interest to see how sensitive prediction of the probability of failure is as the desired values decrease since the enhanced Monte Carlo method is an optimized fitting and extrapolation method.

Each evaluation of the system buckling capacity is preceded by pre-loading the system with the structural self-weight and the nominal traffic loads. The initial load geometric stiffness is introduced already in the pre-loading step and not only used in the perturbation step. This will allow for any nonlinear geometric contributions of the pre-loaded structure to be accounted for. Hence, the updated structural geometry from the deformed structure will add to any introduced imperfections. The traffic loads are defined by the Norwegian Public Road Administration and given in their design guide, Handbook 185 (2009). This definition includes a uniformly distributed line load of 9 kN/m over a 3 m width and three pairs of point loads, each given as 210 kN and separated in the longitudinal directions by 6 and 2.5 m. The uniformly distributed traffic load is also introduced as the perturbation load pattern used in the solution.

The limit state function of the structural reliability, G, is defined by the stability failure considered for the three first buckling modes. Hence, the general bifurcation buckling limit state function can be formulated as:

$$G(\mathbf{X}_R, P_{cr}, P_\gamma, I_m, I_f) = P_{cr}(P_B(\mathbf{X}_R), I_m) - P_\gamma\left(P_T(\alpha, \beta), I_f\right) \tag{11}$$

The limit state, G, is a function of the global system buckling capacity P_{cr} and the load estimated from the traffic action P_γ including the model uncertainties I_m and I_f of the structural capacity and load model (as previously defined). The structural basic random variables, $\mathbf{X}_R$, which are discussed in Sect. 2, and given by the vector:

$$\mathbf{X}_R = [t_{arch}, t_{bracing}, t_{port.\text{column}}, t_{port.\,girder}, D_{arch}, D_{bracing}, D_{port.\text{column}}, D_{por.girder}, H, W, L, \theta], \tag{12}$$

where t is the thickness, and D is the diameter of tubular cross sections, while H, W, L and θ are the four global imperfections, width, length, height and the arch out of plumbness, respectively. The buckling capacity, P_B, is calculated by the perturbation load, $P_{pert,}$ and the buckling load factor BLF found from the FE-analysis, and given as:

$$P_B(\mathbf{X}_R) = P_{pert} \cdot BLF(\mathbf{X}_R), \tag{13}$$

and the traffic load is estimated from the simplified Gumbel distributed traffic load with the corresponding distribution parameters α and δ:

$$P_T = P_T(\alpha, \delta). \tag{14}$$

All parameters used in the structural analysis that are not included as basic random variables will remain as deterministic values only. These are parameters, such as material properties, remaining structural cross sections as well as the geometric distribution of the load.

Typically, the failure mode of the buckling phenomenon will occur without any warning. Hence, for civil engineering structures high reliability is required (Scholten et al. 2004). To achieve the desired accuracy of the estimated failure probability, a high number of simulations are needed. This means that even if the FE analyses can be efficiently organized and quickly executed, they will still demand a large computational effort to reach the minimum number of necessary observed failures within the simulated population.

The probability of failure for the three first buckling modes is calculated, where the first two are out-of-plane buckling modes and the third is an in-plane buckling mode with significantly higher buckling load factor than the first two. The probability of failure is calculated for all three modes, using the limit state function in Eq. (11). Typical buckling modes corresponding to the three first modes are shown in Figs. 5, 6 and 7.

It is of interest to further explore the computational time reduction and show how the enhanced Monte Carlo method can be used on computationally demanding structural systems, using reasonable calculation efforts. A comparison is presented between simply employing the enhanced Monte Carlo simulation strategy directly with a procedure combining the Response Surface Method (RSM) (Bucher 2009)

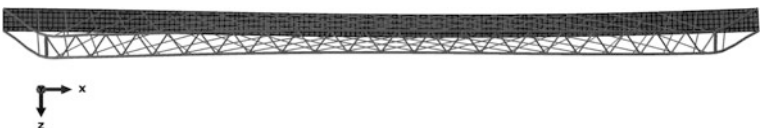

Fig. 5 First estimated buckling mode

Fig. 6 Second estimated buckling mode

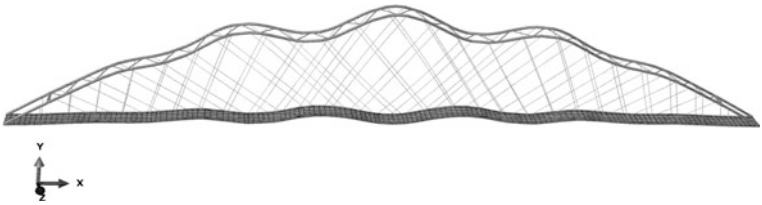

Fig. 7 Third estimated buckling mode

and the enhanced Monte Carlo method. In the former, a relatively large number of FE simulations is used that will require a substantial amount of calculation time. The latter strategy will only need a fraction of the FE simulations and will consequently achieve a considerable reduction in the calculation time. The final sample needed for the enhanced Monte Carlo method when using the response surface method is quickly sampled from the fitted response surface.

The RSM strategy to approximate the true process can be used with different complexity and accuracy. A common approach is to introduce a first- or second-order polynomial function with a set of predictor values corresponding to the number of parameters used to account for main effects as well as predictor values for the interaction and possible quadratic terms. The response surface parameters are then determined, using multiple regression analysis as described by Bucher and Most (2008) and Carley et al. (2004).

The second-order model is widely applied as a useful approximation to the true response surface in a restricted region. The size of the problem also depends on the set of observations used to determine the regression parameters relative to the introduced basic random variables. There are several possible schemes to improve efficiency. For example, an augmented Latin Hypercube Sampling can be used, where the standard deviation of each basic random variable has been doubled to obtain better mapping of the response space of interest with a reasonable number of observations. In the present analysis a simple Monte Carlo simulation method is used, demanding a high number of observations as a basis for the different response surfaces.

The general form of a complete second-order polynomial model for n basic random variables X_i for the regression analysis is given by

$$\eta = p_o + \sum_{i=1}^{n} p_i X_i + \sum_{j=1}^{n} \sum_{i=1}^{n} p_{ij} X_i X_j + \varepsilon, \tag{15}$$

where p_i and p_{ij} are the regression parameters. Finally, the random error term ε may be assumed to be uncorrelated with the basic random variables and normally distributed with zero mean and constant (but unknown) variance. The number of parameters needed for a full quadratic polynomial is given by:

$$v = n(n+1)/2 + n + 1 \tag{16}$$

The present model has $n = 12$ basic random variables, which gives the number of parameters to $v = 91$.

A set of response values with corresponding predictor values needs to be generated. The present investigation includes 12,000 randomly chosen FE-calculations as observations to determine the 91 parameters of the response surface. Figure 8 shows scatter diagrams for each response surface of the different buckling modes. The three diagrams together with the accompanying adjusted coefficient of multiple determination value for all three buckling modes, all found to be $R^2_{adj} > 0.95$, indicate good agreement for the prediction made from the response surface.

As described, the estimation of the probability of failure for $\lambda < 1$ is done by employing the Monte Carlo simulation with or without the response surface. Each system buckling analysis was computed by the bifurcation analysis in Abaqus/Standard. The computational time for a single analysis is approximately 10 s on a standard laptop computer, including time to retrieve results and initiate a new analysis. The total number of simulated system buckling analyses was 3.88×10^5 executed in 6 parallel processes, rendering approximately 8 days and nights of computational time. This was deemed to be a reasonable calculation effort to invest in the present problem using Monte Carlo simulations. The 12,000 observations needed to establish the response surfaces represents approximately one day (6 h) of FE simulations as used in the Monte Carlo estimation. The response surface is then used to simulate a new set of 7.5×10^5 observations to calculate the empirical probability of failure for $\lambda < 1$, which requires about a minute on a standard laptop computer.

The predicted failure probability and reliability index at $\lambda = 1$, given by the fitted optimal curves and the re-anchored and optimized 95% confidence interval, are given in Table 3 for the Monte Carlo simulation and Table 4 for the response surface simulations. The corresponding diagrams for the probability of failure, as predicted by Eq. (6) for λ-values up to one, are shown pairwise in Figs. 9, 10 and 11 mode by mode for the MC- and RSM-simulations. Each of the Figs. 9, 10 and 11

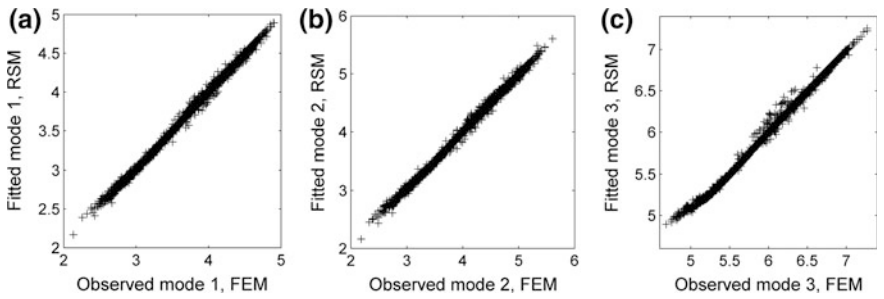

Fig. 8 Scatter plot of obtained results from the FEM procedure, compared to the predicted results by the RSM procedure; **a** buckling mode 1, **b** buckling mode 2, and **c** buckling mode 3

Table 3 Network arch bridge probability of failure for global system buckling, estimated with the three first buckling modes by Monte Carlo simulations

	Pf–	*Pf*	*Pf*+	*β*-	*β*	*β*+	*Δβ*
Mode 1	3.48×10^{-7}	6.46×10^{-7}	10.3×10^{-7}	4.75	4.84	4.96	0.21
Mode 2	1.75×10^{-7}	3.98×10^{-7}	7.09×10^{-7}	4.82	4.94	5.09	0.27
Mode 3	0.29×10^{-9}	1.68×10^{-9}	4.33×10^{-9}	5.76	5.91	6.20	0.44

Reliability index given by $\beta = -\Phi(P_f)$

Table 4 Network arch bridge probability of failure for global system buckling estimated with the three first buckling modes by response surface simulations

	Pf–	*Pf*	*Pf*+	*β*–	*β*	*β*+	*Δβ*
Mode 1	2.73×10^{-7}	4.46×10^{-7}	6.66×10^{-7}	4.83	4.91	5.01	0.18
Mode 2	1.32×10^{-7}	2.45×10^{-7}	3.96×10^{-7}	4.94	5.03	5.15	0.21
Mode 3	0.10×10^{-9}	0.56×10^{-9}	1.65×10^{-9}	5.91	6.09	6.37	0.46

Reliability index given by $\beta = -\Phi(P_f)$

also includes the values established from the fitting procedure, *q, a, b*, and *c* defined for each $p_f(\lambda)$ to be used together with Eq. (6).

The results in Tables 3 and 4 show the failure probabilities for different buckling modes. Table 3 includes results from only FE-simulations and the enhanced Monte Carlo method, while Table 4 includes results from a reduced number of simulations to establish a response surface and then again the enhanced Monte Carlo method. As expected, the probability of failure variations is greater for higher buckling modes than lower modes. In Table 4 the reliability index is slightly higher than in Table 3, indicating a slightly more reliable structure. This is partly due to the good representation of the response surface at the region of interest and partly due to the slightly higher number of samples used from the response surface. This shows that the number of FE simulations chosen for the response surface is sufficient, as also shown by the scatter plots in Fig. 8. If more simulations from the response surface were run, the confidence intervals could also be further reduced. In Figs. 9, 10 and 11 the width of the 95% confidence interval for $\lambda = 1$ can be seen. In Tables 3 and 4 the mean estimated failure probability is presented together with the confidence interval.

To elucidate the increase in the variation of the failure probability of higher modes, a column presents the difference between the reliability indices corresponding to the upper and lower confidence interval limits. This variation clearly increases with increasing buckling modes. Furthermore, comparisons between results within each mode (Tables 3 and 4) indicate that the variation is less for the response surface estimations. The empirically estimated failure probabilities ($\lambda < 1$) oscillate less for RSM than for Monte Carlo simulations only, which are seen when comparing the different diagrams in Figs. 9, 10 and 11. This seems reasonable since the investigated system instability problem is quite smooth over the region covered by the response surface. Hence, even though the response surface is based on a

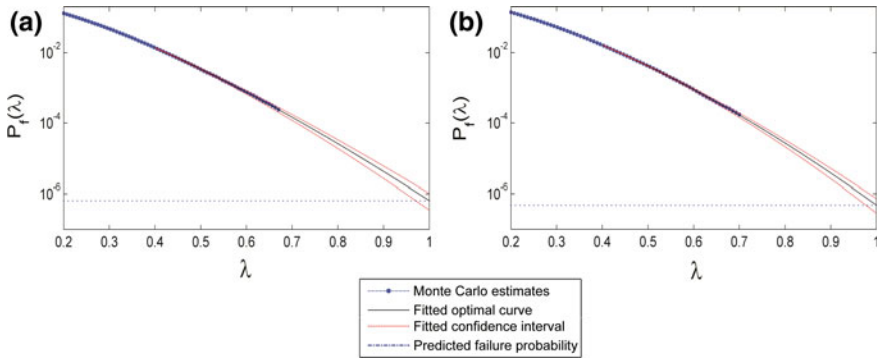

Fig. 9 **a** Log plot of failure probability with buckling mode 1, MC. Parameters of the fitted optimal curve: $q = 0.210$, $a = 15.222$, $b = 0.128$ and $c = 1.322$, **b** Log plot of failure probability with buckling mode 1, MC from RSM. Parameters of the fitted optimal curve: $q = 0.365$, $a = 14.143$, $b = 0.024$ and $c = 1.550$

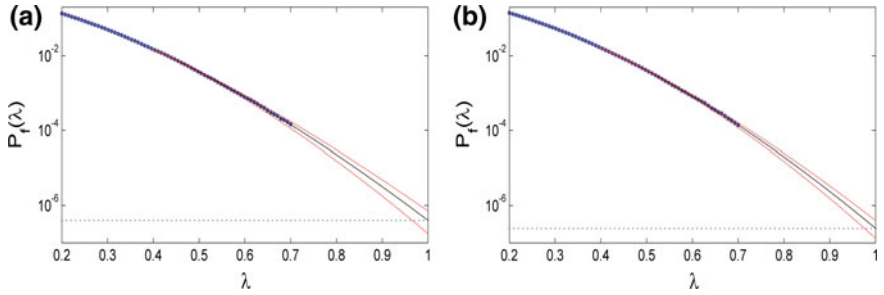

Fig. 10 **a** Log plot of failure probability with buckling mode 2, MC. Parameters of the fitted optimal curve: q = 0.321, a = 14.729, b = 0.052 and c = 1.487, **b** Log plot of failure probability with buckling mode 2, MC from RSM. Parameters of the fitted optimal curve: q = 0.399, a = 14.229, b = 0.003 and c = 1.648

reduced number of FE-simulations, they cover sufficiently detailed behavior of the process, and the final sampling is somewhat larger than the first. It can be seen in all three modes, which show slightly lower predicted failure probabilities ($\lambda = 1$). This demonstrates that the estimation of system probability of failure for a large civil engineering structure can be sufficiently well determined by a moderate number of simulations, the use of a response surface, if based on an appropriate mapping of the response space obtained by FE calculations, and employment of the enhanced Monte Carlo method.

All estimated probabilities of failure comply with the expected desired probability of failure commonly used in designing civil engineering structures, depending on the consequences of failure and failure modes. For example, in Annex B of Eurocode NS-EN 1990 (2008), three different desired reliabilities are given as 10^{-5}, 10^{-6} and 10^{-7}.

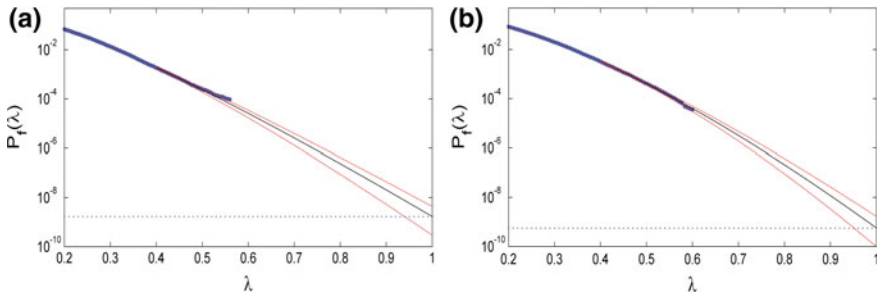

Fig. 11 **a** Log plot of failure probability with buckling mode 3, MC. Parameters of the fitted optimal curve: $q = 0.078$, $a = 22.518$, $b = 0.189$ and $c = 1.161$, **b** Log plot of failure probability with buckling mode 3, MC from RSM. Parameters of the fitted optimal curve: $q = 0.192$, $a = 23.087$, $b = 0.108$ and $c = 1.414$

5 Conclusions

In the present investigation the global buckling reliability of a network arch bridge is assessed by an efficient enhanced Monte Carlo-based method. It has been shown that the method provides good estimates of the reliability of the structural global system with reasonable computational effort. The method is used in the present study to estimate global system buckling failure probability, which allow for possible nonlinear pre-loaded geometric stiffness and linearized buckling, all solved by the FE software Abaqus/Standard. The low values of the probability of failure are in agreement with the desired values in design codes, with a failure event without warning and with great consequences, commonly set to 10^{-7}. The enhanced Monte Carlo method proved to be an efficient technique for reducing the number of simulations needed to reach acceptable levels of uncertainty of the estimated reliability index. The computational time can be drastically reduced by the use of a response surface as a basis for the necessary number of Monte Carlo simulations needed for an accurate estimation of the probability of failure. Hence, the investigation offers a method which not only reduces the calculation cost but also makes it possible to achieve the low failure probability demand of design codes, considering large complex structures with sudden failure modes. This is illustrated by results in both the computational time and uncertainty of the final probability of failure, given by the confidence intervals.

References

Bez R, Bailey S (1993) Traffic load models for bridge evaluation. In: Second international conference on bridge management: surrey, England, 9 pp

Brunn B, Schanack F, Steinmann U (2004) Network arches for railway bridges. In: Advances in assessment, structural design and construction. CIMNE, Barcelona

Bucher C (2009) Computational analysis of randomness in structural mechanics, vol 3., Structures and infrastructures book seriesTaylor & Francis Group, London, UK
Bucher C, Most T (2008) A comparison of approximate response functions in structural reliability analysis. In: Probabilistic engineering mechanics, vol 23, pp 154–163
Carley KM, Kamneva NY, Reminga J (2004) Response surface methodology. In: CASOS technical report (centre for computational analysis of social and organizational systems) CMU-ISRI-04-136, 26 pp
Faber MH (2001) Reliability of exceptional structures. In: World congress safety of modern technical systems, Cologne, Germany
Getachew A (2003) Traffic load effects on bridges, statistical analysis of collected and Monte Carlo simulated vehicle data. Doctoral thesis at KTH-Stockholm, 162 pp
Handbook 185 (2009) Bruprosjektering. In: Norwegian public road administration, 302 pp. ISBN 82-7207-591-1
JCSS (2001) Probabilistic model code—Part 1–3. In: Joint committee on structural safety. ISBN 978-3-909386-79-6
Karpa O, Naess A (2013) Extreme value statistics of wind speed data by the ACER method. J Wind Eng Ind Aerodyn 122:10
Larsen R (2012) The network arch—a slender and transparent bridge structure. In: Nordic steel construction conference, Oslo, Norway, pp 249–258
Li K, Sun K (2011) Stochastic parameters analyze for steel highway bridge members. In: Geotechnical special publication No. 219GSP, ASCE, pp 184–189
Madsen HO, Krenk S, Lind NC (1986) Methods of structural safety. Prentice-Hall, Englewood Cliffs, NJ. ISBN 0-13-579475-7
Melchers RE (1999) Structural reliability analysis and prediction, 2nd edn. Wiley, Chichester, UK
Moen C, Shapiro E, Hart J (2011) Structural analysis and load test of a 19th century iron bowstring arch-truss bridge. J Bridge Eng:31. doi:10.1061/(ASCE)BE.1943-5592.0000341
NS-EN1991-1-2:2003 + NA (2010) Eurocode 1: actions on structures—Part 2: traffic loads on bridges
NS-EN1990:2002 + NA (2008) Eurocode: basis of structural design
Naess A, Leira BJ, Batsevych O (2009) System reliability analysis by enhanced Monte Carlo simulation. Struct Saf 31:349–355
Naess A, Leira BJ, Batsevych O (2011) Reliability of large structural systems. Probab Eng Mech 28:164–168
Nowak A, Lutomirska M, Sheikh Ibrahim FI (2010) The development of live load for long span bridges. Bridge Struct 6(1, 2):73–79
Pi YL, Bradford BU (2002) In-plane stability of arches. Int J Solids Struct:105–125
Romeijn A, Bouras C (2008) Investigation of the arch in-plane buckling behavior in arch bridges. J Construct Steel Res 64:1349–1356
Schanack F (2009) Berechnung der Knicklast in Bogenebene von Netzwerkbögen. Bautechnik 86 (5):249–255
Scholten C, Enevoldsen I, Arnbjerg-Nielsen T, Randrup-Thomsen S, Sloth M, Engelund S (2004) Reliability-based classification of the load carrying capacity of existing bridges. In: Road directorate—ministry of transport Denmark. ISBN 87–7923-774-6
Shinozuka M (1972) Monte Carlo solution of structural dynamics. In: Computers and structures. Pergamon Press, Great Britain, vol 2, pp 855–874
Tveit P (1987) Considerations for design of network arches. J Struct Eng 113(10):2189–2207
Tveit P (2006) Optimal network arches for coastal regions. In: International conference on bridges Dubrovnik, Croatia, pp 721–728
Tveit P (2011) The network arch. bits of manuscript in February 2011 after Lectures in 50 Countries. Internet edition, Grimstad, Norway. http://home.uia.no/pert/index.php/Home
Xiangyang W, Guanghui Z (2010) Bridge reliability analysis based on the FEM and Monte Carlo method. In: International conference on intelligent computation technology and automation, Changsha, China, pp 891–894

Review of Quantitative Reliability Methods for Onshore Oil and Gas Pipelines

Smitha D. Koduru and Maher A. Nessim

Abstract Onshore pipelines provide a low-risk alternative for shipping oil and gas in large quantities. Over the past two decades, it has become standard industry practice to use risk models as a part of pipeline maintenance programs as a tool to rank pipeline segments for repair, identify significant failure threats, and guide operational and integrity management decisions. In recent years, pipeline failures have garnered increased attention from the public resulting in a greater scrutiny of the design, construction, and maintenance practices used by pipeline operators. This provided an incentive for pipeline operators and regulators to embrace a more rigorous and effective risk assessment and management strategies than those common in the oil and gas industry. The objective of this chapter is to provide a review the state-of-the-art reliability methods applicable to onshore oil and gas pipelines. As a part of the review, common threats to pipeline integrity are discussed in the context of how they increase the demand and/or decrease the capacity of the pipeline to withstand applied loads. An overview of the probabilistic models, limit states and reliability methods employed for the assessment of pipeline failures is presented.

1 Introduction

Onshore oil and gas pipelines form a critical part of the energy infrastructure (Yusta et al. 2011). In the United States alone, there are over 400,000 miles (over 700,000 km) of gas and liquid transmission pipelines transporting petroleum products over long distances (PHMSA 2016). In Europe, there are over 140,000 km of gas transmission pipelines (EGIG 2015). On a per unit volume basis, onshore buried pipelines transport petroleum products more safely than road and rail transportation (Wang and Duncan 2014).

S.D. Koduru (✉) · M.A. Nessim
C-FER Technologies (1999) Inc, Edmonton, Canada
e-mail: s.koduru@cfertech.com

P. Gardoni (ed.), *Risk and Reliability Analysis: Theory and Applications*,
Springer Series in Reliability Engineering, DOI 10.1007/978-3-319-52425-2_4

As a part of pipeline maintenance programs, it is common industry practice to employ qualitative risk assessments. The focus of pipeline maintenance programs is to identify high risk locations and prioritize remedial actions based on risk ranking. This focus has resulted in qualitative risk assessment approaches that are primarily relative. These methods assign a risk index for each factor contributing to a pipeline risk and evaluate an overall risk index that is a weighted combination of individual risk factors (Muhlbauer 2004). However, recent failures attributed to an aging pipeline network and the potential resulting consequences, e.g. San Bruno gas pipeline explosion 2010 (NTSB 2015a, b), Kalamazoo river oil spill 2010 (NTSB 2012), have attracted increased attention to pipeline risk assessment models (PHMSA 2016). While qualitative models are easier to employ, they have some inherent limitations for applications involving complex risk interactions. These imitations include a high sensitivity of the rankings to subjective factors that are used to weight the different parameters affecting the risk estimate. Furthermore, qualitative model results are system-specific, which implies that they cannot be used to compare the risk associated with different pipelines or develop risk acceptance criteria consistent with other engineered systems (e.g. nuclear facilities, and aviation).

Due to the above-mentioned limitations of qualitative methods, quantitative risk assessment methods have attracted growing interest in the pipeline industry. Such quantitative methods have been recently adopted for land use planning around buried pipelines in Europe (IGEM/TD/2 2009, NEN 2006). In Canada, quantitative risk assessments and reliability design methods are included as a non-mandatory part of the pipeline design code (CSA Z662 2015).

Risk is quantified as the product of probability of failure and the expected consequence expressed in quantifiable measures, including but not limited to dollar cost, number of fatalities, spill volumes. The objective of this chapter is to review the state-of-the-art in reliability methods as applied to onshore oil and gas pipelines. The primary emphasis of the review is on rigorous quantitative methods used to estimate the probability of occurrence of pipeline failures. The following sections include an explanation of how quantitative reliability methods are applied to pipelines and a definition of the hazards and limit states that are specific to pipelines. Sources of uncertainty, probabilistic models and reliability methods available to estimate the probability of occurrence are discussed next. The chapter ends with a brief overview of the use of reliability analysis in quantitative risk assessments, and suggestions for potential future research by identifying the technical gaps in current methods.

2 Problem Definition

Pipelines are linear assets buried in varying terrain conditions, which are subject to varying hazards dependent on the nature of the terrain. Furthermore, pipelines are subject to capacity deterioration mechanisms over their design life, and require

periodic maintenance actions either to repair or replace the deteriorated pipe. This results in temporal variations in the probability of occurrence of pipeline failures. Depending on the land use, development, and environment around the pipeline, the consequences of a failure also vary with location and time. Therefore, pipeline risk is often annualized and expressed on a per unit length basis.

2.1 Limit States

The primary failure mode of a pressurized pipeline is a release of the product being transported, which is often referred to as a 'Loss of Containment' (LoC). Based on the magnitude of the release and the extent of associated consequences, a failure is typically classified as a small leak or a burst. For natural gas and low vapour pressure (LVP) pipelines, small leaks, which are referred to as "pinholes leaks", do not lead to significant life safety consequences and may lead to limited environmental consequences in the case of LVP pipelines. Bursts can lead to significant safety and environmental consequences, and can be further classified into large leaks and ruptures based on whether or not the initial opening extends axially. A large leak occurs if the resulting opening does not extend beyond the location of initial burst. By contrast, a rupture results from an axial extension of the failure zone by fracture or plastic collapse, leading to more severe consequences than a large leak. Serviceability failure modes, such as local buckling or denting are also relevant limit states that can impinge on pipeline operations but do not lead to loss of containment.

According to the reliability based design and assessment (RBDA) methodology, included in Annex O of CSA Z662 (CSA 2015), limit states for natural gas pipelines are categorized as:

- Ultimate limit states, which include large leaks and rupture and result in significant safety consequences;
- Leakage limit states, which is a leak from an opening of less than 10 mm leading to limited loss of containment that has no significant consequences;
- Serviceability limit states, which include pipeline damage due to yielding, ovalization, denting, excessive plastic deformation and local or global buckling, can lead to service interruption and require repair, but do not lead to product release. Detailed analyses and implementation of monitoring and maintenance programs are required to ensure that the serviceability limit states do not progress to loss of containment.

A detailed list of load cases and the associated limit states and failure modes during the design life of a pipeline have been developed by Nessim and Zhou (2005) and are available in Annex O of CSA Z662 (CSA 2015). The limit state functions associated with the failure modes described above, can result from either a force-controlled or a deformation-controlled loading mechanism depending on the

type of hazard. For example, internal pressure loading imposes a force-controlled demand, for which the limit state function is defined in terms of either applied stress or force. Conversely, natural hazards such as ground movements impose deformation-controlled demand on a buried pipeline, for which the limit state function in terms of applied strain. Limit state functions are generally expressed as,

$$g(\mathbf{x}, t) = r(\mathbf{x}, t) - s(\mathbf{x}, t) \tag{1}$$

where g is the limit state function defined as a function of a vector of $\mathbf{x}$ random variables and time t, while r is the distribution for capacity and s is the distribution for demand, which can also be defined as functions of other basic random variables, such as pipe geometry and material properties, and can also be a function of time for time-dependent limit states such as corrosion and other deterioration mechanisms. The probability of failure is then defined as,

$$\mathrm{P_f}(g \leq 0) = \int .. \int_{(g \leq 0)} f(\mathbf{x}) \mathrm{dx} \tag{2}$$

where $f(\mathbf{x})$ is the joint probability distribution function of the random variables included in the vector $\mathbf{x}$.

Internal pressure, or hoop stress due to internal pressure are examples of force-controlled processes. Capacity to resist internal pressure is often reduced by damage to the pipeline by accidental impacts and progressive deterioration mechanisms such as corrosion and cracks. The pressure-containing capacity of the pipeline at a defect location (either due to impact or deterioration) is modelled analytically using semi-empirical models validated by test data. The calculated capacity is uncertain due to uncertainties in the input model parameters including defect sizes, material properties and pipe dimensions, as well as uncertainties regarding the accuracy of the model itself. Failure mechanisms specific to the nature of loading due to a given hazard and the associated limit state functions are presented in the later sections.

2.2 Hazards

Hazards that cause pipeline failures are typically referred to in the pipeline industry as 'threats' to pipeline integrity. The ASME code for pressure piping (ASME B31.8S 2014) divides the threats into nine categories based on their time dependent nature. These are:

- Time-dependent
  - internal corrosion
  - external corrosion
  - stress corrosion cracking (SCC)

- Stable
  - manufacturing-related defects
  - welding/fabrication related defects
  - equipment failures
- Time-independent
  - third-party/mechanical damage
  - incorrect operational procedures
  - weather-related and outside force.

Other pipeline codes and pipeline incident databases identify further subcategories or merge some of the above-mentioned categories. For example, the pipeline incident[1] database developed and maintained by the Pipeline and Hazardous Materials Safety Administration (PHMSA) of the United States Department of Transportation, divides the incident causes into the following six categories:

- corrosion
- excavation damage
- incorrect operations
- material/weld/equipment failure
- other outside force damage
- all other causes.

In Europe, the European Gas Pipeline Incident Data Group (EGIG) divides the initial causes of pipeline incidents into six categories, namely:

- corrosion
- external interference
- construction defect/material failure
- hot tap made by error
- ground movement
- other or unknown.

In this review, we consider the following broad categories based on the similarities either in the failure mechanisms or in the underlying damage:

- Excavation damage
- Corrosion
- Cracks
- Natural hazards
- Human error
- Other.

Excavation damage occurs due to construction activity over a buried pipeline. This is variously categorized as third-party/mechanical damage, excavation

[1]Incident is defined as any event that led to loss of containment.

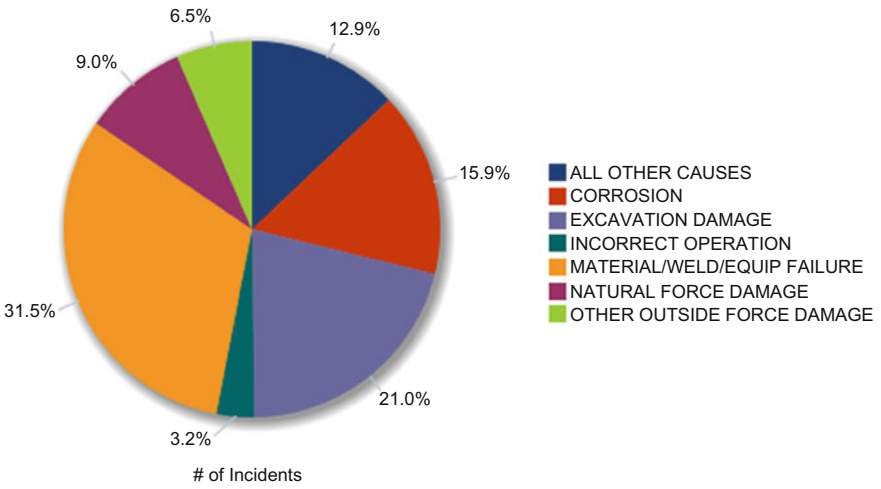

Fig. 1 All reported incidents causes breakdown for onshore gas transmission pipelines (1996–2015) (PHMSA 2016)

damage, and external interference Cracks in the seam weld of a pipeline may occur during the welding/fabrication process, and as such material/weld/equipment failures and construction defect/material failures are combined in a single category in this review. While SCC has a unique growth mechanism, it is included under cracks as the failure mechanisms leading to LoC and the models used to analyze them are similar for all axial cracks including SCC. Incorrect operational procedures, and hot tap made by error, would fall under the human error category of hazards.

Based on incident records for onshore gas transmission pipelines from PHMSA (PHMSA 2016), material/weld/equipment failures, excavation damage, and corrosion rank as the three highest contributing causes over the 20 year period from 1996 to 2015. Figure 1 shows the proportion of incidents due to all the categories considered. EGIG data (EGIG 2015) over the 43 year period from 1970 to 2013 shows external interference as a leading cause followed by corrosion and construction defect/material failure for gas transmission pipelines. Figure 2 shows the failure frequencies associated with the categories considered by EGIG. The PHMSA (PHMSA 2016) incident database for onshore liquids pipelines shows that material/weld/equipment failure, corrosion and incorrect operations are the three highest contributing causes over the 20 year period between 1996 and 2015. Figure 3 shows the proportion of incidents from all threat categories for onshore liquids pipelines from the PHMSA incident database.

Because excavation damage and corrosion are the leading causes of pipeline failures, extensive research is available on methodologies that can be used to calculate the probabilities of failure for these two threats. In the following sections, detailed limit state functions, sources of uncertainty, and reliability methods associated with each hazard are presented.

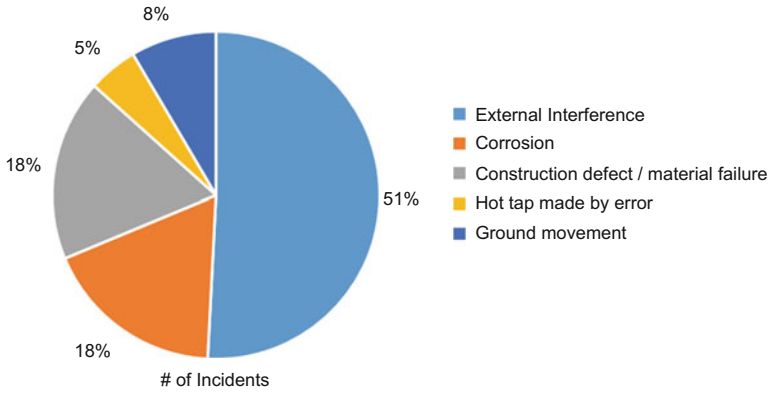

Fig. 2 All reported incidents causes breakdown for onshore gas transmission pipelines (1970–2013) (EGIG 2015)

3 Excavation Damage

Assuming that the occurrence of an equipment impact is a statistically independent event from all other impact events, probability of failure due to excavation damage is expressed as

$$P_{fi} = P(\text{Hit})\, P(\text{LoC}|\text{Hit}) \tag{3}$$

where P_{fi} is the probability of failure due to excavation damage, P(Hit) is the probability of a buried pipeline being impacted by an excavator, and P(LoC| Hit) is the probability of loss of containment conditioned on the pipeline being impacted. When the probabilities of occurrence and failure in Eq. (3) are sufficiently small and the occurrence of more than one failure event is negligible, all the probabilities are approximated by the rate. A possible failure mechanism due to excavation equipment impact is puncture, which is defined as failure due to punching shear and membrane action of the pipe wall (Chen and Nessim 1999). If puncture does not occur, a dent, gouge, or gouged-dent may result from the impact. Following the removal of impact load, gouges and dent-gouges may fail due to the loss of resistance to internal pressure. If immediate failure does not occur, fatigue crack initiation around dents, fatigue growth of gouges and dent-gouges due to pressure cycling could lead to subsequent failures that result in loss of containment. Failure mechanisms due to puncture and damage features such as gouges, and dent-gouges that lead to immediate loss of containment are considered in estimating the probability of failure in this review. Delayed failures due to fatigue are not included.

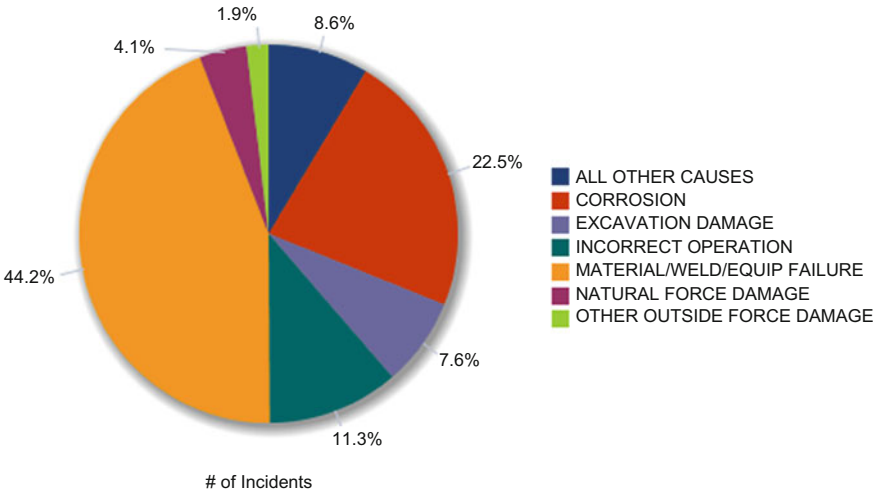

Fig. 3 All reported incidents causes breakdown for onshore hazardous liquids transmission pipelines (1996–2015) (PHMSA 2016)

3.1 Uncertainties

The sources of uncertainty associated with computing the probability of impact on a buried pipe include:

- the rate of excavation activity along the pipeline Right of Way (ROW)
- the depth of cover over the buried pipeline which prevents the intended excavation from reaching the pipeline
- the effectiveness of other preventative or protective measures such as, permanent markers indicating the location of the buried pipe, on-call systems that mark the exact location of the pipe based on prior notification of excavation activities, and protective barriers such as concrete slabs.

To estimate the probability of failure given an impact, sources of uncertainty include the direction and magnitude of the impact force. Depending the type and size of the excavator, the magnitude of the impact force and associated surface area can vary within a wide range. Therefore, failure probability estimation models account for uncertainties in the excavator type, weight, size of the excavator bucket teeth, and model errors associated with deriving the impact force from these parameters (Chen and Nessim 1999). In the case of failure due to dent-gouges and gouges, uncertainties in the size of the damage feature must also be considered. Apart from the uncertainties specific to the occurrence and magnitude of impact, uncertainties exist in the magnitude of internal pressure, and the pipeline parameters affecting the capacity to maintain containment after an impact.

3.2 Models

Fault tree analysis has been widely used to estimate equipment impact rates. The occurrence of excavator impact on a pipeline is often assumed to be a homogeneous Poisson process over the duration of interest and accordingly, annual impact rates over a specified length of pipe are computed based on the activity rate surrounding the pipeline ROW.

Chen and Nessim (1999) have developed one of the first fault tree models that are currently widely used in North America to estimate equipment impact frequencies on a buried pipeline. Basic event probabilities required for this fault-tree model were estimated based on the results of an industry survey. In recent years, other fault tree models to estimate the probability of failure of preventive measures were developed by Chen et al. (2006) and Toes and Rogers (2010). Figure 4 shows a condensed version of the fault-tree and the primary factors affecting the impact frequencies adapted from Chen et al. (2006). The model by Toes and Rogers (2010) accounts for the effect of concrete slab, designed according to the specifications of UK Standard (IGEM 2013), as a protective barrier on the probability of impact.

To estimate the probability of failure given an impact, failure mechanisms due to puncture, burst of gouge or dent-gouge damage features are modelled. Table 1 provides a summary of references describing the capacity models developed to resist each failure mechanism. Random variables associated with limit state functions for each failure mechanism are described in the remainder of this section.

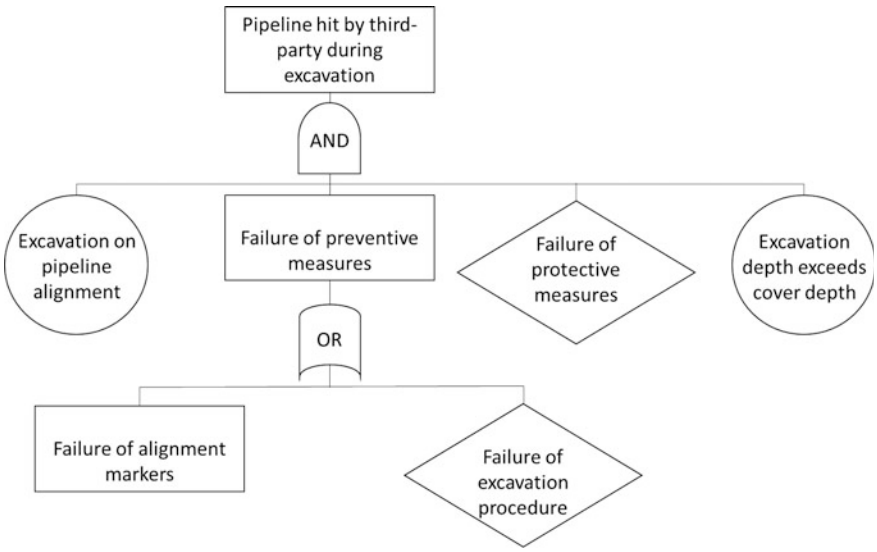

Fig. 4 Simplified fault-tree model for equipment impact (adapted from Chen et al. 2006)

Table 1 Capacity models for equipment impact failure modes

Failure mechanisms	References for models
Puncture	Driver and Playdon (1997) Driver and Zimmerman (1998)
Dent-gouge	EPRG Model (Roovers et al. 2000) CSA Model (Nessim and Zhou 2005)
Gouge	Linkens et al. (1998)
Rupture	Cosham et al. (2008) Nessim and Zhou (2005)

3.2.1 Puncture

The limit state function for puncture, g_p, is defined in the form shown in Eq. (1), with r_p as the capacity to resist the puncture, and q as the demand due to the impact force. Capacity models for puncture can be found in Driver and Playdon (1997) and Driver and Zimmerman (1998). The random variables considered in the semi-empirical function for puncture resistance are:

- diameter
- wall thickness
- length of the indenter
- width of the indenter
- tensile strength of pipe material
- model error of the puncture resistance model.

Impact force is modelled as a function of the excavator mass by Roovers et al. (2000). Chen and Nessim (1999) considered impacts by both excavators and backhoes, and derived the probability distribution of the impact forces as,

$$F(q) = P(\text{excavator})\, F(q|\text{excavator}) + P(\text{backhoe})\, F(q|\text{backhoe}) \tag{4}$$

where F(.) indicates the cumulative distribution function, P(excavator) is the probability of the excavation equipment being an excavator, and P(backhoe) is the probability of the excavation equipment being a backhoe. Empirical models for the impact forces were derived such that force due to an excavator is a function of the excavator weight, while force due to a backhoe is a function of the excavation depth. The probability distribution of the impact force was generated by considering both the variability in the equipment type and the model errors associated with the semi-empirical equations used to calculate the impact force. An alternative approach is to derive the probability distribution from available excavators in the industry and historical data for the dent sizes. Driver and Zimmerman (1998) model the impact force as a shifted gamma distribution based on an industry survey, and Cosham et al. (2008) provide Weibull distribution parameters for the impact force based on records of the dent sizes, pipe geometries and grades in UK Onshore Pipeline operators Association (UKOPA) fault database.

3.2.2 Dent-Gouge

The limit state function for dent-gouge failure, g_{dg}, is a stress-based failure criteria modelled in the form of Eq. (1), with σ_c as the hoop stress capacity and σ_p as the hoop stress demand due to internal pressure. Typically, loading due to internal pressure is either considered to be deterministic and equal to the maximum allowable operating pressure (MAOP), or characterized as a time-independent random variable based on the pressure cycling history. Critical hoop stress resistance is primarily a function of defect dimensions and pipe parameters. Therefore, the random variables considered in calculating the critical hoop stress capacity are:

- gouge depth
- gouge length
- dent depth
- wall thickness
- diameter
- yield strength
- material toughness.

The most commonly employed methods for calculating the critical hoop stress capacity are the semi-empirical models recommended by the European Pipeline Research Group (EPRG) (Roovers et al. 2000) and Nessim and Zhou (2005). The model developed by Nessim and Zhou (2005) is based on previous work by Linkens et al. (1998), Hopkins et al. (1992), and Francis et al. (1997). Both methods are based on elastic-plastic fracture mechanics analysis and assume that the gouge acts as a part-wall or through-wall surface crack and may fail either by brittle fracture or plastic collapse. On the basis of available test data, it is assumed that the effect of the dent is to introduce a bending stress in the pipe wall that does not by itself lead to an immediate loss of containment (Francis et al. 1997). In evaluating σ_p, the dent-gouge is assumed to be aligned with the longitudinal axis of the pipe. If the variability in the dent-gouge direction is included, σ_p is calculated as the stress demand normal to the gouge direction. Nessim and Adianto (2014) account for the variability in the direction of dent-gouge through a calibrated factor of 0.65 of hoop stress.

In contrast to puncture resistance, model error is ignored for dent-gouge resistance in Annex O of CSA Z662 (CSA 2015), Cosham et al. (2008) and Nessim and Adianto (2014). Nessim and Zhou (2005) indicate that model error in estimating dent-gouge resistance is small enough to be ignored. They also mention that if the gouge is assumed to be aligned with the pipe longitudinal axis the conservatism in calculating the applied stress due to this assumption is greater than the variability in the model error. For reliability assessment of dent-gouge damage, Cosham et al. (2008), and Goodfellow et al. (2014) provide Weibull distribution parameters for length and depth of gouge defects. Nessim and Adianto (2014) employ a lognormal distribution for gouge length, and a Weibull distribution for the gouge depth.

3.2.3 Gouge

The limit state function for burst failure of a gouge defect, g_g, is also stress-based with σ_g as the capacity to resist internal pressure at the gouge location and σ_h as the demand due to hoop stress. Capacity to resist hoop stress in the presence of a gouge is evaluated assuming failure due to plastic collapse and not a brittle fracture (Roovers et al. 2000; Cosham et al. 2008). Random variables associated with this limit state function are:

- gouge depth
- gouge length
- wall thickness
- diameter
- yield strength.

3.2.4 Rupture

The limit state functions for puncture for burst of a dent-gouge or gouge model failures that can result in large leaks or rupture. If the probability of failure due to rupture is required, two different formulations may be used, one based on the defect length and the other based on the hoop stress. The limit state function for rupture based on defect length criteria is defined by Cosham et al. (2008) as

$$g_r = l_{cr} - l_g \tag{5}$$

where l_{cr} is the critical length defined as a function of the hoop stress, pipe dimensions and material properties, but does not include the effect of material toughness. An alternative limit state function for $g_{r,}$ based on the rupture stress is of the form in Eq. (1) (CSA 2015). It defines the capacity, σ_{cr} as the critical stress derived based on the formulation in Kiefner et al. (1973) and the demand, σ_h, as the applied hoop stress. In addition to the pipe diameter and wall thickness, σ_{cr} is a function of pipe material properties such as yield strength, fracture toughness, and defect dimensions including depth and length.

3.3 Methods to Estimate the Probability of Failure

The probability of failure due to an impact is a union event of all three failure mechanisms. Therefore, probability of burst is

$$P(\text{LoC}|\text{Hit}) = P(g_p \leq 0) \text{U } P(g_{dg} \leq 0) \text{U } P(g_g \leq 0) \quad (6)$$

If all gouge defects are conservatively assumed to be dent-gouges, then only puncture and dent-gouge limit states are required. Therefore Nessim and Zhou (2005) recommended using only the puncture and dent-gouge limit states. In practice, the probability of failure due to puncture is often ignored as the probability of failure is dominated by burst of a dent-gouge. Therefore, Nessim and Adianto (2014) considered only the dent-gouge limit state function to estimate the probability of failure. Cosham et al. (2008) also ignore the puncture failure mechanism and consider that the failure due to dent-gouge and gouge defects are mutually exclusive, and therefore, the probability of failure due to each limit state function is evaluated separately.

Due to the presence of multiple limit states, the probability in Eq. (6) is commonly determined using the Monte-Carlo Sampling (MCS) method. The Second-Order Reliability Method (SORM) has also been employed to calculate the probability of puncture separately (Chen and Nessim 1999). Cosham et al. (2008) employed direct integration for independent failure probability calculations associated with the dent-gouge and gouge limit states. If the leakage limit state is evaluated separately, the probability of large leak as a result of a dent-gouge is,

$$P(\text{Leak only}|\text{dent} - \text{gouge}) = P(g_{dg} \leq 0) \cap P(g_r > 0) \quad (7)$$

Therefore, the required probability becomes a system reliability problem with two limit states. In order to reduce the computational complexity and avoid the numerical convergence problems that can arise from the use of FORM and SORM, MCS is commonly employed to estimate the probability shown in Eq. (7).

4 Corrosion

Corrosion is a time-dependent deterioration mechanism that reduces the pipe capacity to resist the hoop stresses imposed by the internal pressure. For a given segment of pipeline, failure due to corrosion occurs if any corrosion feature within the segment fails during a specified time interval. Therefore, probability estimation must account for the probability of occurrence of corrosion, the spatial distribution of corrosion features on pipeline surface, the size and growth rates of corrosion features and the likely failure mechanism for each feature. Current In-Line Inspection (ILI) technologies can detect internal and external corrosion features with a high degree of reliability. ILI tools provide estimates of the density and size of corrosion features. However, uncertainties regarding these parameters are not completely eliminated due to the practical limitations of ILI tools in detecting and sizing corrosion features.

4.1 Uncertainties

The uncertainties considered in evaluating the probability of failure due to corrosion are:

- Density of corrosion features
- Initial size of each corrosion feature as defined by its depth, length, and width
- Growth rate of each corrosion feature within the time period of interest.
- Pipeline characteristics affecting the capacity to resist failure under the operating pressure

When ILI tools are employed to detect corrosion features and estimate their sizes, the following uncertainties in tool measurements are included:

- Probability of detection based on feature size
- Probability of correct classification of a corrosion defect
- Depth and length sizing error of the detected corrosion features
- Density and sizing of the undetected features.

4.2 Models

Models required to estimate the failure probability of corrosion features are categorized as occurrence models, growth models, and limit states, as described below.

4.2.1 Occurrence Models

Different types of occurrence models exist for internal and external corrosion, as the underlying corrosion processes and mitigation strategies are different for the two types of corrosion. Internal corrosion occurs primarily due to a reaction between the product and the pipe and is influenced by the product composition, flow characteristics, and pipe profile. Protective measures against internal corrosion include addition of corrosion inhibitors to the product, running cleaning tools to remove deposits in pipe, reducing the water content in the flow and installation of protective liners. External corrosion occurs primarily due to an electro-chemical reaction between the soils surrounding a buried pipe. External coatings on the pipe surface and cathodic protection of the pipe with direct current between the pipe and a sacrificial anode are commonly employed as protective measures against the occurrence of external corrosion.

Models are available to determine internal corrosion rates as a function of water content and other condensates containing carbon dioxide (CO_2), hydrogen sulfide (H_2S), pipe profile, pH, temperature, pressure, velocity, and corrosion inhibitors. Kale et al. (2004) developed a probabilistic model that estimates the probability of

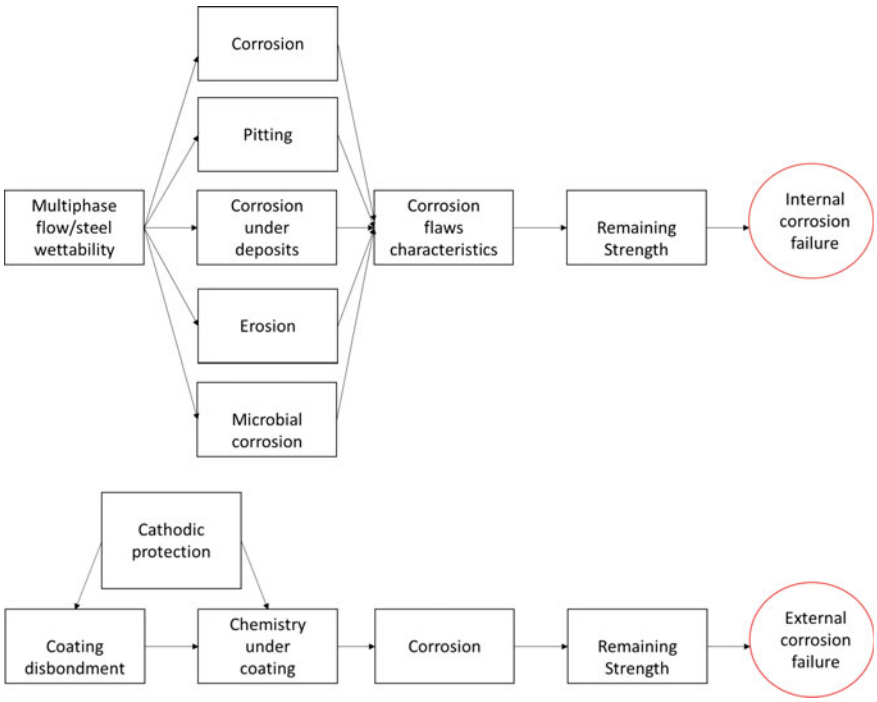

Fig. 5 Causal links for the development of bayesian networks for internal and external corrosion (Ayello et al. 2014)

corrosion at a given location accounting for uncertainties in the pipe elevation profile, the effects of corrosion inhibitors, as well as other pipeline-specific input parameters, such as temperature, pressure, velocity of the flow, and concentration of CO_2, O_2, and H_2S. A model uncertainty factor is also included in the model. The model identifies the most probable locations where corrosion damage is likely to exceed a specified depth threshold.

More recently, Ayello et al. (2014) and Shabarchin and Tesfamariam (2016) employed Bayesian network models to predict the initiation, growth and failure due to both internal and external corrosion. Figure 5 shows the causal links considered in estimating corrosion initiation for internal and external corrosion as adapted from Ayello et al. (2014). The detailed Bayesian network developed for internal corrosion considers the product type and flow characteristics, as well as possible deposits and erosion at pipe fittings such as valves and bends in pipe. The external corrosion Bayesian network considers the condition of the surface coating based on possible damage mechanisms such as excavation impacts, drainage of the surrounding soil due to seasonal rainfall and topography, and soil properties such as porosity, salinity and chemical properties.

Wang et al. (2015) developed a hidden Markov random field model to assess the presence of external corrosion based on a clustering approach.

This model correlates the density and location of external corrosion obtained from ILI tool inspection, with the soil characteristics surrounding the detected features. Based on this information, a random field model is used to predict external corrosion on the basis of soil characteristics such as soil resistivity, pH and salinity. This type of model is advantageous when ILI tools cannot be used for portions of a pipeline, but data regarding the corrosion rates and soil characteristics is available.

Recent developments in ILI technologies have resulted in high detection probability for most internal and external corrosion features on segments of pipelines that are suited for the use of ILI tools. This has resulted in a reduction in the uncertainty associated with corrosion density. However, the probability of detection depends on the size of the corrosion feature. Typically, the probability of detection is modelled as a deterministic exponential function of feature depth such that,

$$P_d = 1 - e^{rd} \tag{8}$$

where P_d is the probability of detection, d is the depth of the corrosion feature and r is a constant characterizing the detection capability of the ILI tool. Distributions for density and size of undetected defects are estimated based on the detected corrosion features and the probability of detection in Eq. (8). Lu et al. (2015) extended this approach by developing a log-logistic model for the probability of detection that depends not only on the feature depth but also on the feature length. As the probability of detection is modelled as a function of both feature length and depth, the probability of undetected features that are long and shallow or short and deep is estimated with improved accuracy. Although this approach was applied to SCC features by Lu et al. (2015), the methodology is also suitable for application to corrosion features.

4.2.2 Growth Models

Since corrosion is a time dependent process, generation of new features and growth of existing features must be considered for reliability evaluation. Occurrence models for internal and external corrosion often address corrosion generation and growth rates based on the same input parameters used to model corrosion initiation. Bayesian networks by Ayello et al. (2014) account of the growth of corrosion features in both depth and length. Miran et al. (2016) considered a power law function for the growth of a corrosion defect depth, and length.

Due to the low growth rate of corrosion features and the significant sizing error associated with ILI measurements, deterministic evaluation of generation and growth rates of individual corrosion features from successive ILI run data has been successful only for high growth rates and accurate corrosion depth estimates obtained from special processing of ILI tool signals. In most cases however, sizing error is large enough to dwarf the true growth rate for individual corrosion features

(Nessim et al. 2008). Therefore, it is standard practice to employ a time independent linear growth rate, which is modelled with a Weibull distribution (CSA 2015).

For pipelines with a high density of corrosion features, population-based growth rates were estimated from multiple ILI runs using hierarchical models (Dann and Maes 2015). This approach utilizes the incremental growth of the mean feature population depth between multiple ILI runs. If features of significant depth were removed due to maintenance actions between the ILI runs, the increment in the mean depth value will be negligible. Also, if new corrosion features with smaller depths are initiated between the ILI runs, the mean depth of the population in the second ILI run will be reduced, rendering this approach ineffective.

Hierarchical Bayesian models for corrosion growth using multiple ILI data were also developed by Al-Amin et al. (2012), and Zhang et al. (2015) in conjunction with stochastic process growth modelling. In these applications, detected features from each ILI run are matched to the features detected in other ILI runs. However, uncertainties in detection and sizing of corrosion features by ILI may lead to challenges in matching corrosion features from multiple inspections. For onshore pipelines, growth models using different stochastic processes are available in the literature. These are broadly divided as:

- Markov process: Hong (1999a, b) employed homogeneous and non-homogeneous Markov processes to estimate the growth of pitting corrosion. The Markov process models the transition states of feature size from one depth interval to a greater depth interval based on the current feature size. The transition probability for a given time interval is independent of the past transition probabilities. Therefore, knowledge of the current size of features will allow modelling of their growth to a critical feature size. More recently, Timashev and Bushinskaya (2015) applied a pure birth Markov process simultaneously to a set of corrosion features to estimate corrosion growth. This approach requires establishing transition probabilities, which are highly dependent on the pipe parameters and the surrounding corrosive environmental features.
- Gamma process: Zhang et al. (2012) and Qin et al. (2015) proposed a non-homogeneous gamma process for modelling corrosion growth. A hierarchical Bayesian model was developed to include the probability of detection, as well as the bias and variance in the depth sizing of the corrosion features. The parameters of the non-homogeneous gamma process growth model are updated based on the imperfect measurements of the same corrosion features with each new inspection.
- Inverse Gaussian process: Increments of corrosion depth are modelled as an inverse Gaussian distribution in this stochastic growth model. The model requires fewer prior distributions to model feature growth and measurement error and yet provides similar accuracy in predicting depth increments as the non-homogeneous Gamma process (Zhang et al. 2013). Similar to the process above, this approach requires feature matching from multiple inspections.

4.2.3 Limit States

For a given corrosion feature, the limit state function for small pin-hole leaks is,

$$g_{sl}(t) = w_t - d_{max}(t) \tag{9}$$

where $g_{sl}(t)$ is the time dependent limit state function for small leaks over a time period t, w_t is the wall thickness of the pipe, and $d_{max}(t)$ is the maximum depth of the corrosion feature which increases as a function of time due to the corrosion process. Similarly, the limit state function for burst is,

$$g_b(t) = r_b(t) - p \tag{10}$$

where $g_b(t)$ is the time dependent limit state function for burst over a time period t, $r_b(t)$ is the capacity of the pipe to resist the internal pressure, and p is the demand due to applied internal pressure. As ILI data provides feature depth and length, most burst pressure capacity models were developed using these sizing parameters and with assumptions regarding the shape of the corrosion feature in order to estimate its cross-sectional area. Standardized models for burst pressure capacity prediction are available in B31G (ASME 2012) and Annex O of CSA Z662 (CSA 2015). Other commonly used models, such as Battelle (Leis and Stephens 1997), DNV-99 (DNV 1999), are employed in an example application by Caleyo et al. (2002). In evaluating the limit state function in Eq. (10) the following random variables are considered:

- Corrosion depth
- Corrosion length
- Growth rate
- Wall thickness
- Yield strength
- Model error.

According to the models in B31G, corrosion depth is the maximum depth of the feature, while CSA model considers the average depth. For features identified through ILI run, the distribution of depth and length are derived from the sizing errors that are specified by the ILI tool manufacturers. Depending on the choice of corrosion growth model, growth rates are either random variables or stochastic processes with time-dependent model parameters. A model error distribution is available for the CSA model from Nessim and Zhou (2005), while the model errors for B31G models are not reported in ASME (2012).

Rupture occurs due to unstable axial extension of a through-wall defect (i.e., maximum corrosion depth is equal to wall thickness). It is defined by the limit state function (CSA 2015),

$$g_r(t) = p_b - p \tag{11}$$

where $g_r(t)$ is the time dependent limit state function for rupture over a time period t, and p_b is the pressure capacity.

4.3 Methods to Estimate the Probability of Failure

Probability of failure for a single corrosion feature, P_i, is evaluated for failure due to a small leak as,

$$P_i(\text{Small Leak}) = P(g_{sl}(t) \le 0) \cap P(g_b(t) > 0) \tag{12}$$

Similarly probability of burst, including large leak or rupture, is defined as,

$$P_i(\text{Burst}) = P(g_{sl}(t) > 0) \cap P(g_b(t) \le 0) \tag{13}$$

The probability due to large leak only will be defined as,

$$P_i(\text{Large Leak}) = P(g_{sl}(t) > 0) \cap P(g_b(t) \le 0) \cap P(g_r(t) > 0) \tag{14}$$

The difference in probability between P_i(Burst) and P_i(Large Leak) will provide the probability of failure due to rupture.

In order to evaluate time-dependent and system probabilities in Eqs. (12)–(14), MCS is commonly adopted. Caleyo et al. (2002) employed First-Order Second Moment (FOSM) and First Order Reliability Method (FORM) to calculate the probability of failure due to corrosion. However, corrosion growth rates are assumed to be linear and deterministic in this application. Zhang and Zhou (2014), proposed a series system formulation using the FORM to evaluate the probabilities for small leak, burst and large leak. In this approach, if t is the duration for which the probability of failure is evaluated, t_{sl} is the time to small leak and t_b is the time to burst, small leak can only occur if ($t_{sl} < t$ and $t_{sl} < t_b$). Similarly, burst can only occur if ($t_b < t$ and $t_b < t_{sl}$). The required probabilities are recast as,

$$P_i(\text{Small Leak}) = P(g_{sl}(t) \le 0) - w_2(t)P_{12}(t) \tag{15}$$

$$P_i(\text{Burst}) = P(g_b(t) \le 0) - w_1(t)P_{12}(t) \tag{16}$$

where $P_{12}(t) = \text{P}(g_{sl}(t) \le 0 \cap g_b(t) \le 0)$, and $w_2(t)\ P_{12}(t)$ and $w_1(t)\ P_{12}(t)$ represent the probability of ($t_b < t_{sl} < t$) and ($t_{sl} < t_b < t$), respectively. Zhang and Zhou (2014) solved for the values of $w_2(t)\ P_{12}(t)$ and $w_1(t)\ P_{12}(t)$ using a "wedge integral" method and a "probability weighting factor" method. Both approaches perform well for burst over a short duration. However, small leak probabilities are underestimated

by both methods. For large leaks, the probability is increasingly underestimated over longer durations.

The annual probability of failure of a pipeline segment of a finite length is determined through different approaches based on the available inspection data. If the data regarding location and sizing of individual corrosion features is unavailable, then the distributions for corrosion depth and length are derived based on a representative data set from a similar pipeline. The annual probability of burst of a finite length of pipe segment is evaluated as,

$$P_b = \rho \cdot P(\text{Burst}) \tag{17}$$

where ρ is the density of the corrosion features over the given length and P(Burst) is the annual probability of failure of a single corrosion feature. It is noted here that the failure of a given corrosion feature is assumed to be independent of the failure of any other feature and the occurrence of simultaneous failure of one or more features is assumed to be negligibly small. If the location and sizing of individual features is known, there are two different approaches for probability evaluation depending on the objective of the reliability assessment. In order to evaluate the annual probability of failure of a pipe segment due to the failure of any corrosion feature, is the corrosion features can be modelled as a series system reliability problem, such that,

$$P_b = 1 - \prod (1 - P_i(\text{Burst})) \tag{18}$$

In modelling as a series system, the failure of each corrosion feature is assumed to be statistically independent of the other corrosion features. While Eq. (18) provides the probability of failure anywhere within the segment, it is representative of failure probability due to one or more features. In order to employ this value in a risk computation, consequence must be quantified due to the failure of *one or more* events. However, consequences are typically quantified for a single LoC event. Using consequence per event in risk calculations with this approach is applicable only when the length of pipeline segment is short enough to assume that the failure due to a single corrosion feature will lead to a replacement of the entire pipe segment. Then, the possibility of a second failure event due to a remaining corrosion feature is eliminated. Alternatively, if probability of failure of two or more events is negligible, the probability of failure evaluated from Eq. (18) can be employed in the risk estimation.

As the consequence due to LoC event is quantified per failure event and pipe segments are considered over longer lengths, it is more common to estimate expected number of failures per segment using the MCS method, such that,

$$F_b = \Sigma n_{fi} / N \tag{19}$$

where F_b is the frequency of burst within a given length of pipe segment, n_{fi} is the number of samples that failed in burst for the ith corrosion feature, and N is the total

number of samples. If probabilities of individual corrosion features are available, then the probability of failure per unit length of pipeline segment is computed as,

$$P_b = \rho \cdot \sum P_i(\text{Burst}) / n_c \tag{20}$$

where n_c is the number of corrosion features with in the given length. This approach provides a conservative estimate for the total risk as the failure due to a corrosion feature is not assumed to prevent a subsequent failure due to another corrosion feature. However, the probability of simultaneous failure of one or more features is assumed to be zero in this approach. Instead of probability of failure, the annualized rate of failure computed using Eq. (20) does not require the assumption of mutually exclusive occurrence of corrosion feature failures. Different approaches defined by Eqs. (17)–(20) are also applied to other corrosion feature failure modes.

5 Cracks

Cracks in buried pipelines are classified as either axial cracks or stress corrosion cracking (SCC). Axial cracks occur as single cracks due to defects in manufacturing, construction and welding of the pipe joints. These are time independent as there is no possibility of new crack initiation and growth. Under normal operating conditions, the axially oriented cracks experience fatigue crack growth caused by fluctuations in the internal pressure and the corresponding hoop stress cycles. A second category of cracks, SCC, occur as crack fields and their crack growth is driven by similar mechanisms as external corrosion. Detection of cracks through ILI technology and the assessment of ILI tool reliability for crack detection is currently an area currently of active research (Skow and LeBlanc 2014; Lu et al. 2015).

Uncertainties to be considered in estimating the probability of failure due to cracks are similar to those listed for corrosion. Growth models for fatigue crack growth depend on the stress intensity factor and the expected number of stress cycles. Initiation and growth models for SCC are based on similar external corrosive factors as external corrosion. SCC in high-pH environments is initiated by pitting corrosion. However, mechanisms for initiation and growth of SCC in near-neutral pH environments is not well-understood (Michael Baker Jr., Inc. 2005), although near-neutral SCC was observed in the ground conditions with high concentrations of dissolved CO_2. Statistical models for the occurrence and growth of SCC have received considerable attention in the literature. Jaske et al. (2002) proposed empirical models for fatigue crack growth based on the well-known Paris Law and for near-neutral pH SCC crack growth based on power law equations. Youzwishen et al. (2004) proposed an empirical model for predicting the occurrence of near-neutral pH based on an exponential function, while Jain et al. (2012) and Ayello et al. (2014) developed Bayesian Network models for high-pH and near-neutral pH SCC.

The burst limit state function for cracks is similar to Eq. (10), which represents burst of a corrosion feature. Models to determine burst due to cracks consider two failure mechanisms: (1) ductile failure due to plastic collapse, and (2) brittle failure due to fracture. Models for the ductile mode of failure are similar for cracks and corrosion features. They are a function of material strength, feature depth and length, and pipe parameters such as wall thickness and diameter. Models for brittle failure, on the other hand, are dependent on the fracture toughness of the material. A few widely-used semi-empirical models exist to predict the burst pressure capacity for a crack. These include the Log-Secant Model (Kiefner et al. 1973), the Modified-Log-Secant Model (Kiefner 2008), and the CorLAS^{TM} Model (Jaske and Beavers 2001). Yan et al. (2014) provide a comprehensive list of available burst pressure prediction models and the model error associated with each. In their study, over a hundred burst pressure results from experimental studies were compared to the model predictions and the coefficient of variation of the model error was estimated. The CorLAS^{TM} Model with 22.8% coefficient of variation has the lowest model error. A further comparison of capacity prediction models with experimental data by Tandon et al. (2014) also indicated significant model errors. Given the high model uncertainty in the capacity predictions, reliability analyses for cracks must properly account of the model error distribution. However, characterization of model error in the burst pressure capacity models is an area of ongoing research.

When fatigue crack growth and SCC crack growth are considered, evaluation of the probability of failure due to cracks requires a time-dependent reliability analysis. The problem of estimating the time-dependent probability of crack failure for a given pipe segment is similar to corrosion. Hence, the same reliability analysis methods for corrosion are applicable to cracks.

6 Natural Hazards

Rizkalla et al. (2008) provided a detailed list of common geotechnical and hydro-technical hazards that affect buried pipelines. These include geotechnical hazards such as ground movement, seismic shaking and liquefaction, as well as hydro-technical hazards caused by scour, bank erosion, debris and floods. Other natural hazards include lightning and forest fires.

Of all the natural hazards, ground movements is the most common. Movement of the soil can induce significant imposed displacement on the buried pipe. These displacements result in bending and axial stresses in the pipeline. The primary sources for ground movement are:

- Slope creep: A gradual soil movement, in horizontal plane to the pipe axis, due to fluctuations in the pore water pressure in the soils.
- Landslides: A sudden ground movement along steep slopes along an inclined plane, primarily in horizontal plane to the pipe axis.

- Subsidence: A gradual vertical downward movement of the soil due to the lowering of ground water table or collapse of underground mines.
- Frost heave: A gradual vertical upward movement of the soil due to the freezing of water in the discontinuous permafrost regions in the arctic. This movement could be periodic depending on the seasonal changes in temperature and moisture content of the soils due to precipitation.
- Thaw settlement: A gradual vertical downward movement of the soil due to thawing of the frozen permafrost soils in the discontinuous permafrost artic regions.
- Earthquakes: Lateral spreading of the soil due to liquefaction, permanent ground displacements due to failure of weak soils and surface faulting across the pipe axis.

Due to the varied nature of ground movement sources, displacement demands on the pipelines can be time dependent (slope creep, subsidence, frost heave and thaw settlement), and spatially distributed (subsidence, frost heave, thaw settlement, and earthquakes). Therefore, uncertainties regarding the ground displacement magnitude over the duration of interest, the location of occurrence of the ground displacement and the mechanical properties of the moving soil dominate the failure probability calculations. For location specific time-independent hazards, such as landslides and liquefiable soils due to ground shaking, quantification of the magnitude of ground displacement is still a source of large uncertainty.

Bending and axial stresses induced by ground movement result in two different modes of failure in a buried pipeline. Excessive compressive stresses can lead to local buckling in the pipe surface. While bucking is typically considered as a serviceability limit state, cyclic hoop stresses at buckling location could result in fatigue cracking and rupture. Axial tensile stresses can lead to rupture of manufacturing cracks in girth welds, which is an ultimate limit state that leads to loss of containment. As ground movements induce deformation-controlled loading, both, serviceability and ultimate limit states are characterized with imposed strain demands and strain capacity of the pipe body and girth weld.

Strain demand due to soil displacement around a buried pipelines are evaluated as a function of the magnitude and direction of ground movement, the length of the moving block of soil, the soil strength parameters and pipe dimensions and material properties. Simplified equations for determining strain demand are limited to particular directions of ground movement relative to the pipe longitudinal axis (Rajani and Morgenstern 1993; Yoosef-Ghodsi et al. 2008). Several empirical models exist for the assessment of compressive strain capacity (Zimmerman et al. 1995; Dorey et al. 2001; Liu et al. 2013) and tensile strain capacity (Wang et al. 2011; Tang et al. 2014). However, there are large uncertainties associated with both strain demands and capacity, in addition to the variabilities inherent in the soil properties that are used to estimate strain demand.

Reliability analyses are rarely conducted for ground movements. Rizkalla et al. (2008) proposed a framework for quantitative risk assessment of geotechnical hazards. However, quantitative reliability methods are not generally accepted for

geotechnical applications due to the lack of sufficient data and large uncertainties in the soil parameters as noted. Zhou (2012) showed an example application for the influence of soil heterogeneity on the probability of failure for longitudinal ground displacements due to slope creep. Nessim et al. (2010) provided a methodology for seismic reliability assessment of buried pipelines due to permanent ground displacement. However, the seismic sources considered in that study were limited to the known fault sources. A comprehensive overview of seismic reliability assessments that identified a number of challenges in determining soil conditions, strain demand, and pipe strain capacity is available in Honegger and Wijewickreme (2013).

7 Human Error

Incorrect operations are primarily caused by human error in the pipeline control room. The effect of human factors on pipeline operations and accounting for heuristics (such as the use of short-cuts or rules of thumb) and biases (such as selective attention, confirmation bias, word-framing resulting in biased decisions) in decision-making is a growing field of interest in the pipeline industry (Harron 2015). However, the effects of human factors including variance in operator performance and operator actions leading to a failure have not been systematically studied in the pipeline industry.

Incorrect operations often lead to overpressure in the pipelines. The effect of incorrect operations can therefore be accounted for in defining the probability distribution of internal pressure which is used in the limit state functions for excavation damage, corrosion and cracks.

8 Conclusion

Reliability analysis in pipeline industry is employed for quantitative risk estimation, which is evaluated as the product of probability of occurrence of loss of containment and the associated consequences. The consequences of a product release can be categorized in terms of life safety, environmental impact and financial losses. Release consequences varies with the type of product released, the release volume, the probability of receptor exposure and the sensitivity of the receptors to the product. Receptors could be human populations, natural habitat, or wildlife. A comprehensive overview of framework for estimation of consequences is available in the risk assessment methodology proposed by Muhlbauer (2004, 2015).

Consequences are dependent on the volume of product release, which in turn depends on the failure mode. Therefore, variations in the estimation of risk is largely dependent on the threats included in the assessment of pipeline integrity, and the estimation of the associated probabilities for different pipeline failure modes.

As mentioned earlier, methodology adopted for combination of failure probabilities due to individual corrosion or crack features, and other time and location dependent hazards, such as ground movements, could lead to significant difference in the estimated risk. In the presence of multiple threats, risk estimation for each threat separately is the ideal approach for proper accounting for risk. Probability estimation for the combined occurrence of multiple failures with a series system reliability approach, as denoted in Eq. (18), will lead to an underestimation of the total risk. Careful consideration of the consequence estimation is required when combined probability of failure is employed in risk assessments.

Reliability methods are widely applied for the evaluation of the probability of loss of containment from pipelines due to excavation damage and corrosion features. Due to the complexity of the limit state functions, the need to consider multiple limit states simultaneously in order to account for different failure modes, and the time-dependent nature of reliability problem, Monte-Carlo Sampling is considered to be the most reliable method for probability estimation. However, it is well-known that the computational time required for Monte-Carlo Sampling can be high, particularly for the computation of very low probabilities. This limits the application of quantitative reliability approaches in the industry. With new advances in numerical analysis approaches, application of finite element analyses to the failure analysis of corrosion, cracks and ground movements has increased (e.g. Fredj et al. 2015; Filho et al. 2014; Hanif and Kenny 2014; Barbas and Weir 2007). In an effort to reduce the number of evaluations of finite element models, response surface methodologies and the use of surrogate models for reliability estimation is an area of growing interest.

As evident from this review, development of efficient reliability analysis methods that address the unique challenges in estimating the probability of pipeline failures has considerable research potential. In order to accelerate the use of quantitative risk assessments within the pipeline industry, there is a significant need for advanced and faster alternatives to Monte-Carlo Sampling that provide accurate and reliable estimates for probability of failure.

References

American society of mechanical engineers (ASME) (2014) Managing system integrity of gas pipelines. AMSE B31.8S-2014, ASME code for pressure piping B31, Supplement to ASME B31.8, Sept 30

American society of mechanical engineers (ASME). 2012. Manual for determining remaining strength of corroded pipelines. ASME B31G-2012, Supplement to ASME B31 code for pressure piping

Al-Amin MM, Zhou WW, Zhang SS, Kariyawasam SS, Wang HH (2012) Bayesian model for calibration of ILI tools. In: ASME. International pipeline conference, vol 2, pipeline Integrity Management, pp 201–208. doi:10.1115/IPC2012-90491

Ayello F, Jain S, Sridhar N, Koch GH (2014) Quantitative assessment of corrosion probability—a bayesian network approach. Corrosion 70(11):1128–1147

Barbas ST, Weir MS (2007) Strain-based design methodology for seismic and arctic regions. In: Proceedings of the 17th international offshore and polar engineering conference, July. The international society of offshore and polar engineers (ISOPE), Lisbon, Portugal, 1–6

Caleyo F, Gonzalez JL, Hallen JM (2002) A study on the reliability assessment methodology for pipelines with active corrosion defects. Int J Press Vessels Pip 79:77–86

Chen Q, Nessim M (1999) Reliability-based prevention of mechanical damage to pipelines. Prepared for the Offshore/Onshore Design Applications Supervisory Committee—Pipeline Research Committee, of Pipeline Research Council International, Inc., Catalog No. L51816, August

Chen Q, Davis K, Parker C (2006) Modeling damage prevention effectiveness based on industry practices and regulatory framework. In: Proceedings of the 6th international pipeline conference. Calgary, Alberta, September 25–29, Paper No. IPC2006-10433

Cosham A, Haswell J, Jackson N (2008) Reduction factors for estimating the probability of failure of mechanical damage due to external interference. International pipeline conference. Calgary, Alberta, September 29–October 3, IPC2008-64345

CSA Group (2015) Oil and Gas Pipeline Systems. CSA Z662-15

Dann MR, Maes MA (2015) Population-based approach to estimate corrosion growth in pipelines. Proceedings of 12th international conference on applications of statistics and probability in civil engineering, ICASP12, July. Vancouver, Canada, pp 12–15

Det Norske Veritas (DNV) (1999) Corroded pipelines: recommended practice DNV- RP-F101. Det Norske Veritas, AS

Dorey AB, Cheng JJR, Murray DW (2001) Critical buckling strains for energy pipelines. Structural Engineering Report No. 237, Department of Civil and Environmental Engineering, University of Alberta, Edmonton, Alberta

Driver R, Playdon D (1997) Limit states design for accidental outside force. Report to National Energy Board of Canada

Driver RG, Zimmerman TJE (1998) A limit states approach to the design of pipelines for mechanical damage. In: Proceedings of 17th international conference on offshore mechanics and arctic engineering (OMAE98), ASME

EGIG (European Gas Pipeline Incident Data Group) (2015) Gas pipeline incidents. 9th report of the european gas pipeline incident data group (period 1970–2013). www.EGIG.eu

Filho JEA, Machado RD, Bertin RJ, Valentini MD (2014) On the failure pressure of pipelines containing wall reduction and isolated pit corrosion defects. Comput Struct 132:22–33

Francis A, Espiner R, Edwards A, Cosham A, Lamb M (1997) Uprating an in-service pipeline using reliability-based limit state methods. Risk-based and limit state design and operation of pipelines. Aberdeen, UK. May 21–22 1997

Fredj A, Dinovitzer A, Sen M (2015) 10th European LS-DYNA conference application of the SPH finite element method to evaluate pipeline response to slope instability and landslides. Wurzburg, Germany

Goodfellow G, Haswell JV, Jackson NW, Ellis R (2014) Revision to the UK pipeline quantitative risk assessment guidelines IGEM/TD/2 and PD8010-3. International pipeline conference, Calgary, Alberta, September 29–October 3, IPC 2014-33218

Hanif W, Kenny S (2014) Mechanical damage and fatigue assessment of dented pipelines using FEA. Proceedings of the 10th international pipeline conference, Calgary, Alberta, September 29–October 3, IPC 2014-33445

Harron L (2015) Human factors. In: Winston Revie R (ed) Oil and gas pipelines: integrity and safety handbook. Wiley, Inc., NJ

Honegger DG, Wijewickreme D (2013) Seismic risk assessment for oil and gas pipelines. In: Tesfamariam and Goda (eds) Handbook of seismic risk analysis and management of civil infrastructure systems. Woodhead Publishing Limited

Hong HP (1999b) Application of the stochastic process to pitting corrosion. Corrosion 55(1): 10–16

Hong HP (1999a) Inspection and maintenance planning of pipeline under external corrosion considering generation of new defects. Struct Saf 21:22–203

Hopkins P, Corder I, Corbin P (1992) The resistance of gas transmission pipelines to mechanical damage. In: CANMET international conference on pipeline reliability, vol. II

Institution of Gas Engineers and Managers (IGEM) (2013) Assessing the risks from high pressure natural gas pipelines. IGEM/TD/2, 2nd Edition, Communication 1764

Jain S, Ayello F, Beavers JA, Sridhar N (2012) Development of a probabilistic model for stress corrosion cracking of underground pipelines using bayesian networks: a concept. In: International pipeline conference, Calgary, Alberta, September 24–28, IPC2012-90340

Jaske CE, Beavers JA (CC Technologies Laboratories, Inc) (2001) Integrity and remaining life of pipe with stress corrosion cracking. Prepared for the Materials Technical Committee, Pipeline Research Council International, Inc. Catalog No. L51928, Houston, Texas

Jaske CE, Veith PH, Beavers JA (2002) Assessment of crack-like flaws in pipelines. corrosion (2002) NACE International. Texas, USA

Kale A, Thacker BH, Sridhar N, Waldhart CJ (2004) A probabilistic model for internal corrosion of gas pipelines. In: Proceedings of IPC 2004 international pipeline conference, Calgary, Alberta, October 4–8, IPC2004-0483

Kiefner (2008) Defect assessment—conclusion: modified Ln-Secant equation improves failure prediction. Oil Gas J 106(38)

Kiefner JF, Maxey WA, Eiber RJ, Duffy AR (1973) Failure stress levels of flaws in pressurized cylinder. Progress in flaw growth and fracture toughness testing, ASTM STP 536, American Society for Testing and Materials, pp 461–481

Leis N, Stephens DR (1997) An alternative approach to assess the integrity of corroded line pipe—part II: alternative criterion. In: Proceedings of 7th international offshore and polar engineering conference, Honolulu, USA, May 25–30, 624–641

Linkens D, Shetty NK, Bilo M (1998) A probabilistic approach to fracture assessment of onshore gas-transmission pipelines. In: Pipes and pipelines international, July–August, pp 5–16

Liu M, Wang Y-Y, Zhang F, Kotian K (2013) Realistic strain capacity models for pipeline construction and maintenance. prepared for US department of transportation. Pipeline and Hazardous Materials Safety Administration, Office of Pipeline Safety, Contract No. DTPH56-10-T-000016, Center for Reliable Energy Systems, Dublin, OH, USA, December

Lu D, Skow J, Keane S (2015) Assessing the probability of detecting crack features using ultrasonic ILI tool run results and excavation data. J Pipeline Eng, 1st Quarter pp 43–51

Michael Baker Jr Inc (2005) Stress corrosion cracking study. Integrity Management Program Delivery Order DTRS5-02-D-70036, Department of Transportation, Research and Special Program Administrations, Office of Pipeline Safety

Miran SA, Huang Q, Castaneda H (2016) Time-dependent reliability analysis of corroded buried pipelines considering external defects. J Infrastruct Syst. doi:10.1061/(ASCE)IS.1943-555X.0000307

Muhlbauer WK (2004) Pipeline Risk Management Manual: Ideas, Techniques, and Resources, 3rd edn. Elsevier Inc

Muhlbauer WK (2015) Pipeline Risk Assessment. Expert Publishing LLC, Austin, TX

National Transportation Safety Board (2015) Enbridge incorporated hazardous liquid pipelines rupture and release. Marshall, Michigan, July 25 2010. Pipeline Accident Report, NTSB/PAR-12/01, Washington, D.C

National Transportation Safety Board (2015) Integrity management of gas transmission pipelines in high consequence areas. Washington, DC, January 27, Safety Study NTSB/SS-15/01

Nessim M, Adianto R (2014) Limit states design for onshore pipelines—design rules for operating pressure and equipment impact loads. In: International pipeline conference, Calgary, Alberta, September 29–October 3, IPC2014–33436

Nessim M, Dawson J, Mora R, Hassanein S (2008) Obtaining corrosion growth rates from repeat in-line inspection runs and dealing with the measurement uncertainties. In: ASME. International pipeline conference, 2008 7th international pipeline conference, vol 2. pp 593–600

Nessim M, Yoosef-Ghodsi N, Honegger D, Zhou J, Wang S (2010) Application of reliability based design and assessment to seismic evaluations. In: International pipeline conference, Calgary, Alberta, September 27–October 1, IPC2010–31557

Nessim MA, Zhou W (2005) Guidelines for Reliability Based Design and Assessment of Onshore Natural Gas Pipelines, Gas Research Institute Report, GRI-04/0229. Des Plaines, IL

PHMSA (Pipeline and Hazardous Materials Safety Administration) (2016) Data and statistics from office of pipeline safety (OPS). United States Department of Transportation (US DOT). http://www.phmsa.dot.gov/pipeline/library/data-stats. Accessed 30 Apr 2016

Qin H, Zhou W, Zhang S (2015) Bayesian inferences of generation and growth of corrosion defects on energy pipelines based on imperfect inspection data. Reliab Eng Syst Saf 144: 334–342

Rajani BB, Morgenstern NR (1993) Pipelines and laterally loaded pipes in an elasto-plastic medium. J Geotech Eng 119(9):1431–1447

Rizkalla M, Read R, O'Neil G (2008) Geohazard management. Rizkalla (ed) Pipeline geo-environmental design and geohazard management. ASME

Roovers P, Boo B, Galli M, Marewski U, Steiner M, Zarea M (2000) EPRG methods for assessing the tolerance and resistance of pipelines to external damage. In: Denys R (ed) Proceedings of the 3rd international pipeline technology conference pipeline technology, Vol II, May 21–24. Elsevier, Belgium. pp 405–425

Shabarchin O, Tesfamariam S (2016) Internal corrosion hazard assessment of oil and gas pipelines using Bayesian belief network model. J Loss Prev Process Ind 40:479–495

Skow JB, LeBlanc L (2014) In-line inspection tool performance evaluation using field excavation data. In: Proceedings of the ASME 2014 10th international pipeline conference, IPC 2014, September 29–October 3, 2014, Calgary, Alberta, Canada

Tandon S, Gao M, Krishnamurthy R, Kariyawasam S, Kania R (2014) Evaluation of existing fracture mechanics models for burst pressure predictions, theoretical and experimental aspects. In: Proceedings of the ASME 2014 10th international pipeline conference, IPC 2014, September 29–October 3, 2014, Calgary, Alberta, Canada

Tang H, Fairchild D, Panico M, Crapps J, Cheng W (2014) Strain capacity prediction of strain-based pipelines. In: Proceedings of the 10th international pipeline conference, IPC 2014, Paper No. IPC2014-33749, Calgary, AB, Canada, September 29-October 3

Timashev SA, Bushinskaya AV (2015) Markov approach to early diagnostics, reliability assessment, residual life and optimal maintenance of pipeline systems. Struct Saf 56:68–79

Toes G, Rogers M (2010) A revised fault tree method for determining the effectiveness of slabbing. GL Noble Denton, Report Number: 9551, Issue: 1.0, May 11

Wang H, Duncan IJ (2014) Likelihood, causes and consequences of focused leakage and rupture of U.S. natural gas transmission pipelines. J Loss Prev Process Ind 30:177–187

Wang H, Yajima A, Liang RY, Castaneda H (2015) A clustering approach for assessing external corrosion in a buried pipeline based on hidden Markov random field model. Struct Saf 56:18–29

Wang YY, Liu M, Song Y (2011) Second generation models for strain-based design. Contract PR-ABD-1—Project 2, Pipeline Research Council International, Inc. August

Yan Z, Zhang S, Zhou W (2014) Model error assessment of burst capacity model for energy pipelines containing surface cracks. Int J Press Vessels Pip 120–121:80–92

Yoosef-Ghodsi N, Zhou J, Murray DW (2008) A simplified model for evaluating strain demand in a pipeline subjected to longitudinal ground movement. In: Proceedings of the 7th international pipeline conference, IPC 2008, Paper No. IPC2008-64415, Calgary, AB, Canada, September 29-October 3

Youzwishen OO, Van Aelst A, Ehlers PF, Nettel A (2004) A statistical model for the prediction of SCC formation along a pipeline. In: Proceedings of IPC 2004 international pipeline conference, Calgary, Alberta, October 4–8, IPC2004-0267

Yusta JM, Correa GJ, Lacal-Arantegui R (2011) Methodologies and applications for critical infrastructure protection: state-of-the-art. Energy Policy 39:6100–6119

Zhang S, Zhou W, Qin H (2012) Inverse Gaussian process-based corrosion growth model for energy pipelines considering the sizing error in inspection data, corrosion science, vol 73, August 2013, pp 309–320

Zhang SS, Zhou WW, Al-Amin MM, Kariyawasam SS, Wang HH (2013) Time-dependent corrosion growth modeling using multiple ILI data. In: ASME. International pipeline conference, vol 4: pipelining in northern and offshore environments; strain-based design; risk and reliability; standards and regulations: pp 693–702

Zhang S, Zhou W (2014) An Efficient methodology for the reliability analysis of corroding pipelines. J Pressure Vessel Technol 136:041701-1:7

Zhang S, Kariyawasam S, Zhou W (2015) Time-dependent reliability assessment for corroding pipelines based on imperfect inspection data. In: Proceedings of 12th international conference on applications of statistics and probability in civil engineering, ICASP12, Vancouver, Canada, July 12–15

Zhou W (2012) Reliability of pressurised pipelines subjected to longitudinal ground movement. Struct Infrastruct Eng 8(12):1123–1135

Zimmerman TJE, Stephens MJ, DeGeer DD Chen Q (1995) Compressive strain limits for buried pipelines. In: Proceedings of the 1995 offshore mechanics and arctic engineering conference, Denmark, June

Part III
Stochastic Dynamics: Methods and Applications

An Intuitive Basis of the Probability Density Evolution Method (PDEM) for Stochastic Dynamics

Alfredo H.-S. Ang

Abstract The recently developed *Probability Density Evolution Method* (PDEM) is described in intuitive terms in order to permit a better understanding and wider application of the PDEM in practical engineering problems, particularly for assessing the risk and reliability of large and complex engineering systems. In implementation, the PDEM is similar, in a limited sense, to the basic Monte Carlo simulation (MCS) in that it also requires deterministic response solutions of a system. However, in principle and in theory it is very different from the MCS. The practical effectiveness of the PDEM is emphasized and illustrated.

1 Introduction

The recent development by Profs. Jie Li and Jianbing Chen of Tongji University, Shanghai, China represents one of the significant recent advances in the field of reliability and risk analyses (Chen and Li 2007, 2008; Li and Chen 2006, 2009). The mathematical theory of the *probability density evolution method* or PDEM has been rigorously established by the authors. The rigorous theory may require good mathematical background to comprehend. However, because of its practical significance in advancing the field of reliability engineering, it is important that the method be more widely understood and appreciated by practicing engineers.

In this spirit, the purpose of this chapter is to provide an intuitive explanation or description of the PDEM, in terms that will enlighten better understanding and/or appreciation of the true significance of the method, especially of its effectiveness in solving complex problems in engineering, without the full exposition of its underlying mathematical and theoretical basis.

A.H.-S. Ang (✉)
University of California, Irvine, USA
e-mail: ahang2@aol.com

P. Gardoni (ed.), *Risk and Reliability Analysis: Theory and Applications*,
Springer Series in Reliability Engineering, DOI 10.1007/978-3-319-52425-2_5

2 Practical Significance of PDEM

The best way to describe the PDEM is that it is similar in implementation to the basic Monte Carlo simulation (MCS), but only in the sense of the required deterministic sample response solutions of a system.

It starts with the deterministic response solution of a system just as with the MCS. However, each simulated deterministic response solution is associated with a mathematically assigned probability; the determination of the associated probability is a non-trivial mathematical problem (Chen and Li 2008). In contrast to the traditional MCS which requires random sampling of all possible deterministic response solutions, the sample size (or representative points) by PDEM is much smaller than that required of the MCS. A sample size of the order of 200–400 is sufficient even for systems with very large number of degrees-of-freedom (e.g., several million) nonlinear dynamic systems.

2.1 Brief Theoretical Basis

The comprehensive and theoretical basis of the PDEM is well documented by Li and Chen (2006, 2009). Summarized below is a brief summary of its fundamental mathematical basis. According to Li and Chen (2006), the probability density evolution equation is

$$\frac{\partial p_{X\Theta}(x,\theta,t)}{\partial t} + \dot{X}(\theta,t)\frac{\partial p_{X\Theta}(x,\theta,t)}{\partial x} = 0 \tag{1}$$

where $p_{X\Theta}(x,\theta,t)$ is the joint PDF of X and Θ; and $\dot{X}(\theta,t)$ is the velocity of the structural response. The initial condition of Eq. (1) is

$$p_{X\Theta}(x,\theta,t)|_{t=0} = \delta(x-x_0)p_{\Theta}(\theta) \tag{2}$$

Equation (1) can be solved with the initial condition of Eq. (2) using finite-difference method.

The solution of Eqs. (1) and (2) may be summarized with the following steps:

1. Generate the "representative or sample points" and their respective probabilities in the solution space. That is, obtain the deterministic solution of the system response for each representative point and its associated probability.
2. Determine the joint PDF using finite-difference method.
3. Apply numerical integration to obtain the numerical values of the PDF.
4. On the basis of the "complete system failure process", the reliability of a system is defined by the one-dimensional PDF of the extreme-value of the ultimate capacity; integration of this PDF yields the system reliability.

The computational implementation of the PDEM is seemingly similar to the MCS—in the sense that it requires the deterministic solution of the system response for each representative point (or sample solution) in the solution space. However, each of the representative points in the PDEM carries an associated probability; determining these associated probabilities for the respective representative points is central to the PDEM and is a significant and non-trivial mathematical problem (Chen and Li 2008). Experience shows that the number of representative points need not be large to obtain accurate results (of the order of 200–400 points even for very large and complex systems). In contrast, the representative points, or sample size, in MCS are randomly generated to virtually cover the entire population of possible deterministic response solutions; in this case, the corresponding number of representative points (with the MCS) can be extremely large compared to that for the PDEM.

2.2 Reliability of Complex Systems

Thus far, for a complex engineering system, the assessment of its reliability invariably requires Monte Carlo simulation (MCS) or its improved versions such as by variance reduction. However, there is a limit to the effectiveness of any MCS method, particularly for complex dynamic and highly nonlinear systems that involve many degrees-of-freedom (e.g., with several million dof) systems. The recent development of the PDEM provides an effective alternative computational tool for the required reliability assessments that can and should serve to widen the practical implementation of the reliability approach particularly for complex engineering systems

Through the application of the PDEM and based on the complete system failure process proposed by Chen and Li (2007), the reliability, R, of a system is defined as the *system capacity is greater than the applied load*, and can be obtained through the integration of a one-dimensional extreme-value PDF of the ultimate system capacity Z_{max}, as follows:

$$R = \int_{\Omega(x)} Z_{\max}(x)dx \tag{3}$$

where $\Omega(x)$ is the safe domain of the system.

It is significant to emphasize that the above procedure, through Eq. (3), completely circumvents the need to identify the possible failure modes of a system and their respective mutual correlations which are necessary in any traditional methods (e.g., Ang and Ma 1981) for numerically assessing system reliability. This is not surprising as the implementation of the PDEM may be interpreted, heuristically, as a "weighted" sampling process similar to the MCS; the non-trivial weight for each sample is the probability associated with each representative point.

3 On Application to Reliability of Complex Systems

The role of the PDEM is especially significant in the assessment of the reliability of a highly complex system, such as a very high-rise building, a long bridge, a long underground tunnel, and others subjected to strong-motion earthquakes or severe wind storms. For such systems, the analysis of its reliability would traditionally rely on Monte Carlo simulations (MCS); however, because of the large number of degrees-of-freedom needed to model a complex system, and also requiring very large sample size (of the order of 10^6 for very small failure probabilities) necessary in any MCS for sufficient accuracy, it could be impractical or too expensive to apply the MCS. With the PDEM, and through the *complete system failure process* (Chen and Li 2007), the reliability of any complex system can be assessed with relative ease and good accuracy.

Moreover, for large or complex systems, the traditional numerical reliability approach (e.g., Ang and Ma 1981) requires the identification of the major potential failure modes of a system which can be many, and the calculation of the failure probabilities of all the different failure modes many of which are mutually correlated. Also, for systems with correlated parameters the problem becomes even more complicated (Fan et al. 2015).

Instead of the traditional approach, the reliability of a system can be defined through the complete system failure process defined by Chen and Li (2007). On this latter basis, the reliability of a system becomes

$$R = \text{Prob}[Z_{max} > 0] \tag{4}$$

where Z_{max} is the maximum ultimate capacity of the system under the load effects; Z_{max} is a function of the system parameters and of the load effects.

4 Numerical Examples

Example 1 (a simple frame) For simplicity in illustration, consider the first example of a one-story one-bay elastic-plastic frame structure as shown in Fig. 1; the moment capacities M_i ($i = 1, 2, 3$) of the three members are mutually correlated

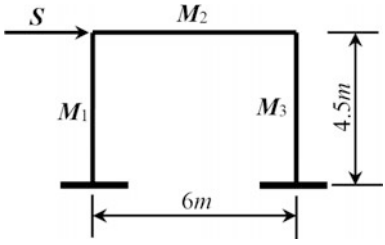

Fig. 1 A simple frame of Example 1

with correlation coefficient, ρ, and is subject to a single load S that is independent of the M_i. The solutions for this example were discussed and illustrated in Fan et al. (2015).

All the M_i are lognormal variables with mean values $\mu_{Mi} = 2000$ KN m and standard deviations $\sigma_{Mi} = 300$ KN m, and S is also a lognormal variable with mean value $\mu_S = 500$ KN and standard deviation $\sigma_S = 200$ KN. The section area of all the elements are 0.3 m $\times$ 0.3 m = 0.09 m^2, and the initial elastic modulus of the material is $E = 2.06 \times 10^5$ MPa.

According to the complete system failure process, the reliability, R, of this system is

$$\begin{aligned} R &= \Pr\{P_{\max}(M_1, M_2, M_3, S) - P(S) > 0\} \\ &= \Pr\{P_{\max}(M_1, M_2, M_3) - S > 0\} \\ &= \Pr\{Z_{\max}(M_1, M_2, M_3, S) > 0\} \end{aligned} \tag{5}$$

In general, especially for a complex structural system, the Z_{max} can be obtained effectively with the PDEM analysis. However, for this simple system, the Z_{max} may be illustrated numerically as follows:

According to the first four moments, $Z_{\max}$ can be expressed by

$$\begin{aligned} Z_{\max}(\Theta) &= \mu_{Z_{\max}} + \sigma_{Z_{\max}}(-l_1 + k_1 U + l_1 U^2 + k_2 U^3) \\ &= 1236018.48 + 287340.58U \\ &\quad - 15824.49U^2 + 4694.75U^3 \end{aligned} \tag{6}$$

Because $Z_{\max}$ is an explicit function of U, it is possible to obtain the analytical solution for its PDF although it is analytically complex; however, its numerical solution can be obtained, as shown in Fig. 2 (dotted line).

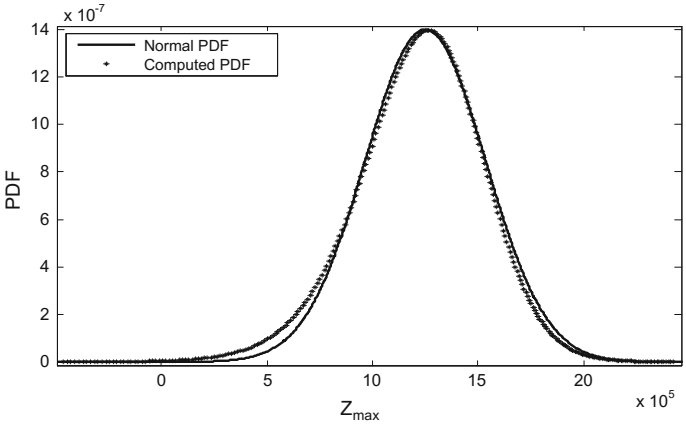

Fig. 2 Comparison of the computed PDF for Z_{max} and the fitted normal PDF

The PDF (dotted line) shown in Fig. 2 can be approximated with the fitted normal PDF as follows,

$$p_{Z_{\max}}(Z) = \frac{1}{\sqrt{2\pi} \times 2.85 \times 10^5} \exp\left(-\frac{1}{2} \left(\frac{z - 1.25 \times 10^6}{2.85 \times 10^5} \right)^2 \right) \tag{7}$$

with mean-value = 1.25×10^6 and standard deviation = 2.85×10^5.

The comparison between the numerical solution for Z_{max} and the fitted normal PDF is shown graphically in Fig. 2.

According to Eq. (4), the safety index of the simple frame is 4.45. This is, of course, the reliability associated only with the variability of information (aleatory uncertainty). As there are unavoidable epistemic uncertainties, assume that (based on engineering judgment) the mean-value of Z_{max} can vary with a c.o.v. of 15% (representing the overall underlying epistemic uncertainty) and a lognormal PDF with a median of 1.0. Then, performing the convolution integration of this log-normal PDF with the fitted normal PDF of Fig. 2 yields (by MCS) the histogram of the safety index of the structure as shown in Fig. 3. Observe that the mean β is 4.45, whereas the 90% β is 5.29, and the 95% β is 5.63.

Example 2 (a tunnel subjected to strong earthquake) This example involves a long underground tunnel subjected to a strong-motion earthquake—the 2008 Wenchuan earthquake in Sichuan, China. The details of the solution for this complex problem are presented in Yue and Ang (2015b); the tunnel-soil system is modeled with

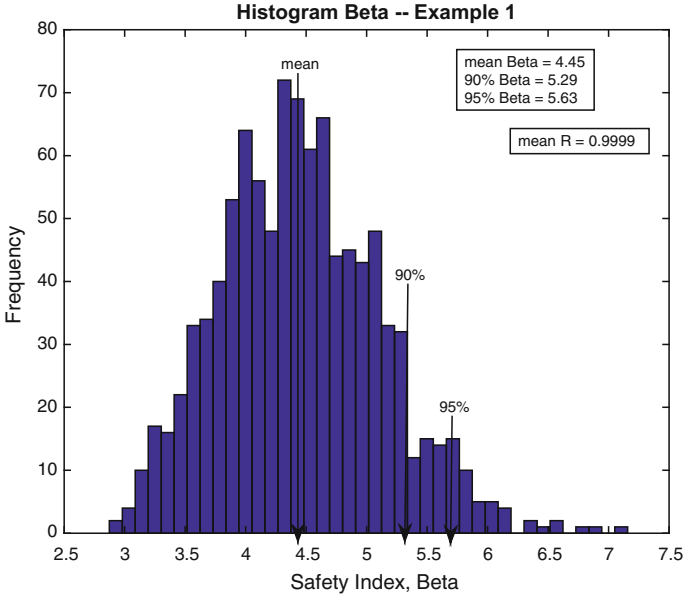

Fig. 3 Histogram of safety index, β, for Example 1

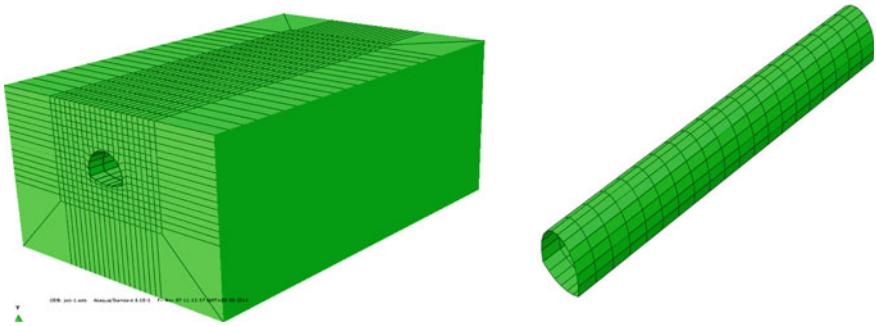

(a) soil-tunnel system (b) tunnel model

Fig. 4 Three-dimensional finite element model

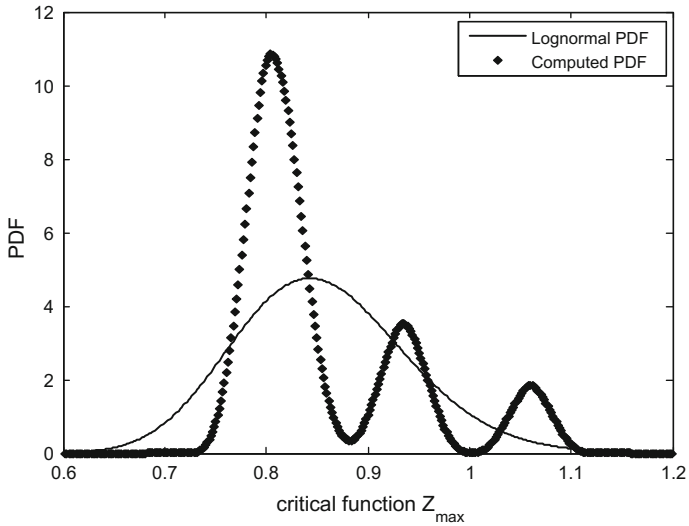

Fig. 5 Computed PDF of Z_{max} and fitted lognormal PDF

3-dimensional finite elements (see Fig. 4) and includes the variability of the natural soil/rock deposit which is modeled as a random field (Vanmarke 1977). Infinite elements on both sides of the tunnel and on bottom longitudinal side are added.

The mean reliabilities of the tunnel, for different R/C tunnel lining thicknesses and ultimate strengths, obtained through Eq. (3) are summarized in Yue and Ang (2015b). Figure 5 shows the PDF of the Z_{max} for the tunnel with a lining thickness of 0.8 m and the ultimate strength of 35 MPa; this figure shows the PDF of the calculated Z_{max} and an approximate fitted lognormal PDF as follows:

$$p(Z) = \frac{1}{\sqrt{2\pi}\sigma z} \cdot \exp\left(-\frac{1}{2}\left(\frac{\ln z - \mu}{\sigma}\right)^2 \right) \tag{8}$$

with $\mu = -0.1613$, and $\sigma = 0.0990$.

On the basis of the fitted lognormal PDF, the mean reliability of the tunnel is 0.94, which is close to the reliability of 0.91 obtained on the basis of the calculated Z_{max}. This reliability represents the effects of only the variability (aleatory uncertainly) of information of the tunnel lining and the surrounding soil/rock properties.

It would be of interest to compare the results of the 2D model (see Yue and Ang 2015a) with those obtained here with the corresponding 3D model. For this particular case, (with t = 0.8 m, and ultimate strength of 35 MPa) calculations with the 2D model would yield a reliability of 0.59 or $\beta = 0.23$, whereas with the 3D model the reliability is 0.91 or $\beta = 1.35$; showing that the 2D model would yield very conservative results.

The above safety indices, of course, does not include the effects of the epistemic uncertainties. To include the effects of the unavoidable epistemic uncertainty, assume (based on subjective judgment) that the median-value of Z_{max} of Fig. 5 will have a c.o.v. of 0.20 with a corresponding lognormal distribution and a median of 1.0. On this basis, and performing a convolution integration using simple Monte Carlo simulations, the histogram of the possible values of the safety index of the tunnel is obtained as shown in Fig. 6, from which the mean, the 90% and 95% values of the respective safety indices are 1.67, 2.13, and 2.33 (corresponding to reliabilities of 0.9525, 0.9834, and 0.9900).

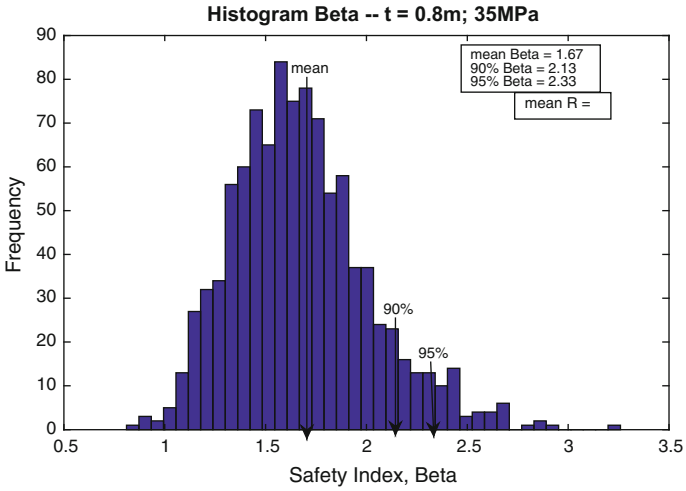

Fig. 6 Histogram of safety index, β, of Example 2 based on fitted lognormal PDF with t = 0.8 m, and 35 MPa

5 Implications to Reliability-Based Design

The PDEM is effective for the analysis of the effects of aleatory uncertainty; however, for design the effects of the epistemic uncertainty must be included. The PDF of the ultimate performance function, Z_{max}, obtained by the PDEM provides a rational and significant basis for including the effects of the epistemic uncertainty in determining the proper safety index for the design of a complex system. In this regard, the process for developing the proper safety index for reliability-based design of a complex structure as a system is described in Ang (2016).

In essence, the process for a reliability-based design of a complex structure as a system can be summarized as follows:

1. Develop the minimum expected life-cycle cost E(*LCC*), design of the system.
2. Applying the PDEM, determine the PDF of the ultimate performance function of the system, Z_{max}.
3. Assess the error (may be subjectively) in the mean-value of Z_{max} to represent the underlying epistemic uncertainty; for practical convenience the PDF of this error may be prescribed as a lognormal distribution with a mean of 1.0 and an appropriate c.o.v. (or its equivalent range of possible errors).
4. Combine the effects of both types of uncertainty through the convolution integral of the two PDFs in Steps 3 and 4. This will yield the PDF (or histogram) of the safety index as a random variable.
5. From the PDF (or histogram) of Step 4, determine the safety index with 90% or 95% confidence appropriate to ensure the safe design of the complete system.

6 Conclusions

- Currently, the reliability assessment of complex engineering systems invariably must rely on Monte Carlo simulations (MCS), but its application to complex systems is limited.
- The PDEM provides an effective alternative procedure for assessing the reliability of complex engineering systems.
- The PDEM represents a recent major break-through in the field of stochastic dynamics, useful in reliability analysis and design of engineering systems, especially relevant for highly complex systems.

Acknowledgements The assistance of Dr. Qingxia Yue and Dr. Wenliang Fan in the preparation of this paper are highly appreciated. Dr. Fan provided the details of Example 1 and various PDFs fitting the respective PDFs of the calculated Z_{max}.

References

Ang AH-S, Ma H-F (1981) On the reliability of structural system. In: Proceedings of third ICOSSAR, Trondheim, Norway

Ang AH-S (2016) Determining safety index for reliability-based optimal design of complex structural systems. J Comput Struct Mech. In: Proceedings of national conference on structural reliability, Sept 2016, Changsha, Hunan, China

Chen JB, Li J (2008) Strategy for selecting representative points via tangent spheres in the probability density evolution method. Int J Numer Methods Eng

Chen JB, Li J (2007) Development-process-of-nonlinearity-based reliability evaluation of structures. Probab Eng Mech

Fan W, Yang P, Ang AH-S, Li Z (2015) Analysis of complex system reliability with correlated random vectors. Probab Mech (submitted for review)

Li J, Chen JB (2006) The probability density evolution method for dynamic response analysis of non-linear stochastic structures. Int J Numer Methods Eng

Li J, Chen JB (2009) Stochastic Dynamics of structures, Wiley

Vanmarcke EH (1977) Probabilistic modeling of soil profiles. J Soil Mech Found Div ASCE 103 (GT11):1227–1246

Yue Q, Ang AH-S (2015a) Nonlinear response and reliability analyses of tunnels under strong earthquakes. Elsevier Publisher (Online Publication)

Yue Q, Ang AH-S (2015b) Reliability evaluation of tunnels under strong-motion earthquakes. In: Proceedings of SRES-Hangzhou, Oct 2015

The Tail Equivalent Linearization Method for Nonlinear Stochastic Processes, Genesis and Developments

Marco Broccardo, Umberto Alibrandi, Ziqi Wang and Luca Garrè

Abstract This chapter aims to provide a general prospective of the Tail Equivalent Linearization Method, TELM, by offering a review that starts with the original idea and covers a broad array of developments, including a selection of the most recent developments. The TELM is a linearization method that uses the first-order reliability method (FORM) to define a tail-equivalent linear system (TELS) and estimate the tail of the response distribution for nonlinear systems under stochastic inputs. In comparison with conventional linearization methods, TELM has a superior accuracy in estimating the response distribution in the tail regions; therefore, it is suitable for high reliability problems. Moreover, TELM is a non-parametric method and it does not require the Gaussian assumption of the response. The TELS is numerically defined by a discretized impulse-response function (IRF) or frequency-response function (FRF), thus allowing higher flexibility in linearizing nonlinear structural systems. The first part of the chapter focuses on the original idea inspiring TELM. The second part offers fourth developments of the method, which were studied by the authors of this chapter. These developments include: TELM in frequency domain, TELM with sinc expansion formula, TELM for multi-supported structures, and the secant hyperplane method giving rise to an improved TELM.

M. Broccardo (✉)
Institut fur Baustatik und Konstruktion, Eidgenossischen Technischen Hochschule (ETH), Zürich, Switzerland
e-mail: bromarco@ethz.ch

U. Alibrandi
Singapore-Berkeley Building Efficiency and Sustainability in the Tropics (SinBerBEST) and Nanyang Technological University (NTU), Singapore, Singapore

Z. Wang
Earthquake Engineering Research and Test Center, Guangzhou University, Guangzhou, China

L. Garrè
DNV GL, Høvik, Norway

P. Gardoni (ed.), *Risk and Reliability Analysis: Theory and Applications*,
Springer Series in Reliability Engineering, DOI 10.1007/978-3-319-52425-2_6

1 Introduction

In structural engineering, significant efforts have been dedicated to the developments of computational methods, which are able to predict the structural response under deterministic excitations. However, in practice, large uncertainties in the geometry, boundary conditions and material are present, and they play a key role in determining the accuracy in predicting responses of interest. Moreover, the nature of several excitations such as earthquakes, wind, or wave loadings, is intrinsically stochastic. Consequently, in presence of these excitations, the structural response is inevitably stochastic, and probabilistic methods of random vibration analysis are necessary.

An important consideration in evaluating failure probabilities is to correctly estimate the tails of the distributions of the structural responses, where failure events for highly reliable systems are located. Further, failure events usually involve nonlinear structural response. Consequently, there are two prevailing elements in the evaluation of the safety and reliability analysis of structural systems that are: (i) An accurate prediction of nonlinear structural responses; and (ii) An accurate estimation of the tail distribution of nonlinear structural responses. The TELM is a recent linearization method (Fujimura and Der Kiureghian 2007), which aims at providing accurate solutions for this class of problems. Taking the pioneering work of Fujimura and Der Kiureghian as a starting point, this chapter aims to provide a general prospective of the methods and a selection of the most recent developments.

TELM genesis finds its roots in the grounding works of Der Kiureghian (2000), and Koo et al. (2005), where FORM (Ditlevsen and Madsen 1996) was pioneered to solve nonlinear random vibration problems. FORM is a time-invariant structural reliability method; therefore, the setup of the dynamic problem needs to be such that the randomness is completely split from time variability. This implies a discretization of the input in terms of a finite set of standard normal Gaussian random variables, and a finite set of time variant functions (Der Kiureghian 2000); moreover, it requires the definition of the failure event as a limit-state function. The limit-state function is defined as the difference between a pre-defined threshold and the nonlinear system response. Negative values of the limit-state function identify the failure domain, and zero values define the frontier of the failure domain (i.e. the limit-state surface). When the system is linear, it can be shown (Sect. 2) that the limit state surface is a hyperplane and failure probability is given by close form solution. Conversely for nonlinear systems, the limit-state surface is generally nonlinear; then, the tail probability is obtained by FORM approximation. In this method, the limit state-surface is approximated by a hyperplane tangent to the point belonging to the limit-state surface and having the highest probability density value. In structural reliability theory, this point is known as the "design point", and it contains important physical information regarding the behavior of the nonlinear system. Departing from these early works, Fujimura and Der Kiureghian developed the TELM and formalized the concept of the tail-equivalent linear system (TELS).

Briefly stated, TELS is the hyperplane introduced by FORM linearization, and it is physically identified by its Impulse-Response Function (IRF) or Frequency-Response Function (FRF). Once the FRF or IRF are identified, linear random vibration theory can be used to determine the statistics of the response. The original method was developed in the time domain for inelastic systems and, in 2008, was extended in frequency domain in the context of marine structures for a nonlinear type of loading (Garrè and Der Kiureghian 2010). Further developments includes: extension of the frequency domain for inelastic structures (Broccardo 2014), multicomponent excitations (Broccardo and Der Kiureghian 2015), nonstationary excitation (Broccardo and Der Kiureghian 2013), sinc expansion (Broccardo and Der Kiureghian 2012), multi-supported structures (Wang and Der Kiureghian 2016), the secant hyperplane method (Alibrandi et al. 2016), and the tail probability equivalent linearization method. Among these, this chapter presents a review of the TELM with sinc expansion, the TELM for multi-supported structures, and the secant hyperplane method.

2 The Original Time Domain TELM

2.1 Input Representation

In TELM, the stochastic excitation is represented by a linear combination of a set of time variant basis functions $\boldsymbol{s}(t) = [s_1(t), \ldots s_N(t)]$ with independent standard normal random coefficients $\mathbf{u} = [u_1, \ldots u_N]^{\mathrm{T}}$,

$$F(t) = \mathbf{s}(t)\mathbf{u}. \tag{1}$$

The choice of the basis functions, $\boldsymbol{s}(t)$, determines the autocorrelation function of the input as well as the physical domain of the discretization. TELM was originally developed in the time domain, using a discretized filtered white-noise, which can be written as

$$F(t) = [\eta(t) * W(t)]U(t) = \int_0^t \eta(t-\tau|\boldsymbol{\theta})W(\tau)d\tau, \tag{2}$$

where * denotes convolution, $U(t)$ is the unit-step function, $W(t)$ is the white-noise process, and $\eta(t|\boldsymbol{\theta})$ is the impulse response function (IRF) of a stable linear filter with parameters $\boldsymbol{\theta}$. TELM implementation of (2) requires discretization of the time axis. For a selected time step Δt and initial time $t_0 = 0$, the white noise $\mathrm{W}(\tau)$ is approximated with the following rectangular wave process:

$$\widehat{W}(t) = \frac{1}{\Delta t} \int_{t_{n-1}}^{t_n} W(\tau) d\tau, \quad t_{n-1} < t \leq t_n \quad n = 1, \ldots, N. \tag{3}$$

Equation (3) is band-limited at frequency $\Omega = \pi/\Delta t$ (rad/s) and, for a given white-noise spectral density S, has the variance $\sigma^2 = 2\pi S/\Delta t$. By defining the standard normal random variables $u_n = \widehat{W}(t_n)/\sigma$, $n = 1, \ldots, N$, Eq. (3) is written in the form

$$\widehat{W}(t) = \boldsymbol{\sigma}(t)\mathbf{u}, \tag{4}$$

where $\boldsymbol{\sigma}(t) = [\sigma_1(t) \ldots \sigma_N(t)]$, and

$$\begin{aligned} \sigma_n(t) = \sigma, \; t_{n-1} < t \leq t_n \quad n = 1, 2, \ldots, N \\ = 0, \text{ otherwise.} \end{aligned} \tag{5}$$

The discrete version of $F(t)$ is obtained by replacing $W(t)$ in Eq. (2) with $\widehat{W}(t)$, that is

$$\widehat{F}(t) = \left[\eta(t|\boldsymbol{\theta}) * \widehat{W}(t)\right] = \mathbf{s}(t)\mathbf{u}, \tag{6}$$

where

$$s_n(t) = \sigma \int_{t_{n-1}}^{t_n} \eta(t - \tau|\boldsymbol{\theta}) d\tau, t_{n-1} < t < t_n \quad n = 1, 2, \ldots N. \tag{7}$$

2.2 Time-Domain Response Representation, and TELS Definition

The linear differential equation of a stable system subject to a stochastic input can be written as

$$L[X(t)] = F(t), \tag{8}$$

where $L[\cdot]$ is a differential operator and $X(t)$ is the response. When the system is linear, the response is obtained by convolving its IRF $h(t)$ with the input excitation i.e.

$$X(t) = \left[h(t) * \widehat{F}(t)U(t)\right] = \mathbf{a}(t)\mathbf{u}, \tag{9}$$

where $\mathbf{a}(t) = [a_1(t), \ldots, a_N(t)]$, $a_n(t) = \int_0^t h(t-\tau)s_n(\tau)d\tau$. Observe that the response is a linear function of the vector $\mathbf{u}$. Conversely, when the system is nonlinear, the response is a nonlinear function of $\mathbf{u}$. In the latter case, for any given $\mathbf{u}$, a numerical scheme can be applied to (8) to compute the response. Therefore, the response $X(t)$, in general, is either an explicit or an implicit function of the standard normal random variables $\mathbf{u}$, i.e. $X(t) \equiv X(t, \mathbf{u})$.

Given a response threshold of interest x at a specific time t_x, the tail probability is defined as $P[x < X(t_x, u)]$. FORM can now be used to compute the tail probability as $\Pr[g(x, t_x, \mathbf{u}) < 0]$, where $g(x, t_x, \mathbf{u}) = x - X(t_x, \mathbf{u})$ denotes the limit-state function. In FORM the first-order approximation of the probability is computed by linearizing the limit-state surface in the standard normal space at the so-called design point $\mathbf{u}^*$. The design point belongs to the limit-state surface $g(x, t_x, \mathbf{u}) = 0$ and has minimum distance from the origin. This distance, denoted β, is known as the reliability index. If the system is linear, the limit-state surface is a hyperplane with gradient $\mathbf{a}(t)$ and the design point and the reliability index are given in closed form (Fujimura and Der Kiureghian 2007) as:

$$\mathbf{u}^*(x, t_x) = \frac{x}{\|\mathbf{a}(t_x)\|} \frac{\mathbf{a}(t_x)^T}{\|\mathbf{a}(t_x)\|}, \tag{10}$$

and

$$\beta(x, t_x) = \frac{x}{\|\mathbf{a}(t_x)\|}. \tag{11}$$

Furthermore, the gradient $\mathbf{a}(t_x)$ can be written explicitly in terms of the design point

$$\mathbf{a}(t_x) = \frac{x}{\|\mathbf{u}^*\|} \frac{\mathbf{u}^{*\mathrm{T}}}{\|\mathbf{u}^*\|}, \tag{12}$$

and the tail probability has the simple and exact solution

$$\Pr[x < X(t_x, \mathbf{u})] = \Phi[-\beta], \tag{13}$$

where $\Phi[\cdot]$ denotes the standard normal cumulative probability function. In the nonlinear case, the design point $\mathbf{u}^*$ is obtained as the solution to the constrained optimization problem $\mathbf{u}^* = \arg\min\{\|\mathbf{u}\| | g(x, t_x, \mathbf{u}) = 0\}$. A gradient based optimization algorithm (Liu and Der Kiureghian 1991) is commonly used to solve this optimization. Given $\mathbf{u}^*$, the limit-state function is expanded in Taylor series at the design point:

$$g\left(x, t_x, \mathbf{u}^*\right) = x - \left[X\left(t_x, \mathbf{u}^*\right) + \nabla_{\mathbf{u}} X\left(t_x, \mathbf{u}^*\right) \cdot \left(\mathbf{u} - \mathbf{u}^*\right) + \text{h.o.t}\right], \tag{14}$$

where h.o.t stands for high order terms. The first-order approximation of $\Pr[g(x, t_x, \mathbf{u}) < 0]$ is then obtained by retaining the linear terms. The hyperplane arising from the linearization completely defines TELS. Let $\mathbf{a}(t)$ denote the gradient vector of this hyperplane. Then, for known $\mathbf{s}_n(t)$, the set of equations

$$\sum_{m=1}^{M} h(t_x - t_m) s_n(t_m) \Delta t = a_n(t_x), \; m = 1, \ldots, M \equiv N, \text{ and } t_x \equiv t_M \tag{15}$$

is solved for the IRF $h(t)$ of the TELS. The time resolution used in (15), denoted by the subscript m, is the same as the time discretization used in (4), i.e., $M \equiv N$. As observed in Fujimura and Der Kiureghian (2007), this is a requirement to solve the system in Eq. (15) for the original TELM in time domain. Nevertheless, for discretization methods using other basis functions, the time resolution M can be selected independently from the number of random variables N. Once the IRF of the TELS is obtained, methods of linear random vibration theory are used to compute the statistics of the response for a specific set of thresholds. These represent first-order approximations of the corresponding statistics of the nonlinear response. Examples of these statistics for nonlinear systems can be found in Fujimura and Der Kiureghian (2007), Der Kiureghian and Fujimura (2009) and Broccardo and Der Kiureghian (2014).

3 TELM Analysis in Frequency Domain

3.1 Input Representation

An alternative to the time-domain discretization is the frequency-domain discretization (Shinozuka 1972; Shinozuka and Deodatis 1991). In this representation, the basis functions are selected as random weighted sine and cosine, which results in the canonical Fourier series with random coefficients. For a selected frequency discretization step $\Delta\omega$, and given discrete frequency points $[\omega_1, \ldots, \omega_K]$ with $\omega_k = \omega_{k-1} + \Delta\omega$, the general representation for a stationary process is written as

$$\widehat{F}(t) = \sum_{k=1}^{K} \sigma_k \left[u_k \sin(\omega_k t) + u_{K+k} \cos(\omega_k t)\right] = \mathbf{s}(t)\mathbf{u} \tag{16}$$

where

$$\mathbf{s}(t) = \left[s_1(t), \ldots, s_K(t); s_{K+1}(t), \ldots, s_{2K}(t)\right], \tag{17}$$

$$s_k(t) = \sigma_k \sin(\omega_k t), \quad s_{K+k}(t) = \sigma_{K+k} \cos(\omega_k t), \tag{18}$$

$$\mathbf{u} = [u_1, \ldots, u_K; u_{K+1}, \ldots, u_{2K}]^{\mathrm{T}}, \tag{19}$$

in which $\sigma_k = \sqrt{2S(\omega_k|\boldsymbol{\theta})\Delta\omega}$, $S(\omega_k|\boldsymbol{\theta})$ is a parametric power spectral density (PSD) and $\boldsymbol{\theta}$ is the set of parameters.

3.2 Frequency-Domain Response Representation, and TELS Definition

In frequency domain, the governing equation of a stable linear system can be written as

$$\mathcal{F}\{L[X(t)]\}(\omega) = \mathcal{F}\{F(t)\}(\omega), \tag{20}$$

$$\mathcal{L}\{\overline{X}(\omega)\} = \overline{F}(\omega), \tag{21}$$

where $\mathcal{F}\{\}$ is the Fourier transform operator, $\mathcal{L}\{\}$ is a linear operator in the frequency domain, and $\overline{X}(\omega)$ and $\overline{F}(\omega)$ are the Fourier transforms of the response and the input excitation, respectively. The steady-state response is obtained as

$$\overline{X}(\omega) = \mathcal{F}\{h(t) * F(t)\}(\omega) = H(\omega)\,\overline{F}(\omega), \tag{22}$$

where $H(\omega) = \mathcal{F}\{h(t)\}(\omega)$ is the frequency-response function (FRF) of the system. Using the the frequency-domain representation Eq. (16), the steady-state response of the linear system is obtained as:

$$\begin{aligned} X(t) &= \mathcal{F}^{-1}\{\overline{X}(\omega)\}(t) = \sum_{k=1}^{K} \sigma_k |H(\omega_k)| [u_k \sin(\theta_k t) + u_{K+k} \cos(\theta_k t)] \\ &= \mathbf{a}(t)\mathbf{u}, \end{aligned} \tag{23}$$

where

$$\mathbf{a}(t) = [a_k(t), \ldots, a_K(t); a_{K+k}(t), \ldots, a_{2K}(t)], \tag{24}$$

$$a_k(t) = \sigma_k |H(\omega_k)| \sin(\theta_k t), \quad a_{K+k}(t) = \sigma_k |H(\omega_k)| \cos(\theta_k t), \tag{25}$$

in which $\theta_k = \omega_k t + \varphi_k$ and $|H(\omega_k)|$ and φ_k respectively represent the modulus and phase of the FRF of the linear system. It can be shown (Garrè and Der Kiureghian 2010) that the following relationships exist between the elements of the gradient vector $\mathbf{a}(t_x)$ and the FRF:

$$|H(\omega_k)| = \frac{\sqrt{a_k(t_x)^2 + \bar{a}_k(t_x)^2}}{\sigma_k}, \tag{26}$$

$$\varphi_k = \omega_k t_x + \tan^{-1}\left[\frac{a_k(t_x)}{a_{K+k}(t_x)}\right]. \tag{27}$$

Given a general nonlinear system and a stochastic input described by Eq. (16), the design point $\mathbf{u}^*$ for the selected threshold and time point is first determined and the gradient vector of the tangent plane, $\mathbf{a}(t_x)$, is computed from Eq. (12). The latter, in conjunction with Eqs. (26)–(27), uniquely defines the FRF of the TELS. Likewise in time domain, once the TELS is defined, then, linear random vibration can be used to compute different statistics of the linearized model.

4 TELM Analysis with Sinc Basis Functions

In this section, we report a brief overview on the use of sinc basis functions for representing band-limited stochastic processes and their implementation in TELM analysis. A broader and more in depth treatment can be found in Broccardo (2014), and Broccardo and Der Kiureghian (2012).

Band-limited stationary processes are an important subclass of stochastic processes because in real applications and computer-based simulations, the spectrum, usually, has a finite band limit. A stationary process is band limited if $S(\omega) = 0$ for $|\omega| > \Omega$, with Ω being the band limit of the process. Within this subclass, the band-limited white noise, i.e., processes for which $S(\omega) = S_0$ for $\omega \leq \Omega$ and 0 otherwise, is paramount. In fact, the band-limited white noise serves as the building block for more general processes that are generated by use of filters and modulating functions (Priestley 1965; Rezaeian and Der Kiureghian 2008).

In this section, we briefly show that the sinc function, defined as $\mathrm{sinc}(t) = \sin(t)/t$, is a suitable choice to construct a series expansion for band-limited, white-noise processes. We restrict our focus to the class of strictly Gaussian processes (i.e., the coefficients of the expansion are Gaussian random variables). For convenience, a scaled version of the sinc function is introduced, i.e.

$$\mathrm{sinc}_{\Delta t}(t) = \frac{\sin\left(\frac{\pi t}{\Delta t}\right)}{\left(\frac{\pi t}{\Delta t}\right)}, \tag{28}$$

with $\Delta t \leq \pi/\Omega$ and Ω being the band limit. It is easy to show that

$$\mathcal{F}[\mathrm{sinc}_{\Delta t}(t)](\omega) = \frac{\Delta t}{2\pi}\Pi_{\pi/\Delta t}, \tag{29}$$

where $\mathcal{F}[\cdot]$ is the Fourier Transform operator, $\Pi_{\pi/\Delta t} = 1$ for $|\omega| < \pi/\Delta t$, and $\Pi_{\pi/\Delta t} = 0$ otherwise. It can be shown (Osgood 2007) that any band-limited function $f(t)$ can be represented by the expansion

$$f(t) = \sum_{n=-\infty}^{\infty} f(n\Delta t)\mathrm{sinc}_{\Delta t}(t - n\Delta t). \tag{30}$$

In signal processing, Eq. (30) is known as sinc expansion or Whittaker-Shannon interpolation formula. Remarkably, the coefficients of the series are simply the sample values of the function at discrete points in time, from which the original function can be exactly reconstructed. It can be shown (Osgood 2007) that

$$\int_{-\infty}^{\infty} sinc_{\Delta t}(t - n\Delta t)sinc_{\Delta t}(t - m\Delta t)dt = \delta_{mn}\Delta t, \tag{31}$$

so that the sinc functions are orthogonal.

By considering the coefficients of the expansion in Eq. (30) as random variables, in particular as i.i.d. zero-mean Gaussian random variables, a stationary, band-limited, zero-mean, white-noise process is represented as

$$W(t) = \sum_{n=-\infty}^{\infty} u_n \sigma sinc_{\Delta t}(t - n\Delta t). \tag{32}$$

where u_n are standard normal random variables and σ is the standard deviation. It can be shown (Broccardo 2014) that the autocovariance function of Eq. (32) is identical to that of a band-limited white noise. The convergence of the series is also investigated in Broccardo (2014).

Considering Eq. (32), Eq. (1) can be rewritten as

$$\widehat{F}(t) = \widehat{W}(t) = \sum_{n=1}^{N} u_n \sigma sinc_{\Delta t}(t - n\Delta t) = \mathbf{s}(t)u, \tag{33}$$

where $\mathbf{s}(t) = [\sigma sinc_{\Delta t}(t - \Delta t), \ldots, \sigma sinc_{\Delta t}(t - N\Delta t)]$ and $\mathbf{u} = [u_1, \ldots, u_N]$. Given the above representation of the input process, the implementation of the sinc expansion into TELM analysis is rather straightforward and it follows the same steps of Sect. 2. It is convenient to rewrite Eq. (15) in a matrix form, i.e.

$$\mathbf{Sh} = \mathbf{a}(t_M), \tag{34}$$

with

$$\mathbf{S} = \Delta t_a \begin{bmatrix} s_1(t_1) & \cdots & s_1(t_M) \\ \vdots & \ddots & \vdots \\ 0 & \cdots & s_N(t_M) \end{bmatrix}, \mathbf{h} = \begin{bmatrix} h(t_M - t_1) \\ \vdots \\ h(t_M - t_M) \end{bmatrix}, \mathbf{a}(t_x) = \begin{bmatrix} a_1(t_M) \\ \vdots \\ a_N(t_M) \end{bmatrix}, \tag{35}$$

where $t_x \equiv t_M$, and Δt_a is the time discretization step for numerical analysis. As we have seen in Sect. 2, the original time-domain discretization requires the same time resolution for both the stochastic discretization and the time discretization, that is $M \equiv N$. In nonlinear structural analysis, Δt_a needs to be chosen sufficiently small in order to guarantee convergence of the solution, and usually this requirement leads to a large number of random variables. However, a large number of these variables represent high frequency content of the excitation, which may not be relevant for the physics of the system. In the sinc formulation, there is no such constraint. In fact, we can select a stochastic discretization rate, Δt_s, in the expansion in Eq. (33) that is independent of Δt_a. Then, observe that Eq. (33) is a time-continuous process, for which a different Δt_a can be chosen. Clearly, Δt_s must satisfy the condition $\Delta t_s < \frac{\pi}{\Omega}$, where Ω is the desired bandwidth.

When $\Delta t_a \neq \Delta t_s$, Eq. (35) is in rectangular form with dimension $N \times M$ (in general $\Delta t_a < \Delta t_s$, which implies $N < M$). In that case, the solution of the system can be found as min-norm solution of the system. However, there is a more straightforward approach to follow. In fact, one can recognize that the IRF is a band-limited function which can itself be expressed with the sinc expansion. Thus, it is sufficient to compute samples of the IRF, and to reconstruct the continuous function by the sinc expansion. In other words, Eq. (35) is transformed into a square system with dimension $N \times N$. This leads to a determined system of N equations in N unknowns, which is solved by inversion as before. Observe that the size of the system is much smaller than in the original formulation. Once the N samples of the IRF are computed, the IRF is reconstructed by the sinc expansion, i.e.,

$$h(t) \simeq \sum_{n=1}^{N} h(n\Delta t) sinc_{\Delta t}(t - n\Delta t). \tag{36}$$

4.1 Numerical Example

In this chapter, only an illustrative single-degree-of-freedom system (SDoF) is presented, in Broccardo and Der Kiureghian (2016) the reader can find a more realistic multi-degree-of-freedom (MDoF) example. The equation of motion of a SDOF is written as

$$m\ddot{U}(t) + c\dot{U}(t) + R^{in}\left[U(t), \dot{U}(t)\right] = F(t), \tag{37}$$

where $U(t)$ is the displacement, m the mass, c the damping coefficient, $R^{in}[\cdot]$ the restoring force, and $F(t)$ the external force. In the case of ground motion, $F(t)$ is written as $F(t) = -m\ddot{U}_g(t)$, where $\ddot{U}_g(\mathrm{t})$ is the ground acceleration, here modeled as a white-noise process. In this example, the non-degrading Bouc-Wen material model, (Wen 1976; Bouc 1967), is selected for characterizing R^{in}, i.e.,

$$R^{in}\left[U(t),\dot{U}(t)\right]=k[\alpha U(t)+(1-\alpha)Z(t)], \tag{38}$$

where α is a nonlinearity parameter with $\alpha=1$ denoting a linear case, k is the elastic stiffness, and $Z(t)$ is the hysteretic response that follows the differential law

$$\dot{Z}(t)=-\gamma\left|\dot{U}(t)\right||Z(t)|^{\bar{n}-1}-\eta|Z(t)|^{\bar{n}}\dot{U}(t)+A\dot{U}(t), \tag{39}$$

in which γ, η, A and $\bar{n}$ are model parameters described in Wen (1976), Bouc (1967) and Haukaas and Der Kiureghian (2004). Structural properties and model parameters are listed in Table 1, while Fig. 1 shows the hysteretic behavior of the system. The response of interest is $X(t)=U(t)$, the point in time selected for the analysis is $t_x=10$ s, and the limit-state function is defined by the threshold $x=3\sigma_0$, with $\sigma_0^2=\pi S m^2/(ck)$ being the mean-square response of the linear $(\alpha=1)$ system. The ground acceleration $\ddot{U}_g(t)$ is modelled as a stationary, zero-mean Gaussian band-limited white noise simulated with the sinc expansion. The spectral density is set at $S=1\ [m^2/(rad\ s^3)]$ for all simulations, while the band limit is varied according to the selected time discretization step t_s.

Table 2 shows the result of TELM analysis for selected band-limited white-noise inputs. In all cases, the analysis integration step $\Delta t_a=0.01$ s is used for numerical integration of the nonlinear response. Figure 2a shows the IRFs for the white-noise inputs with band limits of 2.5 and 50 Hz. Observe that the two results are almost the same. This suggests that the two inputs are essentially equivalent for studying the reliability of the system. Figure 2b shows the frequency response functions (FRFs)

Table 1 Structural properties example 1

m (kg)	u_y (m)	α	c (kNs/m)	k (kN/m)	$\gamma\ 1/(\mathrm{m}^{\bar{n}})$	$\eta\ (1/\mathrm{m}^{\bar{n}})$	$\bar{n}$	A
1E6	σ_0	0.1	(2π) E6	$(2\pi)^2$ E6	$1/(2u_y)^{\bar{n}}$	$1/(2u_y)^{\bar{n}}$	3	1

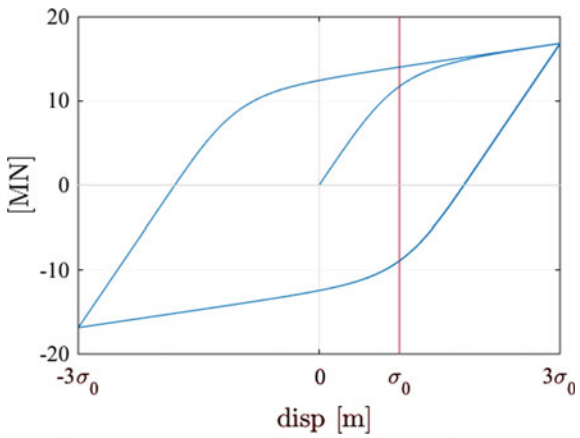

Fig. 1 Hysteretic behavior of the single degree of freedom system

Table 2 Results example 1

Sampling rate Δt_s (s)	Band limit (Hz)	No. Random variables	Reliability index	CPU time (s)
0.010	50.00	1001	3.122	836
0.020	20.00	501	3.135	321
0.050	10.00	201	3.122	291
0.100	5.00	101	3.122	113
0.200	2.50	51	3.133	51

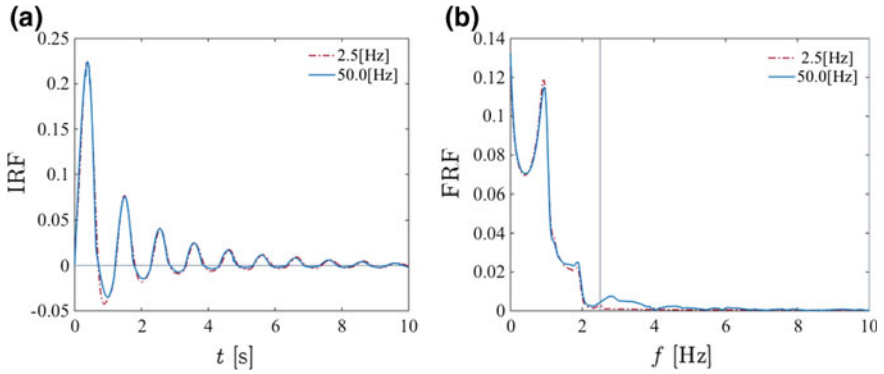

Fig. 2 **a** Impulse-response function for a 2.5 Hz (*red line*) and 50 Hz (*blue line*) band-limited white noise, **b** frequency-response function for the two band-limited white noise. The *grey vertical line* denotes a 2.5 Hz band limit

for the same inputs. From the FRFs, it is evident that the frequencies above 2.5 Hz are not playing a significant role. Thus, we can select a Δt_s according to the desired band limit and use the minimum number of random variables. The last two columns of Table 2 list the reliability index and the CPU time (on a 2.8 GHz processor with 8 GB of RAM) for different Δt_s. Indeed, the use of the sinc expansion and independent selection of t_s leads to significant reduction in the computational time at a negligible loss in accuracy. The sinc function, then can be used to consistently reduce the computational cost. However, a clear knowledge of the input frequency content and of the physic of the system is required. In Broccardo and Der Kiureghian (2016), it is suggested an heuristic criteria that can be applied before implementing the sinc expansion.

5 TELM for Multiple-Supported Excitation Problems

In this section the extension of TELM to multiple-supported excitation analysis is introduced. More details regarding this extension can be found in Wang and Der Kiureghian (2016).

5.1 Representation of Correlated Ground Motions

The stochastic displacement processes, instead of acceleration processes, are used in the formulation of TELM for multiple-support excitation analysis. This is because: (i) It is convenient to use ground displacement as input for structural analysis with multiple-support excitations; and (ii) It is also convenient for formulation of TELS with support displacement processes.

Let an array of zero-mean, jointly stationary Gaussian random processes $[D_1(t) \ldots D_m(t)]$, representing the surface displacement processes for m sites, be expressed as a Fourier series (Chatfield 2003)

$$D_k(t) = \sum_{p=1}^{n/2} [A_{pk} \cos(\omega_p t) + B_{pk} \sin(\omega_p t)],\ k = 1, \ldots, m \tag{40}$$

The Fourier coefficients A_{pk} and B_{pk} are zero-mean, jointly Gaussian random variables and are uncorrelated for different frequencies, i.e. $\mathrm{E}[A_{pk}A_{qk}] = \mathrm{E}[B_{pk}\,B_{qk}] = \mathrm{E}[A_{pk}\,B_{qk}] = 0$ for $p \neq q$. At frequency ω_p, one has (Chatfield 2003)

$$\begin{aligned} \mathrm{E}\left[A_{pk}A_{pl}\right] = \mathrm{E}\left[B_{pk}B_{pl}\right] &= \begin{cases} 2S_{kk}(\omega_p)\Delta\omega, & \text{if } k = l \\ \mathrm{Re}\left[2S_{kl}(\omega_p)\right]\Delta\omega, & \text{if } k \neq l \end{cases} \\ \mathrm{E}\left[A_{pk}B_{pl}\right] = -\mathrm{E}\left[B_{pk}A_{pl}\right] &= \begin{cases} 0, & \text{if } k = l \\ -\mathrm{Im}\left[2S_{kl}(\omega_p)\right]\Delta\omega, & \text{if } k \neq l, \end{cases} \end{aligned} \tag{41}$$

where $S_{kk}(\omega)$ is the two-sided auto-PSD of the displacement process at site k and $S_{kl}(\omega)$ is the cross-PSD of the displacement processes at sites k and l. Thus, given the auto-PSDs and cross-PSDs of the ground displacements, the statistical properties of all the Fourier coefficients are easily determined. The auto-PSDs can be specified using well-known theoretical models.

The cross-PSD between displacement processes at sites k and l can be expressed as

$$S_{kl}(\omega) = \gamma_{kl}(\omega)[S_{kk}(\omega)S_{ll}(\omega)]^{1/2}, \tag{42}$$

where γ_{kl} is the coherency function that characterizes the spatial variability of the ground motion. The coherency function is written as Der Kiureghian (1996)

$$\gamma_{kl}(\omega) = |\gamma_{kl}(\omega)| exp\left\{ i\left[\theta_{kl}^{wp}(\omega) + \theta_{kl}^{sr}(\omega)\right]\right\}, \tag{43}$$

in which the real function $|\gamma_{kl}(\omega)|$ characterizes the incoherence effect, whereas the phase angles $\theta_{kl}^{wp}(\omega)$ and $\theta_{kl}^{sr}(\omega)$ characterize the wave-passage and site-response effects, respectively. Note that, for stationary processes, the coherency function for ground displacements is identical to the coherency function for ground accelerations.

One widely used expression for the incoherence component is Luco and Wong (1986)

$$|\gamma_{kl}(\omega)| = \exp\left[-\left(\frac{\alpha\omega d_{kl}}{\upsilon_s}\right)^2\right], \tag{44}$$

where α is an incoherence factor, d_{kl} denotes the horizontal distance between sites k and l, and υ_s is the shear-wave velocity of the medium. The phase angle due to the wave-passage effect is given by Der Kiureghian (1996)

$$\theta_{kl}^{wp}(\omega) = -\frac{\omega d_{kl}^{L}}{\upsilon_{app}}, \tag{45}$$

in which d_{kl}^{L} is the projected horizontal distance in the longitudinal direction of propagation of waves and υ_{app} is the surface apparent wave velocity. The phase angle due to the site-response effect is given by Der Kiureghian (1996)

$$\theta_{kl}^{sr}(\omega) = \tan^{-1}\frac{\mathrm{Im}[H_k(\omega)H_l(\omega)]}{\mathrm{Re}[H_k(\omega)H_l(\omega)]}, \tag{46}$$

where $H_k(\omega)$ is the FRF of the soil column at site k. A single-degree-of-freedom soil column model is used so that

$$H_k(\omega) = \frac{\omega_k^2 + 2i\zeta_k\omega_k\omega}{\omega_k^2 - \omega^2 + 2i\zeta_k\omega_k\omega}. \tag{47}$$

To fully describe the array of ground displacement processes, $m \times n$ Fourier coefficients in Eq. (40) are required. On the other hand, in the context of TELM, the partially correlated Fourier coefficients should be transformed into the uncorrelated standard normal space. For the $2m$-vector $\mathbf{Y}_p = [A_{p1}\, B_{p1} \ldots A_{pm}\, B_{pm}]^{\mathrm{T}}$ at frequency ω_p, let $\mathbf{\Sigma}_{pp}$ denote the $2m \times 2m$ covariance matrix evaluated via (41). Using a spectral decomposition technique (Li and Der Kiureghian 1993), $\mathbf{Y}_p$ can be transformed into the uncorrelated standard normal space by

$$\mathbf{Y}_p = \sum_{i=1}^{2m} \Omega_{pi} \boldsymbol{\phi}_{pi} u_{pi},\ p = 1,\ \ldots, n/2, \tag{48}$$

where Ω_{pi}^2 and $\boldsymbol{\phi}_{pi}$ are eigenvalues and normalized eigenvectors of the covariance matrix $\boldsymbol{\Sigma}_{pp}$ and u_{pi} are uncorrelated standard normal random variables. Using a subset $2\tilde{m}_p < 2m$ of the terms in Eq. (48) for the largest eigenvalues, the number of random variables can be reduced. The reduction of random variables becomes fairly useful for problems with large set of support points, since high dimensional reliability analysis is computationally demanding. Let

$$\widetilde{\mathbf{T}}_p = \widetilde{\boldsymbol{\Phi}}_p \widetilde{\boldsymbol{\Lambda}}_p,\ p = 1,\ \ldots, n/2 \tag{49}$$

denote the reduced transformation matrix, where $\widetilde{\boldsymbol{\Phi}}_p$ is a $2m \times 2\tilde{m}_p$ matrix of the $2\tilde{m}_p$ highest eigenvectors and $\widetilde{\boldsymbol{\Lambda}}_p$ is a $2\tilde{m}_p \times 2\tilde{m}_p$ diagonal matrix with diagonal elements Ω_{pi} corresponding to the $2\tilde{m}_p$ largest eigenvalues. Equation (48) is then rewritten as

$$\mathbf{Y}_p \cong \widetilde{\mathbf{T}}_p \mathbf{u}_p,\ p = 1,\ \ldots, n/2, \tag{50}$$

where $\boldsymbol{u}_p = [u_{p1} \ldots u_{p(2\tilde{m}_p)}]^T$ is the $2\tilde{m}_p$-vector of uncorrelated standard normal random variables. In this way, the number of random variables for each frequency ω_p is reduced from $2m$ to $2\tilde{m}_p$. Note that $\tilde{m}_p$ may depend on p and may increase as p increases with the upper bound m. This is because the coherency between higher frequency components of a pair of ground motions is weaker than that between lower frequency counterparts. Thus, the total number of random variables is reduced from $m \times n$ to $\sum_{p=1}^{n/2} 2\tilde{m}_p$. Using Eq. (50), the Fourier coefficients A_{pk} and B_{pk} are expressed as

$$A_{pk} = \mathbf{t}_{p(2k-1)} \mathbf{u}_p = \sum_{i=1}^{2\tilde{m}_p} t_{p(2k-1)i} u_{pi},\ p = 1,\ \ldots, n/2,\ k = 1,\ \ldots, m, \tag{51}$$

$$B_{pk} = \mathbf{t}_{p(2k)} \mathbf{u}_p = \sum_{i=1}^{2\tilde{m}_p} t_{p(2k)i} u_{pi},\ p = 1,\ \ldots, n/2,\ k = 1,\ \ldots, m, \tag{52}$$

where $\mathbf{t}_{p(2k-1)}$ and $\mathbf{t}_{p(2k)}$ are respectively the $(2k-1)$-th and $2k$-th row vectors of the reduced transformation matrix $\widetilde{\mathbf{T}}_p$, and $t_{p(2k-1)i}$ and $t_{p(2k)i}$ are the i-th coordinates of $\mathbf{t}_{p(2k-1)}$ and $\mathbf{t}_{p(2k)}$, respectively. Since the Fourier coefficients are uncorrelated for different frequency points, the reduced transformation matrix $\widetilde{\mathbf{T}}_p$ is

computed independently for different p's. Substituting Eqs. (51) and (52) into Eq. (40), one finally obtains

$$D_k(t) = \sum_{p=1}^{n/2} \mathbf{s}_{pk}(t)\mathbf{u}_p = \sum_{p=1}^{n/2} \sum_{i=1}^{2\tilde{m}_p} \mathrm{s}_{pki}(t)u_{pi},\ k = 1, \ldots, m, \tag{53}$$

where $\mathbf{s}_{pk}(t) = [\mathrm{s}_{pk1}(t) \ldots \mathrm{s}_{pk(2\tilde{m}_p)}(t)]$, and

$$\mathrm{s}_{pki}(t) = t_{p(2k-1)i}\cos(\omega_p t) + t_{p(2k)i}\sin(\omega_p t). \tag{54}$$

5.2 *Formulation of TELS for Multiple-Support Excitation Analysis*

The dynamic equilibrium equation for a linear structure with N unconstrained degrees of freedom (DOF) and subjected to m support motions is given by Clough and Penzien (1993)

$$\begin{bmatrix} \mathbf{M} & \mathbf{M}_c \\ \mathbf{M}_c^{\mathrm{T}} & \mathbf{M}_g \end{bmatrix} \begin{Bmatrix} \ddot{\mathbf{X}} \\ \ddot{\mathbf{D}} \end{Bmatrix} + \begin{bmatrix} \mathbf{C} & \mathbf{C}_c \\ \mathbf{C}_c^{\mathrm{T}} & \mathbf{C}_g \end{bmatrix} \begin{Bmatrix} \dot{\mathbf{X}} \\ \dot{\mathbf{D}} \end{Bmatrix} + \begin{bmatrix} \mathbf{K} & \mathbf{K}_c \\ \mathbf{K}_c^{\mathrm{T}} & \mathbf{K}_g \end{bmatrix} \begin{Bmatrix} \mathbf{X} \\ \mathbf{D} \end{Bmatrix} = \begin{Bmatrix} \mathbf{0} \\ \mathbf{F} \end{Bmatrix}, \tag{55}$$

where $\mathbf{X} = [X_1, \ldots, X_N]^{\mathrm{T}}$ is the N-vector of absolute displacements at the unconstrained DOF, $\mathbf{D} = [D_1, \ldots, D_m]^{\mathrm{T}}$ is the m-vector of prescribed support displacements, $\mathbf{M}$, $\mathbf{C}$ and $\mathbf{K}$ are respectively $N \times N$ mass, damping and stiffness matrices associated with the unconstrained DOF, $\mathbf{M}_g$, $\mathbf{C}_g$ and $\mathbf{K}_g$ are $m \times m$ matrices associated with the support DOF, $\mathbf{M}_c$, $\mathbf{C}_c$ and $\mathbf{K}_c$ are $N \times m$ coupling matrices associated with both sets of DOF, and $\mathbf{F}$ is the m-vector of reacting forces at the support DOF.

The conventional approach for analyzing such systems, (Clough and Penzien 1993), decomposes the total displacement vector at the unconstrained DOF into pseudo-static and dynamic components. However, due to the presence of both ground displacement and acceleration processes in the decomposition technique, it is difficult to derive a simple formula to compute TELS.

A displacement-based formulation (Wilson 1998) is a simpler and more effective approach for the present analysis. Using Eq. (55), the equation of equilibrium for the superstructure with specified displacements at the support points is

$$\mathbf{M}\ddot{\mathbf{X}} + \mathbf{C}\dot{\mathbf{X}} + \mathbf{K}\mathbf{X} = -\mathbf{K}_c\mathbf{D} - \mathbf{C}_c\dot{\mathbf{D}}. \tag{56}$$

Assuming the damping forces on the right-hand side are negligible relative to the elastic forces, the displacement-based equilibrium equation can be written in the form

$$\mathbf{M}\ddot{\mathbf{X}} + \mathbf{C}\dot{\mathbf{X}} + \mathbf{K}\mathbf{X} = \sum_{k=1}^{m} \boldsymbol{f}_k D_k(t), \tag{57}$$

where each displacement process $D_k(t)$ is associated with a vector $\boldsymbol{f}_k$ obtained as the negative of the k-th column of the coupling stiffness matrix $\mathbf{K}_c$. Based on Eq. (57), one can write $Z(t)$ in the form

$$Z(t) = \sum_{k=1}^{m} c_k D_k(t) + \sum_{k=1}^{m} \int_0^t h_k^d(t-\tau) D_k(\tau) d\tau, \tag{58}$$

where c_k is a time-invariant coefficient and $h_k^d(t)$ is the IRF for the response quantity of interest relative to a ground displacement at the k-th support DOF. The first sum in Eq. (58) accounts for the contribution of the ground displacement to the response quantity of interest. This term is identical to zero when the response quantity of interest can be defined solely in terms of absolute displacements at the unconstrained DOF. Examples include internal forces in the deck of a bridge. However, when the response quantity involves the ground displacement at a support, then the first term in Eq. (58) must be included. An example is the drift in the pier of a column, which equals the absolute displacement at the top of the pier minus the support displacement. Note that the above formulation does not require decomposition of the response into pseudo-static and dynamic components. Using the Dirac-Delta function, Eq. (58) can be written as

$$Z(t) = \sum_{k=1}^{m} \int_0^t [h_k^d(t-\tau) + c_k \delta(t-\tau)] D_k(\tau) d\tau = \sum_{k=1}^{m} \int_0^t h_k(t-\tau) D_k(\tau) d\tau, \tag{59}$$

in which

$$h_k(t) = h_k^d(t) + c_k \delta(t) \tag{60}$$

is defined as the generalized IRF for the displacement loading at support DOF k. The Fourier transform of $h_k(t)$, assuming it exists, is expressed by

$$H_k(\omega) = H_k^d(\omega) + c_k, \tag{61}$$

where $H_k^d(\omega)$ is the Fourier transform of $h_k^d(t)$. According to Eq. (61) $H_k(\omega)$ may possess a frequency-invariant component.

Substituting the stationary process (53) into (59) one has

$$Z(t, \mathbf{u}) = \sum_{k=1}^{m} \int_0^t h_k(t-\tau) \sum_{p=1}^{n/2} \sum_{i=1}^{2\tilde{m}_p} \mathrm{s}_{pki}(\tau) \mathrm{u}_{pi} d\tau = \sum_{p=1}^{n/2} \boldsymbol{a}_p(t) \mathbf{u}_p = \boldsymbol{a}(t)\mathbf{u}, \tag{62}$$

where $\mathbf{u} = [\mathbf{u}_1 \dots \mathbf{u}_{n/2}]^{\mathrm{T}}$, $\mathbf{u}_p = [\mathrm{u}_{p1} \dots \mathrm{u}_{p(2\tilde{m}_p)}]^{\mathrm{T}}$, $\boldsymbol{a}(t) = [\boldsymbol{a}_1(t) \dots \boldsymbol{a}_{n/2}(t)]$ $\boldsymbol{a}_p = [a_{p1}(t) \dots a_{p(2\tilde{m}_p)}(t)]$, and

$$a_{pi}(t) = \sum_{k=1}^{m} \int_0^t h_k(t-\tau) \mathrm{s}_{pki}(\tau) d\tau, \tag{63}$$

where $\mathrm{s}_{pki}(t)$ is defined in Eq. (54). Equation (63) provides the means for determining the TELS by solving the equation for $h_k(t)$, given the gradient vector $\boldsymbol{a}(t)$ as obtained from the design point. However, $a_{pi}(t)$ is contributed by components from all support DOF and it seems impossible to separately obtain the IRF for each support DOF from Eq. (63).

To tackle the aforementioned problem, one can substitute the original displacement process (40) expressed in terms of correlated Fourier coefficients A_{pk} and B_{pk} into Eq. (59), i.e.

$$Z(t, \mathbf{u}) = \sum_{k=1}^{m} \int_0^t h_k(t-\tau) \sum_{p=1}^{n/2} [A_{pk} \cos(\omega_p \tau) + B_{pk} \sin(\omega_p \tau)] d\tau = \sum_{p=1}^{n/2} \boldsymbol{a}_p'(t) \mathbf{Y}_p = \boldsymbol{a}'(t) \mathbf{Y}, \tag{64}$$

where $\mathbf{Y} = [\mathbf{Y}_1 \dots \mathbf{Y}_{n/2}]^{\mathrm{T}}$, $\mathbf{Y}_p = [A_{p1}\, B_{p1} \dots A_{pm}\, B_{pm}]^{\mathrm{T}}$, $\boldsymbol{a}'(t) = [\boldsymbol{a}_1'(t) \dots \boldsymbol{a}_{n/2}'(t)]$, $\boldsymbol{a}_p'(t) = [a_{p1}'(t) \bar{a}_{p1}'(t) \dots a_{pm}'(t) \bar{a}_{pm}'(t)]$, and

$$a_{pk}'(t) = \int_0^t h_k(t-\tau) \cos(\omega_p \tau) d\tau, \tag{65}$$

$$\bar{a}_{pk}'(t) = \int_0^t h_k(t-\tau) \sin(\omega_p \tau) d\tau. \tag{66}$$

Unlike the gradient vector $\boldsymbol{a}_p(t)$ in (62), the contributions of frequency components from each support DOF in $\boldsymbol{a}_p'(t)$ are separated.

Using Eq. (50), it is easy to show that $\boldsymbol{a}_p'(t)$ and $\boldsymbol{a}_p(t)$ are related by

$$\boldsymbol{a}_p'(t) \widetilde{\mathbf{T}}_p = \boldsymbol{a}_p(t), \; p = 1, \dots, n/2, \tag{67}$$

in which $\widetilde{\mathbf{T}}_p$ is the $2m \times 2\tilde{m}_p$ transformation matrix defined in Eq. (49). Equation (55) provides a means to determine the $2m$-vector $\boldsymbol{a}_p'(t)$ from the $2\tilde{m}_p$-vector $\boldsymbol{a}_p(t)$. However, clearly one cannot have the exact solution of $\boldsymbol{a}_p'(t)$, unless $\widetilde{\mathbf{T}}_p$ is a square matrix, which happens when $\tilde{m}_p = m$ and the number of random variables is not reduced. Using Eq. (41), $\boldsymbol{a}_p'(t)$ can be approximately obtained as

$$\boldsymbol{a}_p^{'}(t) \cong \boldsymbol{a}_p(t)\widetilde{\mathbf{T}}_p^{+},\ p=1,\ \ldots,n/2, \tag{68}$$

where $\widetilde{\mathbf{T}}_p^{+}$ is a $2\tilde{m}_p \times 2m$ pseudo-inverse of $\widetilde{\mathbf{T}}_p$. Furthermore, using Eq. (49), it is easy to show that $\widetilde{\mathbf{T}}_p^{+}$ is given by

$$\widetilde{\mathbf{T}}_p^{+} = \widetilde{\boldsymbol{\Lambda}}_p^{-1}\widetilde{\boldsymbol{\Phi}}_p^{\mathrm{T}},\ p=1,\ \ldots,n/2, \tag{69}$$

where $\widetilde{\boldsymbol{\Phi}}_p$ and $\widetilde{\boldsymbol{\Lambda}}_p$ are defined following Eq. (49). It can be shown that Eqs. (65) and (66) have the form

$$a_{pk}^{'}(t) = \left|H_k(\omega_p)\right| \cos\left(\omega_p t + \varphi_{pk}\right),\ p=1,\ \ldots,n/2,\ k=1,\ \ldots,m, \tag{70}$$

$$\bar{a}_{pk}^{'}(t) = \left|H_k(\omega_p)\right| \sin\left(\omega_p t + \varphi_{pk}\right),\ p=1,\ \ldots,n/2,\ k=1,\ \ldots,m, \tag{71}$$

where $|H_k(\omega_p)|$ is the modulus of the FRF and φ_{pk} is the associated phase angle of the response relative the input ground displacement at the k th support DOF. Using the above equations, one finally has

$$\left|H_k(\omega_p)\right| = \sqrt{\left[a_{pk}^{'}(t)\right]^2 + \left[\bar{a}_{pk}^{'}(t)\right]^2},\ p=1,\ \ldots,n/2,\ k=1,\ \ldots,m, \tag{72}$$

and

$$\tan(\omega_p t + \varphi_{pk}) = \bar{a}_{pk}^{'}(t)/a_{pk}^{'}(t),\ p=1,\ \ldots,n/2,\ k=1,\ \ldots,m \tag{73}$$

In summary, to identify the TELS in multi-support seismic excitation analysis, first the design point $\mathbf{u}^{*}$ of the nonlinear system is used in Eq. (12) to determine the gradient vector $\boldsymbol{a}(t)$. This is then used in Eq. (68) to obtain the transformed gradient vector $\boldsymbol{a}^{'}(t)$. Finally, the modulus and phase of the FRF with respect to each support DOF are computed by use of Eqs. (72) and (73). When the number of random variables is reduced, one can obtain only approximate solutions of the FRFs due to the approximation involved in Eq. (56).

5.3 Random Vibration Analysis

For TELM analysis with multiple-support excitations, applying the principle of superposition to the TELS, the two-sided PSD of the response quantity $Z(t)$ for threshold z is expressed as

$$S_{ZZ}(\omega, z) = \sum_{k=1}^{m} \sum_{l=1}^{m} H_k(\omega, z) H_l^*(\omega, z) S_{kl}(\omega), \tag{74}$$

in which the dependence of the FRFs and the response PSD on the threshold z is explicitly noted. With the auto-PSD of $Z(t)$ obtained from Eq. (74), various response statistics can be conveniently computed using well-known linear random vibration solutions.

6 The Secant Hyperplane Method and the Tail Probability Equivalent Linearization Method

TELM is based on FORM, and with the latter shares the main shortcomings and challenges: (i) In high-dimensional spaces the evaluation of the design point is challenging; (ii) In high-dimensional spaces the sampling points are distant from the design point, consequently some researchers have questioned the applicability of FORM (Valdebenito et al. 2010); (iii) For some problems the FORM approximation is not satisfactory, and it is not possible to know in advance the accuracy of the solution. In this section these issues are discussed. First, the geometry of high-dimensional spaces is described in some detail, and it is shown because FORM, in specific cases, works properly in high dimensions (Broccardo 2014; Alibrandi et al. 2015). Secondly, it is presented a novel linear response surface, named Secant Hyperplane Method (SHM) which improves the accuracy of FORM (Alibrandi et al. 2016). SHM gives rise to the Tail Probability Equivalent Linearization Method (TPELM), which improves the accuracy with respect to TELM (Alibrandi and Mosalam 2016); moreover, it provides credible bounds to the estimation of the quantity of interest. A simple numerical example shows the main features of FORM/SHM and TELM/TPELM in terms of robustness, accuracy and efficiency.

6.1 High-Dimensional Spaces

Typically, the input discretizations both in the time or frequency domain gives rise to high dimensional reliability problems. Recently, it has been shown that in high dimensions all the samples fall far away from the design point (Katafygiotis and Zuev 2008; Valdebenito et al. 2010). This leads to the question regarding the applicability of local approximations like FORM in high dimensions. However, as a matter of fact, FORM has been successfully applied in many applications of stochastic dynamic analysis (Der Kiureghian 2000; Koo et al. 2005; Fujimura and Der Kiureghian 2007; Garrè and Der Kiureghian 2010; Broccardo and Der Kiureghian 2012, 2013, 2015; Alibrandi and Der Kiureghian 2012; Broccardo 2014; Alibrandi and Koh 2015;

Alibrandi et al. 2015; Alibrandi and Mosalam 2016; Wang and Der Kiureghian 2016). To understand how FORM provides sufficiently accurate results in very high-dimensional reliability problems, it is necessary to gain insight into the geometry of very high-dimensional spaces (Alibrandi et al. 2015; Francescetti 2016). The samples drawn from a multivariate normal standard distribution fall within an N-dimensional sphere, and therefore the knowledge of its geometry is paramount.

In a N-dimensional space $u_1, u_2, \ldots, u_N$ the equation of a ball, $B_N(R)$, of radius R, centered in the origin, is $\sum_n^N u_n \leq R^2$. For $n=2$ and $n=3$ the circle and the sphere are obtained, respectively. The surface, $S_N(R)$, of the ball, known as hypersphere, has equation $\sum_n^N u_n = R^2$. The geometry of N-dimensional spheres has some counter-intuitive properties. Some significant ones and their implications within the context of high-dimensional reliability analysis are described below.

Property 1 *In high dimensions, an N-dimensional sphere has finite volume only if* $R > constant \times \sqrt{N}$

Since the volume measures the total "content" of an object, including the internal space, the volume of the N-dimensional ball, $B_N(R)$, and hypersphere $S_N(R)$ are identical. The volume of the hypersphere is defined as $V_n(R) = \mathrm{Vol}[S_N(R)] = K_N R^N$, where K_N is the volume of the N-dimensional unit sphere, i.e.,

$$K_N = \mathrm{Vol}[S_N(1)] = \frac{\pi^{\frac{N}{2}}}{\Gamma\left(\frac{N}{2}+1\right)}, \tag{75}$$

where $\Gamma(\cdot)$ is the Gamma function; moreover, using Stirling's approximation

$$\lim_{N\to\infty} K_N = \lim_{N\to\infty} \frac{\pi^{\frac{N}{2}}}{\Gamma\left(\frac{N}{2}+1\right)} = \frac{1}{\sqrt{N\pi}} \left(\sqrt{\frac{2\pi e}{N}}\right)^N. \tag{76}$$

For $n=1, 2, 3$ we have $K_1 = 2$, $K_2 = \pi$, $K_3 = (4/3)\pi$, while the corresponding volumes are $V_1 = 2R$ (line), $V_2 = \pi R^2$ (circle), $V_3 = \left(\frac{4}{3}\right)\pi R^3$ (sphere), as expected. Figure 3 shows the volume of the unit hypersphere. Observe that K_N increases rapidly up to $N \sim 5$, while for $N > 5$ it decrease and it asymptotically tends to zero for $N \to \infty$. From Eqs. (75) and (76), one can observe that for a large N the radius of a hypersphere of unit volume approaches from above $R_N \sim \left(\frac{1}{\sqrt{2\pi e}}\right)\sqrt{N}$. This implies that in high dimensions the N-dimensional hypersphere has finite volume if $R > constant \times \sqrt{N}$.

Property 2 *Vast majority of the volume of a sphere with radius R lies around a thin shell near the boundary.*

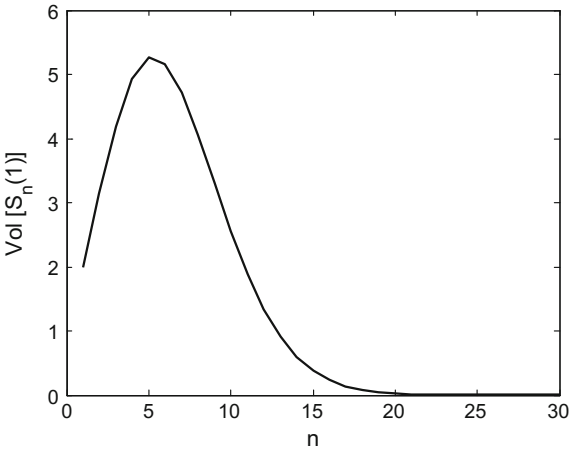

Fig. 3 Volume of the unit hypersphere

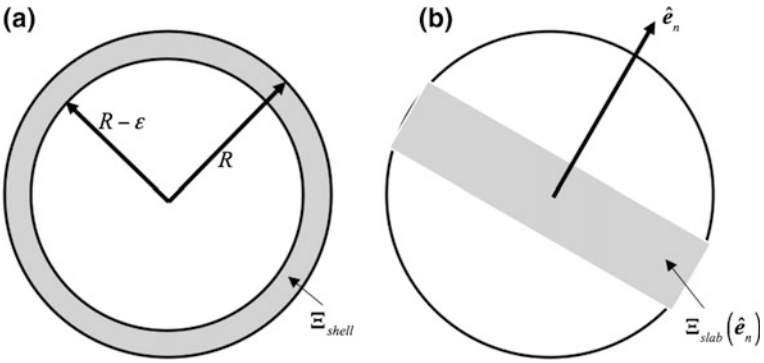

Fig. 4 Concentration of the volume in a hypershere: **a** near a thin shell around the boundary, **b** near an equatorial slab detected by an arbitrarily chosen North Pole

Let us consider a thin shell $S_N(R,\varepsilon)$ of width ε along the surface of a hypersphere of radius R. The volume of the thin shell is given as $\mathrm{Vol}[S_N(R,\varepsilon)] = \mathrm{Vol}[S_N(R)] - \mathrm{Vol}[S_N(R-\varepsilon)]$, i.e. it is equal to the difference between the volumes of two N-dimensional hyperspheres of radius R and $R-\varepsilon$, respectively. Consider the ratio

$$\lambda_N = \frac{\mathrm{Vol}[S_N(R-\varepsilon)]}{\mathrm{Vol}[S_N(R)]} = \frac{K_N(R-\varepsilon)^N}{K_N R^N} = \left(1-\frac{\varepsilon}{R}\right)^N. \tag{77}$$

Observe that for every $0<\varepsilon<R$, $\lambda_N \to 0$ tends to zero as $N\to\infty$. This implies that in high dimensions the center of the sphere is essentially void, and that the

whole volume will be contained in the thin shell $S_N(R,\varepsilon)$, see Fig. 4. This counter-intuitive property of high dimensional geometry is known as the *phenomenon of the volume concentration near the boundary*.

Property 3 *Vast majority of the volume lies near the equator.*

Let us define now the "North Pole" $\hat{\boldsymbol{e}}_n$ as an arbitrarily chosen vector on the hypersphere, while the "equatorial plane" is a hyperplane perpendicular to the North Pole. Having chosen a North Pole vector $\hat{\boldsymbol{e}}_n$, the equatorial hyperplane has equation $\boldsymbol{u}\cdot\hat{\boldsymbol{e}}_n=0$. Consider the equatorial slab bounded by the hyperplanes $\boldsymbol{u}\cdot\hat{\boldsymbol{e}}_n=-\delta_n$ and $\boldsymbol{u}\cdot\hat{\boldsymbol{e}}_n=\delta_n$, so that it is defined as $Slab(\hat{\boldsymbol{e}}_n,\delta_n)\equiv\{\boldsymbol{u}\in R^N\colon -\delta_n\le\boldsymbol{u}\cdot\hat{\boldsymbol{e}}_n\le\delta_n\}$. It can be shown that for $N\to\infty$ the following relationship holds (Francescetti 2016)

$$\frac{\mathrm{Vol}[Slab(\hat{\boldsymbol{e}}_n,\delta_n)]}{\mathrm{Vol}[S_N(R)]}=\frac{1}{\sqrt{2\pi}}\int_{-\delta_n}^{\delta_n}e^{-\frac{t^2}{2}}dt \tag{78}$$

It is seen that the volume of the N-dimensional sphere accumulates near the equator. Note that while the radius of the hypersphere grows as $\sqrt{N}$, the width of the slab is constant. Therefore, in high dimensions all the volume is, surprisingly, concentrated within an equatorial slab which represents a small region with respect to the hypersphere. This because, as above described, the volume of the sphere is finite only if $R\ge constant\times\sqrt{N}$. For illustration, let us choose $N=900$ and $\delta_n=3$, so that gives $\mathrm{Vol}[Slab(\hat{\boldsymbol{e}}_n,\delta_n)]\sim\mathrm{Vol}[S_N(R)]$; it is noted that in this example $R=30$, and $\delta_n/R=0.10$. This property is also known as the phenomenon of the volume concentration near a thin equatorial slab, see Fig. 5. It is here underlined that the North Pole vector represented by the axis $\hat{\boldsymbol{e}}_n$ has been arbitrarily chosen. This implies that all the volume of the sphere is not only concentrated in the equatorial slab detected by the direction $\hat{\boldsymbol{e}}_n$, but also in any slab detected by $\hat{\boldsymbol{e}}_n$, for any $m\ne n$.

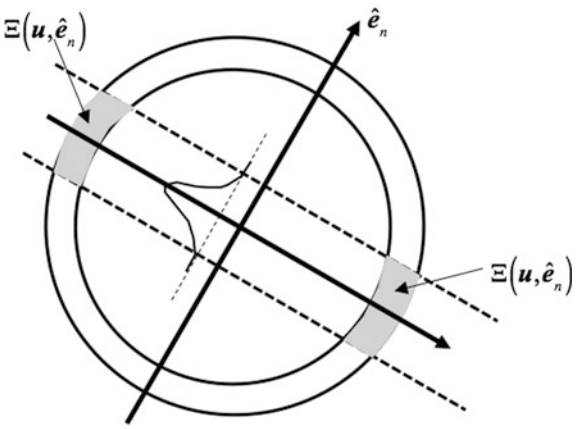

Fig. 5 Samples drawn from a multivariate normal distribution in high dimensions

Summarizing: (i) In high dimensions a hypersphere has finite volume if $> constant \times \sqrt{N}$, (ii) the N-dimensional hypersphere center is void, and almost all the volume concentrates around a thin shell $\Xi_{shell} \equiv S(R, \varepsilon)$ near the boundary, and (iii) Given an arbitrarily North Pole vector, almost all the volume concentrates in an equatorial slab $\Xi_{slab}(\hat{\boldsymbol{e}}_n) \equiv Slab(\hat{\boldsymbol{e}}_n, \delta_n)$, whose width does not depend upon N. As an important consequence of these peculiar properties, the volume concentrates over a relatively very small region $\Xi_{shell}(\hat{\boldsymbol{e}}_n) \equiv \Xi_{shell}(\boldsymbol{u}) \cap \Xi_{slab}(\hat{\boldsymbol{e}}_n)$, irrespective of the chosen North Pole.

6.2 The Multi-variate Normal Standard Distribution

The multivariate normal pdf has equation $f_u(\boldsymbol{u}) = (2\pi)^{-N/2}\exp(-0.5\|\boldsymbol{u}\|^2)$. It can be shown (Katafygiotis and Zuev 2008) that the samples generated from $f_u(\boldsymbol{u})$ belong to an N-dimensional thin shell. Therefore, for any chosen probabilistic direction $\hat{\boldsymbol{e}}_n$, most of the samples belong to a region $\Xi(\boldsymbol{u}, \hat{\boldsymbol{e}}_n) \equiv \Xi_{shell}(\boldsymbol{u}) \cap \Xi_{slab}(\boldsymbol{u}, \hat{\boldsymbol{e}}_n)$, as above defined, see Fig. 5.

It is easy to see that $R = \|\mathbf{u}\|$ follows the chi distribution, whose mean and variance are

$$\mu_R(N) = \sqrt{2}\frac{\Gamma\left(\frac{N+1}{2}\right)}{\Gamma\left(\frac{N}{2}\right)},\ \sigma_R^2(n) = n - \mu_R^2(n). \tag{79}$$

In high dimensions the following asymptotic limits hold:

$$\lim_{N\to\infty} \mu_R(N) = \sqrt{N},\ \lim_{N\to\infty} \sigma_R^2 = \frac{1}{2}. \tag{80}$$

Therefore in high dimensional spaces the samples belong to a thin shell Ξ_{shell} whose average radius is $\mu_{R,N\to\infty} = \sqrt{N}$ and its width is $\mu_{R,N\to\infty} = 1/2$ (Katafygiotis and Zuev 2008; Hurtado 2012; Broccardo 2014). This may also be seen easily by generating, for example, N_s samples from a N-variate normal standard distribution $\boldsymbol{u}^{(k)}$, $k = 1, 2, .., N_s$ and evaluating their distance from the origin $R^{(k)} = \|\boldsymbol{u}\|^{(k)}$. For sufficiently large N, the random variable $R = \|\boldsymbol{u}\|$ approximately follows a Gaussian distribution whose mean and variance are $\mu_{R,N\to\infty}$ and $\sigma_{R,N\to\infty}$, respectively. Here, it is underlined that the sampling points belong *also* to an "equatorial slab" $\Xi_{slab}(\boldsymbol{u}, \hat{\boldsymbol{e}}_n)$, whose semi-width is independent of N. This may be shown by projecting the samples along a generic direction $\hat{\boldsymbol{e}}_n$, obtaining the distance $\delta^{(k)} = \boldsymbol{u}^{(k)}\hat{\boldsymbol{e}}_n$, where the random variable $\delta^{(k)}$ follows a normal standard distribution.

6.3 Structural Reliability Analysis in High Dimensions

The N-dimensional thin shell drawn from the multivariate normal standard distribution is symmetrical around the origin. Therefore, each axis $\hat{\boldsymbol{e}}_n$ can be considered as a probabilistic direction, and each region $\Xi(\boldsymbol{u}, \hat{\boldsymbol{e}}_n)$ is equally important. However, in the framework of structural reliability analysis, because of the presence of a limit state surface, the polar-symmetry of the sphere itself is lost, and a most important direction $\hat{\boldsymbol{e}}_{opt}$ can be defined. The region of probabilistic interest Ω is defined as the intersection between the thin shell $\Xi_{shell}(\boldsymbol{u})$ and the equatorial slab $\Xi_{slab}(\boldsymbol{u}, \hat{\boldsymbol{e}}_{opt})$ containing the limit state $g(\boldsymbol{u}) = 0$, so that $\Omega \equiv \Xi_{opt} = \Xi(\boldsymbol{u}, \hat{\boldsymbol{e}}_{opt})$, see Fig. 6. Here it is noted that, because of the peculiar geometry of these spaces, the target limit state in the region of probabilistic interest may be well approximated by a linear response surface of equation $b_{opt} - \boldsymbol{a}_{opt} \cdot \boldsymbol{u} = 0$, whose slope is $\hat{\boldsymbol{e}}_{opt} = \boldsymbol{a}_{opt} / \|\boldsymbol{a}_{opt}\|$. This because the optimal hyperplane is the best linear classifier of the sampling points belonging to the region of probabilistic interest; consequently the probability of wrong classification is minimum, and the tail probability given by $b_{opt} - \boldsymbol{a}_{opt} \cdot \boldsymbol{u} = 0$ is close to the target. The distance of the optimal hyperplane from the origin along $\hat{\boldsymbol{e}}_{opt}$ is $\delta_{opt} = b_{opt} / \|\boldsymbol{a}_{opt}\| \cong \beta_G$, where β_G is the generalized reliability index, so that $P_f = \Phi(-\beta_G) \cong \Phi(-\delta_{opt})$.

Therefore, in high dimensions the main challenge is finding the "most important direction(s)" $\hat{\boldsymbol{e}}_{opt}$ detecting Ξ_{opt}. The simplest choice is represented from the design point direction $\hat{\boldsymbol{e}}_{opt} = \boldsymbol{a}_{opt} / \|\boldsymbol{a}_{opt}\|$. Extensive numerical experimentation where FORM has been applied has shown the suitability of this choice in many cases of practical interest.

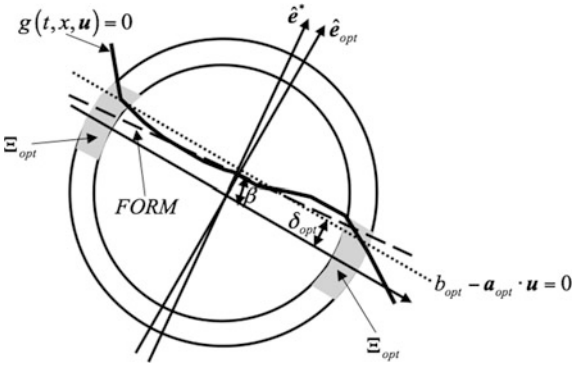

Fig. 6 Samples drawn from a multivariate normal distribution in high dimensions

6.4 Applicability of FORM in High Dimensions

Although FORM is a powerful tool, it has some known drawbacks: (i) in some cases its approximation is not satisfactory, and (ii) it is not possible to know in advance the accuracy of the solution. It is here underlined that for the evaluation of the tail probability, one is not interested in the value $g(t,x,\boldsymbol{u})$ of the limit state function, but in its sign, $z(t,x,\boldsymbol{u}) = sign[g(t,x,\boldsymbol{u})]$. A function, which separates the points belonging to the safe set from the ones belonging to the failure set, is named classifier, since it attributes a class ("safe" or "failure") to each point. The limit state surface $g(t,x,\boldsymbol{u}) = 0$ is the target classifier, while a hyperplane which approximates the limit state, is able to classify correctly only a limited number of points. Clearly, because the hyperplane works well, it is necessary that classify correctly the points at least in the region of probabilistic interest $\Xi_{opt} = \Xi(\boldsymbol{u}, \hat{\boldsymbol{e}}_{opt})$. In this sense FORM may work well because it is able to classify a high number of points, and this happens when the limit state in the region of probabilistic interest does not depart significantly from the FORM hyperplane. In view of the geometry of high-dimensional spaces previously described, the FORM approximation is satisfactory if (i) The design point direction is close to the most important direction, (ii) $\hat{\boldsymbol{e}}^*(t,x) \cong \hat{\boldsymbol{e}}_{opt}(t,x)$, (iii) The limit state is flat, (iv) There are not multiple comparable design points.

6.5 The Secant Hyperplane Method (SHM) for Stochastic Dynamic Analysis

The optimal hyperplane of equation $b_{opt}(t,x) - \boldsymbol{a}_{opt}(t,x) \cdot \boldsymbol{u} = 0$, see also Fig. 6, may give an improvement of the FORM solution, when needed. The optimal hyperplane is determined by considering the reliability problem as a classification approach, giving rise to the Secant Hyperplane Method (SHM) (Alibrandi et al. 2016). The aim of SHM is finding the secant hyperplane $g_{SH}(t,x,\boldsymbol{u}) = b_{sh} - \boldsymbol{a}_{opt}(t,x) \cdot \boldsymbol{u} = 0$ able to classify correctly the highest number of sampling points in the region of probabilistic interest. This task is accomplished by using as a classification approach a method based on the Support Vector Method (SVM). In SVM the margin is defined as the minimum distance between points belonging to different classes, and it is given as $M(t,x) = 2/\|\boldsymbol{a}(t,x)\|$ (Alibrandi et al. 2016). According to the SVM and the theory of the statistical learning, if the two classes are linearly separable, the optimal hyperplane is the one with maximum margin. Since the limit state is not linear, it is not possible to identify a hyperplane, which correctly classifies all the sampling points. To this aim, we relax the classification constraints by introducing "slack variables" $\xi_n(t,x) \geq 0$, giving a measure of the departure from the condition of correct classification. In particular, when $0 < \xi_n \leq 1$ the point is well classified but falls inside the margin, whereas when $\xi_n > 1$ the point is wrongly classified. Finally, if $\xi_n = 0$, the point is classified correctly and it falls outside the margin. In this case, we have a linear model with soft margin since some

points may lie inside the margin. Under this hypothesis, the optimal separating hyperplane has the maximum margin with minimum classification error. Mathematically, the second term can be obtained by minimizing the total number of points wrongly classified through the function $\Phi(\boldsymbol{\xi}) = \sum_{n=1}^{M} I(\xi_n)$, where $I(\xi_n) = 1$ if $\xi_n > 0$, and $I(\xi_n) = 1$ if $\xi_n \leq 0$. Unfortunately, the minimization of $\Phi(\boldsymbol{\xi})$ represents a challenging computational problem, because of the nonlinearity of $I(\xi_n)$. The idea is to approximate the counter function as $\Phi(\boldsymbol{\xi}) \cong \sum_{n=1}^{M} \xi_n$, under the condition $\xi_n \geq 0$. The Secant Hyperplane (SH) is given by the optimization problem:

$$\begin{cases} \min\limits_{w,b,\xi} \frac{1}{2} \|\boldsymbol{a}(t,x)\|^2 + \sum\limits_{n=1}^{M} \xi_n(t,x) & \\ s.t.\, z_i(t,x)[b(t,x) - \boldsymbol{a}(t,x) \cdot \boldsymbol{u}_n] \geq 1 - \xi_n(t,x), & n = 1, \ldots, M \\ \xi_n(t,x) \geq 0 & n = 1, \ldots, M \end{cases} \tag{81}$$

where $\boldsymbol{u}_1, \ldots, \boldsymbol{u}_M$ are M sampling points whose limit state function is $y_n = g(t,x,u_n)$, and $z_n(x,t) = sign[g(t,x,\boldsymbol{u}_n)]$. Note that in the objective function $f(\boldsymbol{a},\xi) = \frac{1}{2}\boldsymbol{a}(t,x)^2 + \sum_{n=1}^{M} \xi_n(t,x)$, the first term maximizes the margin, while the second term minimizes the sum of the errors. The contributions of these two terms could also be weighted $f(\boldsymbol{a},\xi) = (1-C)\frac{1}{2}\|\boldsymbol{a}(t,x)\|^2 + C\sum_{n=1}^{M} \xi_n(t,x)$, with $0 < C < 1$. The margin becomes wider for lower values of C. Observe (Alibrandi et al. 2016) that the slope of the SH is given by all the points internal to the margin, whose width depends on C. Provided the margin is wide enough, the value of C does not affect the convergence of the method. Extensive numerical experimentation has shown that a good tradeoff value is $C = 1/2$, which implies (81). For a given set of classified points, from (81) the secant hyperplane $g_{SH}(t,x,\boldsymbol{u}) = b_{SH}(t,x) - \boldsymbol{a}_{SH}(t,x) \cdot \boldsymbol{u}$ is obtained, together with its lower and upper bounding hyperplanes $g_{LH}(t,x,\boldsymbol{u}) = b_{UH}(t,x) - \boldsymbol{a}_{SH}(t,x) \cdot \boldsymbol{u}$ and $g_{UH}(t,x,\boldsymbol{u}) = b_{LH}\ (t,x) - \boldsymbol{a}_{SH}$ $(t,x) \cdot \boldsymbol{u}$, with $b_{LH} \leq b_{SH} \leq b_{UH}$, see Fig. 7. Correspondingly the secant reliability index $\beta_{SH} = b_{SH} / \|\boldsymbol{a}_{SH}\|$ is obtained, together with the lower and upper reliability indices $\beta_{LH} = b_{LH} / \|\boldsymbol{a}_{SH}\|$ and $\beta_{UH} = b_{UH} / \|\boldsymbol{a}_{SH}\|$, respectively, with $\beta_{LH} \leq \beta_{SH}$ $\leq \beta_{UH}$. With regard to the reliability indices, it is possible to define the failure probabilities $P_{f,LH} = \Phi(-\beta_{UH})$, $P_{f,SH} = \Phi(-\beta_{SH})$, and $P_{f,UH} = \Phi(-\beta_{LH})$, $\Phi[\cdot]$ being the normal standard CDF, while $P_{f,LH} \leq P_{f,SH} \leq P_{f,UH}$. Although $P_{f,LH}$ and $P_{f,UH}$ are bounds of $P_{f,SH}$, they are also the bounds of the target failure probability P_f if one chooses a sufficient number of sampling points such that $P_{f,SH} \cong P_f$. It is however worth noting that with a reduced number of sampling points, whereas $P_{f,SH}$ is quite different from P_f, in some specific cases $P_{f,LH}$ and $P_{f,UH}$ may not bound P_f. In such sense they can be seen as credible lower and upper approximations of P_f, given the available information, represented by the margin-driven simulated samples.

An iterative procedure is implemented in SHM. First a set of sampling points $\boldsymbol{u}^{(k)} = 1, \ldots, K$, along the design point direction $\hat{\boldsymbol{e}}^*(t,x) = \boldsymbol{u}^*(t,x) / \|\boldsymbol{u}^*(t,x)\|$ is chosen. The points belonging to the design point direction are classified (safe and

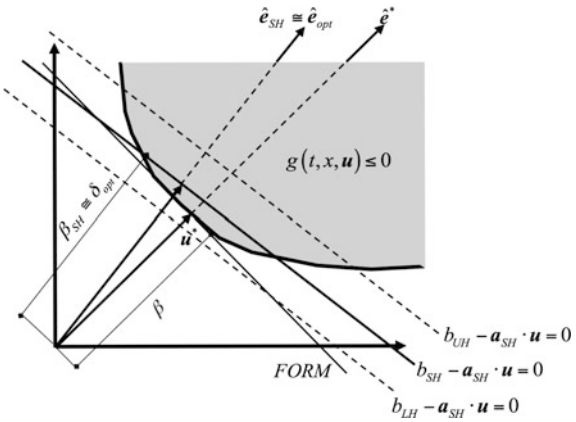

Fig. 7 FORM and SHM for structural reliability analysis

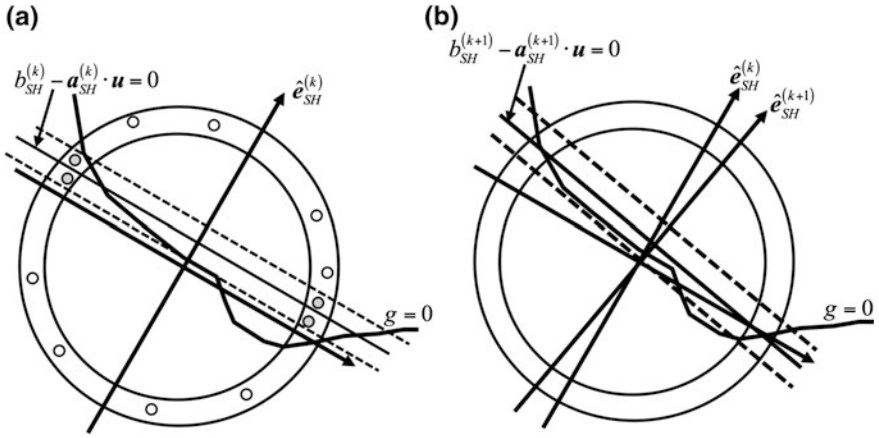

Fig. 8 Iterative procedure underlying SHM. **a** Only the points inside the margin of the k-th secant hyperplane are classified (*filled circles*), **b** building of the (k + 1)-th secant hyperplane

failure points, respectively). A first SH is built through (81), together with its bounding hyperplanes. This first model is likely to be parallel to the FORM hyperplane. Then, an iterative procedure is developed. At the k-th iteration, a new point $\mathbf{u}_k$ inside the margin is chosen and classified; by using (81) the updated SH is determined, as well as the secant reliability index β_{SH} together with its bounds β_{LH} and β_{UH}. The iterative procedure ends when the convergence is achieved. It is noted that the sampling points $\boldsymbol{u}^{(k)}$ are generated through a crude MCS, and they are accepted (with consequent evaluation of the limit state function) only if they fall inside the margin, see Fig. 8. This implies that they belong to the region $\Xi\left(\boldsymbol{u}, \hat{\boldsymbol{e}}_{SH}^{(k)}\right) = \Xi_{shell}(\boldsymbol{u}) \cap \Xi_{slab}(\boldsymbol{u}, \hat{\boldsymbol{e}}_{SH}^{(k)})$, $\hat{\boldsymbol{e}}_{SH}^{(k)}(t,x)$ being the slope of the *SH* at the k-th iteration.

Since $\boldsymbol{u}^{(k)}$ fall far away from the origin, SHM is not affected by the presence of multiple comparable design points. The iterative procedure of SHM adaptively modifies the slope of the hyperplane until it converges to $\hat{\boldsymbol{e}}^{*}_{SH}(t,x)$, the latter being very close to the optimal, i.e. $\hat{\boldsymbol{e}}^{*}_{SH}(t,x) \cong \hat{\boldsymbol{e}}_{opt}(t,x)$. In other words, SHM gives the optimal linear classifier in the sense that it is able to detect the equatorial slab where the maximum linear separability between the safe and the failure sets is achieved.

As noted in Wang and Song (2016) it is not easy to distinguish if a reliability problem is in low or high dimensions. However, the accuracy of SHM is not affected by the number of dimensions: it works well if classify correctly most sampling points in the region of probabilistic interest Ω; the latter being defined as a very narrow region around the design point in low dimensions, or a very small region close to Ξ_{opt} in high dimensions.

The Secant Hyperplane overcomes the main drawbacks of FORM, but it requires an increased computational effort. Extensive numerical experimentation has shown that it requires on average 400–500 analyses for each threshold, in addition to the analyses required to evaluate the design point, irrespective of the number of random variables or the level of the required probability.

6.6 The Tail Probability Equivalent Linearization Method (TPELM)

The Tail-Probability-Equivalent-Linear System (TPELS) based on SHM is defined as the linear system obtained by minimizing the difference between the tail probability of TPELS with respect to the original nonlinear system. The TPELS is a linear system of equation $X_{TPELS}(t,x,\boldsymbol{u}) = \boldsymbol{a}_{TPELS}(t,x)\cdot\boldsymbol{u}$, where

$$\boldsymbol{a}_{TPELS}(t,x) = x\frac{\boldsymbol{w}_{SH}(t,x)}{b_{SH}(t,x)}. \tag{82}$$

It is noted that its limit state function is $g_{TPELS}(t,x,\boldsymbol{u}) = x - \boldsymbol{a}_{TPELS}(t,x)\cdot\boldsymbol{u}$, while its reliability index is $\beta_{TPELS}(t,x) = x/\|\boldsymbol{a}_{TPELS}(t,x)\|$. It is easy to verify that $\beta_{TPELS}(t,x) \equiv \beta_{SH}(t,x)$, and that the two limit state equations $g_{TPELS}(t,x,\boldsymbol{u}) = 0$ and $g_{SH}(t,x,\boldsymbol{u}) = 0$ coincide.

6.7 Numerical Example

It is here considered the case of an oscillator with nonlinear damping where it is known that FORM does not work effectively (Alibrandi et al. 2015, 2016; Alibrandi and Mosalam 2016)

$$m\ddot{X} + c\dot{X}\left[\dot{X}^2 + kX^2\right] + kX = mW(t), \tag{83}$$

where $m = 1$, $c = 1$ and $k = 100$ are the mass, damping and stiffness coefficients, corresponding to a natural frequency $\omega_0 = 10$ rad/s and damping ratio $\zeta_0 = 5\%$. The stochastic ground acceleration is defined as a white-noise process $W(t)$ of intensity $S_w = 1\,\mathrm{m}^2/\mathrm{s}^3$. The probability density function of the response in stationary state is known in closed form (Lutes and Sarkani 2004), and it is used to benchmark the approximations of the tail probability given by FORM and SHM. The system achieves stationarity after about $t = 5$ s, and the frequency step in is chosen as $\Delta\omega = (2\pi)/t = 1.256$ rad/s. The power spectrum density has been discretized from $\omega_1 = 0$ rad/s to $\omega_n = 30$ rad/s, giving rise to $n = 25$ harmonic components and $N = 2n = 50$ standard normal random variables. Let σ^2 be the variance of the response at t. The tail probability is calculated for 12 normalized threshold values x/σ ranging from 0 to 3 with an increment of 0.25.

We use the design point direction as a preliminary important direction for the equatorial slab. It is worth underlining that the evaluation of the design point in high dimensional spaces is challenging. Indeed, the gradient-based procedures are not very efficient in high dimension. Typically, finite element codes do not provide gradients, which can be approximated by the finite differences method. This implies that each iteration of the iterative procedure require $N + 1 = 51$ dynamic computations, so that the computational cost may be excessive. Moreover, in high-dimensional spaces the accuracy of the numerical response gradient is generally poor. These shortcomings may be overcome by using the Direct Differentiation Method (Zhang and Der Kiureghian 1993; Haukaas and Der Kiureghian 2004). Here we determine the design point with a relatively low computational effort using a suitable free-derivative algorithm developed to this aim (Alibrandi and Der Kiureghian 2012; Alibrandi and Mosalam 2016) which requires only 20 analyses per threshold. For the evaluation of the design point through MCFM requires 20 analyses per threshold. SHM reaches convergence after additional 400 analyses, but the quality of the approximation is greatly improved compared to FORM. Figure 9a compares the target tail probability known in closed form (circle markers) with the results obtained by FORM (thin line) and SHM solutions (thick line). The example shows the excellent accuracy of SHM for stochastic dynamic analysis using only 420 analyses per threshold. The good performance of SHM is demonstrated in this example, whereas FORM results are outside the bounds obtained by SHM. In Fig. 9b TELM and TPELM are applied for the evaluation of the first passage probability. Here the comparison of the two tail equivalent linearization methods is developed with MCS with 100,000 samples (represented with circle markers). As expected, it is noted that the results of TELM and TPELM are coherent with the corresponding FORM/SHM, where TPELM outperforms significantly in accuracy TELM.

It should be noted that the hyperplanes corresponding to FORM and SHM hyperplanes can have very different slopes. The results show that the angle between the two hyperplanes may be greater than 40°, especially for low thresholds. FORM

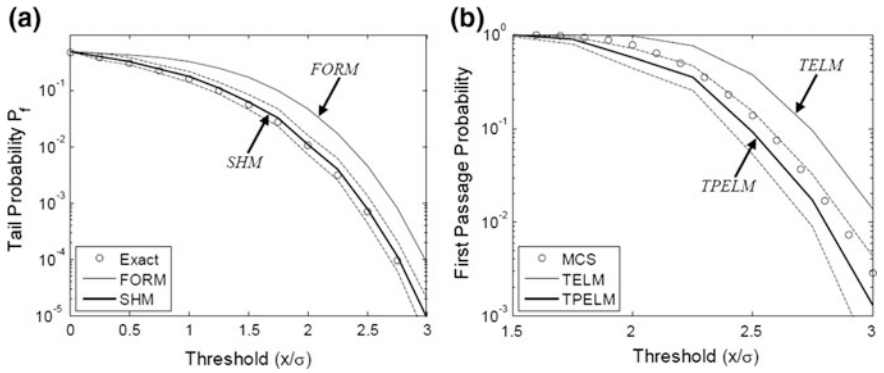

Fig. 9 Response of a SDOF with nonlinear damping. **a** Tail Probability, **b** first-passage probability

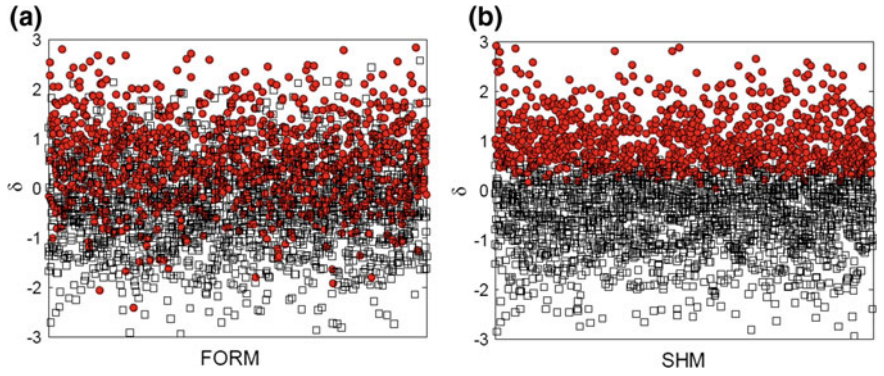

Fig. 10 Classification of a set of 1,000 samples along the direction detected by **a** FORM, **b** SHM

is defined as the tangent plane to the limit state and passing through the design point. SHM detects the optimal direction $\hat{\boldsymbol{e}}_{opt}$ of the equatorial slab, which is equivalent to determining the direction of maximum linear separability between safe points and failure points. For illustration, consider a threshold $x/\sigma = 0.5$, where the angle between the two hyperplanes is $\vartheta = 45°$. In Fig. 10 we present a sample of 1,000 points where the safe points are shown as square markers and failure points as filled circle markers.

In the ordinate axis is represented the distance of the point along the design point direction $\hat{\boldsymbol{e}}^*$ (Fig. 10a) and $\hat{\boldsymbol{e}}_{SH}$ (Fig. 10b). The results show clearly that the direction detected by SHM guarantees a better linear separability between the safe and failure sets, so that SHM is likely to detect the optimal equatorial slab Ξ_{opt}.

7 Conclusions

This chapter presented a general description of the TELM method for solving nonlinear stochastic dynamics problems. Starting from the pioneering use of FORM for solving nonlinear stochastic dynamic problem, the first part of this chapter focuses on the original time-domain development of TELM. The second part of the chapter offers four major advancements of the method, which were studied separately by the authors of this chapter. These developments include: TELM in frequency domain, TELM with sinc expansion formula, TELM for multi-supported structures, and the secant hyperplane method giving rise to an improved TELM. In particular, the frequency-domain discretization offers a different physical interpretation of the linearization method, and it is particularly suitable for stationary excitations. The TELM based on sinc expansion provides a reduction of the number of random variables used to represent the input excitation. In many practical applications, this leads to a significant computational benefit. TELM for multi-supported structures focuses on the extension of the method for nonlinear systems subjected to correlated multi-support seismic excitations. Finally, after a detailed review of the geometry of high-dimensional spaces, the secant hyperplane method is introduced. This leads to a significant improvement of the accuracy of TELM.

References

Alibrandi U, Alani A, Koh CG (2015) Implications of high-dimensional geometry for structural reliability analysis and a novel linear response surface method based on SVM

Alibrandi U, Der Kiureghian A (2012) A gradient-free method for determining the design point in nonlinear stochastic dynamic analysis. Probab Eng Mech 28:2–10. doi:10.1016/j.probengmech.2011.08.018

Alibrandi U, Koh CG (2015) Stochastic dynamic analysis of a marine riser using the first-order reliability method. In: 12th international conference on applications of statistics and probability in civil engineering, ICASP12, Vancouver, Canada

Alibrandi U, Ma C, Koh CG (2016) Secant hyperplane method for structural reliability analysis. J Eng Mech 142:04015098. doi:10.1061/(ASCE)EM.1943-7889.0001024

Alibrandi U, Mosalam KM (2016) Equivalent linearization methods for stochastic dynamic analysis using linear response surfaces

Bouc R (1967) Forced vibration of mechanical systems with hysteresis. In: Proceedings of the fourth conference on non-linear oscillation, Prague, Czechoslovakia

Broccardo M (2014) Further development of the tail-equivalent linearization method for nonlinear stochastic dynamics. University of California, Berkeley

Broccardo M, Der Kiureghian A (2015) Multicomponent nonlinear stochastic dynamic analysis by tail-equivalent linearization. J Eng Mech 04015100. doi:10.1061/(ASCE)EM.1943-7889.0001026

Broccardo M, Der Kiureghian A (2013) Non-stationary stochastic dynamic analysis by tail-equivalent linearization. In: 11th international conference on structural safety and reliability, New York

Broccardo M, Der Kiureghian A (2012) Discretization of stochastic processes in time domain by sinc basis function and application in TELM analysis. In: Proceedings of 16th conference of the international federation of information processing (IFIP) working group 7.5 on reliability and optimization of structural systems

Broccardo M, Der Kiureghian A (2014) Simulation of near-fault ground motions using frequency-domain discretization. In: Tenth U.S. national conference on earthquake engineering frontiers of earthquake engineering, Anchorage, Alaska

Broccardo M, Der Kiureghian A (2016) Simulation of stochastic processes by sinc basis functions and application in TELM analysis. Submitted to: Probabilistic Engineering Mechanics

Chatfield C (2003) The analysis of time series: an introduction, 6th edn. CRC Press

Clough R, Penzien J (1993) Dynamics of structures, Internatio. McGraw-Hill Education, New York

Der Kiureghian A (2000) The geometry of random vibrations and solutions by FORM and SORM. Probab Eng Mech 15:81–90. doi:10.1016/S0266-8920(99)00011-9

Der Kiureghian A (1996) A coherency model for spatially varying ground motions. Earthq Eng Struct Dyn 25:99–111

Der Kiureghian A, Fujimura K (2009) Nonlinear stochastic dynamic analysis for performance-based earthquake engineering. Earthq Eng Struct Dyn 38:719–738. doi:10.1002/eqe

Ditlevsen O, Madsen HO (1996) Structural reliability methods. Wiley, New York

Francescetti M (2016) Some geometry in high-dimensional spaces. http://circuit.ucsd.edu/~massimo/ECE287C/Handouts_files/Geometry.pdf. Accessed 28 Apr 2016

Fujimura K, Der Kiureghian A (2007) Tail-equivalent linearization method for nonlinear random vibration. Probab Eng Mech 22:63–76. doi:10.1016/j.probengmech.2006.08.001

Garrè L, Der Kiureghian A (2010) Tail-equivalent linearization method in frequency domain and application to marine structures. Mar Struct 23:322–338. doi:10.1016/j.marstruc.2010.07.006

Haukaas T, Der Kiureghian A (2004) Finite element reliability and sensitivity methods for performance-based earthquake engineering. Pacific earthquake engineering research center report

Hurtado JE (2012) Dimensionality reduction and visualization of structural reliability problems using polar features. Probab Eng Mech 29:16–31. doi:10.1016/j.probengmech.2011.12.004

Katafygiotis LS, Zuev KM (2008) Geometric insight into the challenges of solving high-dimensional reliability problems. Probab Eng Mech 23:208–218. doi:10.1016/j.probengmech.2007.12.026

Koo H, Der Kiureghian A, Fujimura K (2005) Design-point excitation for non-linear random vibrations. Probab Eng Mech 20:136–147. doi:10.1016/j.probengmech.2005.04.001

Li C, Der Kiureghian A (1993) Optimal discretization of random fields. J Eng Mech 119:1136–1154. doi:10.1061/(ASCE)0733-9399(1993)119:6(1136)

Liu PL, Der Kiureghian A (1991) Optimization algorithms for structural reliability. Struct Saf 9:161–177. doi:10.1016/0167-4730(91)90041-7

Luco JE, Wong HL (1986) Response of a rigid foundation to a spatially random ground motion. Earthq Eng Struct Dyn 14:891–908. doi:10.1002/eqe.4290140606

Lutes LD, Sarkani S (2004) Random vibrations. Elsevier

Osgood B (2007) The Fourier transform and its applications. Lecture notes for EE 261 Stanford University

Priestley MB (1965) Evolutionary spectra and non-stationary processes. J R Stat Soc Ser B 204–237

Rezaeian S, Der Kiureghian A (2008) A stochastic ground motion model with separable temporal and spectral nonstationarities. Earthq Eng Struct Dyn 37:1565–1584. doi:10.1002/eqe.831

Shinozuka M (1972) Digital simulation of random processes. J Sound Vib 25:111–128

Shinozuka M, Deodatis G (1991) Simulation of stochastic processes by spectral representation. Appl Mech Rev 44:191. doi:10.1115/1.3119501

Valdebenito MA, Pradlwarter HJ, Schuëller GI (2010) The role of the design point for calculating failure probabilities in view of dimensionality and structural nonlinearities. Struct Saf 32:101–111. doi:10.1016/j.strusafe.2009.08.004

Wang Z, Der Kiureghian G (2016) Tail-equivalent linearization of inelastic multi-support structures subjected to spatially varying stochastic ground motion. J Eng Mech 451. doi:10.1209/0295-5075/19/6/002

Wang Z, Song J (2016) Cross-entropy-based adaptive importance sampling using von Mises-Fisher mixture for high dimensional reliability analysis. Struct Saf 59:42–52. doi:10.1016/j.strusafe.2015.11.002

Wen Y-K (1976) Method for random vibration of hysteretic systems. J Eng Mech Div 102:249–263

Wilson E (1998) Three dimensional static and dynamic analysis of structures: a physical approach with emphasis on earthquake engineering. Computers and Structures Inc

Zhang Y, Der Kiureghian A (1993) Dynamic response sensitivity of inelastic structures. Comput Methods Appl Mech Eng 108:23–36

Estimate of Small First Passage Probabilities of Nonlinear Random Vibration Systems

Jun He

Abstract Estimates of the small probabilities of failure, i.e., small first passage probabilities, of nonlinear random vibration systems is of great importance in the structural reliability analysis and reliability-based design. Some methods have been developed for estimating the small probabilities, but their computational efficiency is not high enough for analyzing the large-scale systems. In order to overcome the challenge of the computational efficiency of the estimate of the small probabilities, a new method is developed. The method mainly consists of two uncoupled procedures, i.e., modeling the distribution tails of the extreme values of the responses of nonlinear random vibration systems and constructing the Copula of the extreme values of the nonlinear responses. The former is used to estimate the small first passage probabilities of the scalar response processes, while the latter is used to estimate the small first passage probabilities of the vector response processes. Some numerical examples are presented to demonstrate the accuracy and efficiency of the developed method.

1 Introduction

The estimate of the small probabilities of failure of nonlinear dynamic systems to natural hazard excitations, e.g., earthquake ground motion, wind or wave action, is an important part in the structural reliability analysis and reliability-based design. In here, the probability of failure is defined as the probability of first-passage failure, i.e., the probability that the system responses exceed in magnitude the given thresholds in the reference time T. For a structural element, we usually consider a scalar response process in the first-passage failure analysis. However, for a structural system, we have to consider the vector response processes in order to analyze the related first-passage failure.

J. He (✉)
Department of Civil Engineering, Shanghai Jiao Tong University, Minhang, China
e-mail: junhe@sjtu.edu.cn

P. Gardoni (ed.), *Risk and Reliability Analysis: Theory and Applications*,
Springer Series in Reliability Engineering, DOI 10.1007/978-3-319-52425-2_7

The estimate of the small probabilities of failure of nonlinear random vibration systems belongs to random vibration analysis, however, the classical methods developed for random vibration analysis, such as the Monte Carlo method (Shinozuka 1972), equivalent linearization method (Wen 1980), Fokker-Planck equation method (Lin and Cai 2004), moment closure method (Lutes and Sarkani 2004), and so on, cannot efficiently estimate the small probabilities of failure due to the their respective limitations. Therefore, more efficient methods should be developed for the estimate of the small probabilities of failure. Through improving the Metropolis algorithm (Liu 2001), Au and Beck proposed the subset simulation method for estimating the small probabilities of failure (Au and Beck 2001). The subset simulation method is more efficient than the Monte Carlo method and suitable for those nonlinear systems whose deterministic solutions are available. However, the subset simulation method requires a new simulation run when a different and smaller reference time is considered and, therefore, it may still need a lot of CPU time to estimate the small probabilities of failure of nonlinear systems by using the subset simulation method. Based on the equivalent linearization technique and the first-order reliability method (FORM), Fujimura and Der Kiureghian proposed the tail-equivalent linearization method for estimating the distribution tails of the responses of nonlinear random vibration systems, whereby the small probabilities of failure of the systems can be obtained efficiently (Fujimura and Der Kiureghian 2007). In general, the tail-equivalent linearization method is more accurate than the equivalent linearization method and more efficient than the subset simulation method for estimating the small probabilities of first-passage failure of nonlinear random vibration systems. However, in the cases that the non-stationary responses are considered, i.e., the reference time in the failure analysis is relative short, the tail-equivalent linearization method should carry out an equivalent linearization procedure at each discrete time point and, consequently, the computational cost may become high. On the other hand, it is possible to encounter the problem of multiple design points in the tail-equivalent linearization method since the method needs to utilize the design point related to the high response level to determine the unit impulse response function of the equivalent linearization system. Based on the assumption that the extreme value distribution of the nonlinear random response of interest asymptotically approaches a Gumbel distribution or generalized extreme distribution, Naess and Gaidai (2008) and Grigoriu and Samorodnitsky (2014), respectively, proposed the Monte Carlo methods based on extreme value theory for estimating the small probabilities of first-passage failure of nonlinear random vibration systems. However, the Monte Carlo methods require that the reference times are sufficiently long such that the extreme values of the responses of interest can be assumed to follow the Gumbel distribution or generalized extreme value distributions approximately. In 2009, Bucher proposed an asymptotic sampling technique for estimating the small probabilities of failure through using the asymptotic linearity of the generalized reliability index (Bucher 2009). The computational efficiency of the asymptotic sampling technique is almost

the same as that of the subset simulation method. However, the asymptotic sampling technique may also lead to the large discrepancies of the estimates of the small probabilities of failure if the support points required by the method are chosen inappropriately. Overall, although some methods have been developed recently for estimating the small probabilities of first-passage failure of nonlinear random vibration systems, efficient estimate of the small probabilities is still a challenging task.

It has been shown that the small probabilities of first-passage failure are identical to the corresponding exceedance probabilities of the extreme values of the responses considered. Therefore, they can be calculated if the tail distributions of the extreme responses can be determined. As mentioned above, the generalized extreme value distribution has been adopted to fit the extreme values of the nonlinear random responses with sufficiently long reference times. However, in the cases of short reference times, the assumption that the extreme value responses follow the generalized extreme value distribution is invalid and, consequently, the resulting small probabilities of failure may exhibit large numerical errors. Hence, more suitable distributions should be chosen to fit the extreme response distributions, particularly in the tail regions, such that the small probabilities of failure can be estimated with enough high accuracy.

More recently, a new distribution called the shifted generalized lognormal distribution (SGLD) for fitting four moments has been developed (Low 2013). The distribution has a rich flexibility in shape that nearly encompasses the entire skewness-kurtosis region permissible for unimodal densities and has been applied to fit several theoretical distributions and actual datasets with very favorable results, particularly in the tail regions. If we can prove that through defining the suitable parameters the SGLD also has a rich flexibility in fitting the tail distributions of the extreme values of the nonlinear random responses of interest, then we can develop a new method similar to the Monte Carlo simulation methods based on the extreme value theory to estimate the small probabilities of first-passage failure of nonlinear random systems. This new simulation method will be described in detail in below.

2 Brief Description of the SGLD

The SGLD is developed by combining the three-parameter lognormal distribution (Cohen and Whitten 1980) and generalized Gaussian distribution (GGD) (Nadarajah 2005). The three-parameter lognormal distribution is a unimodal and asymmetric distribution. The probability density function (PDF) of a three-parameter lognormal variable X is

$$f_X = \frac{1}{(x-\lambda)\sqrt{2\pi}\sigma}\exp\left\{-\frac{1}{2\sigma^2}[\ln(x-\lambda)-\mu]^2\right\}, \quad x>\lambda \tag{1}$$

where λ, e^{μ} and σ are parameters for location, scale and shape, respectively. The mean, variance and skewness of X are given by

$$\mu_X = \lambda + \exp\left(\mu + \frac{\sigma^2}{2}\right) \tag{2}$$

$$\sigma_X^2 = \left(e^{\sigma^2} - 1\right) e^{2\mu + \sigma^2} \tag{3}$$

$$\gamma_X = \left(e^{\sigma^2} + 2\right)\sqrt{e^{\sigma^2} - 1} \tag{4}$$

Equation (4) indicates that γ_X increases monotonically with σ, and it ranges from zero to infinity. In addition, X approaches the normal distribution when $\sigma \to 0$, in which case the skewness vanishes.

The GGD is a unimodal and symmetric distribution that covers a broad range of kurtosis. Its PDF is given by

$$f_Z(z) = \alpha \exp\left[-\frac{1}{r}\left(\frac{|z-\mu|}{\sigma}\right)^r\right], \quad z \in (-\infty, \infty) \tag{5}$$

$$\alpha = \frac{1}{2r^{1/r}\sigma\Gamma\left(1 + \frac{1}{r}\right)} \tag{6}$$

where μ and σ are the location and scale parameters, and $r > 0$ is the shape parameter that controls the kurtosis, $\Gamma(\cdot)$ denotes the gamma function.

The expressions of the mean, variance and kurtosis of Z can be also derived from Eq. (5):

$$\mu_Z = \mu \tag{7}$$

$$\sigma_Z^2 = \frac{\sigma^2\Gamma\left(\frac{3}{r}\right)}{\Gamma\left(\frac{1}{r}\right)} \tag{8}$$

$$\lambda_Z = \frac{\Gamma\left(\frac{1}{r}\right)\Gamma\left(\frac{5}{r}\right)}{\Gamma^2\left(\frac{3}{r}\right)} \tag{9}$$

Similar to the Gaussian distribution, the PDF defined by Eq. (5) is bell-shaped and unimodal with the mode at $z = 0$. The shape parameter r determines the thickness of the distribution tails. When $0 < r < 2$, the GGD model has a wider tail than the Gaussian distribution and for $r > 2$ it has a narrower tail. The special/limiting cases of the GGD model are: when $r = 1$, the GGD reduces to the Laplace distribution; for $r = 2$, the GGD reduces to the Gaussian distribution; whereas in the limiting case $r \to \infty$ the GGD converges to the uniform distribution in the interval $\left(\mu_Z - \sqrt{3}\sigma_Z, \mu_Z + \sqrt{3}\sigma_Z\right)$.

Through defining $Z = \ln Y$ and introducing location by using $Y = (X - b)/\theta$, the PDF of the SGLD can be obtained from Eq. (5):

$$f_X(x) = \frac{\alpha}{x-b} \exp\left(-\frac{1}{r\sigma^r} \left| \ln \frac{x-b}{\theta} \right|^r \right), \quad x > b \tag{10}$$

where b is the location parameter, θ is the scale parameter, $0 < \sigma$ and $0 < r$ are the shape parameters.

The CDF of the SGLD can be derived from Eq. (11):

$$F_X(x) = \frac{1}{2} + \frac{1}{2} \operatorname{sgn}\left(\frac{x-b}{\theta} - 1 \right) \varrho\left(\frac{1}{r}, \frac{\left| \frac{\ln \frac{x-b}{\theta}}{\sigma} \right|^r}{r} \right), \quad x > b \tag{11}$$

in which $\operatorname{sgn}(\cdot)$ denotes the signum function, and ϱ is the lower incomplete gamma function ratio, i.e., $\varrho(s, z) = \int_0^z t^{s-1} \mathrm{e}^{-t} \mathrm{d}t / \Gamma(s)$.

The PDF defined by Eq. (10) is unimodal and asymmetric for $\sigma > 0$. In the limiting case $\sigma \to 0$ the SGLD converges to the GGD. Other special/limiting cases of the SGLD model are: when $r = 2$ and $b = 0$, the SGLD reduces to the lognormal distribution; when $r = 2$ and $b \neq 0$, the SGLD reduces to the 3-parameter lognormal distribution; when $r = 1$ and $b = 0$, the SGLD reduces to the Log-Laplace distribution; whereas for $r \to \infty$ and $b = 0$ the SGLD converges to the Log-uniform distribution.

By making the substitution $p = F_X(x)$ in the left-side-hand of Eq. (11) and noting that $\operatorname{sgn}((x-b)/\theta - 1) = \operatorname{sgn}(p - 1/2)$, the inverse CDF of the SGLD is obtained as

$$\begin{aligned} x &= F_X^{-1}(p) \\ &= \theta \exp\left\{ \operatorname{sgn}\left(p - \frac{1}{2} \right) \sigma \left[r \varrho^{-1}\left(\frac{1}{r}, \frac{2p-1}{\operatorname{sgn}\left(p - \frac{1}{2}\right)} \right) \right]^{1/\mathrm{r}} \right\} + b, \quad \text{for } p \neq \frac{1}{2} \end{aligned} \tag{12}$$

and $x = b + \theta$ for $p = 1/2$. Where, ϱ^{-1} is the inverse of the lower incomplete gamma function ratio, defined such that $z = \varrho^{-1}(s, \omega)$ corresponds with $\omega = \varrho(s, z)$.

Although the SGLD is a 4-parameter distribution, the parameter estimation of a SGLD only involves two variables, i.e., the shape parameters σ and r, since for each fixed pair (σ, r) the location and scale parameters can be computed from $\theta = \sigma_X/\sigma_Y$ and $b = \mu_X - \theta\mu_Y$, where μ_X and σ_X are the mean value and standard deviation of X and μ_Y and σ_Y are the mean value and standard deviation of the reduced variable $Y = (X - b)/\theta$, which can be computed from the fixed σ and r by the following raw-moments formula [11]

$$\mathrm{E}\left[Y^k\right] = \frac{1}{\Gamma(1/r)} \sum_{n=0}^{\infty} \frac{(k\sigma)^{2n}}{(2n)!} r^{2n/r} \Gamma\left(\frac{2n+1}{r}\right) \tag{13}$$

Since the above SGLD is developed from the three-parameter lognormal distribution, it is only suitable for the case that skewness γ_X is larger than zero. For $\gamma_X < 0$, we can first consider the absolute value of γ_X, and subsequently mirror the resulting PDF about $x = \mu_X$, i.e., replace x by $2\mu_X - x$ on the right-hand-side of Eq. (10). The same operation applies to Eq. (11), expect that the resulting expression should be subtracted from unity. Thus, the PDF and CDF for $\gamma_X < 0$ are given by

$$f_X(x) = \frac{\alpha}{2\mu_X - b - x} \exp\left(-\frac{1}{r\sigma^r} \left| \ln \frac{2\mu_X - b - x}{\theta} \right|^r \right), \quad x < 2\mu_X - b \tag{14}$$

$$F_X(x) = \frac{1}{2} - \frac{1}{2}\mathrm{sgn}\left(\frac{2\mu_X - b - x}{\theta} - 1\right) \varrho\left(\frac{1}{r}, \frac{\left|\frac{\ln\frac{2\mu_X - b - x}{\theta}}{\sigma}\right|^r}{r}\right), \quad x < 2\mu_X - b \tag{15}$$

in which b, θ, σ and r are determined from $|\gamma_X|$.

From Eq. (15), we can derived the inverse CDF for $\gamma_X < 0$

$$\begin{aligned} x &= F_X^{-1}(p) \\ &= 2\mu_X - \theta \exp\left\{ \mathrm{sgn}\left(\frac{1}{2} - p\right) \sigma \left[r\varrho^{-1}\left(\frac{1}{r}, \frac{1-2p}{\mathrm{sgn}\left(\frac{1}{2} - p\right)}\right)\right]^{1/r} \right\} - b, \quad \text{for } p \neq \frac{1}{2} \end{aligned} \tag{16}$$

and $x = 2\mu_X - \theta - b$ for $p = 1/2$.

Given the mean, variance, skewness and kurtosis of X, then the parameters b, θ, σ and r can be estimated by using the method of moments (Low 2013). However, for a nonlinear random vibration system, the computation of the first four moments of the nonlinear random responses often needs a large number of simulations and, consequently, the computational cost may be infeasible. In addition, there may be an unacceptable deviation between the tail of the SGLD with the parameters estimated from the first four moments of the response of interest and the actual tail of the distribution of the response. Hence, a more efficient and accurate parameter estimation method should be proposed when the SGLD is used to fit the tail of the distribution of the nonlinear random response. In here, a new parameter estimation method called 2-level method is proposed, which will be descripted in detail Sect. 4.

3 Small Probabilities of First-Passage Failure

The reliability analysis of a nonlinear random vibration system usually involves the estimation of the small first passage probabilities of a scalar and/or vector response process within the reference time T. For the case of a scalar response process $X(t)$, the expression of the first passage probabilities can be written as

$$P_f(b,T) = P\{\exists \tau \in [0,T]: X(\tau) > b\} \tag{17}$$

in which $\mathrm{P}\{\cdot\}$ is the probability operator and b is the high response threshold level.

The above expression can be equivalently written as

$$\begin{aligned} P_f(b,T) &= 1 - P\{\max_{0\le t\le T} X(t) \le b\} \\ &= 1 - F_A(b) \end{aligned} \tag{18}$$

where $A = \max_{0\le t\le T} \mathrm{X(t)}$ denotes the maximum value of $\mathrm{X(t)}$ within the reference time T and $\mathrm{F}_A(\cdot)$ is the CDF of A.

If the reliability analysis of a nonlinear random vibration system involves a vector response process $(\mathrm{X}_1(\mathrm{t}), \ldots, \mathrm{X}_\mathrm{K}(\mathrm{t}))$, i.e., the first-passage failure is defined as the event that at least one of the component processes of the vector response $(\mathrm{X}_1(\mathrm{t}), \ldots, \mathrm{X}_\mathrm{K}(\mathrm{t}))$ exceeds in magnitude its respective high thresholds within the reference time T, then the small probabilities of first-passage failure can be expressed as

$$\begin{aligned} P_f(b,T) &= P\left\{\exists \tau \in [0,T]: \bigcup_{k=1}^{K} X_k(\tau) > b_k\right\} \\ &= P\left\{\bigcup_{k=1}^{K} A_k > b_k\right\} \end{aligned} \tag{19}$$

in which $b = (b_1, \ldots, b_K)$ denotes the vector thresholds.

Equivalently, the above expression can be rewritten as

$$\begin{aligned} P_f(b,T) &= 1 - P\left(\bigcap_{k=1}^{K} A_k \le b_k\right) \\ &= 1 - F_{\boldsymbol{A}}(b) \end{aligned} \tag{20}$$

where $\mathrm{F}_{\boldsymbol{A}}(\cdot)$ is the joint CDF of $\boldsymbol{A} = (A_1, \ldots, A_\mathrm{K})$.

Equations (18) and (20) show that the small probabilities of first-passage failure of nonlinear random vibration systems can be obtained through computing the exceedance probabilities of the extreme values and multivariate extreme values of the corresponding response processes of the high response threshold levels. In the following section, we will descript an efficient method for modeling the distributions of the extreme values and multivariate extreme values at the tail regions in detail.

4 Extreme Value Distributions of Nonlinear Random Responses

4.1 Marginal Distribution and Its Parameter Estimate

As aforementioned, since the SGLD has such a flexibility and nearly encompasses the entire skewness-kurtosis region permissible for unimodal densities, we use the SGLD to approximate the tail distribution of the extreme value A of the response $X(t)$. The approximate PDF and CDF of A, therefore, can be written as

$$f_A(a) = \frac{\alpha}{x-b}\exp\left(-\frac{1}{r\sigma^r}\left|\ln\frac{a-b}{\theta}\right|^r\right), \quad x > b \tag{21}$$

$$F_A(a) = \frac{1}{2} + \frac{1}{2}\mathrm{sgn}\left(\frac{a-b}{\theta} - 1\right)\varrho\left(\frac{1}{r}, \frac{\left|\ln\frac{a-b}{\theta}\right|^r}{r}\right), \quad x > b \tag{22}$$

for skewness of A is larger than zero, i.e., $\gamma_A > 0$, and

$$f_A(a) = \frac{\alpha}{2\mu_X - b - a}\exp\left(-\frac{1}{r\sigma^r}\left|\ln\frac{2\mu_X - b - a}{\theta}\right|^r\right), \quad a < 2\mu_X - b \tag{23}$$

$$F_A(a) = \frac{1}{2} - \frac{1}{2}\mathrm{sgn}\left(\frac{2\mu_X - b - a}{\theta} - 1\right)\varrho\left(\frac{1}{r}, \frac{\left|\ln\frac{2\mu_X - b - a}{\theta}\right|^r}{r}\right), \quad a < 2\mu_X - b \tag{24}$$

for $\gamma_A < 0$.

Since only two shape parameters σ and r are needed to be estimated to construct a SGLD, when two exceedance probabilities and the corresponding values of A are known, the model parameters b, θ, σ and r can be computed and the resulting SGLD may give the reasonable estimates of the exceedance probabilities that are smaller than the known exceedance probabilities. In most cases, if we want to obtain the exceedance probabilities up to 10^{-4} and even 10^{-5} with sufficient accuracy, the two relatively large exceedance probabilities that are used to estimate the model parameters of the SGLDs can be set to be $P_1 \approx 10^{-1}$ and $P_2 \approx 10^{-2}$.

The estimation of the model parameters b, θ, σ and r of the SGLD generally needs some response samples of the system considered. Therefore, we can approximately estimate the mean μ_A and skewness γ_A of the extreme value A. If $\gamma_A > 0$, then we unchanged the set of the response samples. However, if $\gamma_A < 0$, then we should mirror the set of the response samples about the sample mean μ_A. After the above treatment, we can obtain the two values a_1 and a_2 of A with the exceedance probabilities P_1 and P_2 from the set of the response samples. Through replacing $F_A(a)$ by $1 - P_1$ and $1 - P_2$ on the left-hand-side of Eq. (21) and a by a_1

and a_2 on the right-hand-side of Eq. (22), respectively, we can obtain the following two nonlinear equations

$$1-P_1=\frac{1}{2}+\frac{1}{2}\mathrm{sgn}\left(\frac{a_1-b}{\theta}-1\right)\varrho\left(\frac{1}{r},\frac{\left|\ln\frac{a_1-b}{\theta}\right|^r}{r}\right) \tag{25}$$

$$1-P_2=\frac{1}{2}+\frac{1}{2}\mathrm{sgn}\left(\frac{a_2-b}{\theta}-1\right)\varrho\left(\frac{1}{r},\frac{\left|\ln\frac{a_2-b}{\theta}\right|^r}{r}\right) \tag{26}$$

Utilizing the relationship between the parameters b and θ and the parameters σ and r, the nonlinear equations can be solved by using Newton's method. To accelerate the convergence, as in the method of moments, the initial guess of the iteration solution procedure can be set to $r^{(1)}=2$ and $\sigma^{(1)}$ that satisfies $|\gamma_A|=\left(e^{\left(\sigma^{(1)}\right)^2}+2\right)\sqrt{e^{\left(\sigma^{(1)}\right)^2}-1}$.

Once determining the model parameters b, θ, σ and r, we can obtain the approximate distribution of the response $X(t)$. When the sample skewness γ_A is larger than zero, then the approximate PDF and CDF of $X(t)$ are given by Eqs. (21) and (22). For the case that the sample skewness γ_A is less than zero, the approximate PDF and CDF of $X(t)$ are given by Eqs. (23) and (24).

Apparently, the discrepancies of the estimates of the probabilities P_1 and, particularly, P_2 will contribute to the errors of the small exceedance probabilities of A. Therefore, it is necessary to choose a low discrepancy sampling method, e.g., the pseudo MC simulation method (Dai and Wang 2009) or the correlation-reduction Latin Hypercube sampling (CLHS) method (Owen 1994), to estimate P_1 and P_2.

4.2 Joint Distribution and Its Parameter Estimate

When we think of the $F_{\boldsymbol{A}}(\cdot)$ as an ordinary joint distribution of the random variables $A_1, \ldots, A_K$, we can obtain $F_{\boldsymbol{A}}(\cdot)$ via multivariate Copulas such as multivariate normal Copula, multivariate Clayton Copula and multivariate Gumbel Copula (Nelsen 2006). Since the tail distributions of $A_1, \ldots, A_K$ can be determined by the SGLDs with the parameters estimated by the above descripted 2-level method, from Sklar's theorem the Copulas in terms of the SGLDs can give sufficiently accurate joint probabilities of $\boldsymbol{A}=(A_1, \ldots, A_K)$ at the tail region of interest (Nelsen 2006). Among the above mentioned multivariate Copulas, since it is relatively simple to estimate the Copula parameters of the normal Copula, we use the

multivariate normal Copula to model the joint distribution $F_{\boldsymbol{A}}(\cdot)$. The PDF and CDF of the normal Copula of $\boldsymbol{A}$ are given by Liu and Der Kiureghian (1986).

$$f_{\boldsymbol{A}}(\boldsymbol{a}) = f_{A_1}(a_1) f_{A_2}(a_2) \ldots f_{A_K}(a_K) \frac{\varphi_K\left(\boldsymbol{v}, \boldsymbol{R}^{'}\right)}{\varphi(v_1)\varphi(v_2)\ldots\varphi(v_K)} \tag{27}$$

$$F_{\boldsymbol{A}}(\boldsymbol{a}) = \Phi_K\left(\boldsymbol{v}, \boldsymbol{R}^{'}\right) \tag{28}$$

where $f_{A_k}(\cdot)$ is the SGLD of A_k, $k = 1, \ldots, K$, $\boldsymbol{v} = (v_1, \ldots, v_K)$, in which $v_k = \Phi^{-1}[F_{A_k}(a_k)]$, here $\Phi^{-1}(\cdot)$ is the inverse standard normal CDF, $\varphi(\cdot)$ is the standard normal PDF, and $\varphi_K\left(\boldsymbol{v}, \boldsymbol{R}^{'}\right)$ and $\Phi_K\left(\boldsymbol{v}, \boldsymbol{R}^{'}\right)$ are, respectively, n-dimensional normal PDF and CDF of zero means, unit standard deviations, and correlation matrix $\boldsymbol{R}^{'}$. The elements $\rho_{ij}^{'}$ of $\boldsymbol{R}^{'}$ are defined in terms of the correlation coefficients ρ_{ij} between A_i and A_j through the integral relationship

$$\rho_{ij} = \int_{-\infty}^{\infty} \int_{-\infty}^{\infty} \left(\frac{a_i - \mu_{A_i}}{\sigma_{A_i}}\right)\left(\frac{a - \mu_{A_j}}{\sigma_{A_j}}\right) \varphi_2\left(v_i, v_j, \rho_{ij}^{'}\right) dv_i dv_j \tag{29}$$

where μ_{A_i}, μ_{A_j}, σ_{A_i} and σ_{A_j} are, respectively, the sample mean values and standard deviations of A_i and A_j, which are estimated from the set of the response samples that is used by the 2-level method. The above integral equation can be easily solved by Newton's method.

Once obtaining the marginal and joint distributions of $\boldsymbol{A}$ by using the method described above, we can easily compute the conditional probabilities of $\boldsymbol{A}$, which are identical to the conditional first passage probabilities of the responses of interest. It should be pointed out that only if the mappings $v_k = \Phi^{-1}[F_{A_k}(a_k)]$ are one to one and the correlation matrix $\boldsymbol{R}^{'}$ is positive definite the normal Copula is valid. Since the SGLD $F_A(a_k)$ are continuous and strictly increasing and the differences $\left|\rho_{ij} - \rho_{ij}^{'}\right|$ are small, the preconditions for the normal Copula are always satisfied in the present study.

5 Procedure for the Estimation of Small Probabilities of Failure

According to the above description, the steps for estimating the small probabilities of failure of nonlinear random vibration systems can be summarized as follows:

Step 1. Generate N (in general, $N < 3000$) response samples of the system of interest and estimate their mean values, variances, skewness, skewness and correlation coefficient of $X(t)$ and $\dot{X}(t)$ from the set of response samples.

Step 2. Construct SGLDs fitting the tail distributions of the extreme values of the responses of interest by the proposed 2-level method.
Step 3. Construct the normal Copula fitting the tail of the joint distribution of the extreme values of the responses of interest by the proposed method.
Step 4. Estimate the exceedance probabilities and joint exceedance probabilities of the extreme values of the responses of interest at high threshold levels from the obtained marginal and joint distributions. The estimates of the exceedance probabilities and joint exceedance probabilities are identical to the corresponding small probabilities of first-passage failure of the system.

6 Numerical Examples

6.1 *Investigation of the Efficiency of the 2-Level Method for Estimating the Parameters of the SGLDs*

To illustrate the efficiency of the 2-level method for estimating the parameters of the SGLDs, we consider the four theoretical distributions, i.e., gamma, Weibull, Inverse-Gaussian and F- distributions, which have been used by Low to show the accuracy and flexibility of the SGLD in fitting unimodal distributions (Low 2013). The PDFs of the distributions are given as, respectively

$$f_X(x) = \frac{x^{k-1}\mathrm{e}^{-x}}{\Gamma(k)}, \quad 0 < x < \infty \tag{30}$$

$$f_X(x) = kx^{k-1}\mathrm{e}^{-x^k}, \quad 0 < x < \infty \tag{31}$$

$$f_X(x) = \sqrt{\frac{k}{2\pi x^3}}\mathrm{e}^{-k(x-1)^2/2x}, \quad 0 < x < \infty \tag{32}$$

$$f_X(x) = \frac{1}{x\mathrm{B}(k_1/2, k_2/2)}\sqrt{\frac{(k_1 x)^{k_1} k_2^{k_2}}{(k_1 x + k_2)^{k_1+k_2}}}, \quad 0 < x < \infty \tag{33}$$

in which k, k_1 and k_2 are the distribution parameters and $\mathrm{B}(\cdot)$ is the beta function.

We set $P_1 = 10^{-1}$ and $P_2 = 10^{-2}$ in the following numerical computation. For each distribution, 500 sample sets, each has 2000 samples, are generated by the Latin Hypercube sampling (LHS) method, thereby 500 groups (b, θ, σ, r) are estimated by using the extrapolation method for each distribution. For each distribution, from the resulting 500 SGLDs, 500 groups of the approximate estimates of the exceedance probabilities corresponding to the values $x^* = F_X^{-1}(P^*)$ can be obtained, here $F_X^{-1}(\cdot)$ denote the inverse CDF of the involved variable and P^* are set to be 10^{-4} and 10^{-5}, respectively. Based on the above computation, for each

Table 1 SGLD approximation at the tails of the theoretical distributions[a]

Distributions	$P^* = 10^{-4}$				$P^* = 10^{-5}$			
	Method of moments		2-level method		Method of moments		2-level method	
	Mean $[10^{-4}]$	COV	Mean $[10^{-4}]$	COV	Mean $[10^{-5}]$	COV	Mean $[10^{-5}]$	COV
Gamma								
$k = 1$	1.77	0.453	1.66	0.078	3.24	0.702	2.77	0.134
$k = 2$	1.81	0.411	1.49	0.045	3.21	0.622	2.26	0.070
$k = 3$	1.69	0.354	1.37	0.039	2.76	0.538	1.95	0.057
$k = 4$	1.67	0.353	1.30	0.042	2.65	0.534	1.75	0.062
Weibull								
$k = 2$	1.50	0.197	1.43	0.041	2.25	0.296	2.10	0.060
$k = 3$	1.15	0.129	1.21	0.050	1.41	0.193	1.53	0.067
Inverse Gaussian								
$k = 2$	1.11	0.788	1.68	0.578	1.76	1.321	3.09	0.807
$k = 3$	1.14	0.815	1.61	0.694	1.79	1.430	2.90	0.971
$k = 4$	1.26	0.836	1.60	0.701	2.08	1.472	2.83	1.011
$k = 5$	1.21	0.829	1.55	0.702	1.91	1.406	2.63	1.011
F-								
$k_1 = 5$, $k_2 = 15$	1.90	0.591	0.94	0.147	2.81	0.845	0.86	0.279

[a]*Mean* the mean value of the estimated probability; *COV* the coefficient of variation of the estimated probability

distribution, the mean values and coefficients of variation (COV) of the approximate exceedance probabilities corresponding to x^* are obtained. As compared, from the generated sample sets and the method of moments, we also obtain the corresponding mean value and COV foe each distribution. The computing results are listed in Table 1. It can be seen in Table 1 that, in most cases, the extrapolation method provides better mean values of the estimates of the small exceedance probabilities than the method of moments, and, in all cases, the extrapolation method permits smaller COV of the estimates of the small exceedance probabilities than the method of moments. This indicates that, at least for the four distributions, the extrapolation method is a more efficient method for estimating the model parameters of a SGLD. More numerical analyses demonstrate that with the increase of the number of the samples the accuracy of the extrapolation method becomes higher and the variety of it becomes less. The numerical analyses also show that under the same samples the extrapolation method is always more efficient than the method of moments.

6.2 Hysteretic Oscillator Excited by a Stationary Gaussian Process

Consider a Bouc-Wen hysteretic oscillator subjected to a stationary Gaussian process $F(t)$ which is defined by the set of differential equations

$$\ddot{X} + 2\zeta\omega_0\dot{X} + \omega_0^2[\alpha X + (1-\alpha)U] = F(t) \tag{34}$$

$$\dot{U} = -\gamma\left|\dot{X}\right|U|U|^{n-1} - \beta\dot{X}|U|^n + A\dot{X} \tag{35}$$

in which $\omega_0 = \pi$, $\zeta = 0.05$, $F(t)$ is a stationary Gaussian process with the mean value μ_F and the single-side power spectral density function (PSD) $S_{FF}(\omega) = 1$, and the parameters in the Bouc-Wen law are set to $\alpha = 0.05$, $n = 3$, $A = 1$, and $\gamma = \beta = A/\left(2x_y^n\right)$, where $x_y = 0.5\sigma_0$ is the yield displacement, here $\sigma_0 = 1.5$ is the estimated standard deviation of $X(t)$ at $t = 20$ s to the zero-mean, stationary Gaussian excitation process. The excitation process is expanded by the spectral representation method with the upper-cut frequency $\omega_U = 40\omega_0$ and equal frequency interval $\Delta\omega = 0.1\pi$, i.e.,

$$F(t) = \mu_F + \sum_{i=0}^{N_F}(A_i\cos\omega_i t + B_i\sin\omega_i t) \tag{36}$$

where A_i and B_i are independent normal random variables with mean zero and variances $\sigma_i^2 = 2S_{FF}(\omega_i)\Delta\omega$, here $\omega_i = i\Delta\omega$, and $N_F = \omega_U/\Delta\omega = 400$ is the number of the frequency intervals in discretization. Therefore, there are total 800 variables in the spectral representation and the resulting simulation process has a period $T_0 = 2\pi/\Delta\omega = 20$ s.

The failure of the system is defined as the event that the absolute value of the system response, i.e., $|X(t)|$, exceeds in magnitude the high threshold level b in the reference time $T = 20$ s. First, we consider the case that the mean value of $F(t)$ is $\mu_F = 0$. By using the MC simulation method and CLHS method, we generate, respectively, 1000000 and 2000 response samples of the system. Note that length of time of the samples are all 20 s. Setting $P_1 = 10^{-1}$ and $P_2 = 10^{-2}$ in the extrapolation method, we estimate the model parameters of the SGLDs fitting the extreme response Z, thereby the first passage probabilities of the response $|X(t)|$ are computed by the developed method and plotted in Fig. 1. As compared, the first passage probabilities directly estimated from the 1,000,000 and 2000 response samples are also plotted in Fig. 1. We can see in Fig. 1 that for the small thresholds the first passage probabilities estimated from the developed method almost completely agree with those obtained from the MC simulation method and CLHS, however, for the large thresholds, the first passage probabilities estimated from the developed method based on the 2000 response samples agree very well with those estimated from the developed method based on the 1,000,000 response samples, even for the

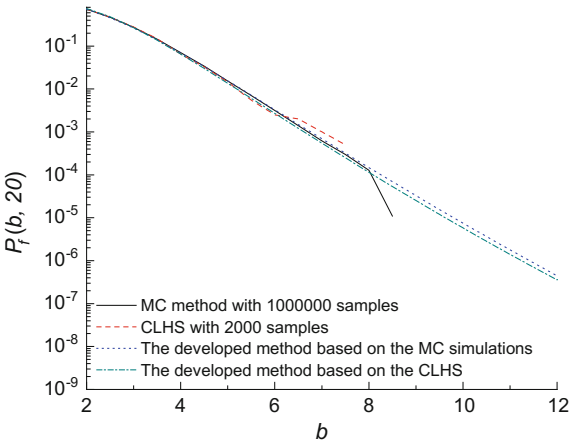

Fig. 1 Estimated first passage probabilities for the case of $\mu_F = 0$ (T = 20 s)

probabilities as low as 10^{-7}, while both the MC simulation method and CLHS method cannot provide useful information about the small first passage probabilities as low as 10^{-7}–10^{-5} since the numbers of the response samples are not sufficiently large.

Secondly, we consider the case that the mean value of $F(t)$ is $\mu_F = 5$. Similarly, we estimate, respectively, the first passage probabilities by using the developed method and the simulation methods and plot them in Fig. 2. It can be seen in Fig. 2 that, for the small thresholds, there is a good agreement between the estimated probabilities. For the large thresholds, there are little deviations between the probabilities estimated by the developed method based on the 2000 response samples generated by the CLHS and those estimated by the developed method based on the 1,000,000 response samples generated by the MC simulation method, however, the deviations are acceptable in the sense that for the same threshold b the

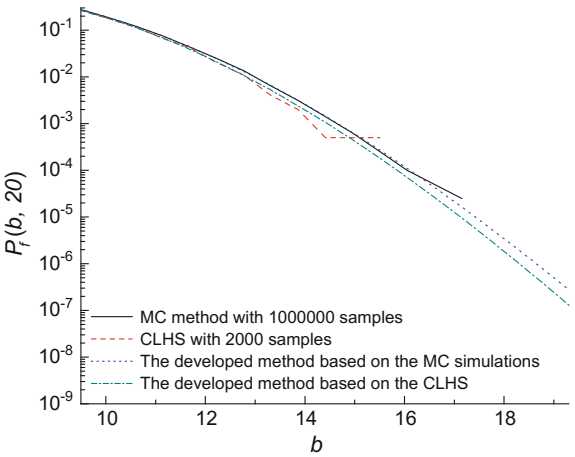

Fig. 2 Estimated first passage probabilities for the case of $\mu_F = 5$ (T = 20 s)

first passage probabilities are of the same order of magnitude. Also, both the MC simulation method and CLHS cannot exactly estimate the small passage probabilities as low as 10^{-7}–10^{-5}.

6.3 Mechanical Model of Two Connected Electric Substation Equipment Items

Consider the mechanical model of two electric substation equipment items connected by a rigid bus conductor fitted with a flexible strap connector, which is subjected to earthquake base motion. The detailed description of the mechanical models of the equipment items has been given by Song and Der Kiureghian (2006). The equation of motion of the system is

$$\boldsymbol{M}\ddot{\boldsymbol{X}} + \boldsymbol{C}\dot{\boldsymbol{X}} + \boldsymbol{R}(\boldsymbol{X}, \dot{\boldsymbol{X}}, U) = -\boldsymbol{L}\ddot{x}_g \tag{37}$$

where

$$\boldsymbol{X} = \begin{Bmatrix} X_1(t) \\ X_2(t) \end{Bmatrix} \tag{38}$$

$$\boldsymbol{M} = \begin{bmatrix} m_1 & 0 \\ 0 & m_2 \end{bmatrix} \tag{39}$$

$$\boldsymbol{C} = \begin{bmatrix} c_1 + c_0 & -c_0 \\ -c_0 & c_2 + c_0 \end{bmatrix} \tag{40}$$

$$\boldsymbol{R}(\boldsymbol{X}, \dot{\boldsymbol{X}}, Z) = \begin{Bmatrix} k_1 X_1(t) - f_s\left[\Delta X(t), \Delta\dot{X}(t), U(t)\right] \\ k_2 X_2(t) - f_s\left[\Delta X(t), \Delta\dot{X}(t), U(t)\right] \end{Bmatrix} \tag{41}$$

$$L = \begin{Bmatrix} l_1 \\ l_2 \end{Bmatrix} \tag{42}$$

where $\ddot{x}_g$ is the base acceleration, $X_i(t)$ is the displacement of the ith equipment item at its attachment point relative to the base, $\Delta X(t) = X_2(t) - X_1(t)$ is the relative displacement between the two equipment items, and the function $f_s\left[\Delta X, \Delta\dot{X}, U\right]$ denotes the resisting force of the rigid bus conductor fitted with a flexible strap connector, which is described by the generalized Bouc-Wen hysteretic law, i.e.,

$$f_s\left[\Delta X, \Delta\dot{X}, U\right] = \alpha k_0 \Delta X + (1-\alpha) k_0 U \tag{43}$$

$$\dot{U} = \Delta\dot{X}\left[A - |U|^n \psi\left(\Delta X, \Delta\dot{X}, U\right)\right] \tag{44}$$

$$\psi(\Delta X, \Delta\dot{X}, U) = \beta_1 \mathrm{sgn}(\Delta\dot{X}U) + \beta_2 \mathrm{sgn}(\Delta\dot{X}\Delta X) + \beta_3 \mathrm{sgn}(\Delta X U) + \beta_4 \mathrm{sgn}(\Delta\dot{X}) + \beta_5 \mathrm{sgn}(U) + \beta_6 \mathrm{sgn}(\Delta X) \tag{45}$$

The parameters related to the system are $m_1 = 1090\,\mathrm{kg}$, $m_2 = 545\,\mathrm{kg}$, $k_0 = 49.2$ kN/m, $k_1 = 172$ kN/m, $k_2 = 538$ kN/m, $l_1 = m_1$, $l_2 = m_2$, $c_0 = 0$, $\zeta_i = c_i/\left(2\sqrt{m_i k_i}\right) = 0.02$, $i = 1, 2$, $\alpha = 0.1$, $A = 1.0$, $n = 1$, $\beta_1 = 0.470$, $\beta_2 = -0.118$, $\beta_3 = 0.0294$, $\beta_4 = 0.115$, $\beta_5 = -0.121$ and $\beta_6 = -0.112$, respectively. In this example, we assume that the ground acceleration $\ddot{x}_g(t)$ is a zero-mean, stationary Gaussian, filtered white-noise process having the Kanai-Tajimi PSD

$$S(\omega) = S_0 \frac{\omega_f^4 + 4\omega_f^2\zeta_f^2\omega^2}{\left(\omega^2 - \omega_f^2\right)^2 + 4\omega_f^2\zeta_f^2\omega^2} \tag{46}$$

with $S_0 = 0.0156\ \mathrm{m^2/s^3}$, $\omega_f = 15.7$ rad/s and $\zeta_f = 0.6$. The random process $\ddot{x}_g(t)$ is represented by the spectral representation, i.e., Equation (22), with equal intervals $\Delta\omega = 0.3$ rad/s and a cut-off frequency of $\omega_U = 120$ (rad/s), which covers about 95% of the area underneath the PSD. Therefore, the period of the simulated process is about 21 s and is described by 800 Gaussian random variables.

By using the MC simulation method and CLHS method, we generate, respectively, 20000 and 2000 response samples of the system. Based on the 20,000 and 2000 samples, we use the developed method to estimate the small probabilities of first-passage failure related to $|X_1(t)|$ and $|X_2(t)|$ and plot them in Figs. 3 and 4, respectively. Note that, in the estimation of the parameters of the SGLDs, the exceedance probabilities P_1 and P_2 are set to $P_1 = 10^{-1}$ and $P_2 = 10^{-2}$ for $A_1 = \max_{0 \le t \le 20}|X_1(t)|$ and $P_1 = 10^{-1}$ and $P_2 = 0.5 * 10^{-2}$ for $A_2 = \max_{0 \le t \le 20}$

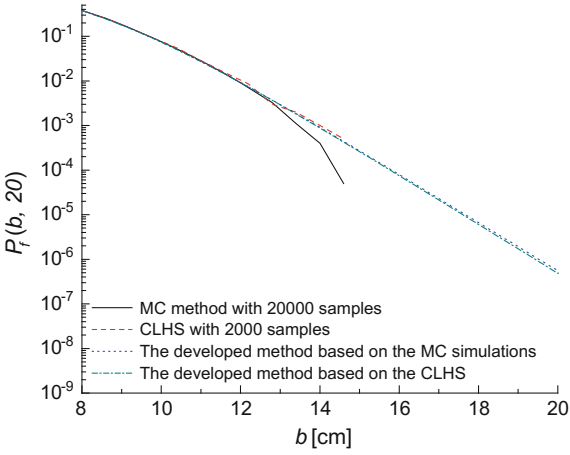

Fig. 3 Estimated first passage probabilities of $|X_1(t)|$

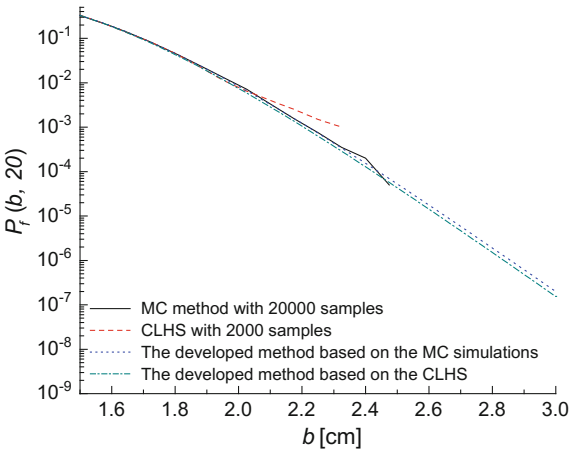

Fig. 4 Estimated first passage probabilities of $|X_2(t)|$

$|X_2(t)|$, respectively. As compared, the first passage probabilities directly estimated from the 20,000 and 2000 samples are also plotted in Figs. 3 and 4. Similar to the above example, Figs. 3 and 4 show that the developed method based on the 2000 response samples generated from the CLHS provide the sufficiently accurate estimates of the small first passage probabilities as low as 10^{-7}, which cannot be directly obtained from the 20,000 samples generated by the MC simulation method and the 2000 samples generated by CLHS.

From the numerical results plotted in Figs. 5 and 6 and the correlation coefficient between the extreme values A_1 and A_2 estimated from the 20,000 and 2000 samples, we use the developed method to estimate the first passage probabilities of the vector thresholds (b_1, b_2) of the vector response process $(|X_1(t)|, |X_2(t)|)$. Figure 5 plots the estimated results based on the 20,000 samples generated by the MC simulation method, in which the thresholds are set to be $8\,\text{cm} \le b_1 \le 20\,\text{cm}$ and $1.6\,\text{cm} \le b_1 \le 3\,\text{cm}$, respectively. The ratio of the estimated results based the 2000 samples generated by the CLHS to those shown in Fig. 6, i.e., $r_{\text{CLHS}-\text{MC}} = p_f^{\text{CLHS}}(\boldsymbol{b}, 20)/p_f^{\text{MC}}(\boldsymbol{b}, 20)$, are also computed and plotted in Fig. 8. It can be seen in Fig. 8 that the ratio $r_{\text{CLHS}-\text{MC}}$ is larger than 0.75 and less than 1, which indicates that the estimated results based the 2000 samples are always slightly less than those based on the 20,000 samples. Figures 5 and 6 also show that in the case that the ratio $r_{\text{CLHS}-\text{MC}}$ is less than 0.9 the first passage probabilities based on the 20,000 samples are less than 10^{-4}. For such small probabilities, the ratio $r_{\text{CLHS}-\text{MC}} \in [0.75, 0.9]$ is acceptable, i.e., the small first passage probabilities estimated based on the 2000 samples generated by the CLHS are sufficiently accurate, as compared with the results estimated based on the 20,000 samples generated by the MC simulation method.

Finally, we consider the conditional first passage probabilities $P\{|X_1(\tau)| > b_1, \tau \in [0, T] || X_2(s)| \le b_2 = 1.8\,\text{cm}, s \in [0, T]\}$ and $P\{|X_2(\tau)| > b_2, \tau \in [0, T] || X_1(s)| \le b_1 = 10\,\text{cm}, s \in [0, T]\}$. The conditional probabilities are estimated from the 20,000 response samples generated by the MC simulation method,

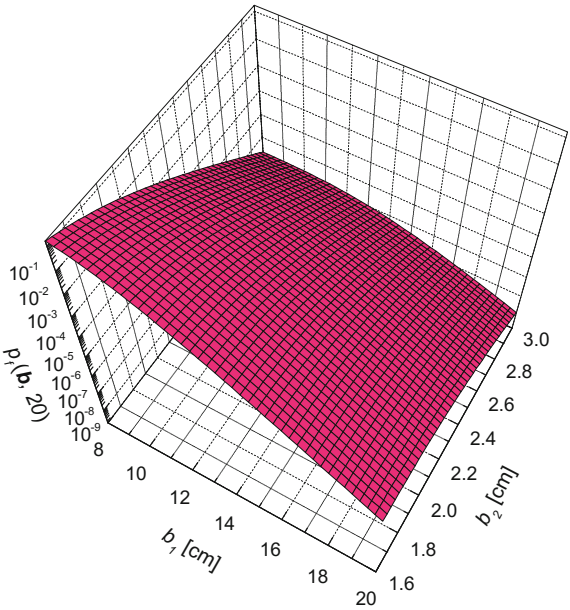

Fig. 5 First passage probabilities of the vector process $(|X_1(t)|, |X_2(t)|)$ estimated from the developed method based on the 20,000 samples

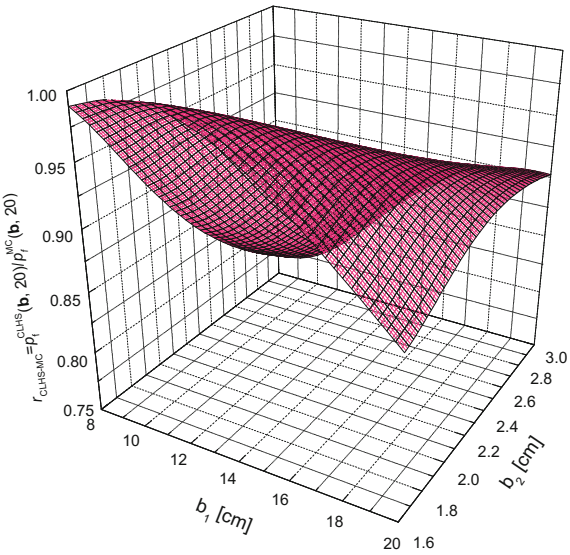

Fig. 6 Ratio of the first passage probabilities of vector response process, $r_{\mathrm{CLHS-MC}} = p_f^{\mathrm{CLHS}}(\boldsymbol{b}, 20)/p_f^{\mathrm{MC}}(\boldsymbol{b}, 20)$

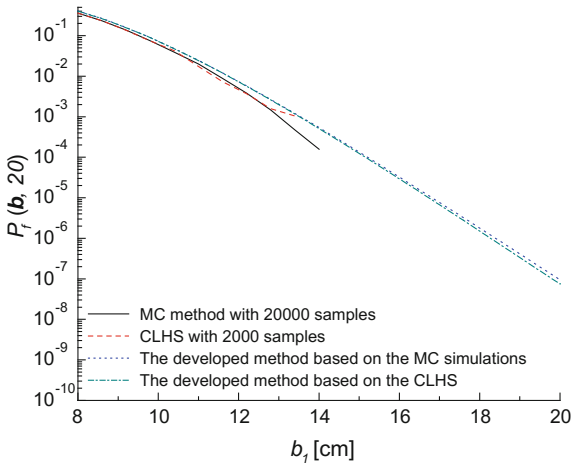

Fig. 7 Estimated conditional first passage probabilities $P\{|X_1(\tau)| > b_1, \tau \in [0,T] || X_2(s)| \leq b_2 = 1.8\,\text{cm}, s \in [0,T]\}$

the 2000 response samples generated by the CLHS, the developed method based on the 20,000 samples and the developed method based on the 2000 samples. The computation results are plotted in Figs. 7 and 8, respectively. Figures 7 and 8 show that the estimates obtained from the developed method based on the 2000 samples agree well with those obtained from the developed method based on the 20,000 samples, including those probabilities as low as 10^{-7}–10^{-5}, while the MC simulation method and the CLHS method cannot give reasonable estimates for the such small conditional first passage probabilities.

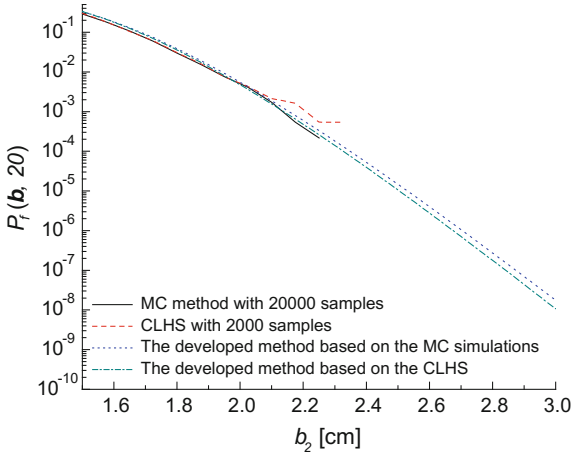

Fig. 8 Estimated conditional first passage probabilities $P\{|X_2(\tau)| > b_2, \tau \in [0,T] || X_1(s)| \leq b_1 = 10\,\text{cm}, s \in [0,T]\}$

6.4 Network Seismic Reliability of a Lifeline Engineering

This example is to illustrate the efficiency and use of the developed method by the seismic reliability analysis of an electrical substation under a stochastic earthquake excitation. The electrical substation is taken from Song (2004) and consists of five equipment items. The equipment items 1 and 2 and equipment items 3 and 4 are connected to each other by three identical assembles of a rigid bus (RB) and an S-shaped flexible strap connector (S-FSC). Other connections are assumed to be sufficiently flexible so as not to cause dynamic interaction. The network graph of the electrical substation is shown in Fig. 9.

For the seismic response analysis, the equipment items are modeled as linear single-degree-of-freedom (SDOF) oscillators and the RB-S-FSCs are modeled as hysteresis elements with additional viscous damping elements. For details of the idealization and its accuracy in interaction studies, see Song (2004).

The equation of motion of the connected equipment items 1 and 2 is defined by Eq. (37), however, the resisting force of the rigid bus conductor fitted with a flexible strap connector (RB-S-FSC) is described by the Bouc-Wen hysteretic law:

$$f_s\left[\Delta X, \Delta \dot{X}, U\right] = \alpha k_0 \Delta X + (1-\alpha) k_0 U \tag{47}$$

$$\dot{U} = \Delta \dot{X}\left[A - |U|^n \left[\beta + \gamma \mathrm{sgn}\left(\Delta \dot{X} U\right)\right]\right] \tag{48}$$

where α represents the post- to preyield stiffness ratio, k_0 is the stiffness of the connector, and A, n, β and γ are the hysteresis model parameters.

The equation of motion for equipment items 3 and 4 is obtained by replacing indices 1 and 2 of Eqs. (37)–(42) with 3 and 4, respectively. Equipment item 5, which has no significant dynamic interaction with other equipment items, is modeled as a stand-alone SDOF oscillator having the equation of motion:

$$m_5 \ddot{X}_5 + c_5 \dot{X}_5 + k_5 X_5 = -l_5 \ddot{x}_g \tag{49}$$

where m_5, c_5, k_5 and l_5 are effective mass, damping, stiffness and external internal inertia force values of the equipment item 5.

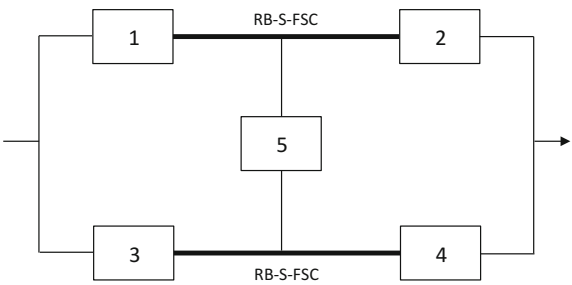

Fig. 9 Network graph of the electrical substation

The parameters of the system are $m_1 = 438\,\text{kg}$, $m_2 = 210\,\text{kg}$, $m_3 = 403\,\text{kg}$, $m_4 = 193\,\text{kg}$, $m_5 = 200\,\text{kg}$, $k_0 = 25.7$ kN/m, $k_1 = 158$ kN/m, $k_2 = 198$ kN/m, $k_3 = 158$ kN/m, $k_4 = 198$ kN/m, $k_5 = 198$ kN/m, $l_i = m_i, i = 1, \ldots, 5$, $c_0 = 0$, $\zeta_i = c_i/\left(2\sqrt{m_i k_i}\right) = 0.02$, $i = 1, \ldots, 5$, $\alpha = 0.206$, $A = 1.0$, $n = 1$, $\beta = 0.175$, $\gamma = 0.176$, respectively. In this example, we assume that the ground acceleration $\ddot{x}_g(t)$ is a zero-mean, stationary Gaussian, filtered white-noise process having the well-known Kanai-Tajimi PSD, which is defined by Eq. (46).

The random process $\ddot{x}_g(t)$ is represented by the spectral representation with equal intervals $\Delta\omega = 0.3$ rad/s and a cut-off frequency of $\omega_U = 120$ (rad/s), which covers about 95% of the area underneath the PSD. Therefore, the period of the simulated process is about 21 s and is described by 800 Gaussian random variable.

From the recursive decomposition algorithm (RDA) (Li and He 2002), the network has 5 disjoint shortest paths and 6 disjoint shortest cuts:

$$L_1 = \{12\} \tag{50}$$

$$L_2 = \{\bar{1}34\} \tag{51}$$

$$L_3 = \{1\bar{2}34\} \tag{52}$$

$$L_4 = \{\bar{1}23\bar{4}5\} \tag{53}$$

$$L_5 = \{1\bar{2}\bar{3}45\} \tag{54}$$

and

$$S_1 = \{\bar{1}\bar{3}\} \tag{55}$$

$$S_2 = \{1\bar{2}3\bar{4}\} \tag{56}$$

$$S_3 = \{\bar{1}3\bar{4}\bar{5}\} \tag{57}$$

$$S_4 = \{\bar{1}\bar{2}3\bar{4}5\} \tag{58}$$

$$S_5 = \{1\bar{2}\bar{3}\bar{4}\} \tag{59}$$

$$S_6 = \{1\bar{2}\bar{3}4\bar{5}\} \tag{60}$$

In this example, the failures of the components are defined as the events that the passage times of the absolute values of the components responses first exceed in magnitude the duration of the earthquake excitation $D = 20$ s. For estimating the 2 threshold levels a_1 and a_2, 2000 response samples of the equipment items are generated by the CLHS. As compared, 20000 response samples are also generated by the Monte Carlo method. Note that each deterministic response in the sampling

Table 2 Model parameters of the SGLDs fitting the extreme value responses

Equipment items	$\boldsymbol{b}$ [cm]	θ	σ	$\boldsymbol{r}$
1	0.514	3.443	0.210	2.201
2	0.435	0.877	0.198	1.859
3	−0.027	3.654	0.177	2.098
4	0.287	0.907	0.178	1.974
5	0.082	1.201	0.153	1.967

is solved by the four-order Rung-Kutta method with the equal time step $\Delta t = 0.02$ s. Skewness of the extreme values of the absolute values of the responses of the equipment items are estimated from the 2000 response samples generated by the CLHS. Estimated skewness are all more than zero. The obtained model parameters are listed in Table 2. Note that the location parameters b listed in Table 2 are slightly more or less than zero such that the tails of the obtained SGLDs agree well with the actual tail distributions of the extreme value responses.

The exceedance probabilities of the extreme value responses of the high thresholds are calculated from the obtained SGLDs. As compared, the exceedance probabilities are also estimated from the 20,000 response samples generated by the MC method. The numerical results show that the exceedance probabilities estimated by the 2-level method are very reasonable for the thresholds considered, however, those estimated by the MC method are unreasonable for the large thresholds since the scale size of the response samples is not large enough.

From the dependence modeling described above, one needs to estimate the correlation coefficients and Kendall's tau of the extreme values of the responses from the generated samples used for marginal distribution modeling, whereby the elements ρ'_{ij} of $\boldsymbol{R}$ of the normal copula, parameter α of the Clayton Copula and parameter β of the Gumbel Copula can be estimated. The sample versions of the correlation coefficients are

$$\rho = \begin{bmatrix} 1.000 & 0.471 & 0.498 & 0.323 & 0.042 \\ 0.471 & 1.000 & 0.239 & 0.405 & 0.252 \\ 0.498 & 0.239 & 1.000 & 0.485 & 0.050 \\ 0.323 & 0.405 & 0.485 & 1.000 & 0.120 \\ 0.042 & 0.252 & 0.050 & 0.120 & 1.000 \end{bmatrix} \tag{61}$$

from which the parameters of the normal Copulas can be computed:

$$\rho' = \begin{bmatrix} 1.000 & 0.473 & 0.496 & 0.324 & 0.043 \\ 0.473 & 1.000 & 0.241 & 0.408 & 0.257 \\ 0.496 & 0.241 & 1.000 & 0.484 & 0.051 \\ 0.324 & 0.408 & 0.484 & 1.000 & 0.122 \\ 0.043 & 0.257 & 0.051 & 0.122 & 1.000 \end{bmatrix} \tag{62}$$

Table 3 The probabilities of the disjoint shortest paths and node-pair reliabilities of the system

Disjoint shortest path	Normal Copula	MC method
$\boldsymbol{L}_1$	0.779049	0.776850
$\boldsymbol{L}_2$	0.075461	0.072200
$\boldsymbol{L}_3$	0.106310	0.113150
$\boldsymbol{L}_4$	0.002593	0.001800
$\boldsymbol{L}_5$	0.001928	0.002000
$\boldsymbol{R}_{sys}$	0.965341	0.966000

Table 4 The probabilities of the disjoint shortest cuts and node-pair reliabilities of the system

Disjoint shortest cut	Normal Copula	MC method
$\boldsymbol{S}_1$	0.013563	0.011750
$\boldsymbol{S}_2$	0.012591	0.014200
$\boldsymbol{S}_3$	0.001807	0.001500
$\boldsymbol{S}_4$	0.004433	0.004550
$\boldsymbol{S}_5$	0.001631	0.001450
$\boldsymbol{S}_6$	0.000635	0.000550
$\boldsymbol{R}_{sys}$	0.965341	0.966000

Based on marginal distribution and dependence modeling, the copulas of the five extreme values of the seismic responses of the electrical substation can be completely determined. It is first assume that the thresholds are $b_1 = 5.0$ cm, $b_2 = 1.5$ cm, $b_3 = 5.0$ cm, $b_4 = 1.5$ cm and $b_5 = 1.5$ cm, respectively. The probabilities of the disjoint shortest paths and cuts as well as the seismic reliability of the electrical substation are calculated from the obtained normal Copulas and listed in Tables 3 and 4. As compared, the probabilities and reliabilities are also estimated by the Monte Carlo method with 20,000 samples and listed in Tables 3 and 4. It can be seen in Tables 3 and 4 that the estimated node-pair reliabilities based on the disjoint shortest paths and cuts are in complete agreement.

For large-size lifeline networks, one can use the Boferroni inequality to reduce the computational cost in estimating the seismic reliability (Li and He 2002). The approximate estimate of the seismic reliabilities can be expressed as

$$R_{sys} \approx \frac{1}{2}\left[1 + \sum_{i=1}^{N'} p_r(L_i) - \sum_{i=1}^{M'} p_r(S_i)\right] \tag{63}$$

where N' and M' are, respectively, the needed numbers of the disjoint shortest paths and cuts, which can be automatically determined by the RDA method when the maximum permissible error of the estimate has been prespecified. The relationship between the maximum permissible error, ε, and the numbers N' and M' is expressed by

Table 5 Approximate estimation of the node-pair reliabilities of the system

Copulas	N'	M'	$\left\lvert 1-\sum_{i=1}^{N'} p_r(L_i)-\sum_{i=1}^{M'} p_r(S_i)\right\rvert\ [\times 10^{-2}]$	R_{sys}
Normal	4	2	1.00	0.968630

Table 6 Five threshold cases of the system

Cases	b_1 [cm]	b_2 [cm]	b_3 [cm]	b_4 [cm]	b_5 [cm]
1	5.1	1.6	5.1	1.6	1.6
2	5.3	1.8	5.3	1.8	1.8
3	5.5	2.0	5.5	2.0	2.0
4	5.7	2.2	5.7	2.2	2.2
5	5.9	2.4	5.9	2.4	2.4

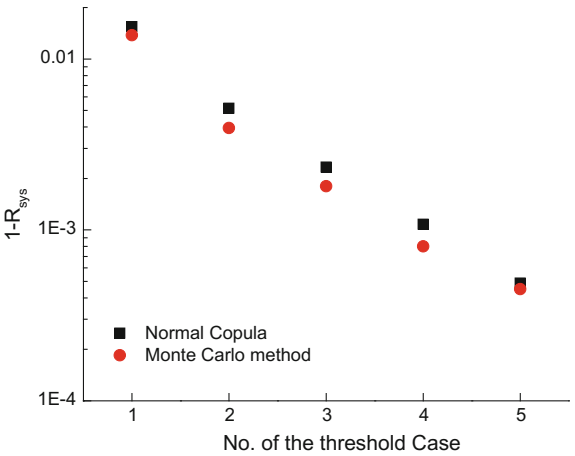

Fig. 10 Node-pair reliabilities for the considered threshold cases

$$\varepsilon = \left| 1 - \sum_{i=1}^{N'} p_r(L_i) - \sum_{i=1}^{M'} p_r(S_i) \right| \tag{64}$$

If we set the maximum permissible error to be $\varepsilon = 1 \times 10^{-2}$, then it only needs four disjoint shortest paths and two or three disjoint shortest cuts to approximately estimate the seismic reliabilities, as illustrated in Table 5.

Secondly, in order to investigate the efficiency of the proposed method in estimating the small probabilities of failure of the electrical substation, we consider the five threshold cases which are listed in Table 6. The seismic reliabilities of the network are estimated, respectively, based on the obtained normal Copula and the Monte Carlo method with 20,000 samples. The numerical results are plotted in

Fig. 10. It can be seen in Fig. 10 that the seismic reliabilities estimated from the normal Copula closely agree with those estimated from the MC method.

7 Conclusions

To efficiently estimate the small probabilities of failure i.e., small first passage probabilities, of nonlinear random vibration systems, a new method is proposed in the present study. The method first uses the SGLDs to approximate the upper tails of the distributions of the extreme response of the system, thereby the small first passage probabilities of the scalar response processes can be approximately estimated. In order to reduce the computational cost to an acceptable level, an efficient parameter estimation method is proposed to estimate the parameters of the SGLDs. Secondly, to efficiently estimate the small first passage probabilities of the vector response processes, the normal Copulas are used to approximate the upper tails of the distributions of the multivariate extreme responses of the system, in which the Copula parameters can be easily estimated based on the response samples that are used to estimate the parameters of the SGLDs modeling the upper tails of the extreme response distributions. Thus, the estimate of the small first passage probabilities of the vector response processes requires little extra computational cost. Two illustrative examples are presented in the present study, which show that the efficiency of the proposed method is high enough in estimating the small probabilities of failure of nonlinear random vibration systems.

References

Au SK, Beck JL (2001) Estimation of small failure probabilities in high dimensions by subset simulation. Probab Eng Mech 16(4):263–277

Bucher C (2009) Asymptotic sampling for high-dimensional reliability analysis. Probab Eng Mech 24(4):504–510

Cohen AC, Whitten BJ (1980) Estimation in the three-parameter lognormal distribution. J Am Stat Assoc 75(370):399–404

Dai H, Wang W (2009) Application of low-discrepancy sampling method in structural reliability analysis. Struct Saf 31(1):55–64

Fujimura K, Der Kiureghian A (2007) Tail-equivalent linearization method for nonlinear random vibration. Probab Eng Mech 22(1):63–76

Grigoriu M, Samorodnitsky G (2014) Reliability of dynamic systems in random environment by extreme value theory. Probab Eng Mech 38:54–69

Liu PL, Der Kiureghian A (1986) Multivariate distribution models with prescribed marginals and covariances. Probab Eng Mech 1(2):105–112

Liu JS (2001) Monte Carlo strategies in scientific computing. Springer Series in Statistics, Springer, Berlin

Li J, He J (2002) A recursive decomposition algorithm for network seismic reliability evaluation. Earthq Eng Struct Dyn 31(8):1525–1539

Lin YK, Cai GQ (2004) Probabilistic structural dynamic-advanced theory and applications. Mc Graw-Hill Inc., New York

Lutes LD, Sarkani S (2004) Random vibrations: analysis of structural and mechanical systems. Elsevier Butterwork-Heinemann, Burlington (MA)

Low YM (2013) A new distribution for fitting four moment and its applications to reliability analysis. Struct Saf 42:12–25

Nadarajah S (2005) A generalized normal distribution. J Appl Stat 32(7):685–694

Nelsen RB (2006) An introduction to copulas. Springer, New York

Naess A, Gaidai O (2008) Monte Carlo methods for estimating the extreme response of dynamical systems. J Eng Mech ASCE 134(8):628–636

Owen AB (1994) Controlling correlations in Latin hypercube samples. J Am Stat Assoc 89 (428):1517–1522

Shinozuka M (1972) Monte Carlo solution of structural dynamics. Comput Struct 2:855–874

Song J (2004) Seismic response and reliability of electrical substation equipment and systems. Doctor thesis. Berkeley, University of California

Song J, Der Kiureghian A (2006) Generalized Bouc-Wen model for highly asymmetric hysteresis. J Eng Mech ASCE 132(6):610–618

Wen YK (1980) Equivalent linearization for hysteretic systems under random excitation. Appl Mech ASME 47(3):150–154

Generation of Non-synchronous Earthquake Signals

Davide Lavorato, Ivo Vanzi, Camillo Nuti and Giorgio Monti

Abstract In this chapter, we describe two procedures to generate earthquake asynchronous signals at different space points for the same seismic event. The foundations of long structures, such as bridges, are placed at distant space points. The earthquake signals at these points have different characteristics and their correct evaluation is important to define design actions. However, design codes around the world do not consider this complex type of action in a consistent manner. The point-to-point signal variation is due both to time lag, since the seismic waves move through the soils with a finite velocity among distant points, and to a change of the signal frequency contents. This depends on physical complex soil-wave interaction phenomena during wave propagation (reflection, refraction, filtering, amplification, etc.). In this chapter, two different generation procedures (PR1 and PR2) to determine the non-synchronous actions at different surface points are shown. Both procedures have been implemented in MATLAB. PR1 generates asynchronous signals at the soil surface. It starts from recorded signals at a few surface points for the same seismic event. PR2 produces asynchronous surface signals by amplifying the bedrock signals obtained by a bedrock propagation process. The inputs for the bedrock propagation are obtained via deconvolution of the recorded surface signals. These latter are also the inputs of the PR1 procedure. Detailed knowledge of soil characteristics is required (soil layers, shear wave velocity profiles, soil density,

D. Lavorato (✉) · C. Nuti
Department of Architecture, University of Roma Tre, Largo G.B. Marzi 10, Rome, Italy
e-mail: davide.lavorato@uniroma3.it

C. Nuti
e-mail: camillo.nuti@uniroma3.it

I. Vanzi
Department of Engineering and Geology, University "G. d' Annunzio", Viale Pindaro 42, Pescara, Italy
e-mail: i.vanzi@unich.it

G. Monti
Department of Structural and Geotechnical Engineering, Sapienza University of Rome, Via Eudossiana 18, Rome, Italy
e-mail: giorgio.monti@uniroma1.it

P. Gardoni (ed.), *Risk and Reliability Analysis: Theory and Applications*,
Springer Series in Reliability Engineering, DOI 10.1007/978-3-319-52425-2_8

nonlinear materials shear moduli and damping curves), which relies on in situ tests. Deconvolution and amplification processes are performed by Equivalent-Linear Earthquake Site Response (1D soil model, SHAKE91 (Schnabel et al. 1972) and EERA (Bardet et al. 2000)). PR1 and PR2 are then applied to an example case. Asynchronous surface signals are generated at eight foundation points of a bridge placed in the Aterno Valley near the city of L'Aquila in Italy, where recordings are available at different recording stations (AQA and AQV) for the same earthquake. The EW component of the strong main shock of 4-6-2009 in L'Aquila is selected as input for the two procedures. Finally, the comparison between the signals resulting by PR1 and PR2 and the input signals recorded at the same points is discussed in term of effects on the structures (acceleration response spectrum) and characteristics of the generated signals (Fourier amplitude spectra, coherences for each frequency) to evaluate the differences between the two procedures and between the procedures and the actually recorded signals.

1 Introduction

Seismic signals (accelerograms) recorded at different surface soil points for the same seismic event are different. This difference is due to a time translation of the signals (time lag) from point to point (the wave moves through two different soil points during a time window) and to a variation of the signal frequency content for effect of soil-wave interaction phenomena (i.e., reflection and refraction of the waves, geometric incoherency, filtering, local amplification or attenuation). These signal variations can be large in case of distant points so that different asynchronous seismic accelerations should be applied at different foundation points of long structures. However, asynchronous seismic action is not evaluated properly in international structural seismic design codes yet. Designers of long structures usually consider either synchronous actions or, in some cases, the effects of non-synchronism due to the time lag difference. This design practice in case of long structures usually can lead to an unsafe design (Monti et al. 1994, 1996; Shinozuka et al. 2000; Tzanetos et al. 2000; Sextos et al. 2003; Nuti and Vanzi 2004, 2005; Lupoi et al. 2005; Carnevale et al. 2010, 2012a, b).

The asynchronous signal transformation from point to point due to the time translation, to the coherency variation and to the different local site effects can be evaluated by means of different models evaluating separately each contribution (Luco and Wong 1986; Vanmarcke and Fenton 1991; Abrahamson et al. 1991; Oliveira et al. 1991; Vanmarcke et al. 1993; Monti et al. 1996; Tzanetos et al. 2000; Shinozuka et al. 2000; Santa-Cruz et al. 2000; Nuti and Vanzi 2004, 2005; Lupoi et al. 2005; Zerva and Zervas 2002; Zerva 2009; Lavorato et al. 2017).

In this chapter, the generation of surface seismic asynchronous signals (accelerograms) by means of two numerical procedures is presented to give designers proper tools and useful indications to obtain meaningful seismic earthquake signals. The proposed procedures provide an innovative contribution to describe

asynchronous surface signals at different points starting from a few available natural accelerometric recordings considering different knowledge levels about the soil.

Firstly, a numerical asynchronous signals propagation procedure is described (Nuti and Vanzi 2004, 2005), which has been implemented by a function framework in MATLAB (Generation of Asynchronous Signals GAS 2.0). These functions have as input the earthquake signals at some points and the soil characteristics for each type of soil crossed by the seismic wave and produce as output the asynchronous signals at points of a random field defined by the user. The propagation procedure considers the point-to-point signals variation due to the frequencies content transformation and to the time lag difference. The signal frequencies content at each point is calculated by assuming a normal distribution of the signal amplitudes. The mean and variance of this normal distribution are obtained from point to point considering the amplitudes of the signals generated at previous point, which were already crossed by the wave by means of the joint conditioned probability theory elaborating the covariance matrix of the propagation problem (Vanmarcke and Fenton 1991). This covariance matrix ($\boldsymbol{\Sigma}$) is built starting from the frequency content of the input signals (power spectra density function PSD) and by the coherence function (ρ) that describes how the signals frequency content changes from point to point as function of the crossed distance and of the crossed soils characteristics.

Next, two different generation procedures (PRocedure 1 (PR1), PRocedure 2 (PR2)) are discussed and applied to a case study to generate surface seismic

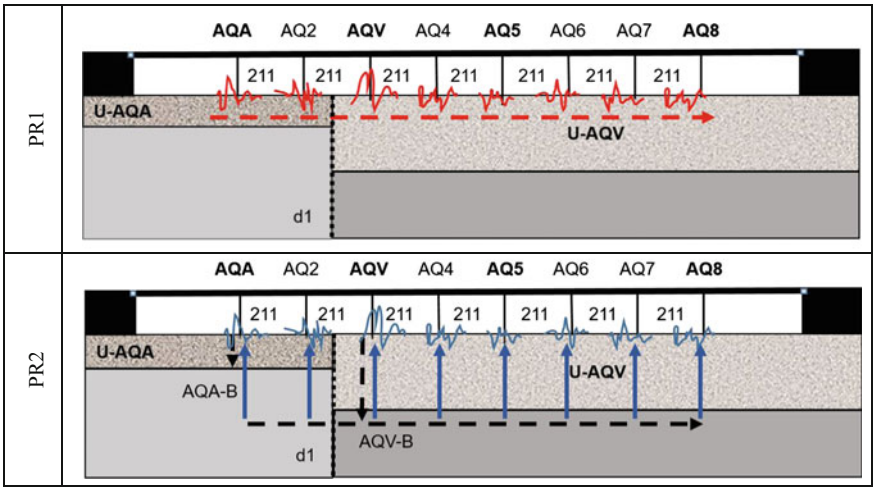

Fig. 1 Generation procedures of asynchronous earthquake signals at surface in correspondence of eight bridge pier foundations: PRocedure 1 (PR1) surface propagation starting from recording accelerograms at AQA and AQV stations propagation (*horizontal dashed line arrow*); PRocedure 2 (PR2) bedrock propagation (*horizontal dashed line arrow*) starting from signals obtained from deconvolution of the surface signals recorded at AQA and AQV (*vertical dashed line arrow*) and next amplification (*vertical arrows*) of the bedrock signals by SHAKE91 (Schnabel et al. 1972) to obtain the surface signals at each bridge foundation [m]

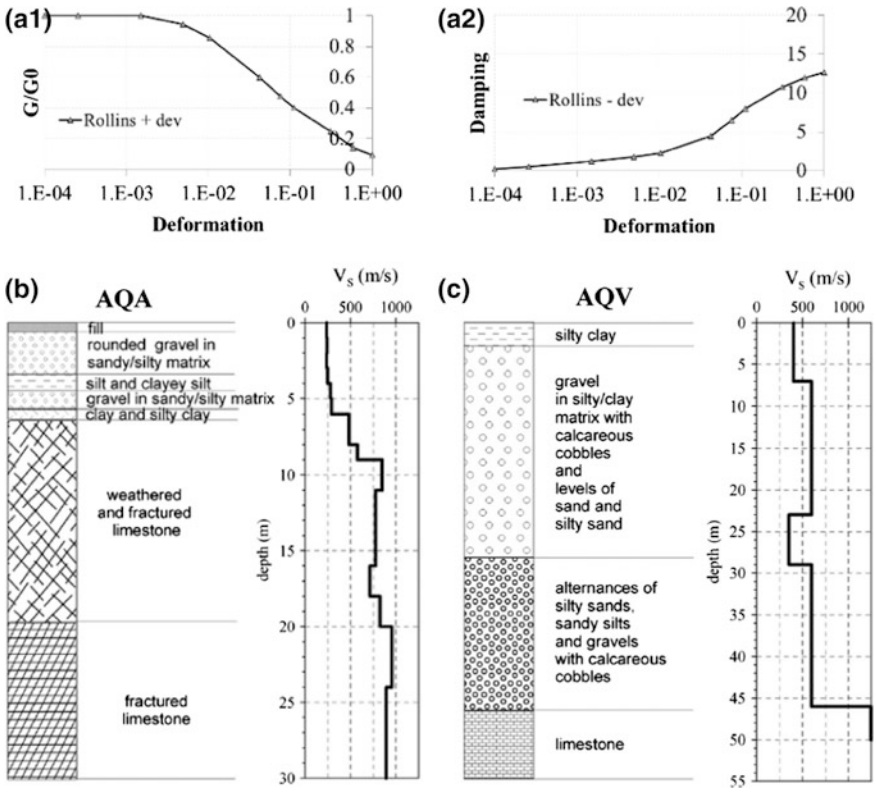

Fig. 2 Soil units U-AQA and U-AQV below AQA and AQV recording stations (Fig. 1) respectively: *first row* shear modulus (**a.1**) and damping curves (**a.2**) proposed for gravel in Rollins et al. (1998). In particular, gravel behavior was well defined by Rollins et al. (1998) mean plus one standard deviation curve for shear modulus and Rollins et al. (1998) mean minus one standard deviation curve for damping; *second row* (**b**, **c**) layers geometries, material types and shear wave (V_s) profiles (reproduced from Lanzo and Pagliaroli 2012)

asynchronous signals (accelerograms) at the foundations of a bridge with eight piers (Fig. 1) located in the Aterno valley near L'Aquila, Italy. Different recording stations are placed in this Valley and so different recordings are available for the same seismic event. Each recording station has an identification code in ITACA database (for example AQA and AQV are two station codes).

The bridge foundations were placed on two soil units (U-AQA and U-AQV, Fig. 1). The soil Unit U-AQA has the soil profile and properties defined under the station AQA (Fig. 2) whereas the soil Unit U-AQV has the soil profile and properties defined under the station AQV (Fig. 2). The components EW recorded at the AQA and AQV stations (Fig. 1) during the main shock (4-6-2009) at L'Aquila were considered as inputs for the two generation procedures. The coherence model (ρ) (Vanmarcke and Fenton 1993) was calibrated by the input signals.

The procedure PR1 generates accelerometric signals directly at the surface, starting from input surface signals and soil characteristics defined in Eurocode 8 (Eurocode 8, ENV 1998-1-1). This solution is simpler as it is direct and it is not necessary to perform local site effect analysis, but it could result less accurate.

The procedure PR2 generates signals at bedrock starting from input signals at bedrock. These input signals are obtained by the deconvolution of the available surface input signals. Finally, the generated bedrock signals are amplified by explicitly considering the local site effects through an equivalent 1D linear analysis. This procedure is more accurate about the soil local effects as it uses a higher knowledge level about the soil (soil layer geometry, nonlinear damping and shear stiffness properties, specific weight, etc.). Furthermore, this procedure allows using the available recorded surface signals at a few points, where the soil characteristics are well-known, to obtain surface signals at points where the recorded signals are not available but where the soil characteristics can be evaluated by in situ tests.

Finally, the comparisons among the signals generated by PR1 and PR2 at AQA and AQV and the input signals recorded at the same points allows evaluating the significance of the generated signals. In particular, 50 signals obtained by the two procedures were compared in terms of Fourier amplitude spectra, coherence between couples of distant points along the bridge and acceleration response spectra.

2 Random Field Propagation Model and Definition of Earthquakes that Vary in Space

The seismic waves signals (accelerograms) recorded at the same time at different points in space for the same seismic event are different. This difference is due to:

- Non-synchronism effects type 1 (NS1): the transformations of the seismic wave frequencies content due to the wave-soil interaction phenomena (reflection, refraction, amplification, etc.).
- Non-synchronism effects type 2 (NS2): the wave reaches a different point after a given time and so there is a time lag (time translation of the signals) among the signals from point to point.

In the last years, several random field (RF) models able to define the spatial variability of earthquakes were presented. These models were developed on the basis of experimental data for simultaneous recordings of the same earthquake (Abrahamson et al. 1991; Oliveira et al. 1991) or on different statistical models (Luco and Wong 1986; Vanmarcke and Fenton 1991, 1993; Monti et al. 1996; Tzanetos et al. 2000; Shinozuka et al. 2000; Santa-Cruz et al. 2000; Nuti and Vanzi 2004, 2005; Lupoi et al. 2005; Zerva and Zervas 2002; Zerva 2009; Lavorato et al. 2017). The models share all a common physical framing, as described by Luco and Wong (1986). However, the evolution presented in Nuti and Vanzi (2004, 2005), is

easier to handle from a mathematical and engineering points of view. It generates asynchronous signals at different space points for a given seismic event starting from acceleration spectra, and has also been upgraded so as to use a real recording as the input.

2.1 Spatial Model of the Earthquakes

The non-synchronism effects can be evaluated assuming that an earthquake acceleration signal at point P in space can be represented via its Fourier expansion as a sum of cosines and sines (Nuti and Vanzi 2004; Nuti and Vanzi 2005):

$$A_P(t) = \sum_k \left(B_{Pk}\ \cos(\omega_k t) + C_{Pk}\ \sin(\omega_k t)\right) \tag{1}$$

In Eq. (1), $A_P(t)$ is the measured acceleration in point P at time t, k is an index varying from 1 to the number of circular frequencies ω_k considered, B_{Pk} and C_{Pk} are the amplitudes of the k-th cosine and sine functions.

Assume the acceleration $A_P(t)$ is produced by a wave moving with velocity V towards a different point in space, say Q, at distance X_{PQ} from P, within a medium (soil) which transmits them without distortion. At point Q, and at time t, we have:

$$A_Q(t) = \sum_k \left(B_{Pk}\ \cos(\omega_k(t-\tau_{PQ})) + C_{Pk}\ \sin(\omega_k(t-\tau_{PQ})\right) \tag{2a}$$

where

$$\tau_{PQ} = X_{PQ}\ \cos(\psi)/V_{app} \tag{2b}$$

In Eq. (2b) ψ is the angle between the vector of surface wave propagation and the vector that goes from P to Q, τ_{PQ} is the time delay of the signal and V_{app} is the surface wave velocity (apparent velocity, Nuti and Vanzi 2004).

Actual recordings at different points in space indicate that Eq. (2a) is "nearly" correct. Since the medium through which the waves travel does distort them, the recording in Q resembles the one in P, the more the shorter the distance between them, and is written as

$$A_Q(t) = \sum_k \left(B_{Qk}\ \cos(\omega_k(t-\tau_{PQ})) + C_{Qk}\ \sin(\omega_k(t-\tau_{PQ})\right) \tag{3}$$

B_{Pk} is correlated with B_{Qk} and C_{Pk} is correlated with C_{Qk} but the B's and C's are independent. The latter is often referred to with the sentence "phase angles are random". The statistical properties of the amplitudes can then be summed up as in

Eq. (4) which is saying that the amplitudes B_{Pk} and C_{Qk} are statistically independent, for any points P and Q, and any circular frequency ω_k, with the only exception of B_{Pk} and B_{Qk} i.e. same circular frequency but different points in space. The same holds for C_{Pk} and C_{Qk}.

$$\begin{array}{ll} B_{Pk1} \text{ independent on } C_{Qk2} & \forall P, Q, k1, k2 \\ B_{Pk1} \text{ independent on } B_{Qk2} & \forall P, Q, k1, k2 \neq k1 \\ C_{Pk1} \text{ independent on } C_{Qk2} & \forall P, Q, k1, k2 \neq k1 \\ B_{Pk} \text{ correlated with } B_{Qk} & \forall P, Q, k \\ C_{Pk} \text{ correlated with } C_{Qk} & \forall P, Q, k \end{array} \tag{4}$$

The amplitudes, which are themselves random variables, are usually assumed normally distributed with zero mean and this assumption is experimentally verified (Vanmarcke and Fenton 1991).

In order to quantify the acceleration time histories in different points in space, Eqs. (1) and (3), all that is needed is a definition of the correlation between amplitudes and of their dispersion, as measured by the variance or, equivalently, of the covariance matrix of the amplitudes.

The covariance matrix ($\mathbf{\Sigma}$) is assembled via independent definition at each frequency of its diagonal terms, the variances at each space point and correlation coefficient between the amplitudes (ρ). The number of generation points n defines the dimension $n \times n$ of the matrix $\mathbf{\Sigma}$. The diagonal terms of $\mathbf{\Sigma}$ are expressed by the power spectral density function (PSD) assumed at each i-th RF generation point. The off diagonal terms of $\mathbf{\Sigma}$ are defined by a correlation coefficient (ρ) which defines the similitude in term of amplitudes for each frequency between two signals generated at two different points and by the PSD functions assumed at these points.

In case of propagation between two points P and Q, the diagonal terms of covariance matrix ($\mathbf{\Sigma}$) are quantified via power spectral density functions PSD_{PP} and PSD_{QQ} at P and Q only. The off diagonal terms (PSD_{PQ}, PSD_{QP}) are obtained by a coherence coefficient ($\rho = \rho_{\omega k}(X)$) and PSD functions ($PSD_{PP}$ and PSD_{QQ}) at the two points P and Q, crossed by the signal during the propagation. The correlation coefficient (ρ) can be expressed via coherency functions.

There are different coherency functions in literature able to describe the coherence variation from point to point for each signal frequency (Harichandran and Vanmarcke 1986; Luco and Wong 1986; Der Kiureghian 1996; Vanmarcke and Fenton 1993; Zerva and Zervas 2002; Zerva 2009). The choice of the appropriate coherence function has be done to overcome also possible numerical errors when the generation procedure is implemented in a computer code. In fact, well-known numerical errors can arise during the elaboration of the problem matrix especially in case of numerical matrix inversion operation. These errors can produce unreliable results due to false numerical matrix singularity.

In this chapter, the selected isotropic frequency-dependent spatial correlation function is described by the following equation (Vanmarcke and Fenton 1993):

$$\rho_{\omega_k}(X) = e^{(-\omega_k |X| / (2\pi V_s s))} \tag{5a}$$

The coherence model between two signals for each circular frequency (ω_k) is a function of the distance (X) between the two points where the signals are generated, the wave shear velocity (V_s) and the coherence parameter s. The coherence parameter s can be calibrated on the basis of two known input earthquake signals.

For the case of study presented in Sect. 2.3, the selected coherence model has overcome possible numerical errors when the covariance matrix ($\mathbf{\Sigma}$) is numerically inverted.

It is important to underline that the generation of a reliable RF of asynchronous accelerometric signals requires the knowledge of a sufficient number of input signals to calculate the PSD functions as function of the complexity of the RF points system. In fact, the generation points of a RF can be placed on a complex site system composed by different soil units (different materials, soil layer geometries, etc.). The effect of soil-wave interaction phenomena can be different for each soil unit and so it is important to consider the specific soil unit effects by a proper input PSD function for each soil unit.

Furthermore, some parameters of the coherence model (ρ) have to be calibrated for the specific generation problem. This calibration can be done by evaluating the experimental coherence ($\rho_e = \rho_e(f_k)$) for each frequency (f_k) between the input signals known at two points and then by tuning the coherence model parameters to obtain numerical coherences similar to the experimental ones in a range of frequencies of interest for the structures analyzed (i.e., for civil structures [0.25, 5 Hz]).

A coherence function parameter tuning can be done, with acceptable approximation from an engineering point of view, by rewriting the Eq. (5a) to have the parameter s as function of the experimental coherence (Eq. 5b):

$$s_k(\rho_e) = -f_k |X| / (\ln(\rho_e) V_s) \tag{5b}$$

where $f_k = \omega_k/(2\pi)$. Then the mean value s_m of the s_k values obtained by Eq. (5b) for each circular frequency ω_k is calculated in the above-defined range of frequencies.

Next, the numerical model for the coherence ($\rho = \rho_{\omega k}(X)$), which is calibrated by Vs and $s = s_m$ parameters, can be used to determine coherence between the signals at different generation points given the point distance X by the Eq. (5a).

After the construction of the covariance matrix, one can focus on the generation procedure for a single cosine component from Eqs. (1) and (3), since the amplitudes at different circular frequencies are independent of each other, and the same holds for the sine and cosine terms. One such cosine component, at points P_1, P_2, …, P_i is: $A_{P1}(t) = B_{P1}\cos(\omega t)$; $A_{P2}(t) = B_{P2}\cos(\omega(t - \tau_{P1P2}))$ … $A_{Pi}(t) = B_{Pi}\cos(\omega(t - \tau_{P1Pi}))$ where, for simplicity, the subscript k has been dropped. The amplitudes B at i

different points are still collectively normally distributed with mean values equal to zero and covariance matrix $\mathbf{\Sigma}$:

$$\mathrm{B} \sim \mathrm{N}(0, \mathbf{\Sigma})$$

$$pdf_B(b) = 2\pi^{-1/2}\det(\mathbf{\Sigma})^{-1/2} e^{-\frac{1}{2}b^T\mathbf{\Sigma}^{-1}b} \tag{6}$$

and can be sampled by recalling that, for collectively normally random variables, conditional distribution are normal.

The formal statement of this rule is:

$$\begin{pmatrix} \mathbf{x}1 \\ \mathbf{x}2 \end{pmatrix} \sim \mathrm{N}\left(\begin{pmatrix} u1 \\ u2 \end{pmatrix}, \begin{bmatrix} \mathbf{\Sigma}_{11} & \mathbf{\Sigma}_{12} \\ \mathbf{\Sigma}_{21} & \mathbf{\Sigma}_{22} \end{bmatrix} \right) \tag{7}$$

where x1 ε R^m, x2 ε R^n and the dimensions of the mean vectors and covariance matrix sub blocks are chosen to match x1 and x2.

Then the conditioned densities:

$$\mathrm{p}(\mathbf{x}2|\mathbf{x}1) = \mathrm{p}(\mathbf{x}1, \mathbf{x}2; \boldsymbol{\mu}, \mathbf{\Sigma}) / \int_{x2 \in R^n} \mathrm{p}(\mathbf{x}1, \mathbf{x}2; \boldsymbol{\mu}, \mathbf{\Sigma}) \mathrm{d}x2 \tag{8}$$

are also Gaussian:

$$\mathbf{x}2|\mathbf{x}1 \sim \mathrm{N}(\boldsymbol{\mu}2 + \mathbf{\Sigma}_{21}\mathbf{\Sigma}_{11}^{-1}(\mathbf{x}1 - \boldsymbol{\mu}1),\ \mathbf{\Sigma}_{22} - \mathbf{\Sigma}_{21}\mathbf{\Sigma}_{11}^{-1}\mathbf{\Sigma}_{12}) \tag{9}$$

Amplitudes sampling, which allows to reconstruct the whole earthquake accelerations random field, can then be done as reported by Vanmarcke and Fenton (1991).

The sampling scheme for B for each circular frequency ω_k is:

- sample the value b_1 of the random variable B_1 at the first considered generation point P1 from a normal distribution with zero mean and variance equal to $\mathbf{\Sigma_{11}}$;

$$\mathrm{N} \sim (0, \mathbf{\Sigma_{11}})$$

- at l-th point, sample the value b_l of the random variable $B_l/b_1, b_2, \ldots, b_{l-1}$ from a normal distribution with mean equal to $\boldsymbol{\mu_2} + \mathbf{\Sigma_{21}\Sigma_{11}^{-1}(x_1 - \mu_1)}$ and variance equal to $\mathbf{\Sigma_{22}\text{-}\Sigma_{21}\Sigma_{11}^{-1}\ \Sigma_{12}}$ (Eqs. 7–9) with:

$$\mathbf{B} = \begin{pmatrix} B_1 \\ B_2 \\ \ldots \\ B_{l-1} \\ B_l \\ \ldots \\ B_n \end{pmatrix} \quad \mathbf{x_1} = \begin{pmatrix} B_1 \\ B_2 \\ \ldots \\ B_{l-1} \end{pmatrix} \quad \mathbf{x_2} = \begin{pmatrix} B_l \\ \ldots \\ B_n \end{pmatrix}$$

$$\boldsymbol{\Sigma_{11}} = \begin{pmatrix} S_{11} & \rho_{12}\sqrt{S_{11}S_{22}} & \cdots & \rho_{1(l-1)}\sqrt{S_{11}S_{(l-1)(l-1)}} \\ \rho_{21}\sqrt{S_{11}S_{22}} & S_{22} & \cdots & \cdots \\ \cdots & \cdots & \cdots & \cdots \\ \rho_{(l-1)1}\sqrt{S_{11}S_{(l-1)(l-1)}} & \cdots & \cdots & S_{(l-1)(l-1)} \end{pmatrix}$$

$$\boldsymbol{\Sigma_{12}} = \begin{pmatrix} \rho_{1l}\sqrt{S_{11}S_{ll}} & \cdots & \cdots & \rho_{1n}\sqrt{S_{11}S_{nn}} \\ \cdots & \cdots & \cdots & \cdots \\ \cdots & \cdots & \cdots & \cdots \\ \rho_{(l-1)l}\sqrt{S_{(l-1)(l-1)}S_{ll}} & \cdots & \cdots & \rho_{(l-1)n}\sqrt{S_{nn}S_{(l-1)(l-1)}} \end{pmatrix}$$

$$\boldsymbol{\Sigma_{21}} = \begin{pmatrix} \rho_{l1}\sqrt{S_{11}S_{ll}} & \cdots & \cdots & \rho_{l(l-1)}\sqrt{S_{(l-1)(l-1)}S_{ll}} \\ \cdots & \cdots & \cdots & \cdots \\ \cdots & \cdots & \cdots & \cdots \\ \rho_{n1}\sqrt{S_{11}S_{nn}} & \cdots & \cdots & \rho_{n(l-1)}\sqrt{S_{nn}S_{(l-1)(l-1)}} \end{pmatrix}$$

$$\boldsymbol{\Sigma_{22}} = \begin{pmatrix} S_{ll} & \cdots & \cdots & \rho_{ln}\sqrt{S_{nn}S_{ll}} \\ \cdots & \cdots & \cdots & \cdots \\ \cdots & \cdots & \cdots & \cdots \\ \rho_{nl}\sqrt{S_{nn}S_{ll}} & \cdots & \cdots & S_{nn} \end{pmatrix} \tag{10}$$

where $S_{ij}(\omega_k) = PSD_{ij}(\omega_k)\, d\omega$, $d\omega$ is the constant circular frequencies difference and $\rho_{ij}(\omega_k)$ is the coherence between the signal at point Pi and the one at point Pj.

Assuming $\mu_1 = \mu_2 = 0$ for the Eq. (6).

- continue partitioning the covariance matrix $\boldsymbol{\Sigma}$ up to the last generation point P_n.

This process must be repeated for all the values of circular frequencies k, and for the sine and cosine terms, and the different components summed up as in Eq. (3). Notice that the signal components for different circular frequencies, once the amplitudes are sampled as described above, can be computed in an efficient way by inverse Fourier transform, possibly using FFT (Fast Fourier transform).

The scaling of the generated signals is done by guaranteeing the same Arias coefficient for input and output (generated) signals. The Arias coefficient measures, in a time window, the strength of a ground motion and is an effective scaling factor for reproducing reliable generated signals. This choice has been made after several numerical attempts using alternative strategies. The earthquake signals usually show a variability of the acceleration during the main duration time windows. There is a first part with low acceleration, a central part with significant acceleration and a final part with low acceleration. In the proposed procedure, the earthquake duration is divided in four time windows (one for the accelerogram part with initial low accelerations, two for the main part and another one for the final part with low acceleration) to obtain Arias scale factor specific for each time windows.

Finally, the effects of the NS2 are included in the propagation procedure by performing a simple temporal translation of the signals at each different space point. The time lag (τ_{PQ}, Eq. 2b) at each point can be calculated by considering the distances crossed by the seismic waves and by assuming an apparent wave velocity (V_{app}, Eq. 2b).

The RF propagation model is based on random extraction from normal distribution, which are defined by mean and standard deviation values at each generation point. For that reason, different random extractions for the same problem inputs produce different generated signals at each RF point. A proper number of different extractions at the same RF point should be performed to analyze the generation results by a statistical point of view considering, at each RF point, mean and mean plus or minus standard deviation curves of the signals characteristics (i.e., Fourier amplitude spectra, coherence in function of the frequencies or acceleration response spectra).

The proposed RF propagation model was implemented in MATLAB by a functions framework named GAS 2.0 (Generation of Asynchronous Signals) that generates asynchronous signals at n points starting from a given number of recorded accelerometric signals for the same seismic event.

2.2 *Case Study: Generation of Surface Asynchronous Signals at the Foundations of a Bridge Located in the Aterno Valley Near L'Aquila, Italy*

The proposed random field (RF) propagation model was applied to generate a RF of surface asynchronous seismic signals at different points of the Aterno valley near L'Aquila, Italy, starting from the recordings of real accelerometric signals, available at a few RF points.

In particular, there are two recording stations AQA and AQV in this valley, which are distant 422 m (Fig. 1); a distance compatible with the length of foundations of a long bridge. For that reason, in this case study, it is possible to consider the generation of asynchronous signals at different foundations points of a bridge and then to compare the generated signals with the ones recorded in correspondence of some bridge foundations, which are given as input of the procedure at some foundations points.

The input accelerometric recordings at stations AQA and AQV permit the calibration of the coherence model parameter (ρ) and the definition of two different input PSD functions for the RF. In this way, it is possible to define two groups of bridge foundations and to assign to each group one of the two PSD functions, considering different local site effects for each foundation group.

The EW components of the accelerometric signals recorded at the two stations AQA and AQV (Fig. 1) during L'Aquila main-shock event (4-6-2009, Magnitude 6.3) are the input signals of the case of study. These components are available in the

Italian earthquake database ITACA (ITalian ACcelerometric Archive, INGV). The main part of the recordings at AQA and AQV was selected considering a time windows of 20.48 s and the recordings at the two different stations were elaborated to have the same zero time. The same zero time was obtained eliminating the time lag difference between the two accelerometric recording zero-times due to the distance between the two stations and to the finite seismic wave velocity. In fact, the seismic wave arrives first in one station (AQA) and then at the second station (AQV).

In this application, the signals were generated in correspondence of eight pier foundations (AQA, AQ2, AQV, AQ4, AQ5-AQ8, Fig. 1) of a bridge with longitudinal axis along the line between AQA and AQV stations (Fig. 1) with an angle ψ of about 27° with respect to the EW line; acronyms are identified in Fig. 1 The distances crossed by the EW components to reach each generation point are measured along the EW line during the propagation process considering this angle. The bridge has a group of two pier foundations (AQA, AQ2) on the soil unit U-AQA, which is characterized by the PSD of the input recording of AQA station, and a second group of six pier foundations (AQV, AQ4, AQ5, AQ6, AQ7, AQ8) on the soil unit U-AQV, which is characterized by the PSD of the input recordings at AQV station (Fig. 1). These two soil units U-AQA and U-AQV have the layer geometries, the shear wave (Vs) profiles and the soil material nonlinear properties given in Fig. 2 by Lanzo and Pagliaroli (2012). These soils properties were selected by Lanzo et al. (2012) by comparing the surface signals obtained by a 1D Equivalent Linear Earthquake Site Response signals with the recorded signals at AQA and AQV stations also in case of a strong earthquake that produces a large nonlinear response of the soil.

In particular, the non-linear mean plus one standard deviation curve for shear modulus (G/G_0) and the mean minus one standard deviation curve for damping (D) proposed for gravel in Rollins et al. (1998) was assumed for the two soil units U-AQA and U-AQV below AQA and AQV. In fact, even if there are different materials in the soil profiles of U-AQA and U-AQV the global profile nonlinear behavior can be simulated very well by 1D equivalent analysis assuming one only G/G_0 curve and one D curve only considering the two different Vs profiles and the two different soil unit's depths.

It is important to underline that the selected seismic event is a near-source one and so the 1D equivalent model for the soil amplification and deconvolution can be improper for the correct signals definition. Furthermore, the station AQA is near the edge of the Aterno Valley and so the 2D local effects are inevitable. For that reason, the 1D model results should be considered with care. However, the obtained signals resulted complete for the analysis and discussion proposed here by an engineering's point of view.

The two soil units have been classified as soil type B in EC8 (Eurocode 8, ENV 1998-1-1) on the basis of the mean value of the shear wave velocity V_s.

2.3 Random Field Generation Procedure PR1 and PR2

The generation of RF of asynchronous signals at the bridge foundations is performed considering two different procedures PR1 and PR2 (Fig. 1) which consider different knowledge levels about the soil.

The procedure PR1 performs a propagation of the EW accelerometric component of the main shock (L'Aquila earthquake, 6-4-2009) directly at surface starting from the EW component recordings at AQA and AQV stations (Fig. 1). The input PSDs (Power Spectral Density function) are calculated by the MATLAB built-in function starting from the EW components recorded at AQA and AQV stations (Fig. 3) during L'Aquila main shock. The PSD of the AQA input signals is the input PSD function for the foundation points AQA and AQ2 whereas the PSD of the AQV input signals is the input PSD function for the foundation points AQV, AQ4-AQ8.

The coherence for each frequency among the generated signals from point to point is described by the coherence model (ρ, Eq. 5a). The mean value (s_m) of the s parameter of the coherence model (ρ) is equal to 9.06 in the range of frequencies [0.25, 5 Hz] (Fig. 3). The s_m parameter was calculated starting from the s values given by Eq. (5b) for each frequency as function of the experimental coherences (Fig. 3). The experimental coherences (ρ_e) for each frequency were calculated by the MATLAB function starting from the two input signals at AQA and AQV stations.

The shear wave velocity Vs in the coherence function (ρ) is assumed equal to 580 m/s, the mean value of the shear velocities in the shear velocity range [360, 800 m/s] for soil type B in EC8 (Eurocode 8, ENV 1998-1-1).

The knowledge level for the soil is low, since V_s is given considering the EC8 soil categories velocities only; moreover, the local site effects are not considered explicitly, rather, by means of the PSDs of the surface recorded input signals only.

The PR2 procedure produces asynchronous signals at surface at each bridge foundation point (Fig. 1) by amplifying the asynchronous signals generated by a propagation procedure (Sect. 2) at the bedrock below each foundation point. The bedrock asynchronous signal propagation has as input the signals obtained by a deconvolution process of the EW components recorded at AQA and AQV stations (Fig. 1) (which are the surface inputs for procedure PR1) during the L'Aquila main shock (4-6-2009). The deconvolution process was performed by an Equivalent-Linear Earthquake Response Analysis, which is implemented in SHAKE91 (Schnabel et al. 1972) or EERA (Bardet et al. 2000), considering the local soil characteristics of U-AQA for the signal recorded at AQA and of U-AQV for the signal recorded at AQV (Fig. 2).

The input PSDs for the bedrock propagation are calculated by the MATLAB built-in function starting from the deconvoluted EW components below at AQA and AQV stations (Fig. 3). The PSD of the bedrock signal below AQA is the input PSD function for the bedrock point below AQA and AQ2, whereas the PSD of the bedrock signal below AQV is the input PSD function for the bedrock points below

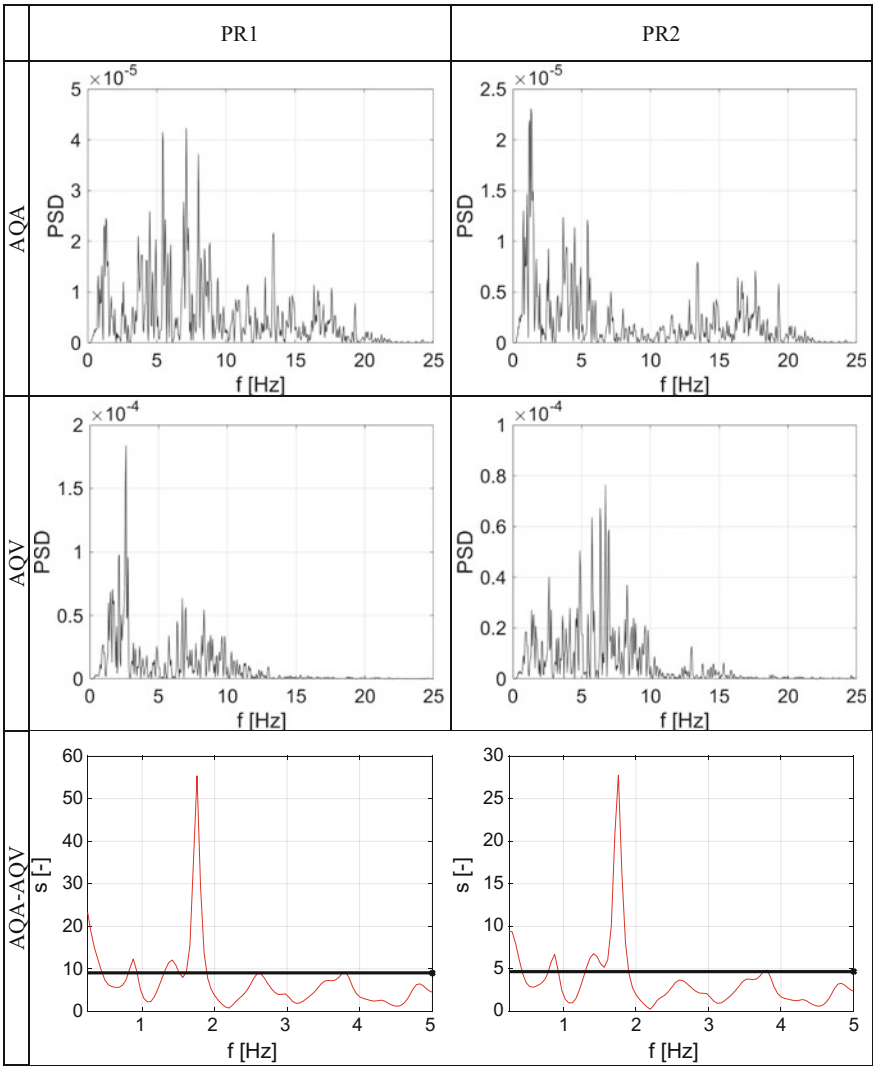

Fig. 3 Generation procedures PR1 (*first column*) and PR2 (*second column*): PSD functions at AQA (*first row*) and AQV (*second row*) stations (Fig. 1) and parameter s of the numerical coherence model (*red line third row*) for each frequency; s_m (mean value of factor s) in the range of [0.25, 5 Hz] (*black line*)

AQV, AQ4-AQ8. The s_m parameter of the coherence model (ρ) is equal to 4.68 in the frequency range [0.25, 5 Hz] (Fig. 3). The s_m parameter was calculated starting from the s values given by Eq. (5b) for each frequency as function of the experimental coherences (Fig. 3). The experimental coherences (ρ_e) for each frequency were calculated by the MATLAB function starting from the two deconvoluted

signals at bedrock below AQA and AQV stations. The shear velocity V_s for the coherence model (ρ) was assumed equal to 1125 m/s. This V_s value is the mean value of the two V_s measured at bedrock below the stations AQA and AQV by in situ tests (Fig. 2, Lanzo and Pagliaroli 2012).

Finally, the generated bedrock signals below each foundation point were amplified by means of SHAKE91 (Schnabel et al. 1972) considering the local soil characteristics of U-AQA for the point AQA and AQ2 and of U-AQV soil units for the point AQV, AQ4-AQ8 (Fig. 1) to obtain the surface signals at each bridge foundation. The input V_s profiles, layer geometry, material shear modulus (G/G_0) and damping (D) nonlinear curves for the amplification below AQA and AQV stations are given in Fig. 2.

For this procedure, the knowledge level for the soil is high, since soil profile geometries and properties have to be defined accurately (i.e., by in situ tests) and the local soil-wave interaction effects are considered explicitly by means of deconvolution and amplification processes.

The propagation of signals at surface and at bedrock during procedure PR1 and PR2, respectively, was performed by the function implemented in GAS 2.0 using the updated proposed generation model (Sect. 2) considering the asynchronous effects NS1 only, which changes the frequencies content of the signals evaluated at different RF points due to the soil-wave interaction phenomena.

The time translation of the generated signals to reproduce the NS2 effects is not applied during the generation procedure. In fact, this study focused on the signals transformations due to NS1 only from point to point during a propagation of a seismic wave. These signal transformations are usually not considered properly during the structural design in case of asynchronous signals analysis and so their effects are discussed with attention here.

2.4 Comparison of the Generated Signals by Procedure PR1 and PR2 at Surface

The asynchronous signals generated at surface by means of PR1 or PR2 procedures were compared in terms of signals characteristics (Fast Fourier Transformation amplitude spectra and coherence among signals at different generation points) and structural response (acceleration response spectra) at bridge foundations AQA, AQV, AQ5 and AQ8 (Fig. 1). These foundation points were selected for the comparison because recordings of the real EW components of the earthquake are available at AQA and AQV points (input of the procedure) and so it is possible to evaluate the reliability of the generated signals.

Furthermore, the points AQ5 and AQ8 were selected for the comparison to evaluate the coherence among points increasingly distant from each other. In particular, the coherence between the generated signals at couples of point AQA-AQV, AQA-AQ5 and AQA-AQ8 were analyzed (Fig. 1).

In particular, fifty asynchronous signals were obtained by means of the two procedures (PR1 and PR2) in correspondence of the selected bridge foundations. These signals were elaborated to obtain Fourier amplitude spectra (FFT-AMP), coherence between couple of distant points along the bridge (Cohere) and acceleration response spectra (Sa). Finally, the mean and mean plus or minus one standard deviation curves of the FFT-AMP, Cohere and Sa curves were calculated at each selected point to perform statistical comparison between the two procedures results.

2.4.1 Comparison Among FFT Amplitude Spectra

The Fast Fourier Transformation amplitude spectra (FFT-AMP) were calculated using MATLAB built-in function for the generated signals at AQA, AQV, AQ5 and AQ8 by means of PR1 and PR2 procedures. The mean curve and the mean plus or minus one standard deviation curves of the FFT-AMP (calculated considering the fifty FFT-AMP of the signals generated at the selected point for each procedure) are shown in Fig. 4, Fig. 5, Fig. 6 and Fig. 7 for the surface points AQA, AQV, AQ5 and AQ8 respectively in the range of frequencies [0, 10 Hz]. This range of frequencies is greater than the one of interest for civil structures [0, 5 Hz] but it allows comparing the two procedures also for higher frequency contents. The green lines in Figs. 4 and 5 represent the FFT-AMP of the input recorded surface signals at AQA and AQV stations.

The comparison among the mean curves of the FFT-AMP of the two procedure (PR1, red line; PR2, blue line, Figs. 4 and 5) with the FFT-AMP of the input signals at AQA and AQV (green line, Figs. 4 and 5) shows that each procedure simulates well the input surface signals frequencies content. In fact, the FFT-AMP values of the input signals (green lines in Figs. 4 and 5) for each frequency are very near to the values of the mean curve of the FFT-AMP obtained from each procedure (red line for PR1, blue line for PR2 in Figs. 4 and 5). Furthermore, the value of the FFT-AMP input signals is for many frequencies included in the FFT-AMP range values defined by the FFT-AMP mean plus (dot black lines in Figs. 4 and 5) or minus (dashed black lines in Figs. 4 and 5) standard deviation curves. For that reason, these two generation procedures are able to produce reliable earthquake signals from a statistical point of view.

2.4.2 Comparison Among Signals Coherences at Different Surface Points

The coherences for each frequency were calculated by the MATLAB built-in function considering the generated signals at the couples of points AQA-AQV, AQA-AQ5 and AQA-AQ8 using procedure PR1 or PR2. This is important as the coherence measures the variation of the signals characteristics during the

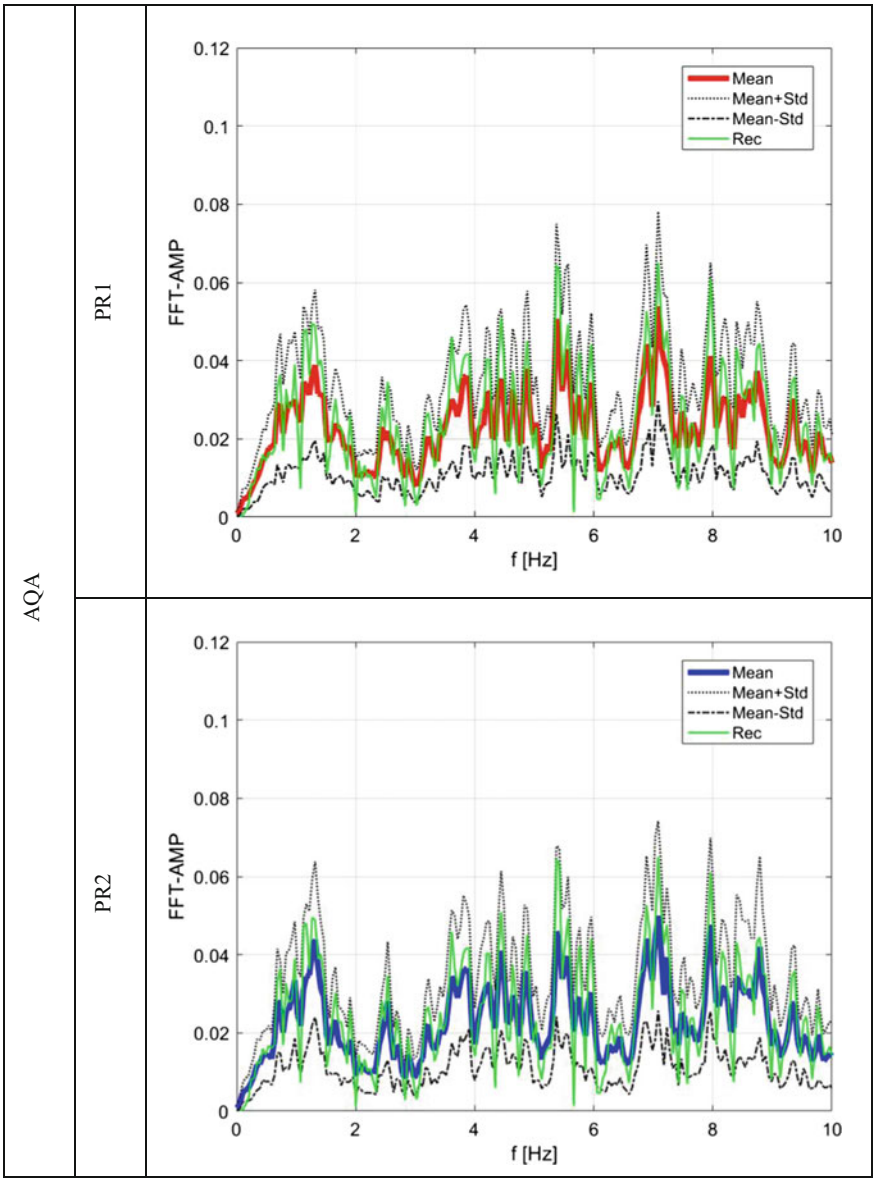

Fig. 4 Comparison between procedure PR1 (*first row*) and PR2 (*second row*) Fourier Amplitude spectra (FFT-AMP) at AQA surface point (Fig. 1); mean of the FFT-AMP considering fifty generations (*red line* for PR1, *blue line* for PR2) and mean plus (*dot black line*) or minus (*dashed black line*) one standard deviation considering fifty generations; The *green lines* are the FFT-AMP amplitude spectra of the recorded signals at AQA

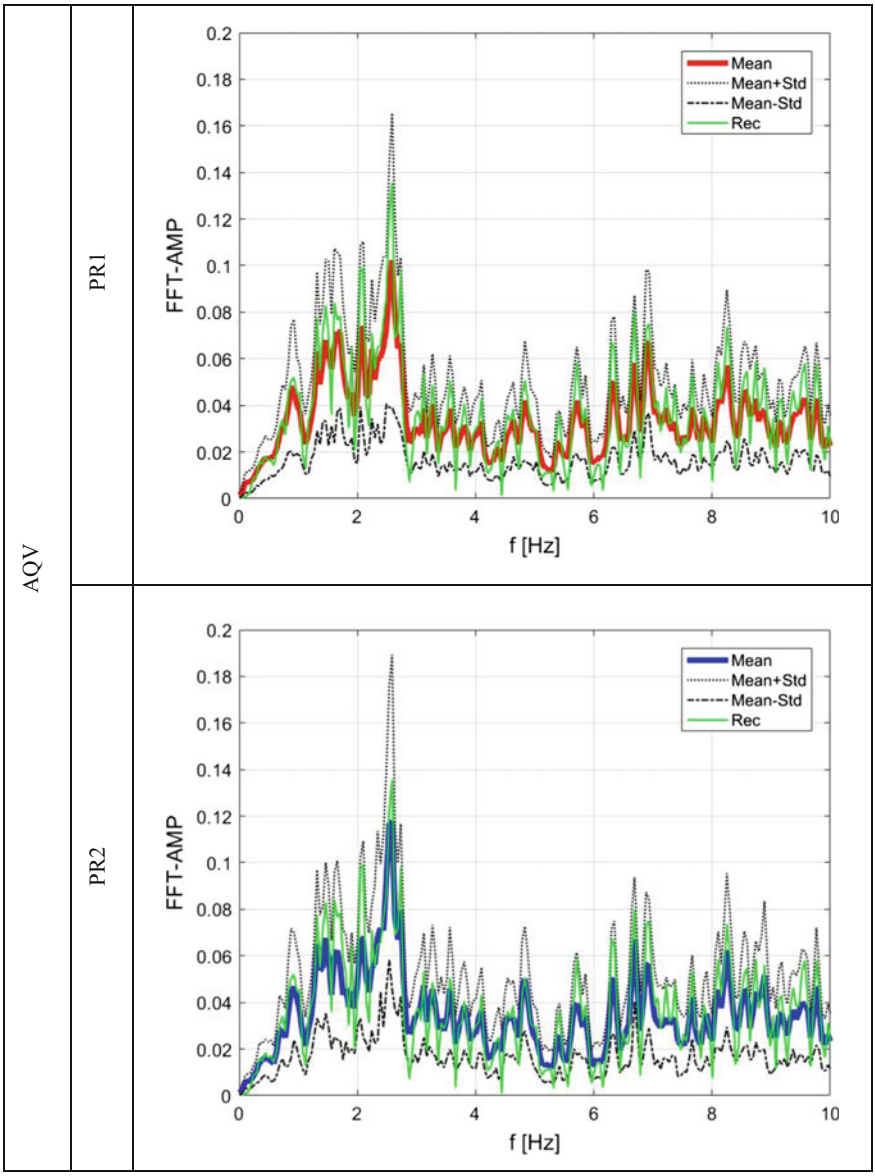

Fig. 5 Comparison between procedure PR1 (*first row*) and PR2 (*second row*) Fourier Amplitude spectra (FFT-AMP) at AQV surface point (Fig. 1); mean of the FFT-AMP considering fifty generations (*red line* for PR1, *blue line* for PR2) and mean plus (*dot black line*) or minus (*dashed black line*) one standard deviation considering fifty generations; The *green lines* are the FFT-AMP amplitude spectra of the recorded signals at AQV

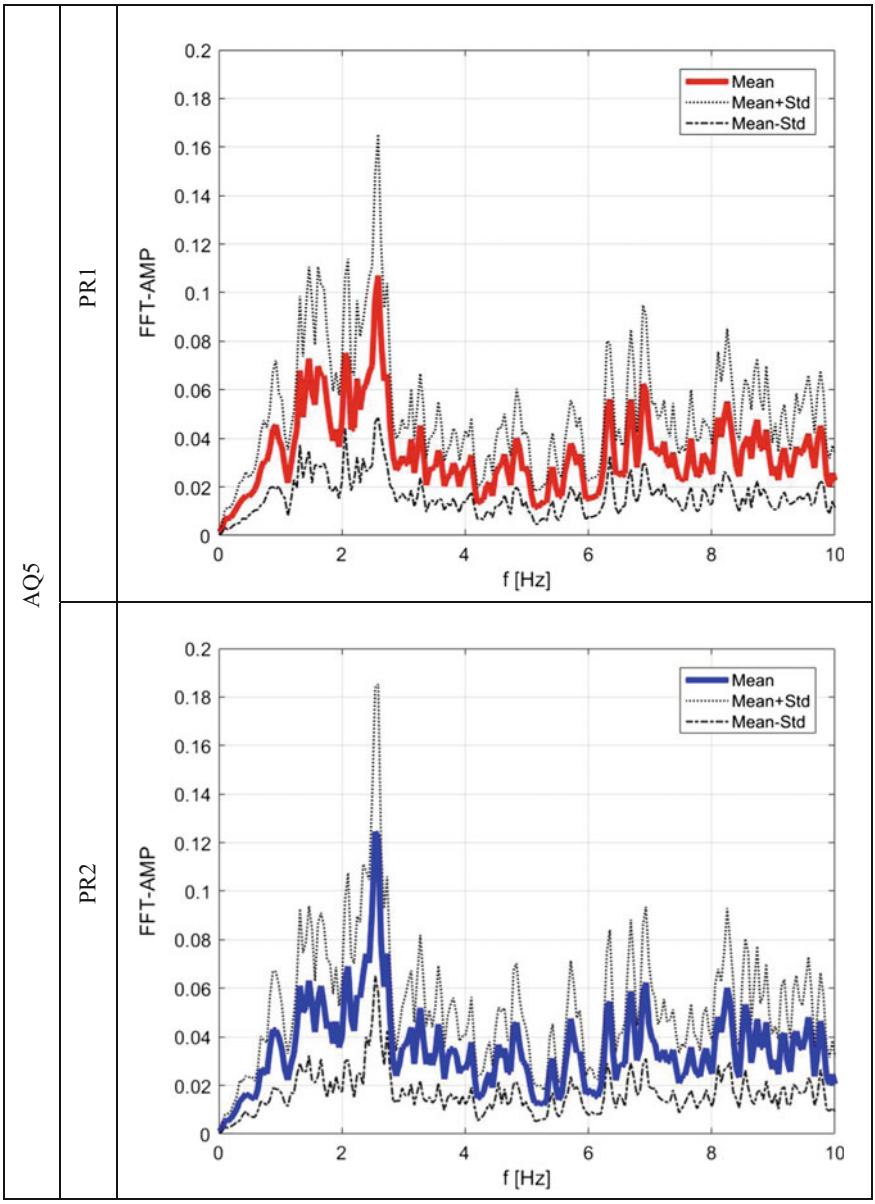

Fig. 6 Comparison between procedure PR1 (*first row*) and PR2 (*second row*) Fourier Amplitude spectra (FFT-AMP) at AQ5 surface point (Fig. 1); mean of the FFT-AMP considering fifty generations (*red line* for PR1, *blue line* for PR2) and mean plus (*dot black line*) or minus (*dashed black line*) one standard deviation considering fifty generations

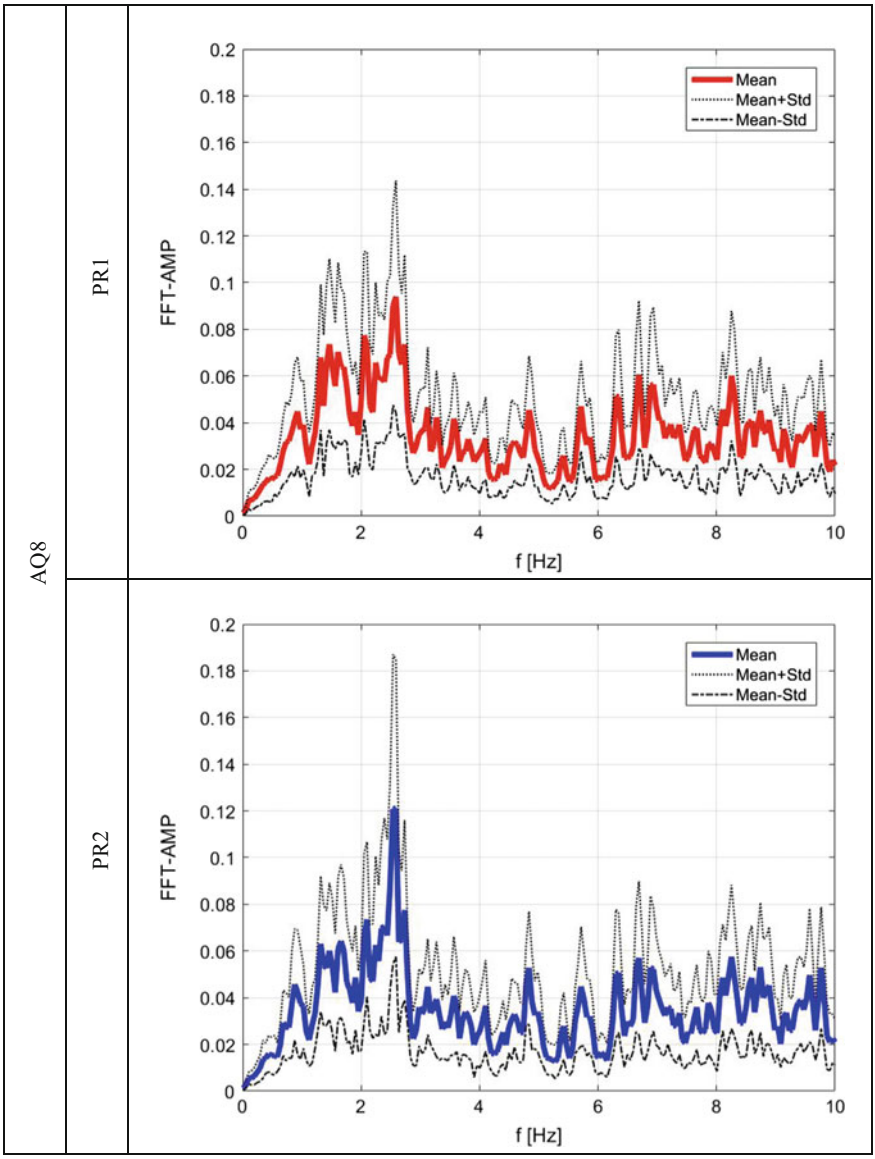

Fig. 7 Comparison between procedure PR1 (*first row*) and PR2 (*second row*) Fourier Amplitude spectra (FFT-AMP) at AQ8 surface point (Fig. 1); mean of the FFT-AMP considering fifty generations (*red line* for PR1, *blue line* for PR2) and mean plus (*dot black line*) or minus (*dashed black line*) one standard deviation considering fifty generations

propagations. This difference among the signals produces relative displacements among the different foundation points.

The effects of these relative displacements (i.e., actions on bridge deck) are very important in the design of long structures (Monti et al. 1994, 1996; Shinozuka et al. 2000; Tzanetos et al. 2000; Sextos et al. 2003; Nuti and Vanzi 2004, 2005; Lupoi et al. 2005, Carnevale et al. 2010, 2012a, b).

However, international codes do not consider or consider improperly these actions, so that unsafe designs can result. The mean curve (red line for PR1, blue line for PR2 in Fig. 8) and the mean plus (dot black line in Fig. 8) or minus (dashed black line in Fig. 8) one standard deviation curves of the coherence, which were calculated considering the fifty coherence curves of the signals generated at the selected point for each procedure are shown in Fig. 8 in the range of frequencies [0, 5 Hz]. The coherences calculated for each frequency by the coherence model (Eq. 5a, black line in Fig. 8), which is assumed for the propagation and calibrated properly for each procedure (PR1 and PR2, Sect. 2.3), are very similar to the value of the mean curve of the coherences calculated between the signals generated by the two procedure (red line for PR1, blue line for PR2 in Fig. 8). Furthermore, the value of the coherence model (black line in Fig. 8) is for many frequencies included in the coherence range values defined by the coherence mean plus (dot black line in Fig. 8) or minus one standard deviation curves (dashed black line in Fig. 8).

The coherence difference due to inevitable numerical errors is small.

2.4.3 Comparison Among the Acceleration Response Spectra Sa

The acceleration response spectrum (Sa) was calculated for each generated signal at bridge foundation points AQA, AQV, AQ5 and AQ8 (Fig. 1) by procedure PR1 or PR2 by a user-defined MATLAB function.

Furthermore, the Sa mean curves (red line for PR1, blue line for PR2 in Figs. 9, 10, 11 and 12) and the mean plus (dot red line for PR1, dot blue line for PR2 in Figs. 9, 10, 11 and 12) or less (dashed red line for PR1, dashed blue line for PR2 in Figs. 9, 10, 11 and 12) one standard deviation curves were calculated considering the fifty Sa of the generated signals for procedure PR1 or PR2 in the range of periods [0, 2.5 s].

The green lines in Fig. 9 and Fig. 10 represent the Sa of the input recorded signals at AQA and AQV respectively. It is evident by the comparison between the mean Sa curves of the generated signals (red line for PR1, blue line for PR2 in Figs. 9 and 10) and the ones of the recorded signals (green line in Figs. 9 and 10) that both procedures PR1 and PR2 are able to generate surface signals with very good agreement with the input recorded ones at AQA and AQV in term of Sa.

Furthermore, the value of the Sa of the input signals (green line in Figs. 9 and 10) is for many periods included in the Sa range values defined by the Sa mean plus (dot red line for PR1, dot blue line for PR2 in Figs. 9 and 10) or minus (dashed red line for PR1, dashed blue line for PR2 in Figs. 9 and 10) one standard deviation curves.

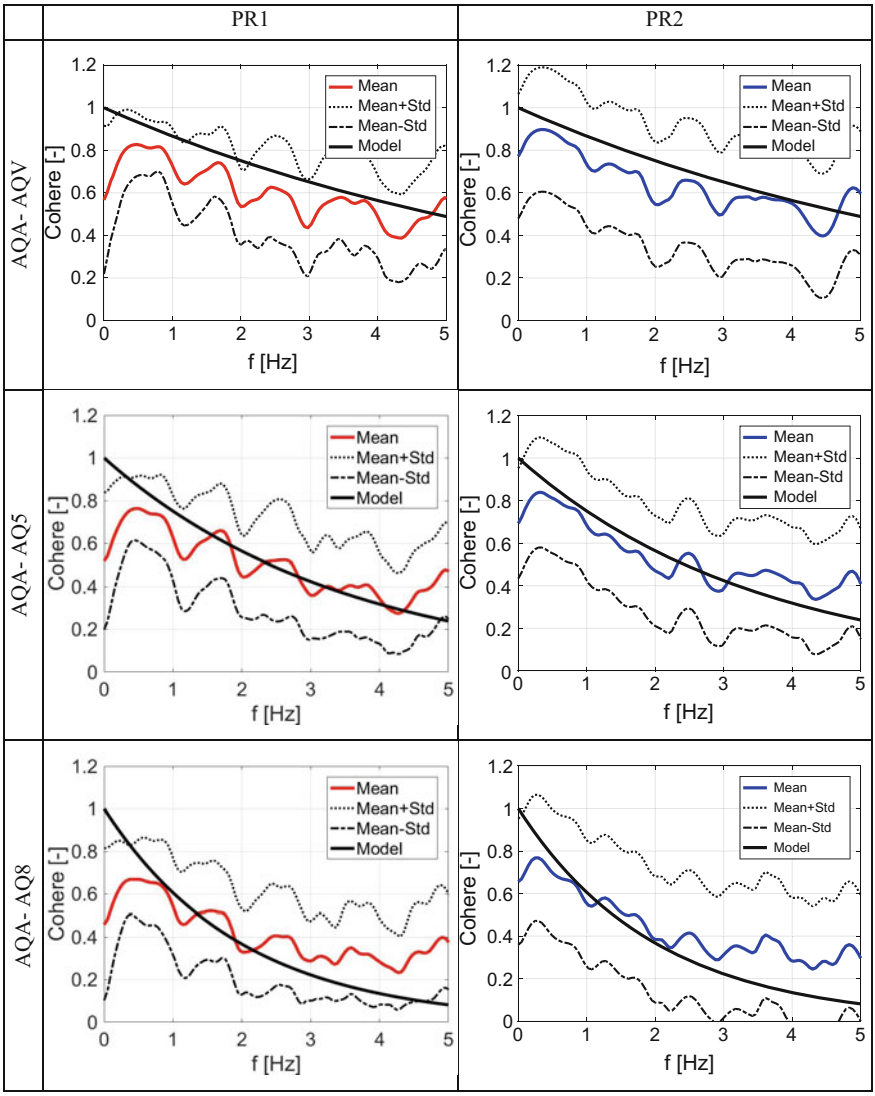

Fig. 8 Comparison between the procedure PR1 (*first column*) and PR2 (*second column*) coherence between the bridge foundations AQA-AQV (*first row*), AQA-AQ5 (*second row*) and AQA-AQ8 (*third row*) (Fig. 1); mean curve of the coherence considering the fifty generations (*red line* for PR1, *blue line* for PR2) and mean plus (*dot black line*) or minus (*dashed black line*) one standard deviation curves considering the fifty generations. The *black line* is the coherence estimated by the coherence numerical model (Eq. 5a) assumed in the generation procedure (GAS 2.0, Sect. 2.1)

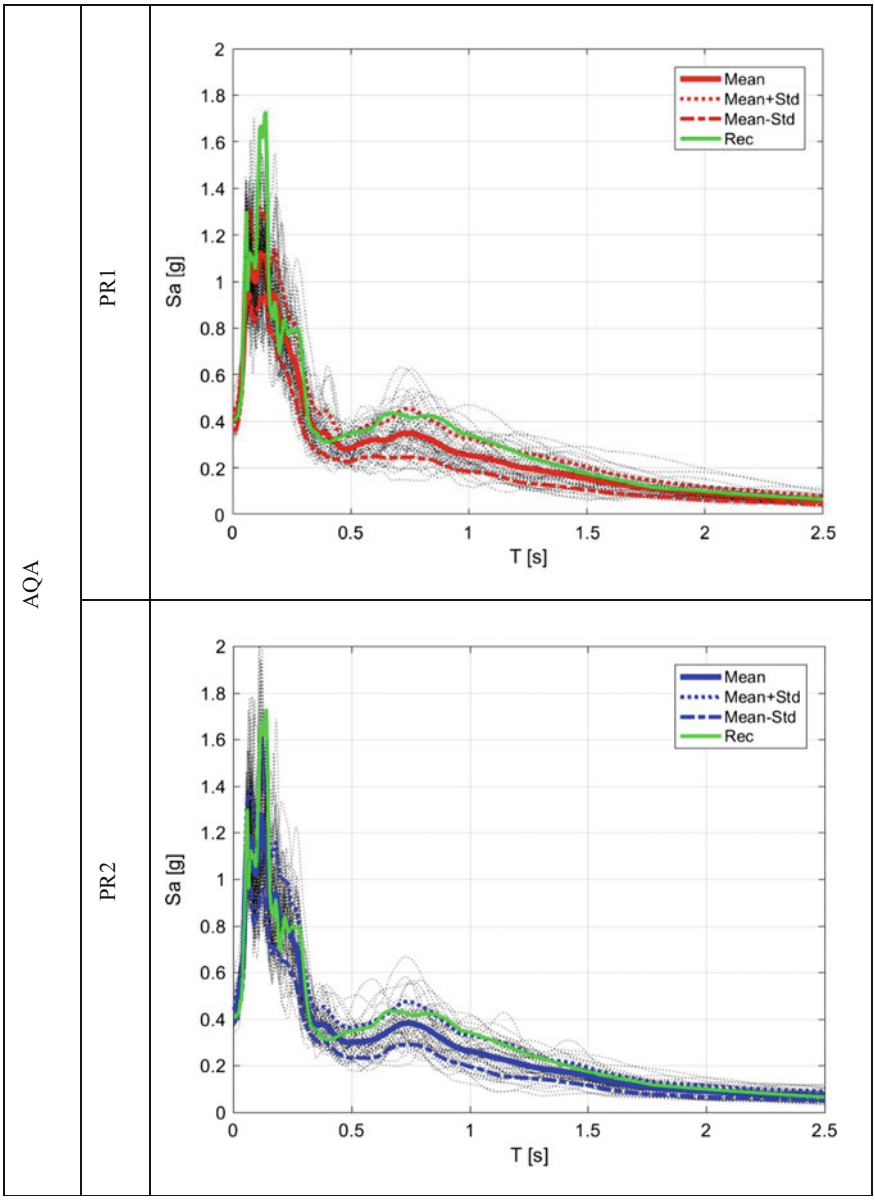

Fig. 9 Comparison between procedures PR1 (*first row*) and PR2 (*second row*) acceleration response spectra (Sa) at AQA bridge foundation (Fig. 1) for each generated accelerograms (*black dot lines*); mean of the Sa considering fifty generations (*red line* for PR1, *blue line* for PR2); mean plus (*dot red line* for PR1, *dot blue line* for PR2) or minus (*dashed red line* for PR1, *dashed blue line* for PR2) one standard deviation considering fifty generations. The Spa of the input accelerograms at AQA is given in *green line*

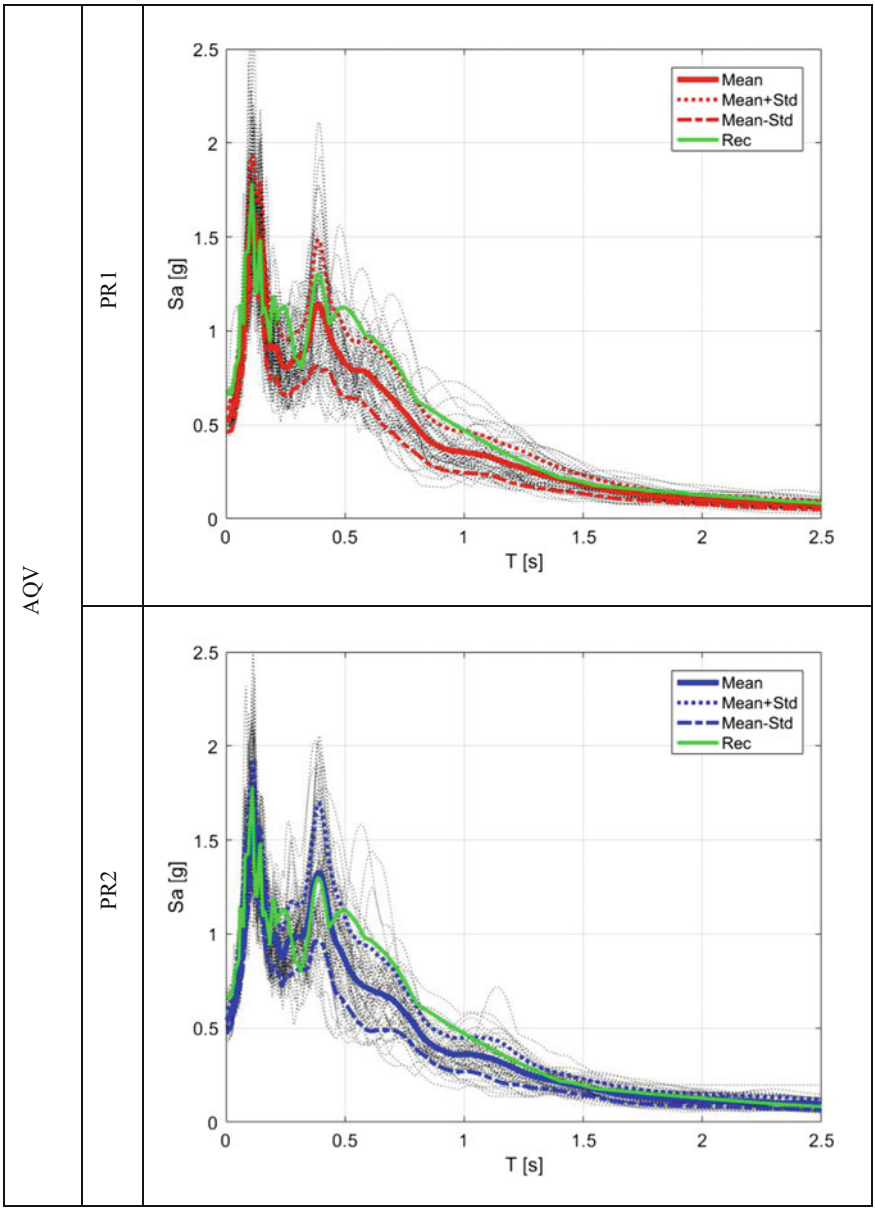

Fig. 10 Comparison between procedures PR1 (*first row*) and PR2 (*second row*) acceleration response spectra (Sa) at AQV bridge foundation (Fig. 1) for each generated accelerograms (*black dot lines*); mean of the Sa considering fifty generations (*red line* for PR1, *blue line* for PR2); mean plus (*dot red line* for PR1, *dot blue line* for PR2) or minus (*dashed red line* for PR1, *dashed blue line* for PR2) one standard deviation considering fifty generations. The Spa of the input accelerograms at AQV is given in *green line*

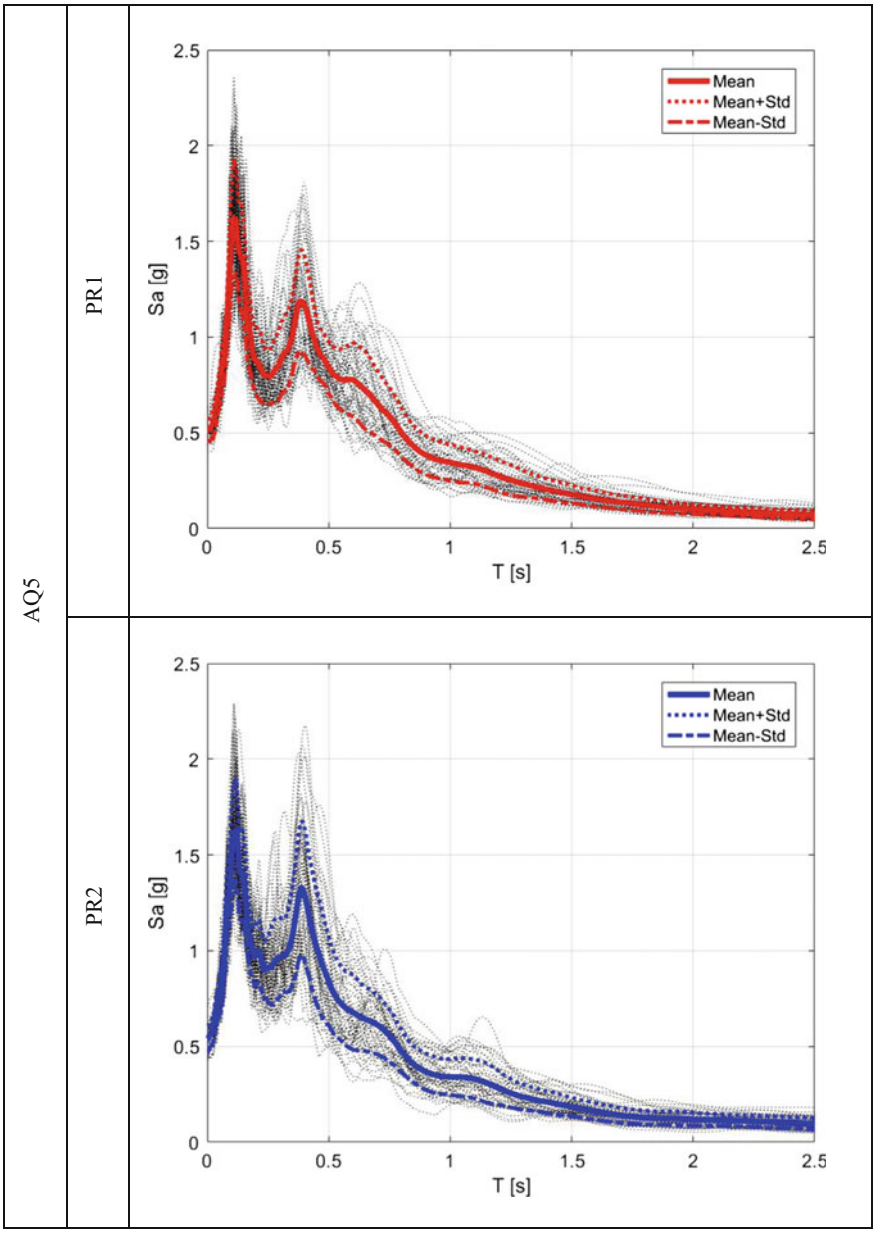

Fig. 11 Comparison between procedures PR1 (*first row*) and PR2 (*second row*) acceleration response spectra (Sa) at AQ5 bridge foundation (Fig. 1) for each generated accelerograms (*black dot lines*); mean of the Sa considering fifty generations (*red line* for PR1, *blue line* for PR2); mean plus (*dot red line* for PR1, *dot blue line* for PR2) or minus (*dashed red line* for PR1, *dashed blue line* for PR2) one standard deviation considering fifty generations

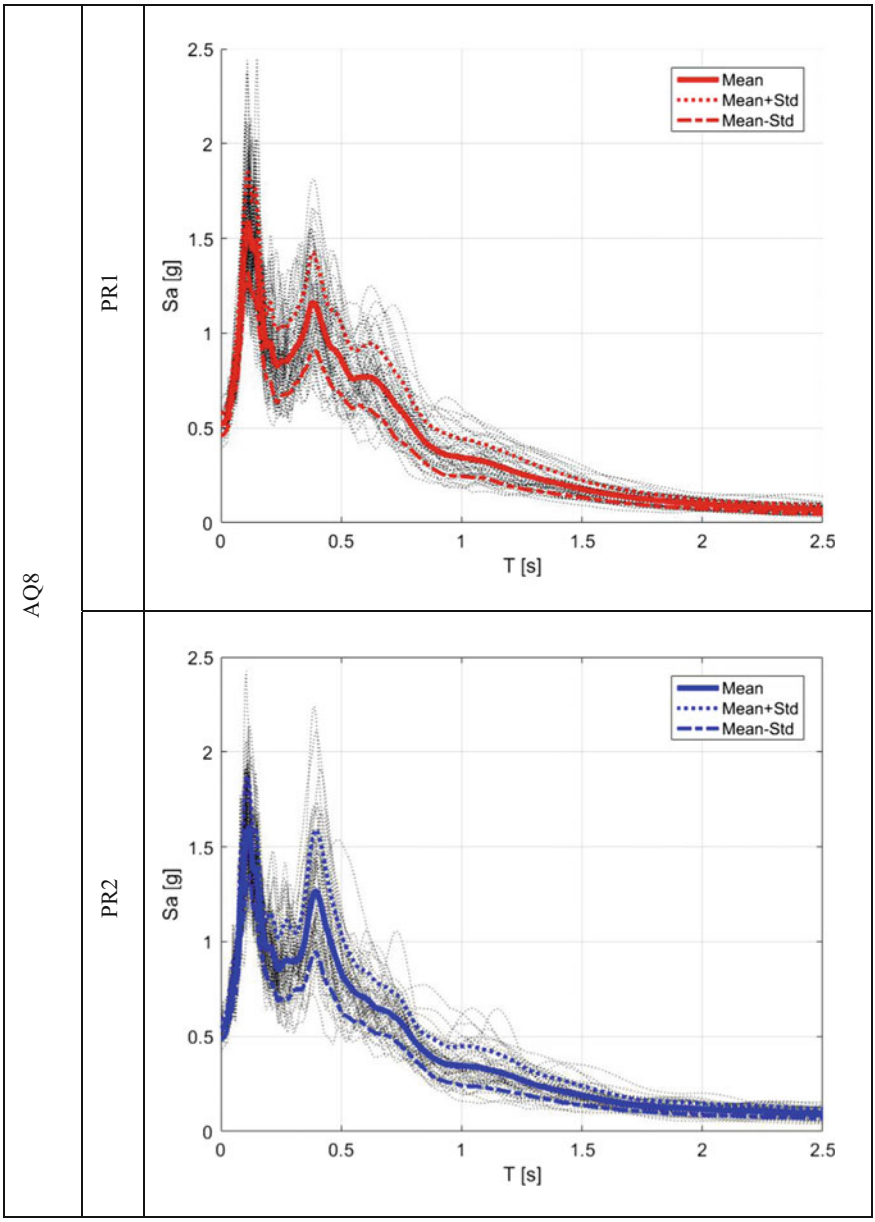

Fig. 12 Comparison between procedures PR1 (*first row*) and PR2 (*second row*) acceleration response spectra (Sa) at AQ8 bridge foundation (Fig. 1) for each generated accelerograms (*black dot lines*); mean of the Sa considering fifty generations (*red line* for PR1, *blue line* for PR2); mean plus (*dot red line* for PR1, *dot blue line* for PR2) or minus (*dashed red line* for PR1, *dashed blue line* for PR2) one standard deviation considering fifty generations

This is important, as the Sa measures the effects of the generated earthquake signals on structures (Monti et al. 1994, 1996; Shinozuka et al. 2000; Tzanetos et al. 2000; Sextos et al. 2003; Nuti and Vanzi 2004, 2005; Lupoi et al. 2005; Carnevale et al. 2010, 2012a, b).

The generated signals can be used in a proper structural long structure design and the proposed procedures represent valid generation tools for designers.

3 Conclusion

In this chapter, a propagation model to generate a random field (RF) of asynchronous earthquake signals at different points for the same seismic event was presented. The model is applied to a real case, and the model results are compared with the real recordings.

Two generation procedures (PR1 and PR2, Fig. 1) are used to obtain asynchronous accelerometric signals at the foundations of a long bridge with eight foundation points. The bridge is placed in the Aterno Valley, where the EW components of the L'Aquila main shock (4-6-2009) accelerometric signals (which are the input for both procedures), were recorded at two stations (AQA and AQV, Fig. 1).

The first procedure PR1 performs an asynchronous earthquake signals generation directly at the soil surface (Fig. 1). The second procedure PR2 performs an asynchronous earthquake signals propagation at bedrock starting from two input bedrock signals (Fig. 1). The asynchronous signals generated at surface by means of PR1 or PR2 procedures are compared in terms of signals characteristics (Fast Fourier Transformation amplitude spectra and coherence among signals at different generation points) and of structural response (acceleration response spectra) at bridge foundations AQA, AQV, AQ5 and AQ8 (Fig. 1).

In particular, fifty asynchronous signals are obtained by means of the two procedures (PR1 or PR2) at each selected foundation point, and elaborated to obtain Fourier amplitude spectra (FFT-AMP), coherence between couple of distant points along the bridge (Cohere) and acceleration response spectra (Sa).

The comparison among the FFT-AMP and Sa curves of the generated signals at AQA and AQV stations by PR1 or PR2 with the ones obtained by the elaboration of the input signals (real seismic recordings) at the same points showed that both the procedures can generate reliable earthquake signals.

The coherences for each frequency calculated by means of the generated signals at distant foundation points along the bridge (AQA-AQV, AQA-AQ5 and AQA-AQ8, Fig. 1) were in good agreement with the ones obtained by the input numerical model assumed in the propagation procedure, for both procedures. The coherence difference due to inevitable numerical errors is small.

This is important as the coherence measures the variation of the signals frequency content during the propagation of the seismic wave from point to point. This difference among the signals characteristics produces relative displacements among the different foundation points, which have to be considered properly during the design of long structures such as bridges (Monti et al. 1994, 1996; Shinozuka et al. 2000; Tzanetos et al. 2000; Sextos et al. 2003; Nuti and Vanzi 2004, 2005; Lupoi et al. 2005; Carnevale et al. 2010, 2012a, b).

Procedure PR2 requires detailed knowledge of the soil properties and produces very similar results to PR1's. However, PR1 is simpler than PR2; besides, few surface recordings are usually available for the same seismic event and there are usually different soil units in correspondence of the foundations of long structures such as bridges.

For that reason, procedure PR2 is also a valid solution to generate surface Random Fields, since it is possible to obtain bedrock signals by the available surface recordings, to perform the bedrock propagation (which is simple since there is only one soil type) and finally to obtain the surface signal. As a final remark, it must be noticed that both (artificial) procedures, produce signals that are in reasonable agreement with the real recorded ones.

Acknowledgements The authors gratefully acknowledge the funding by "The Laboratories University Network of seismic engineering" (ReLUIS) thanks to the research project ReLUIS/DPC 2015-2016. This research is also supported by the Structural Laboratory College of Civil Engineering (Fuzhou University) and the International Joint-Lab (Universities of Roma Tre and Fuzhou).

References

Abrahamson NA, Schneider JF, Stepp JC (1991) Empirical spatial coherency functions for applications to soil structure interaction analyses. Earthq Spectra 7(1):27

Bardet P, Ichii K, Lin CH (2000) A computer program for equivalent-linear earthquake site response analyses of layered soil deposits (EERA). Technical report of Department of Civil Engineering, University of Southern California, USA

Carnevale L, Lavorato D, Nuti C, Vanzi I (2010) Response of continuous deck bridges to non-synchronous seismic motion. Paper presented at the conference sustainable development strategies for constructions in Europe and China, Rome, 19–20 Apr 2010

Carnevale L, Imperatore S, Lavorato D, Nuti C, Silvestri F, Tropeano G, Dezi F (2012) Generation of non-synchronous accelerograms to evaluate the seismic bridge response including local site amplification. Paper presented at the 15th world conference on earthquake engineering

Carnevale L, Imperatore S, Lavorato D, Nuti C, Leoni G, Tropeano G (2012) Assessment of seismic behavior of R.C. bridges under asynchronous motion and comparison with simplified approaches. Paper presented at the 15th world conference on earthquake engineering

Der Kiureghian A (1996) A coherency model for spatially varying ground motion. Earthq Eng Struct Dyn 25:99–111

Eurocode 8, ENV 1998-1-1. Design provisions for earthquake resistance of structures, Part 1-1: General rules—seismic actions and general requirements for structures

Harichandran RS, Vanmarcke E (1986) Stochastic variation of earthquake ground motion in space and time. J Eng Mech 112:154–174

ITACA (ITalian ACcelerometric Archive, http://itaca.mi.ingv.it) INGV, Istituto Nazionale di Geofisica e Vulcanologia, operated by the Italian Civil Protection Department—Presidency of the Council of Ministers (DPC)

Lanzo G, Pagliaroli A (2012) Seismic site effects at near-fault strong-motion stations along the Aterno River Valley during the M′-w = 6.3 2009 L'Aquila earthquake. Soil Dyn Earthq Eng 40:1–14

Lavorato D, Bergami AV, Nuti C, Vanzi I (2017) Generation of asynchronous seismic signals considering different knowledge levels for seismic input and soil. Paper presented at the 16th world conference on earthquake, 16WCEE 2017 Santiago Chile, 9–13 Jan 2017

Luco JE, Wong HL (1986) Response of a rigid foundation to a spatially random ground motion. Int J Earthq Eng Struct Dyn 14:891–908

Lupoi A, Franchin P, Monti G, Pinto PE (2005) Seismic design of bridges accounting for spatial variability of ground motion. Earthq Eng Struct Dyn 34:327–348

MATLAB (matrix laboratory) multi-paradigm numerical computing environment and fourth-generation programming language developed by MathWorks Inc

Monti G, Nuti C, Pinto PE, Vanzi I (1994) Effects of non-synchronous seismic input on the inelastic response of bridges. Paper presented at the II international workshop on seismic design of bridges, Queenstown, New Zeeland

Monti G, Nuti C, Pinto PE (1996) Nonlinear response of bridges under multisupport excitation. J Struct Eng 122(10):1147–1159. doi:10.1061/(ASCE)0733-9445)

Nuti C, Vanzi I (2004) Influence of earthquake spatial variability on the differential displacements of soil and SDF Structures. Technical report of DIS (Department of Structures, University of Roma Tre)

Nuti C, Vanzi I (2005) Influence of earthquake spatial variability on differential soil displacements and SDF system response. Earthq Eng Struct Dyn 34(11):1353–1374

Oliveira CS, Hao H, Penzien J (1991) Ground motion modeling for multiple input structural analysis. Struct Saf 10:79–93

Rollins KM, Evans MD, Diehle NB, Daily WD (1998) Shear modulus and damping relationships for gravels. J Geotech Geoenviron Eng 124(5):396–405

Santa-Cruz S, Heredia-Zavoni E, Harichandran RS (2000) Low-frequency behavior of coherency for strong ground motions in Mexico City and Japan. Paper presented at the 12th world conference on earthquake engineering, Auckland, New Zealand, Paper No. 0076

Schnabel PB, Lysmer J, Seed HB (1972) UCB/EERC-72/12, Earthquake Engineering Research Center, University of California, Berkeley, 1972-12, 92 pp. (480/S36/1972). SHAKE 91—A computer program for conducting equivalent linear seismic response analyses of horizontally layered soil deposits program modified modifications by Idriss IM, Sun JI

Sextos AG, Pitilakis KD, Kappos AJ (2003) Inelastic dynamic analysis of RC bridges accounting for spatial variability of ground motion, site effects and soil-structure interaction phenomena. Part 2: Parametric study. Earthq Eng Struct Dyn 32:629–652

Shinozuka M, Saxena V, Deodatis G (2000) Effect of spatial variation of ground motion on highway structures. Technical report MCEER-00-0013

Tzanetos N, Elnashai AS, Hamdan FH, Antoniou S (2000) Inelastic dynamic response of RC bridges subjected to spatially non-synchronous earthquake motion. Adv Struct Eng 3:191–214

Vanmarcke EH, Fenton GA (1991) Conditioned simulation of local fields of earthquake ground motion. Structural safety, special issue on spatial variation of earthquake ground motion, Jan 1991

Vanmarcke EH, Heredia-Zavoni E, Fenton GA (1993) Conditional simulation of spatially correlated earthquake ground motion. J Eng Mech

Zerva A, Zervas V (2002) Spatial variation of seismic ground motions: an overview. Appl Mech Rev 55(3):271–297, ASME Reprint No AMR 328

Zerva A (2009) spatial variation of seismic ground motions: modeling and engineering applications. CRC Press, Florida

Seismic Response Analysis with Spatially Varying Stochastic Excitation

Katerina Konakli

Abstract Assessment of the seismic vulnerability of extended structures (e.g. bridges and lifelines) as well as of systems of structures covering extended areas requires to properly account for the effects of ground-motion spatial variability. Even in cases with relatively uniform soil conditions, ground motions may exhibit significant variations due to the incoherence and wave-passage effects, respectively manifested as random differences and deterministic time delays. Differential soil conditions cause additional variations in the amplitude and frequency content of the ground motions as these propagate from the bedrock to the surface level. The present chapter describes methods for the modeling of ground-motion spatial variability, the simulation of spatially varying ground-motion arrays and the evaluation of the response of multiply-supported structures to differential support excitations. The pertinent uncertainties in the characteristics of the ground motions are accounted for by employing concepts from stochastic time-series analysis. In particular, the notion of coherency is employed to describe the spatial variability of the ground-motion arrays, which are considered as realizations of a random field at the locations of interest. The statistical properties of the ground motions at separate locations are described through the respective auto-power spectral densities. A statistical characterization of linear structural response to differential support motions is obtained by means of a response-spectrum method, rooted in random vibration theory, while the non-linear response is investigated on the basis of the 'equal-displacement' rule. This chapter is inspired by the doctoral research of the author under the supervision of Professor Armen Der Kiureghian.

K. Konakli (✉)
ETH Zürich, Chair of Risk, Safety and Uncertainty Quantification,
Stefano-Franscini-Platz 5, HIL E23.2, 8093 Zürich, Switzerland
e-mail: konakli@ibk.baug.ethz.ch

P. Gardoni (ed.), *Risk and Reliability Analysis: Theory and Applications*,
Springer Series in Reliability Engineering, DOI 10.1007/978-3-319-52425-2_9

1 Introduction

Several recent earthquake events across the globe highlight the need for improved measures to safeguard people's lives and properties in seismic vulnerable areas. The immense uncertainties associated with the occurrence and the characteristics of future ground motions pose a major challenge in dealing with seismic risk. The work of Professor Armen Der Kiureghian has been fundamental in achieving this goal by offering pioneering methods for addressing uncertainty in the field of earthquake engineering, among his numerous valuable contributions in the broader fields of risk and reliability (e.g. Der Kiureghian and Liu 1986; Der Kiureghian and Ke 1988; Der Kiureghian et al. 1994; Song and Der Kiureghian 2003; Straub and Der Kiureghian 2010).

Inspired by the doctoral work of the author under the supervision of Professor Der Kiureghian, the present chapter focuses on a particular aspect of seismic analysis that is the spatial variability exhibited by earthquake-induced ground motions and its effects on structural response. The importance of incorporating these effects in seismic response analysis arises from the fact that seismic ground motions may exhibit significant variations over distances that are comparable to the dimensions of extended structures, such as bridges and lifelines. Furthermore, the ground-motion spatial variability comes into play when examining seismic vulnerability at a systemic level, considering the infrastructure of entire communities rather than independent structures. It should be emphasized that awareness on the need for a systemic perspective is currently growing in the engineering research community.

This chapter provides an overview on the following topics: the modeling of ground-motion spatial variability, the simulation of spatially varying ground-motion arrays and the response analysis of extended structures subject to differential support excitations. In the relevant methods presented herein, effects of uncertainties are incorporated by considering the ground-motion time histories as realizations of stochastic processes exhibiting spatial correlations. To this end, mathematical tools for time-series analysis in both the time and frequency domains are employed.

Following the Introduction, the coherency function is presented in the next section, as a means of describing the spatial variability of stochastic processes in the frequency domain. Moreover, popular models for the coherency function in the field of earthquake engineering are described. The section continues with the estimation of coherency from ground-motion records, including a case study using accelerograms from the 2004 Parkfield earthquake in California.

The subsequent section describes a method for simulating ensembles of spatially varying ground-motion arrays consistent with a prescribed coherency function. It is underlined that because recorded strong ground-motion arrays remain scarce, methods for generating such arrays synthetically are essential in earthquake engineering research and practice. The method described herein relies on the theory of Gaussian random processes. Two approaches are presented: in the so-called

unconditioned approach, the power spectral density of the acceleration process at a reference site is defined on the basis of a given recorded or synthetic accelerogram. In this case, ensembles of simulated arrays exhibit uniform variability at different locations, a necessary property when these motions are used as input for statistical analyses of structural responses. In the second approach, a specific realization (a recorded or synthetic accelerogram) at a reference site is defined and consistent time histories are simulated at the locations of interest. The latter comprises the conditioned approach.

In the next part of this chapter, the focus is set on methods for the evaluation of structural response to differential support excitations. First, a response-spectrum method is described, rooted in the theory of random vibrations. This method is well known as the Multiple-Support Response-Spectrum (MSRS) rule. Developed by Der Kiureghian and Neuenhofer (1992), the MSRS rule is nowadays incorporated in seismic design codes. The extension of the MSRS rule to account for quasi-static contributions of truncated high-frequency vibration modes, developed by Konakli and Der Kiureghian (2011a), is also presented. In the sequel, effects of spatial variability on the 'equal-displacement' rule, relating mean peak non-linear to mean peak linear structural responses, are discussed.

A summary is included in the final section of this chapter, followed by a grateful acknowledgement to Professor Der Kiureghian.

2 Modeling of Ground-Motion Spatial Variability

2.1 The Coherency Function

The spatial variability manifested in earthquake-induced ground motions can be attributed to three main effects, namely the incoherence, the wave-passage and the site-response effects (Der Kiureghian 1996). The incoherence effect represents random differences in the amplitudes and phases of seismic waves due to reflections and refractions that occur as the waves propagate in the heterogeneous soil medium and also, due to the super-positioning of waves arriving from different parts of an extended source. The wave-passage effect represents the deterministic time-lag that characterizes the arrival of seismic waves at separate locations. The site-response effect represents the influence of varying local soil profiles on the amplitude and frequency content of the bedrock motions as they propagate upwards to the surface. The aforementioned effects are incorporated into the complex-valued coherency function, which models the ground-motion spatial variability in the frequency domain. Details on the coherency function are given in the sequel.

Let $\ddot{u}_k(t)$ and $\ddot{u}_l(t)$ denote a pair of stationary random processes modeling the ground-motion accelerations at locations k and l respectively. The coherency function that characterizes the spatial variability between the two locations is a normalized version of the cross-power spectral density (PSD) of $\ddot{u}_k(t)$ and $\ddot{u}_l(t)$:

$$\gamma_{kl}(\omega) = \frac{G_{\ddot{u}_k\ddot{u}_l}(\omega)}{\left[G_{\ddot{u}_k\ddot{u}_k}(\omega)G_{\ddot{u}_l\ddot{u}_l}(\omega)\right]^{1/2}}. \quad (1)$$

where $G_{xy}(\omega)$ denotes the cross-PSD of the random processes $x(t)$ and $y(t)$, and $G_{xx}(\omega)$ denotes the auto-PSD of process $x(t)$. Although earthquake ground motions are not stationary, the above definition of the coherency function is commonly used to describe their spatial variability under the assumption that the strong-motion phase of an accelerogram is nearly stationary.

In the case of uniform soil conditions, the modulus of the coherency function characterizes the incoherence effect, whereas its phase angle characterizes the wave-passage effect. Der Kiureghian (1996) has shown that, under the assumption of vertical wave propagation from the bedrock level to the ground surface, the site-response effect influences only the phase angle of the coherency function. This assumption can be employed in the case of far-field earthquake records. In this case, the coherency function can be written in the form:

$$\gamma_{kl}(\omega) = |\gamma_{kl}(\omega)| exp\left\{i[\theta_{kl}^{wp}(\omega) + \theta_{kl}^{sr}(\omega)]\right\} \quad (2)$$

where $\theta_{kl}^{wp}(\omega)$ and $\theta_{kl}^{sr}(\omega)$ respectively denote the phase angles due to wave-passage and site-response effects. It is noted that in the case of near-fault motions, site-response effects may also influence the coherency modulus.

Based on the physics of wave propagation and certain simplifying assumptions, it is possible to develop theoretical models to describe the phase angle caused by the wave-passage and site-response effects (the latter for far-field sites). The phase angle due to the wave-passage effect is typically evaluated as (Luco and Wong 1986; Der Kiureghian 1996):

$$\theta_{kl}^{wp}(\omega) = -\frac{\omega d_{kl}^{L}}{\nu_{app}} \quad (3)$$

where d_{kl}^{L} is the projected algebraic horizontal distance in the longitudinal direction of propagation of waves and ν_{app} is the surface apparent wave velocity. Under the assumptions of linear (or linearized) behavior of the soil columns, vertical wave propagation at each site and neglect of dynamic interaction between sites, the phase shift due to the site-response effect is given by (Der Kiureghian 1996):

$$\theta_{kl}^{sr}(\omega) = tan^{-1}\frac{Im[H_k(\omega)H_l(-\omega)]}{Re[H_k(\omega)H_l(-\omega)]} \quad (4)$$

where $H_k(\omega)$ is the frequency-response function for the absolute acceleration response of the soil column at location k.

The inherently random nature of the incoherence effect renders the description of the coherency modulus more challenging. One approach is to use a semi-empirical

model, i.e. a theoretical model employing parameters that can be determined through statistical inference. Another approach is to develop a purely empirical model using data from recorded acceleration arrays. Empirical models account for the complex phenomena that occur during wave propagation and are not captured by simplified mathematical models, but characterize only the specific rupture mechanisms and soil topographies present in the data. Among the most quoted empirical models are those by Harichandran and Vanmarcke (1986) and Abrahamson et al. (1991), which are based on ground motions recorded by two arrays located in an alluvial valley in Taiwan. Ancheta et al. (2011) updated the coefficients of the latter so that the new model additionally fits data from the Borrego Valley Differential Array in California.

One of the most widely used semi-empirical models in engineering applications was derived by Luco and Wong (1986) considering the propagation of shear waves in a random medium. According to this model, the coherency modulus for a pair of acceleration processes at stations k and l separated by a distance d_{kl} is evaluated as:

$$|\gamma_{kl}| = exp\left[-(\alpha d_{kl}\omega)^2\right] \tag{5}$$

in which the coherency drop parameter α is given by $\alpha = \eta/v_s$, where v_s is the average shear-wave velocity of the ground medium along the wave travel-path and η is a constant. Luco and Wong suggested that typical values of α approximately vary from 2×10^{-4} to 3×10^{-4} s/m, whereas Zerva and Harada (1994) proposed an analytical expression for α in terms of the properties and depth of the soil layers at the site under consideration. The Luco and Wong model represents a special case of the model developed by Der Kiureghian (1996) based on the theory of random processes.

2.2 Estimation of the Coherency Modulus

Consider an array of zero-mean, jointly stationary Gaussian ground-acceleration processes at n sites defined by auto-PSDs $G_{kk}(\omega)$, $k = 1, 2, \ldots, n$, and cross-PSDs $G_{kl}(\omega)$, $k, l = 1, 2, \ldots, n$, for $k \neq l$. Let $a_k(t_i)$ and $a_l(t_i)$, $i = 1, \ldots, N$, represent realizations of the acceleration processes at locations k and l respectively, each sampled at equal time intervals Δt, i.e. $t_i = (i-1)\Delta t$. To simplify the algebra, N is considered even. According to Eq. 1, estimation of the coherency function from given realizations requires the respective auto- and cross-PSDs. Under the assumption of ergodicity, these quantities can be estimated from a single realization of a random field, as described below.

An estimator of the auto-PSD of the acceleration record at location k is the periodogram:

$$I_{kk}(\omega_p) = (N\Delta t/4\pi)\left(A_{pk}^2 + B_{pk}^2\right) \tag{6}$$

in which $\omega_p = 2\pi p/N\Delta t$, $p = 1, \ldots, N/2 - 1$, denote discrete frequencies and $\{A_{pk}, B_{pk}\}$ are the Fourier coefficients of the acceleration record (Chatfield 2004). Though asymptotically unbiased, the periodogram is an inconsistent estimator and exhibits erratic behavior. The traditional method to obtain a consistent estimator is to smooth the periodogram over a frequency band (Brillinger 2001). The resulting estimates of the PSD depend on the selected width of the smoothing window and, to a lesser extent, on the type of smoother (Priestley 1981). Because smoothing introduces bias to the estimates, the width of the smoothing window should be selected considering the tradeoff between bias and variance.

A consistent estimator of the cross-PSD of two acceleration records is the smoothed cross-periodogram. The real and imaginary parts of the cross-periodogram are respectively determined by Chatfield (2004):

$$Re\left[I_{kl}(\omega_p)\right] = (N\Delta t/4\pi)\left(A_{pk}A_{pl} + B_{pk}B_{pl}\right) \tag{7}$$

and:

$$Im\left[I_{kl}(\omega_p)\right] = (N\Delta t/4\pi)\left(A_{pk}B_{pl} - A_{pl}B_{pk}\right) \tag{8}$$

Finally, an estimate of the coherency function is obtained by substituting in Eq. 1 the smoothed version of $I_{kl}(\omega)$ in the place of $G_{kl}(\omega)$ and the smoothed versions of $I_{kk}(\omega)$ and $I_{ll}(\omega)$ in the places of $G_{kk}(\omega)$ and $G_{ll}(\omega)$ respectively. To estimate the coherency modulus for a pair of accelerograms at sites k and l, the real and imaginary parts of the coherency function are substituted into the expression $|\gamma_{kl}(\omega)| = \left\{[Re(\gamma_{kl}(\omega))]^2 + [Im(\gamma_{kl}(\omega))]^2\right\}^{1/2}$.

2.3 The Case of the UPSAR Array

Recordings of the UPSAR array during the 2004 Parkfield earthquake in California provided a rare opportunity to examine the coherency function for near-fault strong ground motions. Konakli et al. (2014) investigated the coherency modulus for this particular event and tectonic setting and compared their estimates with commonly used semi-empirical and empirical models. This subsection provides a summary of the analysis and main findings of this study.

The coherency analysis in Konakli et al. (2014) was based on the acceleration time-histories recorded at the 12 operational stations of the UPSAR array. By focusing on inter-station distances 0–500 m, the analysis considered 47 station pairs. Estimates of the coherency modulus were obtained for each station pair and for each of the EW, NS (two horizontal) and UD (vertical) components, by

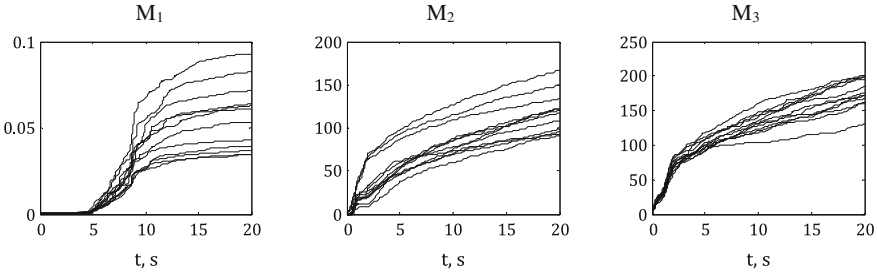

Fig. 1 Evolving measures of variance, predominant frequency and bandwidth of the UPSAR accelerograms in the EW direction

analyzing nearly-stationary segments of the recorded accelerograms. The considered segments were defined by a time window of 7.5 s width, containing the strongest shaking. The selection of the time window was based on an analysis of the following three measures: the integral of the squared acceleration in time (M_1), the cumulative count of zero-level up-crossings (M_2), and the cumulative count of negative maxima and positive minima (M_3). Figure 1 (originally presented in Konakli et al. 2014) shows the time evolution of the aforementioned measures for the accelerograms in the EW direction. Approximately constant slopes of the M_1, M_2 and M_3 curves respectively indicate nearly-constant variance, predominant frequency and bandwidth (Rezaeian and Der Kiureghian 2008). The resulting periodograms for the so selected segments were smoothed using a 5-point Hamming window. Details on the selection of the smoothing window can be found in Konakli et al. (2014).

In order to compare the coherency estimates from the UPSAR recordings to the model by Luco and Wong, values of parameter α in Eq. 5 that fit the UPSAR estimates were determined by means of non-linear least-squares minimization. In examining the coherency at specific distances as a function of frequency, the least-squares minimization was applied on the variance-stabilizing transformation $\tanh^{-1}|\gamma_{kl}|$ (Abrahamson et al. 1991; Ancheta et al. 2011). Figure 2 (originally presented in Konakli et al. 2014) shows the fitter values versus inter-station distances for pairs of components in the NS, EW and UD directions. The figure indicates a strong dependence of α on distance, with α tending to decrease with increasing inter-station distance at a rate that is higher at smaller distances. Overall, the fitted α values for the vertical component are slightly larger than those for the two horizontal components, which tend to be close to each other. This indicates a slightly larger spatial variability among the vertical components than among the horizontal components for the same inter-station distance. The estimated standard deviations of the fitted α values normalized with the respective α values were below 0.2 in all cases.

It is noted that under the assumption of homogeneity, a single estimate of the coherency modulus can be obtained for a relatively narrow inter-station distance bin through averaging. Moreover, under the assumption of isotropy, a single estimate

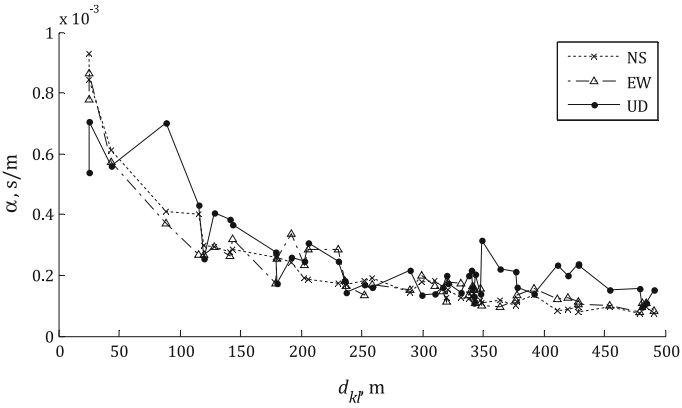

Fig. 2 Fitted α values versus distance using coherency estimates as a function of frequency

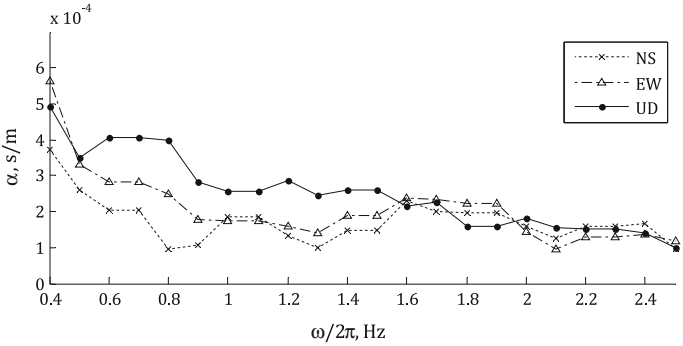

Fig. 3 Fitted α values versus frequency using coherency estimates as a function of distance

can be obtained for the horizontal component of the ground motion. This averaging is important in reducing the noise in the estimates. Fitted α values under the assumptions of homogeneity and isotropy are reported in Konakli et al. (2014).

Next, the behavior of the coherency modulus as a function of inter-station distance is examined at specific frequencies. In this case, the non-linear least-squares minimization is directly applied on $|\gamma_{kl}|$. Figure 3 (originally presented in Konakli et al. 2014) shows the α values obtained for each of the NS, EW and UD components. Frequencies up to 2.5 Hz are shown, because coherency estimates for higher frequencies are dominated by noise. Considering the frequency range below 1.5 Hz, where the effect of noise is relatively small, the figure indicates both direction dependence, with smaller values of α corresponding to the horizontal components, and frequency dependence, with values of α tending to decrease with increasing frequency. The respective estimates of the standard deviation normalized with the fitted α value were below 0.14 in all cases.

According to Figs. 2 and 3, the estimates of α for the UPSAR recordings are within the range suggested by Luco and Wong for distances approximately in the range 100–300 m and for frequencies approximately in the range 0.5–2 Hz. However, unlike the Luco and Wong model where α is a constant, the UPSAR data indicate dependence of α on both inter-station distance and frequency. It is also noted that the rate of decay of the coherency modulus with frequency and distance tends to be higher for the vertical component. This trend is more pronounced for the rate of decay of the coherency modulus with distance at the lower frequencies.

Konakli et al. (2014) further compared estimates of the coherency modulus from the UPSAR recordings with two widely used empirical models. They considered the empirical model by Ancheta et al. (2011) for inter-station distances smaller than 100 m and the model by Harichandran and Vanmarcke (1986) for inter-station distances larger than 100 m. As mentioned earlier in this section, the model by Ancheta et al. (2011) is an update on the earlier model by Abrahamson et al. (1991). For separation distances 100–300 m, the empirical model was found to be in fair agreement with the UPSAR estimates for frequencies up to approximately 4 Hz. For smaller separation distances, the UPSAR coherency modulus was found smaller than that given by the empirical model in the entire frequency range examined, but the trend reversed for separation distances greater than 300 m. These differences indicated a complex dependence of the spatial variability exhibited by earthquake ground motions on source, propagation, topography and site effects.

3 Simulation of Spatially Varying Ground Motions

3.1 The Unconditioned and Conditioned Approaches

The simulation method described in the present section, originally proposed by Konakli and Der Kiureghian (2012a), generates arrays of ground-motion time histories with temporal and spectral non-stationarity, incorporating effects of incoherence, wave passage and differential site response. The method is based on the representation of ground accelerations as realizations of Gaussian random processes and builds upon the earlier works of Vanmarcke and Fenton (1991), Kameda and Morikawa (1992) and Liao and Zerva (2006). The required input comprises: (i) a recorded or synthetic accelerogram at a reference site, (ii) a coherency function that describes the spatial variability of the ground-motion random field and (iii) the frequency-response functions of the soil columns at the locations of interest.

Two approaches are considered. In the unconditioned approach, the simulated motions are consistent with the statistical characteristics of the ground-motion random field at the reference site, derived from the auto-PSD of the given accelerogram. In the conditioned approach, the simulated motions are consistent with the specific realization of the ground-motion random field at the reference site,

represented by the given accelerogram. In the latter approach, the variance of the simulated motions increases with increasing distance from the reference site, which is an undesirable property if the motions are used to perform statistical analysis of structural responses. The unconditioned approach should thus be considered when uniform variance of the simulated motions at different locations is essential.

In both approaches, temporal and spectral non-stationarities are accounted for by considering nearly stationary segments of the given accelerogram. These are used to simulate consistent segments of acceleration time-histories at the target locations, which are appropriately stitched together in the sequel. It is underlined that this method is not directly applicable to near-fault ground motions that contain directivity pulses and thus, cannot be represented as stationary segments even in approximation. One way to include the directivity pulse is to separately model the pulse and superimpose it on a synthetic ground-motion array, the latter generated according to the methodology presented herein.

In the following, after a brief description of the discrete representation of an array of Gaussian processes, the conditioned and unconditioned simulation approaches are outlined for the case of stationary motions. The extension to non-stationary motions is explained in the sequel, followed by an example application.

3.2 Discrete Representation of an Array of Gaussian Processes

Similarly to the previous section, an array of zero-mean, jointly stationary Gaussian acceleration processes at n sites is considered, defined by auto-PSDs $G_{kk}(\omega)$, $k = 1, 2, \ldots, n$, and cross-PSDs $G_{kl}(\omega)$, $k, l = 1, 2, \ldots, n$, for $k \neq l$. Each process is sampled at time instants $t_i = (i-1)\Delta t$, $i = 1, \ldots, N$, with the number of samples N considered even. Such an array of processes can be represented in terms of the finite Fourier series (see, e.g. Chatfield 2004):

$$a_k(t_i) = A_{0k} + \sum_{p=1}^{N/2-1} \left[A_{pk} \cos\left(\omega_p t_i\right) + B_{pk} \sin\left(\omega_p t_i\right)\right] + (-1)^i A_{(N/2)k} \qquad (9)$$

where $\omega_p = 2\pi p/N\Delta t$ are discrete frequencies and $\{A_{pk}, B_{pk}\}$ are the Fourier coefficients. Note that the above representation uses N parameters to describe N observations and can thus be made to exactly fit the given realizations.

The Fourier coefficients $\{A_{pk}, B_{pk}\}$ are zero-mean, jointly Gaussian random variables, uncorrelated for different frequencies, i.e. $\mathrm{E}[A_{pk}A_{qk}] = \mathrm{E}[B_{pk}B_{qk}] = \mathrm{E}[A_{pk}B_{qk}] = 0$ for $p \neq q$. At frequency ω_p, the following relations hold:

$$E\left[A_{pk}\,A_{pl}\right] = E\left[B_{pk}\,B_{pl}\right] = \begin{cases} G_{kk}\left(\omega_p\right)\Delta\omega, & \text{if } k = l \\ Re\left[G_{kl}\left(\omega_p\right)\right]\Delta\omega, & \text{if } k \neq l \end{cases} \tag{10}$$

and

$$E\left[A_{pk}\,B_{pl}\right] = \; -E\left[B_{pk}\,A_{pl}\right] = \begin{cases} 0, & \text{if } k = l \\ Im\left[G_{kl}\left(\omega_p\right)\right]\Delta\omega, & \text{if } k \neq l \end{cases} \tag{11}$$

with $\Delta\omega = 2\pi/N\Delta t$. Obviously, given the auto- and cross-PSDs (or equivalently the auto-PSDs and the coherency function), the variance/covariances of all Fourier coefficients can be determined.

3.3 Simulation of Stationary Motions with the Unconditioned Approach

Let $k = 1, \ldots, n$ denote the index of a target site with frequency-response functions $H_k(\omega)$ and let $\gamma_{kl}(\omega)$ denote the coherency function describing the variability of the motions between two sites k and l. Let $\mathbf{X}_p = [\, A_{p1} \quad B_{p1} \quad \ldots \quad A_{pn} \quad B_{pn} \,]$ denote the set of Fourier coefficients at frequency ω_p and let $\mathbf{\Sigma}_{pp}$ denote the $2n \times 2n$ covariance matrix of these coefficients. The covariance matrix fully defines the zero-mean joint Gaussian distribution of vector $\mathbf{X}_p$. The elements $\mathbf{\Sigma}_{pp,ij}$ of this matrix are determined using Eqs. 10 and 11. The latter equations involve the auto-PSDs $G_{kk}\left(\omega_p\right)$, $k = 1, \ldots, n$, and the cross-PSDs $G_{kl}\left(\omega_p\right)$, $k, l = 1, \ldots, n$, $k \neq l$. To determine the auto-PSDs, first, the auto-PSD of the given realization is estimated through the (optionally smoothed) periodogram given in Eq. 6. In the sequel, the full set of auto-PSDs is obtained in terms of the estimated auto-PSD of the given realization and the site frequency-response functions, using the relation between the PSDs of the surface motions at two locations k and l:

$$G_{ll}(\omega) = G_{kk}(\omega)\,\frac{|H_l(\omega)|^2}{|H_k(\omega)|^2} \tag{12}$$

The above equation is based on the same assumptions as those behind Eq. 4. The full set of cross-PSDs can then be obtained in terms of the auto-PSDs and the given coherency function (see Eq. 1).

Once the covariance matrix is determined, sample vectors from the $2n$-dimensional zero-mean joint Gaussian distribution of $\mathbf{X}_p$ are obtained as $\mathbf{x}_p = \mathbf{L}_p^{\mathrm{T}}\mathbf{z}_p$, where $\mathbf{L}_p$ is an upper triangular matrix such that $\mathbf{L}_p^{\mathrm{T}}\mathbf{L}_p = \Sigma_{pp}$ and $\mathbf{z}_p$ is a $2n$-vector of uncorrelated standard normal variables. A computationally efficient method to obtain $\mathbf{L}_p$ is to write it as $\mathbf{L}_p = \mathbf{D}_p\mathbf{R}_p$, where $\mathbf{D}_p$ is the diagonal matrix of standard deviations and $\mathbf{R}_p$ is the Cholesky decomposition of the correlation matrix.

After sampling at all frequencies $\omega_p = 2\pi p/N\Delta t$, $p = 0, 1, \ldots, N/2$, Eq. 9 is used to obtain the acceleration time-histories at the n sites. Note that the ground motions are fully coherent at $\omega_p = 0$ and the Fourier coefficients have the same values at all locations. Thus, at $\omega_p = 0$, one only needs to sample from a 1-dimensional zero-mean Gaussian distribution with variance $G_{kk}(0)\Delta\omega$.

3.4 Simulation of Stationary Motions with the Conditioned Approach

In the current approach, the Fourier coefficients of the acceleration processes at the target locations are sampled from a joint Gaussian distribution derived by probabilistic conditioning. Consider again the vector of zero-mean Fourier coefficients $\mathbf{X}_p = [\, A_{p1} \quad B_{p1} \quad \ldots \quad A_{pn} \quad B_{pn} \,]$ at frequency ω_p, and the $2n \times 2n$ covariance matrix $\mathbf{\Sigma}_{pp}$ of these coefficients. The vector $\mathbf{X}_p$ is partitioned into two subvectors, $\mathbf{X}_{p1}$ and $\mathbf{X}_{p2}$, with the former including the Fourier coefficients at sites with known ground motions. The conditional distribution of $\mathbf{X}_{p2}$ given $\mathbf{X}_{p1} = \mathbf{x}_{p1}$ is jointly normal with mean:

$$\mathbf{M}_{p,21} = \mathbf{\Sigma}_{pp,21}\left(\mathbf{\Sigma}_{pp,11}\right)^{-1}\mathbf{x}_{p1} \tag{13}$$

and covariance matrix:

$$\mathbf{\Sigma}_{p,22\,11} = \mathbf{\Sigma}_{pp,22} - \mathbf{\Sigma}_{pp,21}\left(\mathbf{\Sigma}_{pp,11}\right)^{-1}\mathbf{\Sigma}_{pp,12} \tag{14}$$

where $\mathbf{\Sigma}_{pp,ij}$ denotes the sub-matrix of $\mathbf{\Sigma}_{pp}$ giving the covariance of vectors $\mathbf{X}_{pi}$ and $\mathbf{X}_{pj}$. The covariance matrix $\mathbf{\Sigma}_{pp}$, is obtained as described in the previous subsection.

The case when the acceleration process is specified at location $k = 1$ only is herein considered. Accordingly, conditioned acceleration time-histories are simulated for locations $k = 2, \ldots, n$. The $2(n-1)$-dimensional joint Gaussian distribution of the Fourier coefficients for the target $n-1$ locations is defined through the conditional mean vector and covariance matrix in Eqs. 13 and 14 respectively. In these equations, $\mathbf{x}_{p1} = [\, A_{p1} \quad B_{p1} \,]$ is the set of Fourier coefficients of the given accelerogram. At each frequency $\omega_p = 2\pi p/N\Delta\mathrm{t}$, $p = 1, \ldots, N/2$, a sample-set of Fourier coefficients for the target locations is obtained as $\mathbf{x}_{p2} = \mathbf{M}_{p,2|1} + \mathbf{L}^{\mathrm{T}}_{p,2|1}\mathbf{z}_p$, where $\mathbf{L}_{p,2\,1}$ is an upper triangular matrix such that $\mathbf{L}^{\mathrm{T}}_{p,2|1}\mathbf{L}_{p,2|1} = \mathbf{\Sigma}_{pp,22|11}$, and $\mathbf{z}_p$ is a $2(n-1)$-vector of uncorrelated standard normal variables. Sampling is not required for $p = 0$, because at $\omega_p = 0$ the ground motions are fully coherent and the Fourier coefficients have the same values at all locations. After the vectors $\mathbf{x}_{p2}$ at all frequencies are obtained, Eq. 9 is used to assemble the realizations of acceleration time-histories at the target locations.

3.5 Extension to Non-stationary Motions

As explained earlier, typical earthquake accelerograms that do not contain a directivity pulse can be seen as consisting of nearly-stationary segments. The segments should be defined so that they maintain nearly time-invariant statistical characteristics, i.e. variance, predominant frequency and bandwidth, respectively measured in terms of the integral of the squared acceleration in time, the cumulative count of zero-level up-crossings and the cumulative count of negative maxima or positive minima (see also the subsection on estimation of the coherency modulus).

The basic idea of the non-stationary extension of the unconditioned simulation is to apply the method described earlier to each "stationary" segment of the given accelerogram and then, for each location, assemble the entire realization by joining together the corresponding simulated segments. Following the segmentation of the given accelerogram, both ends of each segment need to be tapered with appropriate (e.g. cosine-type) functions so as not to introduce fake high-frequency components in the Fourier series. To avoid shifting the segments for different sites, the wave-passage effect is separately applied as a deterministic time-shift on the entire realization. Finally, the shifted accelerograms are further processed following standard techniques in earthquake engineering, i.e. subtraction of the mean value of the entire acceleration time-history, application of a short cosine taper function to set the initial value to zero and application of a high-pass filter to ensure zero residual velocity and displacement. The resulting acceleration time-histories are integrated to obtain the corresponding velocity and displacement realizations.

The non-stationary extension of the conditioned simulation method is performed in a manner similar to that described above for the unconditioned simulation. However, in order to obtain a consistent set of ground motions, the given accelerogram at the reference site must be slightly modified by joining together the tapered segments and post-processing the entire time-history in a manner identical to the simulated motions. The resulting motion at the reference site does not have any random characteristics but is slightly different from the given record. The segmentation and post-processing mainly influence the low-frequency content of the motion, which is more apparent in the displacement waveform. As a result, the displacement time-history of the original record may somewhat differ from the simulated displacement time-history at zero distance. If accurate representation of the displacement time-history of the original record is important, the following alternative procedure can be applied: (a) the low-frequency component of the original record is separated, e.g. by use of a high-pass filter; (b) conditioned non-stationary motions are simulated based on the remaining component; (c) the low-frequency component is added back to the simulated time-histories after it has been deterministically modified to account for the wave-passage effect and, optionally, for the site-response effect.

3.6 Example Application

An example application from Konakli and Der Kiureghian (2012a) is herein presented in brief. Support motions are simulated for an example four-span bridge in California with its five supports located at sites with varying soil conditions. The five supports comprise abutment 1, bent 2, bent 3, bent 4 and abutment 5. The acclererogram at the reference site (abutment 1) is the fault-normal component of the Izmit record from the 1999 Kocaeli earthquake. For further details on the bridge configuration and the characteristics of the ground motion random field, the reader is referred to Konakli and Der Kiureghian (2012a).

Figure 4 shows example sets of support motions generated with the unconditioned and conditioned approaches (left and right graphs respectively). For each example simulation, acceleration, velocity and displacement time-histories at the five supports are shown. Note that both simulation approaches preserve the non-stationary nature of the ground motion and that all records approach zero with increasing time. The motions in the pair of abutments 1 and 5 and the pair of bents 2 and 4 differ only due to incoherence and wave passage, and thus, have the same frequency contents. For any other pair of support motions, the variability is additionally due to the effect of varying soil conditions. These differences in the frequency contents are more apparent in the acceleration than in the velocity and displacement time-histories, with the lower frequency contents indicating softer sites.

Figure 5 shows 5% damped pseudo-acceleration response spectra at each support point for 20 realizations obtained from unconditioned and conditioned simulations (left and right graphs respectively). For the unconditioned case, the variances at all support points are similar, which, as explained before, is a desirable characteristic for ground motions to be used in statistical analyses of structural responses. For the conditioned case, one notes the increasing variance of the spectral amplitude with increasing distance from abutment 1, at which the variance is zero.

Figure 6 compares the acceleration coherency estimates from the simulated motions with the corresponding target theoretical models for an example pair of support points (abutment 1 and bent 3). The real and imaginary parts of the coherency function are shown in the upper and bottom graphs respectively. The coherency estimates are obtained by averaging the estimates from 20 realizations. Excellent agreement of the coherency estimates with the theoretical model validates the accuracy of both the unconditioned and the conditioned approaches (see left and right graphs of the figure respectively). It is noted that an equally good agreement of the estimated coherency with the target theoretical models has also been verified for the other pairs of supports.

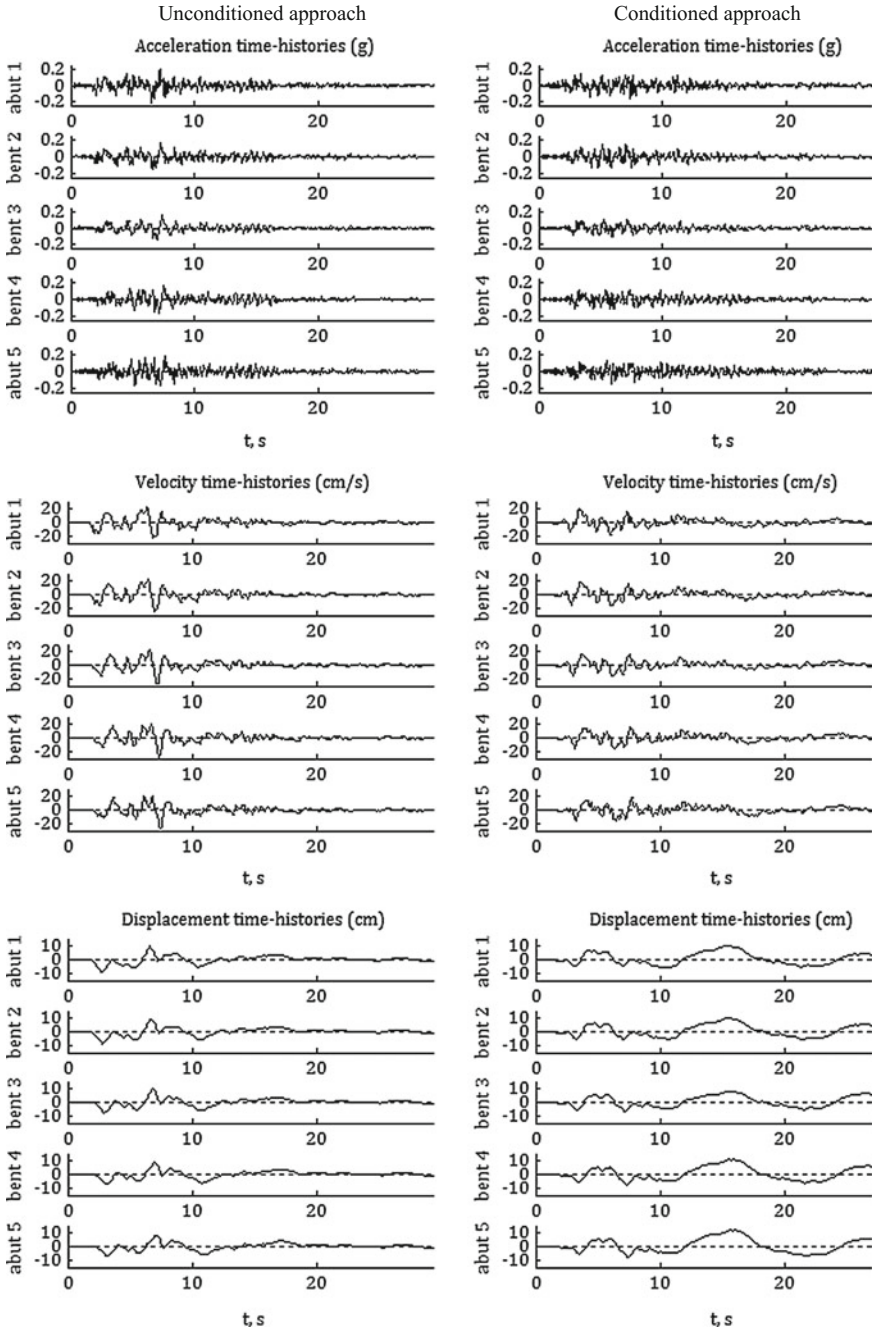

Fig. 4 Example sets of simulated support motions

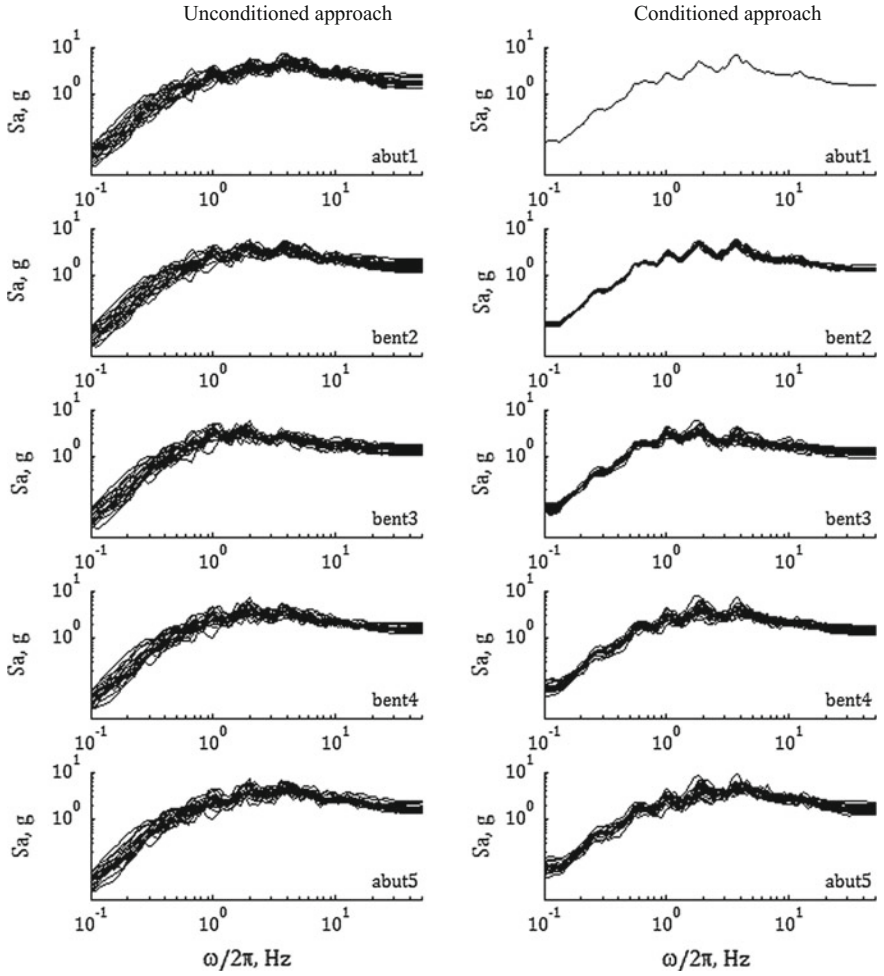

Fig. 5 Pseudo-acceleration response spectra for 20 simulated arrays

4 Structural Response to Differential Support Excitation

4.1 Linear Response Analysis with Response-Spectrum Methods

Analysis of structural response to differential support excitations can be performed using time-history analysis (e.g. Saxena et al. 2000; Sextos et al. 2004; Lou and Zerva 2005; Lupoi et al. 2005) the methods of random vibration (e.g. Dumanogluid and Soyluk 2003; Zembaty and Rutenberg 2002; Zhang et al. 2009; Heredia-Zavoni et al. 2015) or response spectrum methods (e.g. Berrah and Kausel 1992;

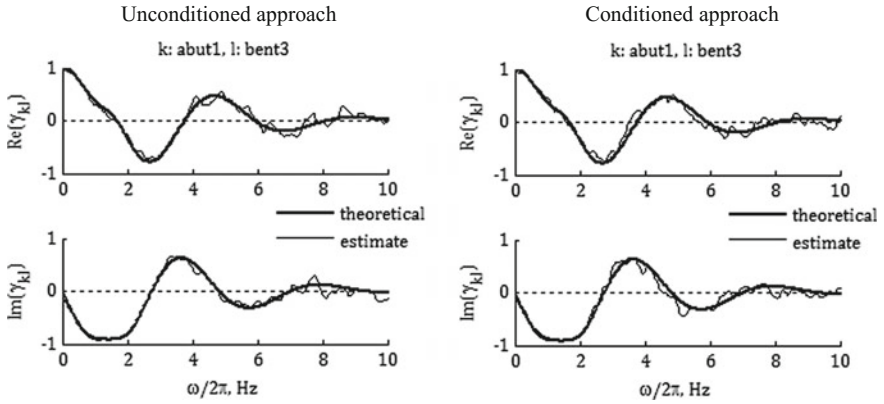

Fig. 6 Acceleration coherency estimates from 20 simulated arrays

Der Kiureghian and Neuenhofer 1992; Konakli and Der Kiureghian 2011a). The random vibration and response spectrum approaches provide a statistical characterization of the response and therefore, their results are not specific to a particular set of ground motions. In this respect, the aforementioned two approaches are deemed advantageous to time-history analysis. Due to the simplicity of characterizing ground motions with response spectra, the response-spectrum approach is particularly appealing in engineering practice.

The Multiple-Support Response-Spectrum (MSRS) rule, developed by Der Kiureghian and Neuenhofer (1992), evaluates the mean peak response of multiply-supported linear structures subjected to spatially varying ground motions. This rule has become a popular method of analysis of multiply-supported structures (see, e.g. Kahan et al. 1996; Soyluk 2004; Wang and Chen 2005; Yu and Zhou 2008; Wang and Der Kiureghian 2014) and is also incorporated by seismic codes (Eurocode 8 1998). The original formulation of this method only considered responses that could be expressed as linear functions of the total displacements at unconstrained degrees of freedom (DOF) of the structure. Konakli and Der Kiureghian (2011a) generalized the original formulation to account for response quantities that also depend on the support motions. Such dependence is pervasive among response quantities of interest; for instance, when rotational DOF are condensed out in the analysis, most response quantities of interest indirectly depend on the support motions. Konakli and Der Kiureghian (2011a) further developed an extended version of the MSRS rule that accounts for quasi-static contribution of truncated high-frequency modes. This extension is particularly important in engineering practice, where computational costs necessitate the truncation of modes beyond a number far smaller than the total number of DOF of the structure. The generalized and extended MRSS rules are described in the sequel.

4.2 The Generalized MSRS Rule

Consider a linear structural system with N unconstrained DOF and subjected to m support motions. Let $\mathbf{x} = [\, x_1 \quad \ldots \quad x_N \,]^{\mathrm{T}}$ denote the N-vector of (total) displacements at the unconstrained DOF and $\mathbf{u} = [\, u_1 \quad \ldots \quad u_m \,]^{\mathrm{T}}$ denote the m-vector of prescribed support displacements. Assuming classical damping, let $\mathbf{\Phi} = [\, \mathbf{\Phi}_1 \quad \ldots \quad \mathbf{\Phi}_N \,]$, ω_i and, ζ_i, $i = 1, \ldots, N$, respectively denote the modal matrix, natural frequencies, and modal damping ratios of the fixed-base structure. Moreover, let $s_{ki}(t)$ denote the normalized response of the ith mode to the kth support motion, obtained as the solution to:

$$\ddot{s}_{ki}(t) + 2\zeta_i \omega_i \dot{s}_{ki}(t) + \omega_i^2 s_{ki}(t) = -\ddot{u}_k(t) \tag{15}$$

A generic response quantity of interest $z(t)$ can be written as a linear combination of the support displacements and the displacements at the unconstrained DOF:

$$z(t) = \mathbf{q}_u^T \mathbf{u}(t) + \mathbf{q}_x^T \mathbf{x}(t) \tag{16}$$

where $\mathbf{q}_u = [\, q_{u,1} \quad \ldots \quad q_{u,m} \,]^{\mathrm{T}}$ and $\mathbf{q}_x = [\, q_{x,1} \quad \ldots \quad q_{x,N} \,]^{\mathrm{T}}$ are coefficient vectors. Equation 16 represents a generalization of the original formulation by Der Kiureghian and Neuenhofer (1992), who considered $z(t)$ a function of $\mathbf{x}(t)$ only. This generalization allows consideration of response quantities that are functions of displacements at both the constrained as well as support DOF, e.g. the drift of a bridge column or an internal force of a structural model with condensed rotational DOF.

Based on principles of modal analysis, Eq. 16 can be written as (Konakli and Der Kiureghian 2011a):

$$z(t) = \sum_{k=1}^{m} a_k u_k(t) + \sum_{k=1}^{m} \sum_{i=1}^{N} b_{ki} s_{ki}(t) \tag{17}$$

where a_k represents the response quantity of interest when the kth support DOF is statically displaced by a unit amount while all other support DOF remaining fixed, and b_{ki} represents the contribution of the ith mode to the response arising from the excitation at the kth support DOF when the normalized modal response $s_{ki}(t)$ is equal to unity. The coefficients a_k and b_{ki} are given by:

$$a_k = q_{u,k} + \mathbf{q}_x^T \mathbf{r}_k \tag{18}$$

where $\mathbf{r}_k$ represents the displacements at the unconstrained DOF when the kth support DOF is displaced by a unit amount, and:

$$b_{ki} = \mathbf{q}_x^T \boldsymbol{\Phi}_i \beta_{ki} \tag{19}$$

where $\beta_{ki} = \boldsymbol{\Phi}_i^{\mathrm{T}} \mathbf{M}\mathbf{r}_k / \boldsymbol{\Phi}_i^{\mathrm{T}} \mathbf{M} \boldsymbol{\Phi}_i$ is the modal participation factor associated with the ith mode and kth support DOF; in the latter expression, $\mathbf{M}$ denotes the mass matrix of the structure associated with the unconstrained DOF. The coefficients a_k and b_{ki} depend only on the structural properties and can be computed by use of any conventional static analysis program (see Konakli and Der Kiureghian 2011a, b, for further details on properties of these coefficients and their computation).

Using Eq. 17 and the principles of stationary random vibration theory, the mean of the peak of the generic response quantity $z(t)$ can be approximately obtained in the form (Der Kiureghian and Neuenhofer 1992):

$$\begin{aligned} &E[\max|z(t)|] \\ &\approx \Bigg[\sum_{k=1}^{m} \sum_{l=1}^{m} a_k a_l \rho_{u_k u_l} u_{k,max} u_{l,max} \\ &+ 2 \sum_{k=1}^{m} \sum_{l=1}^{m} \sum_{j=1}^{N} a_k b_{lj} \rho_{u_k s_{lj}} u_{k,max} D_l(\omega_j, \zeta_j) \\ &+ \sum_{k=1}^{m} \sum_{l=1}^{m} \sum_{i=1}^{N} \sum_{j=1}^{N} b_{ki} b_{lj} \rho_{s_{ki} s_{lj}} D_k(\omega_i, \zeta_i) D_l(\omega_j, \zeta_j) \Bigg]^{1/2} \end{aligned} \tag{20}$$

The preceding equation represents the MSRS combination rule. The mean of the peak response is given in terms of: (i) the structural properties, reflected in the coefficients a_k and b_{ki}, (ii) the mean peak ground displacements $u_{k,\max}$ and the ordinates of the mean displacement response spectra $D_k(\omega_i, \zeta_i)$, and (iii) three sets of correlation coefficients. The latter comprise the coefficients $\rho_{u_k u_l}$, describing the correlation between the kth and lth support displacements, the coefficients $\rho_{u_k s_{lj}}$, describing the correlation between the kth support displacement and the response of the jth mode to the lth support motion, and the coefficients $\rho_{s_{ki} s_{lj}}$, describing the correlation between the responses of the ith and jth modes to the kth and lth support motions respectively.

The correlation coefficient for two processes $x(t)$ and $y(t)$ is defined as:

$$\rho_{xy} = \frac{\int_{-\infty}^{+\infty} G_{xy}(\omega) d\omega}{\left[\int_{-\infty}^{+\infty} G_{xx}(\omega) d\omega \int_{-\infty}^{+\infty} G_{yy}(\omega) d\omega\right]^{1/2}} \tag{21}$$

where $G_{xx}(\omega)$ is the auto-PSD of $x(t)$, and $G_{xy}(\omega) = \gamma_{xy}(\omega)[G_{xx}(\omega) G_{yy}(\omega)]^{1/2}$ is the cross-PSD of $x(t)$ and $y(t)$, with $\gamma_{xy}(\omega)$ denoting the coherency function. The processes involved in the computation of the correlation coefficients of the MSRS rule are the support displacements $u_k(t)$ and the normalized modal responses $s_{ki}(t)$. The auto-PSD of $u_k(t)$ can be obtained in terms of the response spectrum $D_k(\omega, \zeta)$, while the auto-PSD of $s_{ki}(t)$ additionally involves the frequency-response function

of the *i*th mode (see Der Kiureghian and Neuenhofer 1992, for details). It follows that the complete set of correlation coefficients can be obtained in terms of the response spectra at the support DOF, the coherency function and the modal properties of the structure.

Konakli and Der Kiureghian (2012b) investigated the accuracy of the MSRS rule by comparing the MSRS estimates of mean peak structural responses with the corresponding 'exact' mean values obtained by time-history analysis. The considered structural systems comprised four bridge models designed by the California Department of Transportation and characterized by distinctly different configurations and dynamic properties. The focus of the study was set on pier drifts, which are quantities particularly important in performance-based design of bridges. The analysis assumed uniform soil conditions, but incorporated effects of incoherence and wave passage. Support-motion arrays for the time-history analysis were obtained with the unconditioned simulation method, described in the previous section. The study considered two recorded accelerograms as seeds in the simulation of the support motions and two levels of incoherence. For each ground motion random field, 20 ensembles of ground-motions arrays were generated. The mean response spectra of the motions at all supports of a bridge were used as input in the MSRS analysis.

As an example, Fig. 7 shows the time histories of three pier drifts (from different bridges) for a particular ground-motion random field (20 realizations) together with the corresponding MSRS estimates, the latter depicted by horizontal lines. Examining absolute values of the MSRS errors, the mean and standard deviation over all pier drifts and ground-motion random fields considered were found equal to 4.6% and 3.7% respectively. The maximum error observed was 12.3%, but in most cases, the errors were smaller than 10%.

It is emphasized that the MSRS method is intended for use in conjunction with smooth response spectra that represent broadband excitations and a smooth coherency function. In the aforementioned analysis however, jagged response spectra from relatively narrowband excitations were used. Furthermore, the smooth coherency function used for evaluation of the correlation coefficients in the MSRS analysis differs from the actual coherency values for pairs of simulated support motions, which may exhibit fluctuations around the theoretical model. In view of these differences, the reported MSRS errors are deemed remarkably small.

4.3 The Extended MSRS Rule

When high-frequency modes are truncated, an improved approximation of the response can be obtained by accounting for the quasi-static contributions of the truncated modes. If ω_i is large relative to the frequencies of the input excitation, the last term in the left-hand side of Eq. 15 is dominant and the *i*th normalized

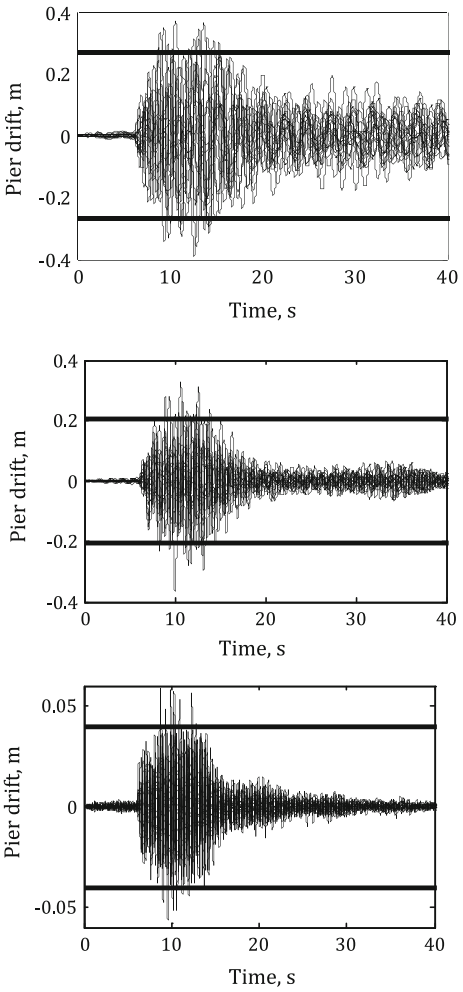

Fig. 7 Response time-histories and corresponding MSRS estimates

modal response to the kth support motion can be approximated by $s_{ki}(t) \approx -\omega_i^{-2}\ddot{u}_k(t)$. Using this relation in Eq. 17 for modes $i > n$ leads to:

$$z(t) \approx \sum_{k=1}^{m} a_k u_k(t) + \sum_{k=1}^{m}\left[\sum_{i=1}^{n} b_{ki} s_{ki}(t) - \sum_{i=n+1}^{N} \frac{b_{ki}}{\omega_i^2}\ddot{u}_k(t)\right] \tag{22}$$

The coefficients b_{ki} for $i > n$ can be eliminated from Eq. 22 by employing the identity (Konakli and Der Kiureghian 2011a):

$$-\sum_{i=1}^{N}\frac{b_{ki}}{\omega_i^2}=-\mathbf{q}_x^T\mathbf{K}^{-1}\mathbf{M}\mathbf{r}_k \tag{23}$$

where $\mathbf{K}$ denotes the stiffness matrix of the structure associated with the unconstrained DOF. By rearranging terms, one obtains:

$$\sum_{i=n+1}^{N}\frac{b_{ki}}{\omega_i^2}=\mathbf{q}_x^T\mathbf{K}^{-1}\mathbf{M}\mathbf{r}_k-\sum_{i=1}^{n}\frac{b_{ki}}{\omega_i^2}=d_k \tag{24}$$

Using the above identity, Eq. 22 can be written in a form that involves the dynamic properties of only the first n modes:

$$z(t)\approx\sum_{k=1}^{m}a_k u_k(t)+\sum_{k=1}^{m}\sum_{i=1}^{n}b_{ki}s_{ki}(t)-\sum_{k=1}^{m}d_k\ddot{u}_k(t) \tag{25}$$

Note that this improved expression of the response additionally involves the support accelerations $\ddot{u}_k(t)$.

Based on Eq. 25 and principles of random vibration theory, the extended MSRS rule that accounts for contributions of truncated modes is obtained as:

$$\begin{aligned}
&E[max|z(t)|]\\
&\approx\Bigg[\sum_{k=1}^{m}\sum_{l=1}^{m}a_k a_l\rho_{u_k u_l}u_{k,max}u_{l,max}\\
&+2\sum_{k=1}^{m}\sum_{l=1}^{m}\sum_{j=1}^{n}a_k b_{lj}\rho_{u_k s_{lj}}u_{k,max}D_l(\omega_j,\zeta_j)\\
&+\sum_{k=1}^{m}\sum_{l=1}^{m}\sum_{i=1}^{n}\sum_{j=1}^{n}b_{ki}b_{lj}\rho_{s_{ki}s_{lj}}D_k(\omega_i,\zeta_i)D_l(\omega_j,\zeta_j)\\
&+\sum_{k=1}^{m}\sum_{l=1}^{m}d_k d_l\rho_{\ddot{u}_k\ddot{u}_l}\ddot{u}_{k,max}\ddot{u}_{l,max}-2\sum_{k=1}^{m}\sum_{l=1}^{m}\rho_{u_k\ddot{u}_l}u_{k,max}\ddot{u}_{l,max}\\
&-2\sum_{k=1}^{m}\sum_{l=1}^{m}\sum_{i=1}^{n}b_{ki}d_l\rho_{s_{ki}\ddot{u}_l}D_k(\omega_i,\zeta_i)\ddot{u}_{l,max}\Bigg]^{1/2}
\end{aligned} \tag{26}$$

The extended MSRS rule adds the last three terms to the original formulation. The first of these terms represents the static contribution of the truncated modes. The second term arises from the covariances of the support displacements and accelerations, while the last term arises from the covariances between the responses of the included modes and the static responses of the truncated modes. These terms involve the peak support accelerations and three sets of correlation coefficients. The new coefficients $\rho_{\ddot{u}_k\ddot{u}_l}$, $\rho_{u_k\ddot{u}_l}$ and $\rho_{s_{ki}\ddot{u}_l}$ respectively describe: the correlation between the ground accelerations at the kth and lth support DOF, the correlation between the ground displacement at the kth support DOF and the ground acceleration at the lth support DOF, and the correlation between the ith modal response to the excitation

at the kth support DOF and the ground acceleration at the lth support DOF. The accuracy of the MSRS coefficients $\rho_{u_k u_l}$, $\rho_{\ddot{u}_k \ddot{u}_l}$ and $\rho_{u_k \ddot{u}_l}$ (the last two appearing only in the extended rule) was examined by Konakli (2013).

For an assessment of the improvement obtained with the extended rule, the interested reader is referred to Konakli and Der Kiureghian (2011a).

4.4 Non-linear Response: The 'Equal Displacement' Rule

Non-linear response-history analysis (RHA) represents the most accurate method for the evaluation of inelastic structural response to a specified set of support motions. However, non-linear RHA faces two important constraints: (i) it is computationally costly and (ii) by providing results that are particular to the selected input time-histories, it has limited ability to characterize effects of uncertainties that surround future ground motions. Although response-spectrum methods overcome these limitations, they are restricted to linear response analysis. It is thus of interest to investigate relations between non-linear responses and their linear counterparts.

Observations by Veletsos and Newmark (1960) on the responses of elasto-plastic and the corresponding linear single-DOF systems gave rise to the 'equal displacement' rule. Under certain conditions, this rule allows estimation of the maximum displacement response of inelastic structures from analysis of their elastic counterparts. The 'equal displacement' rule is particularly useful in displacement-based design procedures (Moehle 1992, Kowalsky 2002), which are of growing interest in performance-based earthquake engineering. Therefore, several studies have been devoted to assessing its accuracy and limitations for different types of structures and ground motions. The applicability of the 'equal displacement' rule for extended structures subjected to differential support motions was investigated by Konakli and Der Kiureghian (2014); a brief description of the analysis and main findings of this study is given next.

Konakli and Der Kiureghian (2014) compared responses from linear and non-linear time-history analyses for idealized models of four actual bridges in California with distinctly different configuration and dynamic properties. They performed statistical analyses of the maximum pier drifts for ground-motion random fields with different frequency contents and spatial variability characteristics. In particular, the analysis considered two seed recorded accelerograms and four cases of spatial variability:

- Case 1 represents uniform support excitations.
- Case 2 incorporates effects of incoherence and wave passage, but assumes uniform soil conditions.
- Case 3 differs from case 2 in considering a higher level of incoherence.
- Case 4 differs from case 2 in assuming varying soil profiles.

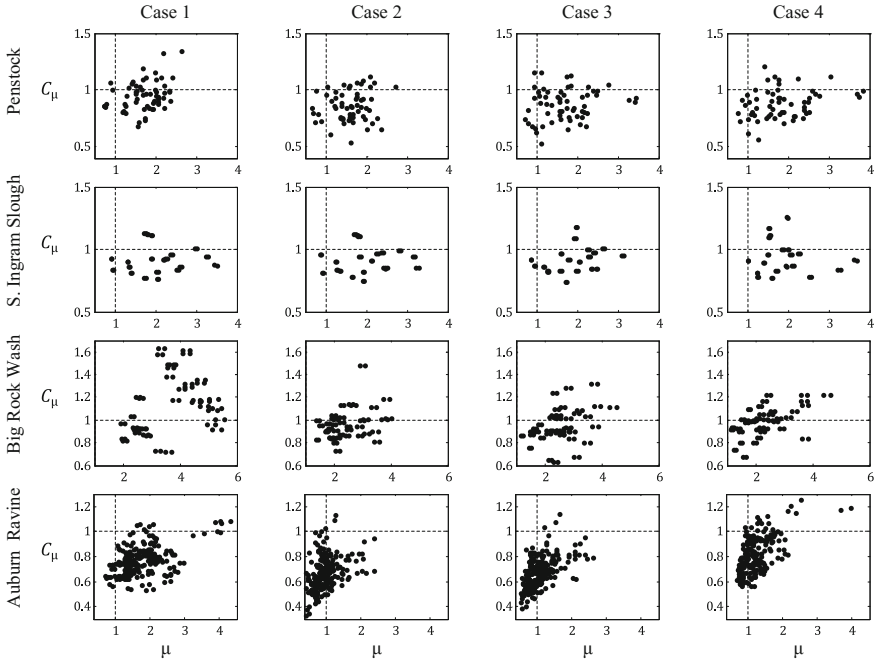

Fig. 8 Inelasticity versus ductility factors

As ensemble of 20 support-motion arrays were simulated for each bridge model and ground-motion random field. Based on the respective pier-drift responses from linear and non-linear RHA, Konakli and Der Kiureghian (2014) analyzed the statistics of two dimensionless response quantities: (i) the ductility factor μ, representing the ratio of peak pier drift from non-linear RHA to the corresponding yield drift, and (ii) the inelasticity factor C_μ, representing the ratio of peak non-linear to peak linear drift. Graphs of inelasticity versus ductility factors for one seed accelerogram are shown in Fig. 8, where graphs in the same row correspond to a single bridge model, whereas graphs in the same column correspond to a certain case of spatial variability.

Under uniform support motions (case 1) and for moderate levels of inelastic behavior, the 'equal displacement' rule was found fairly accurate for cases when the fundamental period of the bridge was beyond the acceleration-controlled range of the response spectrum. For bridges with shorter fundamental periods, the rule was found non-conservative for cases with mean ductility factors in the range from 3 to 4 and overly conservative for cases with mean ductility factors smaller than approximately 2. Wave passage and incoherence (cases 2 and 3) reduced the mean inelasticity factors, but the latter increased when the effect of differential site response was additionally incorporated by locating piers on softer soils (case 4). Effects of spatial variability on the pier-drift response were more pronounced for

longer and stiffer bridges. In most cases, mild or moderate positive linear correlations between inelasticity and ductility factors were observed, with the higher correlations observed for bridges with fundamental periods shorter than the transition period between the acceleration- and velocity-controlled ranges of the response spectrum.

5 Conclusions and Perspectives

This chapter provided an overview on methods for incorporating effects of ground-motion spatial variability in seismic response assessment, based on concepts of stochastic time-series analysis and random vibration theory. The examined topics included the modeling of ground-motion spatial variability, the simulation of spatially varying ground-motion arrays and the evaluation of structural response to differential support motions. The modeling of the ground-motion spatial variability relied on the coherency function; the different elements of this function as well as its estimation based on recorded motions were explained. The presented method for simulating spatially varying ground motions incorporates the incoherence, wave-passage and site-response effects and preserves the temporal and spectral non-stationarity of a specified reference accelerogram. In particular, the unconditioned simulation approach yields arrays with uniform variability that can be used as input for the statistical analysis of structural response. The Multiple-Support Response-Spectrum (MSRS) rule and its extended version were described as a means for obtaining a statistical characterization of the peak linear structural response. Finally, investigations into the relations between peak linear and non-linear responses under effects of ground-motion spatial variability provided insights into the validity of the 'equal displacement' rule in this case of excitation.

Inspired by the particular case of seismic response analysis to correlated support motions, this chapter closes with the hope that methods of stochastic analysis will be more widely employed in engineering practice, as a valuable tool for dealing with the significant uncertainties facing engineering design. The importance of a systemic perspective that properly accounts for the pertinent inter-dependencies and correlations is also emphasized. The most modern research findings in the aforementioned areas can be effectively transferred into engineering practice through the continuing education of engineers, the interactions between research and practice and the systematic research-informed updating of the engineering codes.

Acknowledgements I would like to express my deep gratitude to Professor Armen Der Kiureghian for his excellent academic advising and the invaluable support and encouragement he provided to me not only during my doctoral years, but also in the pursuit of my dreams thereafter. His personality, values and accomplishments are a unique source of inspiration. I have the honor of keeping one of his paintings, depicting the Bay Bridge in San Francisco, a reminder of my very meaningful graduate years at Berkeley that opened up new wonderful horizons in my life.

References

Abrahamson NA, Schneider JF, Stepp JC (1991) Empirical spatial coherency functions for application to soil-structure interaction analyses. Earthq Spectra 7:1–28

Ancheta TD, Stewart JP, Abrahamson NA (2011) Engineering characterization of earthquake ground motion coherency and amplitude variability. In: Earthquake engineering, UCLA civil and environmental engineering, UC Los Angeles

Berrah M, Kausel E (1992) Response spectrum analysis of structures subjected to spatially varying motions. Earthq Eng Struct Dyn 21:461–470

Brillinger RD (2001) Time series: data analysis and theory. Soc Ind Appl Math

Chatfield C (2004) The analysis of time series: an introduction, 6th edn. CRC Press LLC

Der Kiureghian A (1996) A coherency model for spatially varying ground motions. Earthq Eng Struct Dyn 25:99–111

Der Kiureghian A, Ke JB (1988) The stochastic finite element method in structural reliability. Probab Eng Mech 3:83–91

Der Kiureghian A, Liu PL (1986) Structural reliability under incomplete probability information. J Eng Mech 112:85–104

Der Kiureghian A, Neuenhofer A (1992) Response spectrum method for multiple-support seismic excitation. Earthq Eng Struct Dyn 21:713–740

Der Kiureghian A, Zhang Y, Li CC (1994) Inverse reliability problem. J Eng Mech 120: 1154–1159

Dumanogluid A, Soyluk K (2003) A stochastic analysis of long span structures subjected to spatially varying ground motions including the site-response effect. Eng Struct 25:1301–1310

Eurocode 8: Design of structures for earthquake resistance-part 2: bridges (1998)

Harichandran RS, Vanmarcke EH (1986) Stochastic variation of earthquake ground motion in space and time. J Eng Mech 112:154–174

Heredia-Zavoni E, Santa-Cruz S, Silva-González FL (2015) Modal response analysis of multi-support structures using a random vibration approach. Earthq Eng Struct Dyn 44(13):2241–2260

Kahan M, Gibert RJ, Bard PY (1996) Influence of seismic waves spatial variability on bridges: a sensitivity analysis. Earthq Eng Struct Dyn 25:795–814

Kameda H, Morikawa H (1992) An interpolating stochastic process for simulation of conditional random fields. Probab Eng Mech 7:243–254

Konakli K, Der Kiureghian A (2011a) Extended MSRS rule for seismic analysis of bridges subjected to differential support motions. Earthq Eng Struct Dyn 40:1315–1335

Konakli K, Der Kiureghian A (2011b) Stochastic dynamic analysis of bridges subjected to spatially varying ground motions. Report No. 2011/105, Pacific earthquake engineering research center, University of California, Berkeley

Konakli K, Der Kiureghian A (2012a) Simulation of spatially varying ground motions including incoherence, wave-passage and differential site-response effects. Earthq Eng Struct Dyn 41:495–513

Konakli K, Der Kiureghian A (2012b) Evaluation of the accuracy of the Multiple Support Response Spectrum (MSRS) method. In: Proceedings of 15th world conference on earthquake engineering, Lisbon, Portugal

Konakli K (2013) Spatial correlations in seismic response analysis of extended structures. In: 11th international conference on structural safety and reliability, Columbia University, New York

Konakli K, Der Kiureghian A (2014) Investigation of 'equal displacement' rule for bridges subjected to differential support motions. Earthq Eng Struct Dyn 43(1):23–39

Konakli K, Der Kiureghian A, Dreger D (2014) Coherency analysis of the UPSAR array of accelerograms recorded during the 2004 Parkfield earthquake. Earthq Eng Struct Dyn 43 (5):641–659

Kowalsky MJ (2002) A displacement-based approach for the seismic design of continuous concrete bridges. Earthq Eng Struct Dyn 31:719–747

Liao S, Zerva A (2006) Physically compliant, conditionally simulated spatially variable seismic ground motions for performance-based design. Earthq Eng Struct Dyn 35:891–919
Lou L, Zerva A (2005) Effects of spatially variable ground motions on the seismic response of a skewed, multi-span, RC highway bridge. Soil Dyn Earthq Eng 25:729–740
Luco JE, Wong HL (1986) Response of a rigid foundation to a spatially random ground motion. Earthq Eng Struct Dyn 14:891–908
Lupoi A, Franchin P, Pinto PE, Monti G (2005) Seismic design of bridges accounting for spatial variability of ground motion. Earthq Eng Struct Dyn 34:327–348
Moehle JP (1992) Displacement-based design of RC structures subjected to earthquakes. Earthq Spectra 8:403–428
Priestley MB (1981) Spectral analysis and time series. Academic Press, London
Rezaeian S, Der Kiureghian A (2008) A stochastic ground motion model with separable temporal and spectral nonstationarities. Earthquake Eng Struct Dyn 37:1565–1584
Saxena V, Deodatis G, Shinozuka M, Feng MQ (2000) Development of fragility curves for multi-span reinforced concrete bridges. In: Proceedings of the international conference on monte carlo simulation, Principality of Monaco, Austria
Sextos A, Kappos AJ, Mergos P (2004) Effect of soil-structure interaction and spatial variability of ground motion on irregular bridges: the case of the Krystallopigi Bridge. In: Proceedings of the 13th world conference on earthquake engineering, paper No. 2298, Vancouver, BC, Canada
Song J, Der Kiureghian A (2003) Bounds on system reliability by linear programming. J Eng Mech 129:627–636
Soyluk K (2004) Comparison of random vibration methods for multi-support seismic excitation analysis of long-span bridges. Eng Struct 26:1573–1583
Straub D, Der Kiureghian A (2010) Bayesian network enhanced with structural reliability methods: methodology. J Eng Mech 136:1248–1258
Vanmarcke EH, Fenton GA (1991) Conditioned simulation of local fields of earthquake ground motion. Struct Saf 10:247–264
Veletsos AS, Newmark NM (1960) Effect of inelastic behavior on the response of simple systems to earthquake motions. In: Proceedings of the 2nd world conference on earthquake engineering, Japan, vol 2, pp 895–912
Wang J, Chen H (2005) A new spatial coherence model and analytical coefficients for multi-support response spectrum combination. Earthq Eng Eng Vib 6:225–235
Wang Z, Der Kiureghian A (2014) Multiple-support response spectrum analysis using load-dependent Ritz vectors. Earthq Eng Struct Dyn 43(15):2283–2297
Yu RF, Zhou XY (2008) Response spectrum analysis for non-classically damped linear system with multiple-support excitations. Bull Earthq Eng 6:261–284
Zembaty Z, Rutenberg A (2002) Spatial response spectra and site amplification effects. Eng Struct 24:1485–1496
Zerva A, Harada T (1994) A site-specific model for the spatial incoherence of the seismic ground motions. In: Proceedings of the 5th national conference on earthquake engineering, Chicago, Illinois
Zhang YH, Li QS, Lin JH, Williams FW (2009) Random vibration analysis of long-span structures subjected to spatially varying ground motions. Soil Dyn Earthq Eng 29:620–629

Part IV
Sensitivity Analysis and Optimization

Application of CQC Method to Seismic Response Control with Viscoelastic Dampers

Yutaka Nakamura

Abstract The complete quadratic combination (CQC) modal combination rule for seismic analysis of structures is a great achievement of Professor Armen Der Kiureghian. Among the other various uses of the CQC method, this chapter introduces the application of the CQC method to seismic response control of buildings with dampers to highlight the practical value of the CQC method. The expanded CQC method can accurately estimate the maximum response of buildings installed with response control damping devices and enables performance-based placement design of dampers. In this chapter, the performance-based design procedure of a viscoelastic damper (VED) is introduced for finding the storywise distribution of VEDs in a building such that each peak interstory drift coincides with the corresponding prescribed value. The mechanical properties of the employed VED's dependence on amplitude and frequency of the excitation as well as material temperature are taken into account and a mechanical nonlinear four-element model that comprises two dashpot elements and two spring elements is proposed for the VED. The developed performance-based design procedure utilizes equivalent linearization of the VED and the expanded CQC method, which involves modal analysis with complex eigenvalue analysis. Seismic response analyses are carried out for high-rise building models with optimally placed VEDs, with the results demonstrating the effectiveness of the expanded CQC method and the validity of the proposed performance-based placement-design procedure.

1 Introduction

Various dampers and energy dissipation devices have been developed and are widely used to reduce the earthquake response of buildings, such as the viscoelastic damper (VED), metallic hysteretic damper, friction damper, and viscous fluid damper.

Y. Nakamura (✉)
Institute of Technology, Shimizu Corporation, 3-4-17, Etchujima, Koto-Ku, Tokyo 135-8530, Japan
e-mail: yutaka.nakamura@shimz.co.jp

P. Gardoni (ed.), *Risk and Reliability Analysis: Theory and Applications*,
Springer Series in Reliability Engineering, DOI 10.1007/978-3-319-52425-2_10

VEDs were first used in building structures to reduce wind-induced vibrations (Mahmoodi et al. 1987), and have subsequently been studied and used to reduce the earthquake response of buildings (Soong and Dargush 1997; Cheng et al. 2008; Takewaki 2009). As shown in Fig. 1, a typical VED consists of a VE material or a high damping rubber that is bonded between an inner steel plate and an outer steel plate and is subjected to shear deformation. The story-installation-type VED is generally found in three configurations: brace type, wall type, and column type, as shown in Fig. 2. The VED induces a viscous shear force in response to relative interstory drift, causing energy dissipation, and hence, the VE material properties govern the performance and characteristics of the VED.

Mechanical properties of the VED generally show a significant dependence on the amplitude and frequency of the excitation and material temperature depending on the employed VE material. For the use of VEDs in a building, one should consider their nonlinear characteristics and dependence and study the necessary story-wise placement of the dampers to meet the seismic design performance objectives. Although quite a few previous studies have been carried out on the optimum or effective placement of viscous or viscoelastic dampers, these have dealt with the damper as an ideal mechanical model that comprises a linear dashpot element with/without a linear spring element (Zhang and Soong 1992; Chang et al. 1992; Tsuji and Nakamura 1996; Gluck et al. 1996; Takewaki 1997, 2000; Ribakov and Gluck 1999; Takewaki et al. 1999, 2013; Garcia 2001; Singh and Moreschi

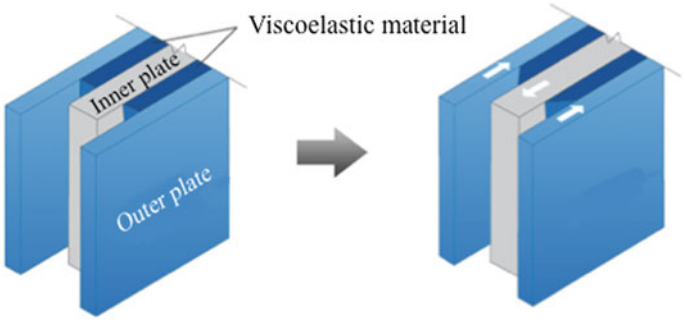

Fig. 1 Principle of VED

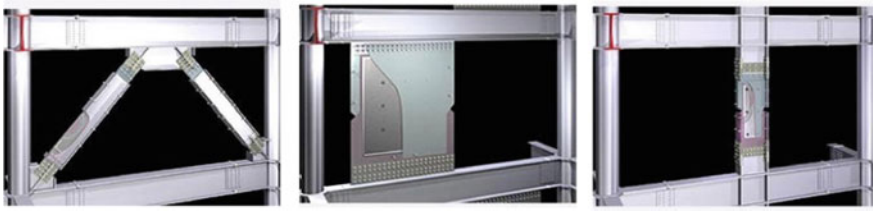

Fig. 2 Configurations of the story-installation-type of VED

2001, 2002; Uetani et al. 2003; Xu et al. 2003; Park et al. 2004; Liu et al. 2004; Lavan and Levy 2005, 2006; Tan et al. 2005; Liu et al. 2005; Silvestri and Trombetti 2007; Cimellaro 2007) and have treated the optimum placement of ideal viscous or viscoelastic dampers installed in a building under seismic excitations. The story-wise placement of supplemental dampers or damping coefficients was found to meet the seismic design constraints or to optimize the values of the target properties. The constraints are mostly imposed on the interstory drifts of a structure subjected to a specified earthquake input, since the interstory drifts can be regarded as the most important seismic design index. The mean peak interstory drifts of the building installed with dampers subjected to the specified design displacement response spectrum can be estimated using the expanded complete quadratic combination (CQC) method, which entails modal analysis with complex eigenvalue analysis (Igusa et al. 1984; Yang et al. 1990).

In addition to the interstory drift criteria, Takewaki (1997) and Takewaki et al. (1999) minimized the sum of amplitudes of the transfer functions evaluated at the undamped fundamental natural frequency of a structure. Lavan and Levy (2005) chose energy-based damage indices based on the hysteretic energy dissipated by the restoring force divided by its hysteretic energy at failure. Tan et al. (2005) and Liu et al. (2005) considered an acceleration-based criterion in addition to the interstory drift criteria. Silvestri and Trombetti (2007) studied various performance indices such as the standard deviation of the roof displacement or the base shear, the average of the standard deviations of the interstory drift angles, and the sum of the standard deviations of the damper forces. Cimellaro (2007) minimized the sum of the norm of the displacement, absolute acceleration, and base shear transfer function evaluated at the fundamental natural frequency.

Various sequential procedures have been proposed to find the optimum placement of the supplemental dampers in a structure. The basic idea is that a controller is optimally located if it is placed at a position where the displacement response of the uncontrolled structure is the largest (Zhang and Soong 1992). To find the optimal location, Gluck et al. (1996) used the solution for the linear quadratic regulator problem, Singh and Moreschi (2001, 2002) employed a gradient-based optimization approach and a genetic algorithm, and Xu et al. (2003) utilized the simplex method. Takewaki (2009) explored the repetitive performance sensitivity analysis, using which the supplemental damper is installed into the story with the highest performance sensitivity.

We have previously developed a wall-type VED using a newly produced VE material with low temperature dependence and proposed a mechanical model for the VED using a nonlinear four-element (NLF) model that comprises two dashpot elements and two spring elements (Nakamura and Kaneko 1998). The NLF model can express the VED dependence on the amplitude and frequency of the excitation and material temperature. In this chapter, after reviewing the developed VED and the proposed NLF model, a placement-design procedure is proposed for the manufactured wall-type VED such that each peak interstory drift is limited to the specified value for a given design response spectrum (Nakamura and Hanzawa 2002; Nakamura et al. 2016). The proposed design procedure utilizes the equivalent

linearization of the VED and the expanded CQC method in the peak response estimation. The validity of the proposed design procedure is demonstrated by design examples of high-rise building models.

2 Review of a Developed VED

The VED generally exhibits large temperature dependence (Chang et al. 1992; Soong and Dargush 1997), which is considered to be a drawback and limits its applicability. A new VED was developed by utilizing a newly produced VE material with low temperature dependence. Based on a series of dynamic tests of the VE material specimen, a mechanical model for the VED was proposed using an NLF model that comprises two nonlinear dashpot elements and two nonlinear spring elements. The validity of the proposed mechanical model of the VED was verified through the dynamic loading tests of a 1/2-scale VED. In this section, the proposed NLF model of the VED is reviewed and its test results are described.

2.1 Mechanical Characteristics of VE Material

The newly developed VE material is made of thermoplastic elastomer of the olefin-styrene series. Table 1 shows the compounding ratios of the VE material. A series of dynamic loading tests were carried out on a test specimen consisting of a 70 mm × 80 mm sheet of the VE material (thickness $d = 5$ mm, total shear area $A_S = 5600$ mm^2) as shown in Fig. 3. The air temperature (T_e) was 20 °C. Figure 4 shows hysteresis loops for an increasing sine wave and for an earthquake interstory drift of the 8th floor of a hypothetical 15-story building (Appendix I).

From the measured hysteresis loop under sinusoidal loading, as shown in Fig. 5, the equivalent shear stiffness, K_{eq}, the equivalent damping coefficient, C_{eq}, and the equivalent damping factor, h_{eq}, were obtained by

$$K_{eq} = \frac{Q}{\delta_{\max}} \tag{1a}$$

$$C_{eq} = \frac{\Delta W}{\pi\, \omega\, \delta_{\max}^2} \tag{1b}$$

Table 1 Compounding ratios of the VE material

	Elastomer	Damping material	Antioxidant
Weight percentage (%)	42–52	42–52	4–8

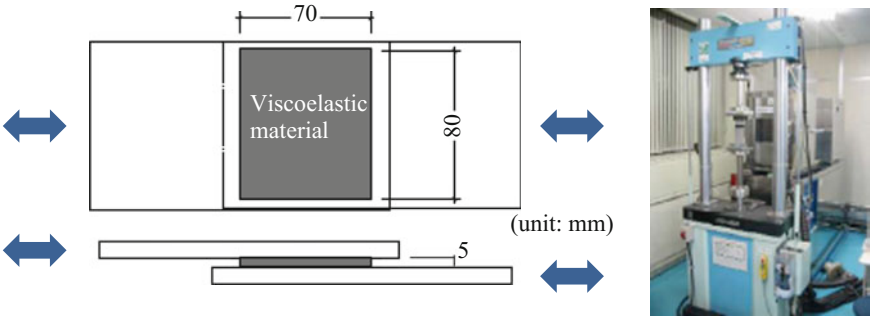

Fig. 3 Test specimen of VE material and the dynamic testing machine

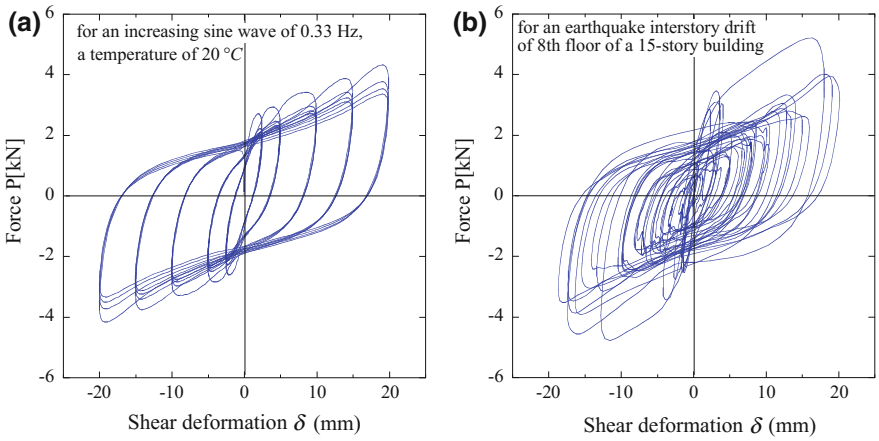

Fig. 4 Resisting force characteristics of VE material

Fig. 5 Evaluation of equivalent stiffness and area of a hysteresis loop

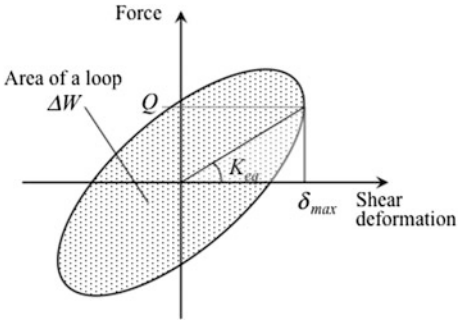

$$h_{eq} = \frac{\omega C_{eq}}{2K_{eq}} \tag{1c}$$

where ω indicates the circular frequency of a sine wave.

Figure 6 shows the obtained values of K_{eq}, C_{eq} and h_{eq} for the shear strain, $\gamma_{\max}(=\delta_{\max}/d)$, of the VE material at air temperature, T_e, of 20 °C, where $\delta_{\max}$ indicates the amplitude of the sinusoidal wave. Figure 6 indicates the amplitude and frequency dependence of the VE material, and both K_{eq} and C_{eq} decrease with increasing $\gamma_{\max}$, while h_{eq} is almost constant at about 0.4 irrespective of the amplitude and frequency of the input.

Figure 7 shows K_{eq} and C_{eq} for T_e = 0–40 °C where K_{eq} and C_{eq} values are normalized by the value at T_e = 20 °C, respectively. This figure indicates that the temperature dependence of K_{eq} and C_{eq} can be well expressed by $\exp\{-0.017(T_e - 20)\}$. The temperature dependence is much smaller than that for the other viscoelastic materials for the VED that have been in practical use.

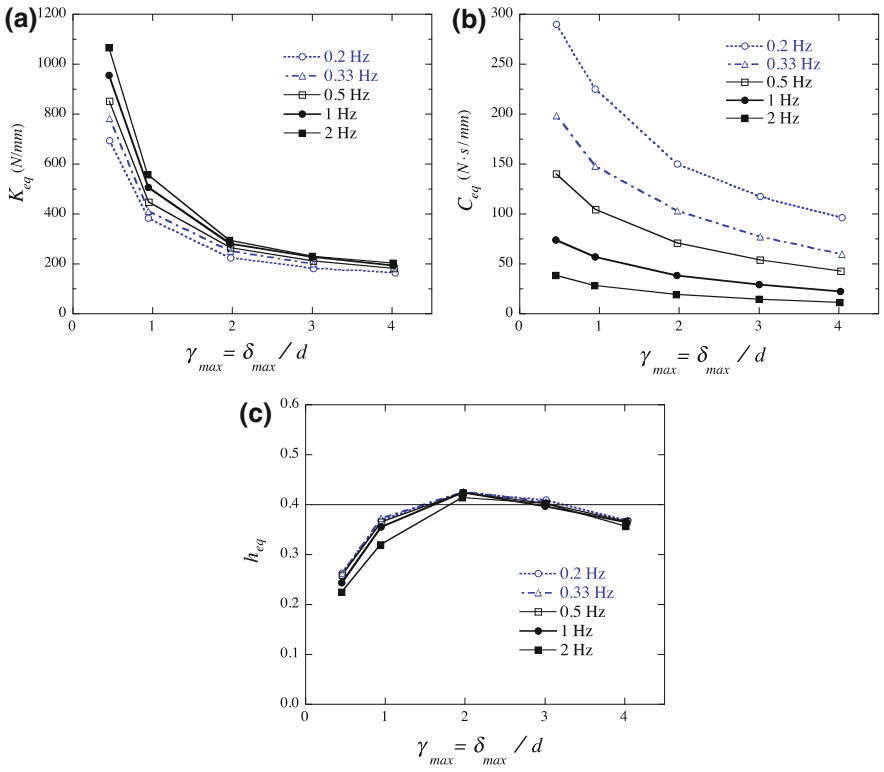

Fig. 6 Amplitude- and frequency-dependency of mechanical characteristics of VE material

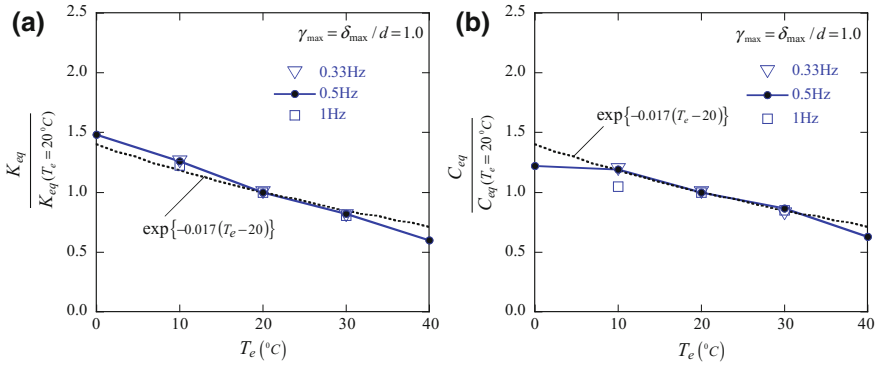

Fig. 7 Temperature-dependency of the equivalent stiffness and damping coefficient of test VE material

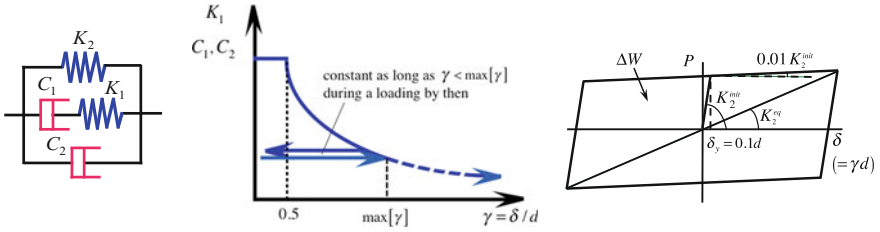

(a) Four-element model (b) Nonlinearity of K_1, C_1 and C_2 (c) Nonlinearity of K_2

Fig. 8 NLF model (**a** Four-element model; **b** Nonlinearity of K_1, C_1 and C_2; **c** Nonlinearity of K_2)

2.2 NLF Model of VE Material

A mechanical model for the VE material was proposed by an NLF model (Nakamura and Kaneko 1998) that comprises two nonlinear dashpot elements and two nonlinear spring elements as shown in Fig. 8 and expressed by Eqs. (2a)–(2d). The four-element model shown in Fig. 8a can express the frequency dependence of the VE material, and the nonlinear characteristics of the four elements shown in Fig. 8b, c can provide the amplitude dependence of the VE material.

The temperature dependence of the VE material is expressed by incorporating the temperature-dependence function, $F_t(T_e)$, in each element as

$$C_1 = 4.76 \times 10^{-1} \gamma^{-0.640} \times \frac{A_s}{d} \times F_t(T_e) \quad (N \cdot s/mm) \tag{2a}$$

$$C_2 = 1.59 \times 10^{-2} \gamma^{-0.395} \times \frac{A_s}{d} \times F_t(T_e) \quad (N \cdot s/mm) \tag{2b}$$

$$K_1 = 2.83 \times 10^{-1} \gamma^{-0.715} \times \frac{A_s}{d} \times F_t(T_e) \quad (N/mm) \tag{2c}$$

$$K_2 = 1.57 \times \frac{0.1 + 0.01(\gamma - 0.1)}{\gamma} \times \frac{A_s}{d} \times F_t(T_e) \quad (N/mm) \tag{2d}$$

$$F_t(T_e) = exp\{-0.017(T_e - 20)\} \tag{2e}$$

where A_s and d indicates the area and the thickness of the VE material, respectively. The coefficients of the four elements are first determined to express the obtained frequency dependence for a fixed shear strain of $\gamma = 200\%$ by trial-and-error, and then nonlinear characteristics with respect to γ are incorporated to express the obtained amplitude dependence (Nakamura and Kaneko 1998).

The equivalent shear stiffness, K_{eq}, and the equivalent damping coefficient, C_{eq}, of the proposed NLF model are expressed as follows.

$$K_{eq}(\omega, \gamma; A_S, d, T_e) = \frac{\omega^2 C_1^2}{K_1^2 + \omega^2 C_1^2} K_1 + K_2 \quad (N/mm) \tag{3a}$$

$$C_{eq}(\omega, \gamma; A_S, d, T_e) = \frac{K_1^2}{K_1^2 + \omega^2 C_1^2} C_1 + C_2 + C_{K_2} \quad (N \cdot s/mm) \tag{3b}$$

where

$$C_{K_2} = \frac{\Delta W}{\pi \cdot \omega \cdot (\gamma d)^2} = \frac{0.622(\gamma - 0.1)}{\pi \cdot \omega \cdot \gamma^2} \times \frac{A_s}{d} \times F_t(T_e) \quad (N \cdot s/mm) \tag{4}$$

and ω indicates the circular frequency of the excitation. Figure 9 shows K_{eq} and C_{eq} obtained from the experimental results of the test VE material and those of the

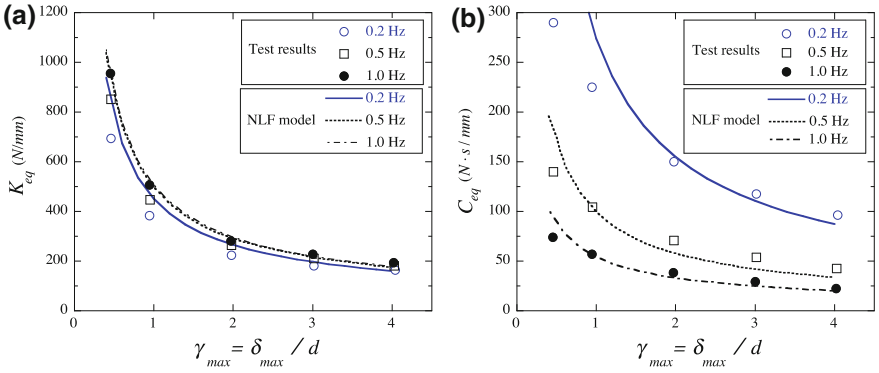

Fig. 9 Equivalent stiffness and damping coefficient of experimental results of VE material and those of proposed NLF model

proposed NLF model. Figure 9 indicates that the proposed NLF model can express the dynamic characteristics of the VE material with good accuracy.

2.3 Dynamic Loading Tests of VED

Using a 1/2-scale model of the wall-type VED, dynamic loading tests were carried out to verify that the resisting force characteristics of the scale VED can be accurately simulated by the proposed NLF model. Figure 10 shows a schematic diagram of a 1/2-scale wall-type VED and the setup of a dynamic loading test. Two VE materials with dimensions of 600 mm × 600 mm and thickness of 10 mm were held between an inner steel plate and an outer steel plate by vulcanizing bonding. The total area of the VE material in the VED, A_s, was 720×10^3 mm^2.

Figure 11 shows an experimental hysteresis loop of the 1/2-scale model VED and that of the test VE material specimen ($A_s = 5.6 \times 10^3$ mm^2, $d = 5$ mm) in Fig. 3 for an earthquake interstory drift of the 8th floor of a hypothetical 15-story building (Appendix I). The vertical axis of Fig. 11 represents the shear stress, τ, which is obtained from the resisting shear force, Q, divided by A_s. The horizontal axis of Fig. 11 represents the shear strain, γ, which is obtained from the applied time-history deformation, δ, divided by the thickness of the VE material, d. The two hysteresis loops in Fig. 11 are very similar, implying that the resisting force of the VE material is proportional to the area of the VE material.

Figure 12 shows an experimental hysteresis loop of the 1/2-scale model VED and a simulation result by the NLF model for an earthquake interstory drift of the 24th floor of a hypothetical 24-story building (Appendix I). The simulation result in Fig. 12 is computed by the NLF model (Fig. 8) and Eqs. (2a)–(2e) which need the

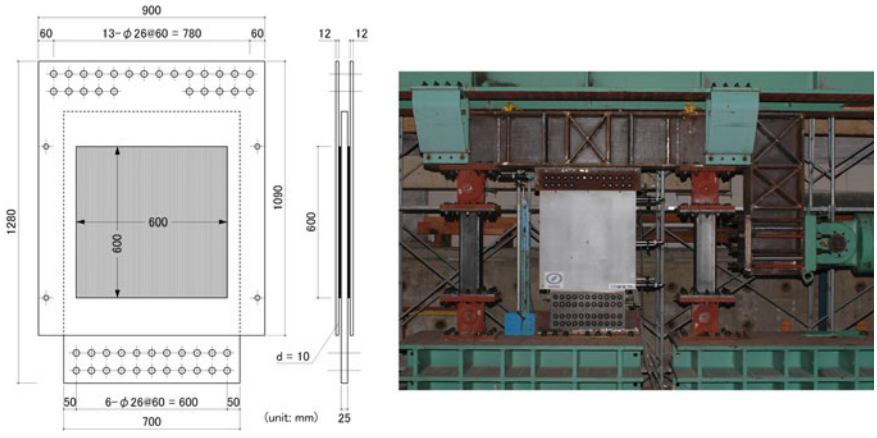

Fig. 10 Schematic diagram of a VED and setup of dynamic loading test

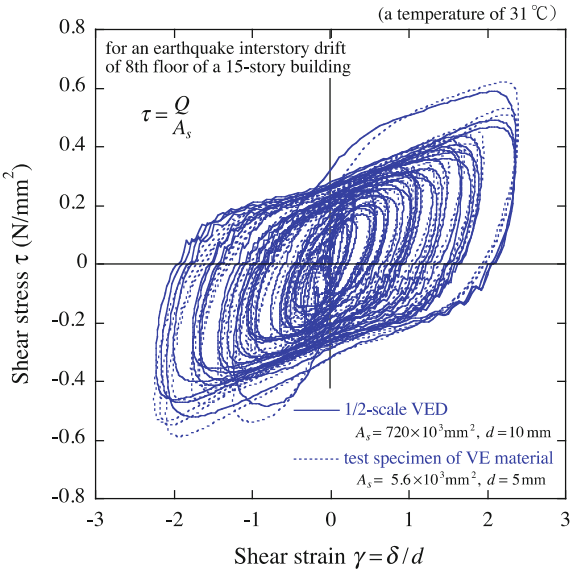

Fig. 11 Resisting force characteristics of test VE material and VED

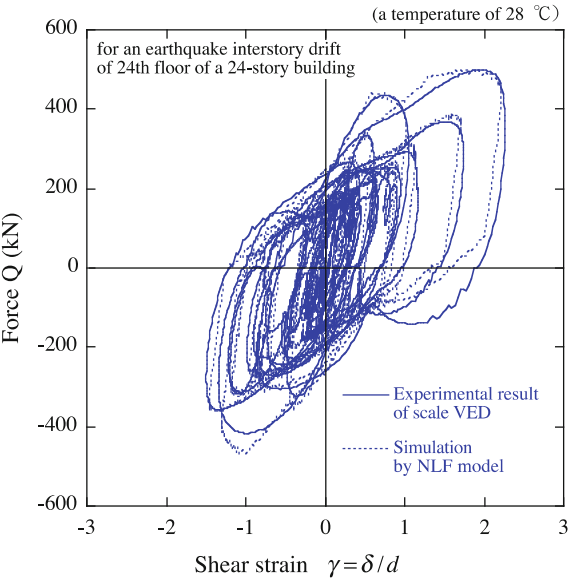

Fig. 12 Resisting force characteristics of mechanical model and experimental results of VED

time-history shear strain, γ, but not the value of ω. The simulations were in good agreement with the experimental result, implying that the mechanical characteristic of the VED can be accurately estimated by the proposed NLF model.

3 Maximum Earthquake Response of a Building with VEDs

The seismic design constraints are generally imposed on the peak responses of a structure subjected to a specified earthquake input. The computational method is proposed here for estimating the peak interstory drifts of a building where VEDs with mechanical characteristics given by the NLF model are used. The mean peak interstory drifts can be estimated by using the equivalent linearization of the VEDs and the expanded CQC method for the specified design displacement response spectrum.

3.1 Equivalent Linearization of VED

The NLF model of the VED can be converted into a linear Voigt model comprising a linear spring and a linear dashpot connected in parallel by utilizing the equivalent linearization. Substituting the maximum shear strain of the VED, $\gamma_{\max}$, for γ in Eqs. (2a)–(2e) and (4), and the fundamental natural period of the building, T_1, for ω in Eq. (4) as $\omega = 2\pi/T_1$, the equivalent shear stiffness, K_D, and the equivalent damping coefficient, C_D, of the converted Voight model shown in Fig. 13 are given by Eqs. (3a) and (3b), respectively for a specified set $\{A_s,\ d,\ T_e\}$.

The maximum shear strain $\gamma_{\max}$ of the VED installed in a story can be evaluated from the interstory drift constraint in a performance-based design. When the peak interstory drift angle is specified as β for the story of a floor height L_s and the mounting component for the VED can be regarded as stiff enough, $\gamma_{\max}$ is given by

$$\gamma_{\max} = \frac{L_s \cdot \overline{\beta}}{d} \tag{5}$$

The fundamental natural period, T_1, of the building installed with the VED can be obtained through the modal analysis explained in the following section. The equivalent linearization of the VED considering the stiffness of the mounting component is described in Appendix II.

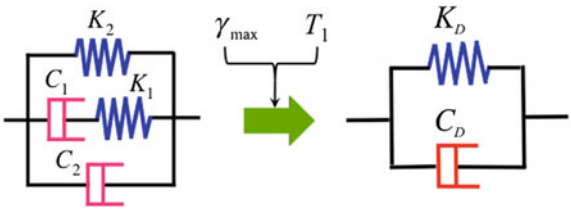

Fig. 13 Equivalent linearization of NLF model

3.2 Modal Analysis by the Expanded CQC Method

Consider a multistory shear building in which the VEDs are installed between the floors. The mean peak response of the building to an earthquake can be estimated using modal analysis. The equivalent shear stiffness, k_{Dj}, and the equivalent damping coefficient, c_{Dj}, of the Voight model of the VED installed at the j-th floor are added to the story shear stiffness, k_{Sj}, and the story damping coefficient, c_{Sj}. The equations of motion of an f-story shear building can then be written as follows:

$$\boldsymbol{M_S}\ddot{\boldsymbol{x}} + (\boldsymbol{C_S} + \boldsymbol{C_D})\dot{\boldsymbol{x}} + (\boldsymbol{K_S} + \boldsymbol{K_D})\boldsymbol{x} = -\boldsymbol{M_S}\mathbf{1}\,\ddot{z} \tag{6}$$

where $x = \{x_1 \ldots x_f\}^T$ and $\mathbf{1} = \{1 \ \ldots \ 1\}^T$ and $\ddot{z}$ denote the horizontal displacements of the floors and the input earthquake acceleration, respectively, $\boldsymbol{M_S}$ denotes the diagonal mass matrix of the structure, $\boldsymbol{C_S}$ and $\boldsymbol{C_D}$ denote the tri-diagonal damping matrices for the structure and for the installed VEDs, respectively, and $\boldsymbol{K_S}$ and $\boldsymbol{K_D}$ denote the tri-diagonal stiffness matrices for the structure and for the installed VEDs, respectively. The damping matrix, $\boldsymbol{C_S} + \boldsymbol{C_D}$, in Eq. (6) represents non-proportional damping, and the eigenvalue problem of Eq. (6) is given using Foss's method (1958) as

$$\begin{aligned} &(\lambda A + B)X = 0 \\ &A = \begin{bmatrix} \mathbf{0} & M_S \\ M_S & C_S + C_D \end{bmatrix}, \quad B = \begin{bmatrix} -M_S & \mathbf{0} \\ \mathbf{0} & K_S + K_D \end{bmatrix}, \quad X = \begin{pmatrix} \lambda u \\ u \end{pmatrix} \end{aligned} \tag{7}$$

Equation (7) gives f pairs of complex conjugate eigenvalues $\{\lambda\}$, and their corresponding eigenvectors $\{u\}$ for damped vibration as listed below.

$$\boldsymbol{\lambda} = \left\{\lambda^{(1)} \cdots \lambda^{(j)} \left(= \lambda_R^{(j)} + i\lambda_I^{(j)}\right) \ldots \lambda^{(f)}; \lambda^{(f+1)} \cdots \lambda^{(f+j)} \left(= \lambda_R^{(f+j)} - i\lambda_I^{(f+j)}\right) \ldots \lambda^{(2f)}\right\} \tag{8}$$

where $\lambda^{(j)}\left(= \lambda_R^{(j)} + i\lambda_I^{(j)}\right)$ and $\lambda^{(f+j)}\left(= \lambda_R^{(f+j)} - i\lambda_I^{(f+j)}\right)$ $(j = 1, 2, \ldots f)$ are a pair of complex conjugate eigenvalues. The natural circular frequency, ω_j, and the damping factor, h_j, of the j-th mode are given by

$$\omega_j = \left|\lambda^{(j)}\right| = \sqrt{\lambda_R^{(j)^2} + \lambda_I^{(j)^2}} \tag{9a}$$

$$h_j = -\frac{\lambda_R^{(j)}}{\omega_j} = -\frac{\lambda_R^{(j)}}{\sqrt{\lambda_R^{(j)^2} + \lambda_I^{(j)^2}}} \tag{9b}$$

The mean peak interstory drifts, $\{\delta_j\}$, of the building subjected to the specified design displacement response spectrum $S_D(\omega; h)$ can be estimated using the expanded CQC method (Igusa, Der Kiureghian and Sackman 1984) as follows:

$$\delta_j = \left[\sum_{r=1}^{N}\sum_{s=1}^{N} S_D(\omega_r; h_r)\cdot S_D(\omega_s; h_s)\cdot\left(\rho_{RR}^{(r,s)} a_j^{(r)} a_j^{(s)} + 2\rho_{RI}^{(r,s)} a_j^{(r)} b_j^{(s)} + \rho_{II}^{(r,s)} b_j^{(r)} b_j^{(s)}\right)\right]^{1/2} \tag{10a}$$

$$a_j^{(r)} = R_e\left[\nu^{(r)}\left(u_j^{(r)} - u_{j-1}^{(r)}\right)\right] \tag{10b}$$

$$b_j^{(r)} = I_m\left[\nu^{(r)}\left(u_j^{(r)} - u_{j-1}^{(r)}\right)\right] \tag{10c}$$

$$\nu^{(r)} = 2I_m\left[\lambda^{(r)}\right]\frac{X^{(r)^T}\boldsymbol{AP}}{X^{(r)^T}\mathbf{A}\mathbf{X}^{(r)}}i \tag{10d}$$

$$P = \begin{Bmatrix}\mathbf{1}\\ \mathbf{0}\end{Bmatrix} \tag{10e}$$

where $R_e[\ ]$ and $I_m[\ ]$ denote the real and imaginary parts of a complex number, respectively, and $\rho_{RR}^{(r,s)}$, $\rho_{RI}^{(r,s)}$, and $\rho_{II}^{(r,s)}$ are the modal cross-correlation coefficients given by Yang et al. (1990) as follows:

$$\rho_{RR}^{(r,s)} = \frac{8\left(h_r + h_s p^{(s,r)}\right)\sqrt{h_r h_s p^{(r,s)}}}{\left(p^{(r,s)} + p^{(s,r)} + 2h_r h_s\right)^2 - 4\left(1-h_r^2\right)\left(1-h_S^2\right)} \tag{11a}$$

$$\rho_{RI}^{(r,s)} = \frac{4\left(p^{(r,s)} - p^{(s,r)} + 2h_r h_s + 2p^{(s,r)}h_S^2\right)\sqrt{h_r h_s p^{(r,s)}}}{\sqrt{\left(1+h_S^2\right)}\left\{\left(p^{(r,s)} + p^{(s,r)} + 2h_r h_s\right)^2 - 4\left(1-h_r^2\right)\left(1-h_S^2\right)\right\}} \tag{11b}$$

$$\rho_{II}^{(r,s)} = \frac{4\left(p^{(r,s)} + p^{(s,r)} + 2h_r h_s\right)\left(h_r + h_s p^{(s,r)}\right)\sqrt{h_r h_s p^{(r,s)}}}{\sqrt{\left(1+h_r^2\right)\left(1+h_S^2\right)}\left\{\left(p^{(r,s)} + p^{(s,r)} + 2h_r h_s\right)^2 - 4\left(1-h_r^2\right)\left(1-h_S^2\right)\right\}} \tag{11c}$$

where $p^{(r,s)} = \omega_r/\omega_s$.

4 Performance-Based Placement-Design Procedure of VED

A placement-design procedure for the VEDs is proposed here such that each peak interstory drift angle $\{\beta_j\}$ of an f-story shear building with a specified set $\{\boldsymbol{M_S}, \boldsymbol{C_S}, \boldsymbol{K_S}\}$ subjected to a design earthquake $S_D(\omega; h)$ would coincide with the prescribed value $\{\beta_j\}$ $(j = 1, 2, \ldots, f)$. Figure 14 presents a design process for finding the distribution of the VEDs' $\{A_j\}$ $(j = 1, 2, \ldots, f)$ that are required to limit the interstory drift angles to the specified target values. Here, $\{A_j\}$ means the total area of the VE material in the dampers at the j-th floor, while the thickness (d) and the temperature (T_e) of the VE material are previously defined.

In the design process shown in Fig. 14, A_j is adjusted by the ratio of the estimated peak interstory drift angle, β_j, to the target value, $\bar{\beta}_j$, and α in the equation in Step [8] is the control parameter, which is specified as $0 < \alpha \leq 1$.

As $\{A_j\}$ values are adjusted in the design process, the T_1 value of the building with VEDs varies. Hence, the estimation in Step [4] of the process should always be

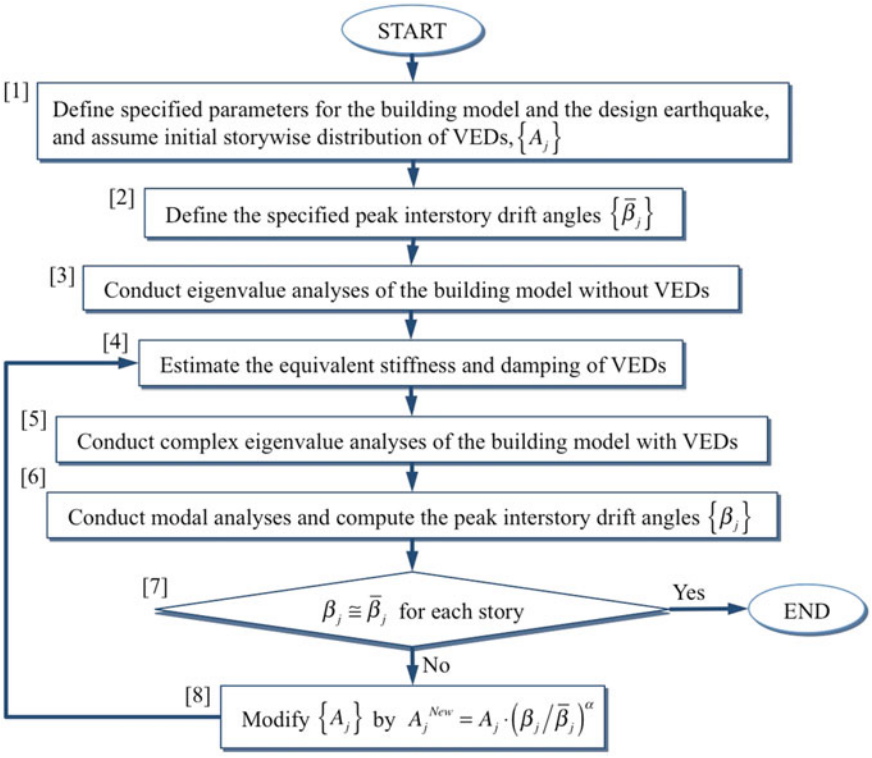

Fig. 14 Design process for placement design of VED for specified peak interstory drifts

based on T_1, which is obtained by the previous eigenvalue analysis. The proposed design procedure utilizes complex eigenvalue analysis, and therefore, can provide the changes in the equivalent natural periods and the equivalent damping factors of the building with VEDs.

5 Design Examples

Below, design examples of the performance-based placements of wall-type VEDs for three high-rise building models such that each peak interstory drift angle is reduced to the prescribed value, are shown. Time history response analyses are carried out for the buildings installed with the necessary number of VEDs to demonstrate the validity of the proposed design procedure.

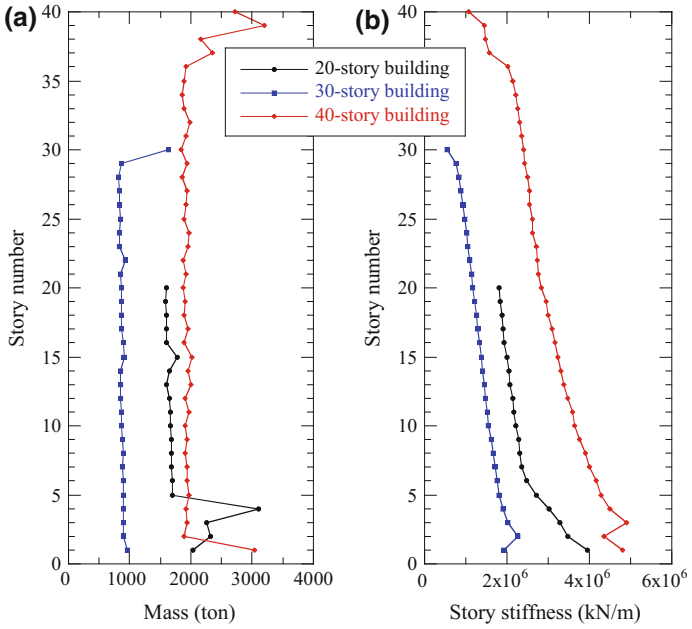

Fig. 15 Mass and story stiffness of 20, 30, and 40-story shear buildings

Table 2 Fundamental natural period and story height of 20, 30, and 40-story shear buildings

	Fundamental natural period (s)	Story height (cm)
20-story shear building	2.06	398
30-story shear building	2.96	410
40-story shear building	4.00	378

5.1 *High-Rise Building Models with Optimally Placed VED*

Consider a 20, 30, and 40-story shear buildings with mass and story stiffness properties as shown in Fig. 15, which are based on actual high-rise buildings.

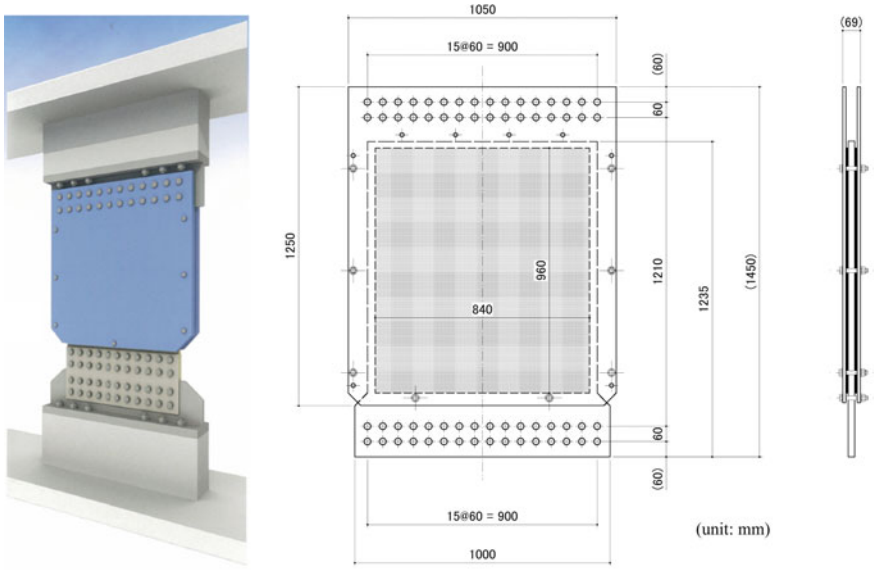

Fig. 16 Wall-type VED

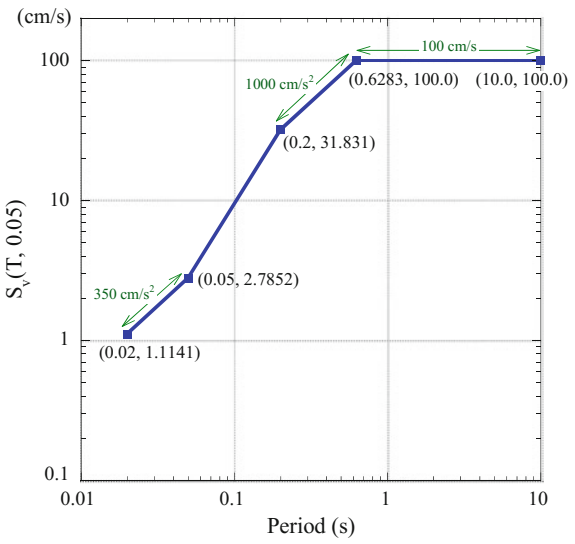

Fig. 17 Design velocity response spectrum

The fundamental natural periods of the buildings without dampers, T_1, and their story heights are shown in Table 2. The damping ratio in the first mode, h_1, is assumed to be 2%, and those in the higher modes are assumed to be proportional to the frequency.

The wall-type VED shown in Fig. 16 is employed to control the peak interstory drifts of the buildings. The VE material is 5 mm in thickness and the total area of the VE material of one wall-type VED is 1.6128 m^2. The ambient temperature is assumed to be 20 °C. The story-wise distributions of $\{A_j\}$ are now determined such that the peak interstory drift angle for all stories is $\beta_j \equiv 1/150$ for the Level 2 design response spectrum specified by the Japan Building Center (Fig. 17). The control parameter α is 0.3 in the design process.

The extracted progress of story-wise distribution of the area of the VE material in the 20-story building is shown in Fig. 18a, together with the estimated peak interstory drift angles in Fig. 18b, which vary according to the story-wise

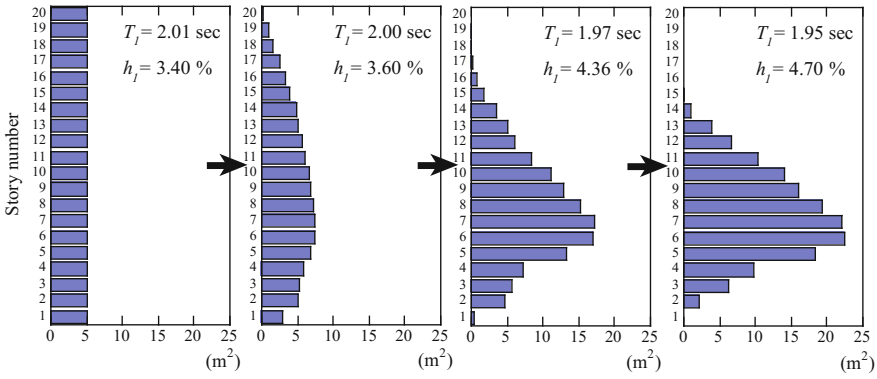

(a) Iterative design process of story-wise distribution of VE material area

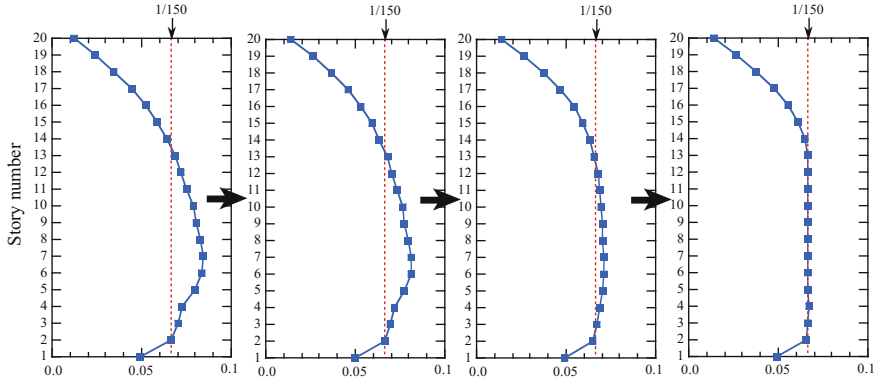

(b) Variation in peak interstory drift angles for the upper distribution of VE material

Fig. 18 Extracted progress of story-wise distribution of VE material area and varying peak interstory drift angles in 20-story building

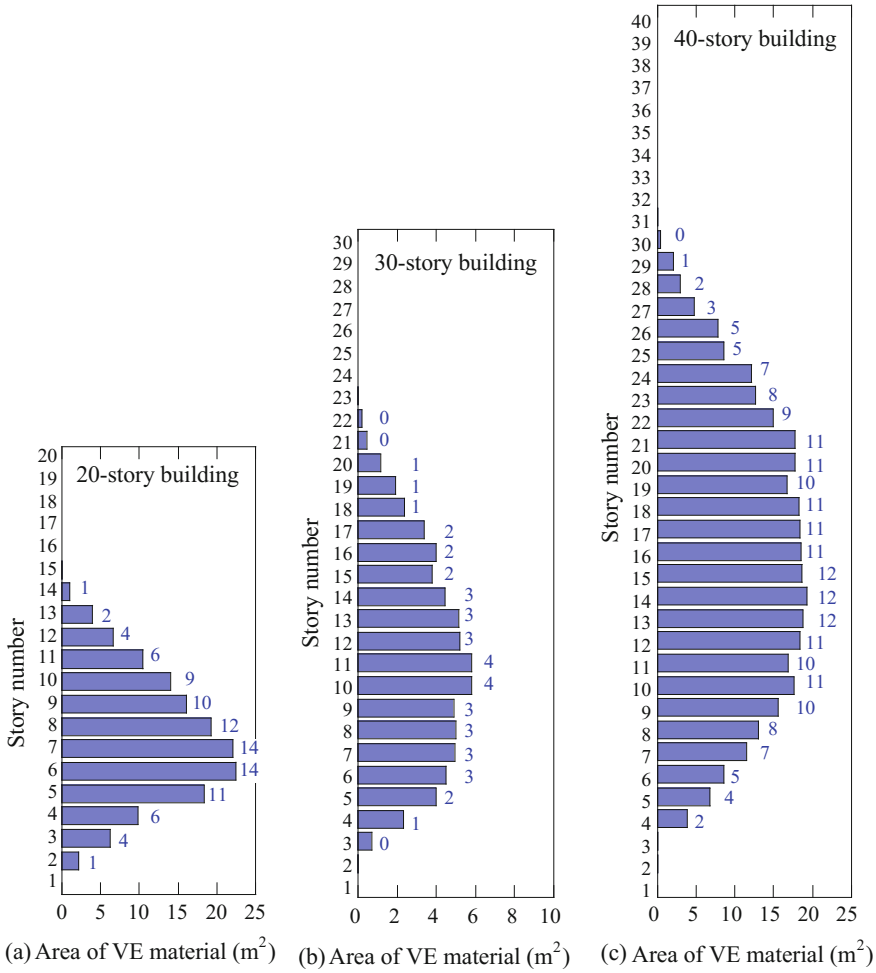

Fig. 19 Story-wise distribution of VE material area and necessary number of VEDs in 20-, 30-, and 40-story buildings designed for maximum story drift angle of 1/150

Table 3 Fundamental natural period and damping factor of buildings with and without VED

	Fundamental natural period (s)		Damping ratio in the first mode (%)	
	Without VED	With VED	Without VED	With VED
20-story building	2.06	1.95	2.0	4.70
30-story building	2.96	2.89		3.32
40-story building	4.00	3.83		4.31

distribution of the area of the VE material. As shown on the left-hand side of Fig. 18a, the story-wise distribution of the VE material is first assumed to be uniform for all floors, and the drift angles are estimated by the expanded CQC method, as shown on the left-hand side of Fig. 18b. The area of the VE material at each floor is adjusted by the ratio of the estimated drift angle to the target value. For the modified VE material distribution, the drift angles are repeatedly estimated and compared to the target value with the modification repeated until the estimated drift angles are sufficiently close to the target value, as shown on the right-hand side of Fig. 18a, b. The variations in T_1 and h_1 computed by the complex eigenvalue analyses during the iterative modification are also shown in Fig. 18a.

Figure 19 shows the obtained story-wise distribution of the area of the VE material and the necessary number of VED in the 20-, 30-, and 40-story buildings designed for a maximum story drift angle of 1/150. The necessary number of VEDs at each story was obtained by dividing the obtained area of the VE material by 1.6128 m^2 (= the area of the VE material of the employed wall-type VED in Fig. 16) and rounding off to a whole number.

The proposed placement-design procedure can evaluate the extent of changes in T_1 and h_1 of the building installed with the necessary VEDs by the complex eigenvalue analyses. Table 3 shows T_1 and h_1 of the building with and without the VEDs. The required VEDs shorten the fundamental T_1 slightly and increase h_1 considerably due to their additional stiffness and damping coefficient. These changes in T_1 and h_1 can provide important information about the dynamic characteristics of the building.

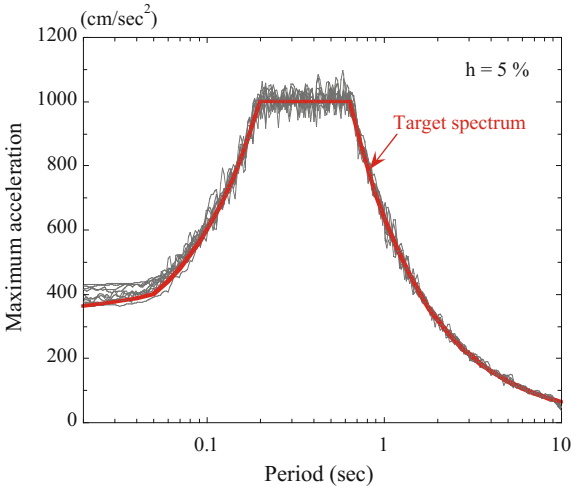

Fig. 20 Acceleration response spectra of 10 synthetic earthquakes with the target spectrum

5.2 *Verification by Time-History Response Analyses*

To demonstrate the validity of the proposed design procedure, the buildings installed with the necessary number of wall-type VEDs (as shown in Fig. 19) were subjected to 10 synthetic earthquakes generated to be compatible with the design response spectrum (Fig. 17). Figure 20 shows acceleration spectra of the 10 synthetic earthquakes with the target spectra. Time-history analyses were conducted

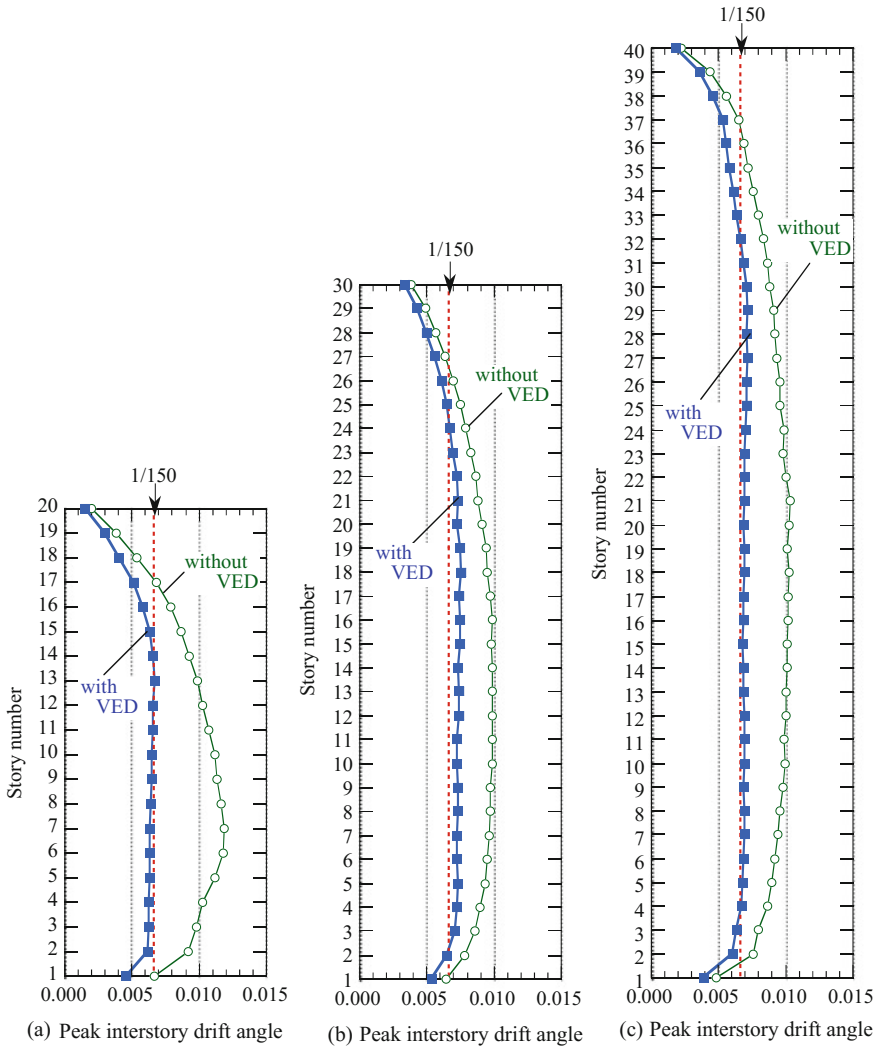

Fig. 21 Story-wise distribution of mean peak interstory drift angles in buildings without VEDs and buildings with VEDs designed for maximum story drift angle of 1/150

using the original mechanical model of the VED, i.e., the NLF model given by Eqs. (2a)–(2e).

Figure 21 shows the story-wise distribution of the mean peak interstory drift angles obtained by time-history analyses of the buildings with and without VEDs. With the exception of the lower and upper floors, where there is no need to install a VED, the mean peak interstory drift angles are found to be controlled to the specified value of 1/150 with enough accuracy.

The mean peak interstory drift angles of the 30-story building in Fig. 21b exceed the target value of 1/150 by about 10%. The errors in Fig. 21 are considered to be caused by the following two disparities between the proposed design procedure and the applied time-history analyses: The design procedure uses the converted Voigt model of the VED, while the time-history analyses use the original NLF model of the VED. The design procedure uses the modal analysis with the specified design response spectrum, while the time-history analyses use the generated synthetic earthquake waves. Considering the uncertainty and dispersion of the earthquake input, this amount of error can be regarded as acceptable, and the target peak responses of a structure can be specified for an appropriate safety margin.

6 Conclusions

Using the expanded CQC method for non-classically damped structures, a performance-based placement-design procedure is developed for finding the story-wise distribution of the manufactured wall-type VED such that each peak interstory drift would be limited to the specified value for a given design response spectrum.

The wall-type VED is installed between the floors in a building, and induces a viscous shear force in response to the relative interstory drift, causing energy dissipation. The wall-type VED studied in this chapter utilizes a newly developed VE material with low temperature dependence. The wall-type VED shown in Fig. 16 has been applied to a few tall buildings in Japan as a practical damper. A mechanical model for the VED can be expressed by an NLF model that comprises two nonlinear dashpot elements and two nonlinear spring elements. The NLF model can express amplitude- and frequency-dependence properties of the VED. The validity of the proposed NLF model of the VED is verified through the dynamic loading tests of a 1/2-scale wall-type VED.

The expanded CQC method is utilized to estimate the peak interstory drifts of a building with installed VEDs subjected to a specified given design response spectrum. In the modal analysis, the NLF model of the VED installed at each story is converted into an equivalent linear Voigt model, which is determined by the prescribed peak interstory drift and the fundamental natural period of the structure.

An algorithm for the placement design of the VED is proposed such that the peak interstory drifts would be limited to a specified value. In the proposed

sequential design process, the area of the VE material in each story is adjusted by the ratio of the estimated peak interstory drift angle to the target value. The necessary number of VEDs at each story is obtained by dividing the obtained area of the VE material by the area of the VE material of the employed single wall-type VED and rounding off the result to a whole number.

Design examples of the performance-based placements of the wall-type VEDs are shown for three high-rise building models. Time-history response analyses are carried out for buildings installed with the necessary number of VEDs subjected to the design response spectrum-compatible synthetic earthquakes. The results demonstrate the effectiveness and validity of the proposed performance-based placement-design procedure.

The developed design procedure utilizes the equivalent linearization of the VED and the expanded CQC method. Therefore, the procedure can be applied not only to the VED but also to other dampers such as metallic hysteretic dampers and viscous fluid dampers, which can be converted into a linear Voigt model framework. Another advantage of the procedure is that the variations in the fundamental natural period and the damping ratio of the structure due to the installed dampers can be evaluated by complex eigenvalue analysis, which provides important information on the dynamic characteristics of the structure.

Acknowledgements The VED in this study was jointly developed by Shimizu Corporation and Sumitomo Riko Company Limited. The author would like to express his appreciation to Sumitomo Riko Company Limited for their significant contribution to development of the VED.

The author was given the opportunity to study and carry out research for two years under Professor Armen Der Kiureghian at University of California, Berkeley; this has increased and deepened the author's knowledge of the modal analysis method (Der Kiureghian and Nakamura 1993; Nakamura et al. 1993). The author would like to express his deep appreciation for the attentive guidance by Professor Der Kiureghian.

Appendix I

Earthquake Interstory Drifts of Hypothetical 15- and 24-story Buildings

The dynamic loading tests of the VE material and the VED make use of simulated earthquake interstory drifts of hypothetical 15- and 24-story buildings subjected to Hachinohe 1968 EW earthquake or El Centro 1940 NS earthquake. The fundamental natural periods of the 15- and 24-story buildings are assumed to be 2 s and 3 s, respectively. Fig. 22 shows the waveforms of the earthquake interstory drifts in Figs. 4b, 11 and 12.

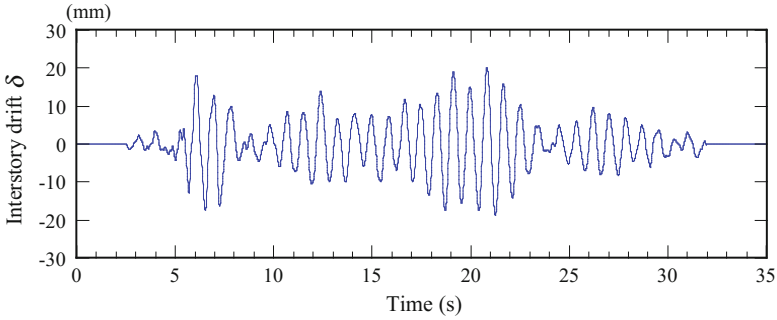

(a) Interstory drift of 8th floor of a 15-story building subjected to Hachinohe 1968 EW earthquake (Figs. 4(b) and 11)

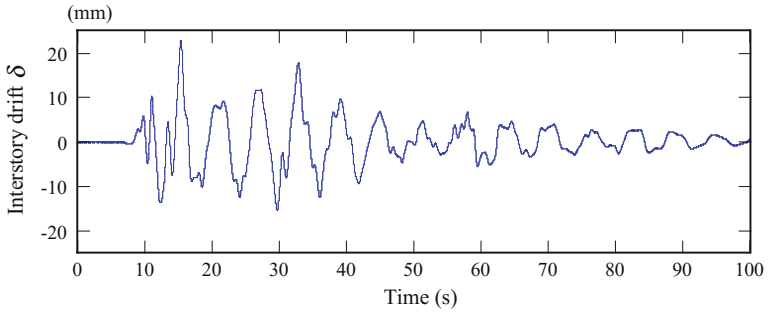

(b) Interstory drift of 24th floor of a 24-story building subjected to El Centro 1940 NS earthquake (Fig. 12)

Fig. 22 Earthquake interstory drifts of hypothetical 15- and 24-story buildings

Appendix II

Voigt Model of VED Considering the Stiffness of the Mounting Component

For consideration of the mounting component's stiffness, K_M the equivalent Voigt model including the mounting component can be constructed. As shown in Fig. 23, the sum of the maximum shear deformation of the VED, $\delta_D = \gamma_{\max} \cdot d$, and the maximum deformation of the mounting component, δ_M, is equal to the specified peak interstory drift, $\delta = L_S \cdot \beta$.

The following equation holds for $\gamma_{\max}$, δ, K_M, and $K_{eq}(\omega, \gamma_{\max})$ and $C_{eq}(\omega, \gamma_{\max})$ of the VED given by Eqs. (3a) and (3b) for a specified set $\{A_s,\ d,\ T_e\}$:

$$\gamma_{\max} \cdot d = \delta \cdot \left\{ \left(1 + \frac{K_{eq}(\omega, \gamma_{\max})}{K_M} \right)^2 + \omega^2 \left(\frac{C_{eq}(\omega, \gamma_{\max})}{K_M} \right)^2 \right\}^{-\frac{1}{2}} \tag{12}$$

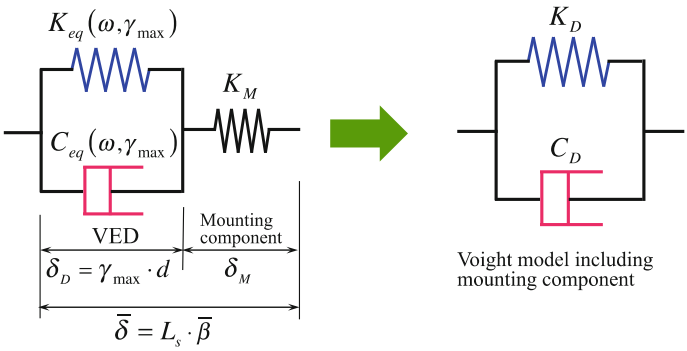

Fig. 23 Equivalent linearization of VED considering the mounting component's stiffness

While Eq. (12) cannot be analytically solved in terms of $\gamma_{\max}$, the value of $\gamma_{\max}$ can be estimated through iterative computations by substituting $L_S \cdot \beta/d$ as an initial value of $\gamma_{\max}$ on the right-hand side of Eq. (12). Once a converged value of $\gamma_{\max}$ is obtained, K_D and C_D of the equivalent Voigt model considering K_M are obtained according to

$$K_D = \frac{K_{eq}(\omega,\gamma_{\max})\left(1+\frac{K_{eq}(\omega,\gamma_{\max})}{K_M}\right)+\omega^2\frac{C_{eq}(\omega,\gamma_{\max})^2}{K_M}}{\left(1+\frac{K_{eq}(\omega,\gamma_{\max})}{K_M}\right)^2+\omega^2\left(\frac{C_{eq}(\omega,\gamma_{\max})}{K_M}\right)^2} \tag{13}$$

$$C_D = \frac{C_{eq}(\omega,\gamma_{\max})}{\left(1+\frac{K_{eq}(\omega,\gamma_{\max})}{K_M}\right)^2+\omega^2\left(\frac{C_{eq}(\omega,\gamma_{\max})}{K_M}\right)^2} \tag{14}$$

where the fundamental natural circular frequency of a building, $\omega = 2\pi/T_1$, is assigned to ω in Eqs. (13) and (14) in the same way as in Sect. 3.1.

References

Chang KC, Soong TT, Oh S-T, Lai ML (1992) Effect of ambient temperature on viscoelastically damped structure. J Struct Eng 118:1955–1973

Cheng FY, Jiang H, Lou K (2008) Damping systems. In: Smart structures. CRC Press, Boca Raton, FL, pp 109–158

Cimellaro GP (2007) Simultaneous stiffness-damping optimization of structures with respect to acceleration, displacement and base shear. Eng Struct 29:2853–2870. doi:10.1016/j.engstruct.2007.01.001

Der Kiureghian A, Nakamura Y (1993) CQC modal combination rule for high-frequency modes. Earthquake Eng Struct Dyn 22:943–956

Foss KA (1958) Coordinates which uncouples the equations of motion of damped linear dynamic systems. J Appl Mech 25:361–364

Garcia DL (2001) A simple method for the design of optimal damper configurations in MDOF structures. Earthquake Spectra 17:387–398

Gluck N, Reinhorn AM, Gluck J, Levy R (1996) Design of supplemental dampers for control of structures. J Struct Eng 122:1394–1399

Igusa T, Der Kiureghian A, Sackman JL (1984) Modal decomposition method for stationary response of non-classically damped systems. Earthquake Eng Struct Dyn 12:121–136

Lavan O, Levy R (2005) Optimal design of supplemental viscous dampers for irregular shear-frames in the presence of yielding. Earthquake Eng Struct Dyn 34:889–907

Lavan O, Levy R (2006) Optimal design of supplemental viscous dampers for linear framed structures. Earthquake Eng Struct Dyn 35:337–356

Liu W, Tong M, Wu Y, Lee GC (2004) Optimized damping device configuration design of a steel frame structure based on building performance indices. Earthquake Spectra. 20:67–89

Liu W, Tong M, Wu Y, Lee GC (2005) Optimization methodology for damper configuration based on building performance indices. J Struct Eng 131:1746–1756. doi:10.1061/(ASCE)0733-9445(2005)131:11(1746)

Mahmoodi P, Robertson LE, Yontar M, Moy C, Feld I (1987) Performance of viscoelastic dampers in World Trade Center Towers. In: Dynamic of structures, structures Congress'87, Orlando, FL

Nakamura Y, Hanzawa T (2002) Performance-based placement design of vibration control dampers. In: Structural engineers world congress SEWC2002. T2-4-a-1, Yokohama, Japan

Nakamura Y, Kaneko M (1998) Mechanical modeling of viscoelastic damper with amplitude- and frequency-dependent properties. In: Proceedings of the second world conference on structural control, vol 1, pp 181–190

Nakamura Y, Der Kiureghian A, Liu D (1993) Multiple-support response spectrum analysis of the golden gate bridge. Earthquake Engineering Research Center, University of California at Berkeley, Report No. UCB/EERC-93/05

Nakamura Y, Hanzawa T, Nomura T, Takada T (2016) Performance-based placement of manufactured viscoelastic dampers for design response spectrum. Front Built Environ 2:10. doi:10.3389/fbuil.2016.00010

Park J-H, Kim J, Min K-W (2004) Optimal design of added viscoelastic dampers and supporting braces. Earthquake Eng Struct Dyn 33:465–484

Ribakov Y, Gluck J (1999) Optimal design of ADAS damped MDOF structures. Earthquake Spectra 15:317–330

Silvestri S, Trombetti T (2007) Physical and numerical approaches for the optimal insertion of seismic viscous dampers in shear-type structures. J Earthquake Eng 11:787–828. doi:10.1080/13632460601034155

Singh MP, Moreschi LM (2001) Optimal seismic response control with dampers. Earthquake Eng Struct Dyn 30:553–572

Singh MP, Moreschi LM (2002) Optimal placement of dampers for passive response control. Earthquake Eng Struct Dyn 31:955–976

Soong TT, Dargush GF (1997) Viscoelastic dampers. In: Passive energy dissipation systems in structural engineering. Wiley, Chichester, pp 127–170

Takewaki I (1997) Optimal damper placement for minimum transfer functions. Earthquake Eng Struct Dyn 26:1113–1124

Takewaki I (2000) Optimal damper placement for critical excitation. Probab Eng Mech 15: 317–325

Takewaki I (2009) Building control with passive dampers. John Wiley & Sons (Asia) Pte Ltd, Singapore

Takewaki I, Yoshitomi S, Uetani K, Tsuji M (1999) Non-monotonic optimal damper placement via steepest direction search. Earthquake Eng Struct Dyn 28:655–670

Takewaki I, Moustafa A, Fujjita K (2013) Optimal placement of visco-elastic dampers and supporting members under variable critical excitations. In: Improving the earthquake resilience of buildings. Springer, London, pp 249–275

Tan P, Dyke SJ, Richardson A, Abdullah M (2005) Integrated device placement and control design in civil structures using genetic algorithms. J Struct Eng 131:1489–1496. doi:10.1061/(ASCE)0733-9445(2005)131:10(1489)

Tsuji M, Nakamura T (1996) Optimum viscous dampers for stiffness design of shear buildings. In: The structural design of tall buildings, vol 5, pp 217–234

Uetani K, Tsuji M, Takewaki I (2003) Application of an optimum design method to practical building frames with viscous dampers and hysteretic dampers. Eng Struct 25:579–592. doi:10.1016/S0141-0296(02)00168-2

Xu Z-D, Shen Y-P, Zhao H-T (2003) A synthetic optimization analysis method on structures with viscoelastic dampers. Soil Dyn Earthquake Eng 23:683–689. doi:10.1016/j.soildyn.2003.07.003

Yang JN, Sarkani S, Long FX (1990) A response spectrum approach for seismic analysis of nonclassically damped structure. Eng Struct 12:173–184

Zhang R-H, Soong TT (1992) Seismic design of viscoelastic dampers for structural applications. J Struct Eng 118:1375–1392

Optimal Design of Reinforced Concrete Section Under Combined Dynamic Action

Michel Kahan

Abstract Wind or earthquake dynamic actions produce combined efforts on structures (axial force, bending moment about one or two axes, …) whose maximum values within a member section can often be represented by an elliptical envelope. The present chapter describes a technique to optimize reinforced concrete sections subjected to this type of dynamic load by adjusting quantities of steel and/or concrete so that the interaction curve characterizing the resistance of the section becomes tangent to the envelope of the maximum combined forces. The method relies on a geometrical transformation from the original space of forces in which the envelope is an ellipse to a so-called "standard normal space" where it becomes the unit circle. In this latter space, the safety margin of the section has a very simple geometric expression and is measurable with well-known tools of reliability analysis. The section parameters (steel and concrete) can then be adjusted in a very efficient way.

1 Foreword

Think of how many people have truly influenced your life. There should not be many. For me, Armen has been one of these very few. An extremely knowledgeable person, a remarkable teacher—the kind who makes you feel clever, and above all, a truly good man, and I hope a friend.

I only studied for six months with him at UC Berkeley, but that changed the course of my PhD, and my vision of engineering. Less certainty, more questioning, and a commitment to turn complex issues into elegant solutions.

I have left the field of research for civil engineering consultancy services some years ago, but I have kept these fundamentals. This chapter, which I first wrote as a

M. Kahan (✉)
SETEC, 42-52 Quai de la Rapée – CS 71230,
75583 Paris Cedex 12, France
e-mail: michel.kahan@setec.fr
URL: http://www.setec.fr/en

P. Gardoni (ed.), *Risk and Reliability Analysis: Theory and Applications*,
Springer Series in Reliability Engineering, DOI 10.1007/978-3-319-52425-2_11

paper in French (Kahan 2002), is dedicated to Armen: it includes reliability techniques and algorithms that Armen taught me, and the core of the chapter is a nice geometrical transformation that turns a complex issue into a relatively simple one, a way of solving problems which Armen might like.

2 Scope

Recent developments in structural analysis include time step analysis of complex structures whose materials behave in a non-linear way or whose large displacements require second order analysis. These sophisticated numerical tools are commonly used to check the behavior of structures subjected to dynamic forces under seismic or wind actions. Thus, given temporal data of the dynamic load (accelerograms for an earthquake or fields of instantaneous wind speeds), it is possible to compute (within model errors) elastic and inelastic strains and check whether or not they remain within acceptable limits that are either determined experimentally or given by standards and codes.

Despite the improvement of numerical analysis, the *design* techniques of the same structures remain voluntarily simple, with the clear objective to cover, in a robust way, a large range of uncertain dynamic actions.

Thus, most engineers will deal mainly with forces instead of strains (at least within the framework of force based design) and will check that the combined dynamic forces remain in a safe domain. Namely, if the section is well designed, the vector of combined forces (axial force N and bending moments M_y, M_z) is a function of time which must remain within the boundaries formed by an interaction curve or surface which represents the resistance capacity of the section. Checking forces this way is equivalent to checking strains only if there is a one-to-one relationship between strains and stresses, such as with linear elastic materials. In all other cases (most of practical cases in fact) force-based design has a more conventional and regulatory purpose than a truly physical meaning.

Most often, an elliptical envelope can be drawn around maximum credible combined forces. It can be thought of as a curve or a surface of equal probability of occurrence of the force vector $\{N, M_y, M_z\}$ or as a curve or a surface that the force vector will out-cross very rarely, with a given probability.

In the following, we assume that the envelope of section forces is elliptical and we will state that a reinforced concrete section is designed in an optimal way if the interaction curve, representing the resistance capacity is completely outside and possibly tangent to the above action envelope.

It is usually a difficult issue to check that every point of the solicitation ellipse lies within the safe domain of the interaction (resistance) curve. In the following, we will review how this is dealt with in practical engineering life, using Leblond's approach (Leblond 1980) where the ellipse is approximated by a polygonal envelope and each corner of the polygon is checked to be within the safe domain.

The core of the original method presented here lies in a geometrical transformation from the original space of section forces {N, M_y, M_z} to a so-called "standard normal space" in which the safety margin of the section can be measured very simply as the distance of the transformed interaction curve to the origin.

In a first stage, we briefly review a numerical method for the analysis of reinforced concrete sections. We then define the limit states, first in terms of local strains, then it terms of combined forces. There can be several limit states corresponding to strain limits in steel or in concrete. The maximum section forces are described, in the original space, by an ellipse in the presented case of a single axis bending moment combined with axial force (or by an ellipsoid in higher dimensions).

We then operate the transformation to the "standard normal space" in which the envelope of forces becomes the unit circle centered about the origin. Optimal design of the section will consist in adjusting dimensional parameters, such as steel and concrete quantities, so that all limit states curves lie outside of the unit circle and, at best, are tangent to it. The measure of the safety margin and the optimization process call on numerical tools well known in reliability analysis.

3 Reinforced Concrete Section Analysis

The optimization process relies on a numerical analysis of reinforced concrete sections. We describe briefly the main steps of a technique that can be used, with emphasis on the elements that are required for the optimization algorithm to follow. The fundamental numerical constraint is that the relationship between sectional strains and forces should be differentiable and its inverse should exist and be differentiable as well.

3.1 Assumptions

Stresses and strains are counted positive when in traction and elongation. Sign conventions for bending moments and axial forces are reported on Fig. 1. Axial forces are counted positive when in traction, a positive bending moment M_y will compress "lower" fibers and a positive bending moment M_z will compress "right hand side" fibers.

With these sign conventions, the vector of reduced forces can be expressed in terms of stress distribution as:

$$T = \begin{cases} N = \int \sigma(y,z)\, dy\, dz \\ M_y = \int (z - z_G)\, \sigma(y,z)\, dy\, dz \\ M_z = -\int (y - y_G)\, \sigma(y,z)\, dy\, dz \end{cases} \quad (1)$$

Equation 1: vector of reduced forces

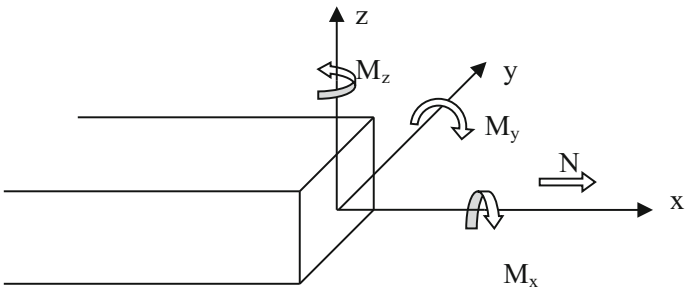

Fig. 1 Sign conventions for bending moments and axial force

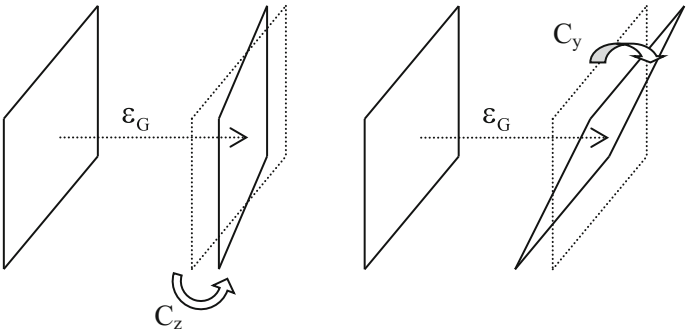

Fig. 2 Strain cinematic

Assuming an Euler-Bernoulli beam model, plane sections remain plane, perpendicular to the mean fiber and isometric. Longitudinal strain of the section fibers can be expressed in terms of the center of gravity longitudinal strain and in terms of curvatures C_y and C_z (cf. Fig. 2) as:

$$\varepsilon_x(y,z) = \varepsilon_G + C_y \cdot (z - z_G) - C_z \cdot (y - y_G) \tag{2}$$

Equation 2: longitudinal strain distribution

With these assumptions, the vector $\boldsymbol{\chi}^T = \{\, \varepsilon_G \quad C_Y \quad C_Z \,\}$ constitutes the *distributor* of longitudinal strains in the section.

3.2 Discretization

To carry out numerical computation, the continuous material is divided in longitudinal fibers of finite cross sections. Longitudinal stress across each of these fibers

is assumed to be constant and equal to the longitudinal stress at the center of mass of the fiber. Equation 1 then becomes:

$$\mathbf{T} = \begin{cases} N = \sum\limits_{\text{fibers}} \sigma(y_s, z_s)\, dS \\ M_y = \sum\limits_{fibers} (z_s - z_G)\, \sigma(y_s, z_s)\, dS \\ M_z = -\sum\limits_{fibers} (y_s - y_G)\, \sigma(y_s, z_s)\, dS \end{cases} \tag{3}$$

Equation 3: vector of reduced forces (discretized version)

In these formulae, (y_s, z_s) and dS are respectively the coordinates of the center of mass and the cross section of the current fiber.

3.3 Constitutive Relations of Materials

The constitutive models relate the strain calculated at the center of mass of the fiber to the stress assumed uniform over the fiber cross section.

For simplicity, we also assume that the stress is a function of the present strain only, independently of the stress-strain history.

In the following, an elastoplastic behavior is assumed for steel, with a slight hardening beyond the yield point (see Fig. 3) which is useful to ensure numerical stability of the strain computation algorithm.

In other words, given the elastic strain $\varepsilon_{el} = \frac{f_e}{\gamma_s E_s}$ (divided, when appropriate, by the partial safety factor γ_s), the constitutive relations are:

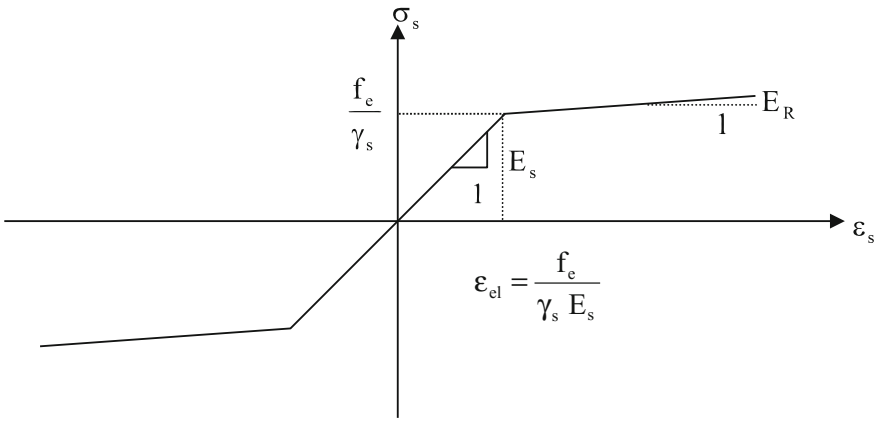

Fig. 3 Elastoplastic relation with hardening for steel fibers

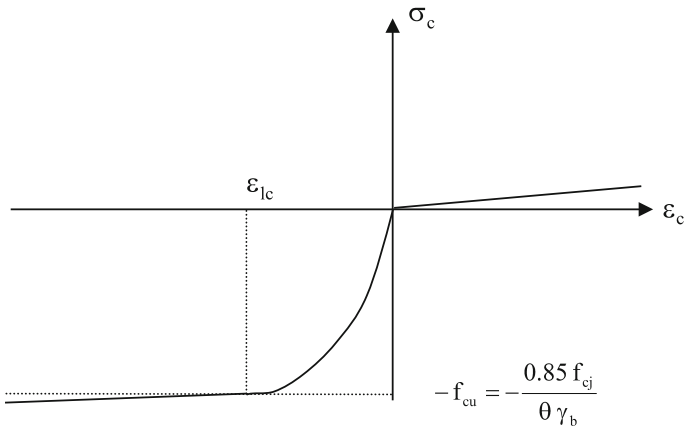

Fig. 4 Constitutive relations for concrete fibers

$$\begin{array}{ccc} \text{if } \varepsilon < -\varepsilon_{el} & \sigma_s = -\frac{f_e}{\gamma_s} + E_R\,(\varepsilon_s + \varepsilon_{el}) & \frac{\partial \sigma_s}{\partial \varepsilon_s} = E_R \\ \text{if } -\varepsilon_{el} < \varepsilon < \varepsilon_{el} & \sigma_s = E_s\,\varepsilon_s & \frac{\partial \sigma_s}{\partial \varepsilon_s} = E_s \\ \text{if } \varepsilon > \varepsilon_{el} & \sigma_s = \frac{f_e}{\gamma_s} + E_R\,(\varepsilon_s - \varepsilon_{el}) & \frac{\partial \sigma_s}{\partial \varepsilon_s} = E_R \end{array} \tag{4}$$

Equation 4: constitutive relations for steel

As far as concrete is concerned, we assumed a parabolic-rectangular stress-strain relationship, widely used in design codes. However we introduced a cracked section elastic modulus $E_{c,\,cracked}$ and a creep modulus $E_{c,\,creep}$ (see Fig. 4) so as to ensure a better stability of numerical algorithms.

With $f_{cu} = \frac{0.85\,f_{cj}}{\theta\,\gamma_b}$ the conventional stress limit for concrete, $\varepsilon_{lc} = -0,002$ the strain limit of the parabolic diagram, $E_b = 11000\,\sqrt[3]{f_{cj}}$ the conventional elastic modulus for concrete (used solely to define residual modulus for creep $E_{c,\,creep}$ and cracking $E_{c,\,cracked}$ made equal to 1/100th of this value, for example) the constitutive relations for concrete fibers are:

$$\begin{array}{ccc} \text{if } \varepsilon_c < \varepsilon_{lc} & \sigma_c = -f_{cu} + E_{c,\,creep}(\varepsilon_c - \varepsilon_{lc}) & \frac{\partial \sigma_c}{\partial \varepsilon_c} = E_{c,\,creep} \\ \text{if } \varepsilon_{lc} < \varepsilon_c < 0 & \sigma_c = -f_{cu}\left(1 - \left(1 - \frac{\varepsilon_c}{\varepsilon_{lc}}\right)^2\right) & \frac{\partial \sigma_c}{\partial \varepsilon_c} = -2\,\frac{f_{cu}}{\varepsilon_{lc}}\left(1 - \frac{\varepsilon_c}{\varepsilon_{lc}}\right) \\ \text{if } \varepsilon_c > 0 & \sigma_c = E_{c,\,cracked}\varepsilon_c & \frac{\partial \sigma_c}{\partial \varepsilon_c} = E_{c,\,cracked} \end{array} \tag{5}$$

Equation 5: constitutive relations for concrete fibers

4 Relations Between Distributor of Longitudinal Strains and the Vector of Reduced Forces

With the previous definitions of the section forces (Eq. 3) and of the distributor of longitudinal strains (Eq. 2), relations of the following type can be established which make use of the constitutive relations for steel and concrete (Eqs. 4 and 5):

$$\mathrm{T}\left(\varepsilon_{\mathrm{G}}, \mathrm{C_y}, \mathrm{C_z}\right) = \begin{cases} \mathrm{N} = \sum\limits_{\text{fibers}} \sigma\left(\varepsilon\left(\varepsilon_{\mathrm{G}}, \mathrm{C_y}, \mathrm{C_z}\right), \text{ material}\right) \mathrm{dS} \\ \mathrm{M_y} = \sum\limits_{\text{fibers}} \left(\mathrm{z_s} - \mathrm{z_G}\right) \sigma\left(\varepsilon\left(\varepsilon_{\mathrm{G}}, \mathrm{C_y}, \mathrm{C_z}\right), \text{ material}\right) \mathrm{dS} \\ \mathrm{M_z} = -\sum\limits_{\text{fibers}} \left(\mathrm{y_s} - \mathrm{y_G}\right) \sigma\left(\varepsilon\left(\varepsilon_{\mathrm{G}}, \mathrm{C_y}, \mathrm{C_z}\right), \text{ material}\right) \mathrm{dS} \end{cases} \tag{6}$$

Equation 6: strain-forces relations

Provided the constitutive relations are differentiable, the derivative of the force vector with respect to each strain distributor parameter can be computed:

$$\boldsymbol{\Delta}(\boldsymbol{\chi}) = \frac{\mathrm{d}\mathbf{T}}{\mathrm{d}\boldsymbol{\chi}} = \begin{bmatrix} \frac{\partial \mathrm{N}}{\partial \varepsilon_{\mathrm{G}}} & \frac{\partial \mathrm{N}}{\partial \mathrm{C_y}} & \frac{\partial \mathrm{N}}{\partial \mathrm{C_z}} \\ \frac{\partial \mathrm{M_y}}{\partial \varepsilon_{\mathrm{G}}} & \frac{\partial \mathrm{M_y}}{\partial \mathrm{C_y}} & \frac{\partial \mathrm{N}}{\partial \mathrm{C_z}} \\ \frac{\partial \mathrm{M_z}}{\partial \varepsilon_{\mathrm{G}}} & \frac{\partial \mathrm{M_z}}{\partial \mathrm{C_y}} & \frac{\partial \mathrm{M_z}}{\partial \mathrm{C_z}} \end{bmatrix} \tag{7}$$

Equation 7: derivative of the force vector with respect to each strain distributor parameter

Conversely, the above relations do not explicitly yield the distributor of strains as a function of external forces ($\mathbf{T}_{\mathrm{ext}}^{\mathrm{T}} = \left\{\mathrm{N_{ext}}, \mathrm{M_{y,ext}}, \mathrm{M_{z,ext}}\right\}$). For that purpose, it is convenient to use a research algorithm, for example of the Newton-Raphson type, in which an arbitrary initial distributor of strains is chosen $\boldsymbol{\chi}^0$ and a series of distributors is computed in the following way:

$$\chi^{\mathrm{n}+1} = \begin{Bmatrix} \varepsilon_{\mathrm{G}}^{\mathrm{n}+1} \\ \mathrm{C_y^{n+1}} \\ \mathrm{C_z^{n+1}} \end{Bmatrix} = \chi^{\mathrm{n}} + \left[\boldsymbol{\Delta}(\boldsymbol{\chi}^{\mathrm{n}})\right]^{-1} \begin{Bmatrix} \mathrm{N_{ext}} - \mathrm{N}(\boldsymbol{\chi}^{\mathrm{n}}) \\ \mathrm{M_{y,ext}} - \mathrm{M_y}(\boldsymbol{\chi}^{\mathrm{n}}) \\ \mathrm{M_{z,ext}} - \mathrm{M_z}(\boldsymbol{\chi}^{\mathrm{n}}) \end{Bmatrix} \tag{8}$$

Equation 8: series of strain distributors

This series converges provided the determinant of the derivative of the force vector with respect to the strain distributor (Eq. 7) does not come close to zero, which explains the hardening chosen for post-yield behavior.

As an example, Fig. 5 shows the result of the research algorithm for a hollow core rectangular pier of exterior dimensions 5 m × 8 m, 40 cm wall thickness

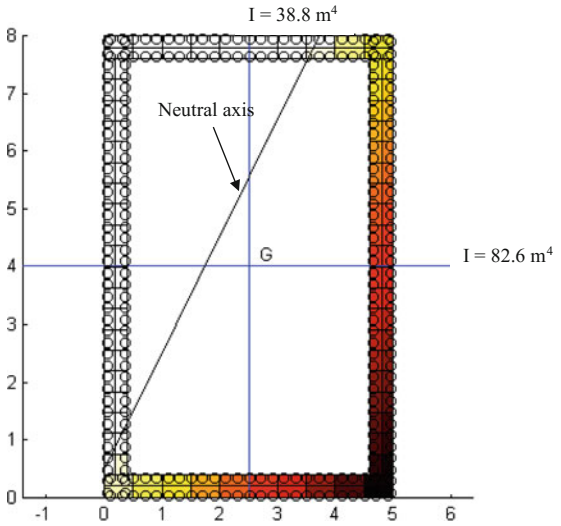

Fig. 5 Example of a pier cross-section

reinforced with 16 mm diameter bars placed every 20 cm on each face (inside and outside) with 3 cm concrete cover. For external forces defined by:

$N = -80$ MN	$M_y = 150$ MN.m	$M_z = 150$ MN.m

The maximum compression stress in concrete is 26.2 MPa (shortening of 0.20%) and the maximum tensile stress in steel 288 MPa (elongation of 0.14%).

This way a bijective relation can be established $\{N \quad M_y \quad M_z\}^T = T\left(\{\varepsilon_G \quad C_y \quad C_z\}^T\right)$. The differentiable properties of this relation will turn out to be particularly interesting in the following optimization of section parameters.

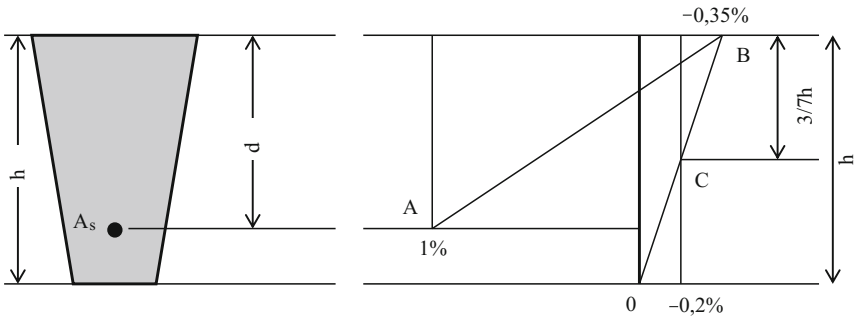

Fig. 6 Strains conventional limit states

5 Limit States

Reinforced concrete codes usually set conventional limits to compression and tensile strains of various materials. For example, tensile strain for steel is limited to 1% (limit state A), compressive strain for concrete to 0.35% (limit state B) and a uniform compression of the section cannot shorten concrete fibers beyond a strain of 0.2% (limit state C). These constraints are summarized in the following diagram for a plane bending moment combined with axial force:

For simplicity of graphical representation, the following discussion will be restricted to the optimization of a reinforced concrete section subjected to a plane bending moment combined with an axial force. The method however extends to loads of more than two components.

In the particular case considered, the three limit states can be characterized by the following functions of the distributor of strains whose components are the strain at the center of mass ε_G and the curvature C_y. A positive sign of one the three functions indicates that the corresponding limit state has not been reached.

Limit state A (maximum tensile strain of steel)	$g_A(\varepsilon_G, C_y) = 0.01 - \varepsilon_G - C_y(z_A - z_G)$ where z_A and z_G are the ordinates of the most tensed steel fiber and of the center of mass of the section	$g_A(\varepsilon_G, C_y) \geq 0$ if the steel tensile limit state has not been reached: (steel strain $\varepsilon(z_A) \leq 0.01$)
Limit state B (maximum compressive strain in concrete)	$g_B(\varepsilon_G, C_y) = 0.0035 + \varepsilon_G + C_y(z_B - z_G)$ where z_B is the ordinate of the most compressed concrete fiber	$g_B(\varepsilon_G, C_y) \geq 0$ if the concrete compressive strain has not been reached: (concrete strain $\varepsilon(z_B) \geq -0.0035$)
Limit state C (average compressive strain in concrete)	$g_C(\varepsilon_G, C_y) = 0.002 + \varepsilon_G + C_y(z_C - z_G)$ where z_C is the ordinate of point C (see Fig. 6)	$g_C(\varepsilon_G, C_y) \geq 0$ if the average concrete compressive strain limit state has not been reached: (concrete strain $\varepsilon(z_C) \geq -0.002$)

These functions are introduced in order to use the formalism of reliability analysis. The safety of section is guarantied when all three functions $g_i(\varepsilon_G, C_y)$ are strictly positive. A limit state is reached as soon as one of function goes to zero. Negative values of a limit state function mean a crossing of the limit state threshold and therefore a "conventional" failure of the reinforced concrete section.

In a (ε_G, C_y) diagram, the curves defined by $g_i(\varepsilon_G, C_y) = 0$ are straight lines bounding the safety domain of the section (Fig. 7).

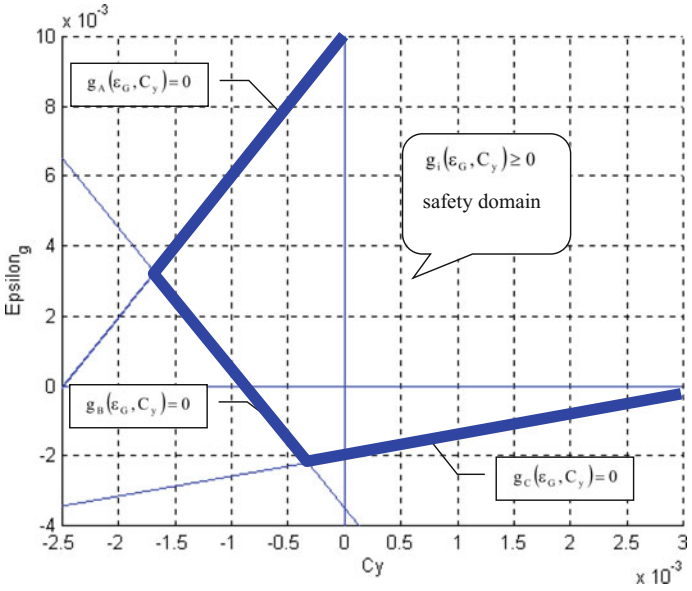

Fig. 7 Limit states in terms of the section strain parameters

6 Interaction Curves

With the transformation $\{ N \quad M_y \}^T = T\left(\{ \varepsilon_G \quad C_y \}^T \right)$ described in paragraph 4, limits states can also be expressed in terms of section forces:

$$\tilde{g}_i(M_y,\ N) = g_i(\varepsilon_G,\ C_y) = g_i\left(T^{-1}(M_y,\ N)\right) \qquad \text{where } i = A,\ B \text{ or } C \tag{9}$$

The $\tilde{g}_i(M_y,\ N) = 0$ curves define the safety domain boundary, now in terms of the section forces (bending moment and axial load). These curves are commonly referred to as interaction curves.

The interaction curves for the reinforced concrete section described in paragraph 4, are presented in Fig. 8 with the more usual axis ($-M_y$, $-N$), $-N$ being thus positive in compression and $-M_y$ positive when it tends to compress the upper fiber:

The A-limit state (steel elongation) bounds the lower part of the safety domain in the above diagram. The B-limit state (extreme concrete fiber crushing) bounds the middle part and the C-limit state (general concrete crushing) bounds the upper part. A simultaneous positive sign of all three $\tilde{g}_i(M_y,\ N)$ functions characterizes the safety domain.

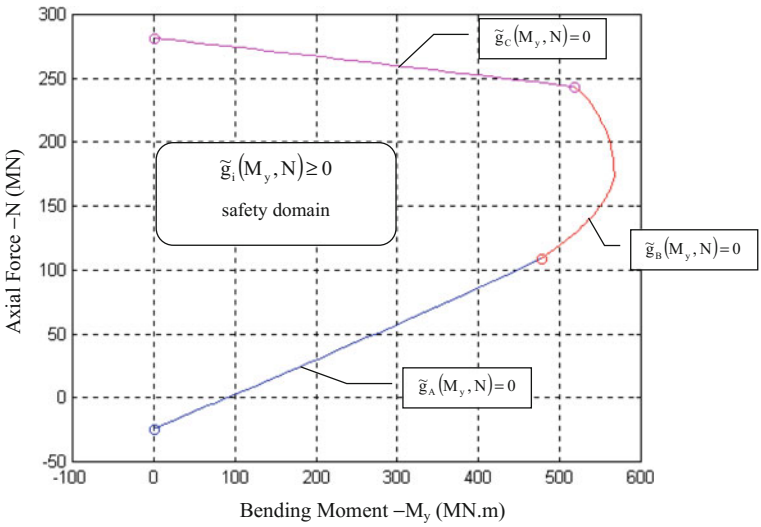

Fig. 8 Interaction diagram (−N, −My)

7 Aerodynamic and Seismic Forces

Aerodynamic and seismic actions are time dependent and are generally considered to be very random phenomena. If these actions were known as functions of time, a dynamic structural analysis could be performed leading to a time dependent force vector within a given section (N(t), $M_y(t)$, $M_z(t)$) which, if the section had been properly designed, would remain constantly within the safety domain bounded by the interaction curves. It is clear that this approach is only conventional since it does not take into account the loading history and inelastic behavior of materials which have a significant impact on the response and capacity of the structure.

Moreover, the load time history is very rarely known in detail. However, it is possible in practice, through a probabilistic or stochastic analysis, to define a curve or a surface boundary (typically an ellipse or an ellipsoid) within which the section forces will remain or, at least, outside of which the section forces will go with a known and very small probability (see Capra and Davidovici 1984).

Take, for example, the bending moment M and axial force N in a beam section resulting from static forces, yielding the static response M_0 and N_0, and seismic forces in one horizontal direction, yielding the dynamic responses $M - M_0$ and $N - N_0$. Assume that M_i and N_i are the response spectrum values of M and N for the ith mode.

If the dynamic response were governed by a sole mode, then the maximum dynamic responses $M - M_0$ and $N - N_0$ would be reached simultaneously.

Because of the multiplicity of vibration modes and partial correlation between modes, maximum axial force and maximum bending moment will not be reached simultaneously.

However, an elliptic envelope of combined bending moment and axial load can be defined as:

$$\left(\frac{M-Mo}{\Delta M}\right)^2+\left(\frac{N-No}{\Delta N}\right)^2-2\,\rho\,\left(\frac{M-Mo}{\Delta M}\right)\,\left(\frac{N-No}{\Delta N}\right)=1-\rho^2$$

where

- Mo and No are the values at rest of axial load and bending moment,
- ΔM and ΔN are the spread of their dynamic variations,
- ρ is the coefficient of correlation between the dynamic variations of axial force and bending moment ($-1 \le \rho \le 1$).

In the one directional seismic example chosen above

$$\Delta M^2=\sum_i\sum_j \rho_{ij}M_iM_j$$

$$\Delta N^2=\sum_i\sum_j \rho_{ij}N_iN_j$$

$$\rho=\frac{\sum_i\sum_j \rho_{ij}M_iN_j}{\Delta M\cdot\Delta N}$$

where the correlation coefficients between modal responses can be inferred from the well-known complete quadratic combination (CQC) rule:

$$\rho_{ij}=\frac{8\sqrt{\xi_i\xi_j\omega_i\omega_j}\left(\xi_i\omega_i+\xi_j\omega_j\right)\omega_i\omega_j}{\left(\omega_i^2-\omega_j^2\right)^2+4\xi_i\xi_j\omega_i\omega_j\left(\omega_i^2+\omega_j^2\right)+4\left(\xi_i^2+\xi_j^2\right)\omega_i^2\omega_j^2}$$

ξ_i and ω_i being respectively the damping ratio and circular frequency of the ith mode.

The ellipse can also be viewed as an isoprobability curve for the "correlated gaussian" vector of section forces.

8 Standard Practice for the Design of a Reinforced Concrete Section

For the section to be properly designed, the above ellipse should remain within the boundary of the section interaction curve (M, N).

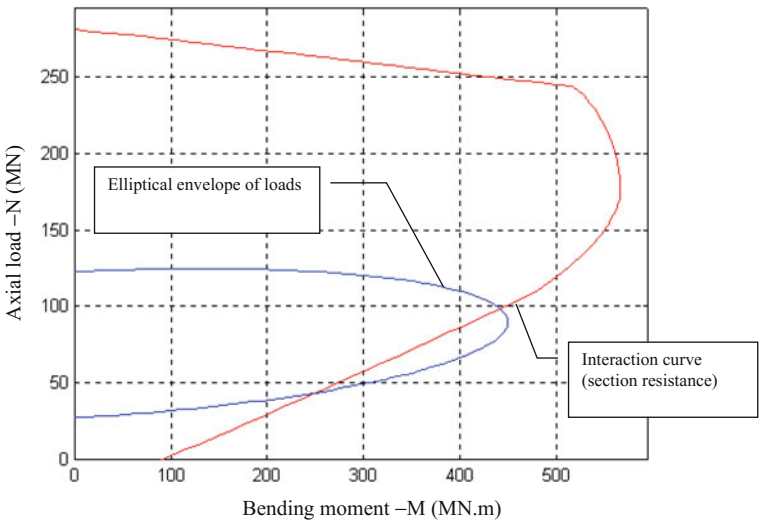

Fig. 9 Elliptical envelope of loads versus interaction curve

Namely, each point of the ellipse should be (and therefore should be checked to be) within the safety domain (see Fig. 9).

In practice (Capra and Davidovici 1984 or Leblond 1980), the problem can been simplified by inscribing the ellipse inside an octagon each side of which is tangent to the ellipse as shown in Fig. 10 (taken from Leblond 1980).

Then one checks that each summit of the octagon, P1 to P8 in Fig. 10, lies within the safety domain, or, which is equivalent, that the corresponding forces do not lead to strains beyond one of the limit states, defined by a steel ratio.

Leblond has shown that the octagon surface is only 5% larger than the ellipse surface, which means that the approximation is accurate enough for engineering purposes.

In three dimension (M_y, M_z, N), the ellipsoid can be inscribed inside a polyhedron with 24 summits and each of these is checked with respect to the limit states.

These many checks will tell, with a good approximation, whether or not the load envelope lies inside the safe domain, but they will not tell what the safety margin is, nor what to do to make a section safe, if it is not.

In particular, this method does not yield the sensitivity of the safety margin to design parameters, such as beam size or steel ratio. In other words, they are not physically speaking and they do not help optimize the section quantities (steel and/or concrete).

The following sections will solve this issue.

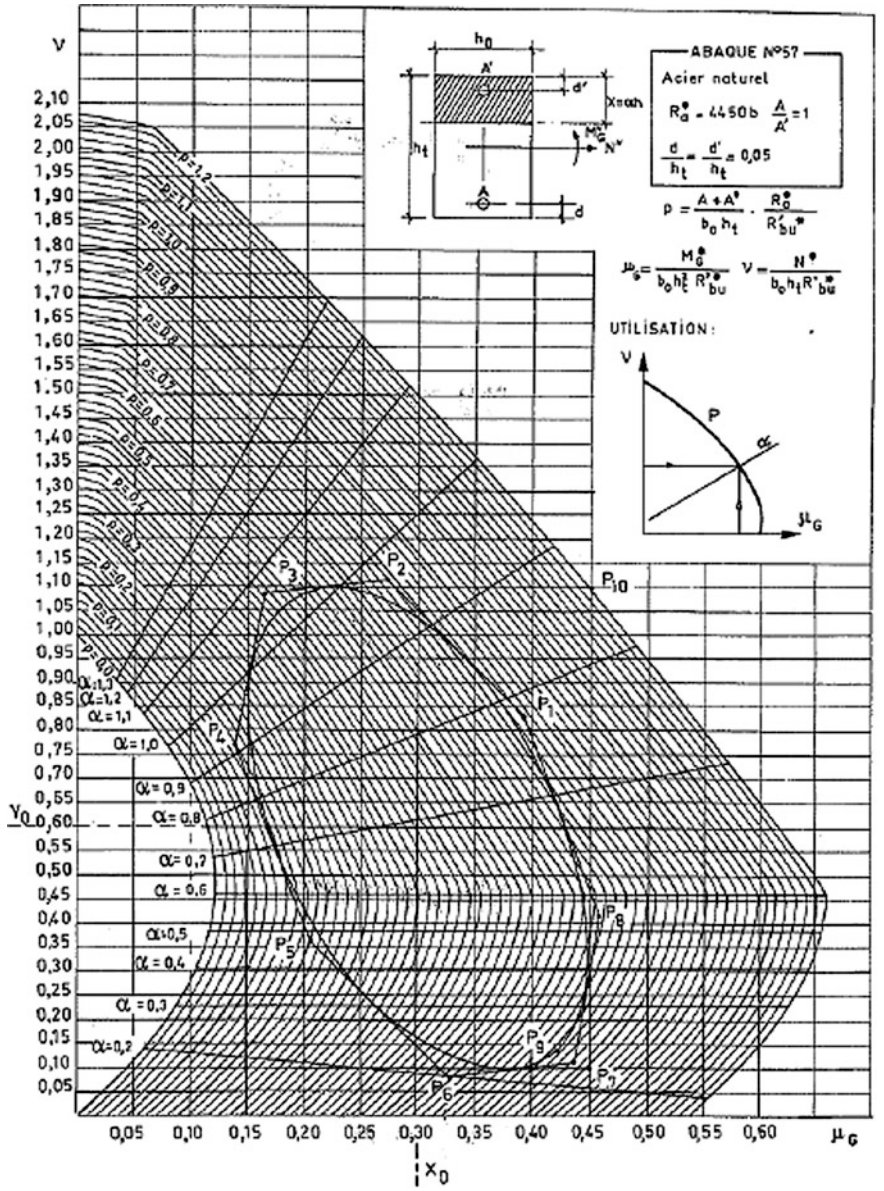

Fig. 10 Approximation of the ellipse with an octagon

9 Improvement of the Design Method—Transformation to the Standard Normal Space

The above problem has a very simple geometrical interpretation in a slightly different space that we will call the "standard normal space", thus referring to reliability theories. One goes from the "original space" (M, N), where we assume that (M, N) is a gaussian vector of correlated random variables, to the standard normal space, where the corresponding variables are gaussian, of unit variance, centered and non correlated, through a linear transformation.

Let us call:

- $\boldsymbol{\mu} = \begin{Bmatrix} M_o \\ N_o \end{Bmatrix}$ the load vector at rest (center of the ellipse in the original space).
- $\mathbf{D} = \begin{Bmatrix} \Delta M \\ \Delta N \end{Bmatrix}$ the vector of maximal dynamic variations (sizing the ellipse in the original space).
- $\mathbf{R} = \begin{bmatrix} 1 & \rho \\ \rho & 1 \end{bmatrix}$ the correlation matrix (giving the tilt of the ellipse in the original space) and $\mathbf{L} = \begin{bmatrix} 1 & 0 \\ \rho & \sqrt{1-\rho^2} \end{bmatrix}$ its lower triangular (Choleski) decomposition so that $\mathbf{L}\mathbf{L}^{\mathrm{T}} = \mathbf{R}$.

The transformation from the original space $\mathbf{x} = \begin{Bmatrix} M \\ N \end{Bmatrix}$ to the standard normal space $\mathbf{u} = \begin{Bmatrix} u_1 \\ u_2 \end{Bmatrix}$ is performed through the following relation:

$$\begin{aligned} \mathbf{u} &= \mathbf{L}^{-1}\mathbf{D}^{-1}(\mathbf{x} - \boldsymbol{\mu}) \\ \mathbf{x} &= \boldsymbol{\mu} + \mathbf{L}\,\mathbf{D}\,\mathbf{u} \end{aligned} \tag{10}$$

Equation 10: transformation to the standard normal space

The Jacobian of the transformation is:

$$\mathbf{J}_{x,u} = \mathbf{D}\mathbf{L} \quad \text{et} \quad \mathbf{J}_{u,x} = \mathbf{L}^{-1}\mathbf{D}^{-1}$$

In the standard normal space, the load envelope is a circle of unit radius centered about the origin.

As the transformation is linear, it preserves tangency from one space to the other and in particular the fact that the load envelope crosses out the interaction curve or not.

Figure 11 shows, for convenience, the interaction curve in the standard normal space. It has been drawn point by point from the interaction diagram in the original space. The following algorithm does not however require that this curve be drawn in the standard normal space.

The limit state functions are also defined in the standard normal space:

$$G_i(\mathbf{u}) = \tilde{g}_i(\mathbf{x}) = g_i\left(\varepsilon_G(\mathbf{x}), C_y(\mathbf{x})\right)$$

In the standard normal space, the section fails when the interaction curve (representing resisting characteristics) penetrates inside the envelope of loads, now represented by the unit circle. This has a simple geometric expression:

Let β be the shortest distance from the origin to the interaction curve;

- if $\beta \leq 1$, the section is insufficiently designed (the load envelope out-crosses the interaction curve),
- if $\beta = 1$, the section is optimally designed for the dynamic loads,
- if $\beta \geq 1$, the section is designed with some margin $(\beta - 1)$ with respect to the dynamic loads.

Note that β is the minimum of the distances to the several limit states $G_i = 0$ measured in the standard normal space.

Thanks to the transformation to the standard normal space, the load envelope is particularly simple (unit circle centered about the origin). However, the interaction curve in this space has no simple expression (just as in the original space, by the way).

We will see in the following that, in order to design the reinforced concrete section in an optimal way, we will not need a literal expression of the interaction curve in that space.

10 Search for a Design Point and Safety Margin

Checking whether a reinforced concrete section is properly designed for dynamic loads sums up to evaluating the distance from the origin to the interaction curve of that section in the standard normal space, or, which is equivalent, the minimum of the distances to the limit states $G_i = 0$ in that space.

For that purpose, we use an algorithm that looks for the "design point" (name borrowed from the reliability theories) which is the closest point to the origin on a limit state curve. This point satisfies the following optimization problem under constraints:

$$\min\{\|\mathbf{u}\| \mid G_i(\mathbf{u}) = 0\}$$

This particular algorithm, called HL-RF or improved HL-RF (see Ditlevsen and Madsen 1996 and Zhang and Der Kiureghian 1995) is well known in reliability analysis. We review the main steps hereafter:

(a) Initialize by fixing tolerances ξ_1 and ξ_2 (for example $\xi_1 = \xi_2 = 10^{-3}$) and a starting point $\mathbf{u}_1$ (typically $\mathbf{u}_1 = [0 \quad 0]^T$ or $\mathbf{x}_1 [M_o \quad N_o]^T$).

(b) At each step, compute $\mathbf{x}_j = \mathbf{x}(\mathbf{u}_j)$ using Eq. 10, then $\mathbf{x}_j = [\,M_j \quad N_j\,]^T$.
The distributor of strains $\boldsymbol{\chi}(\mathbf{x}_j) = [\,\varepsilon_G \quad C_y\,]^T = \left[T^{-1}(M_j, N_j)\right]^T$, comes out of the procedure suggested in paragraph 4, and one finds:

$$G_i(\mathbf{u}_j) = \tilde{g}_i(x_j) = g_i(\boldsymbol{\chi}(\mathbf{x}_j)) \text{ and } \nabla G_i(\mathbf{u}_j)^T = \nabla_x \tilde{g}_i(\mathbf{x}_j)^T \mathbf{J}_{x,u}$$

(note that the limit state function in the normal standard space and its gradients are only computed through their original space counterpart)

$$\text{with } \nabla_x \tilde{g}_i(\mathbf{x}_j) = \begin{bmatrix} \frac{\partial M}{\partial \varepsilon_G} & \frac{\partial N}{\partial \varepsilon_G} \\ \frac{\partial M}{\partial C_y} & \frac{\partial N}{\partial C_y} \end{bmatrix}^{-1} \nabla_\chi g_i(\chi(\mathbf{x}_j)) = \begin{bmatrix} \frac{\partial M}{\partial \varepsilon_G} & \frac{\partial N}{\partial \varepsilon_G} \\ \frac{\partial M}{\partial C_y} & \frac{\partial N}{\partial C_y} \end{bmatrix}^{-1} \begin{Bmatrix} \frac{\partial g_i}{\partial \varepsilon_G} \\ \frac{\partial g_i}{\partial C_y} \end{Bmatrix}$$

Incidentally, note that $\begin{bmatrix} \frac{\partial M}{\partial \varepsilon_G} & \frac{\partial N}{\partial \varepsilon_G} \\ \frac{\partial M}{\partial C_y} & \frac{\partial N}{\partial C_y} \end{bmatrix}^{-1} = \begin{bmatrix} \frac{\partial \varepsilon_G}{\partial M} & \frac{\partial C_y}{\partial M} \\ \frac{\partial \varepsilon_G}{\partial N} & \frac{\partial C_y}{\partial N} \end{bmatrix}$ is computed using Eq. 7.

(c) The direction vector of search for the "descent" algorithm is:

$$\mathbf{d}_j = \frac{-G_i(\mathbf{u}_j) + \nabla G_i(\mathbf{u}_j)^T \mathbf{u}_j}{\|\nabla G_i(\mathbf{u}_j)\|} \frac{\nabla G_i(\mathbf{u}_j)}{\|\nabla G_i(\mathbf{u}_j)\|} - \mathbf{u}_j$$

(d) And the step size λ_j can be either chosen arbitrarily between 0 and 1 (0.2 for example) or by looking for the minimum of a "merit function" (see Zhang and Der Kiureghian, 1995) $m(\mathbf{u}) = 1/2\|\mathbf{u}\|^2 + c\,G(\mathbf{u})$ (where constant $c > \|\mathbf{u}_j\| / \|\nabla G(\mathbf{u}_j)\|$):

$$\lambda_j = \arg \min_{\lambda \in]0,1]} \{m(\mathbf{u}_j + \lambda \mathbf{d}_j) - m(\mathbf{u}_j)\}$$

(e) The next trial point is:

$$\mathbf{u}_{j+1} = \mathbf{u}_j + \lambda_j \mathbf{d}_j$$

(f) Convergence is reached when the trial point is close to the limit state $(G_i(\mathbf{u}_j) \approx 0)$ and when the search direction does not change any more:

- $|G_i(\mathbf{u}_j)/G_i(\mathbf{u}_1)| \le \xi_1$
- $\left\|\mathbf{u}_{j+1} - \boldsymbol{\alpha}_j^T \mathbf{u}_j \boldsymbol{\alpha}_j\right\| \le \xi_2$ where the unit vector giving the direction of search has been defined: $\boldsymbol{\alpha}_j = -\nabla G(\mathbf{u}_j) / \|\nabla G(\mathbf{u}_j)\|$

(g) If the algorithm has not converged, the procedure resumes at step (b),
(h) If it has converged, we define:

- **The design point** $\mathbf{u}^* = \mathbf{u}_j$
- **The direction unit vector** $\boldsymbol{\alpha} = -\nabla G(\mathbf{u}_j) / \|\nabla G(\mathbf{u}_j)\|$
- **The distance to the origin** $\beta = \boldsymbol{\alpha}^T \mathbf{u}^*$

In the numerical example below, we will use the following values: $M_o = 0$, $N_o = 75$ MN, $\Delta M_o = 450$ MN.m, $\Delta N_o = 50$ MN and $\rho = 1/3$.

Applied to the above studied reinforced concrete section, the algorithm (with λ_j fixed at 0.2) converges in 27 iterations and yields a $\beta = 0.8379$ for the steel tension limit state (A) (the more concerned in this particular case) which expresses that the reinforced concrete section is insufficiently designed and lacks of steel.

A small circle shows the design point on Fig. 11 together in the original space of loads and in the standard normal space.

11 Optimization of a Reinforced Concrete Section

An interesting property of the HL-RF algorithm is that one obtains quite easily as by-products the sensitivities of distance β with respect to the system parameters and in particular with respect to the parameters that can change the interaction curve.

Let θ be a multiplication factor of the initial steel quantity in the reinforced concrete section. Namely, any particular steel fiber whose cross section is initially dS_o will turn $\theta\, dS_o$ during the optimization process.

$$\begin{cases} N = \sum_{\text{concrete fibers}} \sigma\big(\varepsilon(\varepsilon_G, C_y), \text{concrete}\big)\, dS + \sum_{\text{steel fibers}} \sigma\big(\varepsilon(\varepsilon_G, C_y), \text{steel}\big)\, \theta\, dS_o \\ M = \sum_{\text{concrete fibers}} (z_s - z_G)\, \sigma\big(\varepsilon(\varepsilon_G, C_y), \text{concrete}\big) dS + \sum_{\text{steel fibers}} (z_s - z_G)\, \sigma\big(\varepsilon(\varepsilon_G, C_y), \text{steel}\big)\, \theta\, dS_o \end{cases} \tag{11}$$

The limit state thus becomes naturally a function of parameter θ.

One shows (Hohenbichler and Rackwitz 1986) that the infinitesimal variation (sensitivity) of β with respect to θ writes:

$\frac{\partial \beta}{\partial \theta} = \frac{1}{\|\nabla G\|} \frac{\partial g}{\partial \theta}(\mathbf{x}^*, \theta)$ where $\mathbf{x}^*$ is the design point in the original space. In order to optimize the steel quantity that lacks in the example we used before, we apply this formula to the steel tension limit state (A):

$$\tilde{g}_A(M, N) = 0.01 - \varepsilon_G(M, N, \theta) - (z_A - z_G) \cdot C_y(M, N, \theta)$$

thus $\frac{\partial \beta}{\partial \theta} = \frac{1}{\|\nabla G\|} \left[-\frac{\partial \varepsilon_G}{\partial \theta} - (z_A - z_G) \frac{\partial C_y}{\partial \theta} \right]$.

The distributor of strain is not an explicit function of N, M, and θ. However, one can compute its partial derivative with respect to parameter θ, that is, with N and M fixed:

$$dN = \frac{\partial N}{\partial \varepsilon_G} d\varepsilon_G + \frac{\partial N}{\partial C_y} dC_y + \frac{\partial N}{\partial \theta} d\theta = 0$$
$$dM = \frac{\partial M}{\partial \varepsilon_G} d\varepsilon_G + \frac{\partial M}{\partial C_y} dC_y + \frac{\partial M}{\partial \theta} d\theta = 0$$

from which we find

$$\frac{\partial \varepsilon_G}{\partial \theta} = -\frac{\frac{\partial N}{\partial \theta}\frac{\partial M}{\partial C_y} - \frac{\partial M}{\partial \theta}\frac{\partial N}{\partial C_y}}{\frac{\partial N}{\partial \varepsilon_G}\frac{\partial M}{\partial C_y} - \frac{\partial M}{\partial \varepsilon_G}\frac{\partial N}{\partial C_y}} \quad \text{and} \quad \frac{\partial C_y}{\partial \theta} = -\frac{\frac{\partial M}{\partial \theta}\frac{\partial N}{\partial \varepsilon_G} - \frac{\partial N}{\partial \theta}\frac{\partial M}{\partial \varepsilon_G}}{\frac{\partial N}{\partial \varepsilon_G}\frac{\partial M}{\partial C_y} - \frac{\partial M}{\partial \varepsilon_G}\frac{\partial N}{\partial C_y}}$$

with

$$\frac{\partial N}{\partial \theta} = \sum_{\text{fibre d'acier}} \sigma\left(\varepsilon\left(\varepsilon_G,\ C_y\right), \text{acier}\right) dS_o$$
$$\frac{\partial M}{\partial \theta} = \sum_{\text{fibres d'acier}} \left(z_s - z_G\right) \sigma\left(\varepsilon\left(\varepsilon_G,\ C_y\right), \text{acier}\right) dS_o$$

which comes out Eq. 11. All other terms were computed previously (Eq. 7).

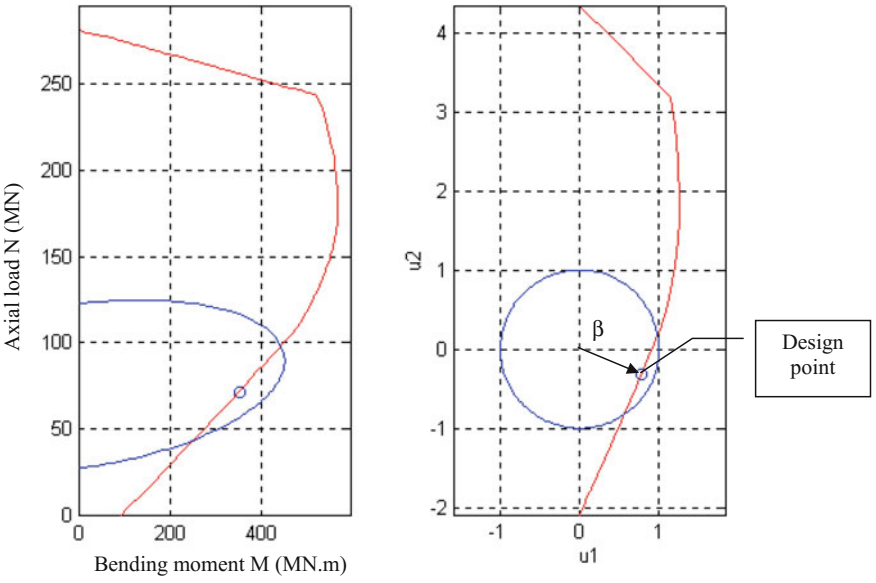

Fig. 11 Resistance and load (original space to the *left*, standard normal space to the *right*)

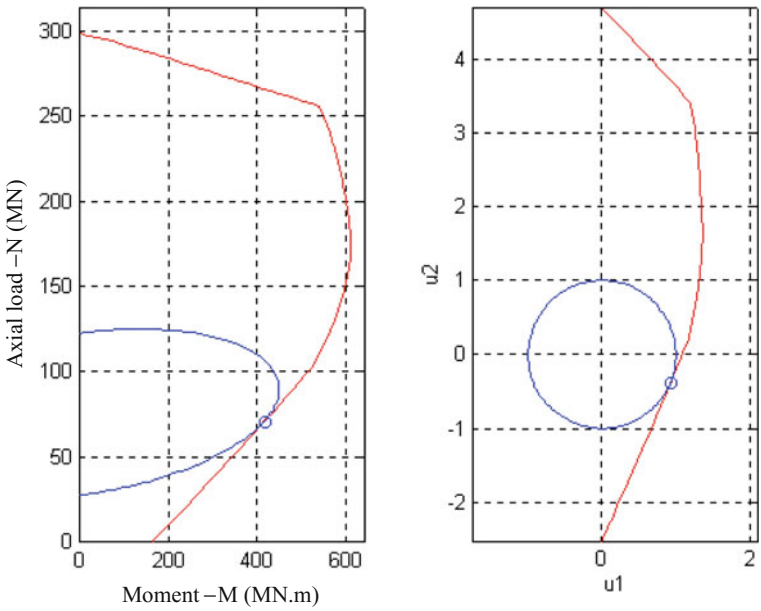

Fig. 12 Load envelope and resistance after optimization

Having thus computed $\frac{\partial \beta}{\partial \theta}$, one finds by first order approximation the increment of parameter θ which is necessary to make the section optimal ($\beta_{optimal} = 1$):

$$\Delta\theta = \frac{1-\beta}{\frac{\partial \beta}{\partial \theta}}$$

Applied to the previous example, this leads to multiply each steel section by 1.8377. With these new steel quantities, one obtains an excellent result as confirmed by the new position of the interaction curve which is (almost) tangent to the load ellipse in the original space and the new index $\beta = 0.9997$ in the standard normal space (Fig. 12). In this case, it is not even necessary to pursue the optimization process beyond this very first step.

12 Conclusion

We changed the elliptic envelope of dynamic load to a unit circle centered about the origin through a simple geometric transformation. In this new space of loads and resistance, called "standard normal space", the vulnerability of the reinforced concrete section with respect to the dynamic load has a very simple geometrical expression: for the section to be safe, the distance β of the origin to the limit state

curves (interaction curves) must be greater or equal to one. The distance β can be viewed as a measure of the safety margin.

The distance β is evaluated using an algorithm well known in the field of reliability of structures. The algorithm converges rapidly and, conveniently, does not require to draw the interaction curves in either space (original M-N space or standard normal space). Furthermore, it is independent of the dimension of the load and resistance space so that the elements derived here extend naturally to higher dimension problems (axial force and two bending moments, shear force, etc.).

The algorithm yields, as a by-product, the sensitivity of margin β to modifications in the section properties (steel quantity, thickness of a concrete member), which allows to optimize material quantities in a very efficient way.

References

Capra A, Davidovici V (1984) Calcul dynamique des structures en zone sismique, Eyrolles

Ditlevsen O, Madsen HO (1996) Structural reliability methods. Wiley

Hohenbichler M, Racwitz R (1986) Sensitivity and importance measures in structural reliability. Civil Eng Syst 3:203–210

Kahan M (2002) Dimensionnement d'une section en béton armé soumise à une enveloppe elliptique de sollicitations dynamiques combinées. Revue française de génie civil 7–8/2002:1283–1308

Leblond L (1980) Calcul sismique par la méthode modale—utilisation des réponses pour le dimensionnement. In: Annales de l'ITBTP, no 380, pp 119–127

Zhang Y, Der Kiureghian A (1995) Two improved algorithms for reliability analysis. In: Rackwitz R, Augusti G, Borri A (eds) Reliability and optimization of structural systems, proceedings of the 6th IFIP WG 7.5 working conference on reliability and optimization of structural systems, 1994, pp 297–304

FORM Sensitivities to Distribution Parameters with the Nataf Transformation

Jean-Marc Bourinet

Abstract The Nataf transformation has been proven very useful in reliability assessment when marginal distributions are statistically known and linear correlation is sufficient for modeling the dependence between random inputs. Under the assumption that the use of FORM is appropriate for the problem of interest, it is often of importance to quantify how the FORM solution is sensitive to the distribution parameters of the random inputs. Such information can be exploited in different contexts including optimal design under uncertainty. This chapter describes how sensitivities to marginal distribution parameters and linear correlation can be assessed numerically in the context of FORM based on the Nataf transformation. The emphasis is on the accuracy of such sensitivities with no other approximations than the one due to numerical integration. In the presented examples, the accuracy of these sensitivities is assessed w.r.t. reference solutions. The sensitivity to correlation brings useful information which are complementary to those w.r.t. marginal distribution parameters. High sensitivities may be detected such as illustrated in the context of stochastic crack growth based on the Virkler data set.

1 Introduction

In time-invariant structural reliability, the failure probability p_f is formulated in terms of a random vector $\boldsymbol{X} = \left(X_1, \ldots, X_n\right)^\mathrm{T}$ representing n uncertain inputs of a system of interest and a limit-state function (LSF) $g : \mathscr{X} \subseteq \mathbb{R}^n \to \mathbb{R}, \boldsymbol{x} \mapsto g(\boldsymbol{x})$ which defines its failure criterion (or a combination of its failure criteria). We conventionally define the failure domain as $\mathscr{F}_{\boldsymbol{x}} = \{\boldsymbol{x} \in \mathscr{X} : g(\boldsymbol{x}) \leq 0\}$ and the safe domain $\overline{\mathscr{F}}_{\boldsymbol{x}}$ as the complementary domain of $\mathscr{F}_{\boldsymbol{x}}$ in $\mathscr{X}$. The failure probability p_f is given by the following n-fold integral:

J.-M. Bourinet (✉)
Université Clermont Auvergne, CNRS, SIGMA Clermont, Institut Pascal,
F-63000 Clermont Ferrand, France
e-mail: bourinet@sigma-clermont.fr

P. Gardoni (ed.), *Risk and Reliability Analysis: Theory and Applications*,
Springer Series in Reliability Engineering, DOI 10.1007/978-3-319-52425-2_12

$$p_{\mathrm{f}} = \int_{g(\boldsymbol{x})\leq 0} f_{\boldsymbol{X}}(\boldsymbol{x})\,\mathrm{d}\boldsymbol{x} = \int_{\mathscr{X}} \mathbb{1}_{\mathscr{F}_{\boldsymbol{x}}}(\boldsymbol{x})\, f_{\boldsymbol{X}}(\boldsymbol{x})\,\mathrm{d}\boldsymbol{x}, \tag{1}$$

in which $f_{\boldsymbol{X}} : \mathbb{R}^n \to \mathbb{R}_+, \boldsymbol{x} \mapsto f_{\boldsymbol{X}}(\boldsymbol{x})$ denotes the joint continuous probability density function (pdf) of $\boldsymbol{X}$, $\mathbb{1}_{\mathscr{F}_{\boldsymbol{x}}}(\boldsymbol{x})$ is the indicator function of the failure domain $\mathscr{F}_{\boldsymbol{x}}$ such that $\mathbb{1}_{\mathscr{F}_{\boldsymbol{x}}}(\boldsymbol{x}) = 1$ if $\boldsymbol{x} \in \mathscr{F}_{\boldsymbol{x}}$, $\mathbb{1}_{\mathscr{F}_{\boldsymbol{x}}}(\boldsymbol{x}) = 0$ otherwise, and $\mathrm{d}\boldsymbol{x} = \mathrm{d}x_1 \ldots \mathrm{d}x_n$.

The reliability problem defined in Eq. (1) is conveniently expressed in the n-dimensional standard normal space $\mathbb{R}^n$ by means of a suitable transformation $T : \mathscr{X} \to \mathbb{R}^n, \boldsymbol{x} = \left(x_1, \ldots, x_n\right)^{\mathrm{T}} \mapsto \boldsymbol{u} = \left(u_1, \ldots, u_n\right)^{\mathrm{T}} = T(\boldsymbol{x})$ constructed such that the following equalities (in distribution) hold:

$$\boldsymbol{U} = T(\boldsymbol{X}) \Leftrightarrow \boldsymbol{X} = T^{-1}(\boldsymbol{U}), \tag{2}$$

where $\boldsymbol{U} = \left(U_1, \ldots, U_n\right)^{\mathrm{T}}$ and U_i for $i = 1, \ldots, n$ are independent normal variates with zeros means and unit standard deviations. Equation (1) rewrites as follows:

$$p_{\mathrm{f}} = \int_{G(\boldsymbol{u})\leq 0} \varphi_n(\boldsymbol{u})\,\mathrm{d}\boldsymbol{u} = \int_{\mathbb{R}^n} \mathbb{1}_{\mathscr{F}_{\boldsymbol{u}}}(\boldsymbol{u})\,\varphi_n(\boldsymbol{u})\,\mathrm{d}\boldsymbol{u}, \tag{3}$$

where $G = g \circ T^{-1}$ denotes the LSF expressed in the standard normal space, $\mathscr{F}_{\boldsymbol{u}} = \{\boldsymbol{u} \in \mathbb{R}^n : G(\boldsymbol{u}) \leq 0\}$ is the failure domain in the standard normal space, $\varphi_n(\cdot)$ denotes the n-dimensional standard normal pdf with independent components and $\mathrm{d}\boldsymbol{u} = \mathrm{d}u_1 \ldots \mathrm{d}u_n$.

Several methods are available for assessing p_{f} from Eq. (3). The reader is invited to refer to general textbooks for a review of well-established techniques with their main advantages and drawbacks. The scope of this chapter will be restricted to the approximation method known as the first-order reliability method (FORM). In a FORM analysis, the objective is to find the point P^* of the limit-state surface (LSS) $\mathscr{F}_{\mathbf{u}}^0 = \{\boldsymbol{u} \in \mathbb{R}^n : G(\boldsymbol{u}) = 0\}$ that is the closest to the origin O in the standard normal space, see e.g. (Ditlevsen and Madsen 2007; Lemaire et al. 2010). This point known as the most probable failure point (MPFP) or design point in structural reliability is the solution of the following quadratic optimization problem under nonlinear constraint:

$$\boldsymbol{u}^* = \arg\min_{\boldsymbol{u}\in\mathbb{R}^n} \frac{1}{2}\boldsymbol{u}^{\mathrm{T}}\boldsymbol{u} \;\text{ subject to }\; G(\boldsymbol{u}) = 0, \tag{4}$$

where $\boldsymbol{u}^*$ is the coordinate vector of P^* in the standard normal space. Several methods are available to solve the optimization problem defined in Eq. (4), including general algorithms such as the usual sequential quadratic programming (SQP) algorithm or a few others which have been specifically tailored to solve Eq. (4), e.g. the HLRF algorithm (Hasofer and Lind 1974; Rackwitz and Fiessler 1978) and the i-HLRF algorithm (Zhang and Der Kiureghian 1994). The so-called Hasofer-Lind reliability index β_{HL} is given by $\beta_{\mathrm{HL}} = \beta = \boldsymbol{\alpha}^{\mathrm{T}}\boldsymbol{u}^*$ where $\boldsymbol{\alpha}$ is a unit vector such that $\boldsymbol{\alpha} = -\nabla G(\boldsymbol{u}^*)/\|\nabla G(\boldsymbol{u}^*)\|$ and ∇ is the gradient operator. Under the assumption of a unique MPFP and a linear (or nearly linear) LSS, the failure probability is well

approximated by the first-order Taylor polynomial of G at $\mathbf{u}^*$. This approximation simply reads $p_{\mathrm{f}}^{\mathrm{FORM}} = \Phi(-\beta)$ where $\Phi(\cdot)$ denotes the standard normal cumulative distribution function (cdf). The following notations will also be used in the sequel: $\Phi^{-1}(\cdot)$ will denote the inverse of the standard normal cdf and $\varphi(\cdot)$ the standard normal pdf.

2 Nataf Transformation

The joint pdf $f_{\boldsymbol{X}}$ is in general not fully known due to insufficient probability information. Our first assumption is that the marginal distributions are known, here defined by their respective marginal cdfs F_{X_i} for $i = 1, \ldots, n$. A second assumption is made regarding the dependence structure of the random vector $\boldsymbol{X}$. In the sequel, we will assume that this dependence can be modeled by the linear correlation between the components of $\boldsymbol{X}$. The linear correlation coefficients of (X_i, X_j)-pairs are denoted by $\rho_{ij} = \rho_{X_i X_j}$ for $i, j = 1, \ldots, n$ and $\mathbf{R} = \left[\rho_{ij}\right]_{1 \le i,j \le n}$ is used for the correlation matrix. Restricting the scope of the reliability analysis to linear correlation is often a practical choice in the case of scarce information. It is important to point out that such an assumption may be questionable as raised by Lebrun and Dutfoy (2009b) and other types of dependence may be better suited.

The transformation T under the above defined assumptions is known as the Nataf transformation (Nataf 1962). This transformation has been introduced in structural reliability by Liu and Der Kiureghian (1986a). Its presentation in the framework of copulas is due to Lebrun and Dutfoy (2009b), from which the text of this section is inspired. In the Nataf transformation, each component X_i of $\boldsymbol{X}$ is first mapped into a uniform random variable V_i on $[0, 1]$ using its cdf F_{X_i}. These uniform random variables V_i are then mapped into correlated standard normal variables Z_i using the inverse cdf of the standard normal distribution, i.e. such that $\boldsymbol{Z} = (Z_1, \ldots, Z_n)^{\mathrm{T}} \sim \mathcal{N}(\mathbf{0}, \mathbf{R}_0)$ where $\mathbf{R}_0$ denotes the correlation matrix of the random vector $\boldsymbol{Z}$. The correlated standard normal variables Z_i are finally mapped into independent standard normal variables U_i using a linear transformation denoted by T_{zu}.

The transformation T is therefore defined as the following composed application:

$$\begin{array}{rccccc} T = T_{zu} \circ T_{vz} \circ T_{xv} : & \mathscr{X} & \to & [0,1]^n & \to & \mathbb{R}^n & \to & \mathbb{R}^n \\ & \boldsymbol{x} & \mapsto & \boldsymbol{v} = T_{xv}(\boldsymbol{x}) & \mapsto & \boldsymbol{z} = T_{vz}(\boldsymbol{v}) & \mapsto & \boldsymbol{u} = T_{zu}(\boldsymbol{z}) \end{array} \tag{5}$$

where $\boldsymbol{x} = (x_1, \ldots, x_n)^{\mathrm{T}}$, $\boldsymbol{v} = (v_1, \ldots, v_n)^{\mathrm{T}}$, $\boldsymbol{z} = (z_1, \ldots, z_n)^{\mathrm{T}}$, $\boldsymbol{u} = (u_1, \ldots, u_n)^{\mathrm{T}}$, and where, for $i = 1, \ldots, n$:

$$v_i = F_{X_i}(x_i) \quad , \quad z_i = \Phi^{-1}(v_i) \ . \tag{6}$$

For the construction of T_{zu}, we assume a linear relation between $\boldsymbol{z}$ and $\boldsymbol{u}$ in the form $\boldsymbol{z} = \mathbf{A}\boldsymbol{u}$. From the definition of the correlation matrix $\mathbf{R}_0$, it is easy to show that

$\mathbf{A}$ can be chosen as the lower-triangular matrix $\mathbf{L}_0$ of the Cholesky decomposition of $\mathbf{R}_0$ (assumed positive definite) such that:

$$\mathbf{R}_0 = \mathbf{L}_0 \mathbf{L}_0^{\mathrm{T}} \,, \tag{7}$$

which defines the transformation T_{zu}:

$$\begin{aligned} T_{zu} \,:\, & \mathbb{R}^n \to \mathbb{R}^n \\ & \boldsymbol{z} \mapsto \boldsymbol{u} = T_{zu}(\boldsymbol{z}) = \mathbf{L}_0^{-1} \boldsymbol{z}. \end{aligned} \tag{8}$$

As described in Lebrun and Dutfoy (2009b), the underlying assumption of the Nataf transformation is that the copula $C_{\boldsymbol{Z}}$ of the random vector $\boldsymbol{Z}$ (or equivalently the copula $C_{\boldsymbol{X}}$ of $\boldsymbol{X}$) is the n-dimensional normal copula parametrized by the correlation matrix $\mathbf{R}_0$.

The joint cdf of $\boldsymbol{Z}$ is therefore assumed to be given by:

$$\begin{aligned} F_{\boldsymbol{Z}}(\boldsymbol{z}) = F_{\boldsymbol{Z}}\left(z_1, \ldots, z_n\right) &= C_{\boldsymbol{Z}}\left(\Phi\left(z_1\right), \ldots, \Phi\left(z_n\right)\right) \\ &= C_{\mathscr{N}_n}\left(\Phi\left(z_1\right), \ldots, \Phi\left(z_n\right); \mathbf{R}_0\right) \\ &= \Phi_n\left(z_1, \ldots, z_n; \mathbf{R}_0\right) \,, \end{aligned} \tag{9}$$

where $C_{\boldsymbol{Z}}$ is the n-dimensional normal copula $C_{\mathscr{N}_n}$ parametrized by the correlation matrix $\mathbf{R}_0$.

The joint pdf of $\boldsymbol{Z}$ therefore reads:

$$\begin{aligned} f_{\boldsymbol{Z}}(\boldsymbol{z}) = f_{\boldsymbol{Z}}\left(z_1, \ldots, z_n\right) &= c_{\boldsymbol{Z}}\left(\Phi\left(z_1\right), \ldots, \Phi\left(z_n\right)\right) \prod_{i=1}^{n} \varphi\left(z_i\right) \\ &= c_{\mathscr{N}_n}\left(\Phi\left(z_1\right), \ldots, \Phi\left(z_n\right); \mathbf{R}_0\right) \prod_{i=1}^{n} \varphi\left(z_i\right) \\ &= \varphi_n\left(z_1, \ldots, z_n; \mathbf{R}_0\right) \,, \end{aligned} \tag{10}$$

where $c_{\boldsymbol{Z}}$ is the density of n-dimensional normal copula parametrized by the correlation matrix $\mathbf{R}_0$, whose expression is:

$$c_{\mathscr{N}_n}\left(u_1, \ldots, u_n; \mathbf{R}_0\right) = \frac{\varphi_n\left(\Phi^{-1}\left(u_1\right), \ldots, \Phi^{-1}\left(u_n\right); \mathbf{R}_0\right)}{\prod_{i=1}^{n} \varphi\left(\Phi^{-1}\left(u_i\right)\right)} \,, \tag{11}$$

where $\varphi_n\left(\cdot; \mathbf{R}_0\right)$ is the n-dimensional standard normal pdf with linear correlation matrix $\mathbf{R}_0$.

The joint pdf in the $\boldsymbol{x}$-space $\mathscr{X}$ is obtained as a direct application of the invariance of the copula $C_{\boldsymbol{Z}}$ by the n strictly increasing transformations $(F_{X_i}^{-1} \circ \Phi)$ for $i = 1, \ldots, n$. We therefore have $C_{\boldsymbol{X}} = C_{\boldsymbol{Z}}$ and $c_{\boldsymbol{X}} = c_{\boldsymbol{Z}}$. The joint pdf of $\boldsymbol{X}$ is therefore given by the following expression:

$$f_{\boldsymbol{X}}(\boldsymbol{x}) = f_{\boldsymbol{X}}(x_1, \ldots, x_n) = c_{\boldsymbol{X}}\left(F_{X_1}(x_1), \ldots, F_{X_n}(x_n)\right) \prod_{i=1}^{n} f_{X_i}(x_i)$$
$$= \frac{\varphi_n(z_1, \ldots, z_n; \mathbf{R}_0)}{\prod_{i=1}^{n} \varphi(z_i)} \prod_{i=1}^{n} f_{X_i}(x_i) \quad , \tag{12}$$

which is the expression given in Eq. (11) of Ref. (Liu and Der Kiureghian 1986a).

The $\mathbf{R}_0$ matrix has not been explicited yet. The elements $\rho_{0,ij}$ of this matrix are defined in terms of the known linear correlation coefficients $\rho_{ij} = \rho_{X_i X_j}$ of X_i and X_j components of $\boldsymbol{X}$. They are obtained from the following equation, for $i, j = 1, \ldots, n$, in which we use the bivariate form of the joint pdf expressed in Eq. (12):

$$\rho_{ij} = \mathbb{E}\left[\left(\frac{X_i - \mu_i}{\sigma_i}\right)\left(\frac{X_j - \mu_j}{\sigma_j}\right)\right]$$
$$= \int_{\mathscr{X}_j}\int_{\mathscr{X}_i}\left(\frac{x_i - \mu_i}{\sigma_i}\right)\left(\frac{x_j - \mu_j}{\sigma_j}\right)\frac{\varphi_2(z_i, z_j, \rho_{0,ij})}{\varphi(z_i)\,\varphi(z_j)} f_{X_i}(x_i) f_{X_j}(x_j)\,\mathrm{d}x_i \mathrm{d}x_j \tag{13}$$
$$= \int_{\mathbb{R}}\int_{\mathbb{R}} h(z_i, z_j, \mu_i, \mu_j, \sigma_i, \sigma_j)\ \varphi_2(z_i, z_j, \rho_{0,ij})\,\mathrm{d}z_i \mathrm{d}z_j,$$

where $\mathscr{X}_i$ and $\mathscr{X}_j$ denote the respective supports of the ith and jth components of the random vector $\boldsymbol{X}$, μ_i and μ_j their respective means, σ_i and σ_j their respective standard deviations,

where $h(z_i, z_j, \mu_i, \mu_j, \sigma_i, \sigma_j) = \left(\frac{F_{X_i}^{-1}(\Phi(z_i)) - \mu_i}{\sigma_i}\right)\left(\frac{F_{X_j}^{-1}(\Phi(z_j)) - \mu_j}{\sigma_j}\right)$,

and where $\varphi_2(z_i, z_j, \rho_{0,ij}) = \varphi_2\left(z_i, z_j; \begin{bmatrix} 1 & \rho_{0,ij} \\ \rho_{0,ij} & 1 \end{bmatrix}\right) = \frac{1}{2\pi\sqrt{1-\rho_{0,ij}^2}}$

$$\exp\left(-\frac{z_i^2 - 2\rho_{0,ij} z_i z_j + z_j^2}{2\left(1-\rho_{0,ij}^2\right)}\right).$$

The Nataf transformation is valid if Eq. (13) admits solutions for all $i, j = 1, \ldots, n$ and if the linear correlation matrix $\mathbf{R}_0$ is positive definite. Such a situation is often met in applications of practical interest as raised in (Liu and Der Kiureghian 1986a).

Finding $\rho_{0,ij}$ solutions of the integral relation defined in Eq. (13) is in general tedious and, for this reason, approximate formulae for $\rho_{0,ij}$ have been derived by Liu and Der Kiureghian (1986a) for most common statistical distributions. These formulas are in general obtained by least-square fitting and therefore approximate, except for a few pairs of distributions. An alternative solution consists in calculating $\rho_{0,ij}$ for $i, j = 1, \ldots, n$ and $i > j$ by numerical integration such as implemented in FERUM 4.x (Bourinet et al. 2009). Such calculations are done only once to define the transformation T and they are fast with any currently available computers. The coefficients $\rho_{0,ij}$ of the $\mathbf{R}_0$ matrix are obtained by a 2D numerical integration as solutions of the following equation for $i, j = 1, \ldots, n$ and $i > j$:

$$\rho_{ij} = \sum_{k=1}^{n_i} \sum_{l=1}^{n_j} \omega_k \omega_l \, h\left(z_k, \mu_i, \sigma_i, z_l, \mu_j, \sigma_j\right) \; \varphi_2\left(z_k, z_l, \rho_{0,ij}\right), \tag{14}$$

where $\left(z_k, z_l\right)$ are the $n_i \times n_j$ integration points and $\omega_k \omega_l$ their respective weights. A Gaussian quadrature rule is applied over the truncated domain $[-6, 6] \times [-6, 6]$. A specific attention must be paid to strongly correlated random variables for accurate $\rho_{0,ij}$ values. A practical rule adopted in FERUM 4.x consists in increasing the number of integration points along each dimension with correlation, ranging from $n_i = n_j = 32$ points along each dimension for absolute values of correlation lower than 0.9 to $1,024$ points for absolute values larger than 0.9995.

3 Sensitivities to Distribution Parameters

In reliability assessment, it is often of interest to evaluate the sensitivity of the failure probability p_f to the distribution parameters which define the joint pdf $f_{\boldsymbol{X}}$. Such sensitivities bring useful information about the role of each random input parameter in failure. Quantifying the importance of these parameters is for instance of great importance in optimal design under uncertainty.

In the sequel, we assume that all the distribution parameters are gathered in a vector denoted by $\boldsymbol{\theta}_f = \boldsymbol{\theta} = (\theta_1, \ldots, \theta_{n_\theta})^\mathrm{T}$ (the subscript f will be dropped for simpler notations). θ_k will designate any given parameter of this vector. These parameters include the statistical moments of the components X_i of the random vector $\boldsymbol{X}$ for $i = 1, \ldots, n$ or any parameters used for defining the corresponding marginal distributions. The correlation coefficients ρ_{ij} of $\mathbf{R}$ for $i, j = 1, \ldots, n$ are also included in $\boldsymbol{\theta}$ when the Nataf transformation is applied.

The sensitivities of the failure probability to distribution parameters are investigated here in the restrictive context of a FORM analysis. Such sensitivities are of course of interest with other methods too. They may be obtained e.g. as a straightforward post processing of a crude Monte Carlo simulation by means of the score function introduced by Rubinstein (1976; 1986). Such an approach has been brought to the structural reliability community by the work of Wu (1994). A similar post processing can also be applied with subset simulation (Au and Beck 2001) as proposed by Song et al. (2009), see also the presentation by Dubourg (2011, pp. 161–163).

In a FORM analysis, the gradient of the failure probability $p_\mathrm{f}^\mathrm{FORM}$ w.r.t. the distribution parameters $\boldsymbol{\theta}$ is given by:

$$\nabla_{\boldsymbol{\theta}} p_\mathrm{f}^\mathrm{FORM} = -\varphi(\beta) \, \nabla_{\boldsymbol{\theta}} \beta. \tag{15}$$

The gradient of the reliability index β w.r.t. $\boldsymbol{\theta}$ reads as follows, as shown in Hohenbichler and Rackwitz (1986):

$$\nabla_{\boldsymbol{\theta}}\beta = \mathbf{J}_{\boldsymbol{u},\boldsymbol{\theta}}\left(\boldsymbol{u}^*;\boldsymbol{\theta}\right)^{\mathrm{T}}\boldsymbol{\alpha}, \tag{16}$$

where $\mathbf{J}_{\boldsymbol{u},\boldsymbol{\theta}}\left(\boldsymbol{u};\boldsymbol{\theta}\right) = \left[\partial u_i/\partial\theta_j\right]_{1\le i\le n\,,\,1\le j\le n_{\boldsymbol{\theta}}}$ represents the Jacobian of the transformation T w.r.t. the distribution parameters $\boldsymbol{\theta}$. Note that this Jacobian is expressed at the MPFP $\boldsymbol{u}^*$ in Eq. (16).

The kth column of this Jacobian matrix for $k = 1, \ldots, n_{\boldsymbol{\theta}}$ can be obtained by differentiating $\boldsymbol{u}$ w.r.t. the given distribution parameter θ_k in Eq. (8):

$$\frac{\partial \boldsymbol{u}}{\partial\theta_k} = \mathbf{L}_0^{-1}\frac{\partial \boldsymbol{z}}{\partial\theta_k} + \frac{\partial\mathbf{L}_0^{-1}}{\partial\theta_k}\boldsymbol{z}. \tag{17}$$

Two main cases deserve attention. The first case appears when θ_k is a correlation coefficient of $\mathbf{R}$. The components $z_i = \Phi^{-1}\left(F_{X_i}\left(x_i\right)\right)$ of $\boldsymbol{z}$ for $i = 1, \ldots, n$ are expressed in terms of the parameters of the marginal distributions of $\boldsymbol{X}$ and therefore does not depend on θ_k. For this reason the first term of Eq. (17) vanishes. Sensitivity to correlation corresponding to this first case is addressed in Sect. 3.1. The second case appears when θ_k is a parameter of a given marginal distribution (e.g. its mean or standard deviation or, more generally, any parameter of this marginal distribution). The dependence of $\boldsymbol{z}$ on θ_k is clear from the transformation $T_{vz}\circ T_{xv}$ defined in Eq. (17). The calculation of the first term of Eq. (17) is therefore needed for assessing the sensitivity to θ_k. The contribution of the second term is less clear and often neglected. It may be however non zero due to μ_i, σ_i, μ_j and σ_j that appear in Eq. (13), which may imply a dependence of $\mathbf{R}_0$ and therefore $\mathbf{L}_0^{-1}$ on θ_k. The sensitivity to parameters of the marginal distributions is addressed in Sect. 3.2.

3.1 Sensitivity to Correlation

Sensitivity to correlation in the framework of the Nataf transformation has been studied in a very few works (Žanić and Žiha 1998, 2001; Bourinet and Lemaire 2008). The methods proposed in Žanic and Žiha (1998, 2001) are based on the approximate formulas $F = \rho_{0,ij}/\rho_{ij}$ of Liu and Der Kiureghian (1986a) derived for pairs of commonly used marginal distributions. Two methods are proposed in the work of Žanić and Žiha, one based on the Cholesky decomposition as later used by Bourinet and Lemaire (2008) and described in the present chapter, the other one based on a spectral decomposition of $\mathbf{R}_0$. The objective here is to assess these sensitivities by numerical integration from the integral problem defined in Eq. (13) in order to obtain highly accurate sensitivities.

The sensitivity to a given correlation coefficient ρ_{ij} of $\mathbf{R}$ requires to evaluate the following expression at $\boldsymbol{u}^*$:

$$\frac{\partial \boldsymbol{u}}{\partial\rho_{ij}} = \frac{\partial\mathbf{L}_0^{-1}}{\partial\rho_{ij}}\boldsymbol{z}. \tag{18}$$

From $\mathbf{L}_0^{-1}\mathbf{L}_0 = \mathbf{I}_{n\times n}$ where $\mathbf{I}_{n\times n}$ is the $n \times n$ identity matrix, we can straightforwardly obtain:

$$\frac{\partial \mathbf{L}_0^{-1}}{\partial \rho_{ij}} = -\mathbf{L}_0^{-1}\frac{\partial \mathbf{L}_0}{\partial \rho_{ij}}\mathbf{L}_0^{-1}. \tag{19}$$

This expression shows that the sensitivity of $\mathbf{L}_0^{-1}$ w.r.t. ρ_{ij} can be obtained from the one of $\mathbf{L}_0$. The evaluation of $\partial \mathbf{L}_0/\partial \rho_{ij}$ is carried out in two steps as described in the following.

In the first step, the sensitivity of $\mathbf{R}_0$ is derived from Eq. (13). All the elements of the matrix $\partial \mathbf{R}_0/\partial \rho_{ij}$ are zeros except the one in the *i*th row and *j*th column which can be expressed as follows:

$$\frac{\partial \rho_{0,ij}}{\partial \rho_{ij}} = \left(\frac{\partial \rho_{ij}}{\partial \rho_{0,ij}}\right)^{-1}. \tag{20}$$

The sensitivity $\partial \rho_{ij}/\partial \rho_{0,ij}$ is assessed from Eq. (21) by numerical integration with the same rule as the one used to solve Eq. (13), see Eq. (14):

$$\frac{\partial \rho_{ij}}{\partial \rho_{0,ij}} = \int_{\mathbb{R}}\int_{\mathbb{R}} h\left(z_i, z_j, \mu_i, \mu_j, \sigma_i, \sigma_j\right)\ \frac{\partial \varphi_2\left(z_i, z_j, \rho_{0,ij}\right)}{\partial \rho_{0,ij}}\mathrm{d}z_i\mathrm{d}z_j. \tag{21}$$

In the second step, the sensitivity of $\mathbf{L}_0$ w.r.t. ρ_{ij} is obtained from the one of $\mathbf{R}_0$ through a step-by-step differentiation of the Cholesky algorithm. The algorithm used for calculating both $\mathbf{L}_0$ and $\partial \mathbf{L}_0/\partial \rho_{ij}$ is given in Appendix.

3.2 Sensitivity to Parameters of Marginal Distributions

For $k = 1, \ldots, n_{\boldsymbol{\theta}}$, we want to assess $\partial \boldsymbol{u}/\partial \theta_k$ in Eq. (17) where θ_k represents any given marginal distribution parameter. Evaluating the first term $\mathbf{L}_0^{-1}\partial \boldsymbol{z}/\partial \theta_k$ is rather standard from the following expression obtained from Eq. (6), for $i = 1, \ldots, n$:

$$\frac{\partial z_i}{\partial \theta_k} = \frac{1}{\varphi\left(F_{X_i}\left(x_i\right)\right)}\frac{\partial F_{X_i}\left(x_i\right)}{\partial \theta_k}, \tag{22}$$

in which $\partial F_{X_i}\left(x_i\right)/\partial \theta_k$ has to be derived for any usual statistical distribution.

Evaluating the second term $\left(\partial \mathbf{L}_0^{-1}/\partial \theta_k\right)\boldsymbol{z}$ is less easy. The sensitivity of $\mathbf{L}_0^{-1}$ to θ_k is obtained in three steps similarly to what was done for the sensitivity of $\mathbf{L}_0^{-1}$ to correlation in Sect. 3.1:

1. We first express the sensitivity $\dfrac{\partial \mathbf{R}_0}{\partial \theta_k}$, as described in the following.
2. $\dfrac{\partial \mathbf{L}_0}{\partial \theta_k}$ is obtained from $\mathbf{R}_0$ and $\dfrac{\partial \mathbf{R}_0}{\partial \theta_k}$ by means of the algorithm given in Appendix.
3. $\dfrac{\partial \mathbf{L}_0^{-1}}{\partial \theta_k}$ is obtained from $\dfrac{\partial \mathbf{L}_0}{\partial \theta_k}$, see Eq. (19).

The sensitivity of $\mathbf{R}_0$ to θ_k is obtained from the following equation. For any $i, j = 1, \ldots, n$, we have:

$$\frac{\partial \rho_{ij}}{\partial \theta_k} = \int_{\mathbb{R}} \int_{\mathbb{R}} \left[\frac{\partial h\left(z_i, z_j, \mu_i, \mu_j, \sigma_i, \sigma_j\right)}{\partial \theta_k} \varphi_2\left(z_i, z_j, \rho_{0,ij}\right) + h\left(z_i, z_j, \mu_i, \mu_j, \sigma_i, \sigma_j\right) \frac{\partial \varphi_2\left(z_i, z_j, \rho_{0,ij}\right)}{\partial \theta_k} \right] \mathrm{d}z_i \mathrm{d}z_j, \tag{23}$$

where:

$$\frac{\partial h}{\partial \theta_k} = \frac{\partial h}{\partial z_i}\frac{\partial z_i}{\partial \theta_k} + \frac{\partial h}{\partial z_j}\frac{\partial z_j}{\partial \theta_k} + \frac{\partial h}{\partial \mu_i}\frac{\partial \mu_i}{\partial \theta_k} + \frac{\partial h}{\partial \mu_j}\frac{\partial \mu_j}{\partial \theta_k} + \frac{\partial h}{\partial \sigma_i}\frac{\partial \sigma_i}{\partial \theta_k} + \frac{\partial h}{\partial \sigma_j}\frac{\partial \sigma_j}{\partial \theta_k}, \tag{24}$$

and:

$$\frac{\partial \varphi_2}{\partial \theta_k} = \frac{\partial \varphi_2}{\partial z_i}\frac{\partial z_i}{\partial \theta_k} + \frac{\partial \varphi_2}{\partial z_j}\frac{\partial z_j}{\partial \theta_k} + \frac{\partial \varphi_2}{\partial \rho_{0,ij}}\frac{\partial \rho_{0,ij}}{\partial \theta_k}. \tag{25}$$

It is first important to notice that the unknown sensitivity $\partial \rho_{0,ij}/\partial \theta_k$ (i.e. the element of $\partial \mathbf{R}_0/\partial \theta_k$ in the ith row and jth column) appears in the integrand of Eq. (23), see last term of Eq. (25). This sensitivity is obtained by solving Eq. (23) by numerical integration, in which we have $\partial \rho_{ij}/\partial \theta_k = 0$. We use again the same rule for numerical integration as the one defined for the calculation of $\mathbf{R}_0$. Note that the partial derivatives of μ_i, μ_j, σ_i and σ_j w.r.t. θ_k in Eq. (24) are all zeros if θ_k is a distribution parameter of a component of $\boldsymbol{X}$ other than X_i or X_j.

4 Application Examples

The results presented in this section are all obtained with FERUM 4.x in which sensitivities to correlation and marginal distribution parameters have been implemented as described in Sect. 3. Please refer to the `mod_corr_solve.m` function and all the additional files included in the sensitivity sub-folder of the FERUM 4.x package.

Table 1 Example 1: definition of marginal distributions of $\boldsymbol{X}$

Component X_i	Type of distribution	Mean μ_i	Standard deviation σ_i
X_1	Lognormal	500	100
X_2	Lognormal	2,000	400
X_3	Uniform	5	0.5

4.1 Example 1: CalRel Example

This first example is taken from CalRel software user's manual (Liu et al. 1989). The marginal distributions of the three components of $\boldsymbol{X}$ are defined in Table 1.

The correlation matrix of the random vector $\boldsymbol{X}$ reads:

$$\mathbf{R} = \begin{bmatrix} 1 & 0.3 & 0.2 \\ 0.3 & 1 & 0.2 \\ 0.2 & 0.2 & 1 \end{bmatrix}. \tag{26}$$

The LSF is given by:

$$g(\boldsymbol{x}) = g(x_1, x_2, x_3) = 1 - \frac{x_2}{1,000x_3} - \left(\frac{x_1}{200x_3}\right)^2. \tag{27}$$

The following results are obtained with the the i-HLRF algorithm: $\beta = 1.7728$, $p_{\mathrm{f}}^{\mathrm{FORM}} = 3.8133 \times 10^{-2}$. Note that very strict convergence criteria are imposed on the FORM solution for highly accurate sensitivities, here up to a 4 digit-accuracy (both e_1 and e_2 errors lower than 10^{-6} with the i-HLRF algorithm, see (Zhang and Der Kiureghian 1994) for details about these criteria).

The sensitivity of β w.r.t. distribution parameters and correlation are respectively listed in Tables 2 and 3. The sensitivities $\partial\beta/\partial\theta_k$ given in Table 2 are based on both terms of Eq. (17). The first term is dominant for all these sensitivities and the second term represents less than 0.2% of the first one. The sensitivity to correlation of this specific example has been studied and presented earlier in Ref. (Žanić and Žiha

Table 2 Example 1: sensitivities w.r.t. parameters of marginal distributions

θ_k	$\partial\beta/\partial\theta_k$	θ_k	$\partial\beta/\partial\theta_k$	θ_k	$\partial\beta/\partial\theta_k$	θ_k	$\partial\beta/\partial\theta_k$
μ_1	−0.0059	σ_1	−0.0079	a_1^a	−3.7390	b_1^a	−4.7855
μ_2	−0.0009	σ_2	−0.0006	λ_2^b	−1.9660	ζ_2^b	−1.6698
μ_3	1.2602	σ_3	−1.1942	λ_3^b	0.9748	ζ_3^b	0.2854

[a] $[a_1, b_1]$ is the support of the uniform distribution of X_1.

[b] $\lambda_i = \mathbb{E}[\ln X_i]$ and $\zeta_i = \sqrt{\mathrm{Var}[\ln X_i]}$ are the parameters of the lognormal distribution of X_i for $i = 2, 3$

Table 3 Example 1: sensitivities to correlation

	Present approach	Forward finite differences	Ref. (Žanić and Žiha 2001)
$\partial\beta/\partial\rho_{21}$	−0.5151	−0.5150	−0.515
$\partial\beta/\partial\rho_{31}$	0.8916	0.8916	0.890
$\partial\beta/\partial\rho_{32}$	0.4688	0.4689	0.468

2001; Bourinet and Lemaire 2008). The results obtained in Ẑanic and Ẑiha (2001) are reported in Table 3 for comparison. The results obtained by means of the proposed numerical integration are in close agreement with those of Žanić and Žiha. Besides, they are also almost equal to those obtained by finite forward differences with perturbations of the correlation coefficients set to $10^{-5}\ \rho_{ij}$.

4.2 *Example 2: Load-Resistance Problem with Correlated Lognormal R and S*

We consider two lognormally distributed random variables $R = X_1$ and $S = X_2$ with a linear correlation $\rho = \rho_{12} = 0.5$. Their respective means are $\mu_1 = 5$ and $\mu_2 = 1$ and their respective standard deviations are $\sigma_1 = 5$ and $\sigma_2 = 1$. The coefficients of variation of X_1 and X_2, respectively $\delta_1 = \sigma_1/\mu_1$ and $\delta_2 = \sigma_2/\mu_2$, are both equal to one. $\delta\ (= \delta_1 = \delta_2)$ will denote this coefficient of variation. The LSF is expressed as follows:

$$g(\boldsymbol{x}) = g(x_1, x_2) = x_1 - x_2. \tag{28}$$

The $\mathbf{R}_0$ matrix of the Nataf transformation is defined by the following expression, which is exact in this specific case, see (Liu and Der Kiureghian 1986a, Table 8):

$$\rho_{0,12} = \frac{\ln\left(1 + \rho_{12}\delta_1\delta_2\right)}{\sqrt{\ln\left(1+\delta_1^2\right)\ln\left(1+\delta_2^2\right)}} = \frac{\ln\left(1+\rho\delta^2\right)}{\ln\left(1+\delta^2\right)}. \tag{29}$$

It is easy to demonstrate that the LSS is linear in the standard normal space, which gives an exact failure probability with FORM. We obtain $p_\mathrm{f} = p_\mathrm{f}^{\mathrm{FORM}} = \Phi(-\beta)$ where β reads:

$$\beta = \frac{\lambda_1 - \lambda_2}{\sqrt{\zeta_1^2 + \zeta_2^2 - 2\rho_{0,12}\zeta_1\zeta_2}} = \frac{\ln\left(\dfrac{\mu_1}{\mu_2}\right)}{\sqrt{2\ln\left(\dfrac{1+\delta^2}{1+\rho\,\delta^2}\right)}} = 2.1218. \tag{30}$$

where $\lambda_i = \mathbb{E}\left[\ln X_i\right] = \ln \mu_i - 0.5 \ln\left(1 + \delta_i^2\right)$ and $\zeta_i = \sqrt{\mathrm{Var}\left[\ln X_i\right]} = \sqrt{\ln\left(1 + \delta_i^2\right)}$ are the parameters of the lognormally distributed X_i for $i = 1, 2$.

The sensitivities w.r.t. the correlation coefficient ρ and the marginal distribution parameters μ_i, σ_i, λ_i and ζ_i for $i = 1, 2$ can be analytically derived. These sensitivities have been assessed by symbolic calculation and, for the sake of concision, only the expression of the sensitivity to correlation is given here:

$$\frac{\partial \beta}{\partial \rho} = \frac{\delta^2 \ln\left(\dfrac{\mu_1}{\mu_2}\right)}{\left(1 + \rho\,\delta^2\right)\left(2 \ln\left(\dfrac{1 + \delta^2}{1 + \rho\,\delta^2}\right)\right)^{\frac{3}{2}}}. \tag{31}$$

The sensitivity to correlation $\partial\beta/\partial\rho$ assessed numerically by the method described in Sect. 3.1 is 2.4585, which is the exact value obtained from Eq. (31).

The sensitivities w.r.t. marginal distribution parameters $\partial\beta/\partial\theta_k$ are listed in Table 4. The sensitivities assessed by the proposed numerical approach are obtained as the sum of two terms $\boldsymbol{\alpha}^{\mathrm{T}}\mathbf{L}_0^{-1}\left(\partial z/\partial\theta_k\right)$ and $\boldsymbol{\alpha}^{\mathrm{T}}\left(\partial\mathbf{L}_0^{-1}/\partial\theta_k\right)z$, representing the respective contributions of the two terms of Eq. (17). The sensitivities derived analytically and considered as reference values are also given for comparison. The sensitivities obtained by the present numerical approach and the reference ones are perfectly matching. It also clearly appears that the contribution of second term of Eq. (17) is not negligible w.r.t. the first one (it however does not contribute in $\partial\beta/\partial\lambda_i$ for $i = 1, 2$).

The importance of the $\boldsymbol{\alpha}^{\mathrm{T}}\left(\partial\mathbf{L}_0^{-1}/\partial\theta_k\right)z$ contribution in the sensitivities w.r.t. marginal distribution parameters have been further investigated for this specific example. The ratio $\left(\partial\beta/\partial\theta_k\right)_{\text{2nd term only}}$ over $\left(\partial\beta/\partial\theta_k\right)_{\text{both terms}}$ (in absolute value and in percents) as defined in Eq. (32) is represented in Fig. 1 as isocontours for $\rho \in [0.1, 0.9]$ and $\delta \in [0.1, 1]$, μ_1 and μ_2 values remaining unchanged.

Table 4 Example 2: sensitivities to marginal distribution parameters

$\partial\beta/\partial\theta_k$	Present approach[a]	Analytical (reference)
$\partial\beta/\partial\mu_1$	$0.5486 - 0.0301 = 0.5184$	0.5184
$\partial\beta/\partial\mu_2$	$-1.2122 - 0.1507 = -1.3629$	−1.3629
$\partial\beta/\partial\sigma_1$	$-0.2849 + 0.0301 = -0.2548$	−0.2548
$\partial\beta/\partial\sigma_2$	$-0.1061 + 0.1507 = 0.0446$	0.0445
$\partial\beta/\partial\lambda_1$[b]	$1.3183 + 0.0000 = 1.3183$	1.3183
$\partial\beta/\partial\lambda_2$[b]	$-1.3183 + 0.0000 = -1.3183$	−1.3183
$\partial\beta/\partial\zeta_1$[b]	$-1.2743 + 0.2509 = -1.0234$	−1.0234
$\partial\beta/\partial\zeta_2$[b]	$-1.2743 + 0.2509 = -1.0234$	−1.0234

[a] In the second column, the two terms of the sum are the respective contributions of the two terms of Eq. (17).

[b] $\lambda_i = \mathbb{E}\left[\ln X_i\right]$ and $\zeta_i = \sqrt{\mathrm{Var}\left[\ln X_i\right]}$ are the parameters of the lognormal distribution of X_i for $i = 2, 3$

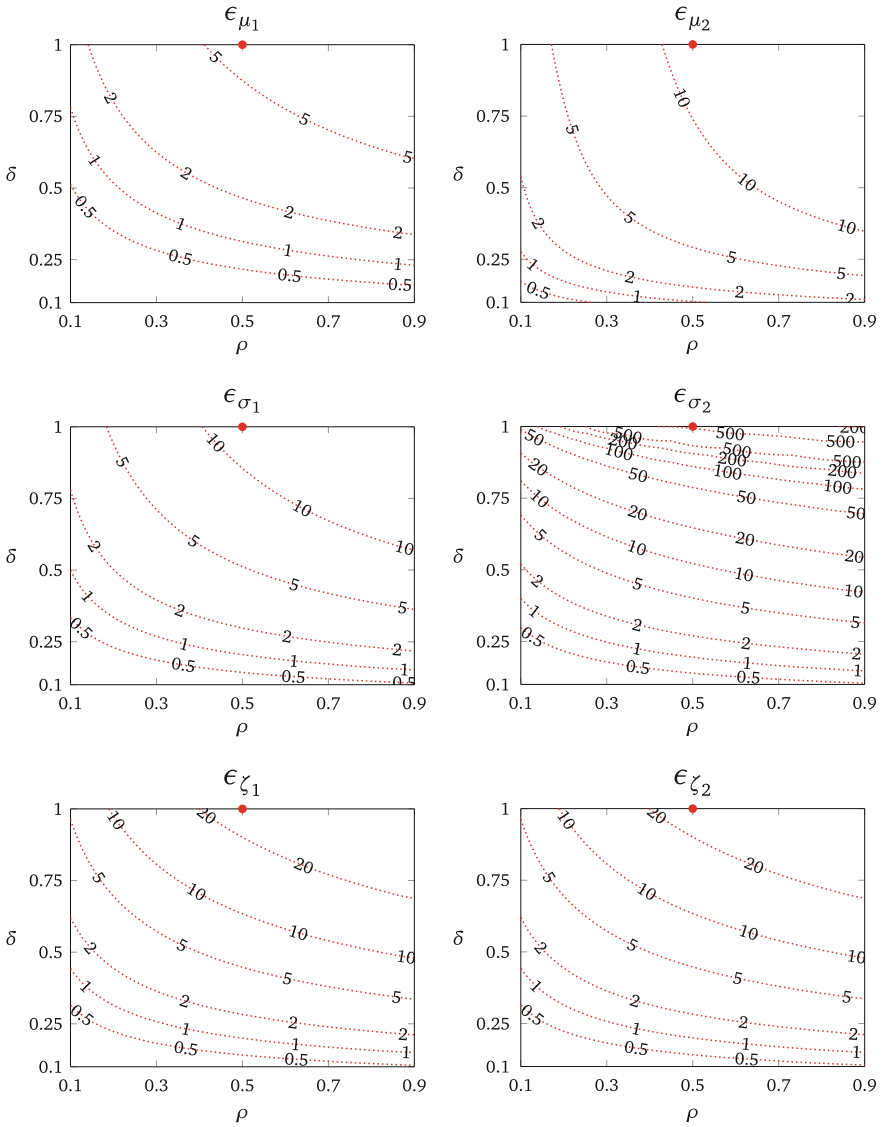

Fig. 1 Example 2: ratio $\varepsilon_{\theta_k}(\rho, \delta)$ for $\theta_k = \mu_i$ (*top*), σ_i (*middle*) and ζ_i (*bottom*), $i = 1, 2$. The *red* plain circle denotes the pair $(\rho, \delta) = (0.5, 1)$ studied in Sect. 4.2

$$\varepsilon_{\theta_k} = 100 \left| \frac{\boldsymbol{\alpha}^{\mathrm{T}} \dfrac{\partial \mathbf{L}_0^{-1}}{\partial \theta_k} \boldsymbol{z}}{\boldsymbol{\alpha}^{\mathrm{T}} \mathbf{L}_0^{-1} \dfrac{\partial \boldsymbol{z}}{\partial \theta_k} + \boldsymbol{\alpha}^{\mathrm{T}} \dfrac{\partial \mathbf{L}_0^{-1}}{\partial \theta_k} \boldsymbol{z}} \right| . \tag{32}$$

This ratio $\varepsilon_{\theta_k}(\rho, \delta)$ is plotted for $\theta_k = \mu_i, \sigma_i$ and ζ_i, $i = 1, 2$. From these plots, it is found that the contribution of the second term in the computed sensitivities grows with ρ and δ. For moderate coefficients of variation (say δ lower than 30%), the contribution of this second term does not exceed 5%. A further analysis has been conducted in order to investigate whether such conclusions could be generalized to other types of distribution than the lognormal one. Accounting for this second term is in fact only needed when at least one component of $\boldsymbol{X}$ has a distribution belonging to Group 2 as defined by Liu and Der Kiureghian (1986a). As a reminder, this group includes the lognormal, gamma, type-II largest value and type-III smallest value distributions. When X_i belongs to Group 2, $\rho_{0,ij}$ (therefore $\mathbf{R}_0$) depends on the coefficient of variation δ_i of X_i, see approximate expressions of $F = \rho_{0,ij}/\rho_{ij}$ given in Liu and Der Kiureghian (1986a). This implies a dependence of $\mathbf{L}_0^{-1}$ on the marginal distribution parameters of X_i and, as a consequence, a non-zero sensitivity of $\mathbf{L}_0^{-1}$ w.r.t. to those parameters.

4.3 Example 3: A Three-Span, Five-Story Linear Elastic Frame Structure Subjected to Lateral Loads

This reliability of a three-span, five-story, linear elastic frame structure subjected to lateral loads is studied in this third example, see Fig. 2. This problem was proposed by Liu and Der Kiureghian (1986b) and studied later in several works (Bucher and Bourgund 1990; Wei and Rahman 2007; Most 2011; Blatman and Sudret 2010; Gong et al. 2014). The problem has $n = 21$ random inputs: 3 applied lateral loads, 2 Young's moduli, 8 moments of inertia and 8 cross-sectional areas. The frame element properties and the statistical properties of each component of $\boldsymbol{X}$ taken in this study are given in Tables 5 and 6 respectively. Linear correlation is considered between the following random inputs:

- loads: $\rho_{P_i P_j} = 0.5$ for $i, j = 1, 2, 3$, $i \neq j$,
- material properties: $\rho_{E_i E_j} = 0.9$ for $i, j = 4, 5$, $i \neq j$,
- moments of inertia: $\rho_{I_i I_j} = 0.13$ for $i, j = 6, \ldots, 13$, $i \neq j$,
- cross-sectional areas: $\rho_{A_i A_j} = 0.13$ for $i, j = 14, \ldots, 21$, $i \neq j$,
- moment of inertias and cross-sectional areas: $\rho_{A_i I_j} = \rho_{I_j A_i} = 0.13$ for $i = 6, \ldots, 13$, $j = 14, \ldots, 21$, except for properties of a single frame element for which we have $\rho_{A_{i+8} I_i} = \rho_{I_i A_{i+8}} = 0.95$ for $i = 6, \ldots, 13$.

Failure is considered when the horizontal displacement at node 1 exceeds 0.2 ft, see Fig. 2. The LSF reads:

$$g(\boldsymbol{x}) = g\left(x_1, \ldots, x_{21}\right) = 0.2 - u_1(\boldsymbol{x}). \tag{33}$$

Note that all the input data that are selected here are those of reference (Most 2011). The same frame structure is studied in all the above mentioned references but it must

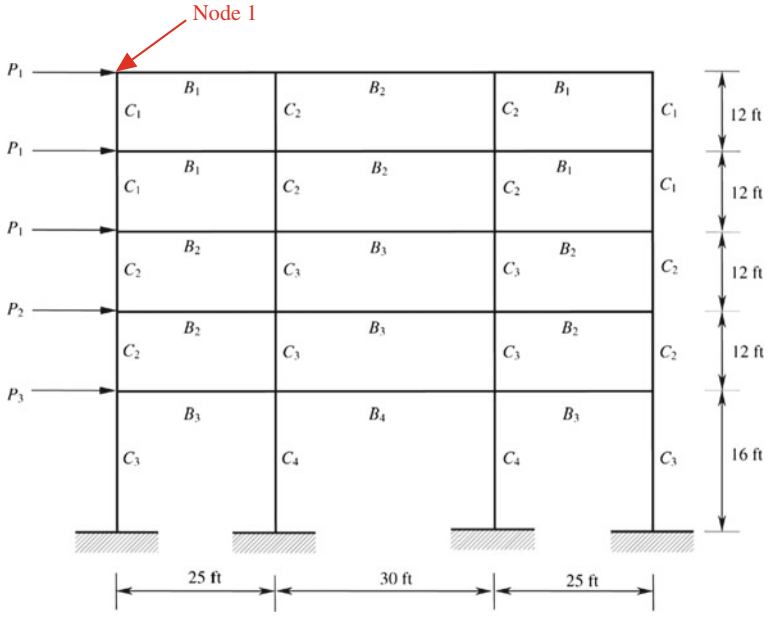

Fig. 2 Example 3: a three-span, five-story, linear elastic frame structure subjected to lateral loads (from (Wei and Rahman 2007))

be pointed out that a few differences exist between the input data used in all these works:

- Distribution type for loads P_{1-3}: Rayleigh in Liu and Der Kiureghian (1986b), Bucher and Bourgund (1990), Most (2011), Gong et al. (2014), lognormal in Wei and Rahman (2007), Blatman and Sudret (2010).
- Distribution types for Young's moduli E_{4-5}, moments of inertia I_{6-13}, cross-sectional areas A_{14-21}: normal in Liu and Der Kiureghian (1986b), Bucher and Bourgund (1990), Wei and Rahman (2007), left-truncated normal in Blatman and Sudret (2010) and lognormal in Most (2011), Gong et al. (2014).
- Coefficients of variation of P_{1-3}: 0.5 for P_{1-3} in Most (2011), Gong et al. (2014), 0.3 for P_1 and 0.4 for P_{2-3} in all the other references.
- Correlation of loads P_{1-3}: no correlation in Wei and Rahman (2007), Blatman and Sudret (2010), correlation of 0.5 in all other references.
- Maximal displacement at node 1 in the LSF: 0.2 ft in Liu and Der Kiureghian (1986b), Bucher and Bourgund (1990), Wei and Rahman (2007), Most (2011), 4 to 9 cm in Blatman and Sudret (2010), 6 cm in Gong et al. (2014).

The results obtained with FORM are $\beta = 3.0340$ and $p_f^{\text{FORM}} = 1.2069 \times 10^{-3}$. The SORM approximations of the failure probability based on the asymptotic formula of Hohenbichler and Rackwitz (1988) are respectively $p_f^{\text{SORM-cf}} = 1.1228 \times 10^{-3}$ and $p_f^{\text{SORM-pf}} = 1.1276 \times 10^{-3}$ with the curvature fitting and point fitting

Table 5 Example 3: frame element properties

Element	Young's modulus	Moment of inertia	Cross-sectional area
B_1	E_4	I_{10}	A_{18}
B_2	E_4	I_{11}	A_{19}
B_3	E_4	I_{12}	A_{20}
B_4	E_4	I_{13}	A_{21}
C_1	E_5	I_6	A_{14}
C_2	E_5	I_7	A_{15}
C_3	E_5	I_8	A_{16}
C_4	E_5	I_9	A_{17}

Table 6 Example 3: definition of marginal distributions of $\boldsymbol{X}$

Component X_i	Type of distribution	Mean μ_i^a	Standard deviation σ_i^a
P_1	Rayleigh	30	9
P_2	Rayleigh	20	8
P_3	Rayleigh	16	6.40
E_4	Lognormal	454, 000	40, 000
E_5	Lognormal	497, 000	40, 000
I_6	Lognormal	0.94	0.12
I_7	Lognormal	1.33	0.15
I_8	Lognormal	2.47	0.30
I_9	Lognormal	3.00	0.35
I_{10}	Lognormal	1.25	0.30
I_{11}	Lognormal	1.63	0.40
I_{12}	Lognormal	2.69	0.65
I_{13}	Lognormal	3.00	0.75
A_{14}	Lognormal	3.36	0.60
A_{15}	Lognormal	4.00	0.80
A_{16}	Lognormal	5.44	1.00
A_{17}	Lognormal	6.00	1.20
A_{18}	Lognormal	2.72	1.00
A_{19}	Lognormal	3.13	1.10
A_{20}	Lognormal	4.01	1.30
A_{21}	Lognormal	4.50	1.50

[a] P_i, E_i, I_i, and A_i are respectively in kip, kip/ft^2, ft^4 and ft^2

(Der Kiureghian et al. 1987) methods. A solution has been obtained by subset simulation (SS) (Au and Beck 2001) with 10^6 samples per level. The failure probability estimate considered as a reference solution is $p_{\mathrm{f\,ref}} = \widehat{p}_{\mathrm{f}}^{\mathrm{SS}} = 1.13 \times 10^{-3}$ with a coefficient of variation of 0.8%. This result in excellent agreement with the one of Ref. (Most 2011) confirms that this reliability problem is characterized by a unique

MPFP with a nearly linear LSS, which makes the use of FORM appropriate here. The sensitivities of β to correlation with FORM are expressed in Eqs. (34–36). All the other correlation sensitivities not given here are less than 0.01. From these results, it appears that all the sensitivities to correlation are lower than zero. The lower the correlation, the safer the frame structure. Moreover it is found that the two most influential correlations are those between the loads P_1 and P_2, on the one hand, and I_{11} and I_{12} (moments of inertia of B_2 and B_3 elements), on the other hand.

$$\left[\frac{\partial \beta}{\partial \rho_{ij}}\right]_{i,j=1-3} = \begin{bmatrix} \times & & \text{sym} \\ -0.18 & \times & \\ -0.06 & -0.01 & \times \end{bmatrix}, \tag{34}$$

$$\left[\frac{\partial \beta}{\partial \rho_{ij}}\right]_{i,j=4-5} = \begin{bmatrix} \times & \text{sym} \\ -0.06 & \times \end{bmatrix}, \tag{35}$$

$$\left[\frac{\partial \beta}{\partial \rho_{ij}}\right]_{i,j=6-13} = \begin{bmatrix} \times & & & & & & & \\ 0.00 & \times & & & & & & \\ 0.00 & -0.01 & \times & & & \text{sym} & & \\ 0.00 & 0.00 & -0.01 & \times & & & & \\ 0.00 & -0.01 & -0.01 & -0.01 & \times & & & \\ -0.01 & -0.02 & -0.04 & -0.02 & -0.05 & \times & & \\ -0.01 & -0.02 & -0.04 & -0.02 & -0.05 & -0.12 & \times & \\ 0.00 & 0.00 & -0.01 & 0.00 & -0.01 & -0.03 & -0.03 & \times \end{bmatrix}. \tag{36}$$

Sensitivities to marginal distribution parameters have also been assessed. The normalized sensitivities $\left(\partial\beta/\partial\theta_k\right)\theta_k$ where $\theta_k = \mu_i, \sigma_i$ for $i = 1, \ldots, 21$ are given in Table 7. The results shows that the reliability of the frame structure is mostly sensitive to the marginal distribution parameters of P_1, E_4 and E_5. The sensitivities w.r.t. the mean and standard deviation of the moments of inertia of the beam elements have lower values, the most important ones being those of I_{11} and I_{12} (note that the reliability was also sensitive to the correlation between these two inputs). The contribution $\boldsymbol{\alpha}^{\mathrm{T}}\left(\partial \mathbf{L}_0^{-1}/\partial\theta_k\right)\boldsymbol{z}$ is negligible in all the computed sensitivities (contribution of less than 2%) as expected from the conclusion drawn in Sect. 4.2.

4.4 Example 4: Crack Propagation Based on the Virkler Data

This last example presented by Bourinet and Lemaire (2008) addresses stochastic crack growth by means of FORM and illustrates the importance of correlation in such a context. All the calculations are based on the experimental data set obtained by Virkler et al. (1979) and the well known Paris-Erdogan crack growth equation. The experiment carried out by Virkler et al. (1979) consisted in recording the crack

Table 7 Example 3: normalized sensitivities w.r.t. mean and standard deviation

X_i	$(\partial\beta/\partial\mu_i)\,\mu_i$	$(\partial\beta/\partial\sigma_i)\,\sigma_i$	X_i	$(\partial\beta/\partial\mu_i)\,\mu_i$	$(\partial\beta/\partial\sigma_i)\,\sigma_i$
P_1	−1.22	−1.93	E_4	2.38	−0.18
P_2	−0.11	−0.09	E_5	1.31	−0.09
P_3	−0.04	−0.03			
I_6	0.09	−0.00	A_{14}	0.00	−0.00
I_7	0.33	−0.02	A_{15}	0.02	−0.00
I_8	0.53	−0.03	A_{16}	0.02	−0.00
I_9	0.30	−0.02	A_{17}	0.00	−0.00
I_{10}	0.38	−0.06	A_{18}	0.03	−0.01
I_{11}	1.06	−0.21	A_{19}	0.02	−0.00
I_{12}	1.02	−0.20	A_{20}	0.00	−0.00
I_{13}	0.20	−0.03	A_{21}	0.00	−0.00

Table 8 Example 4: statistical distributions of m and $\ln C$[a]

Variable	Type of distribution	Mean	Standard deviation	Correlation
m	Normal	2.855	0.166	−0.99795
$\ln C$	Normal	−26.056	0.972	

[a]Units consistent with crack length in mm and stresses in MPa

growth trajectories of 68 samples at 164 equally-spaced measurement points, see Fig. 3, left plot. The test samples were M(T) specimens made of 2024-T3 aluminum alloy of 558.8 mm length, 152.4 mm width and 2.54 mm thickness. The crack was grown from an initial crack length of 9 mm to a final length of 49.8 mm, after a precycling crack growth started from a pre-machined central slit. These specimens were all tested under constant amplitude fatigue loading at a maximum stress level $\sigma_{\max} = 48.36$ MPa and a stress ratio $R = 0.2$.

For each of the 68 trajectories, a crack growth rate versus stress intensity factor (SIF) range curve is obtained based on a 5-point moving least squares linear regression, see Fig. 3, right plot. From each of these curves, a pair of values $(m, \ln C)$ is obtained by linear regression such that:

$$\ln \frac{\mathrm{d}a}{\mathrm{d}N} = \ln C + m \ln \Delta K. \tag{37}$$

Table 8 gives the results obtained from a statistical analysis of the 68 pairs $(m, \ln C)$. It is found that the normality hypothesis can be assumed both for m and $\ln C$. Moreover a linear correlation $\rho = -0.99795$ (very close to -1) is observed between m and $\ln C$ due to the linear regression that is used to find these two parameters. Note that these statistical parameters are consistent with those of other Refs. (Ditlevsen and Olesen 1986; Kotulski 1998).

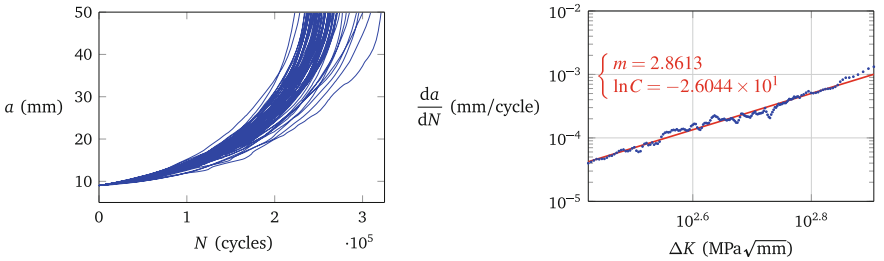

Fig. 3 Example 4: crack length a versus number of cycles N (*left*)—finding m and $\ln C$ from crack growth rate $\mathrm{d}a/\mathrm{d}N$ versus SIF range ΔK curves (*right*)

For reliability assessment, failure is defined when the number of cycles N_r to reach the final crack length $a_\mathrm{f} = 49.8$ mm of the Virkler experiment is lower than a given target number of cycles denoted by N_s. The LSF is therefore expressed as follows:

$$g(\boldsymbol{x}) = N_r(m, \ln C) - N_s, \tag{38}$$

where $\boldsymbol{x} = \left(x_1, x_2\right)^\mathrm{T} = (m,\ \ln C)^\mathrm{T}$ and where N_r is given by:

$$N_r(m, \ln C) = \int_{a_\mathrm{i}}^{a_\mathrm{f}} \frac{1}{C(\Delta K)^m} \mathrm{d}a, \tag{39}$$

in which a_i is the initial crack length, $a_\mathrm{f} = 49.8$ mm is the final crack length and ΔK is the SIF range. For a constant-amplitude fatigue loading of M(T) specimens as applied in the Virkler experiment, we have $\Delta K = K_\mathrm{max}(1 - R)$ where $R = 0.2$ is the stress ratio and K_max is the maximal SIF given by:

$$K_\mathrm{max} = \frac{1 - 0.025(a/W)^2 + 0.06(a/W)^4}{\sqrt{\cos(\pi a/W)}} \sigma_\mathrm{max} \sqrt{\pi a} \tag{40}$$

where a is the current crack length, $W = 152.4$ mm is the width of the test specimen and $\sigma_\mathrm{max} = 48.36$ MPa is the maximum applied stress.

The following three test cases are defined for the subsequent reliability studies:

- Case #1: The initial crack length a_i is considered as deterministic and equal to the minimum crack size of the Virkler experiments, i.e. $a_\mathrm{i} = 9$ mm, and N_s is selected as the average value between the 7th and 8th lowest numbers of cycles of the Virkler tests: $N_s = (237,293 + 237,794)/2 = 237,543.5$ cycles.
- Case #2: The initial crack length a_i is considered as deterministic and equal to 4.4 mm. The target number of cycles N_s is set to 400,000.

Table 9 Example 4, problem 1: FORM results

	Case #1	Case #2	Case #3
a_i (mm)	9	4.4	Exp(1.5, 1.5)
N_s (cycles)	237, 543.5	400, 000	400, 000
β	0.7600	1.8005	1.8399
$p_\mathrm{f}^\mathrm{FORM}$	0.224	3.59×10^{-2}	3.29×10^{-2}
$\partial\beta/\partial\rho^a$	−177.29	−368.22	−6.7092

[a] ρ denotes the correlation between m and $\ln C$

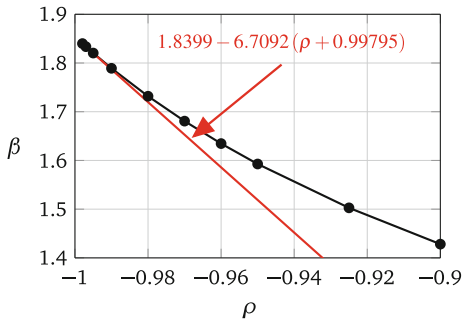

Fig. 4 Example 4, problem 1, case #3: reliability index β versus correlation coefficient ρ between m and $\ln C$

- Case #3: The initial crack length a_i is assumed to be exponentially distributed with a mean and a standard deviation both equal to 1.5 mm. The target number of cycles N_s taken is 400, 000.

4.4.1 Problem 1

This first problem assumes that the random vector $\boldsymbol{X}$ is composed of the two correlated normal variables m and $\ln C$ with distribution parameters given in Table 8 for cases #1 and #2. The exponentially distributed random variable a_i is added to $\boldsymbol{X}$ as an additional component for case #3. The FORM results obtained for the three cases are gathered in Table 9. When the stochastic model involves only m and $\ln C$ as random inputs, a very strong sensitivity of β to the correlation ρ between m and $\ln C$ is observed: −177.29 for case #1 and −368.22 for case #2. For illustration purpose, lowering ρ of 0.001 would approximately result in a reliability index increase of 0.18 and 0.37 for case #1 and #2 respectively. When the initial crack length is considered as random (case #3), the FORM solution appears far less sensitive to ρ. Figure 4 represents how the reliability index β evolves when ρ is varied from −0.99795 to −0.9. It clearly appears that the computed sensitivity $\partial\beta/\partial\rho = -6.7092$ represents the first-order derivative of β at $\rho = -0.99795$.

The failure probability of 0.224 obtained with FORM for Case #1 does not agree in fact with the experimental data. From the definition of the target number of cycles N_s, one would expect a failure probability in the range $\left[7/68, 8/68\right] = [0.103, 0.118]$

since N_s is selected as the average value between the 7th and 8th lowest numbers of cycles of the 68 Virkler tests. The origins of such a difference are investigated in depth in Ref. (Bourinet and Lemaire 2008). First, it can be shown that the difference is not explained by a nonlinearity of the LSS at the MPFP. A SORM analysis gives $p_{\mathrm{f}}^{\text{SORM-cf}} = p_{\mathrm{f}}^{\text{SORM-pf}} = 0.219$ which is close to the FORM approximation (the LSS is almost linear) and still far from $[0.103, 0.118]$. Moreover, it is found that a few samples among the 68 ones of the experimental data set are not correctly classified by the LSS of the selected model (defined by both its LSF g and its random vector $\boldsymbol{X}$), see Figs. 7 and 8 in Bourinet and Lemaire (2008). We can find some points with an experimental number of cycles greater than $N_s = 237,543.5$ that lie in the failure domain ((M)T specimens #9, 23, 41, 54, 62, 63 and 66). Besides, the experimental point corresponding to the first experimental test and characterized by a number of cycles lower than N_s lies in the safe domain, although very close to the LSS, which is not satisfactory too. All these issues are due in fact to an inaccurate representation of the LSF, which results here in a slight underestimation of N_r and *in fine* in a quite important overestimation of the failure probability. This issue is fixed in the sequel by introducing an extra random variable representative of a model error, as described in the subsections related to Problem 2 and 3.

4.4.2 Problem 2

In order to account for a slight underestimation of the number of cycles N_r obtained numerically w.r.t. those found experimentally by Virkler et al., the LSF defined in Eq. (38) is modified as follows:

$$g(\boldsymbol{x}) = k\, N_r(m, \ln C) - N_s, \tag{41}$$

where $\boldsymbol{x} = \left(x_1, x_2, x_3\right)^{\mathrm{T}} = (m,\ \ln C,\ k)^{\mathrm{T}}$ and k follows a Type-I largest value distribution (a.k.a. Gumbel distribution) with a mean equal to 1.027 and a standard deviation equal to 1.91×10^{-2}. This distribution is identified from a statistical analysis of the ratios $N_{\text{exp}}^{(j)}/N_r(m^{(j)}, \ln C^{(j)})$ for $j = 1, \ldots, 68$ where $N_{\text{exp}}^{(j)}$ is the number of cycles of the jth M(T) specimen of the Virkler data set and $(m^{(j)}, \ln C^{(j)})$ are the 68 pairs $(m, \ln C)$ identified from the experimental data. Note that k is assumed independent from both m and $\ln C$. The distributions of m and $\ln C$ are those defined in Table 8. A linear correlation $\rho = -0.99795$ is assumed between m and $\ln C$.

FORM results with model error are given in Table 10 for cases #1 and 2. We can easily show that the 8 (=7 + 1) experimental points that were misclassified with Problem 1 are now correctly placed within the safe and failure domains, see Fig. 9 of Ref. (Bourinet and Lemaire 2008). The failure probability obtained by FORM is now 0.137 and a SORM analysis gives 0.126, which becomes now rather close to the expected 0.103 – 0.118 probability. Regarding sensitivities to correlation, the values

Table 10 Example 4, problem 2: FORM results

	Case #1	Case #2
a_{i} (mm)	9	4.4
N_s (cycles)	237, 543.5	400, 000
β	1.0947	2.0972
$p_{\mathrm{f}}^{\mathrm{FORM}}$	0.137	1.80×10^{-2}
$\partial\beta/\partial\rho^a$	−241.62	−411.16

[a] ρ denotes the correlation between m and $\ln C$

obtained in this new problem are again quite high in absolute value (−241.62 for case #1 and −411.16 for case #2). An alternative problem is proposed which in the next subsection, which avoids such a high sensitivity to correlation.

4.4.3 Problem 3

We now express the linear regression of $\ln C$ on m as follows (Ditlevsen and Olesen 1986):

$$\widehat{\mathbb{E}}\left[\ln C|m\right] = \mathbb{E}\left[\ln C\right] + \frac{\mathrm{Cov}\left[m, \ln C\right]}{\mathrm{Var}\left[m\right]}\left(m - \mathbb{E}\left[m\right]\right), \tag{42}$$

and we make use of the following residual which becomes uncorrelated with m:

$$\varepsilon_{\ln C} = \ln C - \widehat{\mathbb{E}}\left[\ln C|m\right]. \tag{43}$$

The linear regression of $\ln C$ on m can be expressed from the 68 pairs $(m, \ln C)$ identified from the Virkler data set. This linear regression reads:

$$\widehat{\mathbb{E}}\left[\ln C|m\right] = -5.8468m - 9.3623, \tag{44}$$

and we therefore have:

$$\varepsilon_{\ln C} = \ln C + 5.8468m + 9.3623. \tag{45}$$

The distribution parameters of $\varepsilon_{\ln C}$ are inferred from the Virkler data set, see values given in Table 11. The correlation between m and $\varepsilon_{\ln C}$ is close to zero (-9.29×10^{-7}) which now allows us to express the reliability problem in terms of three independent random variables. The LSF with model uncertainty is rewritten in the following form:

$$g\left(\boldsymbol{x}\right) = k\,N_r\left(m, \ln C\right) - N_s, \tag{46}$$

where $\boldsymbol{x} = \left(x_1, x_2, x_3\right)^{\mathrm{T}} = \left(m,\, \varepsilon_{\ln C},\, k\right)^{\mathrm{T}}$ and $\ln C = \varepsilon_{\ln C} - 5.8468m - 9.3623$.

Table 11 Example 4, problem 3: statistical distributions of m, $\varepsilon_{\ln C}$ and k

Variable	Type of distribution	Mean	Standard deviation
m	Normal	2.855	0.166
$\varepsilon_{\ln C}$	Normal	-1.20×10^{-6}	6.22×10^{-2}
k	Gumbel	1.027	1.91×10^{-2}

Table 12 Example 4, problem 3: FORM results

	Case #1	Case #2
a_{i} (mm)	9	4.4
N_s (cycles)	237, 543.5	400, 000
β	1.1050	2.1076
$p_{\mathrm{f}}^{\mathrm{FORM}}$	0.135	1.75×10^{-2}
$\partial\beta/\partial\rho^a$	−0.24	0.68

[a] ρ denotes the correlation between m and $\varepsilon_{\ln C}$

Results obtained by FORM are gathered in Table 12. The failure probabilities with FORM and SORM are respectively equal to 0.135 and 0.124 for Case #1. These results are almost identical to those obtained with Problem 2. The failure probability obtained with SORM is again close to the $[0.103, 0.118]$ expected range. The main difference is that the reliability results are now insensitive to correlation. Near-zero values are obtained for the sensitivity to correlation between m and $\varepsilon_{\ln C}$.

5 Concluding Remarks

In the Nataf transformation, numerical integration can be conveniently applied to define the matrix $\mathbf{R}_0$ but also its sensitivities w.r.t. to distribution parameters, including both marginal distribution parameters and correlation coefficients. The sensitivities of the FORM solution (reliability index and associated failure probability) w.r.t. to these distribution parameters can then be derived through a step-by-step differentiation of the Cholesky decomposition algorithm. These sensitivities are exact in the limits of the accuracy of numerical integration. Several application examples have been presented in order to illustrate the use of these sensitivities in structural reliability with a focus on those w.r.t. correlation. The information gained from these sensitivities enable to rank these distribution parameters by importance, allowing a better understanding of their roles in failure.

Acknowledgements I wish to express my deep gratitude to Prof. Armen Der Kiureghian who has played an important role in the course of my career. His high-quality scientific work has been and still is a great source of inspiration in my research.

Appendix: Determination of $\mathbf{L_0}$ and $\partial \mathbf{L_0}/\partial \rho_{ij}$

// **initialization**
$\mathbf{A} = \left[a_{ij}\right]_{1\le i,j\le n} = \mathbf{R}_0$
$\mathrm{d}\mathbf{A} = \left[\mathrm{d}a_{ij}\right]_{1\le i,j\le n} = \dfrac{\partial \mathbf{R}_0}{\partial \rho_{ij}}$

for $k = 1$ **to** n
  $\mathrm{d}a_{kk} = \mathrm{d}a_{kk} / \left(2\sqrt{a_{kk}}\right)$
  $a_{kk} = \sqrt{a_{kk}}$
  for $i = (k+1)$ **to** n
    $\mathrm{d}a_{ik} = \left(\mathrm{d}a_{ik}\, a_{kk} - a_{ik}\, \mathrm{d}a_{kk}\right) / a_{kk}^2$
    $a_{ik} = a_{ik} / a_{kk}$
  end for
  for $j = (k+1)$ **to** n
    for $i = j$ **to** n
      $\mathrm{d}a_{ij} = \mathrm{d}a_{ij} - \mathrm{d}a_{ik}\, a_{jk} - a_{ik}\, \mathrm{d}a_{jk}$
      $a_{ij} = a_{ij} - a_{ik}\, a_{jk}$
    end for
  end for
end for

$\mathbf{L}_0 = \mathrm{tril}\,(\mathbf{A})$
$\dfrac{\partial \mathbf{L}_0}{\partial \rho_{ij}} = \mathrm{tril}\,(\mathrm{d}\mathbf{A})$

Note: tril (**M**) extracts the lower triangular part of a matrix **M**.

References

Au SK, Beck JL (2001) Estimation of small failure probabilities in high dimensions by subset simulation. Probab Eng Mech 16(4):263–277. doi:10.1016/S0266-8920(01)00019-4

Blatman G, Sudret B (2010) An adaptive algorithm to build up sparse polynomial chaos expansions for stochastic finite element analysis. Probab Eng Mech 25(2):183–197. doi:10.1016/j.probengmech.2009.10.003

Bourinet JM, Lemaire M (2008) FORM sensitivities to correlation: application to fatigue crack propagation based on Virkler data. In: Das PK (ed) Proceedings of 4th international ASRANet colloquium, Athens, Greece, June 25–27, 2008. http://maritime-conferences.com/asranet2010-conference/asranet2008/45%20Bourinet,%20Jean-Marc.pdf

Bourinet JM, Mattrand C, Dubourg V (2009) A review of recent features and improvements added to FERUM software. In: Furuta H, Frangopol DM, Shinozuka M (eds) Proceedings of 10th international conference on structural safety and reliability (ICOSSAR 2009), Osaka, Japan, September 13–17, 2009. CRC Press

Bucher CG, Bourgund U (1990) A fast and efficient response surface approach for structural reliability problems. Struct Saf 7(1):57–66. doi:10.1016/0167-4730(90)90012-E

Der Kiureghian A, Lin HZ, Hwang SJ (1987) Second-order reliability approximations. J Eng Mech 113(8):1208–1225. doi:10.1061/(ASCE)0733-9399(1987)113:8(1208)

Ditlevsen O, Madsen HO (2007) Structural reliability methods. Internet edition 2.3.7. http://od-website.dk/books/OD-HOM-StrucRelMeth-Ed2.3.7.pdf

Ditlevsen O, Olesen R (1986) Statistical analysis of the Virkler data on fatigue crack growth. Eng Fract Mech 25(2):177–195. doi:10.1016/0013-7944(86)90217-1

Dubourg V (2011) Adaptive surrogate models for reliability analysis and reliability-based design optimization. Phd thesis, Université Blaise Pascal, Clermont Ferrand, France. https://tel.archives-ouvertes.fr/tel-00697026v2

Gong JX, Yi P, Zhao N (2014) Non-gradient-based algorithm for structural reliability analysis. J Eng Mech 140(6):04014,029. doi:10.1061/(ASCE)EM.1943-7889.0000722

Hasofer AM, Lind NC (1974) Exact and invariant second-moment code format. J Eng Mech Div 100(1):111–121

Hohenbichler M, Rackwitz R (1986) Sensitivity and importance measures in structural reliability. Civil Eng Syst 3(4):203–209. doi:10.1080/02630258608970445

Hohenbichler M, Rackwitz R (1988) Improvement of second-order reliability estimates by importance sampling. J Eng Mech 114(12):2195–2199. doi:10.1061/(ASCE)0733-9399(1988)114:12(2195)

Kotulski ZA (1998) On efficiency of identification of a stochastic crack propagation. Arch Mech 50(5):829–847. http://am.ippt.pan.pl/am/article/viewFile/v50p829/621

Lebrun R, Dutfoy A (2009b) A generalization of the nataf transformation to distributions with elliptical copula. Probab Eng Mech 24(2):172–178. doi:10.1016/j.probengmech.2008.05.001

Lemaire M, Chateauneuf A, Mitteau JC (2010) Structural reliability. ISTE. doi:10.1002/9780470611708.fmatter

Liu PL, Der Kiureghian A (1986a) Multivariate distribution models with prescribed marginals and covariance. Probab Eng Mech 1(2):105–112. doi:10.1016/0266-8920(86)90033-0

Liu PL, Der Kiureghian A (1986b) Optimization algorithms for structural reliability analysis. Report no. UCB/SEMM-86/09, Department of civil and environmental engineering, University of California, Berkeley

Liu PL, Lin HZ, Der Kiureghian A (1989) CalREL user manual. Report no. UCB/SEMM-89/18, Department of civil and environmental engineering, University of California, Berkeley

Most T (2011) Efficient structural reliability methods considering incomplete knowledge of random variable distributions. Probab Eng Mech 26(2):380–386. doi:10.1016/j.probengmech.2010.09.003

Nataf A (1962) Détermination des distributions dont les marges sont données. Comptes Rendus de l'Académie des Sciences 225:42–43

Rackwitz R, Fiessler B (1978) Structural reliability under combined random load sequences. Comput Struct 9(5):489–494. doi:10.1016/0045-7949(78)90046-9

Rubinstein RY (1976) A monte carlo method for estimating the gradient in a stochastic network, technion, Haifa, Israel. Unpublished manuscript

Rubinstein RY (1986) The score function approach for sensitivity analysis of computer simulation models. Math Comput Simul 28(5):351–379. doi:10.1016/0378-4754(86)90072-8

Song S, Lu Z, Qiao H (2009) Subset simulation for structural reliability sensitivity analysis. Reliab Eng Syst Saf 94(2):658–665. doi:10.1016/j.ress.2008.07.006

Virkler DA, Hillberry BM, Goel PK (1979) The statistical nature of fatigue crack propagation. J Eng Mater Technol 101(2):148–153. doi:10.1115/1.3443666

Žanić V, Žiha K (1998) Sensitivity to correlation in multivariate models. Comput Assist Mech Eng Sci 5(1):75–84

Žanić V, Žiha K (2001) Sensitivity to correlations in structural problems. Transactions of FAMENA 25(2):1–26. https://bib.irb.hr/datoteka/87824.87824-FAMENA2001V25N2.pdf

Wei D, Rahman S (2007) Structural reliability analysis by univariate decomposition and numerical integration. Probab Eng Mech 22(1):27–38. doi:10.1016/j.probengmech.2006.05.004

Wu YT (1994) Computational methods for efficient structural reliability and reliability sensitivity analysis. AIAA J 32(8):1717–1723. doi:10.2514/3.12164

Zhang Y, Der Kiureghian A (1994) Two improved algorithms for reliability analysis. In: Rackwitz R, Augusti G, Borri A (eds) Proceedings of 6th IFIP WG 7.5 working conference on reliability and optimization of structural systems, Assisi, Italy, September 7–9, 1994. Springer, US, pp 297–304. doi:10.1007/978-0-387-34866-7_32

Using FORM for Minimizing the Uncertain Cost of Structural Designs

Terje Haukaas and Stevan Gavrilovic

Abstract This chapter demonstrates the use of the first-order reliability method (FORM) for minimizing expected cost, when the cost is a continuously differentiable function of many random variables and models. The models include construction cost and cost of damage, and typically a finite element model. Assuming these costs are non-negative, the expected cost is the area underneath the complementary cumulative distribution function on the positive cost axis. Points on this distribution function are determined by FORM and numerical integration is employed to calculate the area. Exact derivatives of responses and costs with respect to random variables are propagated through the models and used in FORM. Moreover, exact derivatives of responses and costs with respect to design variables are propagated through FORM in order to have exact derivatives of the expected cost available in the optimization analysis. This framework for minimizing expected cost is implemented in a computer program and illustrated by means of a demonstration example.

1 Introduction

This chapter is written as a tribute to Professor Armen Der Kiureghian on the occasion of the symposium organized in his honor at the University of Illinois at Urbana-Champaign on October 4–5, 2015. Professor Der Kiureghian is a pioneer in the development of reliability methods and other probabilistic methods, and his contributions still stand as the state-of-the-art in the field. Among many examples are the Nataf transformation (Liu and Der Kiureghian 1986) and the gradient-based algorithm for determining curvatures in the second-order reliability method (Der Kiureghian and De Stefano 1991). The objective of this chapter is to demonstrate how FORM has important uses today, even for new problems without classical limit-states. As such, this contribution can perhaps informally be considered an

T. Haukaas (✉) · S. Gavrilovic
Department of Civil Engineering, University of British Columbia, Vancouver, Canada
e-mail: terje@civil.ubc.ca

P. Gardoni (ed.), *Risk and Reliability Analysis: Theory and Applications*,
Springer Series in Reliability Engineering, DOI 10.1007/978-3-319-52425-2_13

extended term paper in Professor Der Kiureghian's famous reliability course CE 229 Structural and System Reliability at the University of California at Berkeley, submitted perhaps a bit late.

The context of this chapter is performance-based earthquake engineering. That means the emphasis is placed on cost rather than stresses and displacements. One paper that develops and demonstrates a popular performance-based methodology is co-authored by Professor Der Kiureghian (Yang et al. 2009). Figure 7 in that paper shows a key indicator of performance: the "loss curve," i.e., the rate of exceedance of a range of dollar values. A shift of the loss curve towards lower cost implies a better design.

Traditional limit-state design is usually part of the structural engineers' considerations even for structures subjected to performance-based engineering. However, in this chapter the focus is solely on performance-based engineering and the loss curve. Consequently, no limit-states appear at first. The objective is solely to identify the structural design that gives the "best" loss curve. The first author of this chapter made initial observations on this problem in two conference papers (Haukaas 2013; Haukaas et al. 2013). The present chapter presents an extension of that work.

2 Methodology

The loss curve mentioned above is essentially a complementary cumulative distribution function for the uncertain loss, i.e., monetary cost, which is a non-negative continuous random variable. Figure 1 is a schematic visualization of a generic loss curve; the probability of exceeding a cost threshold, c, is denoted p. The specific thresholds c_i and probabilities p_i, and the increment Δc, will be explained later. Usually the loss curve does not conform to any standard distribution type but partial descriptors of the distribution can be computed by sampling or other techniques.

In the abovementioned paper by Yang et al. (2009) the criteria by which a structural design is judged is the area underneath the loss curve in the positive portion of the loss axis. It can be shown that this area is the mean annual frequency when the ordinate of the loss curve is given as annual rate of exceedance, and that

Fig. 1 Schematic loss curve

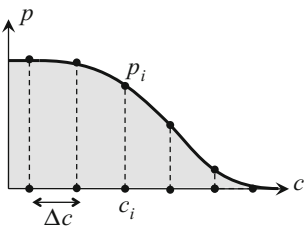

the area is the expected loss when the ordinate of the loss curve is given as probability of exceedance. An informal proof in the latter case is

$$\mu_c = \int_0^\infty c \cdot f(c)dc = -\int_0^\infty c \cdot \frac{G(c)}{dc}dc = -[c \cdot G(c)]_0^\infty + \int_0^\infty 1 \cdot G(c)dc = \int_0^\infty G(c)dc \tag{1}$$

where $f()$ is the probability density function and $G()$ is the complementary cumulative distribution function.

The use of expected loss, i.e., the mean of the cost, as the criterion for design optimization has roots dating back hundreds of years. It is almost 280 years since the use of expected cost as a decision criterion was extended with the concept of nonlinear utility functions to incorporate risk averseness (Bernoulli 1738). In fact, it is more than 70 years since the formal underpinning for making decisions in this way was established (von Neumann and Morgenstern 1944). The present chapter essentially employs a linear utility function, resulting in expected cost minimization, and other decision models, such as minimizing high costs, are not explored here.

The analysis conducted by Yang et al. (2009) was focused on the estimation of repair costs due to earthquake ground motion. For that reason their loss curve contains contributions from repair costs only. In contrast, this paper includes the cost of construction or seismic retrofit, which makes it possible to explore an optimum design. Without the inclusion of the construction cost the best design would be a fortress invulnerable to ground motion. Conversely, with the inclusion of construction cost the expected loss is a convex function of design variables, such as structural dimensions. The result is a convex optimization problem: small dimensions will lead to high repair costs after an earthquake; large dimensions may lead to high construction costs.

Several methods are available for the calculation of the expected cost, i.e., the area underneath the loss curve. The following limitation must here be understood: models are available for evaluating the loss for given realizations of the intervening random variables but the distribution itself is not available. This implies that first- and second-order approximations based on a Taylor expansion of the cost with respect to the random variables (Ang and Tang 2007) is one option. However, a key concern with those approaches is potentially inaccurate estimates of the mean cost. Another option is Monte Carlo sampling from which the mean can estimated. The problem with that approach is that accurate derivatives of the expected cost are unavailable for the subsequent optimization analysis. A third option, based on FORM, addresses both those concerns and is explored in this chapter.

Suppose a FORM analysis is conducted at each cost-threshold, schematically shown in Fig. 1, with the limit-state function

$$g(\mathbf{x}) = c_i - c(\mathbf{x}), \quad i = 1, 2, \ldots, N \tag{2}$$

where $\mathbf{x}$ is the vector of random variables that enter into the models that are employed to calculate the cost $c(\mathbf{x})$, c_i are the cost thresholds, and N is the number of thresholds. The result of each analysis is the probability, p_i, of the cost exceeding the threshold c_i. Numerical integration can be performed, for instance using the trapezoidal rule:

$$E[c] \approx \mu_c^{FORM} = \sum_{i=1}^{N} \frac{(p_{i+1} + p_i)}{2} \cdot (c_{i+1} + c_i), \quad i = 1, 2, \ldots, N \tag{3}$$

where $c_1 = 0$ and hence $p_1 = 1$, while c_N is assumed to be sufficiently high so that p_N is essentially zero. This is an issue related to the selection of the thresholds, c_i, which is addressed next.

3 Cost Thresholds

The accuracy of Eq. (3) depends on the selection of the thresholds c_i. More thresholds in the cost range where the probabilities are non-zero implies higher accuracy but also higher computational cost. Another challenge is that it is not known a priori which cost values are associated with substantial exceedance probabilities.

One approach to address the latter challenge is to conduct a Monte Carlo sampling analysis with a few hundred samples to obtain estimates of the mean and standard deviation of the cost. Then an array of cost thresholds can be laid out in the cost range that will give substantial contributions to Eq. (3). However, this approach is problematic because the mean and standard deviation of the cost can change significantly from one design to another. Hence, the thresholds that are ideal for calculation of the mean cost of the first design may not be suitable for subsequent trial designs. The idea of repeating the sampling for each design is not adopted because that prevents the calculation of exact derivatives of Eq. (3); it would not be possible to analytically tell how a sampling-based threshold value changes due to a change in a random variable realization.

To ensure the availability of exact derivatives an infinite number of cost thresholds is laid out, spaced Δc apart, starting at $c_1 = 0$, so that

$$c_i = (i - 1) \cdot \Delta c, \quad i = 1, 2, \ldots, N \tag{4}$$

The thresholds in Eq. (4) remain fixed throughout the optimization analysis, but not all thresholds are "active" and different thresholds are active for different designs. In fact, the FORM analyses to compute p_i do not commence at c_1 because many of the low-cost thresholds may be associated with $p_i \approx 1$. The approach

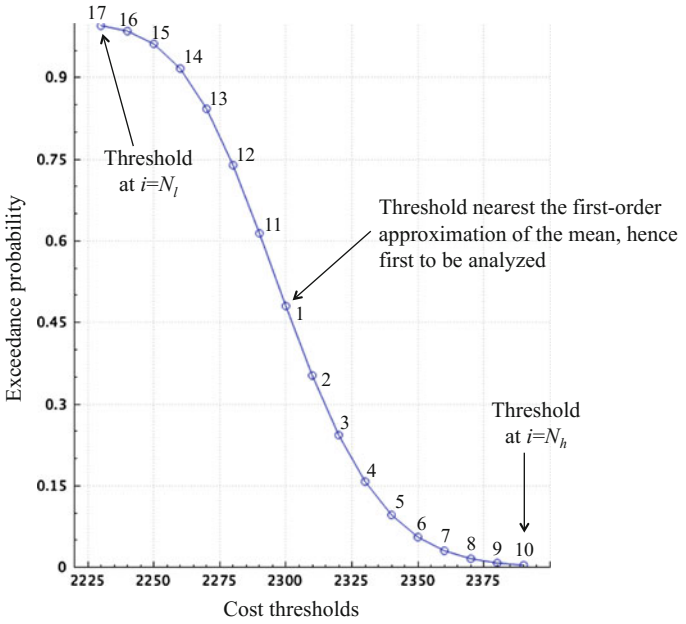

Fig. 2 Loss curve from analysis with the computer program Rts

adopted in this paper is to first compute the first-order second-moment approximation of the mean cost,

$$\mu_c^{FOSM} = c(\mathbf{M_x}) \tag{5}$$

where $\mathbf{M_x}$ is the mean vector for the random variables $\mathbf{x}$. The result in Eq. (5) is readily obtained but as mentioned earlier it may be an inaccurate estimate of the mean cost. Starting at the threshold immediately above μ_c^{FOSM} a FORM analysis is conducted followed by a FORM analysis at the next threshold above, etc. until the computed probability is sufficiently small. Next, a FORM analysis is conducted at the threshold below and nearest μ_c^{FOSM} followed by a FORM analysis at the next threshold below, etc. until the computed probability is sufficiently close to unity.

That procedure is visualized in Fig. 2, where the cost thresholds are numbered by the order in which they are analyzed by FORM. These numbers are *not* the same as $i = 1, 2, \ldots, N$ above. The loss curve in Fig. 2 is obtained with the computer program Rts, which is an extension of the computer program Rt (Mahsuli and Haukaas 2013). Details of the examples analyzed with Rts are provided later in this chapter. The mean cost for the loss curve in Fig. 2 is calculated by the following modified version of Eq. (3):

$$\mu_c^{FORM} = N_l \cdot \Delta c + \sum_{i=N_l}^{i=N_h} \frac{(p_{i+1} + p_i)}{2} \cdot \Delta c \tag{6}$$

where N_l is the value of N at which the probability is sufficiently close to unity and N_h is the value of N at which the probability is sufficiently close to zero. In Eq. (6), the second term is the contribution to the mean from the area under the curve in Fig. 2. The first term is the contribution from the origin, i.e., $i = 0$, to where the curve in Fig. 2 starts. To select N_l and N_h a tolerance probability p_{tol} is employed. Specifically, N_l identifies the first cost threshold at which the probability is above 1-p_{tol} and N_h identifies the first cost threshold at which the probability is below p_{tol}. Obviously other integration schemes can be thought of but Eq. (6) may give a sense of how FORM results are employed to calculate the mean cost.

The variables in the integration scheme in Eq. (6) are p_{tol} and Δc. A value of p_{tol} around or somewhat below 0.01 has given good results in analyses run thus far. The selection of Δc can be more challenging because the standard deviation of the cost may change substantially from one design to another. As a result, one value of Δc may give sufficiently many cost thresholds for one design but not for another. This was not a problem in the analyses conducted here, but several strategies for selecting Δc can be envisioned. One is to select Δc "very small" and let intermittent cost thresholds be active for different designs. Another approach is to use first-order second-moment approximations of the mean and standard deviation of the cost to distribute the thresholds. The important point is that if the cost thresholds move then that must be accounted for in the calculation of the derivative of the expected cost. The calculation of gradients is addressed in a subsequent section.

4 Warm Starts in FORM

Each of the 17 FORM analyses that are carried out to obtain the results shown in Fig. 2 requires several evaluations of the cost, for different realizations of the random variables. In other typical applications the convergence of one FORM analysis requires about 3–10 evaluations of the limit-state function. However, the number of cost evaluations can be reduced when running consecutive FORM analyses like those visualized in Fig. 2. Instead of restarting the search for the design point in FORM from the same random variable realization every time the FORM algorithm can be restarted the previous design point.

The saving in computational cost with that strategy is understood from Fig. 3, which displays results obtained with Rts. The vertical axis in both graphs is the distance from the origin in the standard normal space to the trial points of the FORM algorithm. The horizontal axis is the iteration number of the FORM algorithm. The two graphs in Fig. 3 show the trial points from two different FORM analyses. The graph with more trial points is the result from the first FORM analysis at Point 1 in Fig. 2. The graph with less trial points show the typical result for

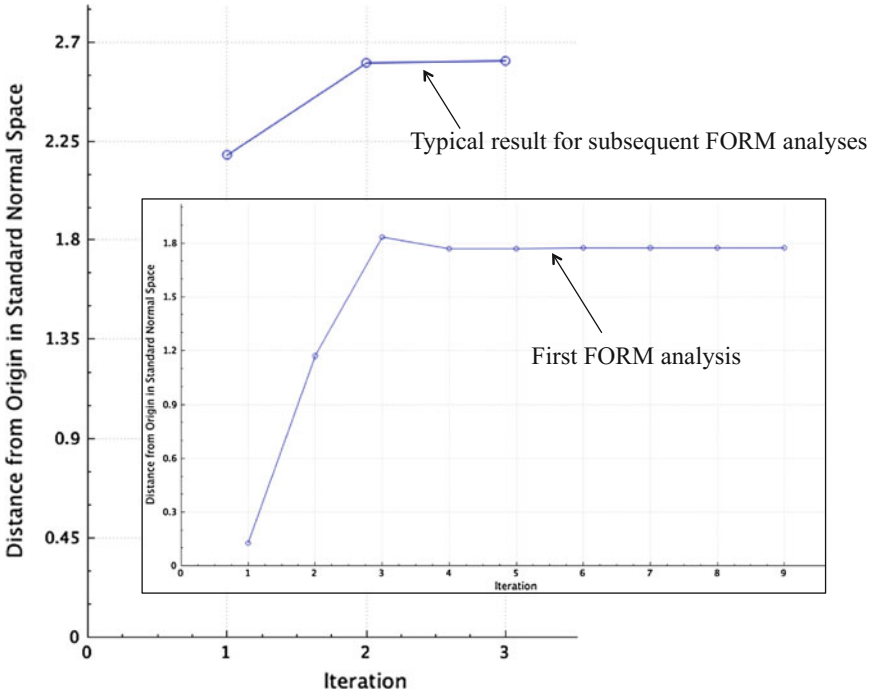

Fig. 3 FORM convergence

subsequent FORM analyses. The latter start at a distance relatively far from the origin and converge with only three evaluations of the cost, signifying a substantial computational cost saving in each FORM analysis. The question whether additional cost evaluations are needed to obtain the gradient vector used in the FORM algorithm is addressed in the next section.

5 Exact Gradients

Professor Der Kiureghian is a pioneer in the derivation and implementation of exact derivatives using the direct differentiation method (Zhang and Der Kiureghian 1993). An important feature of the methodology outlined above is that exact derivatives are propagated through all the intervening models, from finite element analysis through FORM and to the optimization analysis. This means that the exact evaluation of the gradient

$$\nabla c = \frac{\partial c(\mathbf{x})}{\partial \mathbf{x}} \tag{7}$$

is available for the FORM analysis and that the gradient

$$\nabla \mu_c^{FORM} = \frac{\partial \mu_c^{FORM}}{\partial \mathbf{v}} \tag{8}$$

is available for the optimization analysis, where $\mathbf{v}$ are design variables, such as structural dimensions. The exact derivatives are implemented in Rts to run the examples presented below. Differentiation of Eq. (3) yields, due to the fixed cost thresholds,

$$\frac{\partial \mu_c^{FORM}}{\partial \mathbf{v}} = \sum_{i=N_l}^{i=N_h} \frac{1}{2} \cdot \left(\frac{\partial p_{i+1}}{\partial \mathbf{v}} + \frac{\partial p_i}{\partial \mathbf{v}} \right) \cdot \Delta c \tag{9}$$

From FORM, the derivatives of the probabilities are (Der Kiureghian 2005):

$$\frac{\partial p}{\partial \mathbf{v}} = \frac{\partial p}{\partial \beta} \frac{\partial \beta}{\partial c} \frac{\partial c}{\partial \mathbf{v}} = \varphi(\beta) \cdot \frac{1}{\|\nabla G\|} \cdot \frac{\partial c}{\partial \mathbf{v}} \tag{10}$$

because

$$\frac{\partial p}{\partial \beta} = \frac{\partial}{\partial \beta}(\Phi(-\beta)) = -\varphi(\beta) \tag{11}$$

and

$$\frac{\partial \beta}{\partial c} = \frac{1}{\|\nabla G\|} \cdot \frac{\partial g}{\partial c}\bigg|_{\mathbf{x}^*} = \frac{1}{\|\nabla G\|} \cdot \frac{\partial (c_i - c(\mathbf{x}, \mathbf{v}))}{\partial c}\bigg|_{\mathbf{x}^*} = -\frac{1}{\|\nabla G\|} \tag{12}$$

The derivatives $\partial c / \partial \mathbf{v}$ are available in exact form also when finite element models are employed to determine the cost (Haukaas and Der Kiureghian 2005). Figure 4 provides an overview of the propagation of gradients through the model framework. The focus in this chapter is on the three right-most models: FORM,

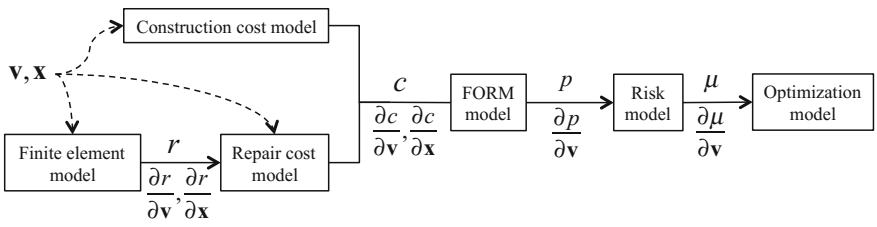

Fig. 4 Propagation of exact derivatives

Risk, and Optimization. The FORM model takes the total cost, c, as input and provides the exceedance probability, p, as output. The FORM model uses the derivative of c with respect to the random variables, $\mathbf{x}$, to achieve convergence. The Risk model repeatedly calls the FORM model to calculate the area underneath the loss curve, i.e., the mean μ. The Risk model accumulates and conveys the derivative of c with respect to the design variables, $\mathbf{v}$, from FORM to the Optimization model. The Optimization model minimizes μ using those derivatives.

6 Demonstration Example

A simple and transparent example is selected to demonstrate the methodology presented above. Consider a simply supported beam subjected to a point load, P, at mid-span. The beam has length L and its rectangular cross-section has height h and width b. The parameters L, b, and P are random variables and h is the design variable. The characteristics of the random variables are provided in Table 1.

The construction cost is formulated proportional to the volume of the beam:

$$c_{constr} = b \cdot h \cdot L \cdot \theta_1 \tag{13}$$

where $\theta_1 = 10^{-5}\$/\text{mm}^3$ is a model parameter to translate beam volume into dollar cost. The repair cost is formulated proportional to the maximum stress in the beam, which is the bending moment over the cross-section modulus:

$$c_{repair} = \frac{3 \cdot P \cdot L}{2 \cdot b \cdot h^2} \cdot \theta_2 \tag{14}$$

where $\theta_2 = 10^3\$/\text{MPa}$ is a model parameter to translate stress into dollar cost.

The objective of the analysis is to minimize the expectation of the total cost, i.e., to minimize

$$\min\{\mu_c\} = \min\{\ \mathrm{E}[c_{constr} + c_{repair}]\ \} = \min\left\{ \int_0^\infty G(c)dc \right\} \tag{15}$$

where the detailed cost models, including discount rates and other factors, are outside the scope of this chapter, and $G(c)$ was defined earlier as the complementary cumulative distribution function of the cost. That function is displayed in Fig. 5a

Table 1 Characteristics of the random variables in the demonstration example

	Distribution	Mean	Coefficient of variation (%)
L	Lognormal	2.0 m	10
b	Lognormal	0.2 m	10
P	Lognormal	5 kN	10

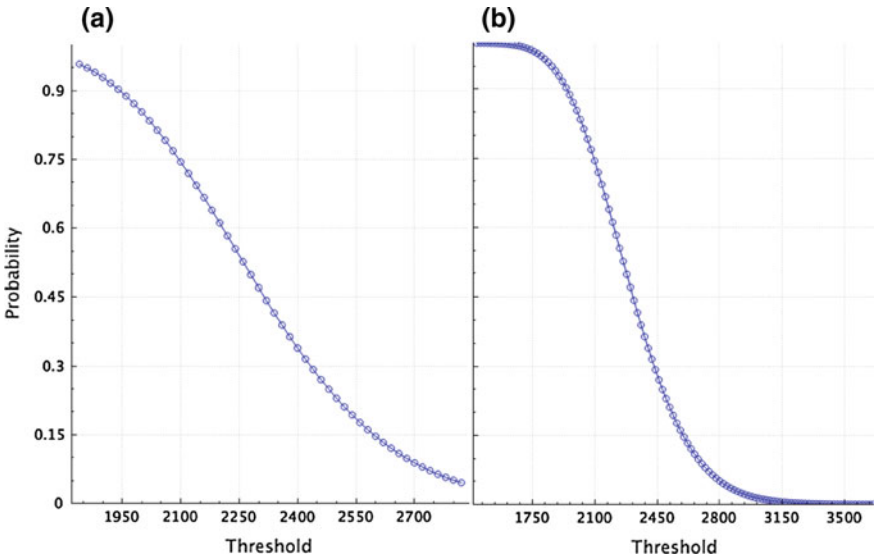

Fig. 5 Initial complementary cumulative distribution function for the total cost

for the beam height $h = 0.5$ m, which is used as initial value for the design variable. The value of the mean for this loss curve according Eq. (6) is \$2,294.77 with $\Delta c = \$20$ and $p_{tol} = 0.05$. Reducing p_{tol} from 0.05 to 0.0001 yields more points in the tails, as shown in Fig. 5b and improves the mean estimate to \$ 2,298.01. A less extreme value $p_{tol} = 0.001$ yields \$2,297.94.

The results shown above are produced with the computer program Rts, which is an extension of the program Rt (Mahsuli and Haukaas 2013) with finite element analysis. The models that are sketched in Fig. 4 are implemented in Rts and Fig. 6 is a screenshot of Rts after convergence of the optimization analysis. The left-most and bottom-most parts of the screen are dedicated to input and output in text form. The main visualization area in the upper-right contains three plots, which are created at run-time. The largest plot shows the loss curve at the optimum design $h = 335.02$, at which the expected cost is \$2,004.03. The convergence towards those optimal values is shown in the lower right plot, with the evolution of the objective function, i.e., the expected cost plotted in blue and the evolution of the design variable value plotted in red. The upper right plot shows the evolution of the last FORM analysis as explained earlier in the context of Fig. 3. In short, Fig. 6 shows the result of the optimization analysis with the example presented in this section.

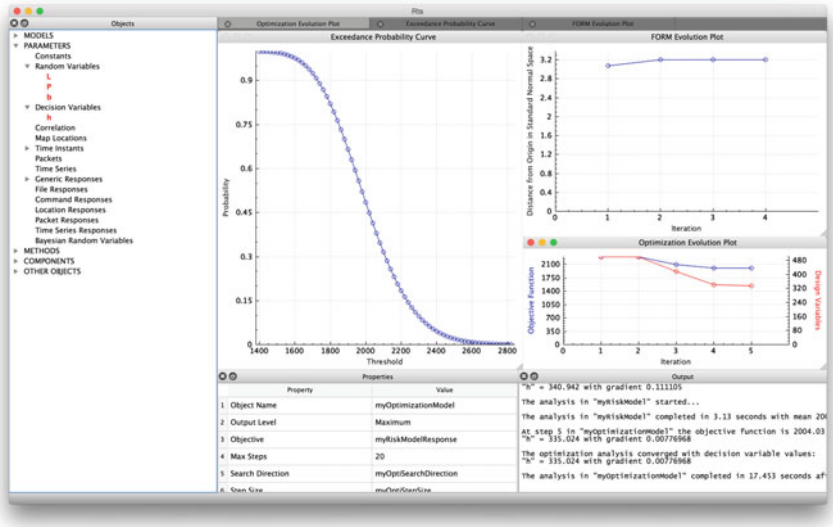

Fig. 6 Screenshot of the computer program after convergence of the optimization analysis

7 Conclusions and Ongoing Studies

A simple example was presented in this paper to illustrate a methodology intended for minimizing the expected cost of more complex building models. The focus on cost is aligned with recent advances in performance-based engineering, and the fundamental idea is that several costs, which depend on many models and random variables, are summed and its mean is minimized. Because a variation in the design variables will make some costs go up and other down, the expected cost is under certain circumstances a convex function suitable for gradient-based optimization.

Several tasks are addressed in ongoing research to go from simple examples to realistic analyses. One task is the creation of information-rich structural models from building information models used in other disciplines of the construction industry. Industry foundation classes are employed as the language by which the information is imported and exported to and from the structural model. The structural model includes non-structural components and content in order to improve cost estimates for damage due to ground shaking, etc.

A related line of research is the creation of detailed models for costs, including construction cost, repair cost, environmental impact cost, downtime cost, and cost of injuries and fatalities. Without comprehensive modeling of hazards and costs the optimization results have limited value.

Other issues being addressed are the feasibility and accuracy of various methods to calculate the expected cost, or other measures of risk, and the feasibility of various optimization algorithms for different problems. The example presented in

this paper is linear elastic with a well-behaved convex objective function. The inclusion of inelastic material behavior, stochastic loading processes, and a life-cycle scope is more challenging and addressed in ongoing studies.

References

Ang AHS, Tang WH (2007) Probability concepts in engineering: emphasis on applications in civil & environmental engineering. Wiley, New York

Bernoulli D (1738) Exposition of a new theory on the measurement of risk. J Econ Soc 22(1): 23–36

Der Kiureghian A (2005). First- and second-order reliability methods. In: Nikolaidis E, Ghiocel DM, Singhal S (eds) Engineering design reliability handbook. CRC Press

Der Kiureghian A, De Stefano M (1991) Efficient algorithm for second-order reliability analysis. J Eng Mech 117(12):2904–2923

Haukaas T (2013) Probabilistic models, methods, and decisions in earthquake engineering. In: Proceedings of the 11th international conference on structural safety & reliability, ICOSSAR 2013, New York

Haukaas T, Allahdadian S, Mahsuli M (2013) Risk measures for minimization of earthquake costs. In: Proceedings of the 11th international conference on structural safety & reliability, ICOSSAR 2013, New York

Haukaas T, Der Kiureghian A (2005) Parameter sensitivity and importance measures in nonlinear finite element reliability analysis. J Eng Mech 131(10):1013–1026

Liu P-L, Der Kiureghian A (1986) Multivariate distribution models with prescribed marginals and covariances. Probab Eng Mech 1(2):105–112

Mahsuli M, Haukaas T (2013) Computer program for multi-model reliability and optimization analysis. J Comput Civ Eng 27(1):87–98

von Neumann J, Morgenstern O (1944) Theory of games and economic behavior. Princeton University Press, Princeton

Yang TY, Moehle J, Stojadinovic B, Der Kiureghian A (2009) Seismic performance evaluation of facilities: methodology and implementation. J Struct Eng 135(10):1146–1154

Zhang Y, Der Kiureghian A (1993) Dynamic response sensitivity of inelastic structures. Comput Methods Appl Mech Eng 108(1–2):23–36

Part V
Statistical Analysis and Probabilistic Models

Model Checking After Bayesian Inference

Matteo Pozzi and Daniele Zonta

Abstract Bayesian analysis provides a consistent logical framework for processing data, inferring parameters and estimating relevant quantities in engineering problems. However, its outcomes are valid conditional to the specific model assumptions. Whether these assumptions are questioned, possibly because of some factors knowingly left out, they can be checked by further analysis of the available empirical data. Again, this can be done inside the Bayesian framework, by probabilistically comparing expanded models with the original one; however, this may be computational impractical in many applications. Test statistics and p-value analysis, historically developed under the frequentist approach but adapted to the Bayesian setting, provide an alternative for model checking coupled with probabilistic inference. In this chapter, we illustrate the relation between p-value analysis and Bayesian model comparison: after presenting it in a general context, we focus on Gaussian linear models under known perturbation, for which this relation can be stated in close formulas, and explore an example outside that domain.

1 Introduction

A key task in engineering analysis is to infer the value of relevant quantities by using a probabilistic model. This model is selected based on expert judgement, physical principles and past empirical observations, and the outcome of the

The original version of this chapter was revised: Incorrect author affiliation has been corrected. The erratum to this chapter is available at https://doi.org/10.1007/978-3-319-52425-2_24

M. Pozzi (✉)
Department of Civil & Environmental Engineering, Carnegie Mellon University,
107b Porter Hall, 5000 Forbes Av, Pittsburgh, PA 15213-3890, USA
e-mail: mpozzi@cmu.edu

D. Zonta
Department of Civil & Environmental Engineering, University of Strathclyde, Glasgow, UK
e-mail: daniele.zonta@strath.ac.uk

P. Gardoni (ed.), *Risk and Reliability Analysis: Theory and Applications*,
Springer Series in Reliability Engineering, DOI 10.1007/978-3-319-52425-2_14

inference process intrinsically depends on it. Further empirical observations offer the opportunity to confirm, revise or reject a candidate model. Bayesian analysis provides a consistent framework to process those observations for model updating and comparison, in the assumption that the set of possible models is exhaustive. In principle, if we could include the complete set in our computational framework, by way of logic we should accept the outcome of the probabilistic inference. In practice, defining a truly exhaustive set of hypotheses is computationally unfeasible in all but highly simplified settings, and agents often leave, more or less consciously, possible alternatives out of the quantitative inference process. Because of this, an agent can question the adopted modelling assumptions and, consequently, the outcome of the analysis: whether the computational model is just an incomplete formalization of the agent's belief, refusing to check it will expose her to the risk of being an "overconfident" Bayesian (Morey et al. 2013).

From a Bayesian perspective, a model is judged as good or bad only in comparison with others. Therefore, formal explicit model checking always requires definition of alternative candidates. However, model checking often follows an implicit practise, based on detecting symptoms that seems in conflict with the assumptions, and deciding to adjust them. p-value analysis provides a quantitative formal procedure for this practice: originally proposed in the frequentist framework, it has been adapted for Bayesian model checking, both in the prior and posterior setting, as proposed by Box (1980), Meng (1994), Gelman et al. (1996, 2014), and discussed by Bayarri and Berger (2000), Kruschke (2013), Morey et al. (2013). By selecting appropriate test statistics, the agent checks her assumptions against possible factors left out of the original setting, and the test outcome can be taken as guidance to confirm or revise that setting. A recent example of test-based checking in engineering analysis is "model falsification", as presented by Goulet et al. (2013), Pasquier and Smith (2015).

In this chapter, we illustrate the relation between p-value analysis and Bayesian model comparison: despite the two procedures look different, it is possible to relate them analytically. As a result, executing a test on a model can be intended as comparing that model with an alternative, specific one. Appropriate tests can assess complicate model assumptions (e.g., a specific noise distribution, the linearity of the response, etc.). However, we start focusing on the simple context of Gaussian linear models under a known possible perturbation, where the equivalence can be shown in close formulas, so that we can identify an appropriate test for comparing the model against a specific alternative, or identify an alternative model implicitly compared by a specific test. In other, more complex contexts, it is not easy to derive these equivalences.

The rest of the chapter is organized as follows. In Sect. 2, we provide a recap on Bayesian model comparison and checking, while in 3 we introduce statistical tests and p-value analysis, discussing prior and posterior model checking. In Sect. 4, we clarify the equivalence between Bayesian model checking and p-value analysis, providing closed form equivalence in the context of Gaussian linear models possibly affected by a known perturbation. These findings are illustrated with numerical examples in Sect. 5, while in Sect. 6 we investigate numerically the possibility of extending these findings outside the Gaussian linear setting. Some concluding remarks are reported at the end of the chapter.

2 Model Checking Using Bayesian Inference

The general problem on discussion in this chapter can be formally stated as follows. Consider a candidate model $\mathcal{M}$ and some empirical observations $\tilde{\mathbf{y}}$: is the model appropriate for processing those data and assessing the value of relevant quantities? What is the criterion whereby we accept (validate) or reject (falsify) it? In this section we recap how model checking should be performed within a Bayesian logical framework.

2.1 Inference Within a Single Model

We start reviewing Bayesian inference inside model $\mathcal{M}$. Parameter set $\boldsymbol{\theta}$, on domain Ω_θ, is defined by a prior probability $p(\boldsymbol{\theta}|\mathcal{M})$, while observable data (i.e. "measures") $\mathbf{y}$ are related to the parameters by a likelihood function $p(\mathbf{y}|\boldsymbol{\theta}, \mathcal{M})$. Predictive distribution of data is given by:

$$p(\mathbf{y}|\mathcal{M}) = \int_{\Omega_\theta} p(\mathbf{y}|\boldsymbol{\theta}, \mathcal{M}) p(\boldsymbol{\theta}|\mathcal{M}) d\boldsymbol{\theta} \tag{1}$$

while posterior distribution by Bayes' rule:

$$p(\boldsymbol{\theta}|\mathbf{y}, \mathcal{M}) = p(\mathbf{y}|\boldsymbol{\theta}, \mathcal{M}) p(\boldsymbol{\theta}|\mathcal{M}) \,/ p(\mathbf{y}|\mathcal{M}) \tag{2}$$

The overall goal of the analysis may be the inference on parameters, or to compute the expected value of a function $f(\boldsymbol{\theta}, \mathcal{M})$, that depends of model and parameter: its corresponding prior and posterior values are:

$$\begin{cases} \mathbb{E}[f|\mathcal{M}] = \int_{\Omega_\theta} f(\boldsymbol{\theta}, \mathcal{M}) p(\boldsymbol{\theta}|\mathcal{M}) d\boldsymbol{\theta} \\ \mathbb{E}[f|\mathbf{y}, \mathcal{M}] = \int_{\Omega_\theta} f(\boldsymbol{\theta}, \mathcal{M}) p(\boldsymbol{\theta}|\mathbf{y}, \mathcal{M}) d\boldsymbol{\theta} \end{cases} \tag{3}$$

Figure 1a reports a basic probabilistic graphical model for this case. In reliability analysis, for example, function f is usually the indicator of a relevant event, e.g. a structural failure. When model $\mathcal{M}$ is assumed, formally f is a binary variable defined as $f = \mathrm{I}[g(\boldsymbol{\theta}, \mathcal{M})]$, where I is the indicator function and $g(\boldsymbol{\theta}, \mathcal{M})$ is the limit state function according to model $\mathcal{M}$. Equation 3, and can be re-written in the form of prior and posterior reliability integrals (Der Kiureghian 2005).

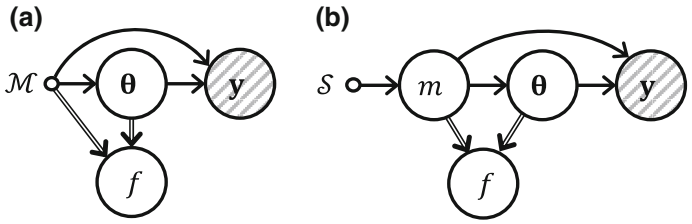

Fig. 1 Probabilistic graphical model for **a** a single model inference and prediction and **b** for multi-model inference and prediction

2.2 Comparison of Models

Bayesian analysis is suitable for explicitly comparing models within a set, stated a priori. Assume that M mutually exclusive and exhaustive models are possible, and indicate with $\mathcal{S}$ their corresponding assumptions. The discrete prior distribution $P(m|\mathcal{S})$ assigns the probability to model m on domain $\{1, \ldots, M\}$. Now both prior distribution, likelihood and function f depends on index m, and Eqs. 1–3 can be re-written using indicator m instead of $\mathcal{M}$. Global predictive distribution is:

$$p(\mathbf{y}|\mathcal{S}) = \sum_{m=1}^{M} p(\mathbf{y}|m)P(m|\mathcal{S}) \tag{4}$$

and updated model probabilities are:

$$P(m|\mathbf{y}, \mathcal{S}) = p(\mathbf{y}|m)P(m|\mathcal{S}) / p(\mathbf{y}|\mathcal{S}) \tag{5}$$

This approach is generally referred to as "model comparison", illustrated by Bretthorst (1996), Jaynes (2003), MacKay (2003) and applied to engineering problems by Beck and Yuen (2004), Zonta et al. (2008), Yuen (2010) Zonta and Pozzi (2015), Wang et al. (2016). Finally, prior and posterior expected value of f now reads:

$$\begin{cases} \mathbb{E}[f|\mathcal{S}] = \sum_{m=1}^{M} \mathbb{E}[f|m]P(m|\mathcal{S}) \\ \mathbb{E}[f|\mathbf{y}, \mathcal{S}] = \sum_{m=1}^{M} \mathbb{E}[f|\mathbf{y}, m]P(m|\mathbf{y}, \mathcal{S}) \end{cases} \tag{6}$$

Figure 1b reports the corresponding graph.

2.3 *Rejecting a Model by Computing Its Posterior Probability*

A special case of model comparison is that where set $\mathcal{S}$ include just two models: candidate model $\mathcal{M}$ and its alternative $\mathcal{A}$, which overall encodes all credible options not incorporated in $\mathcal{M}$. In other words, we are assuming that observations $\mathbf{y}$ are either the outcome of the candidate model $\mathcal{M}$ or the outcome of *something else*, which we make explicit through alternative model $\mathcal{A}$. In this setting, we can rewrite Eq. 5 as:

$$P(\mathcal{M}|\mathbf{y}) = \frac{p(\mathbf{y}|\mathcal{M})P(\mathcal{M})}{p(\mathbf{y}|\mathcal{M})P(\mathcal{M}) + p(\mathbf{y}|\mathcal{A})[1 - P(\mathcal{M})]} \tag{7}$$

highlighting how the posterior distribution of $\mathcal{M}$ depends on its prior probability and the prediction distributions of the measures under $\mathcal{M}$ and $\mathcal{A}$. In this setting, we assume the agent starts assuming model $\mathcal{M}$ (or even a hierarchical model defined by set $\mathcal{S}$, with obvious adjustments in the notation). However, she believes that that option is not the only possible and considers an alternative model $\mathcal{A}$. If the posterior probability of $\mathcal{M}$ is sufficiently high, she can neglect model $\mathcal{A}$ as if this latter hypothesis was disproven by the data. In this case, she is "accepting" model $\mathcal{M}$ and, consequently, she can base her estimate of f, if this is the goal of the analysis, on Eq. 3. On the other hand, if that posterior probability is not high enough, she should use Eq. 6, to avoid the bias due to an incomplete model set: we call this decision "rejecting" model $\mathcal{M}$. We note that, practically, the problem is relevant when the expectation of f given $\mathcal{A}$ is significantly different respect to that given $\mathcal{M}$. When alternative model $\mathcal{A}$ is explicitly available, that decision can be based on Eq. 7: if the posterior probability is below threshold $\bar{P}$, the agent rejects $\mathcal{M}$.

3 Prior and Posterior Model Checking Using *p*-Value Analysis

p-value analysis provides an alternative path to model checking. In this framework, the agent defines a function T of the data, usually called a "test statistic". By transforming the predictive distribution of the measure, $p(\mathbf{y}|\mathcal{M})$, through function $T(\mathbf{y})$, we get the predictive distribution of the statistic, $p(T|\mathcal{M})$. The model is rejected when T is above a selected threshold $\bar{T}$ or, equivalently, when the probability of $\mathcal{M}$ to generate values of T above the observed one (usually called the "*p*-value") is too low, say under threshold $\wp_{\text{thr}}$. While in orthodox statistic the model is calibrated by fixing a value for inner parameters $\boldsymbol{\theta}$, in prior model checking related to Bayesian analysis $\boldsymbol{\theta}$ is a random variable modeled by its prior distribution, and measures are predicted by Eq. 1.

For computing the p-value, we introduce variable $\mathbf{y}'$ as a replicate of the measure, with the same predictive distribution under $\mathcal{M}$, and $T' = T(\mathbf{y}')$ as the corresponding statistics. We want to compute the probability that random variable T' is above $\tilde{T} = T(\tilde{\mathbf{y}})$, where $\tilde{\mathbf{y}}$ indicates the observed data. This is the so-called "prior p-value", $\wp_\pi$. Formally, we can define binary variable $q = \mathrm{I}[T' > \tilde{T}]$, and refer to the graphs in Fig. 4. In graph (a), parameters $\boldsymbol{\theta}$ are not related to the observed data, so the prediction of T' relies on the prior model only, and $\wp_\pi$ is defined as:

$$\wp_\pi = \mathbb{E}[q|\mathcal{M}] = \mathbb{P}[T' > \tilde{T}|\mathcal{M}] \tag{8}$$

or, equivalently, $\wp_\pi = 1 - F_\pi(\tilde{T})$, where F_π is the cumulative distribution corresponding to $p(T|\mathcal{M})$.

The test can also be defined a posteriori, making use of the posterior distribution computed in Eq. 2, and graph (b) is related to the so-called "posterior p-value" $\wp_\omega$ (Meng 1994; Gelman et al. 1996; 2014): parameter $\boldsymbol{\theta}$ and observation $\mathbf{y}$ are now related, and the prediction is based on the posterior distribution:

$$\wp_\omega = \mathbb{E}[q|\tilde{\mathbf{y}}, \mathcal{M}] = \mathbb{P}[T' > \tilde{T}|\tilde{\mathbf{y}}, \mathcal{M}] \tag{9}$$

where the corresponding predictive distribution for the replicate measures is:

$$p(\mathbf{y}'|\tilde{\mathbf{y}}, \mathcal{M}) = \int_{\Omega_\theta} p(\mathbf{y}'|\boldsymbol{\theta}, \mathcal{M}) p(\boldsymbol{\theta}|\tilde{\mathbf{y}}, \mathcal{M}) d\boldsymbol{\theta} \tag{10}$$

Again, posterior p-value can be express as $\wp_\omega = 1 - F_{\omega|\tilde{\mathbf{y}}}(\tilde{T})$, where $F_{\omega|\tilde{\mathbf{y}}}$ is the cumulative distribution corresponding to $p(T'|\tilde{\mathbf{y}}, \mathcal{M})$.

Generally, by using a unique function T, prior and posterior checking cannot define identical rejection regions, even when the threshold of the corresponding the p-values is calibrated *ad hoc*. However, the rejection decision based on function T and p-value threshold $\wp^\pi_{\text{thr}}$ in the prior setting is consistent with that in posterior checking, based on the p-value threshold $\wp^\omega_{\text{thr}}$ and function T_ω defined appropriately, e.g. as follows:

$$T_\omega(\mathbf{y}) = T(\mathbf{y}) - F_\pi^{-1}[1 - \wp^\pi_{\text{thr}}] + F^{-1}_{\omega|\mathbf{y}}[1 - \wp^\omega_{\text{thr}}] \tag{11}$$

where now we use $F_{\omega|\tilde{\mathbf{y}}}$ for referring to the cumulative distribution corresponding to replicate $p(T'_\omega|\tilde{\mathbf{y}}, \mathcal{M})$. While it may be hard to solve Eq. 11, it formally shows the equivalence condition for prior and posterior model checking. However, by reading Fig. 2, it is straightforward to give different meanings to prior and posterior checking: in the prior setting, we evaluate the probability that the prior model, before the updating, generate higher values of the statistic (respect to the observed one), while in the posterior setting we evaluate this probability for the updated model. These alternatives are also related to different computational complexity levels, the evaluating of the posterior p-value being generally harder.

The structure of Eqs. 8–9 closely resembles that of Eq. 3. Because of this, a wide range of numerical methods can be used for solving both problems, including Reliability Methods as FORM or SORM (Der Kiureghian 2005) and Monte Carlo

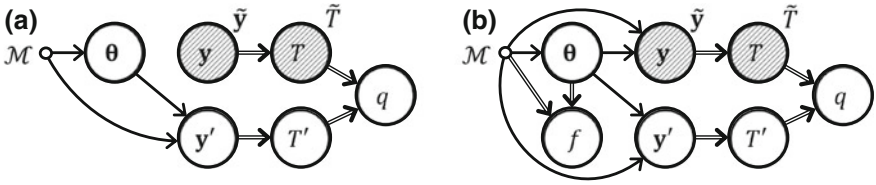

Fig. 2 Probabilistic graphical models for computing prior **a** and posterior **b** p-values

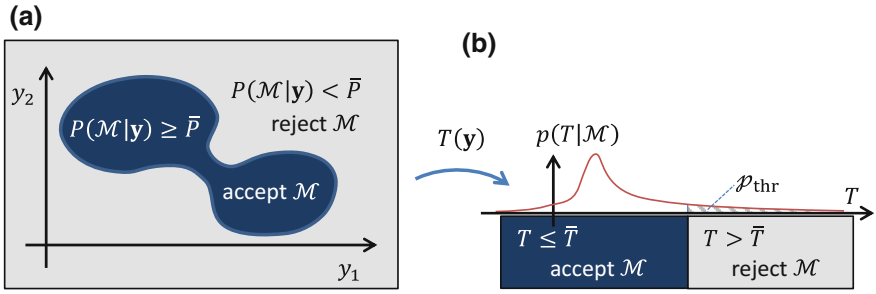

Fig. 3 Pictorial representation of the decision process about accepting/rejecting model $\mathcal{M}$, using Bayesian model comparison **a** and test-based prior checking **b**

methods (Beck and Au 2002). Specifically, the computation of the posterior p-value can be performed via Monte Carlo Markov Chain, also including Reliability Methods (Straub et al. 2016). Moreover, in Fig. 3b we have included the node representing f, to highlight how posterior model checking can be computationally "coupled" with the posterior probabilistic evaluation, as the posterior distribution of $\boldsymbol{\theta}$ is relevant both in Eq. 3b and in Eq. 10. Hence, one could target the problems of evaluating the posterior p-value and the posterior expectation of f (e.g., a failure probability), with a single optimized numerical approach.

Practically, the scope of test-based model checking is humbler than that described in Sect. 2: if $\mathcal{M}$ is rejected, the agent will investigate how to improve the model, without pretending to obtain, as an outcome of the analysis, the complete model set $\{\mathcal{A}, \mathcal{M}\}$, and the corresponding posterior probabilities.

4 Bayesian Selection of Test Statistic

4.1 Bayesian Model Comparison Versus p-*Value Analysis*

In the previous sections, we have reviewed two ways to perform probabilistic model checking: using Bayesian model comparison and p-value analysis. We have seen that, in strict Bayesian terms, accepting/rejecting a candidate model $\mathcal{M}$ requires definition of an alternative model, and decision is based on the calculation

of its posterior probability. On the other hand, in p-value analysis the candidate model is accepted/rejected regardless any explicit alternative model, on the ground of a test statistic. Apparently, the two approaches are incompatible and, not surprisingly, there is a long-standing debate between, say, "radical" and "moderate" Bayesians, with radicals insisting on the logical inconsistency of test statistics and moderates more keen to accept them, under appropriate conditions; a debate which is well represented in the Gelman and Shalizi's paper (2013) and Kruschke's (2013) and Morey et al. (2013) commentaries.

Here we do not enter in this discussion; we just observe that, using either one approach or the other, the outcome of the model checking is always conditional to some assumptions: the alternative model $\mathcal{A}$ in Bayesian model checking; the test statistic T in p-value analysis. When these quantities are in a specific relation among themselves, the model checking based on p-value analysis is, in fact, fully equivalent to that based on the Bayesian model comparison. Figure 3a provides a pictorial representation of Bayesian model checking: the method simply partitions the domain of observations $\mathbf{y}$ into an acceptance region (in dark shade) where $\mathcal{M}$ is more likely than $\bar{P}$ a posteriori, and a rejection one (in light color) where this is not the case. Similarly, a generic test statistic T can be regarded as a map from the domain of observations $\mathbf{y}$ to the real domain, which is divided in an acceptance and a rejection intervals by threshold $\bar{T}$, as in Fig. 3b. Clearly, it is always possible (albeit not always simple) to define a transformation T and a threshold $\bar{T}$ (or $\wp_{\text{thr}}$) mapping the dark and light domains of $\mathbf{y}$ to the corresponding intervals of T. The test statistic thus defined will be perfectly consistent with a Bayesian model checking with alternative model $\mathcal{A}$. The opposite is also true, which is to say that, given a test statistics T and a threshold $\bar{T}$, we can always identify the accept/reject domains in the space of $\mathbf{y}$ and then define an appropriate model $\mathcal{A}$, a prior probability $P(\mathcal{M})$ and a threshold $\bar{P}$ so that Bayesian model checking is compatible with p-value analysis.

In other words, we can always read the practice of using a test statistic in terms of the Bayesian model selection outlined in 2.3 as follows: the agent implicitly assumes an alternative model, that is supposed to generate values of T higher than that of $\mathcal{M}$ and because of this, a high value T raises concern about $\mathcal{M}$, and lower its posterior probability, possibly under $\bar{P}$. So the selection of the statistic is closely related to the candidate and the alternative models. Practically, test statistics can be used when direct application of Eq. 7 is not viable, for example because of the computational complexity of defining $\mathcal{A}$ or evaluating $p(\mathbf{y}|\mathcal{A})$. It is to be noted that some authors propose model checking through test statistics as a path to data exploration, even more effective than direct Bayesian model comparison, because the latter may suffer, in practical implementations, to a high sensitivity to noise parameters (see Gelman and Shalizi 2013, and reference to Lindley 1957).

4.2 Selection of Test Statistics

Similarly to the selection of alternative model $\mathcal{A}$, the selection of test statistic T is based on the agent's belief, experience, and knowledge of the physical problem. Neither $\mathcal{A}$ nor T derives logically from the analysis of $\mathcal{M}$ alone. Although in principle we can always select a test statistic consistent with a Bayesian model comparison, in practice this relationship is not always straightforward. Nonetheless, investigating this correspondence helps us to shed light on how test statistics should be selected.

Let us consider the case when model $\mathcal{A}$ is a complicate extension of $\mathcal{M}$, including additional factors that the agent considers likely negligible. If needed, she can revise the original model, by including these factors. The agent selects a statistics T as a symptom of the neglected factors. If the value of T could be deterministically predicted under $\mathcal{M}$, the default model would be logically disproven whether the observed value $\tilde{T}$ disagreed with such prediction. If, on the other hand, T is uncertain under $\mathcal{M}$, the model cannot be disproven by any value associated with a positive density $p(T|\mathcal{M})$. However, as $\mathcal{A}$ is supposed to give higher values of T, a high statistic may indicate that observations come from $\mathcal{A}$ instead of $\mathcal{M}$. In light of this, the agent can fix a threshold $\bar{T}$ on the statistic, and revise the analysis if $\bar{T}$ is above this value. The selection of threshold $\wp_{\text{thr}}$ on the p-value may be more intuitive than that of $\bar{T}$. If prior p-value $\wp_\pi$ is intended as a random variable, as a function of random measures $\mathbf{y}$, it is uniformly distributed under $\mathcal{M}$, so $\wp_{\text{thr}}$ represents the probability of rejecting $\mathcal{M}$ for measures generated from that model (i.e., of committing a "type I error".), and it is called the test *significance level*. However, it is to be noted that posterior p-value $\wp_\omega$ is not uniformly distributed, even under $\mathcal{M}$, and tends to be concentrated around 50% (Gelman 2013). Intuitively, this happens because, during the inference process, the model is updated to fit the observations and, as a result, observations look less extreme than from the prior point of view (however, posterior p-value can be re-normalized to have uniform distribution). Despite of this, the use of posterior p-value has been advocated (Gelman et al. 2003) for the following reasons. First, when an improper prior distribution is adopted for the model parameters, the distribution of the replicate may be improper as well, and so that of the statistics: hence, the prior p-value may fail to measure the "strangeness" of the measures. For the second argument, consider a region in the parameter domain that, while having high prior probability, receives almost zero posterior probability, e.g. because it is in "bad agreement" with the observed measures, according to model $\mathcal{M}$. By posterior model checking, we do not compare the observed statistic with replicates coming from that region, as it has been ruled-out from the data. On the contrary, prior checking makes use of that region, according to the prior probability. In other words, in posterior checking we compared the measure with the updated model, that is the one we will use if we will accept $\mathcal{M}$.

Even if the agent identifies the factors, left outside $\mathcal{M}$, to be tests against the measures, still the problem remains of selecting an appropriate test, sensitive to

those factors. While the test significance level is invariant respect to the statistic (after selecting $\wp_{\text{thr}}$ and, in the case of posterior analysis, after normalization), the probability of rejecting the model when data are generated from the alternative one (i.e. the so called test *power*) strongly depends on function T. The agent wants the test power to be high, to decrease the probability of a "type II error", accepting $\mathcal{M}$ when measures comes from $\mathcal{A}$. In this next section we investigate how specification of the models is related to the power in a very special setting, that of Gaussian linear model under known perturbation, to illustrate the relation between test statistics and models.

We close this section by specifying some limits of our analysis. First, we do not directly cope with the issue of multiple tests as, in another context, model falsification does (Goulet et al. 2013). Second, we focus on the sensitivity of the test respect to a perturbation in the model, which would bias the inference, without directly addressing the sensitivity of the outcome of the inference process itself (e.g., the risk assessment in an engineering problem), respect of the perturbation.

4.3 Selecting Test Statistics for Linear Gaussian Models

To investigate the relation between p-values and Bayesian model selection, and how to consistently select an appropriate test statistic, we focus on the specific setting of Gaussian linear models (also investigated by Hjort et al. 2006), for which close formulas are available. All computational details are reported in Appendix A. Vector $\boldsymbol{\theta}$ lists random parameters of the default model $\mathcal{M}$, normally distributed (with mean vector $\boldsymbol{\mu}_\theta$ and covariance matrix and $\boldsymbol{\Sigma}_\theta$), linearly related (by matrix $\mathbf{A}$) to response $\mathbf{r}$, while measures $\mathbf{y}$ are affected by an additive zero-mean Gaussian noise $\boldsymbol{\varepsilon}$, with covariance matrix $\boldsymbol{\Sigma}_\varepsilon$. In alternative model $\mathcal{A}$, the additive disturbance (or "perturbation") $\Delta\,\mathbf{r}$ also affects the response, and is linearly related to parameters η by "shape" vector $\mathbf{b}$ (with unitary L-2 norm).

We define test statistic T as a linear function of measures, by vector $\mathbf{v}$ that we can call a "test direction". As the modulus of the direction is immaterial to the p-value analysis, we force it to have unitary L-2 norm. When we refer to the prior p-value, the statistic is normally distributed, and can be normalized so that it is standard normally distributed under $\mathcal{M}$. Under $\mathcal{A}$, the normalized statistics is still normally distributed, with unitary standard deviation and mean μ_π linearly related to scale factor η. The sensitivity α_π of μ_π to η (defined by $\mu_\pi = \alpha_\pi \eta$) depends on $\mathbf{v}$, and the best statistic for prior analysis is that for which α_π is the highest. If, on the other hand, we evaluate the posterior p-value, the normalized statistics is normally distributed with standard deviation σ_ω, zero-mean under $\mathcal{M}$ and with mean μ_ω under $\mathcal{A}$. Re-normalized mean $\mu_\Omega = \sigma_\omega^{-1}\mu_\omega = \alpha_\Omega \eta$ is still linearly related to scale factor η, via sensitivity factor α_Ω. The best statistics for posterior analysis has the highest value of α_Ω.

As illustrates in the appendix, the optimal prior statistics vector $\mathbf{v}_\pi^*$ is parallel to $\mathbf{\Sigma}_Y^{-1}\mathbf{b}$ (where $\mathbf{\Sigma}_Y = \mathbf{A}\,\mathbf{\Sigma}_\theta\mathbf{A}^{\mathrm{T}} + \mathbf{\Sigma}_\varepsilon$ is the covariance matrix of measures $\mathbf{y}$) while the optimal posterior one $\mathbf{v}_\omega^*$ is parallel to $\mathbf{\Sigma}_\varepsilon^{-1}\mathbf{b}$. Therefore, optimal prior and posterior test directions are not the same: they are function not only of $\mathbf{b}$, but also of the noise assumption and, for prior analysis, of the whole measurement uncertainty. However, when the optimal vectors are selected, prior and posterior sensitivities are the same (i.e. $\alpha^* = \alpha_\pi(\mathbf{v}_\pi^*) = \alpha_\Omega(\mathbf{v}_\omega^*) = \sqrt{\mathbf{b}^{\mathrm{T}}\mathbf{\Sigma}_Y^{-1}\mathbf{b}}$); in light of this, the adoption of the prior or the posterior analysis is equivalent, provided that the statistics is carefully selected and threshold identified. In facts, the linear statistics associated to optimal prior and posterior directions are in the equivalence relation described by Eq. 11. When prior and posterior p-values are computed using those optimal directions, they are deterministically related through the following formula:

$$p_\omega = 1 - \Phi[\sigma_\omega \Phi^{-1}(1 - p_\pi)] \tag{12}$$

where Φ is the cumulative standard normal distribution. We plot Eq. 12 in Fig. 4a, for different values of σ_ω that, in turn, depends on perturbation shape, the covariance matrixes of response and of noise. The non-uniform distribution of the posterior p-values under $\mathcal{M}$ is reported in the appendix.

In this setting, a decision rule based on a linear test along the optimal direction is consistent with one based on the posterior probability of model $\mathcal{M}$, when an appropriate threshold on the p-value is selected. This property derives from the Fisher Linear Discriminative Analysis (Fisher 1936, Murphy 2012) and the proof is reported in Appendix A. The prior p-value (again using the optimal direction) is also deterministically related to the posterior probability of $\mathcal{M}$ by Bayes' formula:

$$P(\mathcal{M}|p_\pi) = \frac{1}{1+[1/P(\mathcal{M})-1]\exp\{\mu_\pi[\Phi^{-1}(1-p_\pi)-\mu_\pi/2]\}} \tag{13}$$

Graph (b) shows this relation for $P(\mathcal{M}) = 1/2$ and different values of $\mu_\pi = \alpha^*\eta$, again a function of perturbation shape and covariance matrixes of response and of

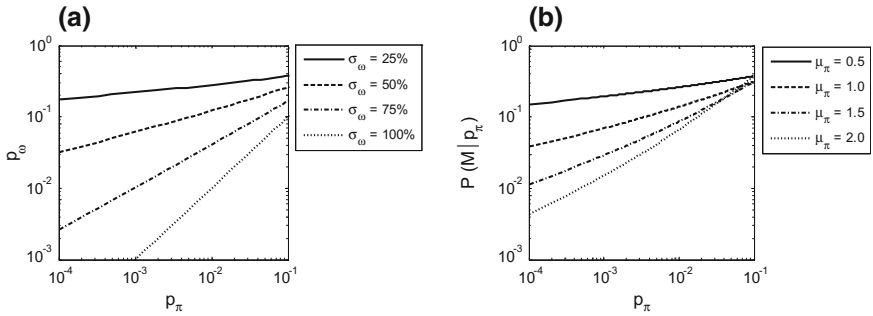

Fig. 4 a) relation between prior and posterior optimal p-values, b) posterior probability of $\mathcal{M}$ as a function of prior p-value

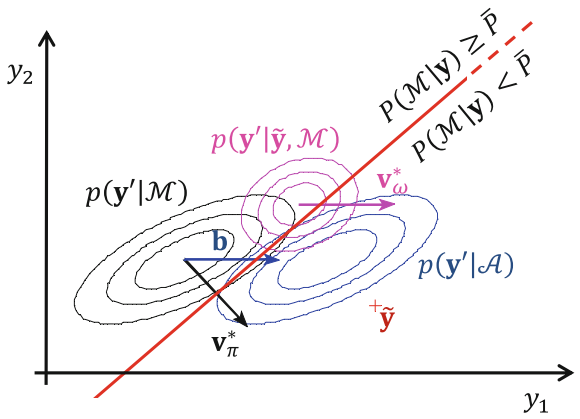

Fig. 5 Example of inference and model checking in Gaussian linear models

noise. The relation is monotonic in a wide range of interest of the parameters. However, the graph allows us to highlight that, as well known (Berger and Sellke 1987), p-values and posterior probabilities can differ for orders of magnitude, and the selection of an appropriate value for $\mathcal{P}_{\text{thr}}$ is generally not identical, or simply related, to that of $\bar{P}$.

Figure 5 summarizes and exemplifies this setting, when vector $\mathbf{y}$ is made up just by two measures. The decision boundary separating the two areas in Fig. 2 is here an hyperplane (a straight line in this example) orthogonal to $\mathbf{v}^*_\pi$, but not necessarily to $\mathbf{v}^*_\omega$. We conclude with a note on optimal directions: posterior direction $\mathbf{v}^*_\omega$ is simpler to compute or define, respect to prior direction $\mathbf{v}^*_\pi$, as the former is independent of $\mathbf{A}$ and $\boldsymbol{\Sigma}_\theta$. In the special case of $\boldsymbol{\Sigma}_\varepsilon$ proportional to the identity matrix, $\mathbf{v}^*_\omega$ coincides with $\mathbf{b}$, so that the posterior test is trivial to define, given the perturbation (as in Fig. 5). This remark highlights a possible benefit of posterior checking.

5 Illustrative Examples of Linear Gaussian Models

5.1 *Toy Example in Data Analysis*

To illustrate the inference process and the test statistics in Gaussian linear model, we start with a toy example. Suppose that, under model $\mathcal{M}$, our prior belief on physical variable θ, say a local strain on a structure, is defined by a normal distribution with mean $\mu_\theta = 100\mu\varepsilon$ and standard deviation $\sigma_\theta = 10\mu\varepsilon$. $N = 5$ direct measures are collected, so matrix $\mathbf{A}$ is actually a column vector of N ones. Marginal homoscedastic noise level is described by standard deviation $\sigma_\varepsilon = 10\mu\varepsilon$, equal to the prior uncertainty. We investigate different scenarios of the noise correlation coefficient ρ_ε (between each pair of measures), ranging from 0 to 1. According to the alternative perturbed model $\mathcal{A}$, the first measure is affected by shift defined by the

product of 1με and positive factor η (so the first entry of vector **b** is 1με, while other entries are zero). We wish to update our knowledge of θ, by processing all measures. Our conclusion would be consistent under $\mathcal{M}$. However, under $\mathcal{A}$, a perturbation affects the first measure, and this may significantly bias our result. The problem we face is to select a statistic able to highlight the perturbation. Clearly, all choices are not equally good for this purpose: any vector **v** with zero at the first entry would produce a statistic insensitive to the perturbation, and consequently unable to discriminate between $\mathcal{M}$ and $\mathcal{A}$. A reasonable candidate statistics is related to a vector with unitary first entry, and zero to all other entries: this statistic identifies T with y_1, that is the only quantity the models disagree about. According to this choice, we will reject $\mathcal{M}$ when y_1 is too high, independently on all other measures. However, y_1 might be high because so is θ, and not because of the perturbation. Being aware of this, we have to fix a high threshold to y_1 and this limits the power of the test. At least in the prior analysis, intuitively we can select a better test; for example, we can compute the difference between y_1 and the mean of all other measures, by a vector **v** that, before normalization, assigns one to the first entry, and value $[-1/(N-1)]$ to each other entry. The idea behind this choice is that, under $\mathcal{M}$, measure y_1 should be similar to the others, no matter what θ is, as all other measures are certainly unperturbed.

In the posterior analysis, on the other hand, we do not need to embed the inference about θ into the test statistic itself, as this follows an explicit Bayesian updating, and we can test measure y_1 in isolation. It turns out that the aforementioned tests are optimal when noise is uncorrelated, in the posterior setting, and in the prior one in the limit case of an improper prior, respectively. The power of the test is reported in Fig. 6a, as the probability of accepting model $\mathcal{A}$ (i.e. of making a "type II error") for thresholds of the prior p-value of 1% and of 10%, and for ρ_ε equal to zero and to 80%: the vertical axis reports the normal quantiles, so that the probability varies linearly with η, starting from the complement of the threshold to one. When measures are positively correlated, is it easier to detect anomalies of the

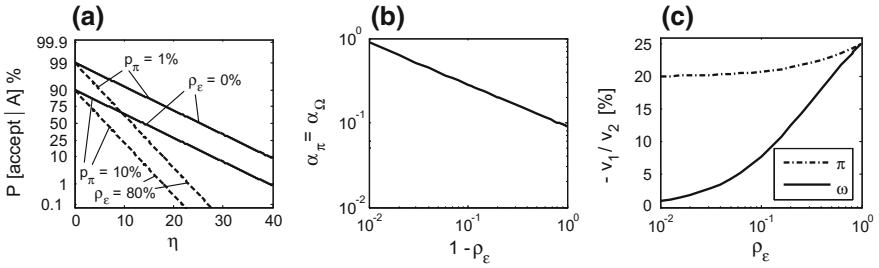

Fig. 6 **a** probability of "type II error" *vs* magnitude of the perturbation, depending on threshold of the prior p-value and noise correlation, **b** sensitivity of the normalized to statistic to noise correlation, **c** optimal direction of the test statistic *vs* noise correlation, for the example in 5.1

first measure, and consequently the test is more powerful. Graph (b) reports the sensitivity α^* as a function of the complement of ρ_ε to one: the power increases monotonically with ρ_ε and, even if it looks linear (in the log-log) scale in this domain, it goes to infinite when ρ_ε goes to one as, in that limit case, measures should be identical under $\mathcal{M}$ and any perturbation can be detected deterministically. Any reasonable unit-length vector assigns the same coefficient to measures in the set $\{y_2, \ldots, y_N\}$, so the ratio between the first coefficient (v_1) and the second one (v_2) is sufficient to describe vector **v**. Hence graph (c), by plotting the opposite of this ratio, fully describes the optimal prior and posterior test statistic, as a function of ρ_ε. For uncorrelated noise, assigning 1 to the first measure, we should assign $(-1/N)$ to all others, in the prior setting and zero in the posterior one. For higher correlation, both settings tend to assign $[-1/(N-1)]$ to all others.

This example illustrates on a simple setting how the optimal test statistic depends on the prior or posterior analysis, and on the model parameters, including the assumption on noise. In this and the following example, model checking using *p*-value analysis is consistent with Bayesian model comparison, as illustrated in Sect. 4.3, according to the Eq. 12–13.

5.2 *Identification of the Stiffness of a Cantilever*

As example of structural identification, consider a uniform cantilever of span L, loaded with a transversal force applied to the tip, instrumented with 10 sensors measuring transversal displacement, evenly separated along the beam, affected by the superposition of two independent noise patterns: a noise independent for each sensor and another one correlated among sensors, with square exponential correlation and correlation length λ, both with standard deviation $10^{-4}L$. In case (i), we consider the identification of the bending flexibility, when model $\mathcal{M}$ assumes no rotation at the fixed end. Parameter θ is $FL^2/3EI$, where F is the force and EI the bending stiffness, and is modelled by a normal distribution with standard deviation $\sigma_\theta = 0.1\%$. In the alternative model $\mathcal{A}$, the cantilever rotates at the edge. Figure 7a reports the standard deviation of the prediction of measure for each sensor, and the rigid perturbation due to edge rotation. Graph (b) reports the optimal prior and posterior test directions when λ is zero (and so sensor noise is uncorrelated). While the posterior optimal direction corresponds to the perturbation, the prior direction does not, because it has to compensate for the flexible component. Graph 6(b) reports the directions when $\lambda/L = 20\%$, showing how the posterior direction can also differ from the perturbation, when noise is correlated. Case (ii) defines an opposite case: the cantilever is assumed to be rigid under model $\mathcal{M}$ and possibly flexible under $\mathcal{A}$. Now parameter θ is FL/k, where k is the rotational stiffness of the edge. Noise and prior parameters are as in case (i), and graphs (d), (e), (f) correspond to (a), (b), (c) for that case, illustrating again how the appropriate test statistic, able to correctly mimic Bayesian model comparison, closely depends on both $\mathcal{A}$ and $\mathcal{M}$.

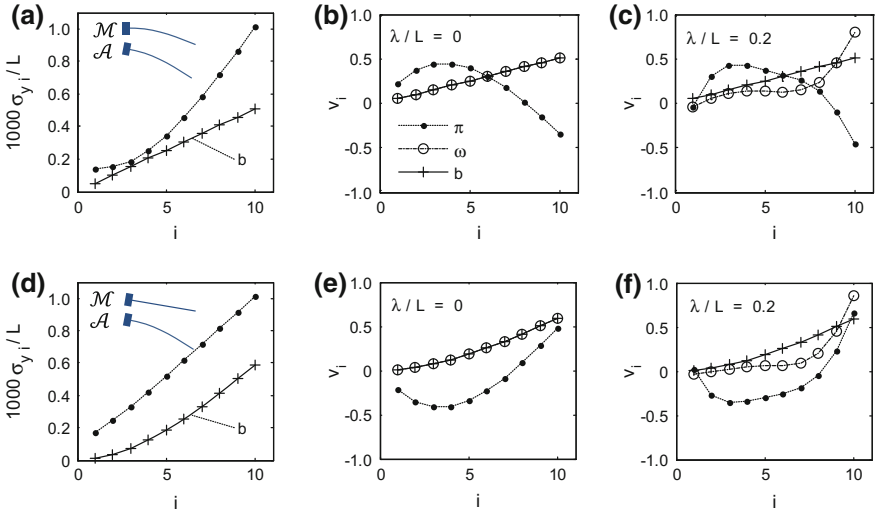

Fig. 7 **a** standard deviation of the sensor measure, **b** optimal statistic directions for uncorrelated noise, **c** optimal statistic directions for correlated noise for case (i), **d–f** corresponding quantities for case (ii) in 5.2

6 Numerical Investigation of a Non-gaussian Model

While in the setting investigated in previous section it is straightforward to define a linear test corresponding to an alternative model and, vice versa, an alternative model corresponding to the linear test, such a pairing is hard to define in a more general context. However, formulas for optimal linear directions, as defined in the Sect. 4.3, can be used outside the linear Gaussian model, as heuristic for identifying a relevant test. In this section, without any attempt of generality, we investigate the performance of those formulas on a specific application outside that domain.

Consider the identification of position and value of load along a uniform beam, of span $L = 5$ m, instrumented with 10 evenly spaced noisy sensors measuring vertical displacement, as in the structural scheme reported in Fig. 8a. Similarly to the application in 5.2, we model the noise affecting the sensors as the superposition of two zero-mean Gaussian noises, each with standard deviation 0.5 mm: the first component is an independent noise, while the second one (independent of the first one) is correlated with squared-exponential function, and correlation length 1.5 m. The load is defined by its position z and its value F, modeled as independent random variables: $z = x/L$ follows a beta$(2, 2)$ distribution, while $f = FL^2/EI$ follows a lognormal distribution $\ln \mathcal{N}\left(\log 0.25, 40\%^2\right)$ (EI being the bending stiffness). According to model $\mathcal{M}$, edges are fixed. In this context, observations $\mathbf{y}$, collected by the sensor set, allow for updating the joint distribution of z and f, and consequently the bending moment profile. In the alternative model $\mathcal{A}$, springs with rotational stiffness k are at the edges. We define that model by dimensionless

parameter $\eta = EI/(kL)$, that is zero under $\mathcal{M}$ and infinite under a simply-supported scheme. By analyzing observations through an appropriate test, we can detect rotation at the edges, and raise concerns on the reliability on the inference based on $\mathcal{M}$. For selecting an appropriate test, we can predict the effect of rotation at the edges that, however, depends on load position. To implement the formulas for optimal direction outlined in Sect. 4.3, we need to define a perturbation shape **b**, and covariance matrix of the measures. As an approximate approach, we compute the perturbation when the load is at the mid-span, i.e. for the expected value of z, and estimate the matrix by generating samples of measures and computing the sample covariance. Figure 8b reports the perturbation shape **b** when load at the mid-span and corresponding prior and posterior statistic directions. Intuitively the prior direction highlights the contribution of the sensors close to the edges (but not too close, as the perturbation is nil at the edges themselves) and do not consider (actually it gives a negative weight) to the sensors close to the mid-span, where model $\mathcal{M}$ predicts high displacements. Here we investigate the power of the corresponding test, by numerical simulations, adopting a numerical scheme similar to that used by Pozzi and Der Kiureghian (2011) and reported in Appendix B. Figure 8c shows the distribution of the p-value under model $\mathcal{M}$ depending on the approach (prior or posterior) and the statistic direction. As expected, the distribution is uniform for prior p-values and it turns out to be almost flat also when direction $\mathbf{v}_{\pi}^{*}$ is selected for posterior analysis. If the perturbation shape **b** or $\mathbf{v}_{\omega}^{*}$ is used for posterior analysis, the corresponding p-value tends to concentrate around 50%. Figure 7d shows the corresponding distributions when the model is perturbed by rotating supports, with η equals to 10%. As expected, p-values tend to the smaller because of the perturbation.

Figure 9 shows the test power as a function of perturbation size η, reporting the probability of a accepting model $\mathcal{A}$ because the p-value is below the selected threshold (i.e., the "type II error" probability). As expected, all curves are monotonic, as a higher perturbation will lead to reject $\mathcal{A}$ with higher probability and, in

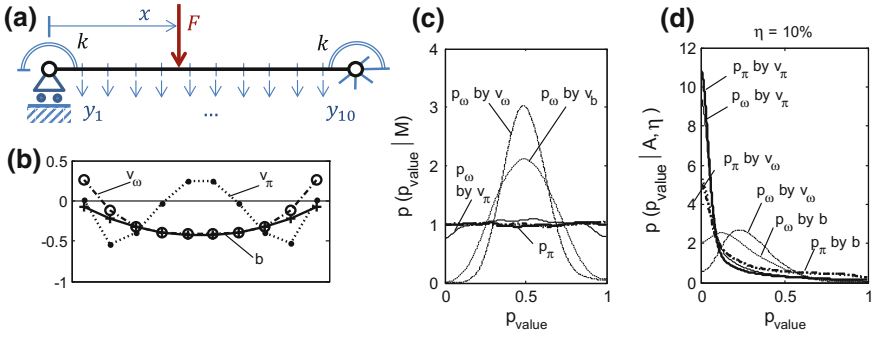

Fig. 8 **a** structural scheme for the numerical investigation or Sect. 6, **b** perturbation and (approximate) optimal statistic directions, **c** p-value distribution under model $\mathcal{M}$ and **d** perturbed model $\mathcal{A}$

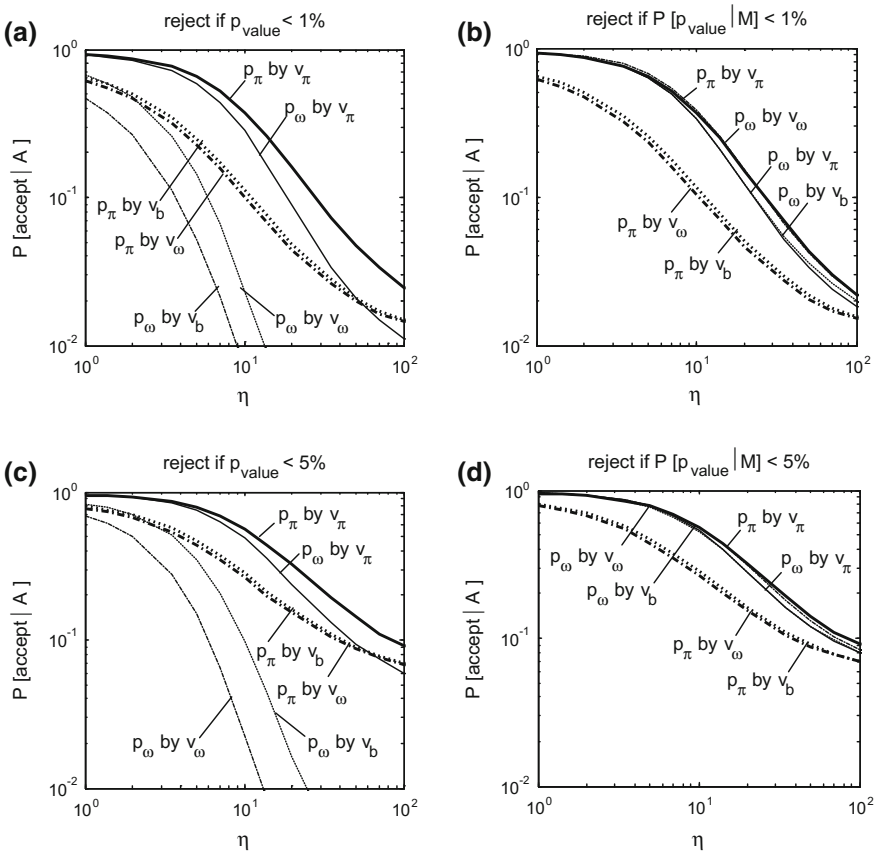

Fig. 9 Power of tests depending on flexibility parameter η, as probability of rejecting model $\mathcal{A}$, depending on prior or posterior setting ($\mathcal{p}_\pi$ or $\mathcal{p}_\omega$), and statistic direction ($\mathbf{v}_\pi^*$, $\mathbf{v}_\omega^*$ or **b**) for **a** a threshold of 1%, **b** a corrected threshold of 1%, **c** a threshold of 5%, **d** a corrected threshold of 5%, for the example in Sect. 6

the prior setting, curves start at the threshold value for η equals to zero. Graph (a) refers to a 1% threshold: in the prior setting, using the suggested direction $\mathbf{v}_\pi^*$ gives the higher power, which is higher than the power using posterior tests. This happens because posterior statistics tends to be concentrated around 50%, but it can be normalized by fixing a threshold not on the *p*-value itself, but on the probability that the *p*-value belongs to a tail of its distribution associated with a fixed probability, as described in 4.3 and Appendix A. Graph (b) adopts this correction, that has virtually no effect on prior analysis: the power of the poster test is almost indistinguishable from the best prior analysis when the suggested direction $\mathbf{v}_\omega^*$ is used. We report the corresponding results for a threshold of 5% in graphs (c) and (d), showing similar results respect to the previous threshold. Even if we cannot

claim that any of these linear tests are able to represent consistently a decision boundary based on probabilistic model comparison between $\mathcal{M}$ and $\mathcal{A}$, the analysis suggests that, at least in this setting, the direction identified by the formulas outlined in 4.3 are useful for the selection of powerful linear tests, and that prior and posterior suggested directions leads to similar power, when the threshold is appropriately corrected.

7 Conclusions

In this chapter, we have investigated the relationship between Bayesian model checking and *p*-value analysis based on test statistics. While Bayesian comparison provides an explicit transparent path to investigate alternative models, *p*-value analysis is an alternative procedure for model checking. We have shown how any test statistic underlies an alternative model that makes the test fully consistent with a rigorous Bayesian model comparison. Similarly, given an alternative model in a Bayesian setting, we can always define a test which yields consistent results as to accept or reject the candidate model. Also, we demonstrated that it is always possible to identify pairs of tests that are equivalent for prior/posterior model checking. We have outlined these equivalences in closed form in the simple setting of Gaussian models under a known constant possibly perturbation, and showed that, under these assumptions, it is slightly easier (somehow "more intuitive") to formulate an appropriate test statistic for posterior model checking, as a function of the perturbation to be investigated, respect to the appropriate test for prior model checking. Outside a liner Gaussian setting, these simple closed form expressions provide only an approximate solution, while the exact correspondence between alternative model and test is not always easily found. In these cases, good engineering intuition is still often the best resource to select an appropriate test statistic.

Generally, our purpose is not to recommend the use of test statistics, but to investigate their meaning and relation with Bayesian analysis. Usually, *p*-value analysis is computationally simpler than model comparison and, as we have noted, the numerical scheme strongly resembles that of classical reliability analysis (in case of prior model checking) and reliability analysis under information (in case of posterior model checking). However, that procedure has several disadvantages respect to explicit Bayesian model comparison. First, as the alternative model is not explicitly defined, the corresponding assumptions cannot be openly discussed. Secondly, as the *p*-values are not posterior probabilities of the candidate model, it may be impractical to put a fixed threshold on their value. Nonetheless, reporting *p*-values after Bayesian inference, for specific reasonable test statistics, may become an interesting practice in probabilistic data analysis related to engineering applications.

Appendix A: Gaussian Linear Models

The Gaussian distribution $\mathcal{N}$ is defined as follows:

$$\mathbf{x} \sim \mathcal{N}(\boldsymbol{\mu}, \boldsymbol{\Sigma}) \Leftrightarrow \log p(\mathbf{x}) = -\frac{1}{2}(\mathbf{x}-\boldsymbol{\mu})^{\mathrm{T}}\boldsymbol{\Sigma}^{-1}(\mathbf{x}-\boldsymbol{\mu}) + \text{constant}$$

The standard normal Gaussian distribution φ and corresponding CDF are defined as:

$$x \sim \varphi \Leftrightarrow x \sim \mathcal{N}(0,1), \quad \Phi(x) = \int_{-\infty}^{x} \varphi(\lambda) d\lambda$$

For each covariance matrix $\boldsymbol{\Sigma}_a$, we indicate by $\boldsymbol{\Lambda}_a$ the corresponding precision matrix $\boldsymbol{\Lambda}_a = \boldsymbol{\Sigma}_a^{-1}$.

Prior distribution	$\boldsymbol{\theta} \sim \mathcal{N}(\boldsymbol{\mu}_\theta, \boldsymbol{\Sigma}_\theta)$
Response	$\mathbf{r} = \mathbf{A}\,\boldsymbol{\theta} \sim \mathcal{N}(\boldsymbol{\mu}_r, \boldsymbol{\Sigma}_r)$ with $\begin{cases} \boldsymbol{\mu}_r = \mathbf{A}\,\boldsymbol{\mu}_\theta \\ \boldsymbol{\Sigma}_r = \mathbf{A}\boldsymbol{\Sigma}_\theta\mathbf{A}^{\mathrm{T}} \end{cases}$
Perturbation	$\Delta\,\mathbf{r}\vert\mathcal{M} = 0 \quad \Delta\,\mathbf{r}\vert\mathcal{A} = \mathbf{b}\,\eta$
Noise distribution	$\boldsymbol{\varepsilon} \sim \mathcal{N}(0, \boldsymbol{\Sigma}_\varepsilon)$
Measures	$\mathbf{y} = \mathbf{r} + \Delta\,\mathbf{r} + \boldsymbol{\varepsilon}$
	$\mathbf{y}\vert\mathcal{M} \sim \mathcal{N}(\boldsymbol{\mu}_Y, \boldsymbol{\Sigma}_Y)$ with $\begin{cases} \boldsymbol{\mu}_Y = \boldsymbol{\mu}_r \\ \boldsymbol{\Sigma}_Y = \boldsymbol{\Sigma}_r + \boldsymbol{\Sigma}_\varepsilon \end{cases}$
	$\mathbf{y}\vert\mathcal{A} \sim \mathcal{N}\left(\boldsymbol{\mu}_Y^*, \boldsymbol{\Sigma}_Y\right)$ with $\boldsymbol{\mu}_Y^* = \boldsymbol{\mu}_r + \mathbf{b}\eta$
Test statistic	$T = \mathbf{v}^{\mathrm{T}}\mathbf{y}$
	$T\vert\mathcal{M} \sim \mathcal{N}\left(\mu_\mathcal{M}, \sigma_\mathcal{M}^2\right)$ with $\mu_\mathcal{A} = \mu_\mathcal{M} + \mathbf{v}^{\mathrm{T}}\mathbf{b}\eta$
	with $\begin{cases} \mu_\mathcal{M} = \mathbf{v}^{\mathrm{T}}\boldsymbol{\mu}_r \\ \sigma_\mathcal{M}^2 = \mathbf{v}^{\mathrm{T}}\boldsymbol{\Sigma}_Y\mathbf{v} \end{cases}$ $T\vert\mathcal{A} \sim \mathcal{N}\left(\mu_\mathcal{A}, \sigma_\mathcal{M}^2\right)$
Prior normalized statistic	$u = \sigma_\mathcal{M}^{-1}(T - \mu_\mathcal{M})$
	$u\vert\mathcal{M} \sim \varphi$
	$u\vert\mathcal{A} \sim \mathcal{N}(\mu_\pi, 1)$ with $\mu_\pi = \sigma_\mathcal{M}^{-1}\mathbf{v}^{\mathrm{T}}\mathbf{b}\eta$
Posterior distribution	$\boldsymbol{\theta}\vert\mathbf{y} \sim \mathcal{N}(\boldsymbol{\mu}_\omega, \boldsymbol{\Sigma}_\omega)$ with
	$\begin{cases} \boldsymbol{\Sigma}_\omega = \left[\boldsymbol{\Lambda}_\theta + \mathbf{A}^{\mathrm{T}}\boldsymbol{\Lambda}_\varepsilon\mathbf{A}\right]^{-1} \\ \boldsymbol{\mu}_\omega = \mathbf{M}\mathbf{y} + \mathbf{c} \end{cases}$ and $\begin{cases} \mathbf{M} = \boldsymbol{\Sigma}_\omega\mathbf{A}^{\mathrm{T}}\boldsymbol{\Lambda}_\varepsilon \\ \mathbf{c} = \boldsymbol{\Sigma}_\omega\boldsymbol{\Lambda}_\theta\boldsymbol{\mu}_\theta \end{cases}$
Replicate distribution	$\mathbf{y}_r\vert\mathbf{y} \sim \mathcal{N}\left(\boldsymbol{\mu}_{Y_r\vert y}, \boldsymbol{\Sigma}_{Y_r\vert Y}\right)$ with
	$\begin{cases} \boldsymbol{\Sigma}_{Y_r\vert Y} = \mathbf{A}\,\boldsymbol{\Sigma}_\omega\mathbf{A}^{\mathrm{T}} + \boldsymbol{\Sigma}_\varepsilon \\ \boldsymbol{\mu}_{Y_r\vert y} = \mathbf{K}\,\mathbf{y} + \mathbf{d} \end{cases}$ and $\begin{cases} \mathbf{K} = \mathbf{A}\,\boldsymbol{\Sigma}_\omega\mathbf{A}^{\mathrm{T}}\boldsymbol{\Lambda}_\varepsilon \\ \mathbf{d} = \mathbf{A}\,\boldsymbol{\Sigma}_\omega\boldsymbol{\Lambda}_\theta\boldsymbol{\mu}_\theta \end{cases}$

Posterior statistics
$$T|\mathbf{y} \sim \mathcal{N}\left(\mu_{T|y}, \sigma^2_{T|Y}\right)$$
$$\begin{cases} \mu_{T|y} = \mathbf{v}^{\mathrm{T}}(\mathbf{K}\mathbf{y} + \mathbf{d}) \\ \sigma^2_{T|Y} = \mathbf{v}^{\mathrm{T}}\boldsymbol{\Sigma}_{Y_r|Y}\mathbf{v} \end{cases}$$

Posterior norm. statistic
$$u' = \sigma^{-1}_{T|Y}\left(T - \mu_{T|y}\right) = \sigma^{-1}_{T|Y}\mathbf{v}^{\mathrm{T}}[\mathbf{V}\mathbf{y} - \mathbf{d}] \text{with } \mathbf{V} = \mathbf{I} - \mathbf{K}$$
$$u'|\mathcal{M} \sim \mathcal{N}\left(0, \sigma^2_{\omega}\right) \text{with } \sigma^2_{\omega} = \sigma^{-2}_{T|Y}\mathbf{v}^{\mathrm{T}}\boldsymbol{\Sigma}_{\varepsilon}\boldsymbol{\Sigma}^{-1}_{Y}\boldsymbol{\Sigma}_{\varepsilon}\mathbf{v}$$
$$u'|\mathcal{A} \sim \mathcal{N}\left(\mu_{\omega}, \sigma^2_{\omega}\right) \text{with } \mu_{\omega} = \sigma^{-1}_{T|Y}\mathbf{v}^{\mathrm{T}}\boldsymbol{\Sigma}_{\varepsilon}\boldsymbol{\Sigma}^{-1}_{Y}\mathbf{b}\eta$$

Uniform posterior stat.
$$u'' = \sigma^{-1}_{\omega}u'$$
$$u''|\mathcal{M} \sim \varphi$$
$$u''|\mathcal{A} \sim \mathcal{N}(\mu_{\Omega}, 1) \text{with } \mu_{\Omega} = \sigma^{-1}_{\omega}\mu_{\omega}$$

p-value
$p = 1 - \Phi(u)$,, defined on $0 \le p \le 1$
[prior p-value p_{π} depends on u, posterior p-value p_{ω} on u']
If $u \sim \mathcal{N}(\mu, \sigma^2)$ and $z = \frac{u-\mu}{\sigma}$, the PDF and CDF of the p-value is: $\begin{cases} p(p) = \frac{\varphi(z)}{\sigma\,\varphi(u)} \\ F(p) = 1 - \Phi(z) \end{cases}$

Optimization of Directions: Prior optimal direction is defined by maximizing sensitivity $\alpha_{\pi} = \partial\mu_{\pi}/\partial\eta$, or its square:

$$\left[\frac{\partial\mu_{\pi}}{\partial\eta}\right]^2 = \left[\sigma^{-2}_{\mathcal{M}}\mathbf{v}^{\mathrm{T}}\mathbf{b}\right]^2 = \frac{\mathbf{v}^{\mathrm{T}}\mathbf{b}\mathbf{b}^{\mathrm{T}}\mathbf{v}}{\mathbf{v}^{\mathrm{T}}\boldsymbol{\Sigma}_{Y}\mathbf{v}} \tag{A1}$$

.
obtaining $\mathbf{v} = \mathbf{v}^*_{\pi} \propto \boldsymbol{\Sigma}^{-1}_{Y}\mathbf{b}$. Posterior optimal direction optimizes $\alpha_{\Omega} = \partial\mu_{\Omega}/\partial\eta$, or its square:

$$\left[\frac{\partial\mu_{\Omega}}{\partial\eta}\right]^2 = \left[\sigma^{-1}_{\omega}\sigma^{-1}_{T|Y}\mathbf{v}^{\mathrm{T}}\boldsymbol{\Sigma}_{\varepsilon}\boldsymbol{\Sigma}^{-1}_{Y}\mathbf{b}\right]^2 = \frac{\mathbf{v}^{\mathrm{T}}\boldsymbol{\Sigma}_{\varepsilon}\boldsymbol{\Sigma}^{-1}_{Y}\mathbf{b}\mathbf{b}^{\mathrm{T}}\boldsymbol{\Sigma}^{-1}_{Y}\boldsymbol{\Sigma}_{\varepsilon}\mathbf{v}}{\mathbf{v}^{\mathrm{T}}\boldsymbol{\Sigma}_{\varepsilon}\boldsymbol{\Sigma}^{-1}_{Y}\boldsymbol{\Sigma}_{\varepsilon}\mathbf{v}} \tag{A2}$$

and, by comparing Eq.A1 and A2, we conclude that: $\mathbf{v}^*_{\omega} \propto \boldsymbol{\Sigma}^{-1}_{\varepsilon}\boldsymbol{\Sigma}_{Y}\mathbf{v}^*_{\pi} \propto \boldsymbol{\Sigma}^{-1}_{\varepsilon}\mathbf{b}$.

Optimal Tests and Bayesian Model Comparison: The predictive distributions of measures $\mathbf{y}$, according to models $\mathcal{M}$ and $\mathcal{A}$, are both normal. This is the setting for linear discriminant analysis and Fisher's linear discriminant analysis (Fisher 1936; Murphy 2012). Specifically, because those distributions have the same covariance matrix ($\boldsymbol{\Sigma}_Y$) and their mean vectors differ by $\mathbf{b}\eta$, the Bayes ratio is a function of $\mathbf{y}$, proportional only to $\exp\left[-\mathbf{y}^{\mathrm{T}}\boldsymbol{\Sigma}^{-1}_{Y}\mathbf{b}\eta\right]$, and the posterior distribution can only be a function of the projection of $\mathbf{y}$ along direction $\boldsymbol{\Sigma}^{-1}_{Y}\mathbf{b}$. In other words, the decision boundary is linear and orthogonal to this direction. By defining $T = \mathbf{v}^{*\mathrm{T}}_{\pi}\mathbf{y}$, with $\mathbf{v}^*_{\pi}$ proportional to $\boldsymbol{\Sigma}^{-1}_{Y}\mathbf{b}$, the prior optimal statistic contains all information relevant for

Bayesian model comparison. Both p-value and posterior probability of $\mathcal{M}$ are monotonic functions of T, so the Bayesian decision boundary is completely defined by a threshold on the p-value. Because of this, optimal prior test is consistent with Bayesian analysis. When posterior optimal direction ($\mathbf{v}_{\omega}^{*}$) is selected (so that $\partial\mu_{\Omega}$ is equal to $\partial\mu_{\pi}$), posterior model checking is consistent with prior optimal checking, and so, again, with model comparison.

Appendix B: Monte Carlo Scheme for Numerical Investigation of the *P*-Value

For the large numerical campaign illustrated in Sect. 6, we have adopted an inference scheme similar to that used in Pozzi and Der Kiureghian (2011), based on Monte Carlo simulations.

Parameter values, noises, measures and statistics are sampled in a forward scheme:

$$\left\{\boldsymbol{\theta}_{(i)}\right\}_{M}^{i=1} \sim p_{\theta|\mathcal{M}} \quad \left\{\boldsymbol{\varepsilon}_{(i)}\right\}_{M}^{i=1} \sim p_{\varepsilon} \quad \mathbf{y}_{(i)} = \mathbf{r}\left(\boldsymbol{\theta}_{(i)}\right) + \boldsymbol{\varepsilon}_{(i)} \qquad T_{(i)} = q\left(\mathbf{y}_{(i)}\right)$$

A second set of independent values is also generated:

$$\left\{\boldsymbol{\theta}_{(k)}\right\}_{N}^{k=1} \sim p_{\theta|\mathcal{M}} \quad \left\{\boldsymbol{\varepsilon}_{(k)}\right\}_{N}^{k=1} \sim p_{\varepsilon} \quad \mathbf{y}_{(k)} = \mathbf{r}\left(\boldsymbol{\theta}_{(k)}\right) + \boldsymbol{\varepsilon}_{(k)} \qquad T_{(k)} = q\left(\mathbf{y}_{(k)}\right)$$

The residual and likelihood function for each pair $\left\{\mathbf{y}_{(k)}, \boldsymbol{\theta}_{(i)}\right\}$ is computed in a N by M matrix as:

$$\boldsymbol{\delta}_{(k,i)} = \mathbf{y}_{(k)} - \mathbf{r}\left(\boldsymbol{\theta}_{(i)}\right) \quad lh_{k,i} = p\left(\mathbf{y}_{(k)} | \boldsymbol{\theta}_{(i)}, \mathcal{M}\right) = p_{\varepsilon}\left[\mathbf{y}_{(k)} - \mathbf{r}\left(\boldsymbol{\theta}_{(i)}\right)\right] = p_{\varepsilon}\left(\boldsymbol{\delta}_{(k,i)}\right)$$

For zero-mean Gaussian noise with precision matrix $\boldsymbol{\Lambda}_{\varepsilon}$, log-likelihood and weight is:

$$\log lh_{k,i} = -\frac{1}{2}\boldsymbol{\delta}_{(k,i)}^{\mathrm{T}}\boldsymbol{\Lambda}_{\varepsilon}\boldsymbol{\delta}_{(k,i)} + \text{constant} \qquad w_{i,k} = lh_{i,k} / \sum_{i=1}^{M} lh_{i,k}$$

where the constant disappears in the ratio defining the weights. The prior p-value associated with measure $\mathbf{y}_{(k)}$ is: $\wp_{\pi_{(k)}} = \frac{1}{M}\sum_{i=1}^{M} \mathrm{I}\left[T_{(i)} > T_{(k)}\right]$

While the posterior p-value associated with the same measures is: $\wp_{\omega_{(k)}} = \sum_{i=1}^{M} \mathrm{I}\left[T_{(i)} > T_{(k)}\right] w_{i,k}$

References

Bayarri MJ, Berger JO (2000) P values for composite null models. JASA 95(452):1127–1142. doi:10.1080/01621459.2000.10474309

Beck JL, Au SK (2002) Bayesian updating of structural models and reliability using Markov Chain Monte Carlo simulation. J Eng Mech 128(4):380–391. doi:10.1061/(ASCE)0733-9399(2002)128:4(380)

Beck JL, Yuen K (2004) Model Selection Using Response Measurements: Bayesian Probabilistic Approach. J Eng Mech 130(2):192–203. doi:10.1061/(ASCE)0733-9399(2004)130:2(192)

Berger JO, Sellke T (1987) Testing a point null hypothesis: the irreconcilability of P values and evidence. JASA 82(397):112–122

Bretthorst GL (1996) An introduction to model selection using probability theory as logic. In: Heidbreder GR (ed) Maximum Entropy and Bayesian Methods. Springer, New York, NY, p 1

Box GE (1980) Sampling and Bayes' inference in scientific modelling and robustness. J R Statist Soc A 143(4):383–430

Der Kiureghian A (2005) First-and second-order reliability methods. In Singhal S, Ghiocel DM, Nikolaidis E (eds) Engineering design reliability handbook. Ch. 4–1. doi:10.1201/9780203483930.ch14

Fisher RA (1936) The Use of Multiple Measurements in Taxonomic Problems. Annals of Eugenics 7(2):179–188. doi:10.1111/j.1469-1809.1936.tb02137.x

Gelman A (2003) A Bayesian Formulation of Exploratory Data Analysis and Goodness-of-fit Testing. Int Stat Rev 71(2):369–382. doi:10.1111/j.1751-5823.2003.tb00203.x

Gelman A (2013) Two simple examples for understanding posterior p-values whose distributions are far from uniform. Electron J Stat 7:2595–2602. doi:10.1214/13-EJS854

Gelman A, Carlin JB, Stern HS, Dunson DB, Vehtari A, Rubin DB (2014) Bayesian data analysis. Chapman & Hall/CRC, London

Gelman A, Meng XL, Stern H (1996) Posterior predictive assessment of model fitness via realized discrepancies. Statistica sinica 6(4):733–760

Gelman A, Shalizi CR (2013) Philosophy and the practice of Bayesian statistics. Br J Math Stat Psychol 66(1):8–38. doi:10.1111/j.2044-8317.2011.02037.x

Goulet JA, Coutu S, Smith IF (2013) Model falsification diagnosis and sensor placement for leak detection in pressurized pipe networks. Adv Eng Inform 27(2):261–269. doi:10.1016/j.aei.2013.01.001

Hjort NL, Dahl FA, Steinbakk GH (2006) Post-processing posterior predictive p values. JASA 101(475):1157–1174. doi:10.1198/016214505000001393

Jaynes ET (2003) Probability theory: The logic of science. Cambridge University Press, Cambridge

Kruschke, JK (2013) Posterior predictive checks can and should be Bayesian: comment on Gelman and Shalizi,'Philosophy and the practice of Bayesian statistics'. Br J Math Stat Psychol 66(1):45–56. doi:10.1111/j.2044-8317.2012.02063.x

Lindley DV (1957) A statistical paradox. Biometrika 44(1–2):187–192

MacKay DJC (2003) Information Theory. Cambridge University Press, Cambridge, Inference and Learning Algorithms

Meng XL (1994) Posterior predictive p-values. Ann Stat 22(3):1142–1160

Morey RD, Romeijn JW, Rouder JN (2013) The humble Bayesian: Model checking from a fully Bayesian perspective. Br J Math Stat Psychol 66(1):68–75. doi:10.1111/j.2044-8317.2012.02067.x

Murphy KP (2012) Machine Learning, a probabilistic perspective. MIT press, Cambridge, MS

Pasquier R, Smith IF (2015) Robust system identification and model predictions in the presence of systematic uncertainty. Adv Eng Inf 29(4):1096–1109. doi:10.1016/j.aei.2015.07.007

Pozzi M, Der Kiureghian A (2011) Assessing the value of information for long-term structural health monitoring. In: Kundu T (ed) SPIE Proceedings Vol 7984. SPIE Conference, Health Monitoring of Structural and Biological Systems 2011. San Diego CA, 7 March 2011

Straub D, Papaioannou I, Betz W (2016) Bayesian analysis of rare events. J Comput Phys 314:538–556. doi:10.1016/j.jcp.2016.03.018

Wang P, Small MJ, Pozzi M, Harbert W (2016) A Bayesian approach for assessing seismic transitions associated with wastewater injections. Bull Seismol Soc Am 106(3). doi:10.1785/0120150200

Yuen KV (2010) Recent developments of Bayesian model class selection and applications in civil engineering. Struct Saf 32(5):338–346. doi:10.1016/j.strusafe.2010.03.011

Zonta D, Pozzi M (2015) The remarkable story of Portogruaro Civic Tower's probabilistic health monitoring. Structural Monitoring and Maintenance 2(4):301–318. doi:10.12989/smm.2015.2.4.301

Zonta D, Pozzi M, Zanon P (2008) Managing the historical heritage using distributed technologies. Int J Archit Herit 2(3):200–225. doi:10.1080/15583050802063691

Batch and Recursive Bayesian Estimation Methods for Nonlinear Structural System Identification

Rodrigo Astroza, Hamed Ebrahimian and Joel P. Conte

Abstract This chapter presents a framework for the identification of nonlinear finite element (FE) structural models using Bayesian inference methods. Using the input-output dynamic data recorded during an earthquake event, batch and recursive Bayesian estimation methods are employed to update a mechanics-based nonlinear FE model of the structure of interest (building, bridge, dam, etc.). Unknown parameters of the nonlinear FE model characterizing material constitutive models, inertia, geometric, and/or constraint properties of the structure can be estimated using limited response data recorded through accelerometers or heterogeneous sensor arrays. The updated nonlinear FE model can be used to identify the damage in the structure following a damage-inducing event. This framework, therefore, can provide an advanced tool for post-disaster damage identification and structural health monitoring. The batch estimation method is based on a maximum a posteriori estimation (MAP) approach, where the time history of the input and output measurements are used as a single batch of data for estimating the FE model parameters. This method results in a nonlinear optimization problem that can be solved using gradient-based and non-gradient-based optimization algorithms. In contrast, the recursive Bayesian estimation method processes the information from the measured data recursively, and updates the estimation of the FE model parameters progressively over the time history of the event. The recursive Bayesian estimation method results in a nonlinear Kalman filtering approach. The Extended

R. Astroza
Facultad de Ingeniería y Ciencias Aplicadas, Universidad de los Andes, Santiago, Chile

H. Ebrahimian
Department of Mechanical and Civil Engineering, California Institute of Technology, Pasadena, CA, USA

J.P. Conte (✉)
Department of Structural Engineering, University of California, San Diego, La Jolla, CA, USA
e-mail: jpconte@ucsd.edu

R. Astroza · H. Ebrahimian
University of California, San Diego, La Jolla, CA, USA

P. Gardoni (ed.), *Risk and Reliability Analysis: Theory and Applications*, Springer Series in Reliability Engineering, DOI 10.1007/978-3-319-52425-2_15

Kalman filter (EKF) and Unscented Kalman filter (UKF) are employed as recursive Bayesian estimation methods herein. For those estimation methods that require the computation of structural FE response sensitivities (total partial derivatives) with respect to the unknown FE model parameters, the direct differentiation method (DDM) is used. Response data numerically simulated from a nonlinear FE model (with unknown material model parameters) of a five-story two-by-one bay reinforced concrete frame building subjected to bi-directional horizontal seismic excitation are used to illustrate the performance of the proposed framework.

1 Introduction

System identification (SID) addresses the problem of constructing mathematical models of a dynamic system using data measured from the system (Ljung 1999). SID is very important in many engineering fields and found applications in a wide range of problems. In particular, in the field of structural engineering, SID can be used to assess changes in a structural system due to a damaging event (e.g., earthquake). This results in the capability of monitoring the state of damage (or health) of a structural system and, therefore, of evaluating the risk involved in the post-disaster occupancy (or operation) of the structure and providing decision support for emergency response. Finite element (FE) model updating, which can be defined as the process of calibrating a FE model to minimize the discrepancy between the measured and FE predicted responses of a structure, is a powerful SID method for structural systems.

Linear FE model updating has been one of the most popular approaches for damage identification (DID) of civil structures. In this technique, linear FE models are calibrated using low amplitude vibration data recorded before and after a potentially damaging event and damage is characterized as the reduction of effective stiffness over one or more regions of the structure. Linear FE model updating is typically solved as a constrained optimization problem. The objective of the optimization problem is to minimize the discrepancy between the measured and FE predicted structural responses, which may consist of time or frequency domain responses or quantities derived therefrom (e.g., modal parameters) (Friswell and Mottershead 1995; Simoen et al. 2015). Despite its popularity in the field of structural engineering, linear FE model updating cannot provide any information about the inelastic response regime in the structural components and system, such as history of plastic deformations, residual deformations, loss of strength, loss of ductility capacity, etc. This information is essential for a comprehensive condition assessment of the structure.

To overcome this limitation, a number of efforts have been undertaken in the field of nonlinear FE model updating of civil structures (Ching et al. 2006; Song and Dyke 2014; Yang et al. 2014) in recent years. Distefano and co-workers contributed pioneering work in this topic in the 1970s (Distefano and Rath 1975a, b; Distefano and Pena-Pardo 1976). The studies presented in the literature have utilized simplified nonlinear structural models with lumped nonlinearities defined

phenomenologically, through for example the Bouc-Wen plasticity model, to describe the hysteretic force-deformation response behavior of the structure at the story level or at the plastic hinge regions. However, such models are not used for high-fidelity mechanics-based structural FE modeling; because they fall short in accurately simulating the nonlinear response behavior of real-world structures under extreme loading conditions. Recently, the problem of updating mechanics-based nonlinear FE models of structures using input-output data recorded during damage-inducing events has been investigated (Shahidi and Pakzad 2014; Astroza et al. 2015; Ebrahimian et al. 2015; Huang et al. 2015). An advanced mechanics-based FE model, updated using the measured input-output data, is able to capture actual damage mechanisms in the structural system and thus can provide accurate information about the presence, location, type, and extent of damage in the structure. Therefore, mechanics-based nonlinear FE model updating can be used for rapid post-event condition assessment, by providing FE prediction of the damage in the structure and risk assessment related to the continued occupancy (or operation) of the structure.

This chapter describes the use of batch and recursive Bayesian estimation methods to update mechanics-based nonlinear FE models of civil structures using input-output dynamic data recorded during an earthquake event. The batch method is based on a maximum a posteriori (MAP) approach, resulting in a constrained nonlinear optimization problem that can be solved using gradient-based or non-gradient-based optimization algorithms. The recursive method results in a nonlinear Kalman filtering approach. The Extended Kalman filter (EKF) and Unscented Kalman filter (UKF) are employed as recursive Bayesian estimation methods. Implementation of the EKF and MAP method requires the FE response sensitivities with respect to the model parameters to be estimated. These sensitivities are computed using the direct differentiation method (DDM), an accurate and computationally efficient approach based on the exact (consistent) differentiation of the FE numerical scheme with respect to the model parameters (Tsay and Arora 1990). An application example is presented based on data simulated numerically from a realistic nonlinear FE model of a three-dimensional (3D) five-story two-by-one bay reinforced concrete (RC) frame building subjected to bi-directional horizontal earthquake excitation.

2 Bayesian FE Model Updating

In this section, different approaches based on the Bayesian inference method are presented for the identification of nonlinear structural FE models. First, a general Bayesian framework for FE model updating or identification of nonlinear FE model parameters is described. Then, the batch and recursive methods for estimating the unknown FE model parameters and quantifying their uncertainty are introduced.

The time-discretized equation of motion of an n-DOF nonlinear FE model of a structural system at time step i can be written as

$$\mathbf{M}(\boldsymbol{\theta})\ddot{\mathbf{q}}_i(\boldsymbol{\theta}) + \mathbf{C}(\boldsymbol{\theta})\dot{\mathbf{q}}_i(\boldsymbol{\theta}) + \mathbf{r}_i(\mathbf{q}_i(\boldsymbol{\theta}), \boldsymbol{\theta}) = \mathbf{p}_i \tag{1}$$

in which $\mathbf{q}_i, \dot{\mathbf{q}}_i, \ddot{\mathbf{q}}_i \in \mathbb{R}^{n \times 1} =$ relative displacement, velocity, and acceleration response vectors at time step i, respectively, $\mathbf{M} \in \mathbb{R}^{n \times n} =$ mass matrix, $\mathbf{C} \in \mathbb{R}^{n \times n} =$ damping matrix, $\mathbf{r}_i(\mathbf{q}_i(\boldsymbol{\theta}), \boldsymbol{\theta}) \in \mathbb{R}^{n \times 1} =$ history-dependent internal resisting force vector, $\boldsymbol{\theta} \in \mathbb{R}^{n_{\boldsymbol{\theta}} \times 1} =$ FE model parameter vector, $\mathbf{p}_i \in \mathbb{R}^{n \times 1} =$ dynamic load vector, which in the case of a rigid base earthquake excitation takes the form $\mathbf{p}_i = -\mathbf{M}\mathbf{L}\ddot{\mathbf{u}}_{g_i}$, with $\mathbf{L} \in \mathbb{R}^{n \times n_{\ddot{\mathbf{u}}_g}} =$ influence matrix and $\ddot{\mathbf{u}}_{g_i} \in \mathbb{R}^{n_{\ddot{\mathbf{u}}_g} \times 1} =$ input ground acceleration vector where $n_{\ddot{\mathbf{u}}_g} =$ number of base excitation components.

From Eq. (1), the response of the FE model at time step i to an earthquake ground motion can be expressed as a nonlinear function mapping the FE model parameters and the input ground acceleration time history to the FE predicted response vector (see (Ebrahimian et al. 2016) for more details), i.e.,

$$\hat{\mathbf{y}}_i = \mathbf{h}_i\left(\boldsymbol{\theta}, \ddot{\mathbf{u}}_{g_{1:i}}\right) \tag{2}$$

In this equation, $\hat{\mathbf{y}}_i \in \mathbb{R}^{n_{\mathbf{y}} \times 1} =$ FE predicted response, $\mathbf{h}_i(\ldots) =$ nonlinear response function of the FE model, $\ddot{\mathbf{u}}_{g_{1:i}} = \left[\ddot{\mathbf{u}}_{g_1}^T, \ddot{\mathbf{u}}_{g_2}^T, \ldots, \ddot{\mathbf{u}}_{g_i}^T\right]^T$. In Eq. (2), at rest initial conditions are assumed for the FE model (i.e., zero initial nodal displacement and velocity vectors).

The dynamic response of civil structures can be recorded using an array of heterogeneous sensors such as accelerometers, GPS antennas, displacement transducers, strain gauges, etc. The measured structural response vector, $\mathbf{y}_i$, can be related to the FE predicted response vector, $\hat{\mathbf{y}}_i$, using the prediction error framework (Ljung 1999), i.e.,

$$\mathbf{v}_i(\boldsymbol{\theta}) = \mathbf{y}_i - \mathbf{h}_i\left(\boldsymbol{\theta}, \ddot{\mathbf{u}}_{g_{1:i}}\right) \tag{3}$$

in which $\mathbf{v}_i$, the simulation error, stands for the discrepancies between the measured and FE predicted responses of the structure. It accounts for the measurement noise, errors in the FE model parameters, and analytical model uncertainties (i.e., physical modeling assumptions). It is ideally assumed herein that the analytical FE model can capture exactly the real-world physics of the structural response and, therefore, the analytical model uncertainties (Haukaas and Gardoni 2011) are neglected. Accounting for the effects of model uncertainties in the nonlinear FE model updating framework presented here is out of the scope of this chapter. Moreover, it is assumed herein that the time history of the input ground acceleration is deterministic and known. By neglecting the effects of model uncertainties and assuming that the measurement noise is Gaussian white, the simulation error at each time step can be modeled as a stationary independent zero-mean Gaussian white noise vector process (i.e., the simulation errors are modeled as statistically independent random

variables across different measurement channels and over the time with a stationary zero-mean Gaussian distribution). Therefore, it follows that

$$p(\mathbf{v}_i) = \frac{1}{(2\pi)^{n_y/2}|\mathbf{R}|^{1/2}} e^{-\frac{1}{2}\mathbf{v}_i^T \mathbf{R}^{-1}\mathbf{v}_i} \tag{4}$$

where $|\mathbf{R}|$ denotes the determinant of the diagonal matrix $\mathbf{R} \in \mathbb{R}^{n_y \times n_y}$ defined as the time invariant covariance matrix of the simulation error vector (i.e., $\mathbf{R} = E(\mathbf{v}_i \mathbf{v}_i^T)$, $\forall i$). The unknown FE model parameter vector $\boldsymbol{\theta}$ is modeled as a random vector (denoted by $\boldsymbol{\Theta}$) according to the Bayesian approach for parameter estimation. Bayes' rule is employed to derive the posterior joint probability density function (PDF) of the model parameters from the time histories of the noisy output measurements and the prior joint PDF of these parameters, i.e.,

$$p(\boldsymbol{\theta}|\mathbf{y}_{1:k}) = \frac{p(\mathbf{y}_{1:k}|\boldsymbol{\theta})p(\boldsymbol{\theta})}{p(\mathbf{y}_{1:k})} \tag{5}$$

in which $\mathbf{y}_{1:k} = \left[\mathbf{y}_1^T, \mathbf{y}_2^T, \ldots, \mathbf{y}_k^T\right]^T =$ time history of the measured response of the structure, and $p(\mathbf{y}_{1:k}|\boldsymbol{\theta}) =$ likelihood function. According to Eq. (3), it follows that

$$p(\mathbf{y}_{1:k}|\boldsymbol{\theta}) = p(\mathbf{v}_{1:k}) = \prod_{i=1}^{k} p(\mathbf{v}_i) \tag{6}$$

The objective of the nonlinear FE model updating framework is to estimate the value (point estimate) of the unknown FE model parameter vector $\boldsymbol{\theta}$ at which the posterior joint PDF of $\boldsymbol{\Theta}$ given the measured structural response is maximum, i.e.,

$$(\hat{\boldsymbol{\theta}})_{\text{MAP}} = \arg\max_{(\boldsymbol{\theta})} p(\boldsymbol{\theta}|\mathbf{y}_{1:k}) \tag{7}$$

where MAP stands for maximum a posteriori estimate. Two different approaches to solve this problem are presented in this chapter: (1) batch Bayesian estimation method, and (ii) recursive Bayesian estimation method.

2.1 Batch Bayesian Estimation Method

In the batch Bayesian estimation method, the entire time history of the measured data is used as a batch of data to update the posterior joint PDF of the FE model parameters and find the MAP estimate. Assuming a Gaussian distribution for the prior joint PDF of $\boldsymbol{\Theta}$ in Eq. (5), and assuming that the entire time history of the measurement data is available from the first to the kth time step, the natural logarithm of the posterior joint PDF can be derived as

$$\log(p(\boldsymbol{\theta}|\mathbf{y}_{1:k})) = c_0 - \frac{kn_{\mathbf{y}}}{2}\log(2\pi) - \frac{k}{2}\log(|\mathbf{R}|) - \frac{1}{2}\sum_{i=1}^{k}\left(\mathbf{y}_i - \mathbf{h}_i\left(\boldsymbol{\theta}, \ddot{\mathbf{u}}_{g_{1:i}}\right)\right)^T \mathbf{R}^{-1}\left(\mathbf{y}_i - \mathbf{h}_i\left(\boldsymbol{\theta}, \ddot{\mathbf{u}}_{g_{1:i}}\right)\right) - \frac{n_{\boldsymbol{\theta}}}{2}\log(2\pi) - \frac{1}{2}\log\left(|\hat{\mathbf{P}}_0|\right) - \frac{1}{2}\left(\boldsymbol{\theta} - \hat{\boldsymbol{\theta}}_0\right)^T \left(\hat{\mathbf{P}}_0\right)^{-1}\left(\boldsymbol{\theta} - \hat{\boldsymbol{\theta}}_0\right) \tag{8}$$

in which $c_0 = -\log(p(\mathbf{y}_{1:k}))$ is a constant, $\hat{\boldsymbol{\theta}}_0$ is the prior mean estimate of $\boldsymbol{\Theta}$, and $\hat{\mathbf{P}}_0$ is the prior covariance matrix of $\boldsymbol{\Theta}$, which quantifies the uncertainties associated with the prior estimates of the FE model parameters.

Here the diagonal entries of matrix $\mathbf{R}$, which are the variances of the components of the simulation error vector, can also be treated as random variables and estimated jointly with the FE model parameters through an extended parameter estimation and measurement noise variance estimation. As discussed in (Ebrahimian et al. 2016), this extended estimation approach enhances the robustness of the FE model updating process. Moreover, it allows for automatic information assimilation from the data measured by heterogeneous sensor arrays without the need to scale the data manually.

The MAP problem defined in Eq. (7) results in the following minimization problem:

$$\left(\hat{\boldsymbol{\theta}}, \hat{\mathbf{r}}\right)_{\text{MAP}} = \arg\min_{(\boldsymbol{\theta}, \mathbf{r})} J\left(\mathbf{r}, \boldsymbol{\theta}, \mathbf{y}_{1:k}, \ddot{\mathbf{u}}_{g_{1:k}}\right) \tag{9}$$

$$J\left(\mathbf{r}, \boldsymbol{\theta}, \mathbf{y}_{1:k}, \ddot{\mathbf{u}}_{g_{1:k}}\right) = \frac{k}{2}\sum_{j=1}^{n_{\mathbf{y}}}\log\left(r_j\right) + \frac{1}{2}\sum_{i=1}^{k}\left(\mathbf{y}_i - \mathbf{h}_i\left(\boldsymbol{\theta}, \ddot{\mathbf{u}}_{g_{1:i}}\right)\right)^T \mathbf{R}^{-1}\left(\mathbf{y}_i - \mathbf{h}_i\left(\boldsymbol{\theta}, \ddot{\mathbf{u}}_{g_{1:i}}\right)\right) + \frac{1}{2}\left(\boldsymbol{\theta} - \hat{\boldsymbol{\theta}}_0\right)^T \left(\hat{\mathbf{P}}_0\right)^{-1}\left(\boldsymbol{\theta} - \hat{\boldsymbol{\theta}}_0\right) \tag{10}$$

in which $\mathbf{r} \in \mathbb{R}^{n_{\mathbf{y}} \times 1}$ is the vector of the diagonal entries of matrix $\mathbf{R}$. This minimization problem is solved using the interior-point method (Byrd et al. 1999), which is a gradient-based minimization algorithm. It requires the computation of the gradient of the objective function with respect to the optimization parameters, which in turn requires the FE response sensitivities with respect to the FE model parameters. The latter can be computed accurately and efficiently utilizing the DDM (e.g., (Tsay and Arora 1990; Kleiber et al. 1997; Zhang and Der Kiureghian 1993)).

The Posterior Cramér–Rao lower bound (PCRLB) theorem (Van Trees 2002) can be used to quantify the parameter estimation uncertainties and to estimate a lower bound for the covariance matrix of the estimated FE model parameters. The lower bounds for the estimation problem shown in Eq. (9) can be derived as (see (Ebrahimian et al. 2016) for more details)

$$\mathrm{Cov}(\boldsymbol{\Theta}) \geq \left(\sum_{i=1}^{k} \left[\left(\frac{\partial \mathbf{h}_i\left(\boldsymbol{\theta}, \ddot{\mathbf{u}}_{g_{1:i}}\right)}{\partial \boldsymbol{\theta}} \right)^T \mathbf{R}^{-1} \frac{\partial \mathbf{h}_i\left(\boldsymbol{\theta}, \ddot{\mathbf{u}}_{g_{1:i}}\right)}{\partial \boldsymbol{\theta}} \right]_{\hat{\boldsymbol{\theta}}, \hat{\mathbf{R}}} + \left(\hat{\mathbf{P}}_0\right)^{-1} \right)^{-1} \tag{11}$$

$$\mathrm{Cov}(R_i) \geq \frac{k}{2} \frac{1}{\hat{r}_i^2} \tag{12}$$

in which R_i is a random variable characterizing the ith diagonal entry of matrix $\mathbf{R}$. The right-hand side of Eq. (11) (which is the inverse of the Fisher Information matrix) can also be approximated by the Hessian matrix of the objective function J in Eq. (10). Therefore, two methods can be utilized to quantify the parameter estimation uncertainty. The first method is based on computing the Fisher Information matrix, as shown in Eq. (11), which is referred to as *Method 1* in this chapter. Referred to as *Method 2*, the second method is based on the computation of the Hessian matrix of the objective function in Eq. (10). The Hessian matrix is a by-product of the optimization procedure and is approximately estimated using the Broyden-Fletcher-Goldfarb-Shanno (BFGS) method (Gill et al. 1981).

2.2 Recursive Bayesian Estimation Method

2.2.1 Extended Kalman Filter (EKF)

The MAP problem defined in Eq. (7) can alternatively be solved using a recursive (time step by time step) solution approach. The MAP estimate of $\boldsymbol{\Theta}$ at time step i is derived by differentiating Eq. (8) with respect to $\boldsymbol{\theta}$ and solving for $\boldsymbol{\theta}$, i.e.,

$$\frac{\partial \log(p(\boldsymbol{\theta}|\mathbf{y}_i))}{\partial \boldsymbol{\theta}} = 0 \quad \Rightarrow \quad \left(\mathbf{y}_i - \mathbf{h}_i\left(\boldsymbol{\theta},\ \ddot{\mathbf{u}}_{g_{1:i}}\right)\right)^T \mathbf{R}^{-1} \frac{\partial \mathbf{h}_i\left(\boldsymbol{\theta},\ \ddot{\mathbf{u}}_{g_{1:i}}\right)}{\partial \boldsymbol{\theta}} - \left(\boldsymbol{\theta} - \hat{\boldsymbol{\theta}}_i^-\right)^T \left(\hat{\mathbf{P}}_i^-\right)^{-1} = \mathbf{0} \tag{13}$$

in which $\hat{\boldsymbol{\theta}}_i^-$ and $\hat{\mathbf{P}}_i^-$ are the prior estimates of the mean and covariance matrix of $\boldsymbol{\Theta}$ at time step i, respectively. Equation (13) is a nonlinear algebraic equation, which can be solved approximately using a first-order approximation of the nonlinear function $\mathbf{h}_i\left(\boldsymbol{\theta},\ \ddot{\mathbf{u}}_{g_{1:i}}\right)$ which represents the nonlinear finite element response function. The first-order Taylor series expansion of $\mathbf{h}_i\left(\boldsymbol{\theta}, \ddot{\mathbf{u}}_{g_{1:i}}\right)$ at $\hat{\boldsymbol{\theta}}_i^-$ can be expressed as

$$\mathbf{h}_i\left(\boldsymbol{\theta}, \ddot{\mathbf{u}}_{g_{1:i}}\right) \cong \mathbf{h}_i\left(\hat{\boldsymbol{\theta}}_i^-, \ddot{\mathbf{u}}_{g_{1:i}}\right) + \mathbf{C}_i\left(\boldsymbol{\theta} - \hat{\boldsymbol{\theta}}_i^-\right) \tag{14}$$

where $\mathbf{C}_i = \left.\frac{\partial \mathbf{h}_i\left(\boldsymbol{\theta}, \ddot{\mathbf{u}}_{g_{1:i}}\right)}{\partial \boldsymbol{\theta}}\right|_{\hat{\boldsymbol{\theta}}_i^-}$ = FE response sensitivity matrix computed at $\boldsymbol{\theta} = \hat{\boldsymbol{\theta}}_i^-$. Substitution of Eq. (14) into Eq. (13) results in the following posterior mean estimate of $\boldsymbol{\Theta}$ at time step i:

$$\hat{\boldsymbol{\theta}}_i^+ = \hat{\boldsymbol{\theta}}_i^- + \left(\mathbf{C}_i^T \mathbf{R}^{-1} \mathbf{C}_i + \left(\hat{\mathbf{P}}_i^-\right)^{-1}\right)^{-1} \mathbf{C}_i^T \mathbf{R}^{-1} \left(\mathbf{y}_i - \mathbf{h}_i\left(\hat{\boldsymbol{\theta}}_i^-, \ddot{\mathbf{u}}_{g_{1:i}}\right)\right) \tag{15}$$

in which $\left(\mathbf{C}_i^T \mathbf{R}^{-1} \mathbf{C}_i + \left(\hat{\mathbf{P}}_i^-\right)^{-1}\right)^{-1} \mathbf{C}_i^T \mathbf{R}^{-1} = \mathbf{K}_i$ is known as the Kalman gain matrix. It can be shown that the Kalman gain matrix can also be expressed as (Simon 2006)

$$\mathbf{K}_i = \hat{\mathbf{P}}_i^- \mathbf{C}_i^T \left(\mathbf{C}_i \hat{\mathbf{P}}_i^- \mathbf{C}_i^T + \mathbf{R}\right)^{-1} \tag{16}$$

Therefore, the posterior mean estimate of $\boldsymbol{\Theta}$ at time step i can be found as

$$\hat{\boldsymbol{\theta}}_i^+ = \hat{\boldsymbol{\theta}}_i^- + \mathbf{K}_i\left(\mathbf{y}_i - \mathbf{h}_i\left(\hat{\boldsymbol{\theta}}_i^-, \ddot{\mathbf{u}}_{g_{1:i}}\right)\right) \tag{17}$$

Using Eqs. (3) and (14), it is obtained that $\mathbf{P}_i^{\boldsymbol{\theta}\mathbf{y}} = \hat{\mathbf{P}}_i^- \mathbf{C}_i^T =$ cross-covariance matrix of $\boldsymbol{\Theta}$ and $\mathbf{Y}$ at time step i. Moreover, it is found that $\mathbf{P}_i^{\mathbf{yy}} = \mathbf{C}_i \hat{\mathbf{P}}_i^- \mathbf{C}_i^T + \mathbf{R} =$ covariance matrix of $\mathbf{Y}$ at time step i. Therefore, it can be concluded that

$$\mathbf{K}_i = \mathbf{P}_i^{\boldsymbol{\theta}\mathbf{y}} \left(\mathbf{P}_i^{\mathbf{yy}}\right)^{-1} \tag{18}$$

The posterior covariance matrix of $\boldsymbol{\Theta}$ can be approximated using the PCRLB theorem as

$$\hat{\mathbf{P}}_i^+ = \left(\mathbf{C}_i^T \mathbf{R}^{-1} \mathbf{C}_i + \left(\hat{\mathbf{P}}_i^-\right)^{-1}\right)^{-1} \tag{19}$$

Using the matrix inversion lemma, it follows that

$$\hat{\mathbf{P}}_i^+ = (\mathbf{I} - \mathbf{K}_i \mathbf{C}_i)\, \hat{\mathbf{P}}_i^- = \hat{\mathbf{P}}_i^- - \mathbf{K}_i \mathbf{P}_i^{\mathbf{yy}} \mathbf{K}_i^T \tag{20}$$

Therefore, at each time step, the prior estimates of the mean and covariance matrix of the parameter vector $\boldsymbol{\Theta}$ are updated to the posterior estimates based on the observed discrepancies between the measured and estimated (predicted) structural responses. The posterior estimates of the mean and covariance matrix of $\boldsymbol{\Theta}$ are then transferred to prior estimates at the next time step and the estimation/updating process continues in time. However, to improve the convergence of the recursive estimation procedure, a random disturbance referred to as process noise is added to the estimation process. This process noise is modeled as a stationary independent zero mean Gaussian white noise random vector, denoted as $\boldsymbol{\gamma}$, with a time-invariant diagonal covariance matrix $\mathbf{Q}$. Thus, at each time step, matrix $\mathbf{Q}$ is added to the

posterior covariance matrix of $\boldsymbol{\Theta}$ to yield the prior covariance matrix of $\boldsymbol{\Theta}$ at the next time step, i.e.,

$$\boldsymbol{\Theta}_{i+1}^{-} = \boldsymbol{\Theta}_{i}^{+} + \boldsymbol{\gamma} \Rightarrow \hat{\boldsymbol{\theta}}_{i+1}^{-} = \hat{\boldsymbol{\theta}}_{i}^{+}, \hat{\mathbf{P}}_{i+1}^{-} = \hat{\mathbf{P}}_{i}^{+} + \mathbf{Q} \tag{21}$$

This recursive MAP estimation procedure using linearization (with respect to $\boldsymbol{\theta}$) of the nonlinear FE model is referred to as the EKF method (Simon 2006). By the linearization of the nonlinear FE model, the likelihood function shown in Eq. (6) will be a Gaussian function of $\boldsymbol{\theta}$. Assuming a Gaussian prior joint PDF of the FE model parameters $\boldsymbol{\Theta}$, the posterior joint PDF will also be Gaussian (see Eq. (5)). Therefore, the MAP estimate is the mean of the posterior joint PDF of $\boldsymbol{\Theta}$.

2.2.2 Unscented Kalman Filter (UKF)

The UKF method is also a recursive MAP estimator similar to the EKF method. Both the prior and posterior joint PDF of the FE model parameters $\boldsymbol{\theta}$ are assumed to be Gaussian at each time step. The UKF, however, uses the unscented transformation (UT) method (Julier and Uhlmann 1997; Wan and van der Merwe 2000), a deterministic sampling approach, to propagate the uncertainty in $\boldsymbol{\Theta}$ through the nonlinear FE model, see Eq. (2), thus circumventing the linearization of the FE model used in the EKF method, see Eq. (14). Therefore, it results in a more accurate estimation of the posterior mean and covariance matrix of the parameter vector $\boldsymbol{\Theta}$, especially for highly nonlinear (FE) models (with respect to $\boldsymbol{\theta}$). The UT provides a more accurate estimation of $\mathbf{P}^{\boldsymbol{\theta}\mathbf{y}}$ and $\mathbf{P}^{\mathbf{y}\mathbf{y}}$ and, therefore, a more accurate estimate of the Kalman gain matrix (see Eq. (18)).

The UKF evaluates the nonlinear FE model at a set of deterministically selected realizations of the FE model parameter vector $\boldsymbol{\Theta}$, referred to as sigma points (SPs) and denoted by $\boldsymbol{\vartheta}_{i}^{-,j}$, taken around the prior mean estimate $\hat{\boldsymbol{\theta}}_{i}^{-}$. In this study, a scaled UT is selected and, therefore, the number of SPs is $(2n_{\boldsymbol{\theta}}+1)$, i.e., $j=1, \ldots, 2n_{\boldsymbol{\theta}}+1$. The weighted sample mean and covariance matrix of the SPs are equal to the prior mean estimate ($\hat{\boldsymbol{\theta}}_{i}^{-}$) and prior covariance matrix estimate ($\hat{\mathbf{P}}_{i}^{-}$) of the parameter vector $\boldsymbol{\theta}$, respectively. The SPs are propagated through the nonlinear FE model yielding

$$\mathbf{y}^{j}{}_{i} = \mathbf{h}_{i}\left(\boldsymbol{\vartheta}_{i}^{-,j}, \ddot{\mathbf{u}}_{g_{1:i}}\right) \tag{22}$$

The mean and covariance matrix of the FE predicted structural response $\mathbf{Y}$, and the cross-covariance matrix of $\boldsymbol{\Theta}$ and $\mathbf{Y}$ are respectively computed as (Astroza et al. 2015)

$$\mathbf{h}_{i}\left(\boldsymbol{\theta},\ \ddot{\mathbf{u}}_{g_{1:i}}\right) = \sum_{j=1}^{2n_{\theta}+1} W_{m}^{j} \mathbf{y}^{j}{}_{i} \tag{23}$$

$$\mathbf{P}_i^{\mathbf{yy}} = \sum_{j=1}^{2n_{\boldsymbol{\theta}}+1} W_c^j \left[\mathbf{y}_i^j - \mathbf{h}_i\left(\boldsymbol{\theta},\ \ddot{\mathbf{u}}_{g_{1:i}}\right)\right]\left[\mathbf{y}_i^j - \mathbf{h}_i\left(\boldsymbol{\theta},\ \ddot{\mathbf{u}}_{g_{1:i}}\right)\right]^T + \mathbf{R} \tag{24}$$

$$\mathbf{P}_i^{\boldsymbol{\theta}\mathbf{y}} = \sum_{j=1}^{2n_{\boldsymbol{\theta}}+1} \mathrm{W}_c^j \left[\boldsymbol{\vartheta}_i^{-,j} - \hat{\boldsymbol{\theta}}_i^{-}\right]\left[\mathbf{y}_i^j - \mathbf{h}_i\left(\boldsymbol{\theta},\ \ddot{\mathbf{u}}_{g_{1:i}}\right)\right]^T \tag{25}$$

where W_m^j and W_c^j denote the mean and covariance weighting coefficients, respectively (Wan and van der Merwe 2000). The Kalman gain matrix, posterior mean and covariance matrix estimates of $\boldsymbol{\theta}$ at time step i are obtained from Eqs. (18), (17), and (20), respectively.

3 Application Example

Simulated dynamic response data from a virtual 3D five-story two-by-one bay RC frame building subjected to bi-directional horizontal seismic excitation are used herein to verify the FE model updating methodologies presented in Sect. 2. A mechanics-based nonlinear FE model of the prototype building, developed in the software framework *OpenSees* (http://opensees.berkeley.edu/), is used for response simulation. The simulated response data are contaminated with additive zero-mean white Gaussian noise and used as measured output data to estimate the parameters characterizing the nonlinear material constitutive laws of the concrete and reinforcing steel.

The structure is designed as an intermediate moment-resisting RC frame located in downtown Seattle, Washington, with Site Class D soil conditions, a short-period spectral acceleration $S_{MS} = 1.37\,g$, and a one-second spectral acceleration $S_{M1} = 0.53\,g$. The building has two bays in the longitudinal direction (X) and one bay in the transverse direction (Z), with plan dimensions of 10.0 × 6.0 m, respectively. The frame has five stories with a floor-to-floor height of 4.0 m. The building is designed according to the 2012 International Building Code (International Code Council (ICC) 2012).

The building has six identical 0.45 × 0.45 m RC columns reinforced with 8 #8 longitudinal reinforcement bars and #3 bars spaced at 150 mm as transverse reinforcement. Grade 75 reinforcing steel is assumed for the columns. Longitudinal beams have a square 0.40 × 0.40 m cross-section and are reinforced with 6 #8 longitudinal reinforcement bars and #3 bars spaced at 100 mm transverse reinforcement. Transverse beams have a rectangular 0.40 × 0.45 m cross-section and are reinforced with 8 #8 longitudinal reinforcement bars and #3 bars spaced at 100 mm as transverse reinforcement. Grade 60 reinforcing steel is assumed for the beams in both directions. Figure 1 shows the overall geometry of the building and the cross-sections of the beams and columns.

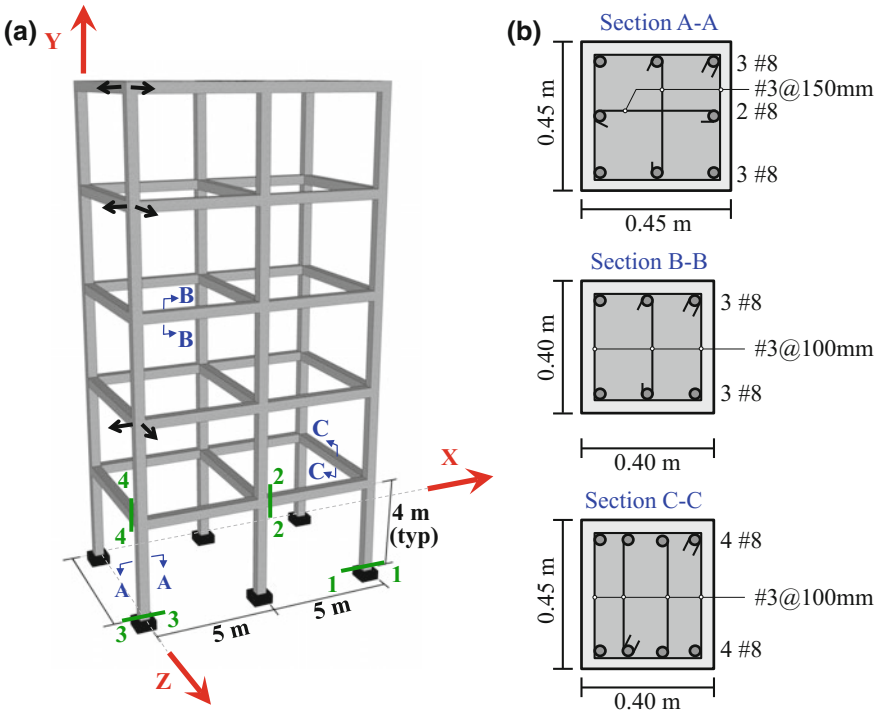

Fig. 1 RC frame building: **a** Isometric view (*black arrows* indicate the locations and directions of the measured acceleration responses), **b** Cross-sections of beams and columns

Figure 2 shows the FE model details for the RC frame building, including FE mesh discretization, nodal masses, and gravity loads applied on the beams. Nonlinear fiber-section displacement-based frame elements (Taucer et al. 1991) are used to model the beams and columns and Gauss-Lobatto quadrature is used for numerical integration along the elements. In this modeling approach, material nonlinearity can spread over various sections monitored along the element, called integration points (IPs). The IPs are further discretized into layers or fibers, the stress-strain behavior of which is governed by nonlinear uniaxial material constitutive laws. Material constitutive models depend on a set of parameters (e.g., elastic modulus, initial yield stress, etc.), the estimation of which is the objective of the nonlinear FE model updating approaches presented in this chapter. It is important to mention that a structure is usually made up of a relatively small number of different structural materials, each represented by a set of material model parameters, therefore the estimation process deals with a limited number of material model parameters, even in the case of large structural systems.

The cross-sections of beams and columns are discretized into longitudinal fibers as illustrated in Fig. 2b. Linear force-deformation models for shear and torsion are

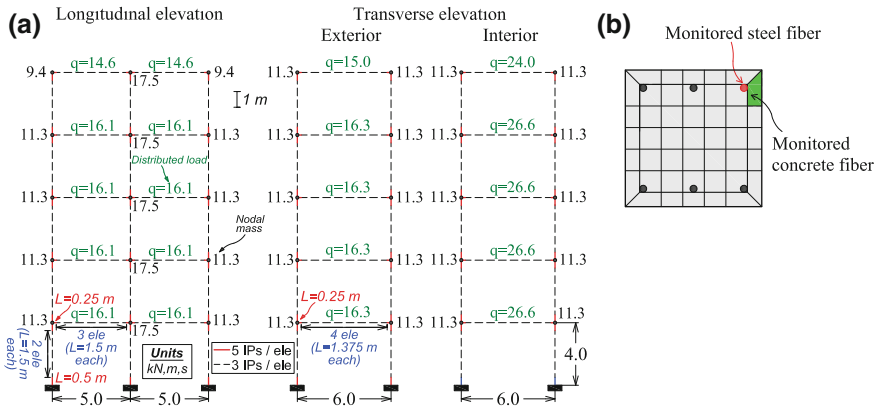

Fig. 2 Finite element model: **a** FE mesh discretization, nodal masses, and distributed loads on beams, **b** cross-section fiber discretization

defined (aggregated) at the section level and along the element, but the shear is coupled with bending only at the element level through equilibrium.

The modified Giuffré-Menegotto-Pinto model (Filippou et al. 1983) is used to model the nonlinear uniaxial stress-strain behavior of the longitudinal steel reinforcing bars. This material model is governed by eight parameters, three of which are primary parameters, while the other five are secondary parameters controlling the curvature of the hysteresis branches between consecutive strain reversal points. The primary material parameters consist of the elastic modulus (E_s), initial yield strength (f_y), and strain hardening ratio (b). These parameters are considered unknown parameters and are estimated through the FE model updating methodology presented herein. The Popovics-Saenz model (Popovics 1973; Saenz 1964; Balan et al. 2001), which is characterized by five material parameters, is used to model the nonlinear uniaxial stress-strain behavior of the concrete fibers The concrete material model parameters are the modulus of elasticity (E_c), peak compressive strength (f_c), strain at peak compressive strength (ε_c), crushing strength (f_u), and strain at crushing strength (ε_u). The values of f_c, ε_c, f_u, and ε_u correspond to the confined state of concrete and for response simulation purposes are determined based on the initial properties of the concrete material. The confinement effects of the transverse reinforcement on the concrete compressive strength and ductility are accounted for by modifying the parameters f_c and ε_c according to Mander et al. (Mander et al. 1988) and ε_u as suggested by Scott et al. (Scott et al. 1982).

Figure 3 shows the uniaxial material constitutive models used for the concrete and reinforcing steel fibers together with their corresponding parameters assumed to be unknown in the estimation phase. A set of material parameter values, referred to hereafter as true values, are assumed for the concrete and reinforcing steel materials in order to simulate the response of the structure. The true material parameter values are: $E^{true}_{s-col} = 200$ GPa, $f^{true}_{y-col} = 517$ MPa, $b^{true}_{col} = 0.01$, $E^{true}_{s-beam} = 200$ GPa, $f^{true}_{y-beam} = 414$ MPa, $b^{true}_{beam} = 0.05$, $E^{true}_{c} = 27600$ MPa, $f^{true}_{c} = 40$ MPa, and $\varepsilon^{true}_{c} = 0.0035$.

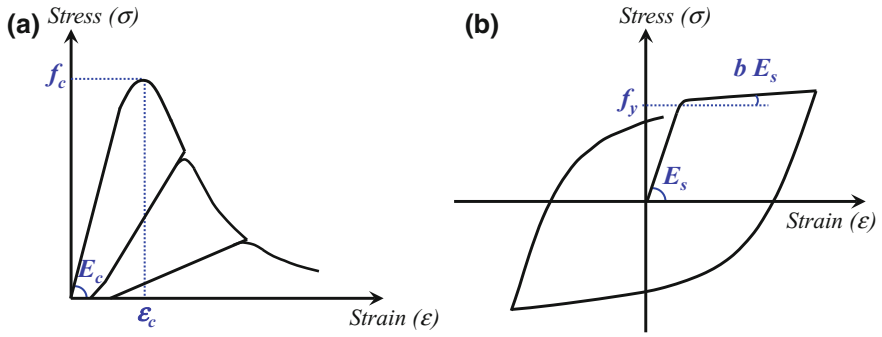

Fig. 3 Uniaxial material models used in the FE model: **a** Concrete, **b** Reinforcing steel

The concrete material parameters f_u and ε_u are not considered as estimation parameters, since they have negligible effects on the simulated response of the structure in this case study.

The damping energy dissipation (beyond the energy dissipated through hysteretic material behavior) is modeled using mass and tangent stiffness-proportional Rayleigh damping (based on the tangent stiffness matrix at the last converged step of analysis). A critical damping ratio of 2% for the first and second modes ($T_1 = 2.01$ s and $T_2 = 0.64$ s, after application of the gravity loads) is considered. Consequently, the mass and stiffness proportional parameters used to describe the Rayleigh damping are $\alpha_M = 0.0948$ and $\beta_K = 0.0031$, respectively.

The horizontal components of the ground acceleration recorded at the Sylmar County Hospital during the 1994 Northridge earthquake (Fig. 4) are used as input base excitation ($\ddot{\mathbf{u}}_g$). The 360° and 90° components are applied in the longitudinal and transverse direction of the building, respectively. They were recorded at a sampling rate of 50 Hz, filtered through a band-pass filter with cutoff frequencies of 0.1 and 23.0 Hz, and have $N = 550$ data samples each. The peak ground accelerations (PGA) of the 360° and 90° components are 0.84 g and 0.60 g, respectively.

3.1 Bayesian FE Model Updating

The nonlinear FE model presented above with the true material parameter values ($\boldsymbol{\theta}^{true} = \left[E^{true}_{s-col}, f^{true}_{y-col}, b^{true}_{col}, E^{true}_{s-beam}, f^{true}_{y-beam}, b^{true}_{beam}, E^{true}_{c}, f^{true}_{c}, \varepsilon^{true}_{c}\right]^T \in \mathbb{R}^{9\times 1}$) is subjected to the earthquake input motion shown in Fig. 4 and used to define the true response of the structure. After completion of the response simulation, the true relative horizontal acceleration responses at the 3rd, 5th, and roof levels in both the longitudinal (X) and transverse (Z) directions (see black arrows in Fig. 1) are contaminated with additive zero-mean Gaussian white noise, which represents the output measurement noise. A 1.0%g root-mean-square (RMS) zero-mean white

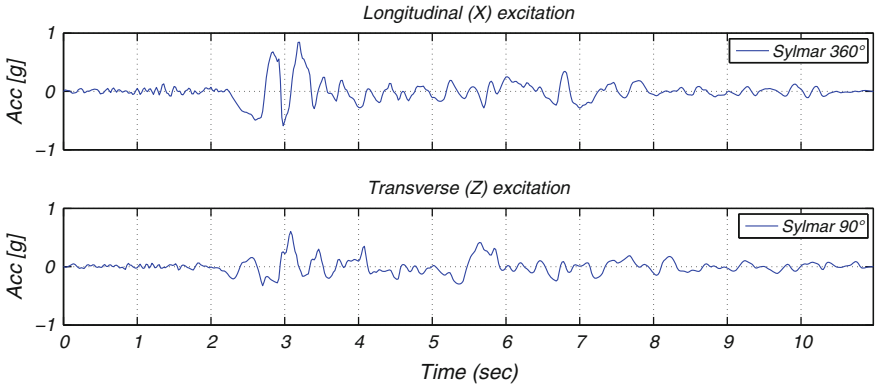

Fig. 4 Ground acceleration records used as seismic input motions

Gaussian noise is added to each simulated relative acceleration response time history, i.e., the actual covariance matrix of the output measurement noise vector is $(0.01\,g)^2\mathbf{I}_6 = 0.96\times10^{-2}\mathbf{I}_6(m/s^2)^2$ where $\mathbf{I}_j = j\times j$ identity matrix. Statistically independent realizations of output measurement noise are used for different acceleration responses. It is noted that a noise level of 1.0%g RMS is considerably larger than the level of noise expected from accelerometers currently used in earthquake engineering applications. Nevertheless, this relatively high level of measurement noise is considered in this study to examine the performance and robustness of the proposed parameter estimation process under extremely noisy measurement conditions. The simulated noisy floor relative acceleration response time histories are used as measured output ($\mathbf{y}$) in the estimation phase. It is assumed that the noiseless seismic input is available in the parameter estimation phase, i.e., the input measurement noise is not considered in this study.

The batch and recursive Bayesian estimation approaches presented in Sect. 2 are used to estimate the unknown FE model parameters ($\boldsymbol{\theta} = [E_{s-col}, f_{y-col}, b_{col}, E_{s-beam}, f_{y-beam}, b_{beam}, E_c, f_c, \varepsilon_c]^T$) and to update the nonlinear FE model of the structure. It is noteworthy that the same FE model is used for response simulation and for parameter estimation, i.e., the effects of modeling errors (or uncertainty) are not considered in this study. The initial estimates (guesses) of the expected values of the model parameters are taken as $\hat{\boldsymbol{\theta}}_0/\boldsymbol{\theta}^{true} = [0.70\,,\ 1.30\,,\ 1.25\,,\ 1.30\,,\ 0.80\,,\ 0.75\,,\ 1.20\,,\ 0.85\,,\ 0.90]^T$.

For the recursive approaches (i.e., UKF and EKF), it is assumed that the output measurement noise is a zero-mean white Gaussian process with a covariance matrix $\mathbf{R} = 0.47\times10^{-2}\mathbf{I}_6(m/s^2)^2$, i.e., a standard deviation (or RMS) of 0.7%g. The assumed amplitude of the measurement noise is purposely chosen to be different from the true amplitude, since in a real-world application the exact measurement noise amplitude is unknown. However, it can be estimated approximately based on the characteristics of the sensors and DAQ system used, experience, and engineering

judgment. Therefore, the estimated amplitude of the measurement noise is not expected to be far from the true value for the various types of sensors involved. Time-invariant first- and second-order statistics are assumed for the process noise, with zero-mean and covariance matrix $\mathbf{Q}_k = \mathbf{Q}$. The diagonal entries of $\mathbf{Q}$ are taken as $(q \times \theta_{0_n})^2$ where $n = 1, \ldots, 9$ and $q = 1 \times 10^{-5}$, i.e., for each of the material parameters ($\hat{\boldsymbol{\theta}}_0$), the RMS of the process noise is taken to be 1×10^{-5} the initial prior mean estimate of the parameter. The initial estimate of the covariance matrix of the model parameters, $\hat{\mathbf{P}}_0$, is assumed to be diagonal (i.e., initial estimates of the FE model parameters are assumed statistically uncorrelated). Diagonal entries of $\hat{\mathbf{P}}_0$ are taken as $(p \times \theta_{0_n})^2$ where $n = 1, \ldots, 9$ and $p = 0.15$, i.e., a coefficient of variation of 15% is assumed for the initial estimates of the FE model parameters.

Two cases are considered in the batch Bayesian estimation approach. In the first case, the unknown FE model parameters ($\boldsymbol{\theta}$) and the diagonal entries of the measurement noise variance matrix ($\mathbf{r} \in \mathbb{R}^{6 \times 1}$) are jointly estimated though an extended optimization process as shown in Eq. (9). The initial estimate of the measurement noise variances is taken as $\hat{\mathbf{r}}_0 = 0.47 \times 10^{-2}[1,\ 1,\ 1,\ 1,\ 1,\ 1]^T (m/s^2)^2$, corresponding to a 0.7%g RMS measurement noise. The feasible search domain for the model parameters is chosen as $0.4\hat{\boldsymbol{\theta}}_0 \leq \boldsymbol{\theta} \leq 2.5\hat{\boldsymbol{\theta}}_0$, where $\hat{\boldsymbol{\theta}}_0$ denotes the vector of initial estimates of the FE model parameters. The feasible search domain for the measurement noise variance is taken as $0.01\hat{\mathbf{r}}_0 \leq \mathbf{r} \leq 100\hat{\mathbf{r}}_0$.

In the second case, only the FE model parameters $\boldsymbol{\theta}$ are estimated, while the measurement noise variances $\mathbf{r}$ are initially estimated (by the same value assumed for the recursive approaches for comparison purposes) and kept constant during the FE model parameter estimation process. In both cases, the parameter estimation uncertainty is quantified by evaluating the CRLB using the two methods presented in Sect. 2.

The optimization convergence criterion consists of two conditions; the optimization process is considered converged when at least one of the following conditions is satisfied:

Condition 1:

$$\left\| \begin{bmatrix} \hat{\tilde{\boldsymbol{\theta}}}_m \\ \hat{\tilde{\mathbf{r}}}_m \end{bmatrix} - \begin{bmatrix} \hat{\tilde{\boldsymbol{\theta}}}_{m-1} \\ \hat{\tilde{\mathbf{r}}}_{m-1} \end{bmatrix} \right\|_2 \leq 10^{-7} \tag{26}$$

Condition 2:

$$\| \nabla J(\boldsymbol{\theta}, \mathbf{r}) \|_\infty \leq 10^{-7} \tag{27}$$

where $\hat{\tilde{\boldsymbol{\theta}}}_m$ is the estimated normalized (with respect to the initial parameter estimates) FE model parameter vector at the m^{th} optimization iteration, $\|\ldots\|_2$ denotes the Euclidean norm, and $\|\ldots\|_\infty$ denotes the infinity norm. It is noted that for the second case study where the vector $\mathbf{r}$ is fixed, only the FE model parameters $\boldsymbol{\theta}$ remain in Conditions 1 and 2.

3.1.1 Discussion of Parameter Estimation Results

Table 1 reports the estimated FE model parameters normalized by the corresponding true values $\left(\theta_n/\theta_n^{true}\right)$ with $n = 1, \ldots, 9$ and Table 2 gives the corresponding coefficient of variations (C.O.V.) defined as $\hat{\sigma}_{\theta_n}/\theta_n$, where $\hat{\sigma}_{\theta_n}$ is the estimated standard deviation of the FE model parameter θ_n. For the recursive approaches, these quantities correspond to the estimation results obtained at the last time step, while for the batch approach, they are the converged values obtained after the convergence criteria presented in Eqs. (26) and (27) are satisfied.

Accurate estimation results are obtained with the different estimation methods, with relative estimation errors less than or equal to 4% for all nine FE model parameters considered in this application example. Material initial stiffnesses (E_{s-col},E_{s-beam}, and E_c) and yield parameters of reinforcing steel (f_{y-col} and f_{y-beam}) are accurately estimated using all the estimation methods. Material model parameters b_{col}, b_{beam}, f_c, and ε_c are estimated with larger relative errors ($\leq$ 4%) and they are associated with larger estimation uncertainty as can be inferred from

Table 1 FE model parameter estimates

Estimation method	FE Model parameter estimates $(\theta_n/\theta_n^{true})$, $n = 1, \ldots, 9$								
	$\frac{E_{s-col}}{E_{s-col}^{true}}$	$\frac{f_{y-col}}{f_{y-col}^{true}}$	$\frac{b_{col}}{b_{col}^{true}}$	$\frac{E_{s-beam}}{E_{s-beam}^{true}}$	$\frac{f_{y-beam}}{f_{y-beam}^{true}}$	$\frac{b_{beam}}{b_{beam}^{true}}$	$\frac{E_c}{E_c^{true}}$	$\frac{f_c}{f_c^{true}}$	$\frac{\varepsilon_c}{\varepsilon_c^{true}}$
UKF	1.00	1.00	1.01	1.00	1.00	0.99	1.00	1.01	0.98
EKF	1.00	1.00	1.04	1.00	1.00	0.99	1.00	1.00	0.99
Batch with noise variance estimation	1.00	1.00	1.01	1.00	1.00	1.00	1.00	0.99	0.98
Batch without noise variance estimation	1.00	1.00	1.02	1.00	1.00	1.00	1.00	1.00	0.98

Table 2 Parameter estimation uncertainty

Estimation method		C.O.V. (%) of FE model parameter $(\hat{\sigma}_{\theta_n}/\theta_n)$								
		E_{s-col}	f_{y-col}	b_{col}	E_{s-beam}	f_{y-beam}	b_{beam}	E_c	f_c	ε_c
UKF	–	0.09	0.06	1.47	0.13	0.08	0.32	0.21	0.87	1.88
EKF	–	0.11	0.07	1.58	0.15	0.09	0.31	0.33	0.95	2.11
Batch with noise var. estimation	Method 1	0.15	0.10	2.27	0.21	0.13	0.43	0.50	1.29	3.03
	Method 2	0.16	0.11	2.45	0.25	0.13	0.33	0.55	1.33	3.45
Batch without noise var. estimation	Method 1	0.11	0.07	1.59	0.15	0.09	0.31	0.35	0.91	2.12
	Method 2	0.11	0.07	1.62	0.15	0.10	0.30	0.32	0.84	2.13

their C.O.V.s that are ranging between 0.3 and 3.5%. Since the measured output responses are less sensitive to b_{col} and ε_c, i.e., less information about these parameters is contained in **y**, larger relative errors and C.O.V.s in their final estimates are observed.

Figures 5 and 6 show the convergence history of the nine FE model parameters using the recursive (UKF and EKF) and batch estimation approaches, respectively. In the case of the recursive approach (Fig. 5), the parameter estimates are observed to converge and therefore the final estimates correspond to stable and converged values. The initial-stiffness related material parameters (E_{s-col}, E_{s-beam}, and E_c) start updating from the first time steps because the output responses are sensitive to elastic-related material parameters at all levels of excitation (and especially at low levels). These parameters converge to their true values at about the 4th second of earthquake excitation. It should be noted that the FE acceleration response sensitivities with respect to E_c are much higher than those to other material parameters during the first two seconds. Since the EKF is based on the analytical linearization (differentiation) of the nonlinear FE response, a large and abrupt jump in the recursive estimate of E_c is observed at the beginning of the excitation. The UKF shows a smoother convergence because this approach circumvents the analytical differentiation of the nonlinear FE response prediction with respect to the estimation parameters. In addition, in the UKF, a parameter controlling the spread of the SPs around the mean value (set equal to 0.01 in this study as suggested in (Wan and van der Merwe 2000)) allows to control the rate of convergence of the filter (see (Astroza et al. 2015) for more details). The other material model parameters start updating at about or after the 2nd second of the earthquake excitation, when the

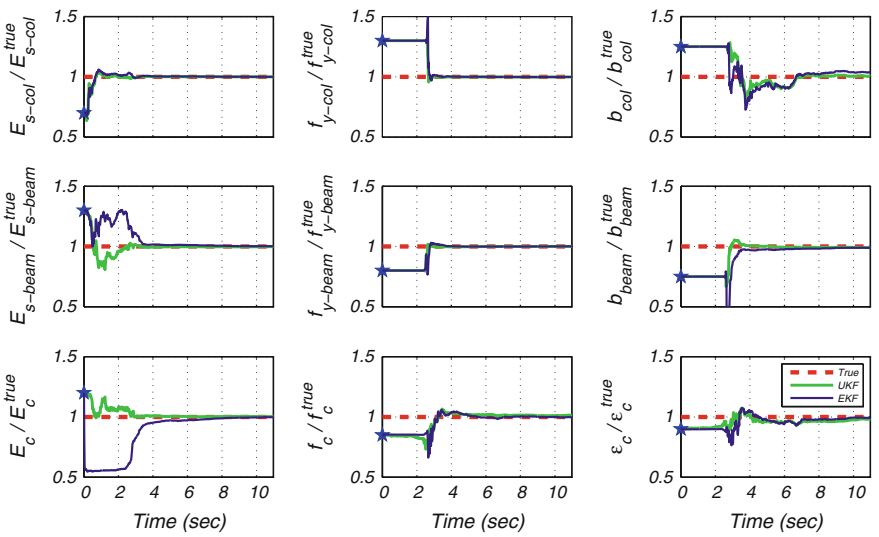

Fig. 5 Time histories of the posterior estimates of the FE model parameters using the recursive approach

amplitude of the excitation increases abruptly (see Fig. 4). The yield strength of the reinforcing steel, the strain hardening ratio of the reinforcing steel in the beams (b_{beam}), and the compressive strength of the concrete (f_c) quickly converge to their true values. Estimates of the strain hardening ratio of the column reinforcing steel (b_{col}) and of the strain at the peak compressive strength of concrete (ε_c) are moving towards and approaching their true values. However, these estimates do not fully stabilize and fluctuate until the end of the time history, because there is not enough information about these two parameters in the output measured response. In the case of the batch estimation approach (Fig. 6), the number of iterations corresponds to the number of evaluations of the objective function defined in Eq. (10). As explained in (Ebrahimian et al. 2016), the spike-like behavior in the convergence histories of the estimated model parameters is due to perturbations applied by the optimization algorithm to escape from the attraction zones of local minima. Both batch estimation solutions (marked by dots in Fig. 6) converge to the true values of the parameters; however, a large number of iterations is required for the extended estimation process, when $\mathbf{r}$ and the FE model parameters $\boldsymbol{\theta}$ are estimated jointly.

Figure 7 shows the convergence histories of the measurement noise variances of the six output response measurements obtained using the batch approach. It is noted that $\mathbf{a}_{ij}$ represents the relative acceleration response of floor i in direction j, where l = longitudinal and t = transverse direction, respectively. The measurement noise variances are correctly estimated for all the response measurements considered, converging to normalized values (with respect to the true variances) between 0.92 and 1.07.

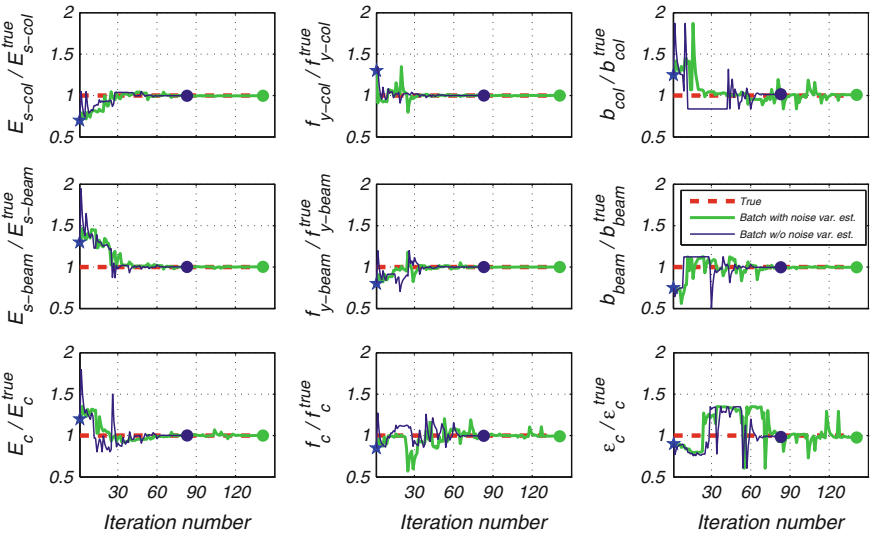

Fig. 6 Convergence histories of the MAP estimates of the FE model parameters using the batch approach

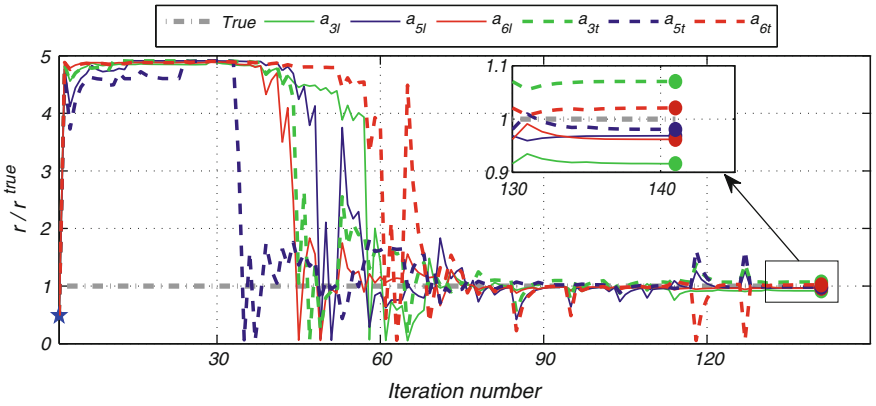

Fig. 7 Convergence histories of the measurement noise variances using the batch approach

Table 3 Relative root mean square error (in %) between the true (noiseless) and estimated relative acceleration response time histories

	Estimation method	Output response measurement					
		a_{3l}	a_{5l}	a_{6l}	a_{3t}	a_{5t}	a_{6t}
$\hat{\boldsymbol{\theta}}_0$	–	58.89	38.33	37.86	39.62	45.48	40.64
$\hat{\boldsymbol{\theta}}$	UKF	0.41	0.28	0.23	0.24	0.24	0.25
	EKF	0.56	0.28	0.22	0.33	0.25	0.30
	Batch with noise var. estimation	0.25	0.22	0.20	0.24	0.22	0.22
	Batch without noise var. estimation	0.26	0.22	0.22	0.27	0.24	0.26

The relative root mean square error (RRMSE) between the true (noiseless simulated) relative floor acceleration response time histories and their estimated counterparts obtained using the final estimates of the FE model parameters ($\hat{\boldsymbol{\theta}}$) are computed and reported in Table 3. The RRMSE between two digital signals $\mathbf{s}^1$ and $\mathbf{s}^2$ with $\mathbf{s}^1$ taken as the reference signal is computed as $RRMSE\ (\%) = \sqrt{\left[1/Ns \sum_{k=1}^{Ns} \left(s_k^1 - s_k^2\right)^2\right]} / \sqrt{\left[1/Ns \sum_{k=1}^{Ns} \left(s_k^1\right)^2\right]} \times 100$, where Ns denotes the total number of data samples (i.e., length) of the signals. The RRMSEs between the true (noiseless) response time histories and their counterparts obtained using the initial estimates of the model parameters ($\hat{\boldsymbol{\theta}}_0$) are also provided for comparison purposes. The very small RRMSEs obtained between the true responses and their estimated counterparts based on final estimates of the FE model parameters confirm the successful performance of all the estimation methods considered herein. These results also confirm that the output measured responses are not very sensitive to the model parameters b_{col} and ε_c, i.e., $\mathbf{y}$ does not contain enough information about these two parameters.

The updated FE model can be used to reconstruct unobserved (unmeasured) responses quantities at global and local levels that can be used to define and quantify damage indices from which the degree of damage throughout the structure can be assessed. Such damage indices include those based on maximum inelastic deformation responses at different scales (e.g., maximum displacement or curvature or strain ductility factors) or normalized cumulative hysteretic energy dissipated (e.g., cumulative displacement, curvature or strain ductility) as a measure of cumulative damage (e.g., low-cycle fatigue), or a combination of both (Cosenza et al. 1993; Park et al. 1985). Figure 8 compares different force-deformation response histories at different scales (structure, section and fiber levels) computed with the true FE model parameters and with the final estimates of the model parameters obtained using the UKF and batch (without noise variance estimation) approaches. The total base shear in the longitudinal and transverse directions (V_b^x and V_b^z, respectively) normalized by the total weight of the building (W) versus the roof drift ratio in the corresponding direction (RDR^x and RDR^z) are plotted in Fig. 8a, b, respectively. The moment (M)

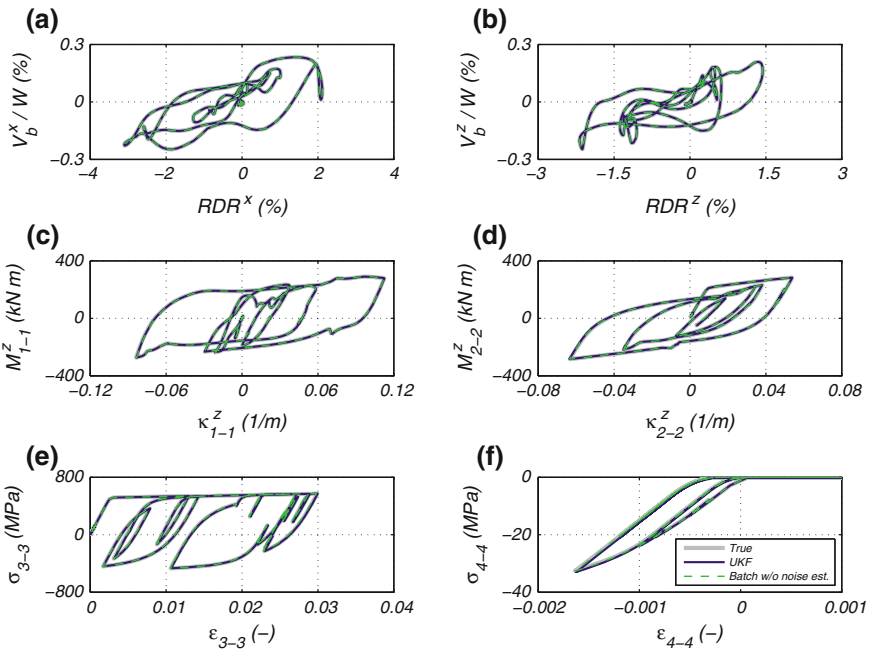

Fig. 8 Comparison of unobserved FE responses computed with the true FE model parameters and final estimates of the FE model parameters obtained using the UKF and batch (without noise estimation) estimation approaches: **a** normalized base shear versus roof drift ratio in the longitudinal direction, **b** normalized base shear versus roof drift ratio in the transverse direction, **c** moment versus curvature at the base of a column (section 1−1 in Fig. 1a), **d** moment versus curvature at the end of a longitudinal beam (section 2−2 in Fig. 1a), **e** stress versus strain of a reinforcing steel fiber at the bottom of a column (section 3−3 in Fig. 1a), **f** stress versus strain of a concrete fiber at the end of a transverse beam (section 4−4 in Fig. 1a)

Table 4 Wall-clock time required for the estimation process of different methodologies

Estimation method	Wall-clock time (hours)
UKF	105
EKF	93
Batch with noise variance estimation	64
Batch without noise variance estimation	52

versus curvature (κ) for sections at the base of a column (section 1−1 in Fig. 1a) and at the end of a 2nd floor longitudinal beam (section 2−2 in Fig. 1a) are shown in Fig. 8c, d, respectively. Fiber level responses are presented in Fig. 8e, f, where the stress (σ) versus strain (ε) of a monitored reinforcing steel fiber at the bottom of a column (section 3−3 in Fig. 1a) and a monitored concrete fiber at the end of a 2nd floor transverse beam (section 4−4 in Fig. 1a) are plotted. The excellent agreement between the true and estimated response based on the final estimates of the model parameters corroborates that the updated FE models can be reliably used for damage identification purposes.

3.2 Computational Cost

In spite of the low-cost high computational power available nowadays, integration of high-fidelity mechanics-based nonlinear FE structural modeling and Bayesian inference methods still requires a significant amount of computational resources and time. Therefore, it is important to study the computational cost associated to the different FE model updating methods. Table 4 reports the wall-clock time required for each estimation approach to update the nonlinear FE model considered herein. The FE model updating using the batch and recursive estimation approaches were run on a desktop workstation with an Intel Core i7 CPU 860 2.80 GHz with 8 GB RAM and a desktop workstation with an Intel Xeon 2.66 GHz processor and 48 GB random-access memory, respectively. The wall-clock time required by the batch approach is 45 to 50% lower than that required by the recursive approaches.

4 Conclusions

This study investigated and compared the performance of a new framework to identify and update mechanics-based nonlinear structural finite element (FE) models using different Bayesian estimation methods. The framework uses recorded input-output data to estimate unknown parameters of advanced mechanics-based nonlinear FE models of the structure of interest, using both batch and recursive approaches. The batch estimation approach consisted of the maximum a posteriori (MAP) method, which results in a nonlinear optimization problem that is solved

using the interior point method, a gradient-based optimization algorithm. The Extended Kalman filter (EKF) and Unscented Kalman filter (UKF) were employed as recursive Bayesian estimation methods.

The proposed methodology was verified using numerically simulated structural response data for a three-dimensional five-story two-by-one bay reinforced concrete (RC) frame building subjected to bi-directional horizontal earthquake excitation. Parameters characterizing the nonlinear material constitutive laws of the reinforcing steel and concrete materials were successfully estimated using the noiseless seismic input data together with limited noisy output response data (6 relative acceleration response time histories). Accurate results were obtained with both batch and recursive estimation methods. Comparison of unobserved response quantities at different scales (structure, component, section and fiber levels) obtained from the updated FE model and the corresponding "true" responses demonstrated the capabilities of the proposed framework for (nonlinear) damage identification purposes. Thus, the updated FE model can be used to reconstruct unmeasured structural responses from the global to local levels. The reconstructed inelastic structural response can be utilized to estimate mechanics-based damage indices and therefore to assess the type and level of damage throughout the structure.

It is noteworthy that the proposed framework is not limited to certain types of FE models, loading conditions, or FE model parameters. Different types of material constitutive models, various types of FE modeling approaches and different types of analysis (e.g., quasi-static, time-dependent, dynamic) can be used with the proposed framework. Furthermore, other time-invariant FE model parameters (e.g., inertia, damping, geometric, and constraint parameters) can be incorporated in the estimation procedure.

Acknowledgements Partial support of this research by the UCSD Academic Senate under Research Grant RN091G – CONTE is gratefully acknowledged. The first author acknowledges the support provided by the Fulbright-CONICYT Chile Equal Opportunities Scholarship. Any opinions, findings, and conclusions or recommendations expressed in this study are those of the authors and do not necessarily reflect those of the sponsors.

References

Astroza R, Ebrahimian E, Conte JP (2015) Material parameter identification in distributed plasticity FE models of frame-type structures using nonlinear stochastic filtering. ASCE J Eng Mech 141(5):04014149

Balan TA, Spacone E, Kwon M (2001) A 3D hypoplastic model for cyclic analysis of concrete structures. Eng Struct 23(4):333–342

Byrd RH, Hribar ME, Nocedal J (1999) An interior point algorithm for large-scale nonlinear programming. SIAM J Optim 9(4):877–900

Ching J, Beck JL, Porter KA, Shaikhutdinov R (2006) Bayesian state estimation method for nonlinear systems and its application to recorded seismic response. ASCE J Eng Mech 132 (4):396–410

Cosenza E, Manfredi G, Ramasco R (1993) The use of damage functionals in earthquake engineering: A comparison between different methods. Earthquake Eng Struct Dynam 22 (10):855–868
Distefano N, Pena-Pardo B (1976) System identification of frames under seismic loads. J Eng Mech Division 102(EM2):313–330
Distefano N, Rath A (1975a) System identification in nonlinear structural seismic dynamics. Comput Methods Appl Mech Eng 5:353–372
Distefano N, Rath A (1975b) Sequential identification of hysteretic and viscous models in structural seismic dynamics. Comput Methods Appl Mech Eng 6:219–232
Ebrahimian H, Astroza R, Conte JP (2015) Extended Kalman filter for material parameter estimation in nonlinear structural finite element models using direct differentiation method. Earthquake Eng Struct Dynam 44(10):1495–1522
Ebrahimian H, Astroza R, Conte JP, de Callafon RA (2016) Nonlinear finite element model updating for damage identification of civil structures using batch Bayesian estimation. Mech Syst Signal Process 84(B):194–222. doi:10.1016/j.ymssp.2016.02.002
Filippou FC, Popov EP, Bertero VV (1983) Effects of bond deterioration on hysteretic behavior of reinforced concrete joints. UCB/EERC-83/19. EERC Report 83-19, Earthquake Engineering Research Center, Berkeley, CA
Friswell MI, Mottershead JE (1995) Finite element model updating in structural dynamics. Kluwer Academic Publishers, Dordrecht, The Netherlands
Gill PE, Murray W, Wright MH (1981) Practical optimization. Academic Press, London, England
Haukaas T, Gardoni P (2011) Model Uncertainty in Finite-Element Analysis: Bayesian Finite Elements. ASCE J Eng Mech 137(8):519–526
Huang Q, Gardoni P, Hurlebaus S (2015) Adaptive reliability analysis of reinforced concrete bridges using nondestructive testing. ASCE-ASME J Risk Uncertain Anal 1(4):04015014
International Code Council (ICC) (2012) International Building Code. Falls Church, VA
Julier SJ, Uhlmann JK (1997) A new extension of the Kalman filter to nonlinear systems. In: 11th international symposium on aerospace/defense sensing, simulation and controls, Orlando, FL
Kleiber M, Antunez H, Hien TD, Kowalczyk P (1997) Parameter sensitivity in nonlinear mechanics: theory and finite element computations. Wiley, England
Ljung L (1999) System identification: theory for the user, 2nd edn. Prentice Hall, Upper Saddle River
Mander JB, Priestley MJN, Park R (1988) Theoretical stress-strain model for confined concrete. ASCE J Struct Eng 114(8):1804–1826
OpenSees—Open system for earthquake engineering simulation. http://opensees.berkeley.edu/. Accessed Nov 2015
Park YJ, Ang AH, Wen YK (1985) Seismic damage analysis of reinforced concrete buildings. ASCE J Struct Eng 111(4):740–757
Popovics S (1973) A numerical approach to the complete stress–strain curve of concrete. Cement Concrete Res 3(5):583–599
Saenz IP (1964) Discussion of 'Equation for the stress–strain curve of concrete, by Desay P, Krishan S. American Concrete Institute (ACI) J 61(9):1229–1235
Scott BD, Park R, Priestley MJN (1982) Stress-strain behavior of concrete confined by overlapping hoops at low and high strain rates. American Concrete Inst (ACI) J 79(1):13–27
Shahidi S, Pakzad S (2014) Generalized response surface model updating using time domain data. ASCE J Struct Eng 140:A4014001
Simoen E, De Roeck G, Lombaert G (2015) Dealing with uncertainty in model updating for damage assessment: a review. Mech Syst Signal Process 56–57:123–149
Simon D (2006) Optimal state estimation: Kalman, H infinity, and nonlinear approaches. Wiley, Hoboken
Song W, Dyke SJ (2014) Real-time dynamic model updating of a hysteretic structural system. ASCE J Struct Eng 140(3):04013082

Taucer FF, Spacone E, Filippou FC (1991) A fiber beam-column element for seismic response analysis of reinforced concrete structures. Report 91/17, EERC, Earthquake Engineering Research Center (EERC), University of California, Berkeley

Tsay JJ, Arora JS (1990) Nonlinear structural design sensitivity analysis for path dependent problems. Part 1: general theory. Comput Methods Appl Mech Eng 81(2):183–208

Van Trees HL (2002) Optimum array processing, Part IV of detection, estimation, and modulation theory. Wiley, New York

Wan EA, van der Merwe R (2000) The unscented Kalman filter for nonlinear estimation. In: IEEE 2000 adaptive systems for signal processing, communications, and control symposium, Lake Louise, AB, Canada

Yang J, Xia Y, Loh CH (2014) Damage detection of hysteretic structures with pinching effect. ASCE J Eng Mech 140(3):462–472

Zhang Y, Der Kiureghian A (1993) Dynamic response sensitivity of inelastic structures. Comput Methods Appl Mech Eng 108(1–2):23–36

Reliability Updating in the Presence of Spatial Variability

Daniel Straub, Iason Papaioannou and Wolfgang Betz

Abstract During the construction and operation of engineering systems, information on their properties and performance becomes available through monitoring and other means of observation. Such information can be used to update predictions of the system's reliability through a Bayesian analysis. We present Bayesian analysis and updating of the reliability of engineering systems that depend on physical quantities that vary randomly in space, which are modelled by means of random fields. The numerical treatment of random fields requires their discretization with a finite number of random variables. To this end, we employ the Expansion Optimal Linear Estimation (EOLE) method, which is shown to be especially efficient in obtaining an approximation of a second-order random field. This property is beneficial for Bayesian analysis in cases where the moment function depends on hyperparameters, such as the correlation length of a random field. We discuss the application of EOLE in the context of BUS, which is a recently proposed framework for Bayesian updating of parameters of engineering systems and the resulting system reliability. In BUS, monitoring data is expressed in terms of an equivalent limit state function such that Bayesian updating can be performed with structural reliability methods. We apply BUS with EOLE to update the reliability of the stability of a foundation resting on spatially variable soil with deformation measurements obtained at an intermediate construction stage.

1 Introduction

Structural reliability is commonly used to assess existing structures, which do not comply with codes and standards due to deterioration or changes in system properties, system demands or code requirements (Ellingwood 1996; Straub and Der

D. Straub (✉) · I. Papaioannou · W. Betz
Engineering Risk Analysis Group, Technische Universität München,
Munich, Germany
e-mail: straub@tum.de
URL: http://www.era.bgu.tum.de

P. Gardoni (ed.), *Risk and Reliability Analysis: Theory and Applications*,
Springer Series in Reliability Engineering, DOI 10.1007/978-3-319-52425-2_16

Kiureghian 2011). Reliability methods have also been employed to appraise the effect of inspection on the reliability of structures and to optimize inspection efforts (Madsen et al. 1989; Faber et al. 2005; Goulet et al. 2015). Along the same lines, they have been utilized to assess the effect of structural health monitoring on a structural system (Pozzi and Der Kiureghian 2011) or site investigations in geotechnical engineering (Papaioannou and Straub 2012). With technological advances in monitoring technology, collecting additional data on structural performance becomes easier and cheaper, and methods to assess the effect of data on the system reliability are thus increasingly required for existing and new structures.

Data influences the system reliability by reducing uncertainty. Strictly, the reliability of an engineering system is not altered by the collection of information alone (Kiureghian 1989; Der Kiureghian and Ditlevsen 2009). However, it is altered by the actions that follow the collection of information. If the reduced uncertainty leads to more targeted actions, sufficient reliability is ensured with lower cost. Bayesian analysis is ideally suited to quantitatively assess the effect of data on the reliability, risk and cost. It allows to consistently combine the data with existing probabilistic models of structural systems, which is particularly relevant when dealing with (rare) failure events (Straub et al. 2016).

When combining data with probabilistic models for reliability analysis, it is often necessary to utilize more advanced mechanical models than for design purposes. Predictions made with simplified (empirical) models used in design processes may not match with the observations on the real structures. One prominent example is the treatment of spatially variable material or soil properties. While it is commonly possible and reasonable to represent such properties by an equivalent homogenous parameter in design calculations, such models can be oversimplifying and lead to erroneous predictions when including data (Papaioannou and Straub 2016). Therefore, there is a significant interest to enable a Bayesian updating of mechanical models with spatially distributed properties for the purpose of reliability assessment.

Bayesian analysis of spatially variable properties is an active field of research (e.g., Marzouk et al. 2007; Koutsourelakis 2009). However, only few investigations on reliability updating in the presence of spatial variability are documented in the literature. These include applications to geotechnical engineering (Papaioannou and Straub 2012), seismic risk (Bensi et al. 2015) and deteriorating structures (Straub 2011b).

This contribution focuses on the representation of random fields in the context of Bayesian analysis and reliability updating. In particular, we discuss the computational benefits of utilizing the Expansion Optimal Linear Estimation (EOLE) proposed in (Li and Der Kiureghian 1993) for discretizing the random field when the a-priori correlation length is uncertain. The recently proposed BUS approach to Bayesian analysis and reliability updating is shortly summarized and its application in the context of random fields is discussed. To demonstrate the approach, we consider an application from geotechnical engineering, where it is common to use observations during the construction phase to ensure the safety of the site; a process that is known as the observational method.

2 Methodology

2.1 Random Field Discretization

Random fields are used to describe spatially variable uncertain parameters. Common examples are soil parameters in geotechnical engineering, environmental loads in structural engineering and topology of multiphase materials in biomechanics. A random field $X(\mathbf{t})$ is defined as a collection of random variables indexed by a continuous spatial parameter $\mathbf{t} \in \Omega \subset \mathbb{R}^d$, with d denoting the spatial dimension. The random field is termed second order if it has finite mean and variance functions. To completely define the random field $X(\mathbf{t})$, the joint distribution of the random variables $\{X(\mathbf{t}_1), X(\mathbf{t}_2), \ldots, X(\mathbf{t}_n)\}$ for any $\{n, \mathbf{t}_1, \mathbf{t}_2, \ldots, \mathbf{t}_n\}$ must be specified. This is straightforward when the random field is Gaussian (i.e. the random variables $\{X(\mathbf{t}_1), X(\mathbf{t}_2), \ldots, X(\mathbf{t}_n)\}$ have the multivariate normal distribution) and the mean function $\mu(\mathbf{t})$ and the autocovariance function $C(\mathbf{t}_1, \mathbf{t}_2)$ are known. However, if the marginal distribution of $X(\mathbf{t})$ is not Gaussian, then a complete definition of the random field in terms of its first and second moment functions is in general not possible. A class of non-Gaussian random fields, termed translation fields, can be defined by a nonlinear transformation of an underlying Gaussian field of the form

$$X(\mathbf{t}) = F_X^{-1}[\Phi(U(\mathbf{t})), \mathbf{t}] \tag{1}$$

where F_X^{-1} is the inverse of the non-Gaussian marginal distribution, Φ is the standard normal distribution and $U(\mathbf{t})$ is a Gaussian random field with zero mean and unit variance. The joint distribution for any selection of points in the spatial domain can then be modeled by a Gaussian copula, also known as the Nataf multivariate distribution (Nataf 1962; Der Kiureghian and Liu 1986). The specification of the auto-correlation coefficient function of $U(\mathbf{z})$ in terms of the one of $X(\mathbf{t})$ involves solving an integral equation.

A random field is said to be second-order (or weakly) homogeneous if its probabilistic structure is invariant to a shift in the spatial parameter up to a second order. A second-order homogeneous random field has constant mean and variance functions and its autocovariance function depends on the difference in location, i.e. $C(\mathbf{t}_1, \mathbf{t}_2) \to C(\Delta\mathbf{t})$ where $\Delta\mathbf{t} = \mathbf{t}_1 - \mathbf{t}_2$. The spatial variability of a second-order homogeneous random field is defined by the autocorrelation coefficient function $\rho(\Delta\mathbf{t}) = \frac{C(\Delta\mathbf{t})}{\sigma^2}$, with σ^2 being the variance of the random field. A common measure of the spatial variability is the scale of fluctuation θ, defined as the integral of $\rho(\Delta\mathbf{t})$ (Vanmarcke 2010). The smaller θ is, the higher is the variability in the sample functions of the random field. An alternative measure for the spatial variability is the correlation length l, defined as the distance $l = \|\Delta\mathbf{t}\|$ for which $\rho(\Delta\mathbf{t}) = e^{-1}$ (Li and Der Kiureghian 1993).

In order to numerically represent the random field $X(\mathbf{t})$, it is necessary to discretize it with a finite number of random variables. Several methods have been proposed for the discretization of random fields, see (Sudret and Der Kiureghian

2000) for a comprehensive review. The efficiency of random field discretization methods depends on their ability to approximate accurately the random field with as few random variables as possible. Accuracy is defined in terms of an error measure such as the mean-square error or the variance error. Efficient random field representations involving small numbers of random variables are beneficial for most numerical methods for uncertainty quantification and reliability analysis.

Random field discretization methods include point methods, spatial average methods and series expansion methods. In point and spatial average methods, the random field is expressed in terms of random variables that correspond to spatial points or averages of discrete parts of the spatial domain. Series expansion methods express the random field as a superposition of products of deterministic spatial functions and random variables, such that each random variable in the expansion has a global influence in the approximation of the random field. Through a proper choice of the spatial functions, series expansion methods are able to describe the spatial variability accurately with much fewer random variables as compared to point or average methods (Sudret and Der Kiureghian 2000). Popular series expansion methods include orthogonal series expansions (Zhang and Ellingwood 1994), the Karhunen-Loève (KL) expansion (e.g., Ghanem and Spanos 1991) and the expansion optimal linear estimation (EOLE) method (Li and Der Kiureghian 1993).

The spatial functions in orthogonal series expansions are chosen as orthogonal functions on the domain of definition of the random field (Zhang and Ellingwood 1994). In particular, the KL expansion employs the eigenfunctions of the autocovariance function of the random field, which are shown to be the optimal choice among all sets of orthogonal functions in the sense that they minimize the global mean square error of the discretization (Ghanem and Spanos 1991). Determination of the eigenfunctions in the KL expansion requires the solution of an integral eigenvalue problem. Aside from a few specific cases, the integral eigenvalue problem needs to be solved numerically resulting in an approximation of the KL expansion. Application of Galerkin-based methods for the solution of the integral eigenvalue problem is time consuming, as they require the assembly of a matrix eigenvalue problem through performing a two-folded integration over the spatial domain (Betz et al. 2014).

The EOLE method proposed in (Li and Der Kiureghian 1993) combines concepts from linear estimation theory and principle component analysis to derive the spatial functions in the representation of the random field. The method can be understood as a numerical KL expansion for the case where the KL eigenvalue problem is solved by the Nyström method (Betz et al. 2014). However, EOLE has the advantage over the Galerkin-based KL expansion that integration is not required to assemble the matrix eigenvalue problem. Hence, the method is particularly efficient in determining the spatial functions in the random field representation. This can be of advantage if the random field description changes throughout the computation, as is the case in Bayesian analysis when the autocovariance function of the random field is described by uncertain (hyper-) parameters.

In the EOLE method, the discrete representation $\widehat{X}(\mathbf{t})$ of the random field $X(\mathbf{t})$ reads

$$\widehat{X}(\mathbf{t}) = \mu(\mathbf{t}) + \sum_{i=1}^{m} \frac{\xi_i}{\sqrt{\lambda_i}} \mathbf{C}_q(\mathbf{t})^T \mathbf{v}_i \tag{2}$$

Here, $\{\lambda_i, \mathbf{v}_i\}$ are the eigenpairs of the covariance matrix of the random variables $X(\mathbf{z}_j)$ corresponding to a set of spatial points $\{\mathbf{t}_j, j = 1, \ldots, q\}$ and $\mathbf{C}_q(\mathbf{t})$ is a $q \times 1$ vector function with j element $C(\mathbf{t}, \mathbf{t}_j)$ (Li and Der Kiureghian 1993). The eigenpairs $\{\lambda_i, \mathbf{v}_i\}$ are evaluated through solving the following matrix eigenvalue problem

$$\mathbf{C}\mathbf{v}_i = \lambda_i \mathbf{v}_i \tag{3}$$

where $\mathbf{C}$ is the covariance matrix of the spatial points with (i, j) element $C(\mathbf{t}_i, \mathbf{t}_j)$. The eigenpairs are arranged in decreasing order of magnitude of the eigenvalues and the first m terms are retained in the EOLE representation. The variables $\{\xi_i, i = 1, \ldots, m\}$ are zero mean orthonormal random variables. If the random field is Gaussian, then $\{\xi_i, i = 1, \ldots, m\}$ are independent standard normal random variables. If it is non-Gaussian then it is not always possible to determine the joint distribution of $\{\xi_i, i = 1, \ldots, m\}$. Therefore, if the random field is defined by a transformation of the type of Eq. (1), it is convenient to apply the EOLE method to discretize the underlying Gaussian field.

The point-wise variance of the EOLE truncation error of $X(\mathbf{t})$ is given by (Li and Der Kiureghian 1993):

$$\mathrm{Var}\left[X(\mathbf{t}) - \widehat{X}(\mathbf{t})\right] = \mathrm{Var}[X(\mathbf{t})] - \sum_{i=1}^{m} \frac{1}{\lambda_i} \left(\mathbf{C}_q(\mathbf{t})^T \mathbf{v}_i\right)^2 \tag{4}$$

This equation can be used to determine the number of terms m in the EOLE representation for a desired accuracy in the approximation of the random field.

2.2 *Reliability Analysis*

Structural Reliability Methods (SRM) have been developed since the 1970 s for computing the (small) probability of failure of engineering systems (e.g., Rackwitz and Fiessler 1978; Der Kiureghian and Liu 1986). The failure event F is described in terms of a limit state function $g(\mathbf{X})$, where $\mathbf{X} = [X_1; X_2; \ldots; X_n]$ is the vector of the n input random variables. By definition, the event F corresponds to

$$F = \{g(\mathbf{X}) \leq 0\} \tag{5}$$

It is helpful to interpret the SRM geometrically: Ω_F corresponds to the domain in the outcome space of $\mathbf{X}$ for which $g(\mathbf{x}) \leq 0$. The probability of the event F is the probability of $\mathbf{X}$ taking a value within Ω_F. It can be computed by integrating the joint probability density function of $\mathbf{X}$, denoted by $f(\mathbf{x})$, over Ω_F:

$$\Pr(F) = \int_{\Omega_F} f(\mathbf{x}) \mathrm{d}x_1 \mathrm{d}x_2 \ldots \mathrm{d}x_n \tag{6}$$

More generally, the event of failure can be defined through a system formulation, as a function of multiple component failure events F_i with corresponding limit state functions g_i. The system failure domain is (Der Kiureghian 2005):

$$\Omega_F = \left\{ \min_{1 \leq k \leq K} \left[\max_{i \in I_1} g_i(\mathbf{x}), \ \ldots, \ \max_{i \in I_K} g_i(\mathbf{x}) \right] \leq 0 \right\}, \tag{7}$$

where I_k is an index set corresponding to the kth cut set of the system. For $K = 1$, this reduces to a parallel system reliability problem; for the case that each cut set contains only one index, this reduces to a series system.

To solve Eq. (6), most SRM involve a transformation of the problem from the original space of the random variables $\mathbf{X}$ to the space of independent standard normal random variables $\mathbf{U}$ by a suitable transformation $\mathbf{U} = \mathbf{T}(\mathbf{X})$. If the joint distribution of $\mathbf{X}$ is of the Gaussian copula class, the transformation of (Der Kiureghian and Liu 1986) can be applied; if the joint distribution of $\mathbf{X}$ is of any arbitrary form, the Rosenblatt transformation can be used (Hohenbichler and Rackwitz 1981). Let G denote the transformed limit state function in standard normal space:

$$G(\mathbf{U}) = g(\mathbf{T}^{-1}(\mathbf{U})) \tag{8}$$

where $\mathbf{T}^{-1}(\mathbf{U}) = \mathbf{X}$ is the inverse transformation from standard normal space to the original outcome space of the random variables. The transformation $\mathbf{T}$ is probability conserving, therefore $\Pr(F) = \Pr(g(\mathbf{X}) \leq 0) = \Pr(G(U) \leq 0)$. In analogy to Eq. (6), the probability of the failure event F is computed by

$$\Pr(F) = \int_{G(\mathbf{u}) \leq 0} \varphi(\mathbf{u}) \mathrm{d}u_1 \mathrm{d}u_2 \ldots \mathrm{d}u_n, \tag{9}$$

where φ is the independent standard multivariate normal probability density function (PDF).

A potentially highly efficient method for approximating the probability of failure is the First-Order Reliability Method (FORM). It approximates the limit state function $G(\mathbf{U})$ by a first-order Taylor expansion at the expansion point $\mathbf{u}^*$, denoted by $G'(\mathbf{U})$. To limit the approximation error, $\mathbf{u}^*$ is selected as the point in the failure domain with the highest probability density value, the most likely failure point (MLFP). The MLFP is found as the point in the domain $\{G'(\mathbf{U}) \leq 0\}$ closest to the origin (Der Kiureghian 2005). The probability $\Pr(G'(\mathbf{U}) \leq 0)$ is equal to the standard normal CDF Φ evaluated at $-\beta_{\text{FORM}}$, where $\beta_{\text{FORM}} = ||\mathbf{u}^*||$ is the distance of $\mathbf{u}^*$ from the origin (for values of $\Pr(G'(\mathbf{U}) \leq 0) < 0.5$). The FROM approximation is therefore

$$\Pr(F) \approx \Pr(G'(\mathbf{U}) \leq 0) = \Phi(-\beta_{\text{FORM}}). \tag{10}$$

The computational bottleneck of FORM is the identification of the design point $\mathbf{u}^*$ through the solution of a constrained geometrical optimization problem. Tailored algorithms exist for this purpose (Liu and Der Kiureghian 1991). Since these are gradient-based methods, the computational cost of the optimization increases with increasing number of dimensions n. FORM-based methods can nevertheless be applied for higher-dimensional problems (Rackwitz 2001; Allaix and Carbone 2015), and have also been shown to perform well for Bayesian updating problems (Straub et al. 2016).

As an alternative to FORM, in this contribution we apply subset simulation (SuS), a SRM that is tailored to work well for problems with larger numbers of random variables. SuS, originally developed in Au and Beck (2001), is an adaptive simulation method. It is based on expressing $\Pr(F)$ as a product of larger conditional probabilities. The conditional probabilities are defined in terms of a set of nested intermediate failure events $F_0 \supset F_1 \supset \cdots \supset F_M = F$, where F_0 denotes the certain event. The probability $\Pr(F)$ can be expressed as:

$$\Pr(F) = \Pr\left(\bigcap_{i=1}^{M} F_i\right) = \prod_{i=1}^{M} \Pr(F_i | F_{i-1}) \tag{11}$$

The intermediate events are defined in standard normal space as $F_i = \{G(\mathbf{U}) \leq b_i\}$, where $b_1 > b_2 > \cdots > b_M = 0$. The values of b_i are chosen adaptively such that the estimates of the conditional probabilities correspond to a chosen value p_0, where typically p_0 is chosen as 0.1. To find b_i, samples of $\mathbf{U}$ conditional on the intermediate failure event F_{i-1} are generated through a Markov Chain Monte Carlo (MCMC) sampling. While SuS can also work in the outcome space of $\mathbf{X}$, the definition of the problem in standard normal space is advantageous as it enables a simpler and efficient MCMC sampling, as shown in (Papaioannou et al. 2015).

2.3 Bayesian Analysis and Reliability Updating

With monitoring or inspections, data $\mathbf{d}$ becomes available, providing information directly or indirectly on the random variables $\mathbf{X}$ in the limit state function. This data can be used to update the prior probability distribution $f_{\mathbf{X}}$ to a posterior distribution $f_{\mathbf{X}|\mathbf{d}}$ following Bayes' rule:

$$f_{\mathbf{X}|\mathbf{d}}(\mathbf{x}) \propto L(\mathbf{x}) f_{\mathbf{X}}(\mathbf{x}) \tag{12}$$

$L(\mathbf{x}) = f_{\mathbf{D}|\mathbf{X}}(\mathbf{d}|\mathbf{x})$ is the likelihood function describing the data. The difficulty lies in the computation of the proportionality constant in Eq. (11). In most cases, analytical solutions are not available and sampling-based approaches are necessary instead (Gelman et al. 2014). MCMC methods are commonly applied for this task, resulting in (correlated) samples from $f_{\mathbf{X}|\mathbf{d}}$ (Beck and Au 2002; Ching and Chen 2007; Straub and Kiureghian 2008; Betz et al. 2016).

The updated probability of failure conditional on the data $\Pr(F|\mathbf{d})$ can – in principle – be calculated by evaluating Eq. (6) with $f_{\mathbf{X}}$ replaced by $f_{\mathbf{X}|\mathbf{d}}$. However, if $f_{\mathbf{X}|\mathbf{d}}$ is known only approximately through samples of the distribution, most structural reliability methods are not directly applicable to evaluate Eq. (6). Hence this approach, albeit seemingly straightforward, does not generally lead to efficient or simple solutions for computing $\Pr(F|\mathbf{d})$.

As an alternative to the direct method, (Straub and Papaioannou 2015), based on earlier ideas from (Straub 2011a), proposed the BUS (Bayesian Updating with SRM) method. It circumvents the problem by formulating an equivalent observation event Z describing the data, which can be used to perform Bayesian analysis within the framework of SRM. The observation event is defined as

$$Z = \{P \leq cL(\mathbf{X})\}, \tag{13}$$

where P is a random variable with standard uniform distribution, and c is a constant that is chosen to ensure that $cL(\mathbf{x}) \leq 1$ for any $\mathbf{x}$.

The observation event Z is equivalent to $\mathbf{d}$ in the sense that updating $\mathbf{X}$ with the event Z leads to the same posterior distribution as updating with $\mathbf{d}$, $f_{\mathbf{X}|Z} = f_{\mathbf{X}|\mathbf{d}}$, as shown in (Straub and Papaioannou 2015). Hence it follows that also $\Pr(F|Z) = \Pr(F|\mathbf{d})$.

The advantage of defining the data through Z is that this event can be represented by a limit state function

$$h(p, \mathbf{x}) = p - cL(\mathbf{x}), \tag{14}$$

such that $Z = \{h(P, \mathbf{X}) \leq 0\}$, in analogy to the definition of the failure event, Eq. (5).

The conditional probability of failure is (Madsen 1987)

$$\Pr(F|Z) = \frac{\Pr(F \cap Z)}{\Pr(Z)}, \tag{15}$$

which corresponds to solving two structural reliability problems:

$$\begin{aligned} \Pr(F|Z) &= \frac{\Pr[g(\mathbf{X}) \leq 0 \ \cap h(P, \mathbf{X}) \leq 0]}{\Pr[h(P, \mathbf{X}) \leq 0]} \\ &= \frac{\int_{g(\mathbf{x}) \leq 0 \ \cap h(p, \mathbf{x}) \leq 0} f_{\mathbf{X}}(\mathbf{x}) \mathrm{d}p \, \mathrm{d}x_1 \mathrm{d}x_2 \ldots \mathrm{d}x_n}{\int_{h(p, \mathbf{x}) \leq 0} f_{\mathbf{X}}(\mathbf{x}) \mathrm{d}p \, \mathrm{d}x_1 \mathrm{d}x_2 \ldots \mathrm{d}x_n} \end{aligned} \tag{16}$$

The numerator is a system reliability problem, whereas the denominator is a component reliability problem whose limit state function is Eq. (13).

In most cases, it is beneficial to solve Eq. (15) in standard normal space. The observation limit state function H in standard normal space is

$$H(\mathbf{u}) = u_0 - \Phi^{-1}\left(cL\left(\mathbf{T}^{-1}(u_1, \ldots, u_n)\right)\right). \tag{17}$$

with Φ^{-1} being the inverse standard normal CDF. U_0 is the standard normal random variable corresponding to P. The probability of the failure event F conditional on the data can now be expressed in terms of the standard normal $\mathbf{U}$:

$$\begin{aligned} \Pr(F|Z) &= \frac{\Pr[G(\mathbf{U}) \leq 0 \ \cap H(\mathbf{U}) \leq 0]}{\Pr[H(\mathbf{U}) \leq 0]} \\ &= \frac{\int_{G(\mathbf{u}) \leq 0 \ \cap H(\mathbf{u}) \leq 0} \varphi(\mathbf{u}) \mathrm{d}u_0 \mathrm{d}u_1 \ldots \mathrm{d}u_n}{\int_{H(\mathbf{u}) \leq 0} \varphi(\mathbf{u}) \mathrm{d}u_0 \mathrm{d}u_1 \ldots \mathrm{d}u_n} \end{aligned} \tag{18}$$

Any SRM is applicable to solve Eq. (15) or (17). Here, SuS is employed as it is efficient in high dimensions. In Eq. (17), the numerator is a subset of the denominator. This allows to reuse the samples generated in the last step of the computation of the denominator in the SuS run for computing the numerator, as described in (Straub et al. 2016).

The BUS algorithm implemented with SuS is illustrated in Fig. 1.

2.4 *Reliability Updating with Random Fields*

Application of BUS for reliability updating with random fields requires the solution of the integrals in Eq. (15), whereby both integrals are infinite dimensional because a random field consist of an infinite number of random variables. In practice, the random field is represented by a finite number of random variables through the

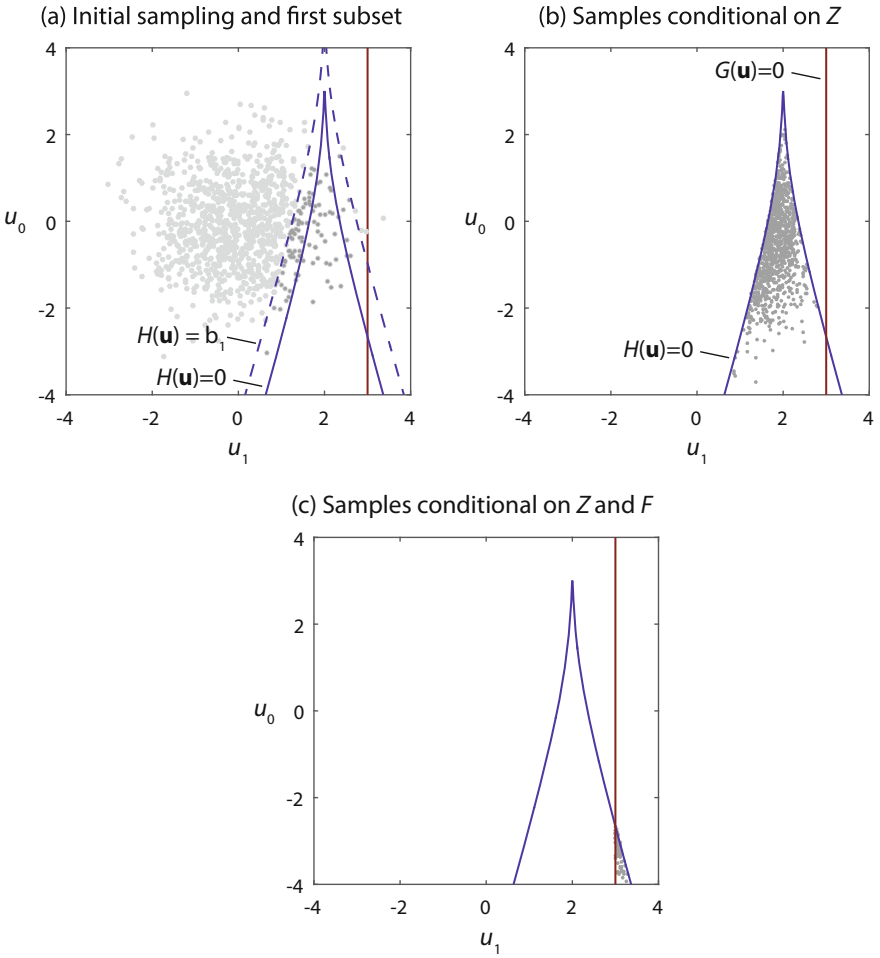

Fig. 1 Illustration of BUS with subset simulation: **a** Initial (Monte Carlo) sampling. The surface of the first subset is indicated with *dashed lines*. The *darker dots* correspond to the samples that fall into this subset and are used as seeds in the MCMC algorithm to generate the samples conditional on the first subset. **b** Samples generated conditional on the observation, $Z = \{H(U) \leq 0\}$. **c** Samples generated conditional on the observation and the failure event, $Z \cap F = \{H(U) \leq 0 \cap G(U) \leq 0\}$. These are the final samples

random field discretization, e.g. according to Eq. (2). If the random field is a translation field and the EOLE method is applied to discretize the underlying Gaussian random field, then the random variables in the discretization are already independent standard normal and a transformation to a standard normal space is not required.

If the variability of the random field is high, reflected by a small scale of fluctuation, then a large number of random variables will be needed to obtain a

small variance error in the EOLE representation. In such case, it is beneficial to apply a SRM that is able to handle efficiently high dimensional problems. In this study, SuS is employed for this purpose.

A main challenge when dealing with random fields in the context of Bayesian updating is the choice of the prior distribution. Prior distributions should reflect the knowledge available before the observations. Often there is uncertainty on the prior knowledge of the parameters of the marginal distribution F_X and/or covariance structure of the random field. This uncertainty can be included through introducing additional random variables. In Bayesian analysis, such random variables are termed hyperparameters to distinguish them from the parameters of the model of the underlying system. Once hyperparametes are included, the probabilistic description of the random field becomes conditional on outcomes of the hyperparameters. This implies that for each realization of the hyperparameters, the spatial functions in the EOLE representation will change. However, as discussed in Sect. 2.1, EOLE is particularly efficient in obtaining the spatial functions, as the assembly of the matrix eigenvalue problem of Eq. (3) can be done in an efficient manner.

If the spatial covariance structure of the random field is represented by means of hyperparameters, the error measure in Eq. (4) depends on the realization of the hyperparameters. A constant (small) error that is independent of the realization of the hyperparameters can only be achieved if the number of EOLE-terms (and, thus, the number of random variables) is selected conditional on the hyperparameters. However, inference algorithms typically require the number of random variables to be constant throughout the analysis. To avoid this problem, the number of EOLE-terms is selected conservatively in this study, by choosing a number of EOLE terms that leads to an acceptable discretization error for most realizations of the hyperparameters. Thereby, it is necessary to verify that for the prior covariance structure with high posterior density the error term is still acceptable.

It is noted that a-posteriori the first- and second-order statistics of the random field will differ from the ones prior to the measurements. For instance, a random field that is second-order homogeneous a-priori will no longer be homogeneous a-posteriori, because of the influence of the locality of the measurements. If the spatial variability of the random field increases considerably conditional on the measurements, the number of random variables in the random field representation of the prior random field might not be sufficient for representing the posterior field. The posterior representation of the random field should therefore be carefully checked.

3 Numerical Investigations

3.1 Problem Description

We consider a problem from geotechnical engineering: The stability of an eccentrically loaded foundation is investigated. Serviceability of the foundation is ensured if the inclination α of the foundation under the final loading P is smaller

than 4 degrees; i.e. the limit-state function describing the associated reliability problem is: $g(\mathbf{X}) = 4° - \alpha(\mathbf{X})$. The foundation is bedded on a soil layer that has a depth of 8 m. The soil is modeled as linear elastic, with a Young's modulus E that is spatially variable, hence described by random field, and a fixed Poisson ratio of 0.35. Beneath the soil layer, a sandstone layer is located, whose influence on the analysis is negligible.

The investigated foundation has a width of 1.5 m; after construction it is loaded eccentrically with load P (Fig. 2). The lever arm of the load is 0.5 m. The load P is uncertain: it follows a Gumbel distribution with mean 1MN and 10% coefficient of variation. At an intermediate construction stage, a centric load F of 0.4MN is applied. The displacements under F at the left and right ending of the foundation are measured $\hat{x}_l = 1$ cm and $\hat{x}_r = 1.5$ cm, see Fig. 2. We utilize an additive model for the combined measurement/modeling errors; the error follows a normal distribution with zero mean and a standard deviation of $\sigma_\varepsilon = 0.5$ cm. The errors associated with $\hat{x}_l$ and $\hat{x}_r$ are correlated with a correlation coefficient of $\rho = 0.9$. It is therefore implied that modeling errors are dominating over measurement errors.

The Young's modulus E of the soil layer is modeled as lognormal random field with a mean of 40 MPa and a coefficient of variation of 50%. The correlation coefficient function between points $\mathbf{t}_1$ and $\mathbf{t}_2$ of the underlying Gaussian random field is $\rho(\Delta\mathbf{t}) = \exp\left(-\sqrt{\Delta t_x^2 + \Delta t_z^2}/l\right)$, where Δt_x and Δt_z are the horizontal and vertical distance between points $\mathbf{t}_1$ and $\mathbf{t}_2$, and l is the correlation length. The correlation length l is modeled as uncertain. As prior distribution for l we select a lognormal distribution that has mean 4 m and a coefficient of variation of 100%.

On each side of the foundation, a soil-stripe of 15 m is modeled explicitly. The random field is discretized using the EOLE method. The EOLE discretization points are distributed uniformly over the domain with 25 points per square meter. The 200 most important terms in EOLE are used to represent the random field.

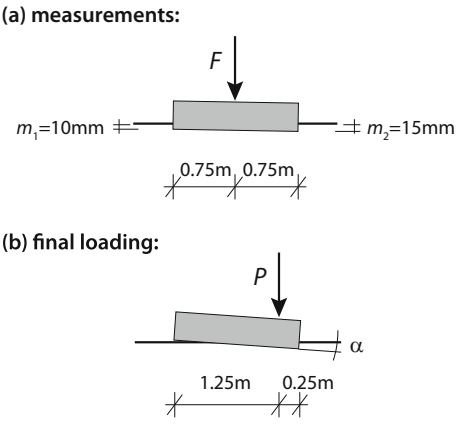

Fig. 2 Loading of the foundation (**a**) during the measurements and (**b**) in the final state

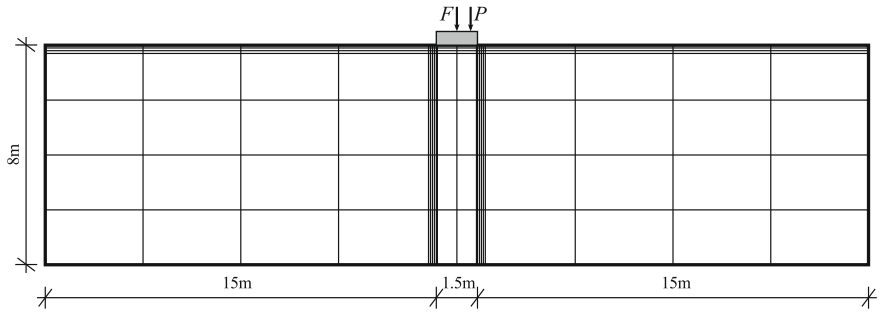

Fig. 3 Finite element mesh used to discretize the soil in the mechanical model: the order of the shape functions is 4

The mechanical model is discretized and solved by means of higher-order finite elements (Szabó et al. 2004). The finite element mesh of the mechanical model is depicted in Fig. 3. The order of the shape functions of the mechanical model is 4.

Samples of the posterior are obtained by means of BUS-SuS with 1000 samples per level. The posterior probability of failure is obtained by an additional run of SuS with 1000 samples per level using the generated posterior samples as basis. Samples of the prior are generated directly. The two computationally challenging tasks are (i) the discretization of the prior random field conditional on the current value of the hyperparameters, and (ii) the computation of the finite element model. In the example at hand, the computational costs of the random field discretization dominate the overall computational costs.

3.2 Results and Discussion

The prior probability of failure is 10^{-2}. The posterior probability of failure conditional on the settlement measurements $\hat{x}_l$ and $\hat{x}_r$ is $3 \cdot 10^{-4}$. The probability of failure estimate is therefore significantly reduced by the measurements performed at the intermediate construction stage.

To further investigate the effect of the measurement on the random variables and the failure event, Table 1 provides mean values and standard deviations of the final load P, correlation length[1] l, and inclination and center settlement of the foundation at final loading under different information. The prior case is compared to different posterior cases: (m) conditional on the measurement, (F) conditional on failure of the foundation (without measurement), and (m&F) conditional on measurement and

[1]Note that the correlation length is defined only for the a-priori case, when the random field is stationary. Strictly, l is the hyperparameter representing the correlation length of the prior random field.

Table 1 Mean values and standard deviations of final load P, correlation length l, and inclination and center settlement of the foundation at final loading. Values are provided for the prior case and different posterior cases: conditional on measurements (m), conditional on failure of the foundation (F) and conditional on a combination of both

	Mean				Standard deviation			
	Prior	Posterior			Prior	Posterior		
		m	F	m&F		m	F	m&F
Final load P	1	1	1.07	1.22	0.1	0.1	0.13	0.16
Corr. length l	4	3.4	6	2.7	4	3.1	4.9	1.5
Inclination (final stage)	1.7	1.7	4.7	4.3	0.7	0.5	0.8	0.3
Final center displ. (final)	4.3×10^{-2}	4.0×10^{-2}	9.8×10^{-2}	7.6×10^{-2}	1.4×10^{-2}	8.9×10^{-3}	2.0×10^{-2}	7.8×10^{-3}

failure. The statistics conditional on failure provide an indication of the parameter values in a failure case, similar to the design point in a FORM analysis.

As expected, the distribution of the final load P is not influenced by measuring displacements in the intermediate construction stage (the m case). However, the mean of P in the case of failure without measurement is lower than in the case with

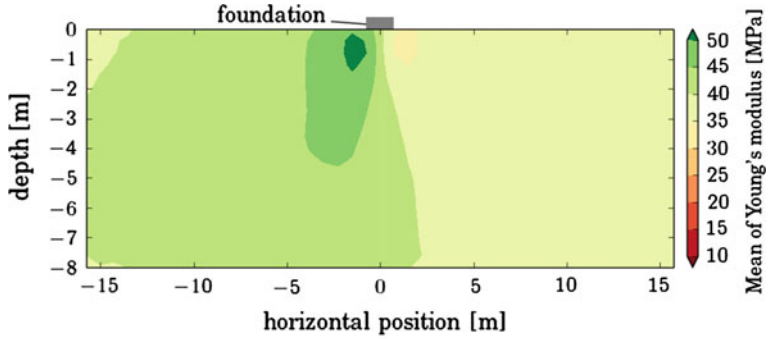

(a) conditional on measurements

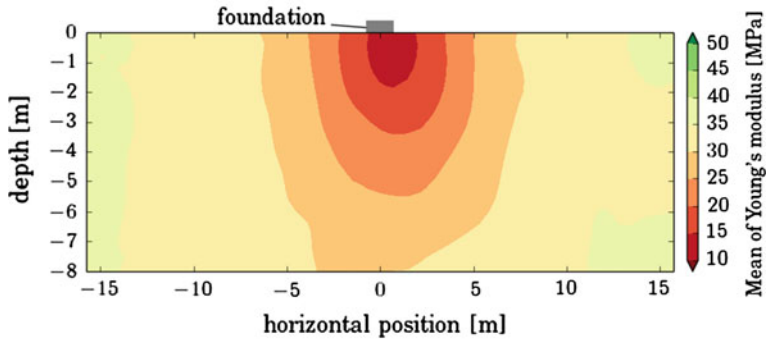

(b) conditional on foundation failure

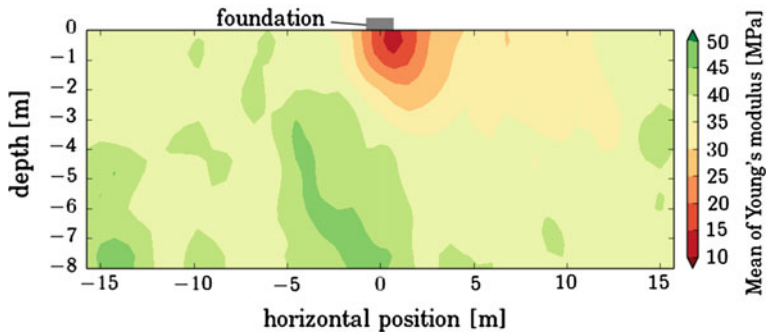

(c) conditional on measurements and foundation failure

Fig. 4 Expected values of the soil stiffness for the three different posterior cases

measurements. Since the measurements reduce the probability of failure, a larger value of P is required in this case to lead to failure.

The expected correlation length l is decreased by the performed measurements. Interestingly, without measurements, larger correlation lengths are associated with failure, whereas smaller correlation lengths are associated with failure once

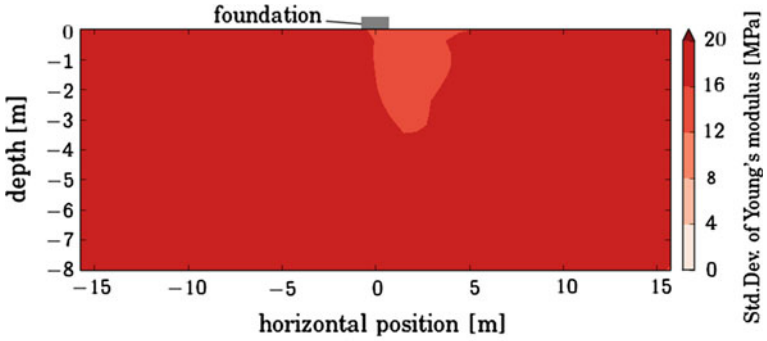

(a) conditional on measurements

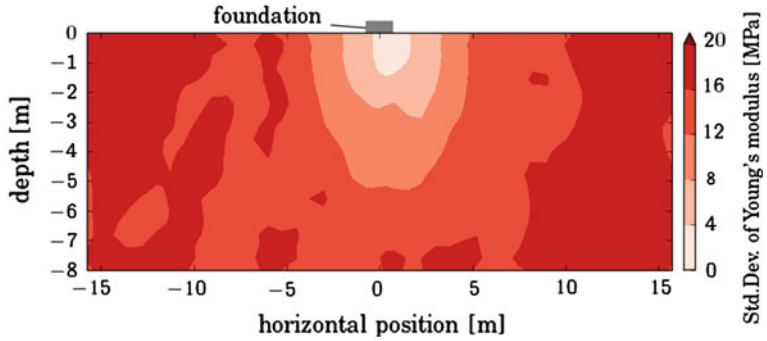

(b) conditional on foundation failure

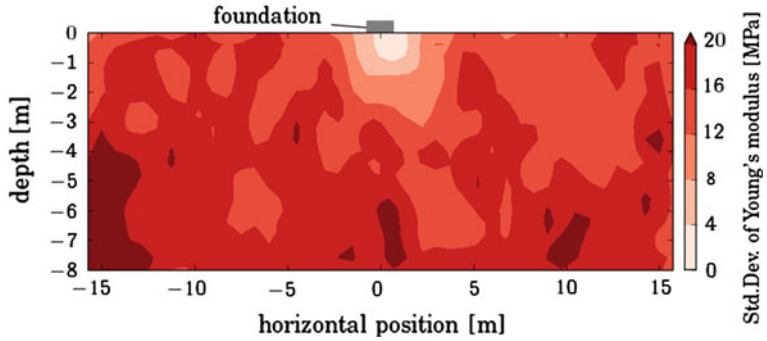

(c) conditional on measurements and foundation failure

Fig. 5 Standard deviation of the soil stiffness for the three different posterior cases

measurements are considered. This indicates that without the measurements, the foundation is expected to fail due to a globally reduced soil stiffness. In contrast, after the measurements are performed, failure is expected as a consequence of a locally reduced soil stiffness.

Even though the measurements clearly reduce the probability of failure, the expected inclination and the expected center settlement of the foundation under final loading are only marginally influenced by the observations. This shows that the main reason for a reduction in the probability of failure is the reduced uncertainty on the soil parameters.

The mean value of the soil stiffness is plotted in Fig. 4 for the three posterior cases. The corresponding standard deviations are illustrated in Fig. 5. The measurements performed at the intermediate construction stage suggests that the stiffness of the soil under the foundation is slightly larger on the left-hand side of the foundation than on the right-hand side (Fig. 4a). Conditioning on failure without the measurements, the expected stiffness of the soil is reduced beneath the foundation with a small shift to the right that increases the inclination of the foundation (Fig. 4b). When conditioning on failure including the measurements, the expected stiffness of the soil suggests a weak spot below the right side of the foundation (Fig. 4c).

The plots of the standard deviations (Fig. 5) show that the standard deviation is primarily reduced in the areas where the mean stiffness changes from the prior to the posterior. These are the areas for which the conditioning on the deformation measurements provides information.

4 Concluding Remarks

Bayesian analysis and reliability updating is a consistent and potentially powerful method to incorporate and combine different information sources for predicting the performance of an engineering system. In many instances, spatially varying properties in these systems should be explicitly represented through random fields. This can lead to potentially demanding computations, and efficient methods for random field discretization are required. In this contribution, we discuss that the EOLE method is beneficial if the analysis includes a random field with an uncertain covariance structure. In these cases, the random field representation will alter in function of the covariance structure, and the efficiency of EOLE in obtaining an approximation of the random field leads to overall reduced computational effort. For Bayesian analysis we apply the BUS approach, which enables the use of classical structural reliability methods to compute the posterior distribution and reliability. The procedure is applied to the updating of the reliability of a shallow foundation with results from displacement measurements. Numerical results show that the reliability estimate can be significantly lowered by including such measurements even if the posterior mean estimates of the soil properties are not more favourable than a-priori, due to the reduction of the uncertainty. Closer

investigation showed that the consideration of the uncertainty in the covariance structure of the random field leads to significant changes in the likely failure modes from the a-priori to the posterior case.

References

Allaix D, Carbone V (2015) An efficient coupling of FORM and Karhunen–Loève series expansion. Eng Comput 1–13

Au S-K, Beck JL (2001) Estimation of small failure probabilities in high dimensions by subset simulation. Probab Eng Mech 16(4):263–277

Beck JL, Au SK (2002) Bayesian updating of structural models and reliability using Markov chain Monte Carlo simulation. J Eng Mech Asce 128(4):380–391

Bensi M, Der Kiureghian A, Straub D (2015) Framework for post-earthquake risk assessment and decision making for infrastructure systems. ASCE-ASME J Risk Uncertain Anal 1 (2):04014003

Betz W, Papaioannou I, Straub D (2014) Numerical methods for the discretization of random fields by means of the Karhunen-Loève expansion. Comput Methods Appl Mech Eng 271:109–129

Betz W, Papaioannou I, Straub D (2016) Transitional markov chain monte carlo: observations and improvements. J Eng Mech 142(5):04016016

Ching J, Chen Y (2007) Transitional markov chain monte carlo method for bayesian model updating, model class selection, and model averaging. J Eng Mech 133(7):816–832

Der Kiureghian, A. (2005). First- and second-order reliability methods. In: Nikolaidis E, Ghiocel DM, Singhal S (eds) Engineering design reliability handbook. CRC Press, Boca Raton, FL

Der Kiureghian A, Ditlevsen O (2009) Aleatory or epistemic? Does it matter? Struct Saf 31 (2):105–112

Der Kiureghian A, Liu P-L (1986) Structural reliability under incomplete probability information. J Eng Mech 112(1):85–104

Ellingwood BR (1996) Reliability-based condition assessment and LRFD for existing structures. Struct Saf 18(2–3):67–80

Faber MH, Sorensen JD, Tychsen J, Straub D (2005) Field implementation of RBI for jacket structures. J Offshore Mech Arctic Eng Trans Asme 127(3):220–226

Gelman A, Carlin JB, Stern HS, Rubin DB (2014) Bayesian data analysis. Taylor & Francis

Ghanem RG, Spanos PD (1991) Stochastic finite elements: a spectral approach. Springer, New York

Goulet J-A, Der Kiureghian A, Li B (2015) Pre-posterior optimization of sequence of measurement and intervention actions under structural reliability constraint. Struct Saf 52:1–9

Hohenbichler M, Rackwitz R (1981) Non-normal dependent vectors in structural safety. J Eng Mech Div Asce 107(6):1227–1238

Kiureghian AD (1989) Measures of structural safety under imperfect states of knowledge. J Struct Eng 115(5):1119–1140

Koutsourelakis P-S (2009) A multi-resolution, non-parametric, Bayesian framework for identification of spatially-varying model parameters. J Comput Phys 228(17):6184–6211

Li C-C, Der Kiureghian A (1993) Optimal discretization of random fields. J Eng Mech 119 (6):1136–1154

Liu P-L, Der Kiureghian A (1991) Optimization algorithms for structural reliability. Struct Saf 9:161–177

Madsen, H. O. (1987). Model updating in reliability theory. In: ICASP 5, International Conference on Applications of Statistics and Probability in Soil and Structures. Vancouver, p 565–577

Madsen HO, Sørensen JD, Olesen R (1989) Optimal inspection planning for fatigue damage of offshore structures. In: Proceedings of the 5th International Conference on Structural Safety and Reliability

Marzouk YM, Najm HN, Rahn LA (2007) Stochastic spectral methods for efficient Bayesian solution of inverse problems. J Comput Phys 224(2):560–586

Nataf A (1962) Statistique mathematique-determination des distributions de probabilites dont les marges sont donnees. Comptes Rendus Hebdomadaires des Seances de l' Academie des Sciences 255(1):42

Papaioannou I, Betz W, Zwirglmaier K, Straub D (2015) MCMC algorithms for subset simulation. Probab Eng Mech 41:89–103

Papaioannou I, Straub D (2012) Reliability updating in geotechnical engineering including spatial variability of soil. Comput Geotech 42:44–51

Papaioannou I, Straub D (2016) Learning soil parameters and updating geotechnical reliability estimates under spatial variability – theory and application to shallow foundations. Georisk (Under review)

Pozzi M, Der Kiureghian A (2011) Assessing the value of information for long-term structural health monitoring. In: SPIE Smart Structures and Materials+ Nondestructive Evaluation and Health Monitoring, International Society for Optics and Photonics

Rackwitz R (2001) Reliability analysis—a review and some perspectives. Struct Saf 23(4): 365–395

Rackwitz R, Fiessler B (1978) Structural reliability under combined random load sequences. Comput Struct 9(5):489–494

Straub D (2011a) Reliability updating with equality information. Probab Eng Mech 26(2):254–258

Straub, D. (2011b). Reliability updating with inspection and monitoring data in deteriorating reinforced concrete slabs. In: Proceedings of 11th International Conference on Applications of Statistics and Probability in Civil Engineering (ICASP)

Straub D, Der Kiureghian A (2011) Reliability Acceptance Criteria for Deteriorating Elements of Structural Systems. J Struct Eng ASCE 137(12):1573–1582

Straub D, Kiureghian AD (2008) Improved seismic fragility modeling from empirical data. Struct Saf 30(4):320–336

Straub D, Papaioannou I (2015) Bayesian updating with structural reliability methods. ASCE J Eng Mech 141(3):04014134

Straub D, Papaioannou I, Betz W (2016) Bayesian analysis of rare events. J Comput Phys 314:538–556

Sudret B, Der Kiureghian A (2000) Stochastic finite elements and reliability—a state-of-the-art report. Department of Civil & Environmental Engineering, University of California, Berkeley

Szabó B, Düster A, Rank E (2004) The p-version of the finite element method. Encyclopedia of computational mechanics

Vanmarcke E (2010). Random fields: analysis and synthesis. Wiley, Hoboken

Zhang J, Ellingwood B (1994) Orthogonal series expansions of random fields in reliability analysis. J Eng Mech 120(12):2660–2677

Bayesian Networks and Infrastructure Systems: Computational and Methodological Challenges

Francesco Cavalieri, Paolo Franchin, Pierre Gehl and Dina D'Ayala

Abstract This chapter investigates the applicability of Bayesian Network methods to the seismic assessment of large and complex infrastructure systems. While very promising in theory, Bayesian Networks tend to quickly show limitations as soon as the studied systems exceed several dozens of components. Therefore a benchmark study is conducted on small-size virtual systems in order to compare the computational performance of the exact inference of various Bayesian Network formulations, such as the ones based on Minimum Link Sets. It appears that all formulations present some computational bottlenecks, which are either due to the size of Conditional Probability Tables, to the size of clique potentials in the junction-tree algorithm or to the recursive algorithm for the identification of Minimum Link Sets. Moreover, these formulations are limited to connectivity problems, whereas the accurate assessment of infrastructure systems usually requires the use of flow-based performance indicators. To this end, the second part of the chapter introduces a hybrid approach that presents the merit of accessing any type of system performance indicator: it uses simulation-based results and generates the corresponding Bayesian Network by counting the outcomes given the various combinations of events that have been sampled in the simulation. The issue of the system size is also addressed by a *thrifty-naïve* formulation, which limits the number of the components that are involved in the system performance prediction, by applying a cut-off threshold to the correlation coefficients between the components and system states. A higher resolution of this *thrifty-naïve* formulation is also obtained by considering local performance indicators, such as the flow at each sink. This approach is successfully applied to a realistic water supply network of 49 nodes and 71 pipes. Finally the potential of this coupled simulation-Bayesian

F. Cavalieri · P. Franchin (✉)
Department of Structural Engineering and Geotechnics, University of Rome "La Sapienza", Via Antonio Gramsci 53, 00197 Rome, Italy
e-mail: paolo.franchin@uniroma1.it

P. Gehl · D. D'Ayala
Department of Civil, Environmental and Geomatic Engineering, University College London (UCL), London WC1E 6BT, UK

P. Gardoni (ed.), *Risk and Reliability Analysis: Theory and Applications*,
Springer Series in Reliability Engineering, DOI 10.1007/978-3-319-52425-2_17

approach as a decision support system is demonstrated, through probability updating given the observation of local evidences after an event has occurred.

1 Introduction

Damage to infrastructure systems reduces their functionality, hindering emergency response as well as normal operations. While vital societal functions (housing, education, production, etc.) are mostly carried out within buildings, or primary systems, these cannot work properly without support from infrastructure, or secondary, systems, which allow movement of goods, services and people (Mieler et al. 2013, 2015).

Research into risk and resilience of infrastructure systems spans across the modeling of the multiple hazards that can hit them, the vulnerability of their components to each or multiple hazards (Gehl and D'Ayala 2015), the systemic consequences of components damage, eventually including cascading effects. The scope of the studies varies from simple risk assessment, the evaluation of the impact of a hazard, to more complex resilience analysis, considering recovery of performance over time, possibly including conventional aging and multiple shocks (Kumar and Gardoni 2014a; Kumar et al. 2015). Moreover, the time horizon is not the only varying factor. Most studies either consider the impact of a future occurrence of a hazard, i.e. they try to forecast for the purpose of planning mitigation and risk-reduction measures (Kumar and Gardoni 2014b), or they perform back-analyses considering past occurrences of hazards to calibrate models (e.g. Cimellaro et al. 2014; Kajitani and Tatano 2009).

Considerably less effort has been put into studying the much more challenging problem of dealing with the hazard in real-time, while it occurs or in the immediate aftermath. The main and most consequential difference between this condition and the previous ones is that information and thus uncertainty is continuously changing and, thus, estimates must be continuously updated in order to support informed decision-making. In this context Bayesian Networks (BNs) have emerged as the tool of choice to provide possible solutions. Bensi et al. (2014) have recently provided a framework, for the seismic hazard case, that integrates BNs with influence diagrams and decision theory. Without entering into the realm of decision-making, this chapter explores some of the challenges that seem to delay adoption of BN for dealing with infrastructure problems of realistic size and complexity. In particular, two such challenges are related to: (a) the computational effort associated with realistically sized networks and (b) the difficulty of describing networked system behavior with physical flow-related performance metrics rather than with simple connectivity ones, in the context of BNs.

While computational effort is a major concern in all types of applications and especially in one that aspires to be performed in real-time, like Bayesian inference in the framework of decision-support systems, the second aspect, i.e. the capability of handling flow-based performance measures is one of conceptual nature. It is

important to state clearly the difference between maximum flow (max-flow) considered in Operations Research theory and the actual physically-driven flows considered herein. Consideration of the latter is paramount in the analysis of infrastructure systems (in particular lifelines), in which tolerance on amount and quality of service to end-users for maintaining serviceability is generally quite low. For instance, most electric appliances do not work if they receive power (i.e. they are connected to some source even in the damaged network) at a voltage lower than about 90–95% of their working range. This results in connectivity-based methods to be unsuitable for the analysis of such systems. Relying on connectivity or computing flows can give a different picture of the actual network performance (Hong et al. 2015). Further, and very relevant to Bayesian inference applications, physical flows can be measured locally and represent excellent evidence, while loss of connectivity or interruption of a source-sink path requires analysis of the network and knowledge of the state of all involved components.

The above two aspects have thus been investigated with reference to two different approaches to systems modeling:

- A number of Minimum Link Set (MLS) formulations of increasing efficiency presented in Bensi et al. (2013), particularly effective but apparently confined to the treatment of connectivity-only problems, and denoted as Option 1 in the following;
- An alternative approximate simulation-based approach, proposed herein and denoted in the following as Option 2, to derive the BN structure and the conditional probability tables (CPTs) from an off-line simulation, implemented using a recently developed open-source infrastructure systems simulation platform (Franchin and Cavalieri n.d., see Sect. 4.2).

2 BN Model of Seismic Hazard

While this chapter focuses on challenges associated with BN modeling of infrastructure systems, a complete BN model including the portion describing the distributed seismic hazard impacting the system was considered, in order to carry out numerical applications.

The distributed seismic hazard model by Bensi et al. (2011) was adopted and used to compare Options 1 and 2. Within such model, sketched in Fig. 1a, an event is described in terms of magnitude and epicenter, while local intensity at each site of interest is modeled by means of a ground motion prediction equation (GMPE), with total variability around the log-mean split between the intra-event and the inter-event model error terms. No amplification is considered and thus the intensity of motion at the surface coincides with the bedrock one.

This model differs from the hazard model included in the simulation platform used to inform BN building according to Option 2 (see below in Sect. 4). The latter is the one developed within the EU-funded collaborative research project

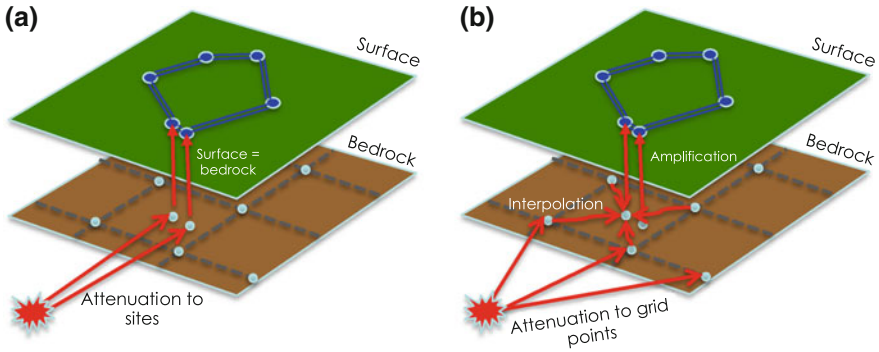

Fig. 1 Sketch of the seismic hazard model: **a** in Bensi et al. 2011, **b** developed in SYNER-G (2012)

SYNER-G (2012), and described in Weatherill et al. (2014). Within such model an event is also generated in terms of magnitude and epicenter (see Fig. 1b), and a GMPE is used to model local intensity, on rock/stiff-soil conditions, but the intensity measure (IM) is predicted at the points of a regular grid that covers the entire study region, thus obtaining a *shake field*. This IM, incorporating the spatial correlation between intra-event residuals at grid points, is then interpolated at each vulnerable component's site from the four closest grid points. The IM values at bedrock are then amplified to obtain surface intensities at the sites of interest. Since the platform is conceived to handle multiple interconnected infrastructural systems and components usually have different fragility models, taking as input different IMs, a number of *secondary* IMs at each site can be finally predicted through a within-site cross-IM correlation model.

In sum, the differences between the implemented seismic hazard BN model (based on Bensi et al. 2011) and the SYNER-G one included in the simulation platform are that in the former (i) no IM interpolation occurs, (ii) no bedrock-surface amplification occurs, and (iii) only one IM is considered. In practice, these differences have been removed by carrying out the simulations used to inform BN building in Option 2 switching off bedrock-surface amplification, and using a seismic grid size of just 500 m, so that the computed IM at the generic site of interest practically coincides with the IMs at the four closest points (in turn, very similar to each other).

For the sake of illustration, Fig. 2 shows the BN portion related to the distributed seismic hazard according to the implemented model, with reference to a trivial five-component system (see Sect. 3, Fig. 5). The log-mean of the intensity for the i-th vulnerable component, $\overline{S}_i$, is retrieved through the adopted GMPE from magnitude M, epicenter location Epi, and source-to-site distance R_i. Correlations between intra-event residuals ε_i are approximated with a Dunnett-Sobel class of Gaussian random variables, U and V_i (Dunnett and Sobel 1955). The logarithm of the intensity, S_i, is obtained as a function of $\overline{S}_i$, ε_i and the inter-event residual η,

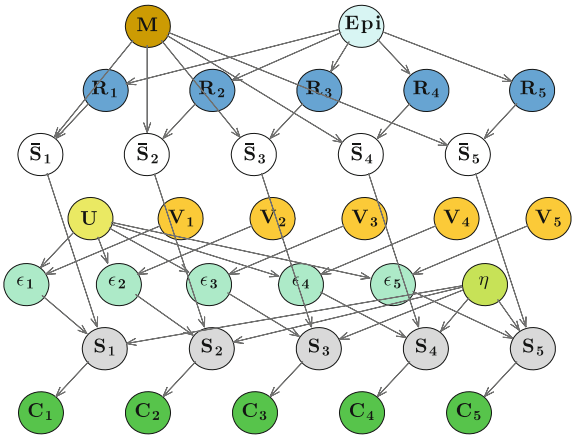

Fig. 2 BN model of distributed seismic hazard, applied to a five-component example system

which is common to all sites. Finally, the C nodes in Fig. 2 represent the damage state of the five components in the system, as a (fragility) function of seismic intensity.

The graphical representation is done with a custom modification of the Bayes Net Toolbox for MATLAB (Murphy 2001), which is used throughout this work to create a BN starting from a given directed acyclic graph (dag) and to perform inference.

3 MLS-Based Approach

Expressing the system performance from all possible combinations of component states constitutes the main computational bottleneck of the BN framework. The most intuitive strategy consists in building a converging BN structure that links all components to a single system node: however, this naïve formulation leads to an exponential increase of the CPT size, which makes inference unfeasible for real-life systems. Therefore Bensi et al. (2013) have introduced BN formulations based on minimum link sets (MLSs), or minimum cut sets (MCSs), in order to decompose a given system into parallel of series sub-systems, or a series of parallel sub-systems. This decomposition enables the application of parallel and series Boolean rules, which can be sequentially assembled into a chain structure instead of the naïve converging structure.

The first step of the MLS-based approach consists in the identification of the MLSs or MCSs of a given system. In the present study, the MLS formulation has been adopted in the applications, while the use of MCSs follows the same principles. A recursive algorithm for finding all the minimal link sets (MLSs) of a system has been implemented and is summarized in Fig. 3. Currently, only edges (representing for instance pipes in water supply systems) can be considered as

Algorithm 1 Finds all MLSs for a source-sink connection in a network

```
1: procedure MLSSEARCH(G, O, D)   ▷ graph G = (V, E), source O, sink D
2:     G* ← G
3:     while path(G*, O, D) exists do      ▷ Until enough edges are removed
4:         p ← shortestPath(G*, O, D)
5:         mls ← (mls, p)
6:         G* ← remove(e ∈ p, G*)          ▷ remove edge e
7:     return mls
```

Fig. 3 Flow chart of the MLS-search algorithm

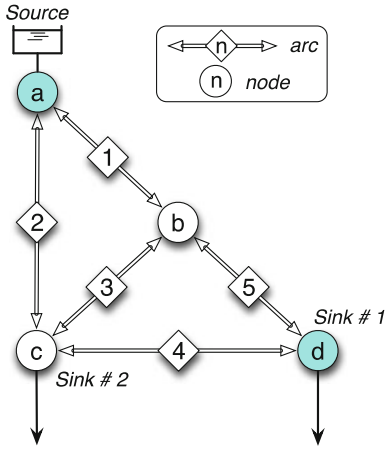

Fig. 4 Five-component example system: only the edges are considered to be vulnerable

vulnerable components. However, the extension of the algorithm to vulnerable nodes is straightforward.

The construction of the BN structure for different levels of the MLS formulation is demonstrated through a trivial water supply system (see Fig. 4). One source is supposed to service two sinks through a system of five vulnerable pipes that are assumed to be undirected. The system metric that is chosen here is the connectivity between the source and sink #1 (i.e. nodes *a* and *d*). Four MLSs are identified between *a* and *d* thanks to the recursive algorithm: {2–4}, {1–5}, {1–3–4} and {2–3–5}.

For comparison purposes, the naïve formulation for this straightforward example is presented in Fig. 5: with five binary components, the CPT for the system node already contains 2^{5+1} elements.

Thanks to the identification of the MLSs, intermediate nodes representing the MLSs can be introduced, as shown in Fig. 6. Fewer component nodes are now contributing to the converging structure of each MLS. However, in the case of larger systems where numerous components might be included in some MLSs, this BN structure would also end up to be limited by the size of CPTs.

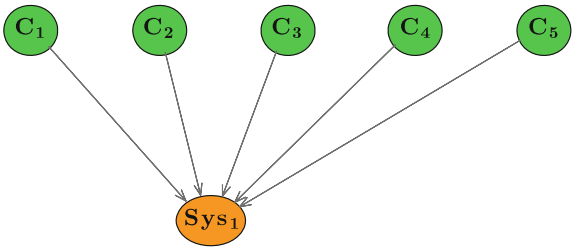

Fig. 5 Naïve formulation for the example system (only system shown, no hazard)

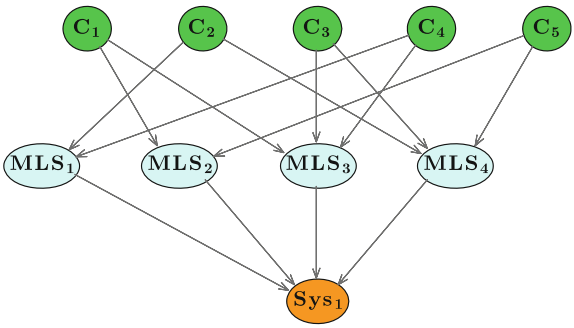

Fig. 6 MLS formulation for the example system

Therefore a second level of the MLS formulation is defined by adopting a chain structure to assemble the MLSs. This efficient MLS formulation uses survival path events (SPEs), which are referred to as "E_S" nodes in the graphs (see Fig. 7). When assembled in chain, they are able to represent each MLS as a survival path sequence. Each SPE is the child of a component node and/or one or more SPE node(s): at each stage of the survival path sequence, it is used to check whether the sequence is still surviving when an additional component is included. While the efficient MLS formulation is useful to reduce the number of parents and the size of CPTs, it tends to generate a large number of SPE nodes when a given component is contributing to a large amount of MLSs: for each participation of a component to a MLS, a new instance of SPE has to be created, thus resulting in ten SPE nodes for five components in the example system.

Therefore a more advanced level of the MLS formulation has been proposed by Bensi et al. (2013), where the SPE chains are coalesced across the different MLSs. The construction of the coalesced BN structure is based on the following steps:

- Assume that the number of instances of each SPE cannot exceed a given value N_i (e.g. start with $N_i = 1$).
- Optimize the connectivity structure between the SPE nodes from all possible permutations. The objective is to obtain a solution with the lowest number of edges.
- The solution must satisfy two constraints: (a) each MLS must be represented by a survival path sequence and (b) each survival path sequence that is defined by the connectivity matrix must correspond to a MLS.

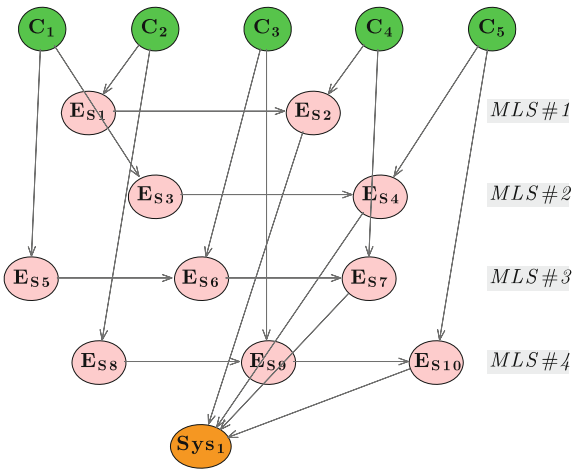

Fig. 7 Efficient MLS formulation with survival path sequences, for the example system

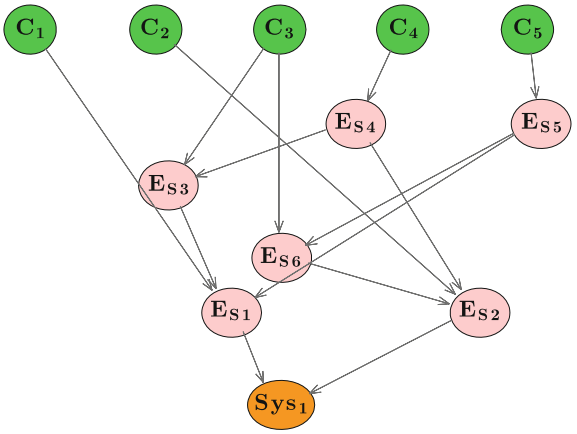

Fig. 8 Efficient MLS formulation with coalesced SPEs, for the example system

- If no adequate solution is found, the optimization procedure is repeated with a higher number of SPEs instances (i.e. $N_i \rightarrow N_i + 1$).

Bensi et al. (2013) have also proposed two additional heuristics in order to reduce the space of the optimization problem. The first one consists in the creation of super-components, which are groups of components that can be assembled in series or in parallel depending on their respective contributions to the MLSs. The second heuristic identifies groups of components that contribute to several MLSs in order to lock their permutation order, thus reducing the size of the optimization space.

This optimization algorithm with the two heuristics has been implemented and applied to the example system. The efficient MLS formulation with coalesced survival path sequences is presented in Fig. 8, where only six SPEs are used (i.e. two SPE instances are required to represent component "C_3").

Table 1 Size and complexity of the various BN structures for the example system

Formulation	# of nodes	# of edges	Max. CPT size
Naïve	6	5	64
MLS	10	14	32
Efficient MLS	16	20	32
Efficient MLS (coalesced)	7	14	16

While the coalesced SPE chains help to drastically reduce the number of nodes in the BN structure, it should be noted that the size of optimization problem increases exponentially with the number and sizes of MLSs. As a result, a significant computation time is spent on the optimization process before the BN inference is performed.

The various modeling approaches are compared in Table 1, with respect to the considered example system.

3.1 Compression Algorithm

As an alternative to the MLS-based formulation, Tien and Der Kiureghian (2015) have introduced a compression algorithm that is applied to the system CPT when the naïve formulation is used. The authors take advantage of the repeating structure of the CPT to jointly apply two compression methods:

- Algorithm 1: representation of the data by consecutive bits of the same value (i.e. runs).
- Algorithm 2: for mixed values that cannot be efficiently compressed for algorithm 1, a Lempel-Ziv algorithm (Ziv and Lempel 1977) based on the encoding of recurring phrases is applied.

In the example provided by Tien and Der Kiureghian (2015), only system and component nodes are considered, without the hazard assessment part. Consequently, these variables belong to a single clique and the variable elimination algorithm is used to perform the inference. This enables to sequentially update the compressed CPT when a variable is eliminated. The authors have shown that the memory storage space only increases linearly with the compression algorithm, whereas the computation time due to the compression operations has an exponential rate with respect to the number of components. Tien and Der Kiureghian (2015) have partially solved the computational time issue through a careful ordering of the component variables within the system CPT and by taking advantage of single-component MLSs.

However, the compression algorithm has only been demonstrated for a trivial BN structure where the hazard assessment has been left out: in the case of more generic systems, such as the ones presented in this study, the variable elimination algorithm may not be used anymore and the ordering of the variables becomes less

transparent. Moreover, seismic intensity nodes have to be added to the clique containing the system nodes, which may complicate the structure of the table of potentials and dramatically reduce the efficiency of the compression algorithm. It is also unclear how sum and product operations can be performed on the compressed matrices without requiring preliminary decompression/recompression operations. Therefore the compression algorithm approach has not been considered in the following benchmark, pending further investigation of the aforementioned issues.

3.2 Application to a Water Supply Network

The most efficient MLS approach, based on the coalescence of SPE chains, was tested with reference to a small academic example network, taken from Kang and Lee (2015). The network is a water supply system (WSS) composed of seven nodes, two of which are water sources and one is a sink or demand node (see Fig. 9). The eleven edges (pipes) are the only vulnerable components. The only seismic source, whose activity parameters are indicated in Fig. 9, is discretized into 12 epicenter locations (that will be the 12 possible states of the "Epi" node in the

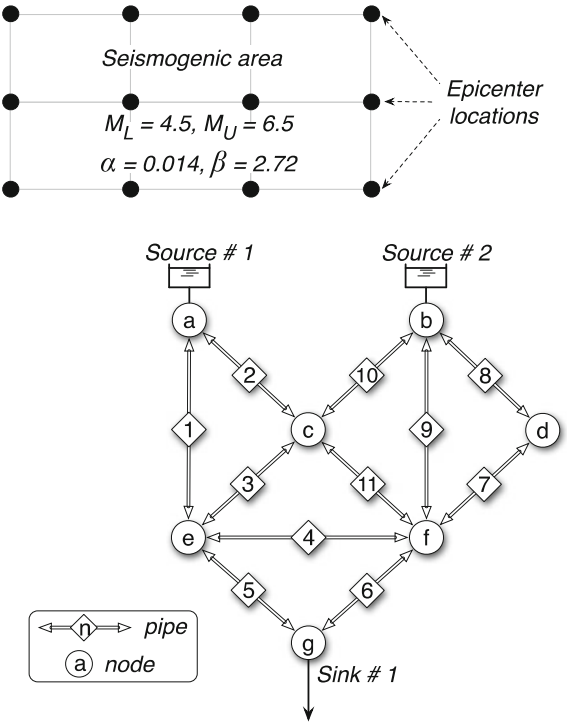

Fig. 9 Water supply network taken from Kang and Lee (2015)

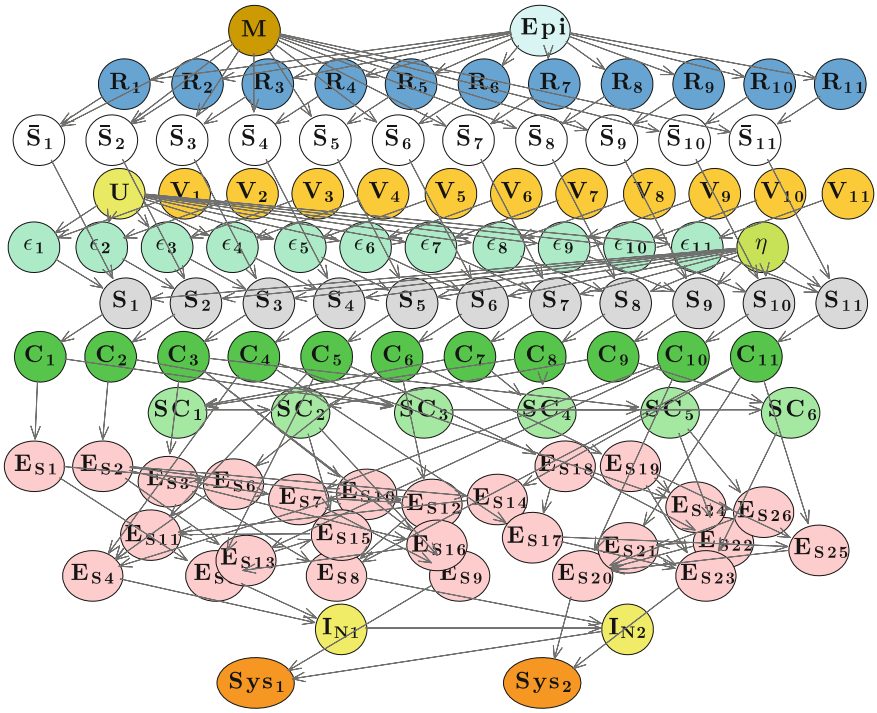

Fig. 10 BN model for the example system (efficient MLS formulation with coalesced SPEs)

BN). For this system, two connectivity problems can be defined, dealing with the existence of at least one path between each of the two sources and the only sink.

The optimization procedure has been applied to the water supply network in order to build the efficient MLS formulation with coalesced SPEs, as shown in Fig. 10. The "SC_i" nodes represent the super-components that are created by the first heuristic proposed by Bensi et al. (2013): series super-components identify groups of components that always appear together in the MLSs, while parallel super-components identify components that appear in different MLSs while sharing these MLSs with the same set of other components. This step enables a drastic reduction of the total number of nodes in the BN, i.e. from 206 nodes with the efficient MLS formulation to 108 nodes with the coalesced version.

Two algorithms are applied to the BN model, i.e. Junction-Tree (JT) for exact inference and Likelihood Weighting (LW) for an approximate solution (with 10^5 or 2×10^5 samples). The posterior distribution of two variables, i.e. earthquake magnitude and intensity measure at component #4, given the disconnection of one of the source-sink paths, is presented in Fig. 11. The global shape of the updated distributions is satisfyingly captured by the approximate inference, however local differences around the distribution tails may prove to be unacceptable, especially in the context of infrastructure risk where low-probability high-impact events are

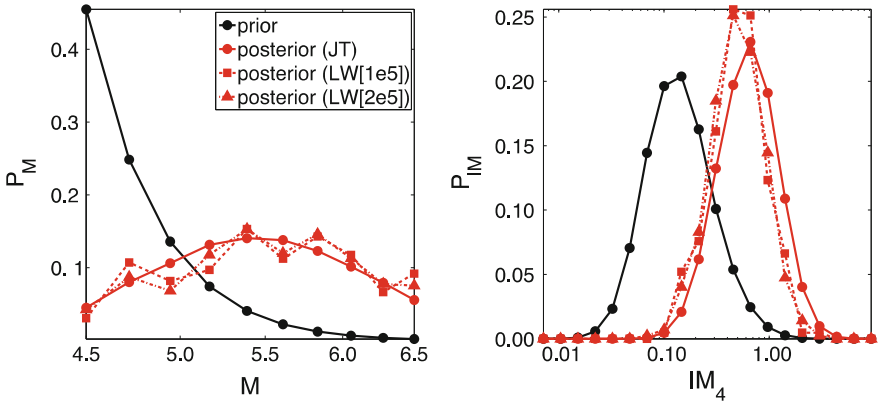

Fig. 11 Prior and posterior distributions for probability of magnitude (*left*) and IM = PGA (*right*); posterior are computed by JT and LW

Table 2 Performance measures of the different MLS formulations

Statistics	Efficient MLS	Efficient MLS (coalesced)
# of SPE nodes	132	34
Maximum clique size	24,576,000	196,608,000
Inference time (JT) (s)	11.5	57.7
Inference time (LW – 10^5) (s)	315.1	161.2

crucial. Moreover, doubling the number of samples in LW does not seem to greatly reduce the error rate. Therefore the use of exact inference algorithms such as JT appears to be the only viable option, even though sampling algorithms are able to cope with larger and more complex BNs.

As expected, the results that are provided by the two different MLS formulations (i.e. coalesced or not) are absolutely identical. In terms of inference performance, however, the efficiency of the two BN models is compared in Table 2. As stated above, the coalesced formulation leads to a dramatic reduction in the number of SPE nodes. However, even when the optimization time is excluded, the JT inference time is actually significantly greater than for the non-coalesced MLS version. This surprising observation is due to the fact that, while reducing the number of nodes, the coalesced formulation creates highly connected and interdependent chains of SPEs. As a result, the cliques that are generated during the initialization of the JT algorithm are almost ten times larger with the coalesced version. The impact of the clique size on the JT inference is essential: this is confirmed by the inference times that are obtained with the LW algorithm, which just propagates probabilistic outcomes through all the BN nodes without building up cliques. Therefore the application to this small water supply system has shown that the efficient MLS formulation with coalesced SPEs is not necessarily the most suitable approach,

Table 3 Qualitative description of the main criticalities that are involved in the various BN modeling options

Formulation	MLS search	SPE optimization	Compression	Inference (clique size)
Naïve				X
Efficient MLS	X			X
Efficient MLS (coalesced)	X	X		X
Naïve with compression	X		X	

since the complexity of BN is more determined by the clique size than the number of nodes or edges.

This section has detailed and reviewed various modeling approaches to solve BNs for larger systems. Their application to small examples has revealed several pending issues and computational bottlenecks, which are summarized as follows (see Table 3):

- When exact algorithms such as JT are applied, the main issue is the size of the cliques that are assembled. They depend on the CPT size of the nodes (i.e. number of parents and discrete states), but also on the more global connectivity of the "vicinity" of the nodes, which is much more difficult to apprehend and quantify.
- The MLS formulation requires the preliminary identification of MLSs, which can be a non-trivial and time consuming task for larger systems (i.e. recursive algorithm).
- The aggregation of SPE chains does not guarantee the reduction of the complexity of the BN. Moreover, the initial optimization step to build up the coalesced SPE chains can lead to significant computation times, especially if numerous SPE instances are required.
- The compression algorithm proposed by Tien and Der Kiureghian (2015) is also based on the identification of MLSs in order to sequentially construct the system CPT, while the compression operations end up converting memory storage space into high computation time.

As shown in Table 3, there is no straightforward modeling option that can solve all types of systems. Each approach presents some computational bottlenecks, since it appears that solving one issue (e.g. CPT or clique size) usually comes at the expense of time-consuming preliminary steps (e.g. MLS search or optimization of SPEs). Therefore, unfortunately, the recent advances in BN modeling for infrastructure risk assessment do not offer all the tools that are necessary to tackle larger systems. Moreover, the systems that have been used for this demonstration are based on binary component states with connectivity-based performance metrics. Far greater challenges are raised when capacity or serviceability metrics are considered, since the use of connectivity-based MLSs or MCSs is not relevant anymore.

4 Simulation-Based Approach

4.1 The Thrifty Naïve (t-Naïve) Formulation

The proposed approach makes use of raw component and system performance data, obtained from a system simulation of n_r runs, to develop the structure of the BN portion related to system performance (i.e., the "lower" BN portion including only components and performance metrics nodes, C and P) and to estimate the CPTs of the performance nodes P by simple counting. The CPTs of the remaining nodes (associated to the n_c components as well as the hazard-related random variables) are derived analytically, as in the MLS-based approach. Off-line simulation results are provided in the form of a $n_r \times (n_c + n_P)$ state matrix, containing, for each simulation *run*, the state indicator for each of the n_c components plus the values of the n_P performance metrics.

Doguc and Ramirez-Marquez (2009) were apparently the first to propose such a use of system-component data pairs to support automated BN building. They focused on one advantage of such a BN setup, which is the fact that the resulting BN, unlike expert-driven ones, can be easily and continuously updated to follow changes in system configuration as well as the availability of new data. They came up with an algorithm that has polynomial complexity [$O(n^2)$], it is quadratic in the number of nodes, which is very attractive in terms of containment of the computational effort increase with the network size, but has also the undesirable feature of being dependent on component ordering. The method proposed herein retains the same quadratic complexity but is independent of component ordering.

Beside inference of the BN structure from system-components data pairs, the simulation-based approach has another important upside which is the most valued one with respect to the objective of the presented work and the reason to propose it: there are no limitations on the type of performance metrics that can be handled, thus connectivity-based measures can be considered as with the MLS-based formulation, but no extra conceptual or practical effort is required to work with flow-based ones.

The starting point is the simplest system description, with all the n_c component nodes C directly linked to each and every system performance node P: this is referred to hereafter as first variant of the naïve formulation, in which results from a system simulation can be used only to train the CPTs of P nodes. These CPTs size increases exponentially with the network size, the total number of entries being m^{n+1} where m is the common number of possible states for C and P nodes, and n is the number of components (2^{n+1} being the case of binary systems of binary components), and more generally $\prod m_i$ over the C nodes and the system performance node of interest.

The proposed approach starts from the naïve BN structure and reduces the number of edges by eliminating those corresponding to a low component-system correlation, as measured by ρ_{min}. For this reason it is named *thrifty naïve* formulation (again, first variant, meaning direct link between C and P nodes). Once the BN structure is obtained, CPTs of P nodes are computed by counting. It is worth

noting that only edges are removed from the BN, while all the component nodes are retained and can be object of Bayesian inference.

The resulting BN structure depends on the choice of the correlation thresholds ρ_{min} (one for each P node) below which edges are removed from the BN. In the examples to follow (see Sects. 4.2 and 4.3), the threshold values were chosen in order to "significantly" reduce the number of edges and the choice is judged by comparing its performance to the MLS-based formulations, for cases where they can be contrasted; a thorough sensitivity study of the final results to $\rho_{\min}$, and the consequent search for an optimal number of links that are retained for each performance metric, are left to future work.

The effectiveness of the proposed method relies on the extent to which the influence of each component is related to the performance of interest. In every system the importance of components will in general vary and some will be more relevant than others, think for instance to graph articulation points or bridges, whose loss can collapse the graph into disconnected portions. More specifically, however, the maximum gain would be obtained when only a limited number of components is related to a given performance, possibly on a geographical basis, a criterion of physical proximity. Based on this idea an improved version of the thrifty naïve formulation can be obtained by including intermediate nodes I between the C and P nodes, corresponding to simpler local performance metrics, for instance the percent demand satisfaction at a given sink node, rather than on the entire network. In this second variant the off-line simulation results are used to compute correlations between C nodes and I nodes, as well as between I nodes and P nodes. Similarly to the first variant, only the BN edges linking nodes with correlation higher than the selected correlation thresholds are retained, while the remaining ones are deleted from the BN. Obviously, selecting very low thresholds yields the second variant of the naïve formulation, with all BN edges retained. Once the BN structure is obtained, the CPTs of I and P nodes are computed by counting. With reference to the performance metrics considered in this work (see next Section), which are based on quantities computed at sink nodes, the number of such intermediate nodes per metric equals the number of sinks.

4.2 *The Object-Oriented Platform for Infrastructure Systems Modeling and Simulation (OOFIMS)*

A software platform for quantitative probabilistic seismic risk analysis, namely Object-Oriented Framework for Infrastructure Modeling and Simulation (OOFIMS), has been recently developed (Franchin and Cavalieri n.d., 2013) within SYNER-G (2012), as a computational tool to assess the vulnerability to earthquakes of an urban area including buildings, lifelines and critical facilities. The tool, coded in MATLAB® (The MathWorks 2011) language according to the object-oriented paradigm (OOP),

allows to model and analyze the performance of interconnected/interdependent infrastructure systems and sets of buildings, at the urban/regional scale, in ordinary or "disturbed" conditions (e.g., due to the impact of a natural or man-made hazard). It was conceived from the beginning as an open framework and is currently being extended to include multiple natural hazards, e.g. flood hazard (Cavalieri et al. 2015), and community resilience assessment (Franchin and Cavalieri 2015).

The features of the proposed simulation-based approach will be shown in the next sections with reference to WSS case studies. The functional model for this network, as implemented in OOFIMS, consists of the $N + E$ steady-state nonlinear flow equations (Houghtalen et al. 2009):

$$\begin{cases} \mathbf{A}_D^T \mathbf{q} - \mathbf{Q}(\mathbf{h}_D) = \mathbf{0} \\ \mathbf{R}|\mathbf{q}|\mathbf{q} + (\mathbf{A}_D \mathbf{h}_D + \mathbf{A}_S \mathbf{h}_S) = \mathbf{0} \end{cases} \tag{1}$$

where N and E are the number of internal (non-source) nodes and of edges, respectively. The first N equations express flow balance at the internal nodes (sum of incoming and outgoing flows equals zero), while the next E equations express the flow resistance of the edges. The subscripts D and S denote the partitions (of vectors and matrices) referred to the N internal or demand nodes and M source nodes, respectively. The matrices $\mathbf{A}_D$ ($E \times N$) and $\mathbf{A}_S$ ($E \times M$) are sub-matrices of the $E \times (N + M)$ matrix $\mathbf{A}$, containing 0, 1 and -1 terms as a function of the network connectivity. The vectors $\mathbf{h}_D$ ($N \times 1$) and $\mathbf{h}_S$ ($M \times 1$) are the corresponding partitions of the $(N + M) \times 1$ vector $\mathbf{h}$ collecting the N unknown water heads in the internal nodes and the M known water heads in the source nodes. The $E \times 1$ vector $\mathbf{q}$ collects the unknown flows in the E edges, and $\mathbf{R}$ is the $E \times E$ diagonal matrix of resistances, with terms $r_i = u_i \cdot L_i$, where $u_i = \beta \cdot D^{-5}$ (according to Darcy's law) and L_i is the i-th edge length. The above set of equations expresses the flow analysis in "head-driven" mode, since the flows actually delivered, $\mathbf{Q}(\mathbf{h}_D)$, are reduced with respect to the end-user demands, $\mathbf{Q}$, if the (unknown) heads at internal nodes fall below thresholds $\mathbf{h}_{min}$; the latter are usually set as the average building heights in the areas served by the nodes, incremented by five meters water column. For the generic internal node this is written as:

$$Q_i(h_{D,i}) = \begin{cases} Q_i \cdot \frac{h_{D,i}}{h_{i,min}}, & \text{if} \quad h_{D,i} < h_{i,min} \\ Q_i, & \text{if} \quad h_{D,i} \geq h_{i,min} \end{cases} \tag{2}$$

This approach is preferred to the solution with fixed demands ("demand-driven" mode), especially for the perturbed seismic conditions, where satisfaction of prescribed demands is not guaranteed (it's an assessment rather than a design problem).

Concerning the physical damageability of vulnerable components, i.e. the edges or pipes, the latter were assigned only two states (intact/broken) and lognormal

fragility curves, in place of Poisson repair rates,[1] in order to make the two approaches (MLS-based and t-Naïve) comparable.

Among the numerous performance metrics implemented in OOFIMS, two system-level metrics for WSS are of interest in this work.

The first metric is the Connectivity Loss (CL), introduced by Poljanšek et al. (2012). This connectivity-based index measures the average reduction in the ability of sinks to receive flow from sources. The same metric is also often called Simple Connectivity Loss (SCL), in order to distinguish it from the Weighted Connectivity Loss (WCL), in which the number of sources connected to the sinks is weighted, e.g. in terms of sum of the inverse of (free-flow) travel times on the paths between sinks and sources: for this reason, hereafter the acronym SCL is employed:

$$\mathrm{SCL} = 1 - \frac{1}{n_d} \sum_{i=1}^{n_d} \frac{N_{i,d}}{N_{i,0}} \tag{3}$$

where n_d is the total number of sinks or demand nodes, while $N_{i,d}$ and $N_{i,0}$ are the number of sources connected to the i-th sink, for the damaged and intact network, respectively. It should be noted that this metric cannot be measured but must be evaluated through a system analysis. This makes collecting evidence in terms of SCL for Bayesian updating problematic. This problem, however, is not related to SCL only, but to connectivity measures in general, which require looking at the entire network in order to establish whether paths exist in the damaged configuration.

As opposed to SCL, the System Serviceability Index (SSI) is a flow-based and "measurable" system-level performance metric, defined by Vanzi (1995) for electric power networks. With reference to water supply systems, the metric takes the form:

$$\mathrm{SSI} = 100 \frac{\sum_{i=1}^{n} Q_i(h_{D,i})}{\sum_{i=1}^{n} Q_i} \tag{4}$$

where $Q_i(h_{D,i})$ and Q_i have been defined above and are referred to the damaged and undamaged conditions, respectively. The SSI index varies between 0 and 100, assuming the value 0 when there is no solution for the flow analysis and 100 when the WSS remains undamaged after the earthquake, or the water head at all sink nodes is larger than the threshold. The metric is measurable and does not require a system analysis (of course it does in an analytical simulation framework, but it does not need one in an actual physical network). It does require only knowledge of the Q values at sink nodes, which can be obtained locally without knowledge of conditions at other parts of the network.

The number of connected sources N and the flow Q are the quantities used to define the intermediate nodes in the improved t-Naïve formulation illustrated in the previous section.

[1]In OOFIMS line-like components such as pipes, embankments, etc. have Poisson vulnerability models with rate of failure per km as a parameter, which is used to establish rupture or leakage of each segment.

4.3 *Kang and Lee Water Supply System by the t-Naïve Formulation*

In order to compare it to Option 1, the proposed simulation-based approach is first applied to the Kang and Lee (2015) example network. In order to allow the computation of the two system-level performance metrics introduced above, SCL and SSI, the network was modified with the addition of one source and one sink, as shown in Fig. 12.

Vulnerable components (pipelines) have two states: intact (1 in the matrix) and broken (2 in the matrix). A Monte Carlo simulation of $n_r = 10{,}000$ runs was carried out, which provided a state matrix of 10,000 rows by 13 columns ($n_c = 11$ plus $n_P = 2$). Table 4 shows an excerpt of such state matrix as provided by OOFIMS, with four further columns, added for use in the second variant of the proposed approach, reporting the number of connected sources N and the ratio between delivered flow and end-user demand $Q(h_D)/Q$, for each of the two sinks in the example and each simulation run. The highlighted rows, in the last six columns, expose the inadequacy of purely connectivity metrics. In fact, even though both sinks are connected to all sources (SCL = 0), the head losses in the network, due to earthquake-induced damage, cause heads at sinks to fall below thresholds, thus preventing end-user demands to be fully delivered (SSI < 100%). This underlines the need to carry out

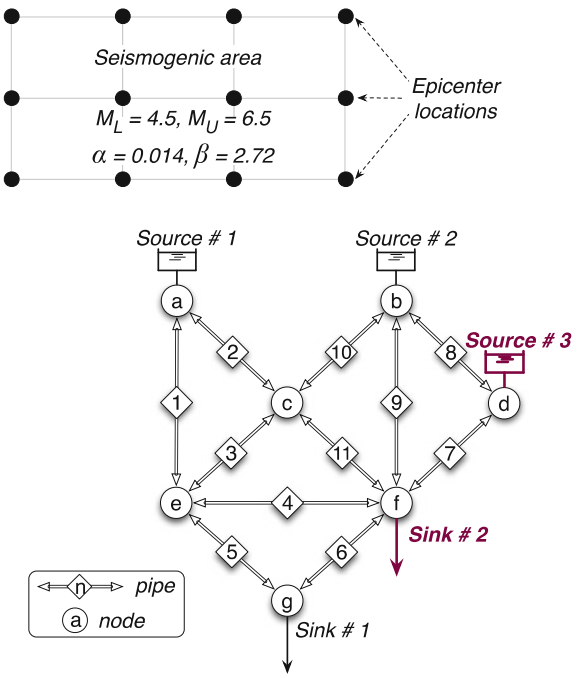

Fig. 12 Water supply network taken from Kang and Lee (2015), with one source and one sink added

Table 4 Excerpt of the state matrix provided by OOFIMS

States (1 = intact, 2 = broken) of the eleven components														# conn. sources		Q/Q_0	
Run	C_1	C_2	C_3	C_4	C_5	C_6	C_7	C_8	C_9	C_{10}	C_{11}	SCL (%)	SSI (%)	Sink1	Sink2	Sink1 (%)	Sink2 (%)
1	1	1	1	1	1	1	1	2	1	2	1	0	100	3	3	100	100
2	1	1	1	1	1	1	1	1	1	1	1	0	100	3	3	100	100
3	1	1	1	1	1	1	1	1	1	1	1	0	100	3	3	100	100
4	1	1	1	1	1	1	1	1	1	1	1	0	100	3	3	100	100
5	1	1	1	2	1	1	1	1	1	1	1	0	11	3	3	9	13
6	1	1	1	1	1	1	1	1	1	1	1	0	100	3	3	100	100
7	2	1	1	2	1	1	1	1	1	1	1	0	8	3	3	3	12
8	1	1	1	1	1	1	1	1	1	1	1	0	100	3	3	100	100
9	1	2	1	1	1	1	1	1	1	1	1	0	100	3	3	100	100
10	1	1	1	1	1	1	1	1	1	2	1	0	100	3	3	100	100
11	1	1	1	1	1	1	2	1	1	1	1	0	41	3	3	75	19
12	1	1	1	1	1	1	1	1	1	1	1	0	100	3	3	100	100
13	1	1	1	1	1	1	1	1	1	1	1	0	100	3	3	100	100
14	1	1	1	1	1	1	1	1	1	1	1	0	100	3	3	100	100
15	1	1	1	1	1	1	1	1	1	2	1	0	100	3	3	100	100
16	2	1	1	1	1	1	2	1	1	1	1	0	0	3	3	0	0
17	2	2	1	1	1	1	1	1	1	1	1	33	68	2	2	40	86
18	1	1	1	1	1	1	1	1	1	1	1	0	100	3	3	100	100
19	1	1	1	1	1	1	1	2	2	1	1	0	41	3	3	74	18
20	1	1	1	1	1	1	1	1	1	1	1	0	100	3	3	100	100
21	1	1	1	1	1	1	2	1	1	1	1	0	41	3	3	75	19
22	1	1	1	1	1	1	1	1	1	1	1	0	100	3	3	100	100
23	1	1	1	1	1	1	1	1	1	1	1	0	100	3	3	100	100
24	1	1	1	1	1	1	1	1	1	1	1	0	100	3	3	100	100
25	1	1	1	1	1	1	1	1	1	1	1	0	100	3	3	100	100
26	1	2	1	2	1	1	1	1	1	1	1	0	1	3	3	0	2
27	1	1	1	1	1	1	1	1	1	1	1	0	100	3	3	100	100
28	1	1	1	1	1	1	1	1	1	1	1	0	100	3	3	100	100

flow analysis, which includes connectivity, for all lifelines (e.g., power and gas networks), in order to get an estimate of the actual serviceability at end-user nodes.

The BN model with distributed hazard and the first variant (i.e. without intermediate nodes I) of the naïve formulation for the system part is shown in Fig. 13. As can be seen, all the $n_c = 11$ components are linked to both P nodes, representing SCL and SSI, respectively. The latter are continuous variables, and for this example were discretized into ten states. As a consequence, the size of their CPTs results to be $10 \times 2^{11} = 20480$: this is a really large number, considering the size of this small example network.

Figure 14 presents a sketch of the correlation-based procedure to switch from the naïve to the thrifty naïve formulation. For each P node, $n_c = 11$ correlation coefficients are computed and then, based on the two selected thresholds (for SCL and SSI), only four edges between C and each P node are retained. This is graphically represented in the figure by means of shades of grey, where lighter color means higher correlation (white is one, black is zero), and only components 1, 2, 7 and 9 are retained for metric P_1 = SCL, and components 4, 7, 9 and 11 for metric P_2 = SSI (components 7 and 9 belong to both sets, and their importance is confirmed once one recognizes that they are direct links between Source 3 and 2, respectively, and Sink 2). Figure 15 shows the resulting reduced BN, in which the CPTs of both P nodes have size equal to $10 \times 2^4 = 160$.

As explained above, in the second variant of the thrifty naïve formulation the simulation results are used to compute correlation between the component nodes and the intermediate nodes, as well as between the latter and the performance

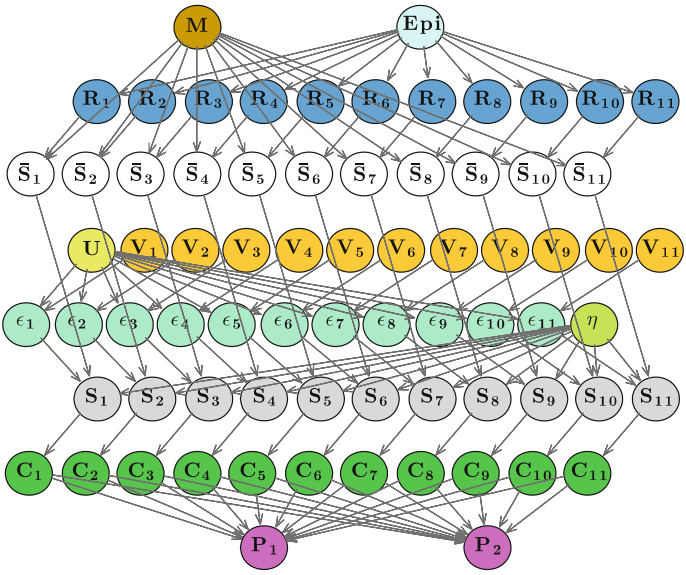

Fig. 13 BN model with distributed hazard and naïve formulation (first variant)

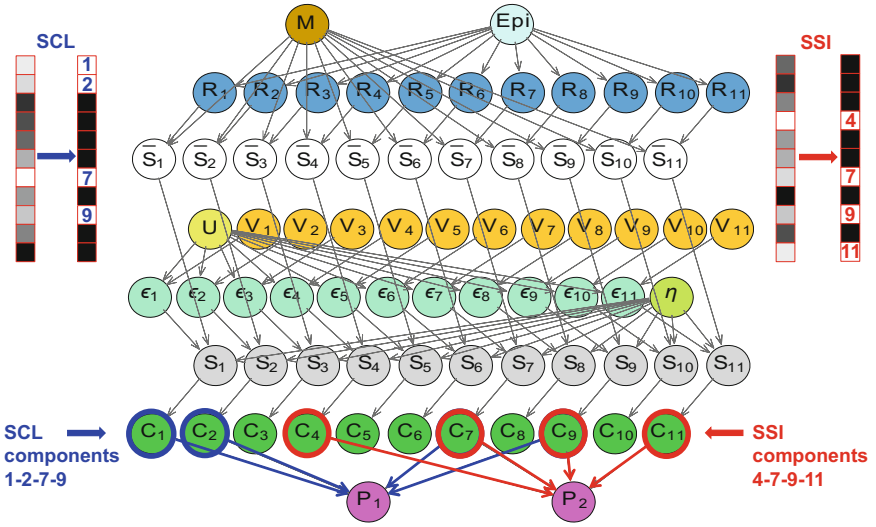

Fig. 14 Correlation-based procedure to switch from naïve to thrifty naïve formulation (first variant)

nodes. Because the number of the I nodes equals the number of sinks for both P nodes, in this example four intermediate nodes were introduced, as shown in Fig. 16. Given the different nature (connectivity-/flow-based) of the two employed

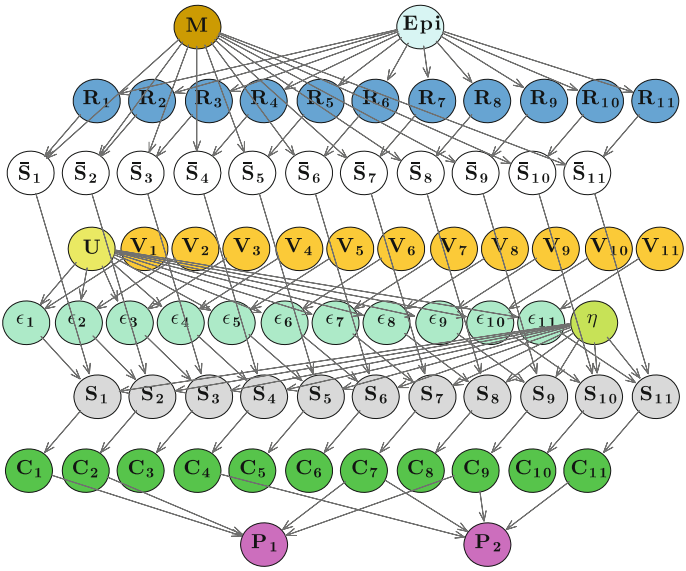

Fig. 15 BN model with distributed hazard and thrifty naïve formulation (first variant): only four links are retained for each metric

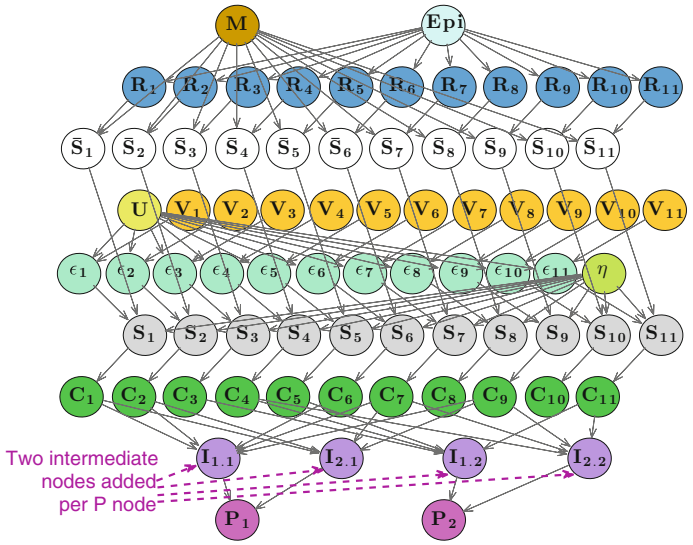

Fig. 16 BN model with distributed hazard and thrifty naïve formulation (second variant), with introduction of two intermediate nodes per P node

performance metrics, the two couples of intermediate nodes were treated differently. In particular, for the I nodes connected to P_1 (i.e., SCL) node, correlation was computed between components' states and the number of connected sources, for each sink; on the other hand, for the I nodes connected to P_2 (i.e., SSI) node, correlation between components' states and the ratio between delivered flow and end-user demand, for each of the two sinks, was taken into account (see Table 4). Figure 16 shows the final BN model, with some links between BN nodes already deleted based on the selected correlation thresholds. It should be noted that, given the small number (i.e., two) of sink nodes for this example, the thresholds were selected in order to retain the links between intermediate nodes and their respective P nodes, producing a naïve formulation between I and P nodes: the CPTs of P nodes were thus derived analytically. Figure 16 gives an immediate outlook of how the network components differently contribute to the sink states and hence to final metrics. In particular, it can be noted that some components (#8 and #10) are not linked to any sink node, meaning that do not play an important role in the network performance assessment.

Figure 17 summarizes and compares the results obtained with the two approaches, the efficient MLS-based and the simulation-based t-Naïve. Two intuitively related types of evidence on performance nodes P were considered: total disconnection of sinks from sources (SCL = 1) and severe reduction of delivered water flow at sinks (SSI < 20%). The performance was tested with reference to the posterior distribution of magnitude and IM, i.e. the peak ground acceleration (PGA): in order to investigate the dependency on edge elimination of both variants of the t-Naïve formulation, the IM was computed at two component sites, one of which (#7) results to be linked to intermediate or performance nodes (depending on

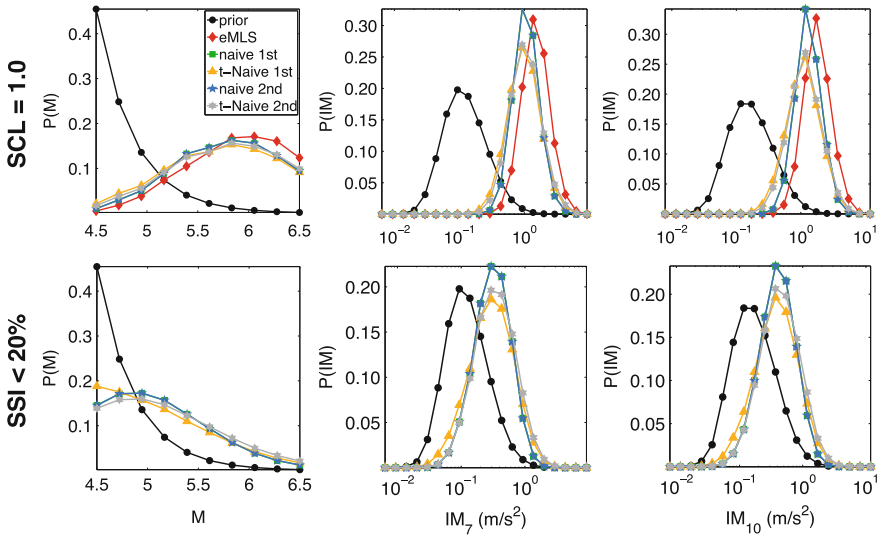

Fig. 17 Comparison between the different approaches and formulations

the considered variant), while the other one (#10) is disconnected (i.e., not directly connected) in both configurations (see Figs. 15 and 16). In Fig. 17 the prior distributions of such quantities are also reported for convenience. Since Option 1 (eMLS in the figure) can handle only connectivity problems, it was possible to test its performance only for the case of evidence on SCL. In particular, such performance was compared with that of Option 2, with reference to four formulations: naïve (all links present) and thrifty naïve (some links deleted on the base of correlation), both for the first and the second variant of the simulation-based approach. The comparison is encouraging, showing a good match between Option 1 and Option 2 posterior distributions. It can also be noted that for all three quantities considered, the two naïve curves are superimposed, while the two thrifty naïve curves are very close to each other: this means that there is no great gain in employing the second variant rather than the first one, at least for this simple example and the quantities considered here. Concerning the second evidence (SSI < 20%), the four formulations of the simulation-based approach were considered, again showing no substantial difference between each other.

The different approaches were also compared in terms of computational effort, using a laptop with a 2 GHz i7 quad core CPU and 8 GB RAM. The outcome is reported in Table 5, in terms of computational times (in seconds). It has to be noted that such times are related only to the automated set-up of the BN model and the inference, and do not include the time for MLS search (0.6”), which is needed for option 1, and for the OOFIMS simulation (49’ 7” for 10^4 samples), needed for option 2. Table 5 highlights the great time reduction for both variants of the thrifty naïve formulation. The second variant of the naïve formulation is clearly slower than the first one, due to the increased number of nodes. Naïve formulation times are higher than those of option 1, which performs well for this small example, relative to connectivity issues. However, the MLS-based approach becomes intractable when dealing with larger examples.

4.4 A Larger, Realistically Sized Example

In order to prove the capabilities of the proposed simulation-based approach in handling larger, realistically sized networks, the water supply system whose

Table 5 Computational times (in seconds)

Evidence	SCL = 1			SSI < 20%		
Method	M	IM_7	IM_{10}	M	IM_7	IM_{10}
eMLS (coalesced)	9.0	9.1	9.0			
Naïve 1st	26.9	25.9	26.0	26.0	26.7	26.1
t-Naïve 1st	3.3	3.2	3.3	3.3	3.2	3.3
Naïve 2nd	42.8	43.1	43.1	45.3	45.1	43.8
t-Naïve 2nd	2.9	2.9	3.0	2.9	2.9	2.9

topology is sketched in Fig. 18, together with the indication of node types (water sources, sinks), was considered. As can be noted, the graph is characterized by a grid or mesh-like topological structure, typical in urban areas where the main arcs connect suburbs or districts, and can be considered as a transmission/distribution (TD) system. The topology was generated using the network model developed by Dueñas-Osorio (2005). Such model, already used by Franchin and Cavalieri (2015), aims to represent real TD systems, based on the ideal class of the *d-lattice-graph*, an unweighted, undirected, regular graph of dimension d with vertices joined to their lattice neighbors according to specified rules. First, the number of vertices n is fixed in order to obtain a square grid, since TD models exist on adjacency matrices of square topologies. Then, m edges of the complete graph (an aperiodic TD substrate) are retained with a probability of existence equal to p_m. This probability can be estimated empirically for each network typology, and the expression provided by Dueñas-Osorio (2005) for water systems is:

$$p_m = 0.60 \cdot n^{-0.05} \tag{5}$$

The total number of nodes is 49, five of which are constant-head water sources, 25 are sinks/demand nodes and the remaining ones are joints. A total of 71 cast iron pipes connect the nodes. Only one seismogenic area (activity parameters indicated in Fig. 18), discretized into nine epicenter locations, is present.

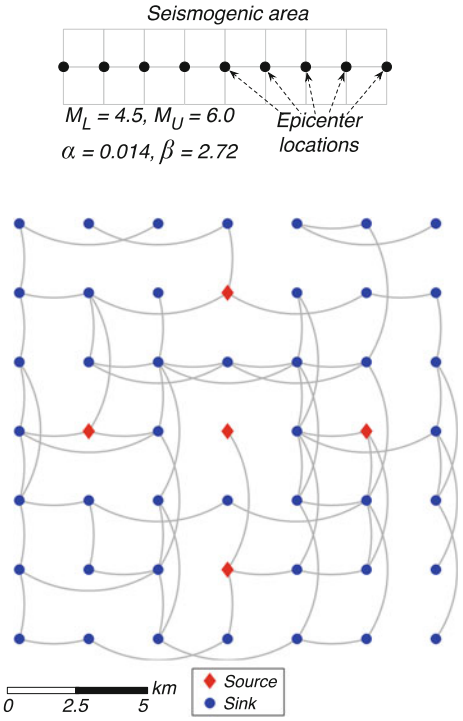

Fig. 18 Topology of the synthetic water supply system used as a realistic case study

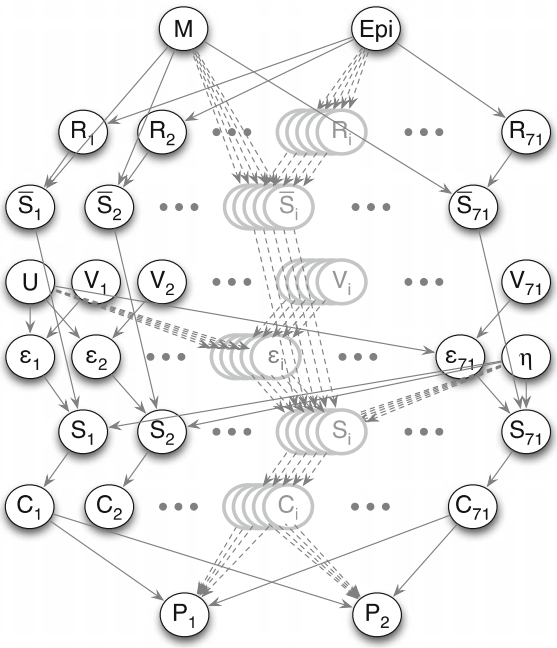

Fig. 19 BN model with distributed hazard and first variant of the thrifty naïve formulation

Given the size of the system, the MLS-based approach results to be unfeasible and was not applied. Further, for this example the large number of pipes, i.e. vulnerable components that are assigned a C node in the BN model, prevents the application of the naïve formulation, so that only the thrifty naïve formulation was used for both variants of the simulation-based approach.

For the sake of clarity, a simplified sketch of the BN model with distributed hazard and the first variant of the thrifty naïve formulation for the system part is shown in Fig. 19. C nodes are linked directly to P nodes, without an intermediate nodes layer; in particular, some C nodes are linked to one or both P nodes, while others (e.g. C_2) are left disconnected based on correlation, meaning their role in the network performance assessment is not paramount.

Figure 20 shows a sketch of the second variant of the thrifty naïve formulation for the considered water supply system. As can be noted, a layer is added between C and P nodes, including one intermediate BN node for each sink node in the system and per P node, for a total of 50 intermediate nodes. Links between C, I and P nodes are again retained based on correlation.

Figure 21 compares the results obtained with the two variants of the thrifty naïve formulations, in terms of the quantities (magnitude and IM, i.e., PGA) and evidence (SCL = 1 and SSI < 20%) already introduced in Fig. 17 for the Kang and Lee example. To investigate the dependency on edge elimination, the component sites selected in this case for the IM computation are #63, which is linked to at least one I or P node (depending on the considered variant), and #27, which results to be disconnected (i.e., not directly connected) in both configurations.

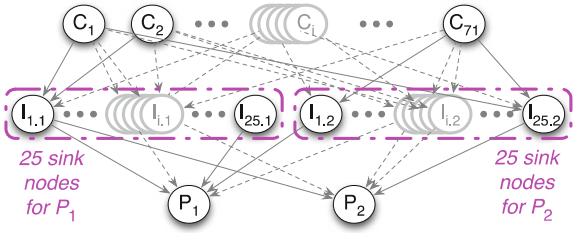

Fig. 20 BN model for the second variant of the thrifty naïve formulation (only system shown)

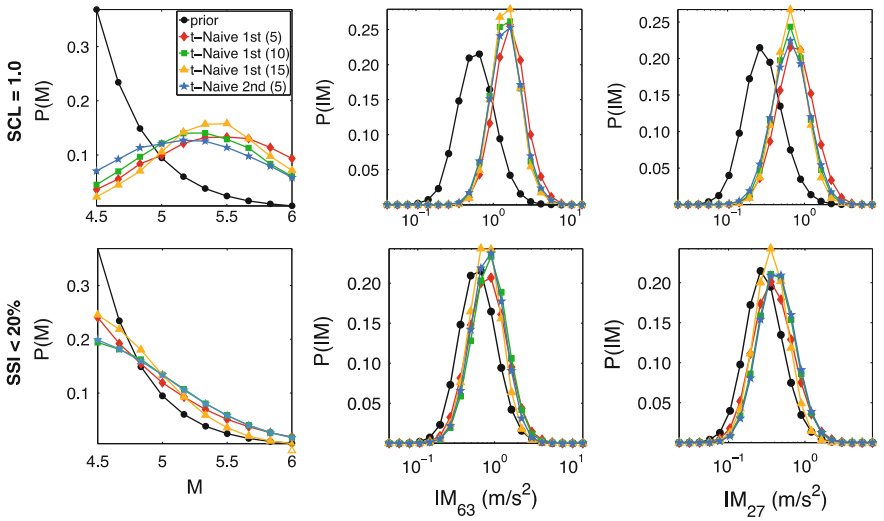

Fig. 21 Thrifty naïve formulation: comparison between the first variant (with three different numbers of component nodes linked to P nodes) and the second one (with five intermediate nodes linked to P nodes)

The first variant was tested with three different numbers, that is 5, 10 and 15, of C nodes connected to both P nodes; on the other hand, the performance of the second variant was analyzed with reference to only one configuration, involving a variable number (one to seven) of C nodes connected to I nodes and as low as five I nodes linked to both P nodes. Such a small number is justified by considering that in this case the CPTs of P nodes soon become very large, being I nodes not binary, as are C nodes: in particular, the 25 I nodes related to P_1 (i.e., SCL) have six states, indicating the number of connected sources (0, 1, 2, 3, 4, 5), while the ones related to P_2 (i.e., SSI) were assigned five states, based on demand discretization.

Despite the very small numbers of directly connected nodes in both variants, the comparison is again encouraging. The number of connected components does not seem to cause important variations in the results, making the approach robust against the threshold selection and definitely feasible to handle realistic systems.

Table 6 Computational times

Evidence	SCL = 1			SSI < 20%		
Method	M	IM_{63}	IM_{27}	M	IM_{63}	IM_{27}
t-Naïve 1st (5)	14.2''	14.3''	14.3''	14.4''	14.4''	14.4''
t-Naïve 1st (10)	26.0''	26.6''	26.4''	26.1''	26.6''	26.7''
t-Naïve 1st (15)	17'13''	17'30''	17'30''	17'20''	17'22''	17'22''
t-Naïve 2nd (5)	1'35''	1'40''	1'42''	1'35''	1'39''	1'35''

All curves show a right-shift that is more evident for the SCL = 1 evidence than for SSI < 20%, as expected. The proximity of the different curves for all three quantities in the subplots indicates that, relatively to the quantities considered here, the choice of one variant rather than the other one is almost indifferent.

The computational times, using the same laptop indicated above, resulted to be totally acceptable (see Table 6), especially if related to a non-academic example. The displayed times do not include the 95' 50" time needed to carry out the OOFIMS simulation (10^4 samples). Comparing the times of the first variant of t-Naïve formulation for the three different numbers of components, it is clear how computational time is far from being linear with the increment of connected components, due to exponential increase in CPT size.

The great convenience of using the second variant in place of the first one, is given by the presence of intermediate nodes (explicitly representing the sink nodes), in particular the ones linked to P_2 node. In fact, such nodes allow the user to handle flow quantities not only at the global/system level (i.e., for SSI computation) but also at the local/node level.

As already pointed out in the introduction, one of the possible goals of setting up a BN model is the possibility to deal with the hazard consequences in real-time, that is feeding the model with evidence as soon as it appears and consequently updating all the probability distributions of interest in the framework of decision-support systems. In the emergency phase following a seismic event, assessing the number of sources connected to a sink, or estimating SCL or SSI might be not feasible in a timely manner. Typical evidence in such a scenario are local in nature, like intensity measurements at strong-motion stations, magnitude values from P-waves, all available in a very short time frame from seismological agencies and often online, but also even though later, state of components as observed in the field or measurements of service levels in network demand nodes. An example of this application is shown in Fig. 22, where the posterior distribution of flow ratio at node #15 is based on the evidence of the actually delivered flow at another sink node. In order to gain insight into the influence of the distance from the "evidenced" sink node, a low serviceability evidence ($Q_i(h_{D,i}) < 20\%\ Q_i$) was put on two different nodes, one of which (#16, the "close" one) is adjacent to node #15, while the second one (#25, the "distant" one) is located in another sector of the network. As expected, Fig. 22 clearly shows how the close node heavily impacts node #15, whereas the influence of the same type of evidence put on the distant node is negligible.

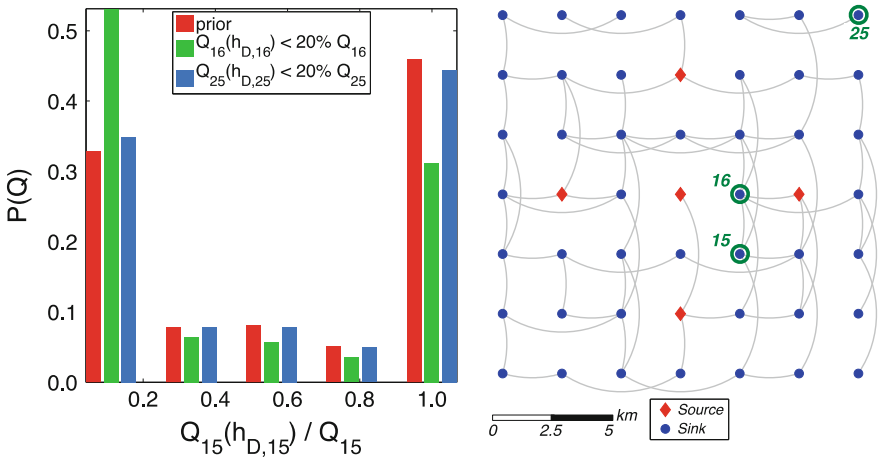

Fig. 22 Prior and posterior probability distributions of flow ratio at sink node #15: evidence on actually delivered flow at sink #16 (the "close" one) and sink #25 (the "distant" one)

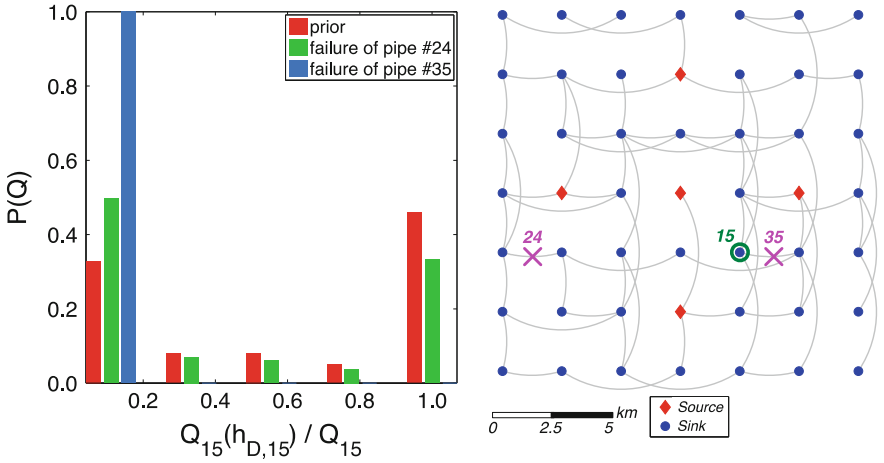

Fig. 23 Prior and posterior probability distributions of flow ratio at sink node #15: evidence on failure of pipe #35 (the "close" one) and pipe #24 (the "distant" one)

Another type of local evidence that can be obtained quickly (and sometimes also easily, without digging) is represented by the breakage of a pipe. Similarly to what was done for the evidence on the flow, the influence of the distance from the evidenced pipe on the posterior distribution of flow ratio at node #15 was investigated, by putting the breakage evidence on a "close" pipe (#35) and a "distant" pipe (#24). Also in this case, the outcome was expected: the close pipe heavily impacts node #15, with a 100% probability to experience a flow ratio lower than 20%, whereas the distant node has small or negligible influence (see Fig. 23).

5 Conclusions and Future Work

Management of infrastructure systems damaged by an external hazard in real-time is a daunting task that can be theoretically tackled by means of a Bayesian Network model. Real-sized networks, however, pose a computational challenge to the use of BNs and, further, existing efficient formulations seem to be confined to connectivity-based models of networked systems. System performance as assessed by connectivity-based and flow-based models can be different, and flows are also better quantities to be used as evidence in Bayesian updating. The chapter investigates these two problems, i.e. the computational limits of available BN models for infrastructure systems and the consideration of actual physical flows in the infrastructure network model. Two approaches are considered. One is an efficient and exact formulation based on Minimum Link Set modeling of the problem, proposed by Bensi et al. (2013) and used as a benchmark, at least for connectivity problems.

The second is an alternative simulation-based approach, proposed by the authors, in which raw component and system performance data, coming from a Monte Carlo simulation of the infrastructure system model, are used to develop the structure of the BN portion related to system performance and to estimate CPTs by counting. The initial naïve formulation is replaced by a more efficient thrifty-naïve one, where BN nodes related to vulnerable components are all kept, while several links between these nodes and system performance nodes are deleted on the base of correlation. The results, comparable with efficient MLS-based ones on connectivity problems, are encouraging. One upside of the proposed approach is the possibility to handle flow-based problems, with the computation of actual flows as determined by physical flow equations (in place of the commonly considered max-flow). The second application showed that such approach allows one to handle larger and realistic networks.

In the field of seismic risk assessment, most random variables are continuous and in this work were discretized. Future work aims to explore the sensitivity to discretization and the possibility to handle Gaussian/conditional Gaussian variables with the junction tree engine. Further, OOFIMS, the computational platform used to produce the components-system data set to support the proposed approximate BN model, can account for multi-state components (e.g. pipes can be intact, leaking or broken): such extension of the approach is straightforward and underway.

Acknowledgements The authors gratefully acknowledge for financial support: the European Commission through grant agreement no. 244061 for the SYNER-G collaborative research project and grant agreement no. 603960 for the INFRARISK collaborative research project, and the Italian Civil Protection Department through grant Reluis RS6.

References

Bensi M, Der Kiureghian A, Straub D (2011) A Bayesian network methodology for infrastructure seismic risk assessment and decision support. Report Number 2011/02, Pacific Earthquake Engineering Research Center, University of California, Berkeley, CA

Bensi M, Der Kiureghian A, Straub D (2013) Efficient Bayesian network modeling of systems. Reliab Eng Syst Saf 112:200–213

Bensi M, Der Kiureghian A, Straub D (2014) Framework for post-earthquake risk assessment and decision making for infrastructure systems. ASCE-ASME J Risk Uncertainty Eng Syst Part A: Civ Eng. http://ascelibrary.org/doi/abs/10.1061/AJRUA6.0000810. Accessed 18 July 2016

Cavalieri F, Franchin P, Ko SY, Giovinazzi S, Hart DE (2015) Probabilistic assessment of increased flooding vulnerability in Christchurch City after the Canterbury 2010–2011 earthquake sequence, New Zealand. Paper presented at the 12th international conference on applications of statistics and probability in civil engineering (ICASP12), Vancouver, BC, Canada, 12–15 July 2015

Cimellaro GP, Solari D, Bruneau M (2014) Physical infrastructure interdependency and regional resilience index after the 2011 Tohoku Earthquake in Japan. Earthq Eng Struct Dynam 43 (12):1763–1784

Doguc O, Ramirez-Marquez JE (2009) A generic method for estimating system reliability using Bayesian networks. Reliab Eng Syst Saf 94(2):542–550

Dueñas-Osorio L (2005) Interdependent response of networked systems to natural hazards and intentional disruptions. Ph.D. thesis, Georgia Institute of Technology

Dunnett CW, Sobel M (1955) Approximations to the probability integral and certain percentage points of a multivariate analogue of Student's t-distribution. Biometrika 42(1/2):258–260

Franchin P, Cavalieri F n.d. OOFIMS Object-Oriented Framework for Infrastructure Modeling and Simulation. https://sites.google.com/a/uniroma1.it/oofims/. Accessed 18 July 2016

Franchin P, Cavalieri F (2013) Seismic vulnerability analysis of a complex interconnected civil Infrastructure. In: Tesfamariam S, Goda K (eds) Handbook of seismic risk analysis and management of civil infrastructure systems. Woodhead Publishing Limited, Cambridge, UK pp 465–513. ISBN-13: 978 0 85709 268 7. doi:10.1533/9780857098986.4.465

Franchin P, Cavalieri F (2015) Probabilistic assessment of civil infrastructure resilience to earthquakes. Comput Aided Civ Infrastruct Eng 30(7):583–600

Gehl P, D'Ayala D (2015) Integrated multi-hazard framework for the fragility analysis of roadway bridges. Paper presented at the 12th international conference on applications of statistics and probability in civil engineering (ICASP12), Vancouver, BC, Canada, 12–15 July 2015

Hong L, Ouyang M, Peeta S, He X, Yan Y (2015) Vulnerability assessment and mitigation for the Chinese railway system under floods. Reliab Eng Syst Saf 137:58–68

Houghtalen RJ, Akan AO, Hwang NHC (2009) Fundamentals of hydraulic engineering systems, 4th edn. Prentice Hall, Boston, MA

Kajitani Y, Tatano H (2009) Estimation of lifeline resilience factors based on surveys of Japanese industries. Earthq Spectra 25(4):755–776

Kang WH, Lee YJ (2015) Efficient post-hazard probabilistic flow analysis of water pipe networks. Paper presented at the 12th international conference on applications of statistics and probability in civil engineering (ICASP12), Vancouver, BC, Canada, 12–15 July 2015

Kumar R, Gardoni P (2014a) Effect of seismic degradation on the fragility of reinforced concrete bridges. Eng Struct 79:267–275

Kumar R, Gardoni P (2014b) Renewal theory-based life-cycle analysis of deteriorating engineering systems. Struct Saf 50:94–102

Kumar R, Cline D, Gardoni P (2015) A stochastic framework to model deterioration in engineering systems. Struct Saf 53:36–43

Mieler M, Stojadinovic B, Budnitz RJ, Mahin SA, Comerio MC (2013) Toward resilient communities: a performance-based engineering framework for design and evaluation of the built environment. PEER-2013/19, Pacific Earthquake Engineering Research (PEER) Center, University of California, Berkeley. http://escholarship.org/uc/item/36m5v2rd.pdf. Accessed 18 July 2016

Mieler M, Stojadinovic B, Budnitz R, Comerio M, Mahin S (2015) A framework for linking community-resilience goals to specific performance targets for the built environment. Earthq Spectra 31(3):1267–1283

Murphy K (2001) The Bayes Net toolbox for Matlab. Comput Sci Stat 33(2):1024–1034

Poljanšek K, Bono F, Gutiérrez E (2012) Seismic risk assessment of interdependent critical infrastructure systems: the case of European gas and electricity networks. Earthq Eng Struct Dynam 41(1):61–79

SYNER-G (2012) Collaborative Research Project, funded by the European Union within Framework Programme 7 (2007–2013), under Grant Agreement no. 244061. http://www.syner-g.eu/. Accessed 18 July 2016

The MathWorks Inc. (2011) MATLAB® R2011b, Natick, MA

Tien I, Der Kiureghian A (2015) Compression and inference algorithms for Bayesian network modeling of infrastructure systems. Paper presented at the 12th international conference on applications of statistics and probability in civil engineering (ICASP12), Vancouver, BC, Canada, 12–15 July 2015

Vanzi I (1995) Seismic reliability of electric power networks. PhD thesis. Department of Structural Engineering and Geotechnics, Sapienza University of Rome, Italy (in Italian)

Weatherill G, Esposito S, Iervolino I, Franchin P, Cavalieri F (2014) Framework for seismic hazard analysis of spatially distributed systems. In: Pitilakis K, Franchin P, Khazai B, Wenzel H (eds) SYNER-G: systemic seismic vulnerability and risk assessment of complex urban, utility, lifeline systems and critical facilities. Springer Netherlands, pp 57–88. Online ISBN: 978-94-017-8835-9, doi:10.1007/978-94-017-8835-9_3

Ziv J, Lempel A (1977) A universal algorithm for sequential data compression. IEEE Trans Inf Theory 23(3):337–343

Bayesian Network Methods for Modeling and Reliability Assessment of Infrastructure Systems

Iris Tien

Abstract Infrastructure systems are essential for a functioning society. These systems, however, are aging and subject to hazards of increasing frequency and severity. This chapter presents novel Bayesian network (BN) methodologies to model and assess the reliability of complex infrastructure systems. BNs are particularly well suited to the analysis of civil infrastructures, where information about the systems is often uncertain and evolving in time. In this environment, BNs handle information probabilistically to support engineering decision making under uncertainty, and are capable of updating to account for new information as it becomes available. This chapter addresses one of the major limitations of the BN framework in analyzing infrastructure systems, namely the exponentially increasing memory storage required as the size and complexity of the system increases. Traditionally, this has limited the size of the systems that can be tractably modeled as BNs. Novel compression and inference algorithms are presented to address this memory storage challenge. These are combined with several heuristics to improve the computational efficiency of the algorithms. Through the application of these algorithms and heuristics to example systems, the proposed methodologies are shown to achieve significant gains in both memory storage and computation time. Together, these algorithms enable larger infrastructure systems to be modeled as BNs for system reliability analysis.

1 Introduction

Infrastructure systems are essential for a functioning society, from distributing the water we drink, to delivering the electricity we need, to enabling transport of people and goods from source points to destination points. Our nation's infrastructure, however, is aging and becoming increasingly unreliable with potentially severe

I. Tien (✉)
School of Civil and Environmental Engineering, Georgia Institute of Technology, 790 Atlantic Drive, Atlanta, GA 30332-0355, USA
e-mail: itien@ce.gatech.edu

P. Gardoni (ed.), *Risk and Reliability Analysis: Theory and Applications*,
Springer Series in Reliability Engineering, DOI 10.1007/978-3-319-52425-2_18

consequences. These systems are complex, comprised of many interconnected and interdependent components, and they are subject to increasing hazards, both natural and man-made. While the ideal solution may be to replace every component in every system, the reality is that resources are limited. Given a complex infrastructure network, system reliability analyses are required to identify the critical components and make decisions regarding inspection, repair, and replacement to minimize the risk of system failure.

The information that we have about our infrastructure systems is often uncertain and evolving in time. Sources of uncertainty include discrepancies between initial design and construction, probabilistic degradation of systems, and exposure to stochastic hazards over time. In addition, we often receive new information about these systems, e.g., from observations, inspections, or repair actions, to incorporate into current system assessments. Bayesian networks (BNs) are an ideal framework to address these challenges. BNs are able to both update the network when new information becomes available, and handle information probabilistically to support engineering decision making under conditions of uncertainty.

2 Bayesian Networks (BNs)

A Bayesian network (BN) is a directed acyclic graph comprised of nodes and links, as shown in the example in Fig. 1. Each node represents a random variable and each link the probabilistic dependency between the variables (Jensen and Nielsen 2007). In constructing a BN, each node in the graph is described by a set of mutually exclusive and collectively exhaustive states. For discrete random variables, the description of these states is straightforward. For continuous random variables, methods have been developed to perform exact inference in continuous linear Gaussian BNs (Lauritzen and Jensen 2001; Madsen 2012), where inference is the process of making conclusions about uncertain quantities in the system based on data or observations. For non-Gaussian variables, simulation methods such as Markov-chain Monte Carlo can be used (Neal 1993). Otherwise, continuous random variables can be discretized.

Figure 1 shows a BN model for five random variables $X = \{X_1, \ldots, X_5\}$. Looking at X_4, we see arrows into the node from X_1 and X_2. In BN terminology, X_4

Fig. 1 An example of a BN

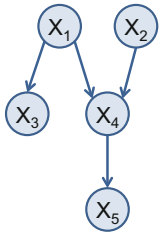

is called a "child" node of X_1 and X_2, and X_1 and X_2 are called the "parent" nodes of X_4. Children nodes are defined conditionally on the parent nodes. Specifically, for discrete nodes, a conditional probability table (CPT) is attached at each node that describes the conditional probability distribution of the node given the states of its parents. Nodes without parents, i.e., X_1 and X_2, are known as root nodes, and are defined by their marginal probability distributions. Together, the conditional and marginal probability distributions define the joint distribution over all random variables X in the network according to the rule

$$p(\mathbf{x}) = \prod_{i=1}^{n} p(x_i|Pa(x_i)) \tag{1}$$

where $p(\mathbf{x}) = \Pr(X_1 = x_1 \cap X_2 = x_2 \cap \cdots)$ is the joint probability mass function of the random variables, $p(x|y) = \Pr(X = x|Y = y)$ denotes the conditional probability mass function of random variable X given the outcome $Y = y$ of another random variable, and $Pa(x_i)$ indicate the parent nodes of x_i for $i = 1, \ldots, n$ total nodes in the network.

2.1 Advantages of BNs

As a probabilistic framework, the BN it is well suited for modeling and analyzing the reliability of systems. Relationships between variables, representing component states, are modeled probabilistically and the likelihood that a node is in a particular state is measured in degrees of belief. This is particularly useful in an environment where information is uncertain, including in the analysis of infrastructure systems, where information is oftentimes scarce, incomplete, or probabilistic in nature. Furthermore, the BN allows a transparent framework for modeling, which facilitates model review and verification by disciplinary experts who may not be familiar with probabilistic methods.

In addition, the BN framework allows for updating of the probability distributions as new information, or evidence, becomes available. When evidence, e.g., the information that a node is in a particular state, on one or more variables is entered into the BN, the information propagates through the network to yield updated probabilities in light of the new observations. This capability of updating is particularly advantageous when the information on which the analysis of a system is based is evolving. In infrastructure reliability assessment, this enables decision making based on the most up-to-date information, e.g., after an action is taken to repair or replace a component of the system, or a particular component failure is observed. It also enables system planning based on different scenarios, e.g., after a natural hazard event such as an earthquake has occurred.

2.2 Limitations of BNs

One of the major limitations of the BN framework, however, is the size and complexity of the system that can be tractably modeled as a BN. In particular, the CPTs associated with each node in the BN can grow enormously large when a node has many parents, each having many states. This happens in systems with many components. Thus, despite its advantages, BNs have been limited in their use for system reliability analysis.

2.3 BNs for Analyzing System Reliability

Previous studies using BNs for system reliability analysis have been limited, focusing on generating BNs from conventional system modeling methods, such as reliability block diagrams (Torres-Toledano and Succar 1998; Kim 2011) and fault trees (Bobbio et al. 2001). The systems studied have been small, comprised of 5, 8 (Mahadevan 2001), or 10 components. In BN studies to model the reliability of slightly larger systems, including a system of 16 components in Boudali and Dugan (2005), the authors state that this "large number" of components makes it "practically impossible" to solve the network without resorting to simplifying assumptions or approximations. It is clear that even a network of 16 components is not enough to create a full model of many real-world systems.

Another approach has been topology optimization as proposed in Bensi et al. (2013), which converts BNs with converging structures into chain-like BN models based on survival or failure path sequences. This formulation minimizes clique sizes to more efficiently model large systems as BNs. The proposed optimization program, however, must consider the permutation of all component indices and, therefore, may itself become intractably large for large systems.

2.4 Conditional Probability Tables (CPTs)

The limitation in the size of a system that can be tractably modeled as a BN is due to the CPTs that must be associated with each node in the BN. The CPT defines the conditional probability distribution of the variable represented by the node given the states of its parents. Specifically, in the case of a discrete node, the CPT provides the conditional probability mass function of the node, given each of the mutually exclusive combinations of the states of its parent nodes. As an example, for the BN given in Fig. 1, Table 1 gives the CPT of X_4 given the states of its parents X_1 and X_2. Here, a binary system is considered such that the nodes X_1, X_2, and X_4 each have two possible states, 0 or 1.

Table 1 Conditional probability table for X_4 from BN of Fig. 1

X_1	X_2	X_4	
		0	1
0	0	$\Pr(X_4=0\|X_1=0,X_2=0)$	$\Pr(X_4=1\|X_1=0,X_2=0)$
	1	$\Pr(X_4=0\|X_1=0,X_2=1)$	$\Pr(X_4=1\|X_1=0,X_2=1)$
1	0	$\Pr(X_4=0\|X_1=1,X_2=0)$	$\Pr(X_4=1\|X_1=1,X_2=0)$
	1	$\Pr(X_4=0\|X_1=0,X_2=1)$	$\Pr(X_4=1\|X_1=1,X_2=1)$

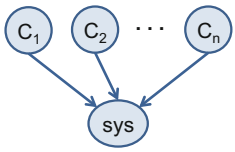

Fig. 2 BN of a system comprised of n components

The size of a CPT grows exponentially with the number of parents of the node in the graph. If each node has m states, then the CPT consists of m^{n+1} elements, where n is the number of parents. The CPT of the binary node X_4, which has two binary parents, consists of $2^3 = 8$ elements as shown in Table 1. It is noted that, using total probability, the conditional probability of a random variable X_i being in any given state will be the complement of the sum of the conditional probabilities of the variable being in all other states, i.e., $1 - \sum_{j=1}^{m-1} p(x_i = j|Pa(x_i))$. This value can be computed based on the other stored entries if desired. For example, in Table 1, $\Pr(X_4 = 1|X_1 = 0, X_2 = 1) = 1 - \Pr(X_4 = 0|X_1 = 0, X_2 = 1)$. If this is done, then the total number of elements that must be stored in the CPT is $m^{n+1} - m^n$. As n increases, however, this remains a computationaly intractable problem.

2.5 BN Formulation for Infrastructure Systems

In modeling infrastructure system reliability, the states of components that comprise the system are represented as the nodes of the graph. The model includes a node representing the system state. Because the state of the system depends on the states of its components, the BN model is defined with the system state as a child of the nodes representing the component states, i.e., links are directed from component nodes to the system node, as shown in Fig. 2.

Thus, for a binary system comprised of $n = 100$ total components, for example, the CPT for the system node consists of $2^{101} = 2.5 \times 10^{30}$ individual elements. This poses a significant memory storage challenge in constructing and analyzing the BN. The exponential increase with each additional parent node quickly renders the

problem intractable. Therefore, BN modeling of systems has been limited to small systems, typically of no more than 20 binary components. The methodologies presented in this chapter address this problem of exponentially increasing memory storage demand with increasing system size to enable large infrastructure systems to be modeled as BNs for reliability assessment.

3 Compression Algorithm

Consider a binary system, where each component as well as the system are in one of two possible states, survival or failure. Observe that the component states deterministically define the system state, i.e., for any combination of the component states, the system is in either a survival or a failure state. Such a model is particularly useful for studying the reliability of infrastructure systems, such as gas, power, or transportation systems, where the states of individual gas pipelines, electrical transmission lines, or roadways directly determine the state of the infrastructure system. In this case, the CPT associated with the system node has a special property. Let the failure and survival states of the system be defined as 0 and 1, respectively. Since for each distinct combination of component states the system state is known with certainty, the system CPT is comprised solely of 0 s and 1 s, with the values given in a single vector.

The novel algorithms described in this chapter first proposed in Tien and Der Kiureghian (2013) and later developed in Tien (2014) and Tien and Der Kiureghian (2016) take advantage of this property, specifically through a data compression process. It is noted that while the methodologies presented focus on binary systems, they can be extended to multi-state flow systems, e.g., where the component states are discretized values of a flow capacity, e.g., 0, 50 and 100% of maximum capacity. In such a system, just as the failure and survival states of individual components determine the state of the system, the flow capacities of components determine the flow capacity of the overall system. In both cases, for any specified states of components states, the state of the system is deterministically known, and the process for data compression described can be used.

Data compression is the process of reducing the number of bits required to store a given dataset. Several methods have been developed for compressing data, including both lossy and lossless methods. In lossy compression, nonessential information is removed from the dataset to reduce storage requirements. The compressed dataset is an approximation of the original dataset. In lossless compression methods, redundancy in a dataset is exploited to reduce the number of bits required to store the data without loss of any information. A dataset compressed using lossless compression can be fully reconstructed, i.e., decompressed completely accurately. The developed compression algorithm described in this chapter

is based on two lossless compression techniques, described briefly in the following sections.

3.1 Run-Length Encoding

In a set of data to be compressed, a run is defined as consecutive bits of the same value. In run-length encoding, runs are stored as a data value and count (Hauck 1986). For example, in compressing a sequence of white and black pixels, respectively indicated by "W" and "B," a sequence of 18 W's is stored as the count 18 and the data value W. Thus, the memory storage requirement is reduced from 18 elements to 2. Run-length encoding is well suited for data with many consecutively repeated values. However, mixed values are stored literally, which results in little gain for mixed data. For example, alternating white and black pixels results in the compressed dataset 1W1B1W1B ⋯, which in fact doubles the memory storage requirement compared to the uncompressed form WBWB ⋯. An example of run-length encoding is shown below:

Uncompressed dataset	WWWWWWWBWWWWWBBWWWWWWWWW
Compressed dataset	7W1B5W2B10W

In the dataset, the initial run of 7 W's is stored as 7 W, followed by one B stored as 1B, followed by a run of 5 W's stored as 5 W, etc. Thus, the original dataset comprised of 25 elements is compressed to a dataset of 10 total elements. Of course, gains achieved by employing run-length encoding to compress a given dataset depend on the number and length of runs in the dataset.

3.2 Lempel-Ziv

Techniques based on the classical Lempel-Ziv algorithm (Ziv and Lempel 1977) find patterns in the data, construct a dictionary of phrases, and encode based on repeated instances of phrases in the dictionary. While there are several techniques developed to construct the dictionary, the major advantage of the Lempel-Ziv algorithm lies in the ability to call the phrases in the dictionary at each repeated instance of a phrase, while having to store just one instance of the phrase in the dictionary. An example of the Lempel-Ziv algorithm with the corresponding dictionary is shown below:

Uncompressed dataset	WWBWBBWBWWBB
Compressed dataset	∅W1B2B2W3

Dictionary:

Phrase number	1	2	3	4
Full phrase	W	WB	WBB	WBW
Encoded as	∅ W	1B	2B	2 W

In constructing the dictionary, begin with the empty set ∅. The dictionary is then dynamically constructed as the data is processed through. In the dataset, the first bit is W, which is encoded as the empty set ∅ plus a W. Next is another W, which has appeared before as phrase 1, to which the bit that follows, B, is appended. Thus, phrase 2 is created as phrase 1 (W) plus a B, which is added to the dictionary. This process continues until arriving at the end result of the compressed dataset of ∅W1B2B2W3.

The key idea in Lempel-Ziv is to find patterns in the dataset to be compressed and to utilize the repetitions of those patterns to achieve savings in memory storage demand. In the example given, the relatively short length of the dataset resulted in limited savings in the compression. However, as the size of the dataset gets larger and the number of repeated phrases increases, the gains achieved by employing the Lempel-Ziv algorithm to compress the dataset also increase.

3.3 Developed Compression Algorithm

The developed compression algorithm integrates both run-length encoding and Lempel-Ziv concepts to compress the system CPT of the BN. Both techniques result in lossless compression. Therefore, no approximations or assumptions are made in the compression of the system CPT.

A run is defined as consecutive bits of the same value. In the binary case, bits can take one of two values: 0 or 1 to indicate failure or survival, respectively. A consecutive sequence of 0's is called a "0 run," and a consecutive sequence of 1's is called a "1 run." Phrases are comprised of at least two elements, the first value and a sequence of the differing second value. The dictionary for the proposed algorithm is comprised of these phrases. Note that this definition of a phrase is different from the standard Lempel-Ziv definition.

Figure 3 shows the flowchart for the developed compression algorithm for a binary system with n components and with $\{MCS\}$ denoting the set of minimum cut sets (MCSs) of the system. The output of the compression algorithm is the compressed system CPT, $cCPT_{sys}$, and the accompanying dictionary of phrases, d_0. Steps of the algorithm are described below.

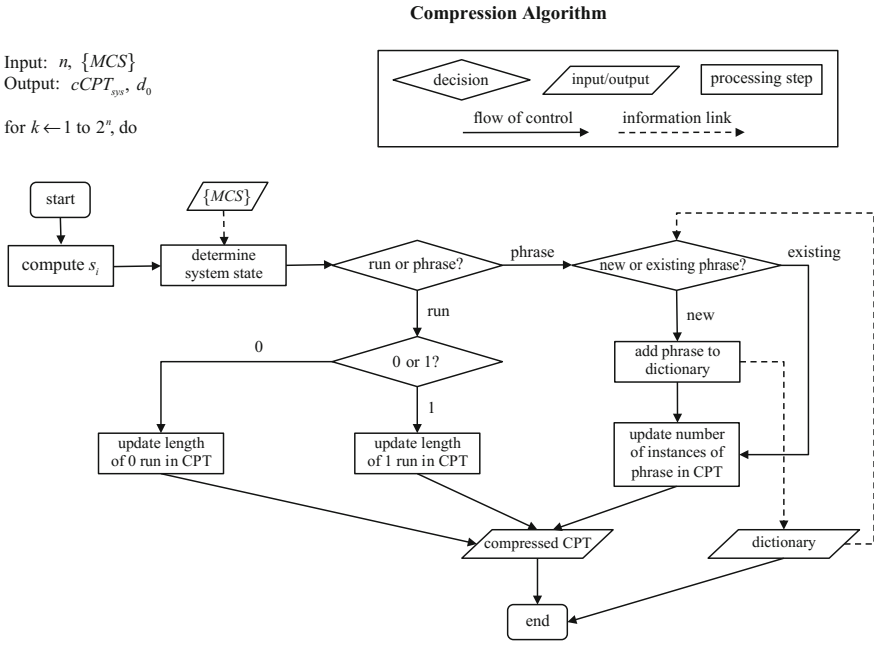

Fig. 3 Flowchart of compression algorithm

For each row $k = 1, \ldots, 2^n$ of the system CPT, the component states $s_1, \ldots, s_n$ are computed in terms of the row number based on the specific pattern used in defining the table. The table is constructed with $C_1, \ldots, C_n$ organized from left to right. Each row of the CPT is one of the mutually exclusive combinations of component states. The specific pattern used to organize these states is: C_1 is in state 0 for rows $k = 1, \ldots, 2^{n-1}$ and in state 1 for rows $k = 2^{n-1} + 1, \ldots, 2^n$; C_2 is in state 0 for rows $k = 1, \ldots, 2^{n-2}$, in state 1 for rows $k = 2^{n-2} + 1, \ldots, 2^{n-1}$, in state 0 for rows $2^{n-1} + 1, \ldots, 2^{n-1} + 2^{n-2}$, and in state 1 for rows $2^{n-1} + 2^{n-2} + 1, \ldots, 2^n$; etc. This pattern continues through C_n. Utilizing this pattern in constructing the CPT, the state of component i, $i = 1, \ldots, n$, in row k of the CPT is determined according to the rule

$$s_i = \begin{cases} 0 & \text{if} \quad ceil\left(\frac{k}{2^{n-i}}\right) \in \text{odd} \\ 1 & \text{if} \quad ceil\left(\frac{k}{2^{n-i}}\right) \in \text{even} \end{cases} \tag{2}$$

where $ceil(x)$ is the value of x rounded up to the nearest integer. For example, for a system comprised of 20 components, the state of C_{15} in row 450,000 is 0 because $ceil\left(\frac{450000}{2^{20-15}}\right) = 14063$ is odd. Note that using the above rule, the data on component states in the CPT is easily removed without any loss of information.

For each row, the component states are checked against $\{MCS\}$ to determine the system state. If all of the components comprising at least one MCS have failed, then the system is in the fail state; if not all components in any of the MCSs have failed, then system is in the survival state. This value of the system state is then encoded in compressed form as a run or a phrase. Runs can be 0 runs or 1 runs, and as the number of consecutive repeated values increases, the length of the run is increased. When a phrase is encountered, the phrase is checked against the contents of the dictionary to determine if the phrase is an existing one that has already been stored in the dictionary, or if it is a new one that must be added to the dictionary. Each phrase in the dictionary is fully defined by four variables: (1) the phrase number, p, (2) the first value in the phrase, v_1, (3) the second and subsequent values in the phrase, v_2, and (4) the length of the phrase L_p. Once the existing or new phrase has been identified, the number of repeated instances of the particular phrase, denoted n_p, is updated.

Each row of the compressed CPT is comprised of three values: (1) an indicator variable that defines whether the row is the beginning of a run or a phrase; (2) if a run, the value r of the run; if a phrase, the phrase number p in the dictionary; and (3) if a run, the length L_r of the run; if a phrase, the number n_p of repeated instances of the phrase. Therefore, a run is defined by the values $\{\text{run}, r, L_r\}$ and a set of phrases is defined by the values $\{\text{phrase}, p, n_p\}$. Once all rows of the system CPT have been processed, the end result of the compression algorithm is the compressed CPT, $cCPT_{sys}$, and the dictionary, d_0. The size of this data is typically orders of magnitude smaller than the size of the original CPT (Tien and Der Kiureghian 2013).

3.4 Application to an Example System

To illustrate the developed compression algorithm, it is applied to the example system shown in Fig. 4, which is adopted from Bensi et al. (2013). The system consists of a parallel subsystem (C_1, C_2, C_3) and series subsystems (C_4, C_5, C_6) and (C_7, C_8). For this system, the set of MCSs is $\{MCS\} = \{(C_1, C_2, C_3, C_4), (C_1, C_2, C_3, C_5)(C_1, C_2, C_3, C_6), (C_7), (C_8)\}$.

The BN formulation of the system is shown in Fig. 5. The full system CPT is shown in Table 2. The first 8 columns give the states of components $C_1, \ldots, C_8$,

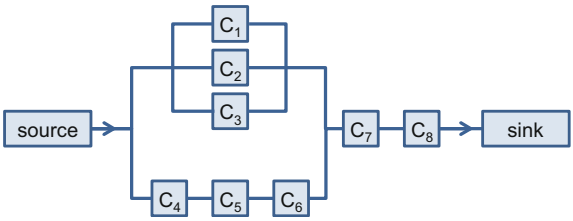

Fig. 4 Example system

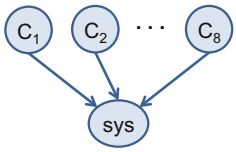

Fig. 5 BN formulation of the example system

Table 2 System CPT for example system

C_1	…	C_7	C_8	*sys*
0	…	0	0	0
0	…	0	1	0
0	…	1	0	0
0	…	1	1	0
⋮		⋮	⋮	⋮
1	…	0	0	0
1	…	0	1	0
1	…	1	0	0
1	…	1	1	1

constructed according to the pattern described in Sect. 3.3. The right-most column gives the state of the system given the states of the components in that row. Because the system is comprised of 8 components, the system CPT consists of $2^8 = 256$ rows.

3.4.1 Construction of Compressed CPT

The implementation of the proposed compression algorithm proceeds by processing through the rows $k = 1, \ldots, 2^n$. Note that we only need to compress the vector of system states, i.e., the right-most column in the CPT. There is no need to compress the entire CPT as the component states in any row, i.e., the values in columns $1, \ldots, n$, can be determined according to the rule given in Eq. (2).

In row $k = 1$, $\{s_1, \ldots, s_8\} = \{0, \ldots, 0\}$. As all components in the system are in the failed state, clearly the system is also in the failed state. More rigorously, checking against $\{MCS\}$, we see that all components in the first MCS, (C_1, C_2, C_3, C_4), have failed. Therefore, $sys = 0$. Note that once we find that all components in a MCS are in the failed state, we need not check the component states against the remaining MCSs as the failure of any one MCS indicates failure of the system.

As we continue through the rows $k = 2, \ldots, 31$, we find the system to be in the failed state, until we reach row $k = 32$. Therefore, the compressed CPT begins with a 0 run of length 31. At $k = 32$, $\{s_1, \ldots, s_8\} = \{0, 0, 0, 1, 1, 1, 1, 1\}$. Checking against $\{MCS\}$, we see that none of the MCSs have failed. In fact, the path from

source to sink flows through C_4, C_5, C_6, C_7, C_8. Thus, $sys = 1$, and we have reached the end of the initial 0 run. Looking at $k = 33$, $\{s_1, \ldots, s_8\} = \{0, 0, 1, 0, 0, 0, 0, 0\}$. We see that the component in the fourth MCS (C_7) has failed. Therefore, $sys = 0$ and we have a phrase beginning at row $k = 32$. Had the value in row $k = 33$ been $sys = 1$, we would have had a 1 run.

At this point, we have not yet encountered any phrases and our dictionary is empty. Therefore, this is the beginning of a new phrase. For $k = 34$ and $k = 35$, $sys = 0$. At $k = 36$, $sys = 1$, indicating the end of the phrase. The full phrase, therefore, is $\{1, 0, 0, 0\}$ for $k = 32, \ldots, 35$, which is stored in the dictionary as $\{1, 1, 0, 4\}$. These four values indicate that the phrase number is $p = 1$, the first value in the phrase is $v_1 = 1$, the second and subsequent values in the phrase are $v_2 = 0$, and the length of the phrase is $L_p = 4$. Note that in the binary case, v_1 and v_2 are complements, so knowing one value enables us to know the other. However, while it is not necessary to store both values in the initial construction of the compressed system CPT, in the subsequent process for inference, v_1 and v_2 can take values different from 0 and 1 and are no longer guaranteed to be complements. Therefore, during inference, we must store both v_1 and v_2, and all four values to define the phrase are recorded in this stage as well for consistency.

After determining $sys = 1$ for $k = 36$, we continue for $k = 37, \ldots, 39$ with the system state $sys = 0$ and for $k = 40$ with the system state $sys = 1$, thus we again encounter the phrase $sys = \{1, 0, 0, 0\}$. This is now an existing phrase that we call from the dictionary. Therefore, in the compressed system CPT, we reference phrase $p = 1$ and increase the number of instances of this phrase by 1. We continue through the remaining rows $k = 40, \ldots, 2^n = 256$. Once we have processed all the rows of the system CPT, the end result for the compressed CPT and the dictionary are as given in Tables 3 and 4, respectively.

Tables 3 and 4 indicate that the total number of elements to be stored for the compressed system CPT is 9 and for the dictionary is 4 for a total of 13 elements. This is not counting the table headings, which are included for reference here and need not be stored when implementing the compression algorithm in a computer.

Table 3 Compressed system CPT for example system

Run or phrase	*r or p*	L_r or n_p
Run	0	31
Phrase	1	56
Run	1	1

Table 4 Dictionary for example system

p	v_1	v_2	L_p
1	1	0	4

Note that we can check that the total number of rows represented in the compressed CPT corresponds with the total number of rows of the system full CPT. From Tables 3 and 4 for the example system, we start with a run of length 31, have 56 instances of a phrase of length 4, and end with a run of length 1. This equals $31 + 56 \times 4 + 1 = 256$ rows of the original CPT that are now stored in the compressed CPT. Thus, all the information in the original CPT is stored in the compressed CPT and the compression is lossless. The total number of elements that must be stored during the construction of the BN has been reduced from $2^8 = 256$ total elements in the original CPT to 13 in the compressed CPT. In a system with a large number of components, the amount of data reduction can be even more dramatic than that observed for this small example system.

4 Inference Algorithm

Once the Bayesian network (BN) model of a system has been constructed, inference is required to draw conclusions about the system. There are both exact and approximate methods for inference. Approximate methods are generally sampling based, including importance sampling (Salmeron 2000; Yuan and Druzdzel 2006) and Markov chain Monte Carlo (Gilks et al. 1996; Beck and Au 2002) methods. In theory, these methods converge to the exact solution for a sufficiently large number of samples. In practice, however, the rate of convergence is unknown and can be slow (Straub 2009). This is especially true when simulating events that are a priori unlikely. The number of simulations required to achieve a sufficiently large sample for convergence can become prohibitive. In addition, many engineering applications of BN methods for system reliability analysis require near-real time updating, e.g., for post-hazard system assessment and decision support. For these applications, approximate methods that are computationally intensive are not appropriate. Therefore, exact methods of inference are preferred and are considered here. In the following sections, the two major algorithms used for exact inference, variable elimination (VE) and junction tree (JT), are briefly described.

4.1 Variable Elimination (VE)

In the VE algorithm (Dechter 1999), our objective is to perform inference on the "query" node, the node for which the updated probability distribution is of interest. To do this, we eliminate all the other nodes in the network, one by one, until we are left with the query node—hence the name of the algorithm, variable elimination.

Elimination of each node corresponds to summing of the joint distribution over all states of the node to be eliminated, resulting in an intermediate factor λ that is used during the next step of elimination. For example, for the system shown in Fig. 2 with components C_1 to C_n, suppose we are interested in the updated distribution of the state of component C_1, given a particular state *sys* of the system. The VE calculation for this query is

$$\begin{aligned} p(C_1, sys) &= \sum_{C_2} \cdots \sum_{C_n} p(C_1)p(C_2)\cdots p(C_{n-1})p(C_n)CPT_{sys} \\ &= p(C_1) \sum_{C_2} p(C_2) \cdots \sum_{C_{n-1}} p(C_{n-1}) \sum_{C_n} p(C_n)CPT_{sys} \\ &= p(C_1) \sum_{C_2} p(C_2) \cdots \sum_{C_{n-1}} p(C_{n-1})\lambda_n \\ &\quad \cdots \\ &= p(C_1)\lambda_2 \end{aligned} \tag{3}$$

where CPT_{sys} is the conditional probability table for the system node in the BN and λ_i is the intermediate factor, in the form of a table, created after the elimination of node C_i. Nodes $C_2, \ldots, C_n$ have been eliminated to arrive at the query node, C_1. It is noted that the order in which the variables in a network are eliminated results in different memory storage and computation time requirements for the VE algorithm. The selection of an optimal elimination ordering, however, is an NP-hard problem. Depending on the structure of the network, heuristics can be developed to improve efficiency in elimination ordering. This topic is addressed in Sect. 6.

4.2 Junction Tree (JT)

The JT algorithm (Spiegelhalter et al. 1993) breaks down the network into smaller structures, called "cliques," which are subsets of the nodes in the BN. The conditional probability tables associated with each clique are called "potentials," and the JT is initialized by computing the potentials over all cliques. The advantage of the JT algorithm comes from breaking down the full BN into cliques. For a network structured as shown in Fig. 2 with components C_1 to C_n, however, the JT is comprised of only one clique of size $n+1$. As the size of the system increases, computation of the potential over this clique during the initialization of the JT increases exponentially and becomes intractable. Therefore, the VE algorithm is adopted here, together with the compression of data, for inference.

4.3 Developed Inference Algorithm

In the proposed inference algorithm, we eliminate variables one by one to arrive at the query node, with the intermediate factor λ_i created after the elimination of component C_i. The key to being able to perform inference on the BN constructed using the compression algorithm described in Sect. 3 is that the λ_i's are also compressed using the same compression algorithm as for CPT_{sys}. Further, the inference algorithm is developed to handle both the compressed CPT_{sys} and λ_i without decompressing or recompressing.

Let CPT_{sys} denote the conventional uncompressed full system CPT, and $cCPT_{sys}$ the compressed system CPT constructed by running the compression algorithm. Similarly, λ_i represents the uncompressed intermediate factor after elimination of the i th component, with $i = 0, n, \ldots, 1$ being the order of elimination, and $c\lambda_i$ the corresponding compressed intermediate factor. $i = 0$ indicates that no components have been eliminated. Therefore, $\lambda_0 = CPT_{sys}$ and $c\lambda_0 = cCPT_{sys}$. Let m_i indicate the number of rows in $c\lambda_i$. During the compression of CPT_{sys}, an accompanying dictionary d_0 is constructed, which defines the phrases present in $cCPT_{sys}$.

For the developed inference algorithm, we begin with $cCPT_{sys}$ and d_0. We then eliminate the components in the order $n, \ldots, 1$. At each step, we directly construct, row by row, $c\lambda_i$ from $c\lambda_{i+1}$ ($c\lambda_n$ from $c\lambda_0 = cCPT_{sys}$), and d_i from d_{i+1} (d_n from d_0). Similar to the rows of the compressed system CPT, each row j of $c\lambda_i$, $j = 1, \ldots, m_i$, is comprised of three values: (1) an indicator variable that defines whether the row is the beginning of a run or a phrase; (2) if a run, the value r_i^j of the run; if a phrase, the phrase number p_i^j in the dictionary; and (3) if a run, the length $L_{r_i}^j$ of the run; if a phrase, the number $n_{p_i}^j$ of repeated instances of the phrase. Each row of d_i defines a phrase, which is fully defined by four variables: (1) the phrase number p, (2) the first value in the phrase, v_1, (3) the second and subsequent values in the phrase, v_2, and (4) the length of the phrase L_p.

The inference algorithm is given below. Let $\{p_f\}$ denote the vector of length n defining the failure probabilities of components $C_1, \ldots, C_n$ so that $p_{f,i} = \Pr(C_i = 0)$ is its ith element. If the component nodes have parents, the parent nodes are eliminated first so that the component failure probabilities are marginalized. We define two quantities: S_i^j the run or phrase start row number in λ_i defined by row j of $c\lambda_i$, and R^j the remainder after processing row j of $c\lambda_i$ (defined in Table 5). Because the remainder is reset after the elimination of node i, it does not carry subscript i. Also, let Q define the set of query nodes (or components) and E denote the set of nodes (components) for which evidence is entered.

Table 5 Rules for constructing $c\lambda_i^j$

Switch			r_i^j or p_i^j	$L_{r_i}^j$ or $n_{p_i}^j$	R^j
Run	$S_{i+1}^j \in$ odd	$L_{r_{i+1}}^j \in$ odd	r_{i+1}^j	$\left(L_{i+1}^j - 1\right)/2$	$r_{i+1}^j \times \Pr(C_i = 0)$
		$L_{r_{i+1}}^j \in$ even	r_{i+1}^j	$L_{i+1}^j/2$	0
	$S_{i+1}^j \in$ even	$L_{r_{i+1}}^j \in$ odd	$r_{i+1}^j \times \Pr(C_i = 1) + R^{j-1}$ (also $r_i^{j+1} = r_{i+1}^j$)	1 (also $L_{r_i}^{j+1} = \left(L_{i+1}^j - 1\right)/2$)	0
		$L_{r_{i+1}}^j \in$ even	$r_{i+1}^j \times \Pr(C_i = 1) + R^{j-1}$ (also $r_i^{j+1} = r_{i+1}^j$)	1 (also $L_{r_i}^{j+1} = \left(L_{i+1}^j - 2\right)/2$)	$r_{i+1}^j \times \Pr(C_i = 0)$
Phrase	$S_{i+1}^j \in$ odd	$L_{p_{i+1}}^j \in$ odd	p_{i+1}^j	$n_{p_{i+1}}^j$	$v_{2_{i+1}}^j \times \Pr(C_i = 0)$
		$L_{p_{i+1}}^j \in$ even	p_{i+1}^j	$n_{p_{i+1}}^j$	0
	$S_{i+1}^j \in$ even	$L_{p_{i+1}}^j \in$ odd	p_{i+1}^j	$n_{p_{i+1}}^j$	0
		$L_{p_{i+1}}^j \in$ even	p_{i+1}^j	$n_{p_{i+1}}^j$	$v_{2_{i+1}}^j \times \Pr(C_i = 0)$

Inference Algorithm

Input: $n, \{p_f\}, cCPT_{sys}, d_0, Q, E$
Output: $\Pr(Q|E)$
For $i \leftarrow n$ down to 1, do

If $i \in Q$
    Reorder λ_{i+1} such that component i is ordered to extreme left, i.e., numbered 1.
    $c\lambda_{i+1}^{\text{reordered}} \leftarrow \lambda_{i+1}^{\text{reordered}}$ using compression algorithm.
    Do not increment i.

Else for $j \leftarrow 1$ to m_{i+1}, do
    Switch {run, phrase}, $S_{i+1}^{j} \in$ {odd, even}, $\left(L_{r_{i+1}}^{j} \text{ or } L_{p_{i+1}}^{j}\right) \in$ {odd, even}.
    Construct $c\lambda_i$ and d_i according to the case rules in Tables 5 and 6.
    Increment i.

end

Tables 5 and 6 show the rules for different cases to construct $c\lambda_i$ and d_i, respectively. In both tables, the cases are shown in the left three columns. In Table 5 for $c\lambda_i$, the fourth and fifth columns list the run or phrase values, and the last column is an update of the remainder for row j. The case for a run with $S_{i+1}^{j} \in$ even involves the remainder from the preceding row of $c\lambda_i$. The last column of the table lists the remainder value for the jth row of $c\lambda_i$. This is updated for possible use for the next row of $c\lambda_i$ or d_i. In Table 6 for d_i, the last three columns list the first and second values of the new phrase and its length. When $S_{i+1}^{j} \in$ even, the first phrase value involves the remainder corresponding to the preceding row of $c\lambda_i$.

With the rules described in Tables 5 and 6, the developed inference algorithm is thus able to handle both CPT_{sys} and λ_i in compressed form without decompressing or recompressing. This enables the savings in memory storage requirement achieved from implementing the compression algorithm during construction of the BN to be preserved through the process of inference.

4.4 Example System

To illustrate the proposed inference algorithm, we apply it to the example system shown in Fig. 4. We define the prior probabilities of failure as 0.2 for the parallel components and 0.01 for the series components, such that $\{p_f\} = \{0.2, 0.2, 0.2, 0.01, 0.01, 0.01, 0.01, 0.01\}$ for components $C_1, \ldots, C_8$.

Table 6 Updating d_i for a new phrase starting in row j of $c\boldsymbol{\lambda}_i$

Switch			$v^j_{1_i}$	$v^j_{2_i}$	$L^j_{p_i}$
Phrase	$S^j_{i+1} \in$ odd	$L^j_{p_{i+1}} \in$ odd	$\left[v^j_{1_{i+1}} \times \Pr(C_i = 0)\right] + \left[v^j_{2_{i+1}} \times \Pr(C_i = 1)\right]$	$v^j_{2_{i+1}}$	$\left[\left(L^j_{i+1} - 3\right)/2\right] + 1$
		$L^j_{p_{i+1}} \in$ even	$\left[v^j_{1_{i+1}} \times \Pr(C_i = 0)\right] + \left[v^j_{2_{i+1}} \times \Pr(C_i = 1)\right]$	$v^j_{2_{i+1}}$	$\left[\left(L^j_{i+1} - 2\right)/2\right] + 1$
	$S^j_{i+1} \in$ even	$L^j_{p_{i+1}} \in$ odd	$R^{j-1} + \left[v^j_{1_{i+1}} \times \Pr(C_i = 1)\right]$	$v^j_{2_{i+1}}$	$\left[\left(L^j_{i+1} - 1\right)/2\right] + 1$
		$L^j_{p_{i+1}} \in$ even	$R^{j-1} + \left[v^j_{1_{i+1}} \times \Pr(C_i = 1)\right]$	$v^j_{2_{i+1}}$	$\left[\left(L^j_{i+1} - 2\right)/2\right] + 1$

4.4.1 Results of Implementing Inference Algorithm

We begin with the compressed system CPT $cCPT_{sys}$ given in Table 3 and the accompanying initial dictionary d_0 given in Table 4. Suppose we are interested in the backward inference problem of obtaining the posterior probability distribution of C_1 given the observation that the system has failed. Our elimination order is $8, \ldots, 1$. In the first step of the elimination process, we are eliminating C_8. For reference, the uncompressed intermediate factor λ_8 created after this elimination is shown in Table 7.

For the proposed inference algorithm, however, we need not work with matrices in uncompressed form. We will be constructing $c\lambda_8$ directly from $cCPT_{sys}$ as follows. $cCPT_{sys}$ consists of 3 rows; therefore, $m_{sys} = 3$. Looking at row $j = 1$ of $cCPT_{sys}$, we see that it is a run; we are starting in row 1, so $S^1_{sys} \in$ odd; and the length of the run is 31, so $L^1_{r_{sys}} \in$ odd. Therefore, in constructing $c\lambda^1_8$, we use the rules in the first row of Table 4.1: $r^1_8 = r^1_{sys} = 0$, $L^1_{r_8} = \left(L^1_{sys} - 1\right)/2 = (31-1)/2 = 15$, and we have a remainder $R^1 = r^1_{sys} \times \Pr(C_8 = 0) = 0$.

Moving to row $j = 2$, we have a phrase that starts in row 32 with a phrase length of 4. Therefore, we use the last row of Table 5 to construct $c\lambda^2_8$: $p^2_8 = p^2_{sys} = 1$, $n^2_{p_8} = n^2_{p_{sys}} = 56$, and we have a remainder $R^2 = v^2_{2_{sys}} \times \Pr(C_8 = 0) = 0$. Because we are now dealing with phrases, we also need to update our dictionary d_8 with this new phrase starting in row $j = 2$ of $c\lambda_8$. Given the even starting row number and even phrase length, we are again using the last row, now in Table 6, to update d_8: $v^2_{1_8} = R^1 + \left[v^2_{1_{sys}} \times \Pr(C_8 = 1)\right] = 0 + [1 \times 0.99] = 0.99$, $v^2_{2_8} = v^2_{2_{sys}} = 0$ and $L^2_{p_8} = \left[\left(L^2_{sys} - 2\right)/2\right] + 1 = 2$.

Here, we see that the run values r and the values of the phrases v_1 and v_2 can take on values other than 0 or 1, even in the binary case, as we multiply by component failure probabilities that are different from 0 or 1. However, the intermediate factors λ_i can still be compressed because the calculations for each row only involve the failure probability of one component so that the number of values

Table 7 Uncompressed intermediate factor λ_8 constructed after elimination of C_8 in the example system

C_1	…	C_6	C_7	λ_8
0	…	0	0	0
0	…	0	1	0
0	…	1	0	0
0	…	1	1	0
⋮		⋮	⋮	⋮
1	…	0	0	0
1	…	0	1	0.99
1	…	1	0	0
1	…	1	1	0.99

Table 8 Compressed intermediate factor $c\lambda_8$ constructed after elimination of C_8 in the example system

Run or phrase	*r or p*	L_r or n_p
Run	0	15
Phrase	1	56
Run	0.99	1

Table 9 Dictionary d_8 constructed after elimination of C_8 in the example system

p	v_1	v_2	L_p
1	0.99	0	2

that the runs and phrases can take on is still finite. Continuing with the example system for row $j = 3$ results in the constructed $c\lambda_8$ and d_8 shown in Tables 8 and 9, respectively.

We continue the elimination process until we have eliminated the variables $C_2, \ldots, C_8$ and arrive at the query node of interest C_1. Our original inference question was to obtain the posterior probability distribution of C_1 given an observation of system failure. From the VE process, we obtain the joint probability $p(C_1, sys)$, which we divide by $p(sys)$ to arrive at the final result: $p(C_1|sys = 0) = [0.20930.7907]$ for C_1 being in the failure or survival state, respectively. Thus, given the observation that the system has failed, the probability of failure for C_1 has been updated from a prior failure probability of 0.2 to a posterior failure probability of 0.2093.

Comparing the uncompressed intermediate factor λ_8 given in Table 7 with the compressed $c\lambda_8$ and accompanying dictionary d_8 given in Tables 8 and 9, respectively, we see that the memory storage requirements have been reduced from $2^7 = 128$ elements to a total of 13 elements, 9 for $c\lambda_8$ and 4 for d_8. Checking the total number of rows represented in $c\lambda_8$ with the total number of rows of the full λ_8 shows the compression to be lossless, and it is again emphasized that there is no need to decompress $cCPT_{sys}$ or any of the λ_i values to compute $c\lambda_i$ for the inference algorithm. Similar reductions in memory storage are achieved at each step of the elimination process.

5 Performance of Algorithms

To evaluate the performance of the developed algorithms, we apply them to two test example systems, comparing the performance of the new algorithms to existing methods in terms of both memory storage and computation time.

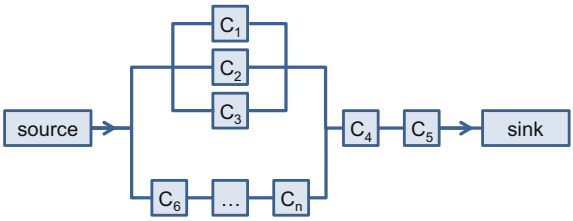

Fig. 6 Example test system: expanded with increased number of components in series subsystem

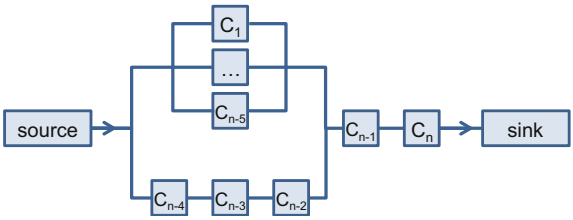

Fig. 7 Example test system: expanded with increased number of components in parallel subsystem

5.1 Test Example Systems

We begin with the example system adopted from Bensi et al. (2013) shown in Fig. 4. The system is comprised of 8 components and consists of a parallel subsystem, $\{C_1, C_2, C_3\}$, and two series subsystems, $\{C_4, C_5, C_6\}$ and $\{C_7, C_8\}$. Because the objective is to see how the proposed algorithms scale, we increase the number of components in the first two subsystems to a total number of components in the system n. The systems obtained by increasing the number of components in the series and parallel subsystems are shown in Figs. 6 and 7, respectively. The BN formulation of these expanded systems is as shown for the general system in Fig. 2.

The resulting analyses of these two expanded systems demonstrates how the proposed algorithms perform compared to existing algorithms for systems of increasing size. While the above systems can be more efficiently represented as a system of three supercomponents, each supercomponent representing a series or parallel subsystem, as described in Pages and Gondran (1986) and used in Der Kiureghian and Song (2008), here we disregard this advantage in order to investigate the system size effect. Supercomponents are discussed in Sect. 6.3.

5.2 Memory Storage

Figure 8 shows the performance of the new algorithms compared to existing methods in terms of memory storage. The maximum number of values that must be stored in memory during the running of the algorithms, plotted on a logarithmic scale, is used as a proxy for the memory storage requirements of each algorithm.

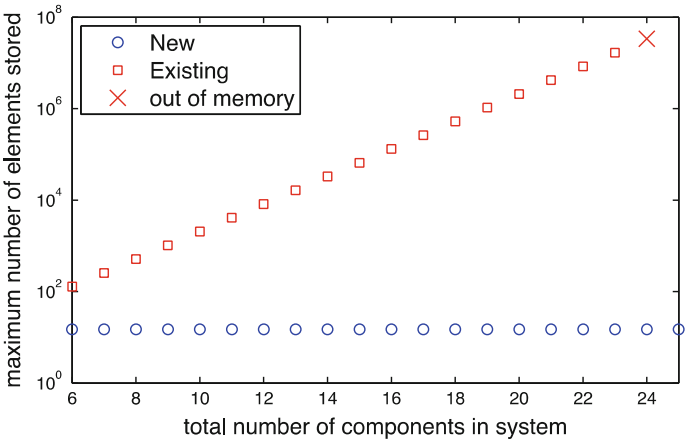

Fig. 8 Memory storage requirements for proposed new algorithm compared to existing method as a function of system size

Algorithms are run in Matlab v7.10 on a 32 Gb RAM computer with 2.2 GHz Intel Core i7 processor.

In Fig. 8, the values for the "New" proposed algorithm are the maximum from the initial construction of the BN (including elements in both the compressed system CPT and accompanying phrase dictionary) and during the inference process (including elements in both the intermediate factors λ_i and accompanying phrase dictionaries at each elimination step). The values for the "Existing" algorithm indicate the maximum number of elements stored using the existing junction tree (JT) algorithm, as implemented in the Bayes Net Toolbox by Murphy (2001). The "X" mark indicates the maximum size of the system after which the existing algorithm can no longer be used because the memory demand exceeds the available memory storage capacity.

Figure 8 shows that the proposed new algorithm achieves significant gains in memory storage demand compared to existing methods. For the existing JT algorithm, the memory storage demand, as measured by the maximum number of values that must be stored, increases exponentially with the number of components in the system. In fact, the algorithm runs out of memory for a system comprised of more than 24 components. The memory storage demand using the proposed new algorithm not only does not increase exponentially, but remains constant, even as the number of components in the system increases. The total number of values stored is 15, compared to 2^{n+1} for the size of the full system CPT.

5.3 Computation Time

Figure 9 examines computational efficiency of the algorithms, and shows the computation times required to run the new compared to existing algorithms as a function of increasing system size (increasing the number of components in the series subsystem). Computation times are broken into the various functions for each algorithm. For each system size, from left to right: "New—compression" indicates the time required to compress the system CPT using the proposed compression algorithm; then the time required to perform forward inference on the system given $\{C_1 = 0\}$ and the time to perform backward inference on the component C_1 given $\{sys = 0\}$, respectively, using the proposed inference algorithm; "Existing—initialization" indicates the times required to initialize the BN using the existing JT algorithm; then the times required to perform forward inference and backward inference using JT. Results for increasing the number of components in the parallel subsystem were similar.

Figure 10 compares the computation times for the proposed algorithm for the two systems in Figs. 6 and 7 broken down into times to: compress the system CPT, perform forward inference on the system given the state of component C_1, and perform backward inference on component C_1 given the state of the system. The solid bars are for the case where the size of the system is increased by increasing the number of components in the series subsystem, and the bars with diagonal hatching are for the case where the size of the system is increased by increasing the number of components in the parallel subsystem.

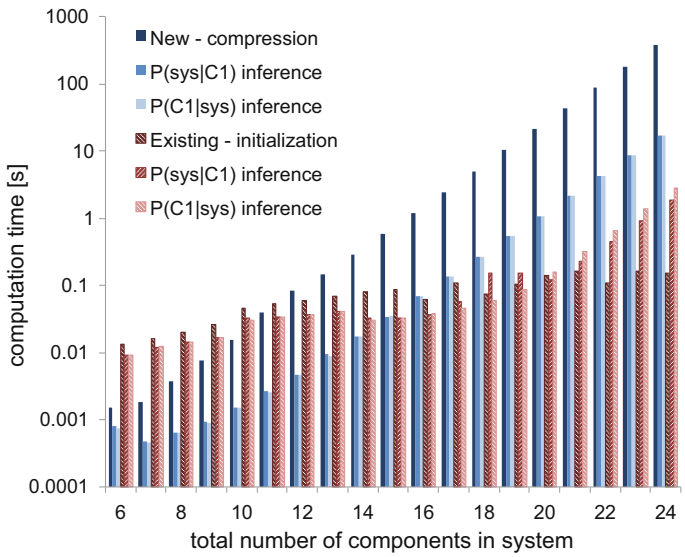

Fig. 9 Computation times for new algorithm compared to existing method as a function of system size

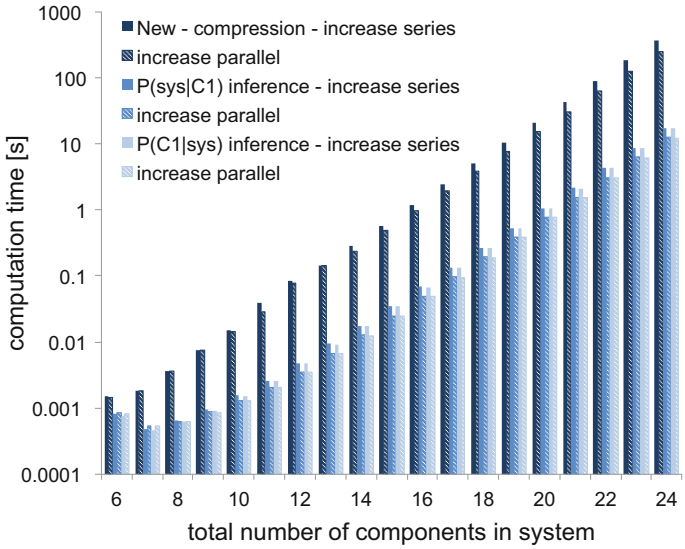

Fig. 10 Computation times for new algorithm when increasing components in the series compared to parallel subsystems

In Fig. 10, we see that the algorithm performs slightly better in the initial compression of the system CPT and in both inference scenarios for the systems with an increased number of parallel components compared to series components. The algorithm, therefore, is better suited to systems that can be formulated as few MCSs comprised of many components each, compared to systems formulated as many MCSs of few components each. In the latter case, it is preferable to use an MLS formulation of the system.

Looking at Figs. 8 and 9 together, we see the classic storage space-computation time trade-off as described in Dechter (1999). Figure 8 shows the significant gains in memory storage demand achieved by the proposed new algorithm compared to the existing JT algorithm; while in Fig. 9, we see that the new algorithm requires longer computation times than the existing algorithm. We note, however, that as systems become larger, i.e., for systems comprised of more than 20 components, the time to perform inference for both the new and existing algorithms is exponentially increasing with the system size. For the existing algorithm, this is due to the increasing clique size for the JT. For the new algorithm, the increase in computation time is due to the computations needed for compressing the CPTs and performing inference with compressed intermediate factors λ_i during the variable elimination process.

It is important to note that the natures of the memory and time constraints are fundamentally different. Memory storage is a hard constraint. If the maximum size of a CPT exceeds the storage capacity of a program or machine, no analysis can be performed. While it is true that memory can be distributed, e.g., in cloud storage,

there still exists a hard limit on the maximum. In contrast, computation time is more flexible. Indeed, various recourses are available to address the computational time, such as parallel computing. Thus, some system reliability problems that simply could not be solved using existing algorithms because of limited computer memory now can be solved using the proposed algorithms. Even so, the accompanying increase in computation time can sometimes be prohibitive, particularly when considering the scale of real-world infrastructure systems. The following sections describe methods developed to improve the computational efficiency of the proposed algorithms such that the algorithms achieve gains along both memory storage and computation time measures.

6 Heuristic Augmentations

Three heuristic augmentations to the proposed algorithms are presented in this section. The first two utilize the ordering of the components for both the compression and inference algorithms, while the third addresses the BN formulation of the system to improve computational efficiency.

6.1 Heuristic for Compression Algorithm

To compress the full system CPT, the compression algorithm must run through each of the 2^n distinct combinations of component states (rows of the CPT). This leads to an exponentially increasing computation time for compressing the system CPT. However, knowledge about the structure of the system can be used to reduce the number of rows to be analyzed. For example, if component C_i on its own constitutes a MCS, i.e., failure of C_i leads to system failure, we need not check the states of other components when C_i is in the failed state.

In general, as discussed in Sect. 4, determining the optimal ordering of nodes in a BN is an NP-hard problem. The heuristic employed here is to order the MCSs by size, and order the components such that those in the smallest MCSs are numbered first and appear to the left in the CPT. Knowing where these components appear in the CPT enables us to know which rows in the CPT need not be processed when running the compression algorithm. In general, given the states of the components $s_1, \ldots, s_n$ for a system of n components, the corresponding row number r of the CPT is determined according to the rule

$$r = 1 + \sum_{i=1}^{n} s_i \times 2^{n-i} \tag{4}$$

Thus, given a particular ordering of components comprising an MCS of a known size, we can easily determine the rows where the system is in the failed state.

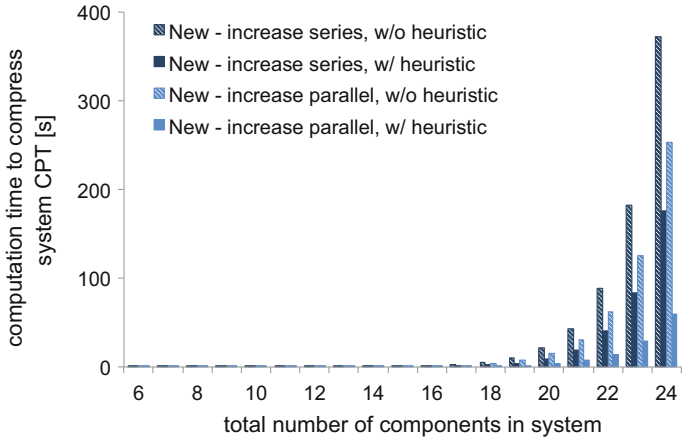

Fig. 11 Computation times to compress the system CPT without versus with heuristic implemented

For example, if component C_1 constitutes an MCS on its own, we know that for rows $1, \ldots, 2^{n-1}$ the system is in the failed state. If, instead, components C_1 and C_2 constitute a MCS, then we know that for rows $1, \ldots, 2^{n-2}$ the system is in the failed state. We call these "0 intervals," i.e., intervals of rows in the system column of the CPT that are in the 0 state. For this heuristic, if a row number in the CPT is determined to be within a 0 interval, we know that in that interval, we are in a 0 run and we are able to directly move to updating the length of the 0 run in the CPT. Therefore, the full compression algorithm need only process through the rows between the 0 intervals. This reduces the number of rows that are processed and results in reduced time spent on compression.

Figure 11 shows the result of applying this heuristic to the example systems presented in Sect. 5.1. The dashed and solid bars show the computation times required to compress the system CPT without and with the heuristic, respectively. In the example systems, the two components comprising the second series subsystem each on their own comprise a MCS. Therefore, these components are numbered first and appear to the left in the CPT. Specifically, for the system in Fig. 6, components C_4 and C_5 are renumbered 1 and 2, and for the system in Fig. 7, components C_{n-1} and C_n are renumbered components 1 and 2.

In Fig. 11, we see the reduction in computation times achieved by employing the heuristic for the compression algorithm. In addition, comparing the results for systems with increasing number of components in the series versus parallel subsystems, we see that, consistent with the results in Fig. 10, the algorithm performs better for the latter case. Thus, the algorithm is better suited to systems formulated as few MCSs of many components each, compared to systems formulated as many MCSs of few components each.

6.2 Heuristic for Inference Algorithm

Similar to the heuristic for the compression algorithm, the heuristic for the inference algorithm looks to ordering the components in a particular way to improve computational efficiency. During variable elimination, when we arrive at the query node, it is necessary to move it to the very left end of the CPT. This requires reordering of the elements in the intermediate factor λ_i, which is a computationally demanding effort. The heuristic employed here is to order the components such that query components appear as far to the left in the CPT as possible. This minimizes the number of operations that must be performed to reorder λ_i.

Figure 12 shows the result of applying this heuristic to the example systems presented in Sect. 5.1. The computation times for forward and backward inference in systems with an increasing number of components in the series and parallel subsystems are plotted. Figure 12a, b c respectively show the results from using the existing JT algorithm and the proposed new algorithm without and with the heuristic employed. The C_1 labeled in the figures on which inference is performed refers to the component numbered C_1 in Figs. 6 and 7. When implementing the heuristics, the compression algorithm heuristic results in the two components in the second series subsystem being renumbered as C_1 and C_2. Therefore, in implementing the inference algorithm heuristic, the query node is ordered next as C_3 in the reordered formulation of the system.

Comparing Fig. 12a, b, we see that the new algorithm without the heuristic employed requires longer computation times for inference than the existing JT algorithm. In addition, the computation times for both algorithms increase exponentially as the system size increases. However, in Fig. 12c we see that with the heuristic employed, the new algorithm achieves computation times that are orders of magnitude smaller than either of the other algorithms: four orders of magnitude faster than the new algorithm without the heuristic employed, and three orders of magnitude faster than the existing JT algorithm.

In addition, and more importantly given the effect for large systems, the computation times are linearly, not exponentially, increasing with system size. The reason for this is that when the heuristic is employed, the computation time becomes a function of not the full size of the λ_i s, which exponentially increase with the system size, but the size of the compressed λ_i s, which we have seen remain constant with increasing system size. With the memory storage savings already demonstrated, these heuristics utilizing a more effective ordering of the components significantly improve the computational efficiency of both the compression and inference algorithms.

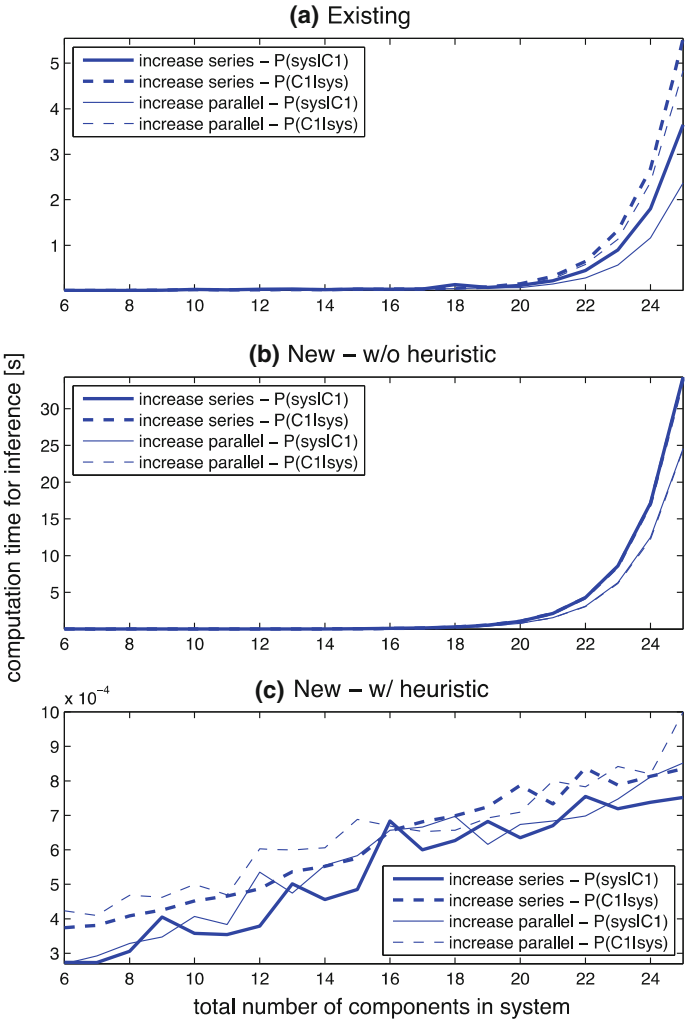

Fig. 12 Computation times for forward and backward inference using the existing algorithm **a** and new algorithm without **b** and with **c** the heuristic implemented

6.3 Algorithm for Supercomponents

Finally, in the previous sections, analyses of the example systems from Sect. 5.1 were purposely performed using a naïve formulation of the system with components each treated individually in order to test the performance of the proposed algorithm. In practice, systems can be more efficiently represented by grouping subsets of components into "supercomponents" (SCs) in a multi-scale modeling approach (Der Kiureghian and Song 2008). We apply the idea of SCs to the

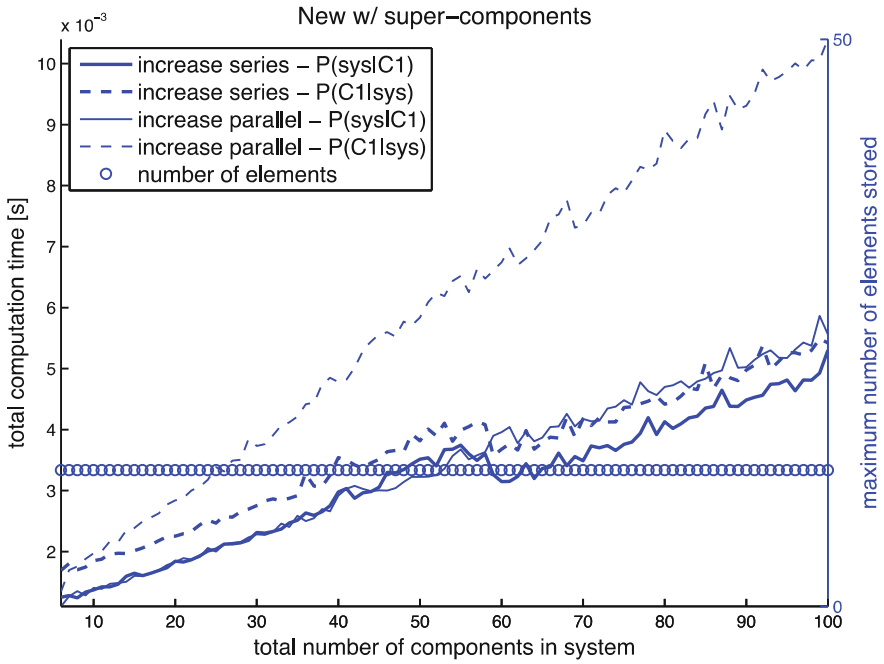

Fig. 13 Computation times and memory storage requirements for proposed new algorithm with supercomponents implemented

example systems described in Sect. 5.1, grouping the components in series and parallel subsystems into single SCs. Figure 13 shows the results in terms of both computation time (left *y*-axis, solid and dashed lines) and memory storage (right *y*-axis, circles) for systems of increasing size. Total computation times represent both the time for compression and the time for forward or backward inference. The maximum number of elements that must be stored during both the compression and inference processes are used as a proxy for the memory storage requirements of the proposed algorithms.

In Fig. 13, we see that the total number of components in the system is now shown up to 100 components. Looking at the magnitude of the computation time first, the total computation time is on the order of 10^{-2} s for a 100-component system. Looking at the trend in computation time as the size of the system increases, it is notably linearly, rather than exponentially, increasing. With regards to memory storage, we see that the maximum number of elements that must be stored remains constant, even as the total number of components in the system increases. Thus, significant gains have been achieved in both memory storage demand and computational efficiency with the proposed algorithm.

7 Application: Power System

With the objective of reliability assessment of infrastructure systems in mind, the proposed algorithms are applied to analyze the reliability of the 4-substation power network from Ostrom (2004) shown in Fig. 14, which was also investigated by Der Kiureghian and Song (2008). The network consists of 3 inputs and 1 output, and 59 components numbered 1–59, where the circles, slashes, and squares represent circuit breakers, switches, and transformers, respectively. Power can flow along any black line, including between substations via the connections shown. Additionally, for this system, the method of SCs is implemented, representing each triplet of switch-breaker-switch as a SC, as shown in Fig. 15, where the dashed squares represent SCs.

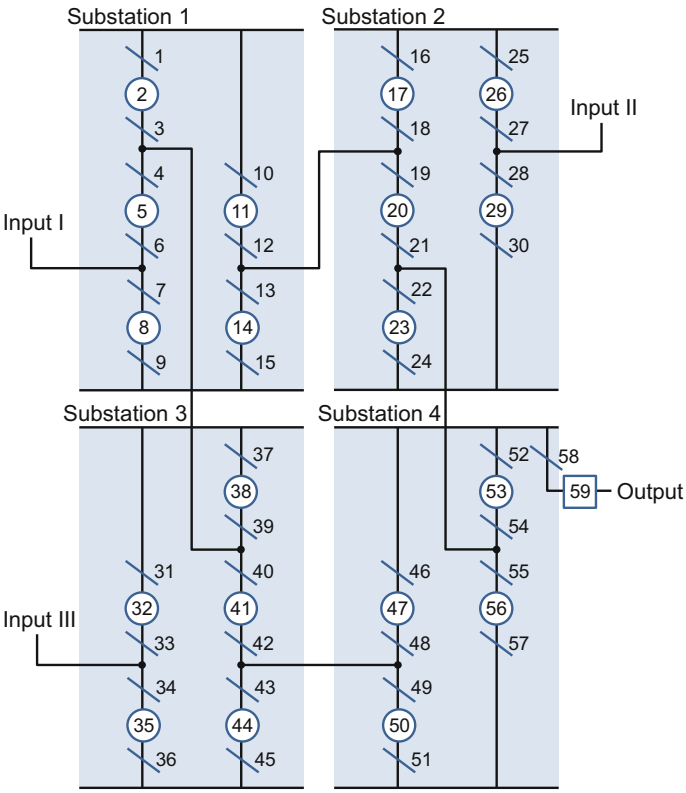

Fig. 14 Power system application

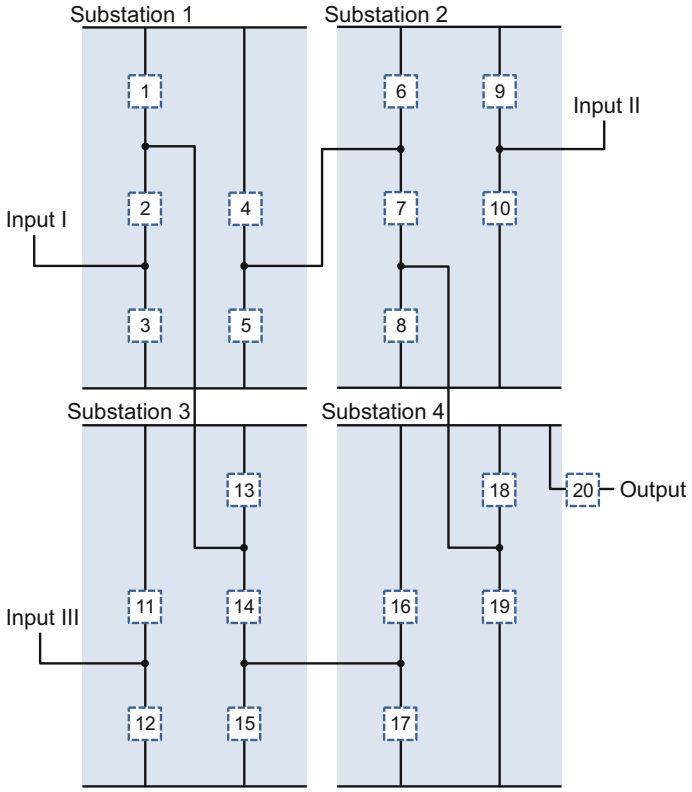

Fig. 15 Power system application with supercomponents implemented

7.1 Inference

Given an infrastructure system comprised of many interconnected components, as the system shown in Fig. 14 is, system risk and reliability analyses enable the identification of critical components to support decision making regarding inspection, repair, and replacement. Inference is required to perform these analyses. Figures 16 and 17 show the results of performing this forward and backward inference, respectively, for the power system application. To facilitate comparison across components, all components are initialized with a prior probability of failure of 0.1.

Figure 16 gives the probability of system failure given component failure for each of the components 1–59. The results of this forward inference support decision making in the management of the power system to minimize the risk of system failure. For example, knowing that probability of system failure is 100% if components 58 or 59 fail clearly indicates the importance of these two components and the need for regular inspection or retrofit of these components to ensure system

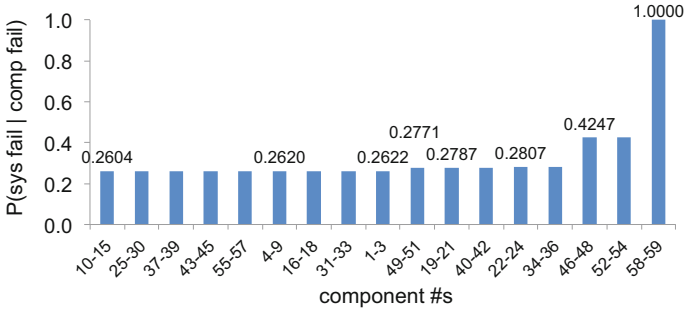

Fig. 16 Results of forward inference for power system application

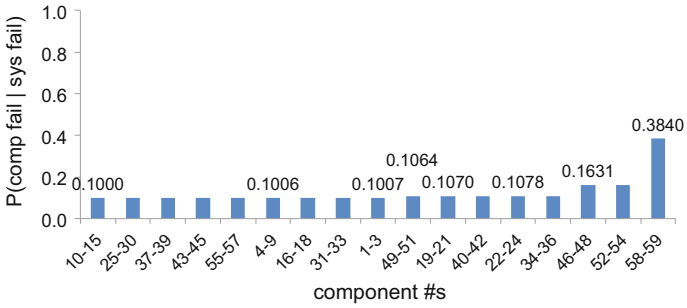

Fig. 17 Results of backward inference for power system application

performance. At a less extreme level, we see that, for example, components 46-48 are more critical than components 10–15. If failed, the updated probability of system failure is 0.4247 compared to 0.2604.

Figure 17 gives the probability of component failure given system failure for each of the components 1–59. The results of this backward inference support decision making in the repair of the power system to identify what may have led to system failure after the failure event has been observed. For example, the probability that components 58 or 59 have failed has been updated from a prior failure probability of 0.1 to 0.3840. In contrast, components 10–15 remain at a probability of failure of 0.1. We see that the evidence on the system state is not informative for these components, and the updated probability of failure equals the prior failure probability.

7.2 Performance of New Algorithms

In demonstrating the ability to perform both forward and backward inference using the proposed algorithm, the performance of the algorithm in terms of both

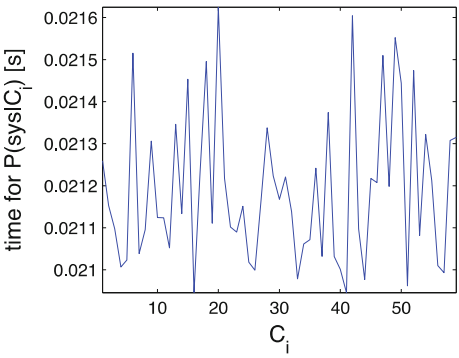

Fig. 18 Computation times for forward inference for power system application

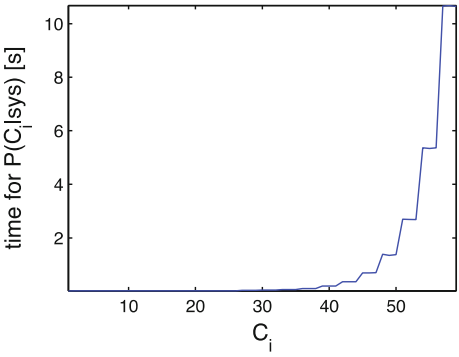

Fig. 19 Computation times for backward inference for power system application

computational efficiency and memory storage requirements is examined. For the power system shown in Fig. 14, the time required to compress the system CPT is 12.8 s. The computation times required for performing forward and backward inference are given in Figs. 18 and 19, respectively.

From Fig. 18, the average time required to compute the probability of system failure given component failure is 0.0212 s. In Fig. 19, we see an exponential increase in the computation time as the component number increases. This is explained by the reordering of the intermediate factor λ_i that must be performed when arriving at a query node during the VE inference process. Therefore, the heuristic for the inference algorithm proposed in Sect. 6.2 should be implemented whereby queries are ordered to the left in the CPT. Doing so, computation times will be in the lower range, e.g., for components 1–20, when performing backward inference.

Finally, the memory storage requirements are assessed. The maximum number of elements that must be stored to perform forward and backward inference are 707 and 1059 elements, respectively. While this may not seem particularly small, this is in comparison to a memory storage demand of $2^{59} = 5.8 \times 10^{17}$ elements for a system of $n = 59$ components. Therefore, the ability to construct the BN and perform inference using the proposed algorithms with only 10^3 elements needed

represents an orders of magnitude reduction in memory demand. Thus, the proposed algorithms achieve significant gains in both memory storage and computation time. Together with the heuristics, this enables large infrastructure systems to be modeled as BNs for reliability assessment.

8 Conclusions

This study presents novel Bayesian network (BN) methodologies for modeling and reliability assessment of infrastructure systems. The chapter proposes a compression algorithm that significantly reduces the memory storage requirements for the BN modeling of systems. The algorithm compresses the conditional probability table (CPT) associated with the system node in the BN as a combination of runs and phrases. The sizes of the compressed CPT and the associated phrase dictionary are typically orders of magnitude smaller than the size of the original CPT.

The proposed inference algorithm is able to perform both backward and forward inference on the compressed matrices. The algorithm utilizes variable elimination to perform exact inference, where the intermediate factors created after each elimination step are also stored in compressed form. No decompression or recompression of these factors during the inference calculations is necessary. This enables the savings in memory storage achieved by implementing the compression algorithm to be preserved through the inference process.

The gains achieved by the compression algorithm in memory storage are accompanied by a trade-off in computation time. Several heuristics, including efficient component ordering and employing supercomponents, are presented to improve computational efficiency. Through the application of the developed algorithms and heuristics to example systems, the ability to model systems of increasing size with orders of magnitude savings in both memory storage and computation time is demonstrated. Together, these algorithms enable larger systems to be modeled as BNs for system reliability analysis.

Infrastructure systems are complex. In an environment of limited resources, system reliability analysis is essential to identify the critical components of a system to make decisions to inspect, repair, or replace. The BN-based algorithms described in this study enable modeling of infrastructure systems at a level of detail and complexity not previously possible. Implementation of these methodologies is a step towards making more efficient and more effective engineering decisions about our infrastructure systems both now and for the future.

Acknowledgements The author would like to acknowledge the guidance, insights, and support of Armen Der Kiureghian during her time at the University of California, Berkeley. Support from the National Science Foundation Graduate Research Fellowship and University of California Chancellor's Fellowship for Graduate Study is also acknowledged.

References

Beck JL, Au SK (2002) Bayesian updating of structural models and reliability using Markov chain Monte Carlo simulation. J Eng Mech 128(4):380–391

Bensi M, Der Kiureghian A, Straub D (2013) Efficient Bayesian network modeling of systems. Reliab Eng Syst Saf 112:200–213

Bobbio A, Portinale L, Minichino M, Ciancamerla E (2001) Improving the analysis of dependable systems by mapping fault trees into Bayesian networks. Reliab Eng Sys Saf 71(3):249–260

Boudali H, Dugan JB (2005) A discrete-time Bayesian network reliability modeling and analysis framework. Reliab Eng Syst Saf 87:337–349

Dechter R (1999) Bucket elimination: a unifying framework for reasoning. Artif Intell 113:41–85

Der Kiureghian A, Song J (2008) Multi-scale reliability analysis and updating of complex systems by use of linear programming. Reliab Eng Syst Saf 93:288–297

Gilks WR, Richardson S, Spiegelhalter DJ (1996) Markov chain Monte Carlo in practice, 1st edn., vol 17. Chapman and Hall, London, pp 486

Hauck, E. L, "Data compression using run length encoding and statistical encoding," U.S. Patent 4 626 829 A, December 2, 1986

Jensen FV, Nielsen TD (2007) Bayesian networks and decision graphs, 2nd edn. Springer, New York

Kim MC (2011) Reliability block diagram with general gates and its application to system reliability analysis. Ann Nucl Energy 38:2456–2461

Lauritzen SL, Jensen F (2001) Stable local computation with conditional gaussian distributions. Stat Comput 11(2):191–203

Madsen AL (2012) Belief update in CLG Bayesian networks with lazy propagation. In: Proceedings of the 22nd conference on uncertainty in artificial intelligence

Mahadevan S, Zhang R, Smith N (2001) Bayesian networks for system reliability reassessment. Struct Saf 23:231–251

Murphy KP (2001) The Bayes net toolbox for matlab. In: Computing science and statistics: proceedings of the interface, vol 33, October 2001

Neal RM (1993) Probabilistic inference using Markov chain Monte Carlo methods, Technical Report CRG-TR-93-1. University of Toronto, Department of Computer Science

Ostrom D (2004) Database of seismic parameters of equipment in substations. Report to pacific earthquake engineering research center. http://peer.berkeley.edu

Pages A, Gondran M (1986) System reliability: evaluation and prediction in engineering. Springer, New York

Salmeron A, Cano A, Moral S (2000) Importance sampling in Bayesian networks using probability trees. Comput Stat Data Anal 34:387–413

Spiegelhalter DJ, Dawid AP, Lauritzen SL, Cowell RG (1993) Bayesian analysis in expert systems. Stat Sci 8(3):219–247

Straub D (2009) Stochastic modeling of deterioration processes through dynamic Bayesian networks. J Eng Mech 135(10):1089–1099

Tien I, Der Kiureghian A (2013) Compression Algorithm for Bayesian Network Modeling of Binary Systems. In Deodatis G, Ellingwood B, Frangopol D (eds) Safety, reliability, risk and life-cycle performance of structures and infrastructures. New York, CRC Press, pp 3075–3081

Tien I (2014) Bayesian network methods for modeling and reliability assessment of infrastructure systems. Doctoral Thesis, University of California, Berkeley

Tien I, Der Kiureghian A (2016) Algorithms for Bayesian network modeling and reliability assessment of infrastructure systems. Reliab Eng Syst Saf 156:134–147

Torres-Toledano JG, Succar LE (1998) Bayesian networks for reliability analysis of complex systems. Lect Notes Artif Intell 1484:195–206

Yuan C, Druzdzel MJ (2006) Importance sampling algorithms for Bayesian networks: principles and performance. Math Comput Model 43(9–10):1189–1207

Ziv J, Lempel A (1977) A universal algorithm for sequential data compression. IEEE Trans Inf Theory 23(3):337–343

Kriging Interpolation Strategy for Finite-Element-Based Surrogate Responses of DCB Delamination Tests

Salvatore Sessa and Nunziante Valoroso

Abstract A procedure for computing the surrogate response of Finite Element models based on kriging interpolation is presented. A set of computer experiments is run for random occurrences of a target material parameter in order to build the data set necessary to the calibration of the interpolation model. Kriging parameters are defined via the Matérn 5/2 variance function and via average functions related to the expected trend of Finite Element analyses to get data consistent with the physics of the simulated experiment. Application of the surrogate model is detailed for the case of pure mode-I bending of a symmetric Double Cantilever Beam bonded specimen and the effectiveness of the proposed procedure is demonstrated both in terms of accuracy and computational effort.

1 Introduction

Gaussian regression or kriging, named after the research originally carried out by Krige (1951), is a family of interpolation methods for scattered data in which interpolated values are modeled by a Gaussian process. Its basic idea amounts to predicting the value of a function at a given point as the weighted average of observed data with weights being defined by means of a stochastic model related to the cross–covariance of observations. Main appeal of kriging interpolation consists in its ability to compute unknown function values quite fast regardless of the complexity of the observed data and, at the same time, to provide the estimation of a confidence interval. The popularity of kriging methods has rapidly grown in recent years and it has been profitably applied in many different contexts involving computer experiments (Santner et al. 2003).

S. Sessa (✉)
University of Naples Federico II, via Claudio 21, Naples, Italy
e-mail: salvatore.sessa2@unina.it

N. Valoroso
Centro Direzionale, isola C4, University of Naples Parthenope, Naples, Italy
e-mail: nunziante.valoroso@uniparthenope.it

P. Gardoni (ed.), *Risk and Reliability Analysis: Theory and Applications*,
Springer Series in Reliability Engineering, DOI 10.1007/978-3-319-52425-2_19

In the present chapter a kriging–based procedure is developed for obtaining the surrogate of a Finite Element (FE) model of a bonded specimen under pure mode-I loading to be used for identification purposes. FE-based inverse identification of a cohesive model describing mode-I fracture in adhesive joints has been recently investigated in Valoroso et al. (2013). The calibration procedure consists of a non-linear programming problem in which a least-square error function expressing the gap between measured and computed quantities is minimized.

The approach developed in Valoroso et al. (2013) has been shown to provide better estimates of mode-I adhesive fracture energy G_{Ic} of bonded specimens compared to data reduction schemes suggested in the test standard ISO25217 Adhesives (2009). The latter rely upon either corrected beam theories (Blackman et al. 1991) or compliance calibration methods (Berry 1960) and require as data set the values of total load P, the end relative displacement δ and of the crack length l_a recorded during the test. Inverse procedures based on FE model updating are however expensive since they require a large number of time-consuming direct FE computations. In this context, use of a suitably calibrated surrogate model can bring identification to a significantly higher level of efficiency.

The surrogate model discussed in this work uses the responses of a set of FE simulations of a symmetric Double Cantilever Beam (DCB) under mode-I bending as observed data of kriging interpolation. Specifically, a set of random points is generated in a suitable interval of the target material parameter and at each point a FE analysis is run to get the corresponding *observed* response. A kriging model built from such *observations* that allows to evaluate the surrogate response and the relevant confidence interval has been recently carried out in Sessa and Valoroso (2015). Herein the developments presented in Sessa and Valoroso (2015) are taken one step further using specifically developed functions that define the average trends and cross–correlation of the structural responses. It is worth emphasizing that the calibration of a kriging model can be computationally demanding; this is however balanced by the negligible cost of surrogate response evaluations, that basically amount to a set of linear, direct evaluations. When applied to experimental campaigns, where specimen geometries and test protocols are usually fixed, the proposed procedure results in globally improved performances compared to usual FE model updating procedures. Actually, in such cases the surrogate model has to be generated only once and its redundant use requires linear computations only.

Outline of the chapter is as follows. The test protocol and the FE model that are being used for identification purposes are presented in Sect. 2. In Sect. 3 is described the kriging interpolation procedure; calibration of the kriging model is then tackled in Sect. 4 along with applications and numerical results that show the capabilities of the proposed approach. Computations refer to the experimental campaign of mode–I fracture tests carried out on bonded aluminum DCB specimens documented in Valoroso et al. (2013), Fedele et al. (2012). Finally, Sect. 5 summarizes advantages and limitations of the proposed approach along with future research directions.

2 Mode-I Delamination Test Parameter Identification

Standard tests for obtaining the mode-I adhesive fracture energy G_{Ic} of bonded joints are performed on DCB specimens whose typical geometry is sketched in Fig. 1a. In the experimental campaign documented in Valoroso et al. (2013) experiments were carried out following the ISO 25217 standard prescriptions. Epoxy-bonded aluminum specimens were tested under quasi-static loading using the electromechanical material testing system shown in Fig. 1b and crack advancement as well as load and end-displacement of the DCB were continuously recorded.

Rough load–deflection curves obtained from typical delamination tests are shown in Fig. 2a, where are reported the load values P $[N]$ recorded by the load cell against the opening end displacement δ $[mm]$ of the DCB.

The rough experimental curves depicted above are far from being smooth and regular as it would be expected based on the Linear Elastic Fracture Mechanics argument. A direct identification of fracture parameters via beam theories or compliance-based methods starting from such data would therefore be quite difficult wherever possible. In the approach presented in Valoroso et al. (2013) inverse

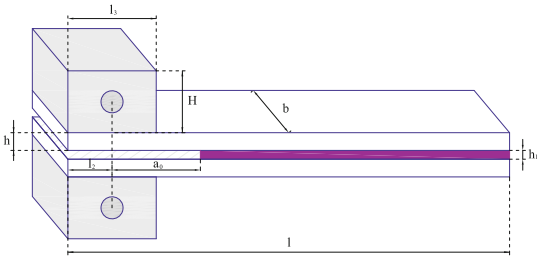

(a) Specimen geometry

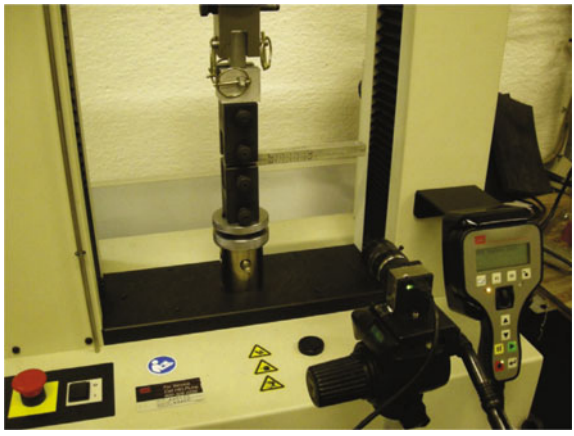

(b) Electromechanical device configuration

Fig. 1 DCB delamination test

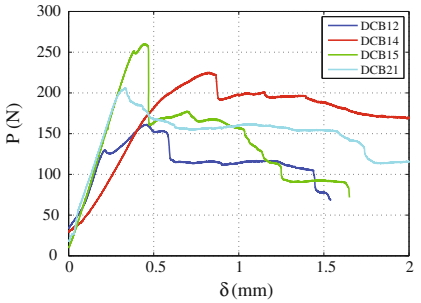

(a) Mode–I delamination test: Experimental load-deflection curves

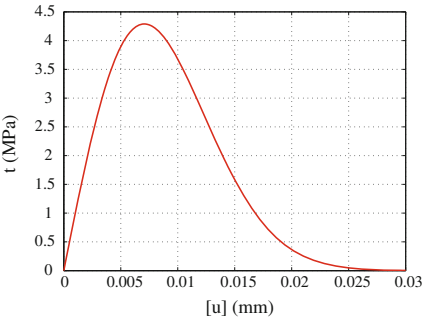

(b) Exemplificative tractionseparation relationship to be identified

Fig. 2 Load–deflection and Stress–strain curves

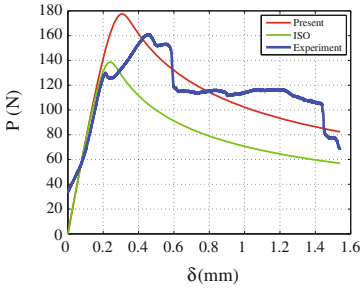

(a) Experimental VS computed load-deflection curves of DCB12 specimen

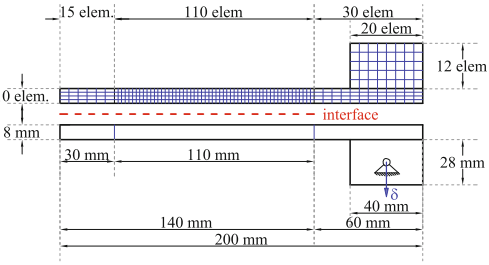

(b) DCB specimen with end load blocks. Geometry and FE mesh used for identification

Fig. 3 Load–deflection response and specimens geometry of DCB delamination tests

identification is carried out using a FE model updating scheme in which the adhesive layer is simulated via zero-thickness interface elements and the intrinsic cohesive zone model originally presented in Valoroso and Champaney (2006) and Valoroso and Fedele (2010). The traction-separation profile for pure mode-I response is sketched in Fig. 2b. The adhesive fracture parameters are computed via an optimization algorithm which minimizes the error in mean–square sense between the FE computed response and the one measured experimentally. Figure 3a compare the results of identification carried out on the bonded DCB specimen against the rough experimental response. Namely, the recorded load–deflection curve is plotted in blue while the green and the red curves represent the responses computed using the FE model sketched in Fig. 3b and the values of the adhesive fracture energy G_{Ic} computed using the ISO 25217 procedures and the model updating scheme, respectively.

Identification based on model updating is recognized to be more reliable in this case. However, its computational cost is quite high and can rapidly become prohibitive even with high-performance computing facilities when the complexity of the

model being analyzed and the number of material parameters object of the identification increase. This motivates the interest in developing surrogate or meta-models to replace direct FE analyses for identification purposes.

3 Kriging Interpolation

An effective approach for computing surrogate responses starting from scattered data is based on kriging interpolation. It consists of a form of Bayesian inference on observed data whereby the surrogate response is computed by means of weighted average of known values with weights defined via Gaussian regression. The function of interest is modeled as a Gaussian process defined by a prior normal distribution; then, a set of values associated with a spatial location is observed and the covariance of these evidences is computed. This defines, for each of the observations, a Gaussian likelihood function which is combined with the prior one in order to get an updated, posterior Gaussian process. Surrogate response provides the best linear unbiased prediction. The recondite action of the weighted average, concealed in the definition of the weights, consists in computing the expected value of the posterior Gaussian process at the point of interest.

Aim of the present application of kriging interpolation is to define the surrogate response by means of the responses usually employed in the inverse identification of a DCB test. Specifically, it is defined in terms of a load–deflection relationship $P\left(\delta, G_{Ic}\right)$ and the crack extension $l_a\left(\delta, G_{Ic}\right)$ where δ is the opening displacement of the DCB and G_{Ic} is the Mode-I critical energy release rate.

The predicted responses are defined via the following relationships:

$$\begin{aligned} P^{\star}\left(\delta, G_{Ic}\right) &= m_P\left(\delta\right) + \sum_{\alpha=1}^{n} \lambda_{\alpha}^{P}\left[P\left(\delta_{\alpha}, G_{Ic\alpha}\right) - m_P\left(\delta_{\alpha}\right)\right] \\ l_a^{\star}\left(\delta, G_{Ic}\right) &= m_{l_a}\left(\delta\right) + \sum_{\alpha=1}^{n} \lambda_{\alpha}^{l_a}\left[l_a\left(\delta_{\alpha}, G_{Ic\alpha}\right) - m_{l_a}\left(\delta_{\alpha}\right)\right] \end{aligned} \tag{1}$$

where δ_P and δ_{l_a} are the response averages and λ_{α}^{P} and $\lambda_{\alpha}^{l_a}$ are the regression weights depending on the cross–covariance of the n observations and δ_{α} and $G_{Ic\alpha}$ are the values of parameters at each observation. Average functions that serve to fit the expected trend of the responses are defined as:

$$\begin{aligned} m_P\left(\delta\right) &= a_0\delta + a_1\delta\exp\left(-a_2\delta^{a_3}\right) \\ m_{l_a}\left(\delta\right) &= b_0 + b_1\delta + b_2\delta^2 + b_3\delta^3 \end{aligned} \tag{2}$$

where a_i and b_i with $i = 1, \ldots 3$ are fitting parameters; the regression weights in Eq. 1 are computed as:

$$\begin{aligned} \lambda^{P} &= \mathbf{K}_{P}^{-1}\mathbf{k}_P\left(\delta, G_{Ic}\right) \\ \lambda^{l_a} &= \mathbf{K}_{l_a}^{-1}\mathbf{k}_{l_a}\left(\delta, G_{Ic}\right) \end{aligned} \tag{3}$$

Matrices $\mathbf{K}_P$ and $\mathbf{K}_{l_a}$ are the cross–covariances of the observed data while $\mathbf{k}_P$ and $\mathbf{k}_{l_a}$ contain the cross–covariance at the point $\left(\delta, G_{Ic}\right)$. For both quantities, a Matérn 5/2 variance model (Santner et al. 2003) is adopted in this work.

The surrogate model is completely defined by Eqs. (1)–(3) once the kriging parameters are known. Fitting of such parameters is described in the following section.

4 Parameter Calibration and Numerical Application

In order to calibrate the model, a set of observed data is required. To this end, it is necessary to choose a set of observation points in terms of the control variable δ and of the model parameter G_{Ic}. Owing to the peculiar test protocol, the opening displacement δ has been discretized between 0 mm and 2.3 mm with step equal to 0.1 mm. Observation values of the critical energy release rate G_{Ic} are randomly generated over a suitable domain. The observed structural responses, i.e. the load–deflection $P\left(\delta_\alpha, G_{c\alpha}\right)$ and the crack extension $l_a\left(\delta_\alpha, G_{c\alpha}\right)$, are therefore computed via direct FE analyses, see also Sect. 2.

Once that the set of observations is defined, average trends are numerically computed and parameters a_i and b_i are easily evaluated by a least–square curve fitting. Figure 4a, b show the structural responses of eight randomly generated observations (blue curves) in terms of load-deflection and crack extension plotted against the opening displacement δ. For any given value of δ, the red curves represent the average of the numerically computed curves while the black curves provide the average trends defined by Eq. (2) fitted to the numerical data.

In an analogous way, a curve fitting procedure allows to obtain the Matérn 5/2 covariance functions depicted in Fig. 5.

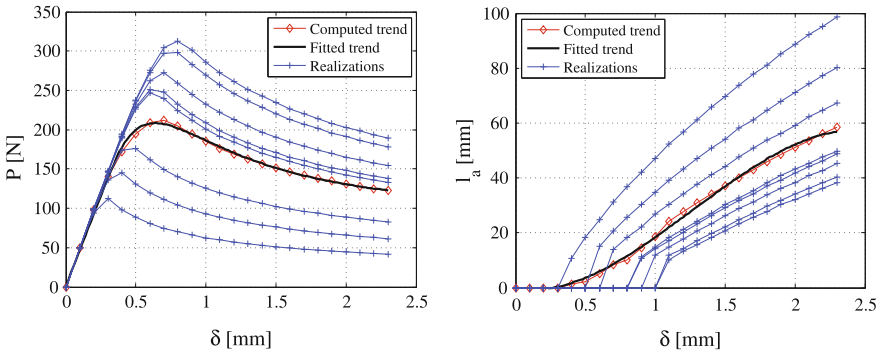

(a) Load–deflection (b) Crack length

Fig. 4 Fitting of response average trends on randomly–generated occurrences

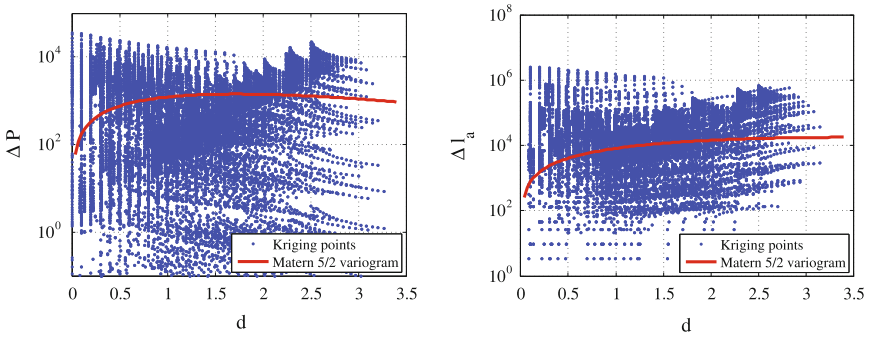

(a) Load–deflection (b) Crack length

Fig. 5 Fitting of response covariances by means of Matern 5/2 functions on randomly–generated occurrences

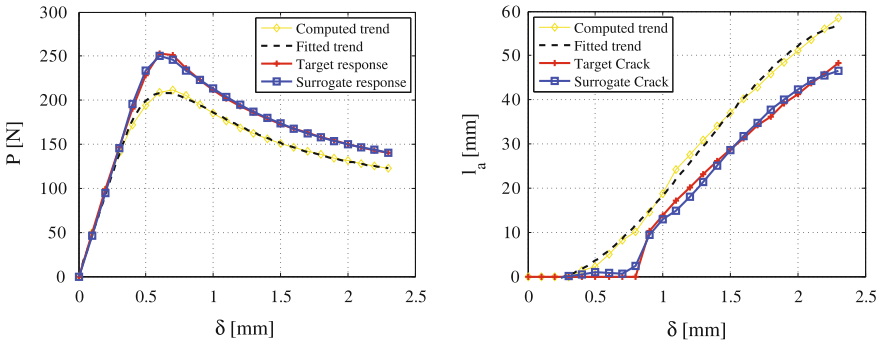

(a) Load–deflection curve (b) Crack propagation curve

Fig. 6 DCB delamination test surrogate models validation by FE–computed target responses

Once regression weights and average trends have been defined, the surrogate model is obtained via Eq. 1. Figure 6a, b show a comparison between surrogate responses and direct FE computations in terms of load-deflection and crack extension, respectively. The surrogate responses computed via Eq. 1 with a 24 observations data set and the responses computed for the same values of the parameters via a direct FE analysis turn out to be undistinguishable.

4.1 Discussion

Figure 6a, b show a substantial matching of the surrogate responses with respect to the finite–element ones. Crack length response is affected by fluctuations in the tail regions because of the peculiar discontinuity of such response. In general, the

Table 1 Surrogate model computational times

Analysis	Time (s)
FEM	90
Krig. 8 obs.	0.5
Krig. 16 obs.	1.75
Krig. 24 obs.	4.8

maximum error results less than 2%, i.e. of the same order of magnitude of typical modeling errors and approximation errors affecting Finite Element analysis results.

The remarkable accuracy obtained using the kriging model is accompanied by a significant reduction in computational cost of response evaluation, see e.g. Table 1. In particular, for a direct forward FE analysis taking about 90 s, a kriging model with 24 observations requires less than 5 s. In this sense, the use of a kriging surrogate model can be very effective for inverse analyses which usually requires thousands of direct forward computations of the structural responses.

5 Conclusions

The surrogate of a FE model based on kriging interpolation has been presented. Kriging interpolates observed data of a function of interest in order to predict unknowns values of a function at an given points in the space of model parameters. In particular, the procedure discussed herein uses as observations the outcomes of forward FE analyses run for random occurrences of a target material parameter.

For the case of mode-I fracture propagation in a bonded DCB specimen analyzed in this work the performances in terms of computing times are noteworthy. Namely, calibration of the kriging model required 24 complete FE analyses in the preliminary stage. Once the meta-model has been set up, an analysis based on the surrogate model runs 20 times faster than a direct forward FE computation. This renders the method most effective whenever redundant computations are required, and in particular in inverse analyses aiming to identify model parameters from experimental data.

A first possible extension of the procedure presented in this chapter concerns the case of multi-parameter analyses. In such cases the procedure can be extended to deal with a multi–dimensional parameter setting provided that the definition of the cross–covariance is suitably adapted to account for possible relationships between the model parameters. This topic is the object of ongoing research.

References

Berry JP (1960) Some kinetic considerations of the Griffith criterion for fracture–II: equations of motion at constant deformation. J Mech Phys Solids 8(3):207–216

Blackman B, Dear JP, Kinloch AJ, Osiyemi S (1991) The calculation of adhesive fracture energies from double-cantilever beam test specimens. J Mater Sci Lett 10(5):253–256

Fedele R, Sessa S, Valoroso N (2012) Image Correlation-Based Identification of Fracture Parameters for Structural Adhesives. Tech Mechanik 32:195–204

ISO25217: Adhesives (2009) Determination of the mode I fracture energy of structural adhesive joints using double cantilever beam and tapered double cantilever beam specimens. Geneva, Switzerland

Krige DG (1951) A Statistical Approach to Some Mine Valuation and Allied Problems on the Witwatersrand. M.Sc. Thesis, University of the Witwatersrand, Faculty of Engineering

Santner T, Williams B, Notz W (2003) The design and analysis of computer experiments. Springer, New York

Sessa S, Valoroso N (2015) Use of Kriging to surrogate finite element models of bonded double cantilever beams. In: Proceedings of ICASP12—International Conference on Applications of Statistics and Probability in Civil Engineering, Vancouver

Valoroso N, Champaney L (2006) A damage-mechanics-based approach for modelling decohesion in adhesively bonded assemblies. Eng Fract Mech 73(18):2774–2801

Valoroso N, Fedele R (2010) Characterization of a cohesive-zone model describing damage and de-cohesion at bonded interfaces. Sensitivity analysis and mode-I parameter identification. Int J Solids Struct 47(13):1666–1677

Valoroso N, Sessa S, Lepore M, Cricrí G (2013) Identification of mode-I cohesive parameters for bonded interfaces based on DCB test. Eng Fract Mech 104:56–79

Part VI
Life-cycle and Resilience Analysis and Financial Tools

Life-Cycle Analysis of Engineering Systems: Modeling Deterioration, Instantaneous Reliability, and Resilience

Gaofeng Jia, Armin Tabandeh and Paolo Gardoni

Abstract This chapter proposes a novel general stochastic formulation for the Life-Cycle Analysis (LCA) of deteriorating engineering systems. The formulation rigorously formalizes the different aspects of the life-cycle of engineering systems. To capture the probabilistic nature of the proposed formulation, it is named Stochastic Life-Cycle Analysis (SLCA). The life-cycle of an engineering system is shaped by deterioration processes and repair/recovery processes, both characterized by several sources of uncertainty. The deterioration might be due to exposure to environmental conditions and to both routine and extreme loading. The repair and recovery strategies are typically implemented to restore or enhance the safety and functionality of the engineering system. In the SLCA, state-dependent stochastic models are proposed to capture the impact of deterioration processes and repair/recovery strategies on the engineering systems in terms of performance measures like instantaneous reliability and resilience. The formulation integrates the state-dependent stochastic models with the previously developed Renewal Theory-based Life-Cycle Analysis (RTLCA) to efficiently evaluate additional system performance measures such as availability, operation cost, and benefits. The proposed SLCA can be used for the optimization of the initial design and mitigation strategies of engineering systems accounting for their life-cycle performance. As an illustration, the proposed SLCA is used to model the life-cycle of a reinforced concrete bridge, subject to deteriorations caused by corrosion and earthquake excitations. The deteriorated bridge column is repaired using Fiber Reinforced

G. Jia
Department of Civil and Environmental Engineering, Colorado State University, Fort Collins, CO, USA
e-mail: gjia@colostate.edu

A. Tabandeh · P. Gardoni (✉)
Department of Civil and Environmental Engineering, MAE Center: Creating a Multi-Hazard Approach to Engineering, University of Illinois at Urbana-Champaign, 205 North Mathews Avenue, Urbana, IL, USA
e-mail: gardoni@illinois.edu

A. Tabandeh
e-mail: tabande2@illinois.edu

P. Gardoni (ed.), *Risk and Reliability Analysis: Theory and Applications*, Springer Series in Reliability Engineering, DOI 10.1007/978-3-319-52425-2_20

Polymer (FRP) composites. The results show that the deterioration processes significantly affect the performance measures of the example bridge.

1 Introduction

Engineering systems are typically designed for a service life that might last for several years. In particular, there is an increasing attention toward sustainability (Gardoni and Murphy 2008), which calls for engineering systems to have longer service lives. However, different deterioration mechanisms might adversely impact the duration of the service life. Kumar and Gardoni (2014a, b) and Kumar et al. (2009, 2015) identify two types of deterioration mechanisms that can occur in most engineering systems: (1) gradual (progressive) deterioration (e.g., due to corrosion (Vu and Stewart 2000; Choe et al. 2009; Zhong et al. 2010; Gardoni and Rosowsky 2011; Gardoni and Trejo 2013), Alkali-Silica reaction (Eck Olave et al. 2015a, b), fatigue, and crack growth); and (2) shock (sudden) deterioration (e.g., due to damages from extreme events like earthquakes, hurricanes, floods, blasts and other natural or anthropogenic hazards) (Sanchez-Silva et al. 2011; Kumar et al. 2015).

Life-Cycle Analysis (LCA) provides a rational framework to plan and evaluate design and mitigation strategies for engineering systems and can promote the sustainable use of the existing resources (van Noortwijk and Frangopol 2004; Joanni and Rackwitz 2008; van Noortwijk and van der Weide 2008; Kumar and Gardoni 2014b; Gardoni et al. 2016). In general, during its life-cycle, a system experiences alternating phases of being in use and of being down. The deterioration mechanisms affect the variables that define the system (e.g., material properties, member dimensions, and imposed boundary conditions). The state of the variables, then define the state of the system (also called system state). The system state, measured in terms of, for example, its instantaneous reliability, degrades over time and when it falls below a prescribed acceptable threshold an intervention is triggered. Therefore, for a complete LCA of deteriorating engineering systems, it is critical to model and incorporate the deterioration processes, the recovery process, and the associated uncertainties (Ellingwood and Yasuhiro 1993; Mori and Ellingwood 1994; Ciampoli and Ellingwood 2002; Choe et al. 2009; Sanchez-Silva et al. 2011; Kumar and Gardoni 2014b).

Resilience has been proposed as a desirable feature of engineering systems to maximize the time they are in service providing the needed level of functionality (e.g., Gardoni and Murphy 2008; Murphy and Gardoni 2011). Murphy and Gardoni (2011) argued that one strategy to effectively reduce the impact of a hazard is to improve the engineering systems' (and more generally the society's) resilience and ability to respond to a disaster in a timely and well-informed way.

This chapter proposes a novel general stochastic formulation for the LCA of deteriorating engineering systems, named Stochastic Life-Cycle Analysis (SLCA). The key elements of the proposed SLCA include the mathematical modeling of the deterioration and recovery processes along with a probabilistic resilience analysis.

The proposed formulation models the service life performance of an engineering system by integrating the models on the state-dependent deterioration (Jia and Gardoni 2017a) and on the state-dependent recovery and resilience analysis (Sharma et al. 2017). The SLCA integrates the deterioration and recovery models with the Renewal Theory-based Life-cycle Analysis (RTLCA), previously proposed by Kumar and Gardoni (2014b), to efficiently evaluate additional system performance measures such as the instantaneous probability of being in service, availability, the costs of operation and failure of the system, and the benefit for a finite time horizon. Furthermore, this chapter evaluates the resilience of deteriorating systems over time, which can be used as a target attribute within the SLCA to optimize design and mitigation strategies.

For the modeling of deterioration, we adopt the general stochastic model proposed by Jia and Gardoni (2017a, b). This model predicts the system state as a function of the values of the state variables that vary with time due to multiple deterioration processes. Current models that consider multiple deteriorations, model them as independent processes (Kumar et al. 2009; Sanchez-Silva et al. 2011; Kumar and Gardoni 2014b; Kumar et al. 2015; Riascos-Ochoa and Sánchez-Silva 2015). In contrast, the model from Jia and Gardoni (2017a, b) explicitly considers the interaction among different deterioration processes. Within this model, either deterministic, probabilistic, or stochastic models (addressing various uncertainties) can be incorporated to describe the changes in state variables due to the deterioration processes. Once the time-varying state variables are modeled, they can be used in existing capacity and demand models (e.g., those developed by Gardoni et al. 2002, 2003 for reinforced concrete bridges) to predict the system state. A capacity model gives a measure of a quantity of interest that the system can sustain (e.g., a deformation or force that the system can accommodate or carry) and a demand model gives a measure of the corresponding quantity of interest that the system is asked to sustain, given the characteristics of the system and possibly other external conditions (e.g., the deformation or force imposed by a possible seismic load).

When the deteriorated system undergoes a recovery, the values of the state variables may change due to the completion of different recovery activities. Also, it is possible that the values of state variables change due to the occurrence of disrupting events (i.e., shocks), that might occur before the completion of the recovery. For the recovery modeling, we adopt the stochastic model proposed by Sharma et al. (2017). As in the deterioration modeling, this model predicts the system state as a function of the values of the state variables. Since the desired values of the state variables are specified (typically in a probabilistic sense) after the completion of each recovery activity, we can use the state variables in the appropriate probabilistic capacity and demand models to determine the corresponding system state as in the deterioration modeling. The impact of disrupting shocks on the state variables during the recovery is modeled in the same way as when the system is in use (i.e., in the deterioration modeling). We then use the estimated values of the state variables, at any time during the recovery, in the appropriate capacity and demand models to determine the corresponding system state.

For the purpose of resilience analysis, we use the mathematical model in Sharma et al. (2017). In this model, the resilience associated with a given system state and recovery strategy (which together determine the shape of the recovery curve) is characterized by a set of partial descriptors. Such partial descriptors have the following desirable properties: (1) they are simple and have clear interpretations, and (2) any set (of partial descriptors) can be augmented with additional descriptors in a systematic way. The first property facilitates the use of the partial descriptors in practice and the communication of the levels of resilience to the public and stakeholders. The second property makes the model flexible and able to characterize resilience associated with any recovery curve with the desired accuracy (i.e., an increasing number of partial descriptors can be used to completely define the recovery curve).

The rest of the chapter is organized into six sections. The next section reviews the RTLCA for the estimation of various life-cycle performance measures. Section 3 discusses the general modeling of the system performance over its service life, including the deterioration and recovery modeling. Section 4 presents the estimation of the instantaneous reliability. Section 5 discusses the resilience analysis. Section 6 illustrates the proposed SLCA by modeling the life-cycle performance of an example reinforced concrete (RC) bridge. Finally, the last section summarizes the chapter and draws some conclusions.

2 Life-Cycle Analysis

This section discusses the RTLCA and the computation of performance measures such as availability, the cost of operation, and benefit according to Kumar and Gardoni (2014b).

During its service life, a deteriorating system generally experiences alternating phases of being in use (i.e., the system is functioning) and of being down (i.e., the system is removed from service for repairs or replacement). Figure 1 schematically illustrates the life-cycle performance of a deteriorating system in terms of an indicator, $Q(t)$ (e.g., instantaneous reliability or functionality) as a function of time t. Within each cycle, $Q(t)$ degrades due to either gradual deterioration (leading to continuous changes in $Q(t)$) or shock deterioration (leading to sudden changes in $Q(t)$). When $Q(t)$ falls below a prescribed acceptable threshold, Q_{acc}, an intervention is triggered; hence, the system is removed from the full operation and undergoes a recovery process with an initial residual state Q_{res} to restore a desired target state Q_{tar}. We use I_i to denote the ith intervention event, being triggered at time t_{I_i}, and L_i to denote the ith renewal cycle, ending at time t_{L_i} when the system is restored to state Q_{tar} and a new cycle (i.e., the $(i+1)$th cycle) starts.

Overall, the length of the ith cycle, T_{L_i}, corresponds to the period between the end of the $(i-1)$th cycle and the end of the ith cycle, i.e., $T_{L_i} := t_{L_i} - t_{L_{i-1}}$. As shown in the figure, we can further divide T_{L_i} and write it as $T_{L_i} = T_{I_i} + T_{D_i}$,

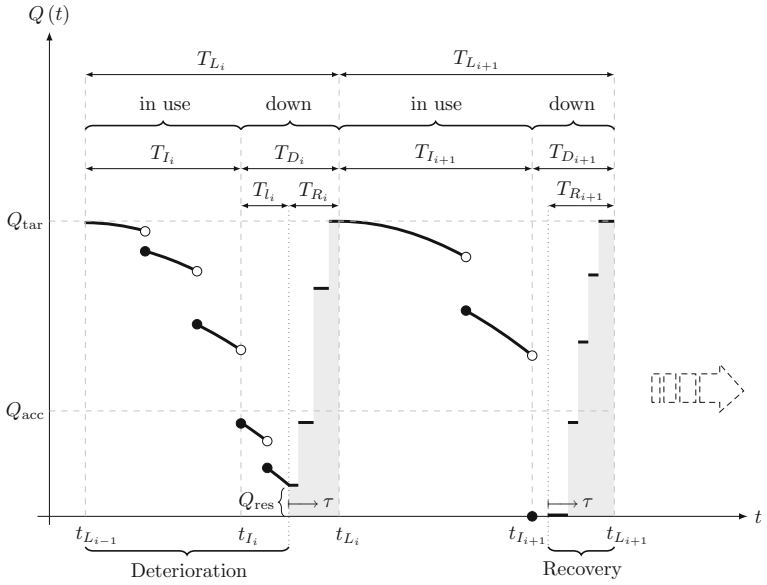

Fig. 1 Illustration of the life-cycle performance of a system

where T_{I_i} is the period in which the system is in use ($T_{I_i} := t_{I_i} - t_{L_{i-1}}$), and T_{D_i} is the down time ($T_{D_i} := t_{L_i} - t_{I_i}$).

For some systems, there might be a time delay (lag period) between the intervention and the start of the recovery process. To account for the possible lag period, we write $T_{D_i} = T_{l_i} + T_{R_i}$, where T_{l_i} is the lag period and T_{R_i} is the recovery time. We use $\tau \in [0, T_R]$ to denote the elapsed time since the beginning of the recovery. During the lag period (e.g., from t_{I_i} to $t_{I_i} + T_{l_i}$) $Q(t)$ may further degrade. Note that intervention I_i in the figure is *preventive* because the prescribed criterion (i.e., $Q(t_{I_i}) \leq Q_{\text{acc}}$) is met. However, intervention I_{i+1} is *essential* because the system experiences a full loss of performance and $Q_{\text{res}} = 0$ (e.g., an ultimate failure has occurred).

Under the assumption of the renewal theory, $\{T_{L_i}\}_{i \in \mathbb{N}}$ forms a sequence of statistically independent and identically distributed (*s.i.i.d.*) random variables.

A renewal event, L_i, can be either L_R or L_F (i.e., renewal because of a repair or a replacement due to failure), with probabilities $\mathbb{P}(L_R) := \mathbb{P}(L_i \equiv L_R)$ and $\mathbb{P}(L_F) := \mathbb{P}(L_i \equiv L_F)$. Using the fact that the events L_R and L_F are disjoint and collectively exhaustive, we have $\mathbb{P}(L_R) + \mathbb{P}(L_F) = 1$, and can write

$$f_{T_L}(t) = f_{T_L|L_R}(t|L_R)\mathbb{P}(L_R) + f_{T_L|L_F}(t|L_F)\mathbb{P}(L_F), \tag{1}$$

where $f_{T_L}(t)$ is the Probability Density Function (PDF) of T_{L_i}; $f_{T_L|L_R}(t|L_R)$ is the conditional PDF of T_{L_i} given that $L_i \equiv L_R$; and $f_{T_L|L_F}(t|L_F)$ is the conditional PDF of T_{L_i} given that $L_i \equiv L_F$. Similarly, for T_{I_i} we have

$$f_{T_I}(t) = f_{T_I|L_R}(t|L_R)\mathbb{P}(L_R) + f_{T_I|L_F}(t|L_F)\mathbb{P}(L_F). \tag{2}$$

The remaining of this section presents the estimation equations for different life-cycle performance measures that were first derived by Kumar and Gardoni (2014b). Based on the assumptions of the renewal theory (i.e., $\{T_{L_i}\}_{i\in\mathbb{N}}$ is a sequence of *s.i.i.d.* random variables), the estimation equations only need the PDFs and probabilities in Eqs. (1) and (2) for the first renewal cycle, which are the same as those for the *i*th renewal cycle for any *i*. Such PDFs and probabilities can be obtained from the modeling of the deterioration and recovery processes, discussed in Sect. 3.

2.1 Availability

The availability of a system during a time interval $[0, t]$ is defined as the fraction of time during which the system is available (or in use), i.e., $A(t) := \int_0^t \mathbf{1}_{\{\text{inuse at } \xi\}} d\xi / t$. The expected value of the availability is simply $\mathbb{E}[A(t)] = \int_0^t \mathbb{P}_S(\xi) d\xi / t$, where $\mathbb{P}_S(t)$ is the instantaneous probability that the system is in use at time t and can be calculated as

$$\mathbb{P}_S(t) = [1 - F_{T_I}(t)] + \int_0^t \mathbb{P}_S(t-\xi) f_{T_L}(\xi) d\xi. \tag{3}$$

2.2 Cost of Operation, Failure Losses, and Benefit

The operation cost, $C_{Op}(t)$, includes the total cost of repairs and replacement of the system in order to operate it up to time t. The expected value of $C_{Op}(t)$ can be computed as

$$\mathbb{E}\left[C_{Op}(t)\right] = \int_0^t \left\{\bar{c}_{Op}(\xi) + \mathbb{E}\left[C_{Op}(t-\xi)\right]\right\} e^{-\gamma\xi} f_{T_L}(\xi) d\xi, \tag{4}$$

where $\bar{c}_{Op}(\xi) := \mathbb{E}[c_{Op_1}|T_{L_1} = \xi]$ and c_{Op_1} is the cost of the repair or replacement occurring between events I_1 and L_1, and γ is the discount rate to compute the Net Present Value (NPV) of the cost.

The additional costs incurred in the life-cycle of the system includes the failure losses, $C_L(t)$, arising from, for example, injuries, deaths or damage to properties. The expected value of the failure losses can be calculated as

$$\mathbb{E}[C_L(t)] = \mathbb{P}(L_F) c_L e^{\gamma T_D} \int_0^{t+T_D} e^{-\gamma\xi} f_{T_L|L_F}(\xi|L_F) d\xi + \int_0^t \mathbb{E}[C_L(t-\xi)] e^{-\gamma\xi} f_{T_L}(\xi) d\xi, \tag{5}$$

where c_L is the loss corresponding to the event I_1, and T_D in this equation is the down-time after an ultimate failure (e.g., $T_{D_{i+1}}$ in Fig. 1, where $Q_{\text{res}} = 0$).

In addition to the incurred costs, an important consideration in the LCA is the benefit of operating a system, $B(t)$. If b represents the benefit of having the system in use for a unit time, the expected benefit can be obtained as

$$\mathbb{E}[B(t)] = b \int_0^t \mathbb{P}_S(\xi) e^{-\gamma\xi} d\xi. \tag{6}$$

We can write the expected net benefit as $\mathbb{E}[B_{\text{net}}(t)] = \mathbb{E}[B(t)] - \mathbb{E}[C_{\text{tot}}(t)] - C_C$, where $\mathbb{E}[C_{\text{tot}}(t)] = \mathbb{E}[C_{Op}(t)] + \mathbb{E}[C_L(t)]$ is the expected total cost and C_C is the construction cost.

The estimation equations for the variance of the above quantities, i.e., availability, cost of operation, failure losses, and benefit, can be derived similarly and can be found in Kumar and Gardoni (2014b). Next, we discuss the modeling of the deterioration and recovery processes, which give the PDFs and probabilities required to estimate the above quantities.

3 Performance Analysis

This section discusses the modeling of the system state under the deterioration-recovery cycles. We first present the general model for the deterioration processes and then present the model for the recovery process.

3.1 Modeling of Deterioration Processes

To model the deterioration processes and their impact on the system state, we use the general stochastic model proposed by Jia and Gardoni (2017a). This model predicts the system state as a function of the values of the state variables that might vary with time due to multiple deterioration processes. This model (as briefly described in this section) is adopted here because it allows the consideration of multiple deterioration processes and their interactions.

3.1.1 State Change Due to Deterioration

Figure 2 illustrates the overall flowchart of the stochastic model. The modeling starts with the vector of external conditions/variables at time t, $\mathbf{Z}(t)$, partitioned into (1) environmental conditions/variables (such as temperature, atmospheric pressure, and relative humidity) denoted as $\mathbf{E}(t)$, and (2) shock intensity measures, denoted as $\mathbf{S}(t)$. The external conditions influence the deterioration that the system may be subject to. Let the vector $\mathbf{X}(t) = [X_1(t) \cdots X_j(t) \cdots X_{n_x}(t)]^T$ denote the state variables of the structural system at time t. Also let $\mathbf{X}_0 := \mathbf{X}(t=0)$ denote the initial state variables at a reference time $t=0$ (e.g., the initial time of construction of the system). Due to the impacts of multiple deterioration processes (with potential interactions between them), the state variables typically change with time. The changes in $\mathbf{X}(t)$ lead to changes in the capacity of the system, $C(t)$, as well as in the demand, $D(t)$, imposed by external conditions. The adopted model focuses on modeling $\mathbf{X}(t)$. Once $\mathbf{X}(t)$ is modeled, it can be used in existing capacity and

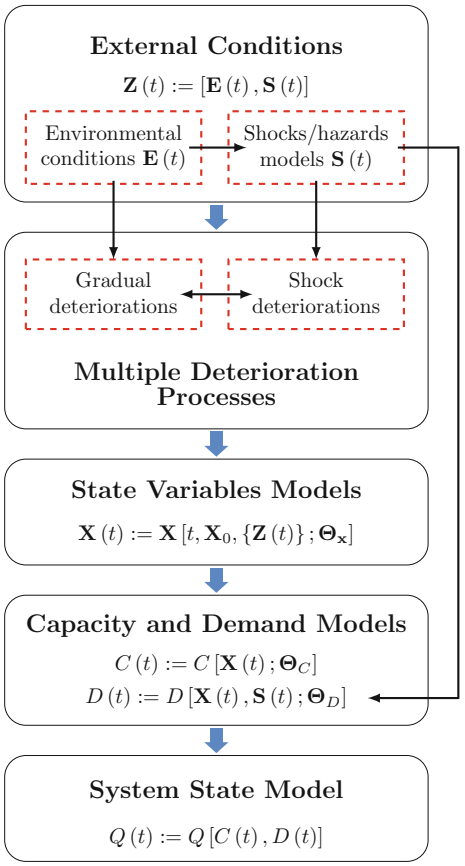

Fig. 2 Overall flowchart for the stochastic model of the deterioration processes and their impact on the system state (Adapted from Jia and Gardoni 2017a)

demand models (as described in the next section), to predict the system state, measured in terms of an indicator $Q(t)$.

The vector of state variables at time t can be written as

$$\mathbf{X}(t) = \mathbf{X}_0 + \int_0^t \dot{\mathbf{X}}(\xi) d\xi, \tag{7}$$

where $\dot{\mathbf{X}}(\xi)$ is the instantaneous rate of state change at time ξ due to the deterioration processes. Suppose the system is subject to m deterioration processes and let $\dot{\mathbf{X}}_k(t)$ denote the rate of state change due to the kth deterioration process. To capture the dependency of the rate on time/age, the state variables of the system at time t, $\mathbf{X}(t)$, and the external conditions, $\mathbf{Z}_k(t)$, we write $\dot{\mathbf{X}}_k(t)$ as

$$\dot{\mathbf{X}}_k(t) := \dot{\mathbf{X}}_k[t, \mathbf{X}(t), \mathbf{Z}_k(t); \boldsymbol{\Theta}_{\mathbf{x},k}], \tag{8}$$

where $\mathbf{Z}_k(t)$ represents the external conditions that have an impact specifically on the kth deterioration process, and $\boldsymbol{\Theta}_{\mathbf{x},k}$ is a vector of model parameters related to the impact of the kth deterioration process. This formulation is different from existing ones where $\dot{\mathbf{X}}_k(t)$ only depends on time.

We can then write $\dot{\mathbf{X}}(t)$ as the sum of the rates associated to individual deterioration processes as

$$\dot{\mathbf{X}}(t) = \sum_{k=1}^{m} \dot{\mathbf{X}}_k[t, \mathbf{X}(t), \mathbf{Z}_k(t); \boldsymbol{\Theta}_{\mathbf{x},k}]. \tag{9}$$

As a special case, if the $\dot{\mathbf{X}}_k[t, \mathbf{X}(t), \mathbf{Z}_k(t); \boldsymbol{\Theta}_{\mathbf{x},k}]$'s only depend on time, i.e., $\dot{\mathbf{X}}_k[t; \boldsymbol{\Theta}_{\mathbf{x},k}]$, the state variables computed from Eqs. (7) and (9) would be the same as those computed using the models available in literature (i.e., in Kumar et al. 2015). The vector $\mathbf{X}(t)$ is a function of time t, the sequence of all external conditions from time 0 to t, $\{\mathbf{Z}(t)\}$, and the vector of model parameters $\boldsymbol{\Theta}_{\mathbf{x}} = (\boldsymbol{\Theta}_{\mathbf{x},1}, \ldots, \boldsymbol{\Theta}_{\mathbf{x},m})$. Therefore, $\mathbf{X}(t) := \mathbf{X}[t, \mathbf{X}_0, \{\mathbf{Z}(t)\}; \boldsymbol{\Theta}_{\mathbf{x}}]$, $\dot{\mathbf{X}}_k(t) := \dot{\mathbf{X}}_k[t, \mathbf{X}(t), \mathbf{E}_k(t); \boldsymbol{\Theta}_{\mathbf{x},k}]$ for gradual deterioration processes, and $\dot{\mathbf{X}}_k(t) := \Delta\mathbf{X}_k[\mathbf{X}(t_{k,i}^-), \mathbf{S}_k(t_{k,i}); \boldsymbol{\Theta}_{\mathbf{x},k}]\delta(t - t_{k,i})$ for $t_{k,i}^- < t \le t_{k,i+1}^-$ for shock deterioration processes, where $\Delta\mathbf{X}_k[\cdot]$ is the change due to the ith shock, occurring at time $t_{k,i}$, $\mathbf{X}(t_{k,i}^-)$ is the state variable at time $t_{k,i}^-$ (i.e., right before $t_{k,i}$), and $\delta(\cdot)$ is the Dirac delta function.

To implement this model, we need to establish and calibrate specific models for the changes of the state variables for each deterioration process. The formulation here is general and can incorporate either a deterministic, probabilistic, or stochastic model. Jia and Gardoni (2017a) proposed a non-homogeneous state-dependent Markov process model for gradual deterioration which is able to capture the associated uncertainties and also the time/age and state-dependence of the deterioration process. The Gamma process, commonly used in the literature to model the gradual deterioration (van Noortwijk et al. 2007; Li et al. 2015), is just a special case (i.e., purely age dependent) of this more general stochastic model.

For shock deterioration, two aspects need to be considered: one aspect is the modeling of the characteristics of the shocks, including the occurrence rate/frequency and the intensity; the other aspect is estimating the change of the state variables due to a shock with a given intensity. Stochastic models such as Poisson processes, either homogeneous (i.e., with constant occurrence rate) (Ellingwood and Yasuhiro 1993; van Noortwijk et al. 2007; Kumar et al. 2009; Kumar and Gardoni 2013, 2014a) or non-homogeneous (i.e., with time-varying occurrence rate) (Kumar and Gardoni 2012; Iervolino et al. 2014; Li et al. 2015), have been used to model the random occurrence of shocks. To predict $\dot{\mathbf{X}}_k(t)$'s due to shocks, we may use analytical models, if available, or develop/adopt probabilistic predictive models as those in Kumar and Gardoni (2012, 2014a).

3.1.2 Stochastic Capacity and Demand Models

Given the state variables at time t, $\mathbf{X}(t)$, the capacity of the system can be expressed as

$$C(t) := C[\mathbf{X}(t); \boldsymbol{\Theta}_C], \tag{10}$$

where $C[\mathbf{X}(t); \boldsymbol{\Theta}_C]$ is a capacity model and $\boldsymbol{\Theta}_C$ is a set of parameters of the capacity model. Similarly, the demand that the shock (described by its intensity measure(s) $\mathbf{S}(t)$) imposes on the system can be expressed as

$$D(t) := D[\mathbf{X}(t), \mathbf{S}(t); \boldsymbol{\Theta}_D], \tag{11}$$

where $D[\mathbf{X}(t), \mathbf{S}(t); \boldsymbol{\Theta}_D]$ is a demand model and $\boldsymbol{\Theta}_D$ is a set of parameters of the demand model. Note that $\boldsymbol{\Theta}_C$ and $\boldsymbol{\Theta}_D$ in Eqs. (10) and (11) do not include $\boldsymbol{\Theta}_{\mathbf{x}}$. As an example, the capacity and demand models in Eqs. (10) and (11) can follow the general forms proposed by Gardoni et al. (2002) and (2003). Here, the models in Eqs. (10) and (11) additionally include the time dependence into the formulations (Choe et al. 2008, 2009; Pillai et al. 2010; Kim et al. 2012; Kumar and Gardoni 2012; Gardoni et al. 2013). More generally, any appropriate capacity and demand models that take the state variables as input can be adopted in the formulation.

3.2 Modeling of the Recovery Process

To model the recovery of deteriorated systems, we use the stochastic model proposed by Sharma et al. (2017). This section briefly reviews this model. The recovery model consists of (1) modeling the occurrence times of the changes in the system state due to the recovery activities or disrupting shocks that could happen during the recovery process (between the initiation of the recovery activities and

before the beginning of a new renewal cycle), and (2) predicting the system state after each change. Next, we briefly discuss this model.

3.2.1 State Change Due to Recovery

The modeling of the recovery process starts with developing a work plan that specifies all of the required recovery activities (i.e., their types and numbers). The recovery work is divided up to a level of detail such that the information about individual activities (e.g., expenditure and required time) can be obtained from the readily available resources (e.g., the RS Means database (Means 2008)). The information about different activities from available resources is typically for a standard situation (i.e., standardized crews, equipment, methods, and weather conditions). Therefore, the initial estimates of the durations or expenditures of the recovery activities might need to be updated based upon the availability of the budget, materials, skilled labors, or weather conditions. The estimates of the durations of the individual activities can be combined to estimate the overall recovery duration. The occurrence of disrupting shocks (e.g., seismic shocks occurring before the completion of the recovery) might change the scope of the recovery work and the initial estimate of the recovery duration. The extent of the change depends on the occurrence time of the shock during the recovery process as well as its intensity.

Recovery activities that together lead to a change in the system state can be grouped into recovery steps. The number of completed recovery steps by any time $\tau \in [0, T_R]$, is modeled as a Poisson process with a mean function $\Lambda_r(\tau)$. Sharma et al. (2017) proposed the following probabilistic predictive model for $\Lambda_r(\tau)$, developed following Gardoni et al. (2002):

$$\mathcal{T}[\Lambda_r(\tau, \boldsymbol{\psi}; \boldsymbol{\Theta}_r)] = \sum_{k=1}^{p_r} \theta_{r,k} h_{r,k}(\tau, \boldsymbol{\psi}) + \sigma_r \varepsilon_r, \tag{12}$$

where $\mathcal{T}(\cdot)$ is a transformation function of $\Lambda_r(\tau, \boldsymbol{\psi}; \boldsymbol{\Theta}_r)$; $\Lambda_r(\tau, \boldsymbol{\psi}; \boldsymbol{\Theta}_r)$ is the predicted mean function; $\boldsymbol{\psi}$ is a set of influencing factors (e.g., budget and weather condition); $\boldsymbol{\Theta}_r = (\boldsymbol{\theta}_r, \sigma_r)$ is a set of model parameters, in which $\boldsymbol{\theta}_r = (\theta_{r,1}, \ldots, \theta_{r,p_r})$; $h_{r,k}(\tau, \boldsymbol{\psi})$'s are a set of explanatory functions; and $\sigma_r \varepsilon_r$ is an additive model error term (additivity assumption), in which σ_r is the standard deviation of the model error that is assumed to be independent of τ (homoskedasticity assumption) and ε_r is a standard normal random variable (normality assumption). The transformation $\mathcal{T}(\cdot)$ is used to approximately satisfy the homoskedasticity, normality, and additivity assumptions. Note that we can update $\boldsymbol{\Theta}_r$ based on the data from similar recovery activities in other projects or the recorded data in ongoing activities in the considered project using a Bayesian approach as in Gardoni et al. (2007).

The recovery steps correspond to reaching milestones for which the state variables, $\mathbf{X}(\tau)$, have desired values (typically, in a probabilistic sense). Note that $\mathbf{X}(\tau)$ in the recovery modeling might not necessarily consist of the same set of state

variables as those in the deterioration modeling. This is because the recovery process may introduce new state variables to the model or replace a subset of state variables in the deterioration modeling with new ones. For example, if a retrofit is implemented using Fiber Reinforced Polymer (FRP) composites, $\mathbf{X}(\tau)$ will include new variables that define the FRP and/or its properties. The impact of disrupting shocks on $\mathbf{X}(\tau)$ is modeled in the same way as it is modeled in the deterioration modeling (before the beginning of the recovery process) as discussed in the previous section.

Combining the deterioration and recovery models, we can write the state variables for every $t \in [t_{I_i} + T_{l_i}, t_{L_i}]$ as

$$\mathbf{X}(t) := \left\{ \begin{array}{l} \mathbf{X}[\tau, \mathbf{X}(t_{I_i} + T_{l_i}), \{\mathbf{Z}(t)\}; \boldsymbol{\Theta}_{\mathbf{x}}, \boldsymbol{\Theta}_r] \\ \mathbf{X}[\tau, \mathbf{X}_0, \{\mathbf{Z}(\tau)\}; \boldsymbol{\Theta}_{\mathbf{x}}, \boldsymbol{\Theta}_r] \end{array} \right\}, \tag{13}$$

where $\mathbf{X}[\tau, \mathbf{X}(t_{I_i} + T_{l_i}), \{\mathbf{Z}(t)\}; \boldsymbol{\Theta}_{\mathbf{x}}, \boldsymbol{\Theta}_r]$ is the subset of state variables which are shared between the deterioration and recovery models, in which $\mathbf{X}(t_{I_i} + T_{l_i})$ is the set of state variables at the beginning of the recovery process obtained from the deterioration model, and $\mathbf{X}[\tau, \mathbf{X}_0, \{\mathbf{Z}(\tau)\}; \boldsymbol{\Theta}_{\mathbf{x}}, \boldsymbol{\Theta}_r]$ is the subset of state variables which are augmented due to the recovery process, in which $\mathbf{X}_0$ is the initial state variables at the time they are added to the system during the recovery process.

3.2.2 Stochastic Capacity and Demand Models

As in the deterioration modeling, we can use the estimated $\mathbf{X}(\tau)$ from the recovery modeling in existing capacity and demand models to determine the capacity of the system and the imposed demand (or capacities and demands in the case of multiple modes of failure). For example, Tabandeh and Gardoni (2014, 2015) developed probabilistic capacity and demand models for FRP-retrofitted RC bridges (as a repair strategy for deteriorated bridge columns) which take $\mathbf{X}(\tau)$ as inputs and estimate the corresponding capacities and demands.

4 Reliability Analysis

In this section, we obtain the instantaneous reliability of the system at any time during its service life. Let $g(t) := C(t) - D(t)$ denote a limit-state function such that $g(t) \leq 0$ defines the failure to meet a specified performance level. Then, we define the conditional failure probability (or fragility) at time t, given the occurrence of a shock with intensity measure(s) $\mathbf{S}(t)$ as $F[\mathbf{S}(t); \boldsymbol{\Theta}] := \mathbb{P}[g(t) \leq 0 | \mathbf{S}(t)]$, where $\boldsymbol{\Theta}$ includes all of the parameters needed for modeling the state variables and the corresponding capacities and demands (i.e., $\boldsymbol{\Theta} = (\boldsymbol{\Theta}_{\mathbf{x}}, \boldsymbol{\Theta}_C, \boldsymbol{\Theta}_D)$ for $t \in [t_{L_{i-1}}, t_{I_i} + T_{l_i}]$ and $\boldsymbol{\Theta} = (\boldsymbol{\Theta}_{\mathbf{x}}, \boldsymbol{\Theta}_r, \boldsymbol{\Theta}_C, \boldsymbol{\Theta}_D)$ for $t \in [t_{I_i} + T_{l_i}, t_{L_i}]$). To incorporate the uncertainty in $\boldsymbol{\Theta}$ in computing $F[\mathbf{S}(t); \boldsymbol{\Theta}]$, there are two possible options (Gardoni et al. 2002).

First, we may ignore the uncertainty in $\boldsymbol{\Theta}$ and obtain a point estimate of the fragility as $\hat{F}[\mathbf{S}(t)] := F[\mathbf{S}(t); \boldsymbol{\Theta}]$, where $\boldsymbol{\Theta}$ is a fixed value of $\boldsymbol{\Theta}$ (e.g., the mean value). Alternatively, we can consider the uncertainty in $\boldsymbol{\Theta}$ to obtain a predictive estimate of the fragility as $\tilde{F}[\mathbf{S}(t)] = \int F[\mathbf{S}(t); \boldsymbol{\Theta}] f(\boldsymbol{\Theta}) d\boldsymbol{\Theta}$, where $f(\boldsymbol{\Theta})$ is the PDF of $\boldsymbol{\Theta}$. Given the fragility function at t, $F[\mathbf{S}(t)]$ (i.e., $\hat{F}[\mathbf{S}(t)]$ or $\tilde{F}[\mathbf{S}(t)]$), we can write the instantaneous failure probability $P_f(t)$ as

$$P_f(t) = \int F[\mathbf{S}(t)] f[\mathbf{S}(t)] d\mathbf{S}(t), \tag{14}$$

where $f[\mathbf{S}(t)]$ is the PDF of $\mathbf{S}(t)$. Using $\hat{F}[\mathbf{S}(t)]$ in Eq. (14) leads to a point estimate of the failure probability (i.e., $\hat{P}_f(t)$) and using $\tilde{F}[\mathbf{S}(t)]$ leads to a predictive estimate of the failure probability (i.e., $\tilde{P}_f(t)$). We can compute the failure probability in Eq. (14) using a stochastic simulation approach (see Jia and Gardoni 2017b and Sharma et al. 2017 for more details). The instantaneous reliability is simply $R(t) = 1 - P_f(t)$.

5 Resilience Analysis

This section briefly reviews the model for resilience analysis proposed by Sharma et al. (2017). Sharma et al. (2017) introduced the *Cumulative Resilience Function* (CRF) $\breve{Q}(\tau)$ which gives the overall recovery progress by time τ. Considering the life-cycle performance indicator, $Q(t)$, we can take $\breve{Q}(\tau) = Q(t)$ for all $\tau \in [0, T_R]$. Once $\breve{Q}(\tau)$ is defined, we can use it to define the *Instantaneous Rate of the Recovery Progress* proposed by Sharma et al. (2017) according to the following three mathematical formulations.

Definition 1 When the CRF is a continuous function of time, the instantaneous rate of the recovery progress is obtained as the time derivative of the CRF. Mathematically, the instantaneous rate can be written as $q(\tau) = d\breve{Q}/d\tau$, for all $\tau \in [0, T_R]$, which is called the *Resilience Density Function* (RDF). Note that the RDF is undefined at possible finite set of points, where the CRF is not differentiable (i.e., CRF is a continuous function of order 0).

Definition 2 When the CRF is a piecewise constant function, the RDF can no longer be defined because of the discontinuity in the CRF. In such cases, the *Resilience Mass Function* (RMF) is defined as $q(\tau) = \sum_{k=0}^{\infty} \Delta\breve{Q}(\tau_k)\delta(\tau - \tau_k)$, for all $\tau \in [0, T_R]$, where $\Delta\breve{Q}(\tau_k) := \breve{Q}(\tau_k) - \breve{Q}(\tau_k^-)$ is the size of the sudden change in CRF at the discontinuity point $\tau = \tau_k$ (where $\tau_0 := 0$); and $\delta(\cdot)$ is the Dirac delta function. To reflect that at τ_0 the CRF is equal to Q_{res} (typically nonzero), we define $\Delta\breve{Q}(0) := Q_{\text{res}}$.

Definition 3 In general, the CRF might be a combination of the previous two cases, where $Q(\tau)$ is a piecewise continuous function. In this case, the instantaneous rate is written as

$$q(\tau) = \tilde{q}(\tau) + \sum_{k=0}^{\infty} \Delta\tilde{Q}(\tau_k)\delta(\tau - \tau_k), \quad \tau \in [0, T_R], \tag{15}$$

where $\tilde{q}(\tau)$ is the RDF, corresponding to the continuous part of the CRF and $\Delta\tilde{Q}(\tau_k)\delta(\tau - \tau_k)$ is the RMF, accounting for the discontinuities of the CRF.

The CRFs or RDFs/RMFs of systems provide complete information about the recovery process and the associated resilience. To help the interpretation of the CRF, RDF and RMF, one can see the analogy between their definitions and those of the Cumulative Distribution Function (CDF), Probability Density Function (PDF) and Probability Mass Function (PMF) that are used to describe random variables in probability theory.

Sharma et al. (2017) also define partial descriptors to capture the key characteristics of resilience. Such partial descriptors are summarized next. The *Center of Resilience*, ρ_Q, of a given recovery process that we use in this chapter, is defined as

$$\rho_Q := \frac{\int_0^{T_R} \tau q(\tau) d\tau}{\int_0^{T_R} q(\tau) d\tau} = \frac{Q_{\text{res}}}{Q_{\text{tar}}} \rho_{Q,\text{res}} + \frac{\bar{Q}_{\text{res}}}{Q_{\text{tar}}} \rho_{\bar{Q},\text{res}}, \tag{16}$$

where $Q_{\text{res}}/Q_{\text{tar}}$ is the contribution of the residual state to ρ_Q, in which $Q_{\text{tar}} := \breve{Q}(T_R)$; $\rho_{Q,\text{res}} := \tau_0$ is the center of resilience, when considering only the residual state; $\bar{Q}_{\text{res}}/Q_{\text{tar}}$ is the contribution of the recovery process to ρ_Q, in which $\bar{Q}_{\text{res}} := Q_{\text{tar}} - Q_{\text{res}}$; and the $\rho_{\bar{Q},\text{res}} := [\int_0^{T_R} \tau\tilde{q}(\tau)d\tau + \sum_{k=1}^{\infty} \tau_k \Delta\tilde{Q}(\tau_k)\mathbf{1}_{\{0 \le \tau_k \le T_R\}}]/\bar{Q}_{\text{res}}$ is the center of resilience, when considering only the recovery process. Since $\tau_0 = 0$, Eq. (16) simplifies into

$$\rho_Q = \frac{\bar{Q}_{\text{res}}}{Q_{\text{tar}}} \rho_{\bar{Q},\text{res}}. \tag{17}$$

The expression for ρ_Q in Eq. (17) distinguishes between the roles of the residual system state (which affects $\bar{Q}_{\text{res}}$) and the recovery process (which affects $\rho_{\bar{Q},\text{res}}$) in the quantification of resilience. Being able to decouple the two contributions facilitates the determination of the acceptable level of resilience, as an intervention criterion, in terms of a balance between the system state in the immediate aftermath of a disruption and the corresponding recovery duration. We also note that the value of ρ_Q depends on the choice for $\breve{Q}(\tau)$ (e.g., functionality or instantaneous reliability). As a result, the interpretation of the obtained results for ρ_Q and decisions about the acceptable level of resilience depend on such choice.

As a generalization, the nth *resilience moment* is defined as

$$\rho_Q^{(n)} := \frac{\int_0^{T_R} \tau^n q(\tau) d\tau}{\int_0^{T_R} q(\tau) d\tau} = \frac{Q_{\text{res}}}{Q_{\text{tar}}} \rho_{Q,\text{res}}^{(n)} + \frac{\bar{Q}_{\text{res}}}{Q_{\text{tar}}} \rho_{\bar{Q},\text{res}}^{(n)}, \tag{18}$$

where $\rho_{Q,\text{res}}^{(n)} := \tau_0^n$ and $\rho_{\bar{Q},\text{res}}^{(n)} := [\int_0^{T_R} \tau^n \tilde{q}(\tau) d\tau + \sum_{k=1}^{\infty} \tau_k^n \Delta\tilde{Q}(\tau_k) \mathbf{1}_{\{0 \le \tau_k \le T_R\}}] / \bar{Q}_{\text{res}}$. We can use $\rho_Q^{(n)}$'s to capture various characteristics of the RDF/RMF, including its dispersion and skewness (see Sharma et al. 2017 for further details). Any CRF and RDF/RMF can be completely characterized in terms of all the $\rho_Q^{(n)}$'s. The expression of the resilience moments in Eq. (18) can also account for the impact of disrupting shocks by letting $\Delta\tilde{Q}(\tau_k) < 0$ when a shock occurs at $\tau = \tau_k < T_R$.

Analogously to the instantaneous reliability, we define the *instantaneous resilience* of a system to account for the effect of deterioration processes on the resilience of the system. The proposed mathematical expression for the instantaneous resilience, quantified in terms of ρ_Q, is

$$\rho_Q(t) = \int \rho_Q[\mathbf{S}(t)] f[\mathbf{S}(t)] d\mathbf{S}(t), \tag{19}$$

where $\rho_Q[\mathbf{S}(t)]$ is the center of resilience, considering the system state at time t and given that the system undergoes a recovery process due to the occurrence of a shock with intensity measure(s) $\mathbf{S}(t)$ which affect both the $\bar{Q}_{\text{res}}$ and $\rho_{\bar{Q},\text{res}}$; and $f[\mathbf{S}(t)]$ is the PDF of $\mathbf{S}(t)$. To account for the uncertainty in $\boldsymbol{\Theta}$, when computing $\rho_Q[\mathbf{S}(t)]$, we can use a point estimate $\hat{\rho}_Q[\mathbf{S}(t)]$ in Eq. (19) which leads to a point estimate of the instantaneous resilience $\hat{\rho}_Q(t)$. Alternatively, we can use a predictive estimate $\tilde{\rho}_Q[\mathbf{S}(t)]$ which leads to a predictive estimate of the instantaneous resilience $\tilde{\rho}_Q(t)$.

6 Illustrative Example

In this section, we illustrate the proposed SLCA by modeling the life-cycle performance of an example RC bridge subject to gradual deterioration due to chloride-induced corrosion and shock deterioration due to seismic excitations. The deteriorated bridge then undergoes a recovery process that consists in repairing the columns using FRP composites. In this example, when the intervention is triggered, if $Q_{\text{res}} = 0$ a full replacement is carried out; otherwise, a repair is carried out. As part of the SLCA, we evaluate the impact of the deterioration processes and the selected repair strategy on the resilience of the RC bridge over its service life. As a benchmark problem, we consider the RC bridge with one single-column bent in Kumar and Gardoni (2014b). Figure 3 shows the configuration of the bridge together with a schematic layout of the hypothetical site of the bridge with respect to a fault (for modeling the seismic hazard).

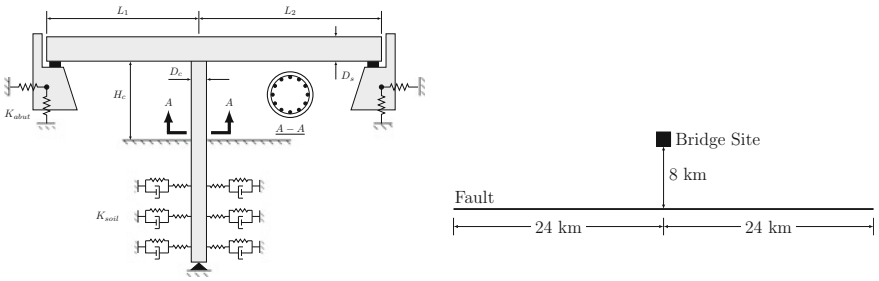

Fig. 3 The considered RC bridge and schematic layout of the hypothetical site

6.1 *Modeling of Deterioration of RC Bridges Due to Corrosion and Seismic Excitations*

For the deterioration due to corrosion, we consider the reduction of the diameter of the reinforcement steel and its impact on the structural properties of the RC bridge column such as moment curvature characteristics (e.g., ultimate curvature capacity) and pushover characteristics (e.g., stiffness). For the deterioration due to seismic excitations, we consider the stiffness reduction and damage accumulation due to low-cycle fatigue. Essentially, we are modeling both the impact on the state variables $\mathbf{X}$ (e.g., reinforcement steel diameter) and the resultant impact on structural properties (e.g., ultimate curvature capacity, stiffness, damage index), which are functions of the state variables $\mathbf{X}$. Modeling the structural properties directly is convenient in this case because they are the direct inputs to the probabilistic capacity and demand models used later.

Corrosion and seismic damage interact. For example, the initiation and the rate of corrosion of reinforcement steel in RC bridges may be accelerated by the formation of cracks caused by past earthquakes. Otieno et al. (2010) found that even small cracks (with width less than 0.4 mm) may significantly impact the initiation and propagation of corrosion. The deterioration modeling discussed in Sect. 3.1 allows us to model the interaction between corrosion and seismic damage.

6.1.1 Deterioration Due to Corrosion

To consider the impact of earthquakes on the corrosion initiation, we model the corrosion initiation time as

$$T_{\text{corr}} = \min(t_{\text{corr}}, t_1), \tag{20}$$

where t_{corr} is a random variable representing the corrosion initiation time as described in Choe et al. (2008) (i.e., without considering the impact of earthquakes); and t_1 is the time of the first damaging shock (i.e., an earthquake such that

$S_a > s_{a0}$, where s_{a0} is a specified threshold beyond which cracks open in the concrete). The environmental exposure conditions (e.g., submerged, tidal, splash, atmospheric) affect the chloride concentration on the surface which in turn influences t_{corr}. So, $\mathbf{E}(t)$ (introduced in Sect. 3.1) includes such exposure conditions. Equation (20) means that if the corrosion has not initiated before the damaging shock, it will initiate immediately after that, considering the formation of cracks. This assumption is supported by the results in Otieno et al. (2010). Overall, as the rate of earthquakes increases, the corrosion initiation time, T_{corr} (or more specifically t_1), shifts towards lower values, compare to the case without considering earthquake impacts (i.e., $T_{\text{corr}} = t_{\text{corr}}$).

To consider the impact of earthquakes on the corrosion rate, we use the following time-dependent model of the diameter of the reinforcement steel (i.e., one of the state variables in $\mathbf{X}$) according to Jia and Gardoni (2017a):

$$d_b(t, T_{\text{corr}}) = \begin{cases} d_{bi}, & t \le T_{\text{corr}} \\ d_b\left(t_{N(t)}, T_{\text{corr}}\right) - (r_a)^{N(t)} \frac{1.0508\left(1-\frac{w}{c}\right)^{-1.64}}{d} \left[(t - T_{\text{corr}})^{0.71} - \left(t_{N(t)} - T_{\text{corr}}\right)^{0.71}\right], & T_{\text{corr}} < t \le T_f, \\ 0, & t > T_f \end{cases} \tag{21}$$

where $d_b(t, T_{\text{corr}})$ is the diameter at time t for a given T_{corr}; $d_{bi} := d_b(0, T_{\text{corr}})$ is the diameter at time 0; $t_{N(t)}$ is the time of occurrence of the $N(t)$th shock whose spectral acceleration S_a satisfies $S_a > s_{a0}$ (s_{a0} is a specified threshold—possibly the same value already considered for Eq. (20)—beyond which the existing cracks may be widened and some self-healed cracks may be reopened, which may accelerate the corrosion process (Otieno et al. 2010); r_a is the acceleration factor adopted to accelerate the corrosion rate after each shock (i.e., the ratio between corrosion rate after and before each shock); w/c is the water-to-cement ratio; d is the cover depth of the RC section; and T_f is the time when $d_b(t, T_{\text{corr}})$, in theory, reaches zero. Equation (21) modifies the time-dependent model for the reinforcement steel diameter in Choe et al. (2008) and Choe et al. (2009) by incorporating the corrosion rate acceleration due to earthquakes as proposed in Jia and Gardoni (2017a). For $r_a = 1$, the corrosion rate is not accelerated after the earthquake, i.e., Equation (21) is equivalent to the equation in Choe et al. (2008). Note that the effect of corrosion acceleration due to earthquakes becomes more obvious as time increases, and also larger r_a leads to faster reduction of d_b. Equation (21) is a particular case of the general expression $\mathbf{X}(t) = \mathbf{X}_0 + \int_0^t \dot{\mathbf{X}}(\xi) d\xi$ in Eq. (7).

In this example, we assume the submerged exposure condition (which affects t_{corr}) and for corrosion acceleration, we set $s_{a0} = 0.1\ g$ and $r_a = 1.2$. These numerical values are assumed for illustrating the proposed formulation. This chapter is concerned with the development of a general mathematical formulation and the specific assessment of s_{a0} and r_a is beyond its scope. Additional studies should assess the most appropriate values of s_{a0} and r_a for specific structure and site.

The changes in d_b lead to changes in the moment curvature characteristics such as ultimate curvature capacity of the RC section, ϕ_u, and the pushover characteristics such as pre-yield lateral stiffness, K, and the displacement at yield, Δ_y. When considering the seismic damage, we model directly such derived structural properties. To combine the corrosion and seismic damage, we convert the effect of corrosion on $\mathbf{X}$ into the effects on the structural properties. Based on $d_b(t, T_{\text{corr}})$ from Eq. (21), we can estimate the corresponding state-dependent values of $\phi_u(t)$, $\Delta_y(t)$, and $K(t)$. Jia and Gardoni (2017a) developed probabilistic models for these structural properties. These models are calibrated based on data from virtual experiments (i.e., moment curvature analyses and pushover analyses) using different combinations of d_{bi} and $d_b(t, T_{\text{corr}})$.

6.1.2 Deterioration Due to Seismic Excitations

To model the deterioration due to seismic excitations, we first need to model the seismic hazard, including the occurrence of damaging earthquakes and the PDF of their intensity measure(s), (i.e., S_a in this example). Following Kumar and Gardoni (2012), the occurrence of earthquake mainshocks is modeled as a homogeneous Poisson process, and between the mainshocks, the occurrence of aftershocks is modeled as a non-homogeneous Poisson process. The time-varying rate of aftershocks is given by the modified Omari's law (Omari 1894; Utsu et al. 1995)

$$\lambda(t_a, m; m_m) = \frac{10^{\upsilon_0 + \upsilon_1 (m_m - m)}}{(t_a + \upsilon_2)^{\upsilon_3}}, \tag{22}$$

where $\lambda(t_a, m; m_m)$ is the mean daily rate of aftershocks with magnitude m or larger at time t_a, following a mainshock of magnitude m_m; υ_0, υ_1, υ_2, and υ_3 are model parameters and are related to the regional seismicity. Typical values are in the range $\upsilon_0 \in [-3, -0.5]$, $\upsilon_1 \in [0.35, 1.7]$, $\upsilon_2 \in [0.01, 0.1]$, and $\upsilon_3 \in [0.7, 1.5]$ (Reasenberg and Jones 1989; Godano et al. 2014). We assume the following values for the model parameters in Eq. (22): $\upsilon_0 = -1.67$, $\upsilon_1 = 0.91$, $\upsilon_2 = 0.05$, and $\upsilon_3 = 1.08$. For the mainshocks, we assume $\upsilon_0 = 3.8$. These values are typical of seismically active regions. For the fault considered in this example, we assume that it can generate earthquakes with magnitudes up to 8.0. We note that small earthquakes have an associated $S_a < 0.1\,g$ at the bridge site (therefore corrosion does not initiate/accelerate after their occurrence). Similarly, medium to large earthquakes have an associated $S_a > 0.1\,g$ at the bridge site (therefore corrosion does initiate/accelerate after their occurrence).

Given the occurrence rate of the earthquakes and the site layout in Fig. 3, we obtain the values of S_a at the site by performing a probabilistic seismic hazard analysis for the mainshock-aftershocks sequence. The details of the seismic hazard analysis can be found in Kramer (1996) and Yeo and Cornell (2009). Next, we estimate the corresponding changes in $\mathbf{X}$ (e.g., establish a model for $\Delta\mathbf{X}_k[\mathbf{X}(t_{k,i}^-), \mathbf{S}_k(t_{k,i}); \boldsymbol{\Theta}_{\mathbf{x},k}]$ as

discussed in Sect. 3.1) or, more specifically, the impact on the structural properties for a given value of S_a. In this example, we use the probabilistic models developed by Kumar and Gardoni (2014a) that predict the degradation of static pushover properties of RC columns as a function of $\mathbf{X}$ and S_a. The specific properties that we consider are as for the gradual deterioration: the ultimate curvature capacity of the RC section, ϕ_u, and the pushover characteristics such as pre-yield lateral stiffness, K, and the displacement at yield, Δ_y. Additional details on the development of state-dependent models using the probabilistic models developed in Kumar and Gardoni (2014a) can be found in Jia and Gardoni (2017b).

To estimate the time-varying capacity and demand, we use the predicted time-varying state variables and structural properties in the probabilistic capacity model developed by Gardoni et al. (2002) and the demand model developed by Gardoni et al. (2003). In terms of failure modes, in this example we focus on the dominant deformation failure (Gardoni et al. 2002).

6.2 Modeling of Recovery Process

Figure 4 shows the developed work plan for the repair of the deteriorated bridge column, using FRP composites. In this example, we consider FRP application as the sole recovery step. This means that the recovery activities in the work plan might continuously progress over time but the performance (e.g., reliability) of the system changes only after applying FRP on the bridge column. Table 1 shows the estimates of the durations of the individual activities in the work plan, using data from RS Means database (Means 2008) and similar projects (see Saini and Saiidi 2013). The table also shows the set of predecessors (recovery activities needed before a specific activity can start) of each activity. The information on the predecessors is required to estimate the completion time of the recovery process. In this example, because there is only one recovery step, the completion time of the recovery step is directly the completion time of the recovery process.

The recovery time is estimated by simulating the durations of the recovery activities in the plan. For this purpose, we model the duration of each individual recovery activity with a Beta distribution and use stochastic activity network scheduling techniques (Duncan 1996) to simulate the progression of the work and estimate the completion time. Note that when the number of recovery steps is more than one, we can use the same approach to generate data for the completion times of different recovery steps and then use the generated data to estimate $\boldsymbol{\Theta}_r$ in Eq. (12).

The recovery process introduces new state variables (i.e., $\mathbf{X}[\tau, \mathbf{X}_0, \{\mathbf{Z}(\tau)\}; \boldsymbol{\Theta}_{\mathbf{x}}, \boldsymbol{\Theta}_r]$ in Eq. (13)), which are FRP properties: thickness, tensile strength, and Young's modulus. The recovery process also affects $\phi_u(t)$ and $\Delta_y(t)$ (but not $K(t)$), the extent of which depends on the FRP properties. The FRP properties are determined such that the repaired system achieves a desired state. In this example, we assume that the repair of the deteriorated bridge improves its

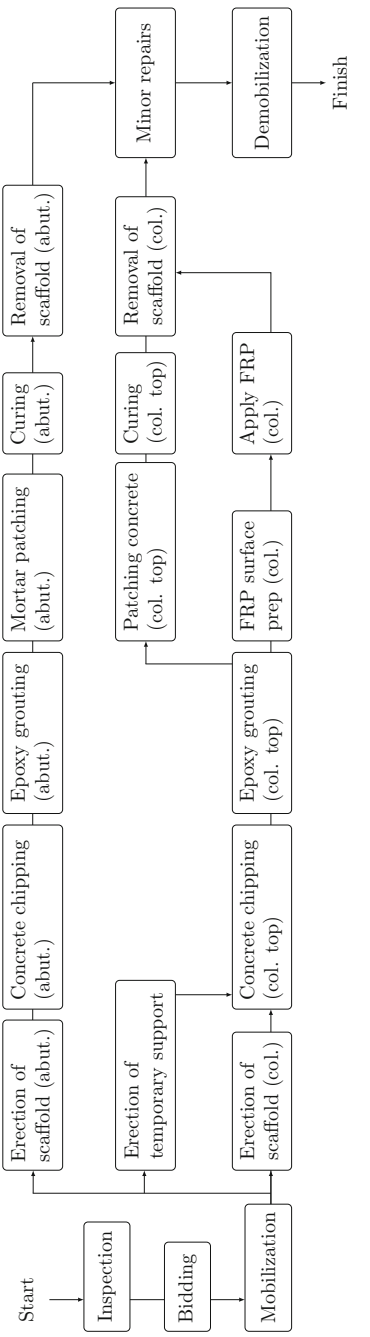

Fig. 4 Work plan for the repair of the deteriorated RC bridge, using FRP composites (Adapted from Sharma et al. 2017)

Table 1 The time table of the required recovery activities to repair the deteriorated RC bridge with FRP composites

Number	Activity	Duration (days)			Predecessor
		Lower bound	Most likely	Upper bound	
1	Inspection	2	3	5	
2	Bidding	15	20	30	1
3	Mobilization	5	7	15	2
4	Erection of scaffold (abutment)	1	2	3	3
5	Erection of temporary support	1	2	3	3
6	Erection of scaffold (pier)	1	2	3	3
7	Concrete chipping (abutment)	1	2	3	4
8	Epoxy grouting (abutment)	1	2	3	7
9	Mortar patching (abutment)	1	2	3	8
10	Curing (abutment)	7	10	15	9
11	Removal of scaffold (abutment)	1	2	3	10
12	Concrete chipping (pier top)	1	2	3	4 and 5
13	Epoxy grouting (pier top)	2	3	3	12
14	Patching concrete (pier top)	1	2	3	13
15	Curing (pier top)	7	10	15	14
16	FRP surface prep (pier)	0.5	1	2	15
17	Apply FRP (pier)	0.5	1	2	16
18	Removal of scaffold (pier)	0.5	1	2	15 and 17
19	Minor repairs	3	4	5	11 and 18
20	Demobilization	0.5	1	2	19

reliability by 10 percent with respect to the as-built condition. The FRP properties are then designed accordingly to meet this target reliability. The possible disrupting shocks during the recovery only affect $\phi_u(t)$, $\Delta_y(t)$, and $K(t)$ because they are functions of the original state properties of the column, but not of the new state variables because it is assumed that the recovery process ends after applying the FRP.

6.3 Results and Discussion

6.3.1 Instantaneous Reliability and Resilience

We estimate the reliability and resilience of the RC bridge, using Eqs. (14) and (19). Figure 5a shows the calculated time-variant predictive fragility, $\tilde{F}(t, S_a)$, and the PDF of S_a, $f(S_a)$, at $t = 0$ and 150. Figure 5b shows the corresponding instantaneous failure probability, $\tilde{P}_f(t)$. Figure 5b also shows the confidence band (between the 0.15 quantile and the 0.85 quantile) due to the epistemic uncertainty in the model parameters $\boldsymbol{\Theta}$. Here, S_a is the intensity measure of a possible future earthquake, while the bridge has been deteriorating over the period $[0, t]$ because of both corrosion (according to Sect. 6.1.1) and seismic excitations experienced before the one with intensity S_a (according to Sect. 6.1.2). As expected, the $\tilde{F}(t, S_a)$ and $\tilde{P}_f(t)$ increase with time due to the impact of deterioration processes. In particular, Fig. 5b shows that the failure probability of the as-built bridge significantly increases over 150 years (on average, from $\tilde{P}_f(t=0) = 5.1 \times 10^{-4}$ to $\tilde{P}_f(t=150) = 6.4 \times 10^{-1}$). This observation clearly shows that without considering the deterioration process, we are substantially underestimating the failure probability.

Figure 6a shows the calculated predictive resilience surface, $\tilde{\rho}(t, S_a)$, and $f(S_a)$ at $t = 0$ and 150, and Fig. 6b shows the predictive instantaneous resilience, $\tilde{\rho}(t)$. Figure 6b also shows the confidence band due to the epistemic uncertainty in $\boldsymbol{\Theta}$. At any given time t, $\tilde{\rho}(t, S_a)$ shows the impact on resilience (i.e., $\bar{Q}_{\text{res}}/Q_{\text{tar}}$) due to a disrupting shock, in terms of its S_a, after which the system undergoes the recovery process. Such impact becomes more significant with time, where a unit increase of S_a leads to a larger change in $\tilde{\rho}(t, S_a)$ at the later stages of the bridge service life than the earlier stages. Due to the impact of deterioration, the resilience of the bridge decays over time which is represented by the increasing trend of $\tilde{\rho}(t, S_a)$ and $\tilde{\rho}(t)$ over time.

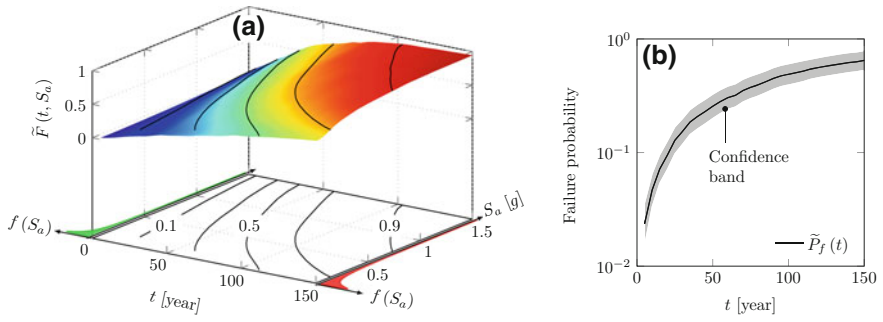

Fig. 5 Calculated **a** time-variant fragility and **b** instantaneous failure probability of the example RC bridge, considering the deterioration due to corrosion and seismic excitations

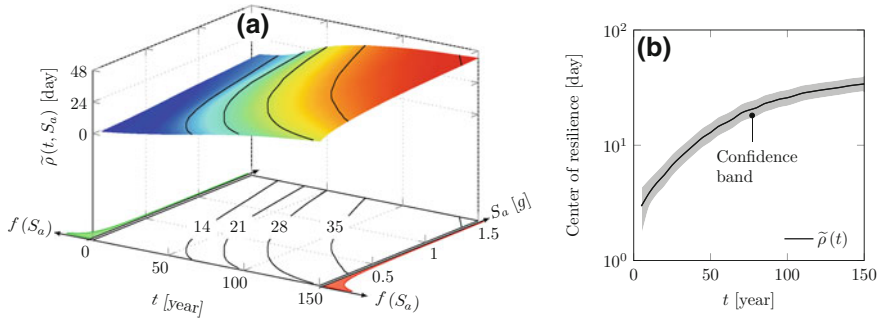

Fig. 6 Calculated **a** resilience surface and **b** instantaneous resilience of the example RC bridge, considering the deterioration due to corrosion and seismic excitations

6.3.2 Life-Cycle Performance Measures

To estimate the life-cycle performance measures, we have to first specify an intervention criterion. In this example, we determine the intervention time based on a prescribed acceptable resilience level, ρ_{acc}. With this choice, the decision about the intervention time not only accounts for the system state in the immediate aftermath of a disruption (i.e., $\bar{Q}_{\text{res}}/Q_{\text{tar}}$) but also for the recovery time needed to put back the system into the operation (i.e., $\rho_{\bar{Q},\text{res}}$). Alternatively, one could determine the intervention time based on an acceptable $R(t)$ level. We assume that there is a lag period, T_l, of 3 months between the intervention time and the beginning of the recovery. Because the recovery is not instantaneous, it is important to consider (as the proposed formulation allows us to do) the likely extra damage to the bridge due to aftershocks during the lag period.

Due to the repair of the deteriorated column with FRP composites, the performance of the RC bridge in the following cycles would be different from the one before the repair. One might expect, for example, that the deterioration rate after the repair is faster because the corrosion has already started and, in addition, we have to account for the deterioration of FRP composites. We assume that the considered 10% improvement in the initial system state compensates for the faster deterioration rate such that the assumption of the renewal process, namely that the T_{L_i}'s are *s.i.i.d.*, still holds. Note that the assumption of having a renewal process is only related to the calculation of life-cycle performance measures and does not affect the instantaneous reliability and resilience calculations.

Figure 7 shows the calculated $f_{T_l}(t)$, $f_{T_l|L_F}(t|L_F)$, and $f_{T_l|L_R}(t|L_R)$ for $\rho_{\text{acc}} = 28$ days as the acceptable level of resilience. The corresponding value of $\mathbb{P}(L_R)$ is 0.624. If we consider two other options for ρ_{acc} (i.e., 21 and 14 days), we see that $\mathbb{P}(L_R)$ tends to increase as ρ_{acc} decreases (i.e., $\mathbb{P}(L_R) = 0.777$ and 0.903, respectively). This trend is expected, because the smaller values of ρ_{acc} mean more frequent repairs and therefore fewer replacements (i.e., larger value of $\mathbb{P}(L_R)$). The marginal and conditional PDFs of T_L, $f_{T_L}(t)$ and $f_{T_L|L_F}(t|L_F)$, can be calculated using

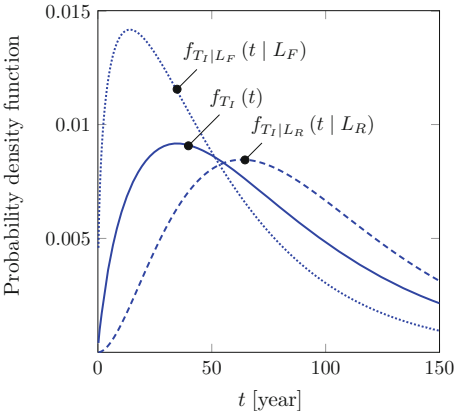

Fig. 7 Calculated PDFs $f_{T_I}(t)$, $f_{T_I|L_F}(t|L_F)$, and $f_{T_I|L_R}(t|L_R)$ for $\rho_{\text{acc}} = 28$ days

the relation $T_L = T_I + T_D$, where the distribution of T_D is obtained from the recovery process. Because the contribution of T_I to T_L dominates in this example, the marginal and conditional PDFs of T_L are close to those of T_I, and are not shown in Fig. 7.

Once we have $f_{T_I}(t)$, $f_{T_L}(t)$, $f_{T_I|L_F}(t|L_F)$, and $f_{T_L|L_F}(t|L_F)$, we use them in the equations presented in Sect. 2 to estimate the life-cycle performance measures. In this example, we only consider the costs and benefits to the bridge's owner. The same formulation could include the costs and benefits to the bridge's users. We assume that the operation cost is proportional to the bridge's replacement value and for the current example, we assume $\bar{c}_{Op} = 0.2C_C$. Also, we assume $c_L = 2C_C$, $\gamma = 0.04$ year^{-1}, and $b = 0.1C_C$ year^{-1}according to Kumar and Gardoni (2014b). The value of the discount rate, γ, is related to a country's level of development, where a value of γ between 0.02 and 0.08 is typical for developed countries (Thoft-Christensen 2012). The benefit of having the bridge in use for a unit time, b, is typically determined based on the product of the average daily traffic on the bridge throughout a year and the average benefit derived from each vehicle passing the bridge (Thoft-Christensen 2012). The quantities in the following analyses and figures are normalized by C_C.

Figure 8 shows the instantaneous probability of being in use, $\mathbb{P}_S(t)$, and the expected availability, $\mathbb{E}[A(t)]$, as functions of time. The relations are plotted for three different values of ρ_{acc}. In Fig. 8a, we observe that (for all the three values of ρ_{acc}) $\mathbb{P}_S(t)$ initially decreases, and then gradually increases toward an asymptotic value. The initial decrease is because as the system operates it deteriorates and becomes more likely to be out of service for a repair or replacement. The instantaneous probability of being in use reaches a minimum at the most likely time of the first repair or replacement. After, $\mathbb{P}_S(t)$ starts to increase because a repair or replacement has typically taken place. We also observe that at t larger than the most likely time of the first repair or replacement, $\mathbb{P}_S(t)$ is larger for smaller values of ρ_{acc}. This is because having more repairs is likely to prevent an ultimate failure that would result in being out of service for an extended period of time. A similar

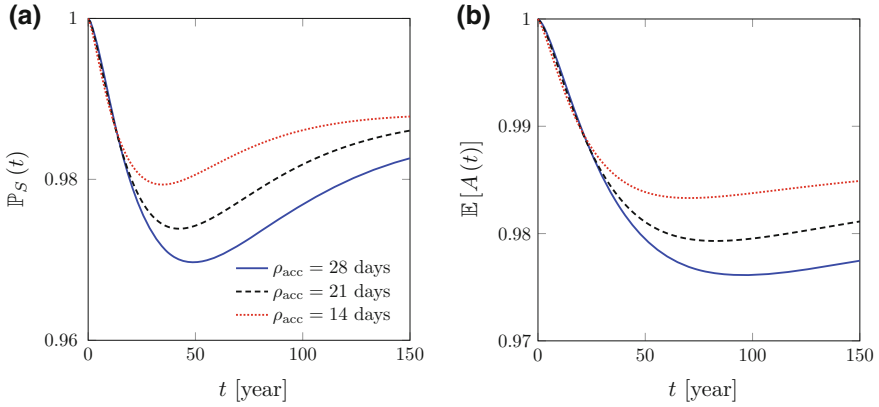

Fig. 8 The effect of ρ_{acc} on the **a** instantaneous probability of being in use and **b** availability of the RC bridge over time

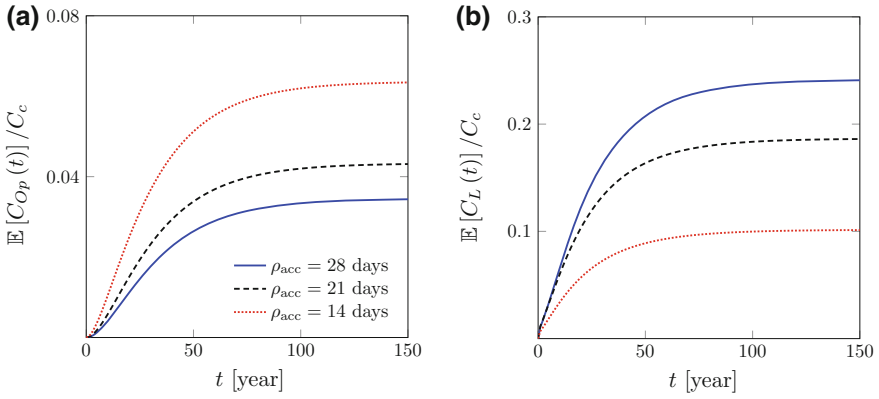

Fig. 9 The effect of ρ_{acc} on the **a** operation cost and **b** failure loss over time

observation can be seen in Fig. 8b for $\mathbb{E}[A(t)]$, where in the long term, smaller values of ρ_{acc} (frequent repairs) lead to higher $\mathbb{E}[A(t)]$.

Using Eq. (4) and the value for $\bar{c}_{Op}$, we can estimate the expected operation cost, $\mathbb{E}[C_{Op}(t)]$. Figure 9a shows $\mathbb{E}[C_{Op}(t)]$ as a function of time and ρ_{acc}. We observe that the larger values of ρ_{acc} lead to larger values of $\mathbb{E}[C_{Op}(t)]$. This is because in the long term more frequent repairs help to avoid the replacement cost due to the occurrence of an ultimate failure.

Figure 9b shows $\mathbb{E}[C_L(t)]$ as a function of time and ρ_{acc}. We observe that the value of $\mathbb{E}[C_L(t)]$ increases with time for all three cases and after $t \approx 80$ years it becomes almost constant. This leveling behavior is because the discount rate makes the costs associated with the events occurring after a sufficiently long period irrelevant to the decision made at $t = 0$. We also observe that $\mathbb{E}[C_L(t)]$ decreases as

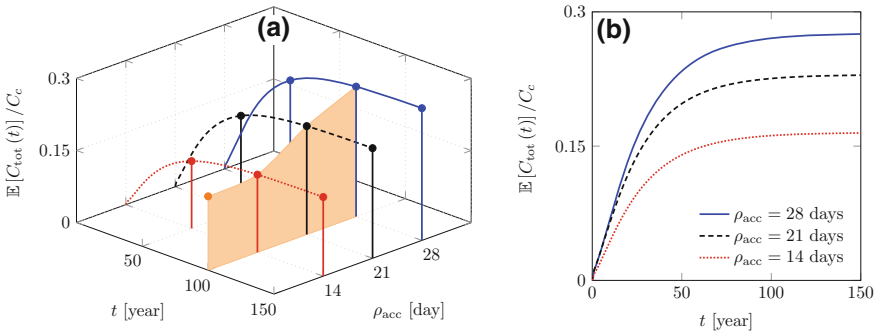

Fig. 10 The effect of ρ_{acc} on the expected total cost over time

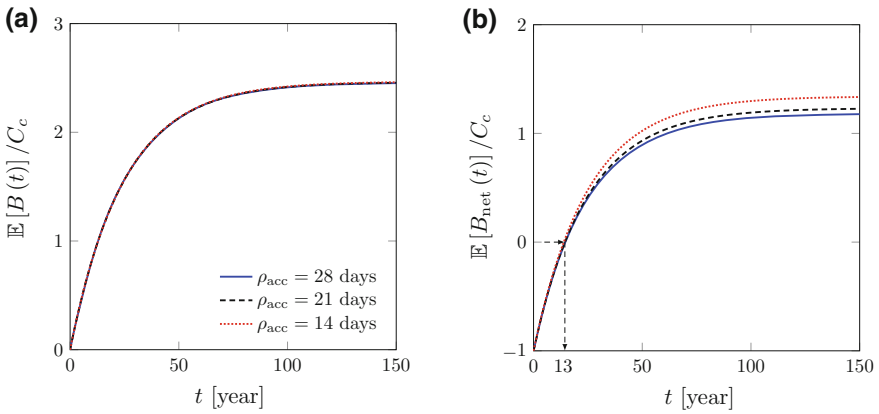

Fig. 11 The effect of ρ_{acc} on **a** the expected benefit and **b** the expected net benefit over time

ρ_{acc} decreases. This is because smaller ρ_{acc} means frequent repairs, smaller $\mathbb{P}(L_F)$, and therefore lower $\mathbb{E}[C_L(t)]$. Comparing the numerical values of $\mathbb{E}[C_{Op}(t)]$ and $\mathbb{E}[C_L(t)]$, we see that $\mathbb{E}[C_L(t)]$ is significantly larger.

Figure 10 shows the expected total cost $\mathbb{E}[C_{\text{tot}}(t)] = \mathbb{E}[C_{Op}(t)] + \mathbb{E}[C_L(t)]$ as a function of time and ρ_{acc}. The trend over time of $\mathbb{E}[C_{\text{tot}}(t)]$ is similar to those of $\mathbb{E}[C_{Op}(t)]$ and $\mathbb{E}[C_L(t)]$. Because in this example $\mathbb{E}[C_L(t)]$ is significantly larger than $\mathbb{E}[C_{Op}(t)]$, the values of $\mathbb{E}[C_{\text{tot}}(t)]$ are similar to those of $\mathbb{E}[C_L(t)]$. The obtained results show that when considering the expected total cost, an optimal mitigation strategy would use the smallest value of ρ_{acc} (among the three considered). Figure 10a also shows the variation of $\mathbb{E}[C_{\text{tot}}(t=100)]$ as a function of $\rho_{\text{acc}} \in \{7, 14, 21, 28\}$. We observe that $\mathbb{E}[C_{\text{tot}}(t=100)]$ is the largest for $\rho_{\text{acc}} = 28$ days. This is because $\mathbb{E}[C_L(t=100)]$ is the largest for $\rho_{\text{acc}} = 28$ days and it dominates $\mathbb{E}[C_{\text{tot}}(t=100)]$.

Figure 11 shows the expected benefit $\mathbb{E}[B(t)]$ and the expected net benefit $\mathbb{E}[B_{\text{net}}(t)]$. We observe that $\mathbb{E}[B(t)]$ increases with time and after $t \approx 100$ years the

rate tends to zero. The leveling behavior is because the discount rate makes the long term benefits irrelevant to the decision made at $t=0$. This is similar to the consideration of the long term costs when computing $\mathbb{E}[C_{\text{tot}}(t)]$. In this example, we observe that the differences in the values of $\mathbb{E}[B(t)]$ for the three values of ρ_{acc} are not significant. This is because the value of $\mathbb{E}[B(t)]$ depends on $\mathbb{P}_S(t)$, which is not significantly different for different values of ρ_{acc} for small values of t, as shown in Fig. 8a and the differences in $\mathbb{P}_S(t)$ for larger values of t are tapered down by the discount rate. Figure 11b shows that $\mathbb{E}[B_{\text{net}}(t=0)]/C_C = -1$ because there is no accumulated benefit at $t=0$ but there is a construction cost ($\mathbb{E}[B_{\text{net}}(t)] = \mathbb{E}[B(t)] - \mathbb{E}[C_{\text{tot}}(t)] - C_C$). After $t \approx 13$ years, the expected benefit generated by the example bridge exceeds the costs, for all the three values of ρ_{acc}. As a result, $\mathbb{E}[B_{\text{net}}(t)]$ becomes positive. We observe that $\mathbb{E}[B_{\text{net}}(t)]$ increases as ρ_{acc} decreases. This is because $\mathbb{E}[B(t)]$ is almost the same for the three values of ρ_{acc} but the $\mathbb{E}[C_{\text{tot}}(t)]$ decreases as ρ_{acc} decreases.

It is important to note that the figure does not imply that the $\mathbb{E}[B_{\text{net}}(t)]$ increases indefinitely by decreasing ρ_{acc}. When the frequency of interventions exceeds the frequency of the occurrence of earthquakes, $\mathbb{E}[C_{\text{tot}}(t)]$ increases without gains in $\mathbb{E}[B(t)]$. As a result, $\mathbb{E}[B_{\text{net}}(t)]$ would start decreasing. A full optimization is beyond the scope of this chapter. However, the proposed SLCA can be used directly in an optimization process to find, for example, the optimal ρ_{acc}. In addition, while this chapter reported results for the expected values of costs and benefits, an optimal design and mitigation strategy can also be investigated considering the tails of the distributions of $C_{Op}(t)$, $C_{\text{tot}}(t)$, and $B_{\text{net}}(t)$.

7 Conclusions

This chapter proposed a general stochastic formulation for the Life-Cycle Analysis (LCA) of deteriorating engineering systems, named Stochastic Life-Cycle Analysis (SLCA). The life-cycle of an engineering system is shaped by deterioration processes and repair/recovery process, both characterized by several sources of uncertainty. In the SLCA, state-dependent stochastic models are proposed to capture the impact of deterioration processes and repairs/recovery strategies on the engineering systems in terms of performance measures like instantaneous reliability and resilience. The proposed formulation integrates the state-dependent stochastic models with the previously developed Renewal Theory-based Life-Cycle Analysis (RTLCA) to efficiently evaluate additional system performance measures such as availability, operation cost and benefits.

The formulation is illustrated through the life-cycle analysis of an example RC bridge subject to deterioration caused by corrosion and seismic excitations. For the recovery process, the deteriorated bridge column is repaired with FRP composites. Resilience is used to defined an intervention criterion that triggers the repair of the deteriorated system. With this choice, the decision about the intervention time

accounts for both the system state in the immediate aftermath of a disruption and the recovery time to put back the system into the operation. The results show that the deterioration processes significantly impact both the instantaneous failure probability and resilience of the example bridge. The level of impact is such that the estimated failure probability of the undamaged bridge significantly underestimates the probability of failure of the deteriorated bridge. The results also indicate that for longterm service life, it is generally economically advantageous to have frequent repairs which reduce the probability that the bridge would be out of service for an extended period of time. While beyond the scope of this chapter, the proposed SLCA can be used in the full optimization of the initial design and mitigation strategies of engineering systems accounting for their life-cycle performance.

Acknowledgements The research herein was supported in part by the Center for Risk-Based Community Resilience Planning funded by the U.S. National Institute of Standards and Technology (NIST Financial Assistance Award Number: 70NANB15H044). The views expressed are those of the authors, and may not represent the official position of the National Institute of Standards and Technology or the U.S. Department of Commerce.

References

Choe D-E, Gardoni P, Rosowsky D, Haukaas T (2008) Probabilistic capacity models and seismic fragility estimates for RC columns subject to corrosion. Reliab Eng Syst Saf 93:383–393

Choe D-E, Gardoni P, Rosowsky D, Haukaas T (2009) Seismic fragility estimates for reinforced concrete bridges subject to corrosion. Struct Saf 31:275–283

Ciampoli M, Ellingwood BR (2002) Probabilistic methods for assessing current and future performance of concrete structures in nuclear power plants. Mater Struct 35:3–14

Duncan W (1996) A guide to the project management body of knowledge. Management 1:459

Eck Olave MK, Bracci JM, Gardoni P, Trejo D (2015a) Performance of RC columns affected by ASR. I : Accelerated exposure and damage. J Bridg Eng 20:4014069

Eck Olave MK, Bracci JM, Gardoni P, Trejo D (2015b) Performance of RC columns affected by ASR. II : Experiments and assessment. J Bridg Eng 20:4014070

Ellingwood BR, Yasuhiro M (1993) Probabilistic methods for condition assessment and life prediction of concrete structures in nuclear power plants. Nucl Eng Des 142:155–166

Gardoni P, Der Kiureghian A, Mosalam KM (2002) probabilistic capacity models and fragility estimates for reinforced concrete columns based on experimental observations. J Eng Mech 128:1024–1038

Gardoni P, Mosalam KM, Der Kiureghian A (2003) Probabilistic seismic demand models and fragility estimates for RC bridges. J Earthq Eng 7:79–106

Gardoni P, Reinschmidt KF, Kumar R (2007) A probabilistic framework for Bayesian adaptive forecasting of project progress. Comput Civ Infrastruct Eng 22:182–196

Gardoni P, Murphy C (2008) Recovery from natural and man-made disasters as capabilities restoration and enhancement. Int J Sustain Dev Plan 3:317–333

Gardoni P, Rosowsky D (2011) Seismic fragility increment functions for deteriorating reinforced concrete bridges. Struct Infrastruct Eng 7:1–11

Gardoni P, Trejo D (2013) Seismic reliability of deteriorating reinforced concrete (RC) bridges. In: Tesfamariam S, Goda K (eds) Handbook of seismic risk analysis and management of civil infrastructure systems. Woodhead Publishing Ltd, Cambridge, UK, pp 514–535

Gardoni P, Trejo D, Kim YH (2013) Time-variant strength capacity model for GFRP bars embedded in concrete. J Eng Mech 139:1435–1445
Gardoni P, Guevara-lopez F, Contento A (2016) The life profitability method (LPM): a financial approach to engineering decisions. Struct Saf 63:11–20
Godano C, Lippiello E, de Arcangelis L (2014) Variability of the b value in the Gutenberg-Richter distribution. Geophys J Int 199:1765–1771
Iervolino I, Giorgio M, Polidoro B (2014) Reliability of structures to earthquake clusters. Bull Earthq Eng 13:983–1002
Jia G, Gardoni P (2017a) A general stochastic framework for modeling deteriorating engineering systems considering multiple deterioration processes and their interactions. Struct Saf (to be submitted)
Jia G, Gardoni P (2017b) Life-cycle analysis of reinforced concrete bridges using a new model for deterioration. Eng Struct (to be submitted)
Joanni A, Rackwitz R (2008) Cost-benefit optimization for maintained structures by a renewal model. Reliab Eng Syst Saf 93:489–499
Kim YH, Trejo D, Gardoni P (2012) Time-variant reliability analysis and flexural design of GFRP-reinforced bridge decks. J Compos Constr 16:359–370
Kramer SL (1996) Geotechnical earthquake engineering. Prentice-Hall, Inc.
Kumar R, Gardoni P, Sanchez-Silva M (2009) Effect of cumulative seismic damage and corrosion on the life-cycle cost of reinforced concrete bridges. Earthq Eng Struct Dyn 38:887–905
Kumar R, Gardoni P (2012) Modeling structural degradation of RC bridge columns subjected to earthquakes and their fragility estimates. J Struct Eng 138:42–51
Kumar R, Gardoni P (2013) Stochastic modeling of structural deterioration in infrastructure systems. In: Tesfamariam S, Goda K (eds) Handbook of seismic risk analysis and management of civil infrastructure systems. Woodhead Publishing Ltd, Cambridge, UK, pp 410–434
Kumar R, Gardoni P (2014a) Effect of seismic degradation on the fragility of reinforced concrete bridges. Eng Struct 79:267–275
Kumar R, Gardoni P (2014b) Renewal theory-based life-cycle analysis of deteriorating engineering systems. Struct Saf 50:94–102
Kumar R, Cline DBH, Gardoni P (2015) A stochastic framework to model deterioration in engineering systems. Struct Saf 53:36–43
Li Q, Wang C, Ellingwood BR (2015) Time-dependent reliability of aging structures in the presence of non-stationary loads and degradation. Struct Saf 52:132–141
Means R (2008) Building construction cost data, 67th edn. Reed Construction Data, Kingston, MA
Mori Y, Ellingwood BR (1994) Maintaining reliability of concrete structures. II: Optimum inspection/repair. J Struct Eng 120:846–862
Murphy C, Gardoni P (2011) Evaluating the source of the risks associated with natural events. Res Publica 17:125–140
Omari F (1894) On the aftershocks of earthquakes. J Coll Sci 7:111–200
Otieno MB, Alexander MG, Beushausen H-D (2010) Corrosion in cracked and uncracked concrete—influence of crack width, concrete quality and crack reopening. Mag Concr Res 62:393–404
Pillai RG, Hueste MD, Gardoni P et al (2010) Time-variant service reliability of post-tensioned, segmental, concrete bridges exposed to corrosive environments. Eng Struct 32:2596–2605
Reasenberg PA, Jones LM (1989) Earthquake hazard after a mainshock in California
Riascos-Ochoa J, Sánchez-Silva M (2015) A unified formalism for modeling and reliability estimation of degrading systems. In: 12th international conference on applications of statistics and probability in civil engineering, ICASP12. Vancouver, Canada, 12–15 July, pp 1–8
Saini A, Saiidi MS (2013) Post-earthquake damage repair of various reinforced concrete bridge components. Caltrans Final Rep, CA 14
Sanchez-Silva M, Klutke GA, Rosowsky DV (2011) Life-cycle performance of structures subject to multiple deterioration mechanisms. Struct Saf 33:206–217
Sharma N, Tabandeh A, Gardoni P (2017) Resilience analysis: a mathematical formulation to model resilience of engineering systems. Sustain Resil Infrastruct (to be submitted)

Tabandeh A, Gardoni P (2014) Probabilistic capacity models and fragility estimates for RC columns retrofitted with FRP composites. Eng Struct 74:13–22

Tabandeh A, Gardoni P (2015) Empirical Bayes approach for developing hierarchical probabilistic predictive models and its application to the seismic reliability analysis of FRP-retrofitted RC bridges. ASCE-ASME J Risk Uncertain Eng Syst Part A: Civil Eng 1(2):04015002

Thoft-Christensen P (2012) Infrastructures and life-cycle cost-benefit analysis. Struct Infrastruct Eng 8:507–516

Utsu T, Ogata Y, Matsu'ura SR (1995) The centenary of the Omori Formula for a decay law of aftershock activity. J Phys Earth 43:1–33

van Noortwijk JM, Frangopol DM (2004) Two probabilistic life-cycle maintenance models for deteriorating civil infrastructures. Probab Eng Mech 19:345–359

van Noortwijk JM, van der Weide J a M, Kallen MJ, Pandey MD (2007) Gamma processes and peaks-over-threshold distributions for time-dependent reliability. Reliab Eng Syst Saf 92:1651–1658

van Noortwijk JM, van der Weide JAM (2008) Applications to continuous-time processes of computational techniques for discrete-time renewal processes. Reliab Eng Syst Saf 93:1853–1860

Vu KAT, Stewart MG (2000) Structural reliability of concrete bridges including improved chloride-induced corrosion models. Struct Saf 22:313–333

Yeo GL, Cornell CA (2009) A probabilistic framework for quantification of aftershock ground-motion hazard in California. Earthq Eng Struct Dyn 45–60

Zhong J, Gardoni P, Rosowsky D (2010) Stiffness degradation and time to cracking of cover concrete in reinforced concrete structures subject to corrosion. J Eng Mech 136:209–219

Fragility Curves of Restoration Processes for Resilience Analysis

Gian Paolo Cimellaro

Abstract In literature the fragility curves are usually adopted to evaluate the probability of exceedance of a given damage state. This chapter presents for the first time a procedure for developing fragility curves of restoration processes which can be adopted for resilience analysis. The restoration process describes the capacity to recover from a system failure and it is one of the most uncertain variables in the resilience analysis therefore, the problem should be treated in probabilistic terms. In the chapter, a method is proposed for evaluating the Restoration Fragility Functions (RFF) of a given system following an extreme event. The restoration curves have been built empirically using the data obtained by a discrete event simulation model of the system considered. Different restoration processes obtained through Monte Carlo simulations have been analyzed statistically to determine the probability of exceedance of a given restoration state. Then, Restoration Fragility Functions (RFF) are obtained using the Maximum Likelihood Estimation (MLE) approach assuming a lognormal cumulative distribution function. The method has been applied to an Emergency Department of a hospital during a crisis, because these buildings are critical facilities which should withstand after an earthquake in order to assist injuries. Two different case studies have been compared: the Emergency Department (ED) with and without emergency plan.

1 Introduction

Hospitals are critical facilities which affect the emergency response after a catastrophic event such as a strong earthquake. The non-functionality of an Emergency Department (ED) during an emergency might significantly impact the health care services and affect the recovery process. The hospital's capability to remain accessible and able to function at maximum capacity, providing its services to the community when they are most needed can be evaluated using the resilience

G.P. Cimellaro (✉)
Politecnico di Torino, Corso Duca Degli Abruzzi 24, 10129 Turin, Italy
e-mail: gianpaolo.cimellaro@polito.it

P. Gardoni (ed.), *Risk and Reliability Analysis: Theory and Applications*,
Springer Series in Reliability Engineering, DOI 10.1007/978-3-319-52425-2_21

indicators (Cimellare et al. 2016). A possible resilience indicator for health care facilities is the waiting time, which is the time a patient waits from the moment he/she walks in the ED until he/she receives the first service from medical personnel (Cimellaro et al. 2010, 2011). A key role in the evaluation of the resilience indicator is played by the recovery time and the shape of the restoration curve, because they are both uncertain quantities. Therefore, in this chapter a procedure for building fragility curves of restoration processes called Restoration Fragility Functions (RFF) which can be adopted for resilience analysis, is presented. RFFs are introduced to take into account the uncertainties of the restoration process. In detail, RFFs are defined as the probability of exceedance of a given restoration process when a certain damage state occurs. To calculate the RFF it is necessary to define the functionality (Q) of the system considered and the recovery time. The Emergency Department (ED) of the Umberto I Mauriziano Hospital in Turin Italy is considered as case study. After building and calibrating a Discrete Event Simulation (DES) model of the Emergency Department (ED) using real data collected on site, different scenarios has been tested by modifying the patient arrival rate and changing the number of available emergency rooms. In this research two scenarios have been considered: the ED with emergency plan applied and the ED in normal condition. RFFs of both cases are compared.

1.1 State of the Art

In the current state-of-art, fragility functions describe the conditional probability that a structure, a nonstructural element or in general a system, will exceed a certain damage state, assuming a certain demand parameter (e.g. story drift, floor acceleration etc.) or earthquake intensity level (e.g. peak ground acceleration (PGA), peak ground velocity (PGV) or spectral acceleration (SA)) is reached. Usually, fragility functions take the form of lognormal cumulative distribution functions, having a median value and logarithmic standard deviation, (Porter et al. 2007). The first attempts to introduce uncertainties in the restoration processes of infrastructures such as bridges is present in the work of Zhou and Frangopol (2014) where they defined the probability of a bridge experiencing different performance and functionality levels (e.g. one lane closed, all lanes closed). They were inspired by the Federal Highway Administration (FHWA 1995), which following ATC-13 (ATC-13 1985), modeled the restoration process of bridge functionality by a normal cumulative distribution function corresponding to each bridge damage state considered. In fact, the recovery functions are highly dependent on their associated damage states. For example, a bridge categorized in a severe damage state may need more time to be restored to its full functionality compared to a bridge slightly damaged. On the other hand, in this paper, the recovery functions are computed for three different Damage States (DS), no damage, moderate damage and complete damage. For each DS a characteristic restoration curve is defined.

2 Restoration Fragility Functions

This chapter presents for the first time a procedure for building fragility curves of restoration processes which can be adopted for resilience analysis. RFF is the probability of exceedance of a given restoration curve (rf) when a certain Damage State (DS) occurs for a given earthquake intensity measure I. The general definition of RFF based on earthquake intensity I is given by

$$RFF(i) = P\left(RF_j \geq rf_{DS1} \middle| DS = DS1, I = i\right) \tag{1}$$

where the $RF_j = j$th restoration function; $rf_j =$ restoration function associated to a given damage state $DS(1, 2, n)$; $I =$ earthquake intensity measure which can be represented by $pga =$ peak ground acceleration; $pgv =$ peak ground velocity; PVS =pseudovelocity spectrum; $MMI =$ modified Mercalli intensity scale, etc.; and $i =$ given earthquake intensity value. The main difference between RFF and standard fragility functions is that the RFF is correlated to a given Damage State (DS). In other words, RFF is conditional on DS and I, while standard fragility curves are only conditional on the intensity measure I.

3 Methodology

The RFF are evaluated using the experimental data of the restoration curves collected by the numerical analyses of the model considered. Different output can be considered, but in this specific case, the waiting time (WT) spent by patients in the emergency room (ER) before receiving care. (Cimellaro et al. 2010), is considered as an indicator of functionality. In particular, the following relationship has been used to define its functionality Q:

$$Q = \frac{WT_0}{WT} \tag{2}$$

where WT_0 is the acceptable waiting time in regular condition, when the hospital is not affected by a catastrophic event, and WT is the waiting time collected during the simulation process. When the WT is less or equal to WT_0, the value of Q is equal to 1, meaning that the hospitals functionality is at its maximum. Different restoration functions (rf) associated at different damage states have been chosen. Then, for each simulation, the probability of exceedance of a given restoration curve (rf) has been calculated. The frequency of exceedance at a given instant is defined as

$$f = \frac{N}{N_{tot}} \tag{3}$$

where N is the number of times when the restoration curves exceed the restoration curve associated at a given damage state; N_{tot} is the number of simulations. Finally the probability of exceedance of a given restoration state has been calculated by

$$P_{ex} = \frac{\sum f_i}{T} \tag{4}$$

where $\sum f_i$ is the sum of the frequencies at each time instant, while T is the length of the simulation (e.g. $T = 12\,days$ in the case study). Finally, different methods to fit fragility curves are compared such as:

1. MLE method: maximum likelihood method;
2. SSE method: sum of squared errors;

4 Case Study: The Mauriziano Hospital in Turin

The Umberto I Mauriziano Hospital located in Turin, Italy (Fig. 1) has been considered as case study to show the applicability of the methodology. The hospital is located in the southeast part of the city, at almost 3 Km from downtown. It was built in 1881 but it was bombed several times during World War II. This explains why several buildings have been rebuilt or added. Presently the hospital includes 17 units, which correspond to different Departments and it covers an overall surface of

Fig. 1 The Mauriziano hospital in Turin, Italy

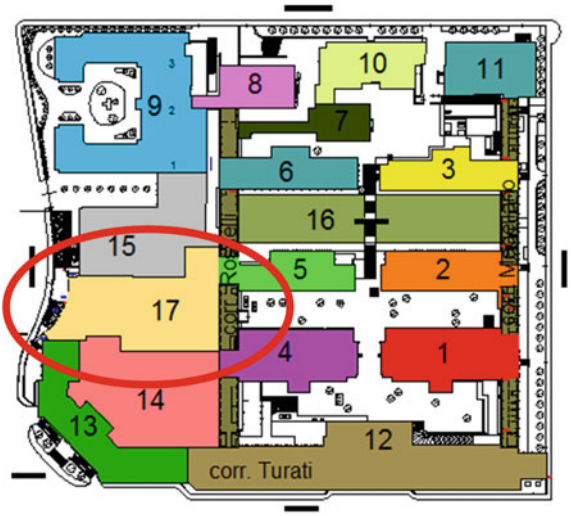

Fig. 2 Hospitals units emergency department building

52827 m^2. Only the Emergency Department (building 17) has been modeled in this case study (Fig. 2).

A discrete event simulation model (DES) of the emergency department has been developed (Fig. 3) using ProModel version 7.0, downloaded on February 15, 2014.

Discrete event simulation models represent useful tools to test Emergency Plans response under a rapid increase in the volume of incoming patients. Using discrete-event Monte Carlo computer simulation, hospital administrators can model different scenarios of the hospital to see how they compare to the desired performance

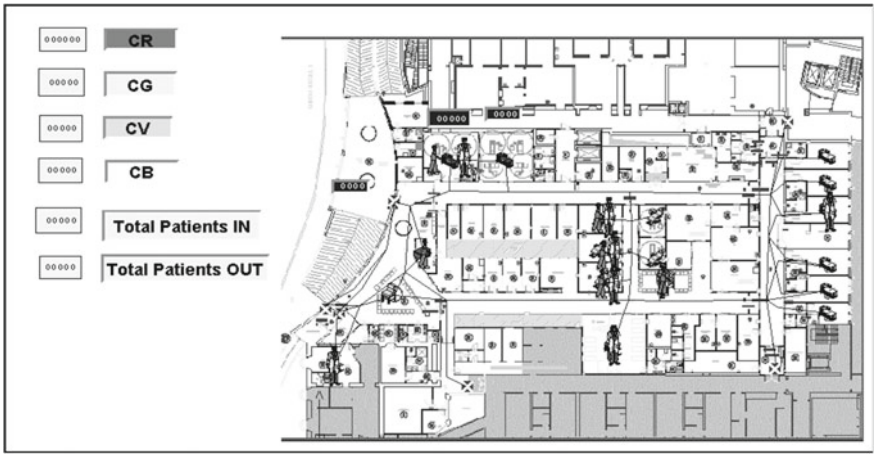

Fig. 3 DES model of the Mauriziano hospital in promodel

(Morales 2011). Moreover, DES model allows investigating and planning the use of hospital resources (Šteins 2010). The data input of the model is the patient's arrival rate in normal operating conditions, which has been extracted by the hospital's register statistics. These data have been used to calibrate the model. During the emergency, the increments of patients entering in the ED has been obtained using the data collected in a Californian hospital during 1994 Northridge earthquake. The pattern of the Northridge patient arrival rate is given in (Cimellaro et al. 2011). Then the patients' arrival rate has been scaled to the seismic hazard in Turin using a procedure based on the Modified Mercalli Intensity (MMI) scale. An earthquake with a return period of 2500 years has been considered, assuming a nominal life for a building of strategic importance of 100 years according to the Italian seismic standards (NTC-08 2008). RFFs both with and without emergency plan are compared. The emergency plan is considered effective if the waiting time obtained when the emergency plan is applied is significantly lower than the waiting time obtained under emergency conditions when the emergency plan is not active.

4.1 Hospital Performance and Restoration Functions (rf)

Generally, the performance of a hospital under seismic hazard is quantified considering all its possible damage states. The performance of the Emergency Department (ED) is quantified within this paper by mapping the current damage state to a value between 0 and 1.0. Assuming a certain damage state occurs in the hospital, then different restoration functions (rf) can be applied to the damaged structure to restore its functionality. However, the restoration functions (rf) of the ED are highly dependent on their associated damage states. For example, an ED categorized in a severe damage state may need more time to be restored to its full functionality compared to an ED slightly damaged, so some rfs have more probability to happen with respect to others.

4.2 Numerical Results

As outputs of the model, the waiting times of the ED when the emergency plan is active have been collected for different scenarios. Three different damage states (DS) have been considered:

1. DS = Fully operational/No Damage (n = 0);
2. DS = Moderate Damage (n = 1);
3. DS = Severe Damage (n = 2);

where *n* is the number of emergency room not functional because damaged by the earthquake. For each *DS*, several simulations have been conducted by changing the intensity of the seismic event using the methodology described above. The intensity

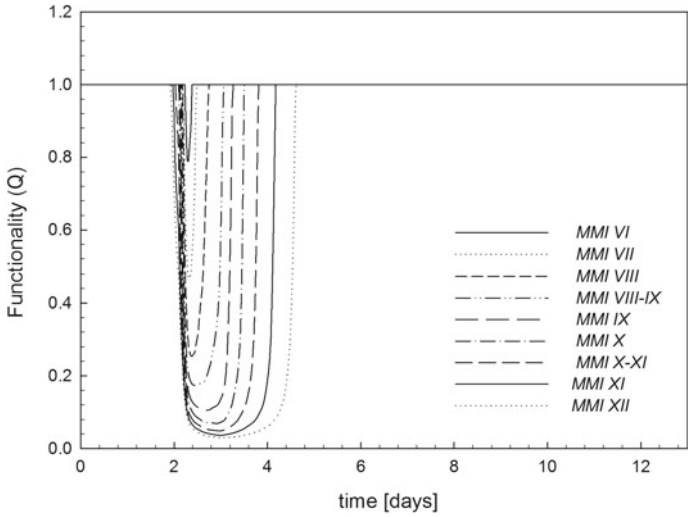

Fig. 4 Functionality curves as a function of seismic intensity, no damage (n = 0)

has been increased by means of scale factors that multiplied the patient arrival rate. Three different Restoration Functions (RFs) have been chosen as comparison. The results are shown in the following paragraphs. The functionality Q of the ED has been evaluated for increasing seismic intensities based on the Modified Mercalli Intensity (MMI) scale (Fig. 4, 5 and 6). Each graph shows different damage states (DS):

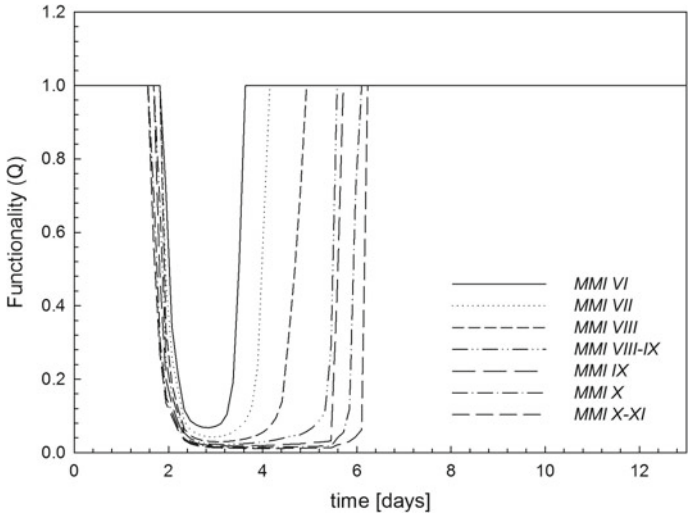

Fig. 5 Functionality curves as a function of seismic intensity, moderate damage (n = 1)

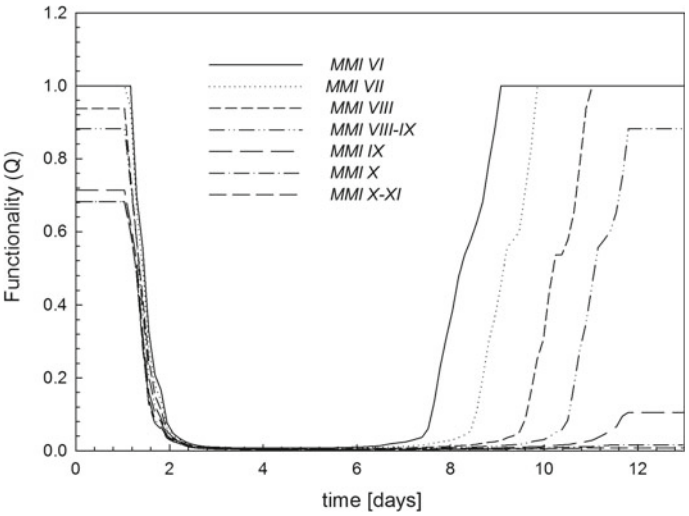

Fig. 6 Functionality curves as a function of seismic intensity, severe damage (n = 2)

- Emergency plan fully operational with n = 0, where n is the number of emergency room not available because damaged by the earthquake (Fig. 4);
- Emergency plan affected by moderate damage (n = 1) (Fig. 5);
- Emergency plan affected by severe damage (n = 2) (Fig. 6);

As shown in the graphs, the functionality is reduced and the recovery time increases when two emergency rooms are not operative. The functionality is also dependent on the seismic intensity. As the seismic intensity increases, the restoration curves take longer recovery time to get back at their initial functionality. In Fig. 7 for higher seismic intensities, the functionality at the end of the simulation doesn't reach the ideal value, showing that the emergency department is not yet back to its original operating condition.

In this case study, the Modified Mercalli Intensity (MMI) scale has been adopted, but other parameters such as peak ground acceleration (PGA), peak ground velocity or spectral acceleration (SA) can also be used. Three restoration functions (rf) associated to specific damage states have been chosen to calculate the fragility restoration curve. The rfs chosen in this study refer to the functionality curve assuming no damage (RF0), moderate damage (RF1) and complete damage (RF2). As shown in Fig. 7, RF0 has a restoration time of 1 day, while RF1 and RF2 have restoration times of 2 days and 6 days respectively. The restoration time t_r specifies how long the ED takes to recover from a disaster.

The restoration fragility functions for each damage state scenario have been calculated. RFF is the probability that a given restoration function rf (Fig. 7) is reached when a certain damage state (DS) occurs for a given earthquake intensity measure I.

In Fig. 8, 9 and 10 the probability of restoration are plotted. The lognormal cumulative distribution function is used to fit the data, to provide a continuous estimate

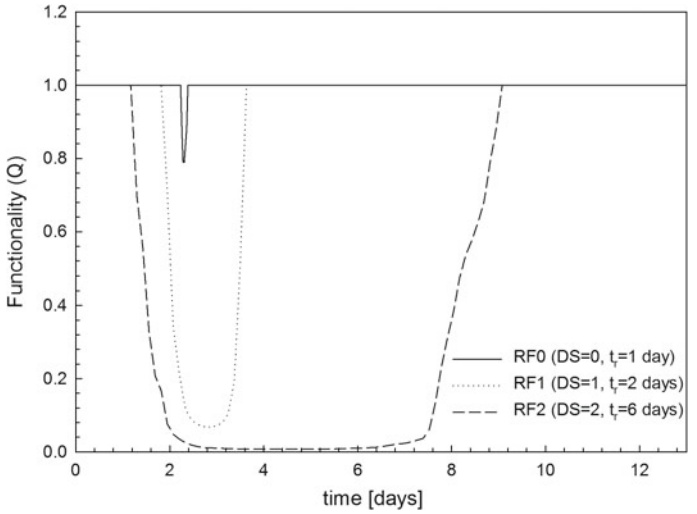

Fig. 7 Restoration functions assuming earthquake of magnitude VI

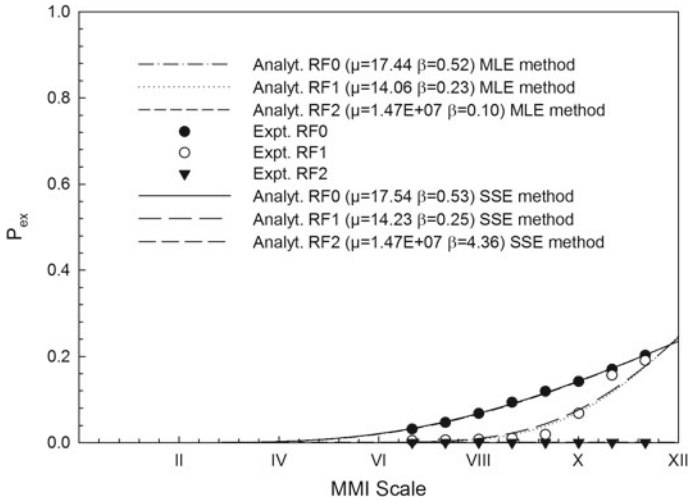

Fig. 8 RFF given DS = 0 (no damage) using MLE and SSE methods, ED with emergency plan applied

of the probability of restoration as a function of MMI. Two different methods to fit fragility curves are compared:

- MLE method: maximum likelihood method;
- SSE method: sum of squared errors;

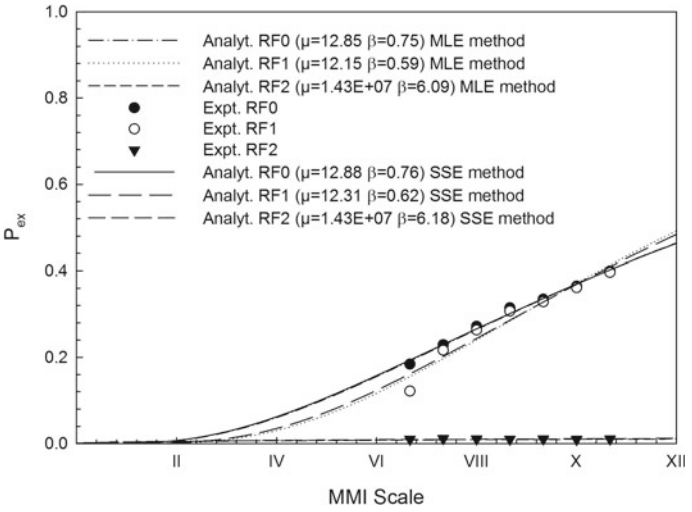

Fig. 9 RFF given a DS = 1 (moderate damage) using MLE and SSE methods, ED with emergency plan applied

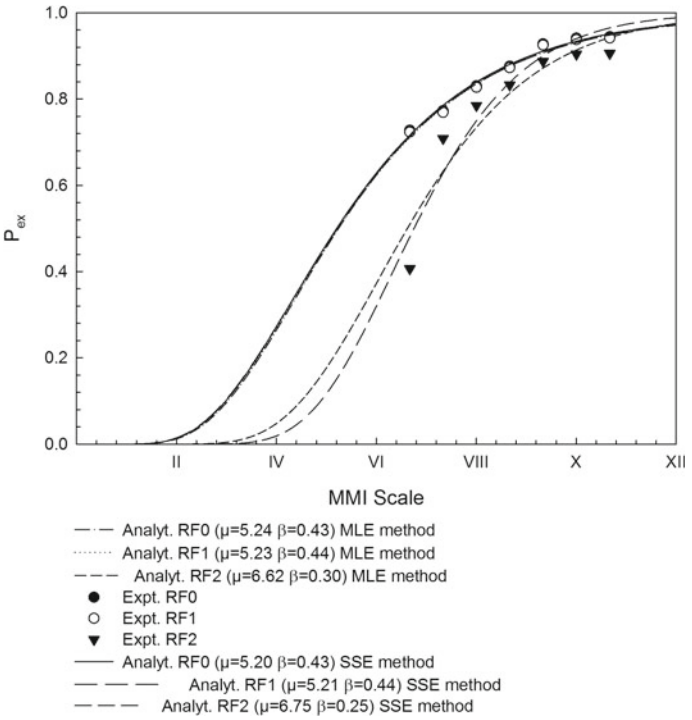

Fig. 10 RFF given a DS = 2 (severe damage) using MLE and SSE methods, ED with emergency plan applied

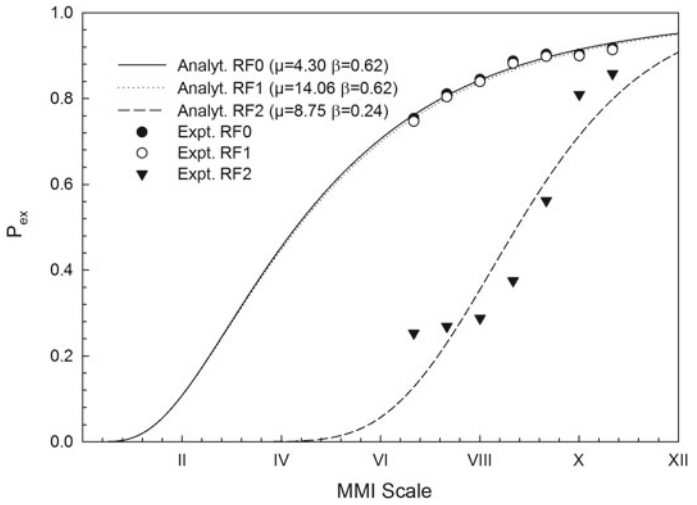

Fig. 11 RFF given a DS = 0 (no damage) using MLE method, ED without emergency plan

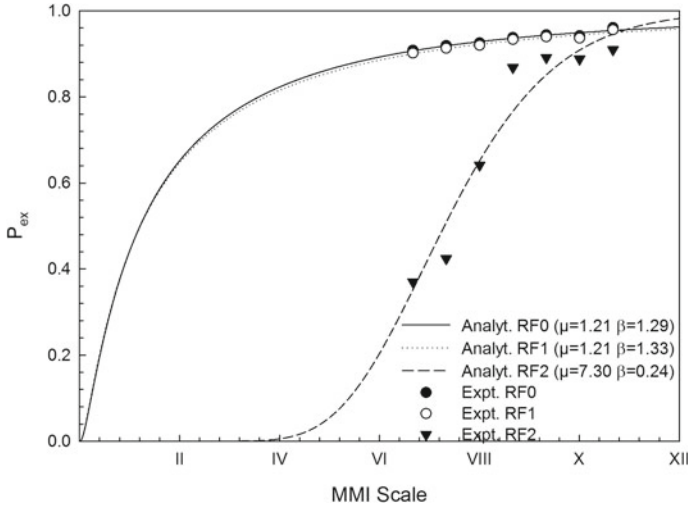

Fig. 12 RFF given a DS = 1 (moderate damage) using MLE method, ED without emergency plan

As shown in Fig. 8, 9 and 10, the two fitting methods have similar results. In Fig. 8 the probability of exceedance the restoration function RF0 increases with the increment of the MMI. For higher MMI, the probability of exceedance of RF1 reaches the probability of exceedance of RF0. In Fig. 8 the same behavior can be observed. In Fig. 8 the probabilities of exceedance of RF0 and RF1 overlap. The RRF related to RF2 increases considerably respect to the previous DSs.

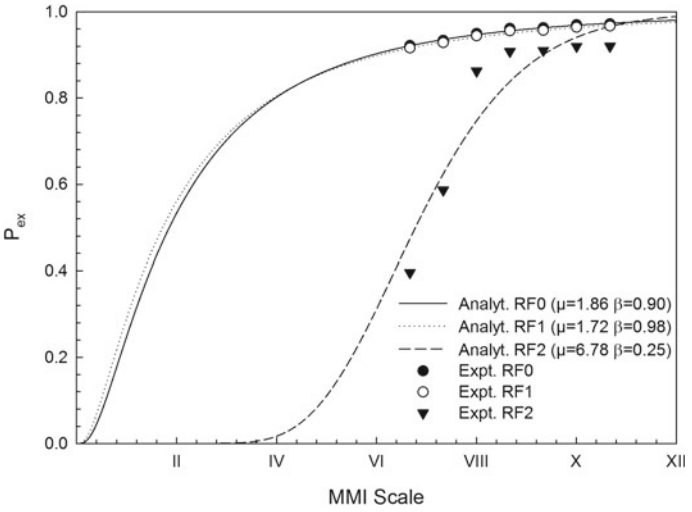

Fig. 13 RFF given a DS = 2 (severe damage) using MLE method, ED without emergency plan

Figures 11, 12 and 13 show the RFFs related to the ED without emergency plan. Results and comparison between RFFs of both cases are presented in the following paragraph.

4.3 RFF Comparison Between ED with and Without Emergency Plan Applied

As can be seen in Figs. 8, 9, 10, 11, 12 and 13, the probability of exceedance of a given restoration curve is higher without emergency plan than when the emergency plan is applied. Therefore, the emergency plan can be considered effective, since the waiting time when the emergency plan is applied is significantly lower than the waiting time without emergency plan. However, the only exception is in Figs. 10 and 13, when the damage state is severe (DS = 2), because in that case the RRFs of both case scenarios mainly overlap.

5 Conclusions

The chapter presents a methodology for building Restoration Fragility Functions (RFF), which describe the probability of exceedance a given restoration curve associated to a given damage state. The reasons for introducing RFFs is because the restoration process is one of the most uncertain variables in the resilience analysis

therefore, it is necessary to consider it in probabilistic terms. Restoration fragility functions can be a useful tool to define resilience of a hospital network. They can be used to estimate the restoration process of the emergency department as a function of the seismic intensity. The main difference between RFF and standard fragility functions is that the RFF is correlated to a given damage state (DS). In other words, RFF is conditional on *DS* and *I*, while standard fragility curves are only conditional on the intensity measure *I*. The method has been applied to the model of the Emergency Department of an existing hospital during a crisis when the emergency plan is applied and in regular condition. The data used for building the fragility curves are related only to the yellow code, while the restoration functions (RF) refer to three damage states (*DS*).

Acknowledgements The research leading to these results has received funding from the European Research Council under the Grant Agreement n. ERC IDEal reSCUE 637842 of the project IDEAL RESCUE–Integrated DEsign and control of Sustainable CommUnities during Emergencies.

References

ATC-13 (1985) Atc-13 earthquake damage evaluation data for california. Report, Applied Technology Council

Cimellaro GP, Reinhorn AM, Bruneau M (2010) Organizational metamodel for hospital emergency department. 14th European conference on earthquake engineering. Ohrid, Republic of Macedonia

Cimellaro G, Reinhorn AM, Bruneau M (2011) Performance-based metamodel for health care facilities. Earthquake Eng Struct Dynam 40(11):1197–1217. doi:10.1002/eqe.1084

Cimellaro GP, Renschler C, Reinhorn AM, Arendt L (2016) PEOPLES: a framework for evaluating resilience. J Struct Eng, ASCE, 142(10). Doi:10.1061/(ASCE)ST.1943-1541X.0001514

FHWA (1995) National bridge inventory (nbi) database. www.fhwa.dot.gov/bridge/nbi.htm

Morales G (2011) Using discrete event computer simulation to analyze the effects of proposed changes to personnel in a hospital medical laboratory. M.S. thesis, The University of Texas – Pan American, Ann Arbor

NTC-08 (2008) Nuove Norme Tecniche per le Costruzioni (NTC08) (in Italian). Consiglio Superiore dei Lavori Pubblici, Ministero delle Infrastrutture, Gazzetta Ufficiale della Repubblica Italiana, 4 febbraio 2008, n. 29

Porter K, Kennedy R, Bachman R (2007) Creating fragility functions for performance-based earthquake engineering. Earthquake Spectra 23(2):471–489

Šteins K (2010) Discrete-event simulation for hospital resource planning – possibilities and requirements. Ph.D. thesis, Linköping University, Norrkoping

Zhu B, Frangopol D (2014) Risk assessment of bridges with partially or fully closed lanes. In: FRE Chen, Frangopol, Ruan (eds) Bridge Maintenance, Safety, Management and Life Extension. Taylor and Francis Group, London, pp 290–294

A Decision Support Tool for Sustainable and Resilient Building Design

Umberto Alibrandi and Khalid M. Mosalam

Abstract In this chapter, an integrated approach for a holistic (involving notions of safety, resiliency and sustainability) building design is presented to select the optimal design alternative based on multiple conflicting criteria under uncertainty. A *probabilistic framework* of the Multi-Attribute Utility Theory (MAUT) is adopted, where MAUT is developed in conjunction with Performance-Based Engineering (PBE) approach, giving rise to a general framework, namely the PBE-MAUT. In PBE-MAUT different design alternatives may be ranked based on the expected utility. The discrepancies from the expected utility theory may be modelled through a risk-averse modelling of the utility functions based on the individual perceptions, or a more detailed description of the consequences valuable to the decision makers. Moreover, a risk-averse decision-maker towards extreme events can consider suitable quantiles or superquantiles. The distribution of the utility function is obtained from the First Order Reliability Method (FORM) which, through the design point, gives also the most critical realizations of the consequences for different degrees of risk aversion. The decision-making process is dynamic, in the sense that the optimal decision changes accordingly when new information is available. Such dynamic behavior is effectively represented using the Bayesian analysis, here modeled by combining PBE-MAUT with the Bayesian Network (BN). In this manner, the proposed framework represents a powerful Decision Support Tool (DST) for holistic building design. The BN, in conjunction with an array of sensors, can also be effectively used to determine the multi-criteria optimal decision considering the building lifecycle for a sustainable and resilient building design. The key features of the DST are demonstrated by an application to an office located on the Create Building, in Singapore.

U. Alibrandi (✉)
SinBerBEST – Singapore Berkeley Building Efficiency and Sustainability in the Tropics – Nanyang Technological University, 1 Create Way, 138062 Create Tower, Singapore
e-mail: umbertoalibrandi@gmail.com

K.M. Mosalam
Department of Civil and Environmental Engineering, University of California, 723 Davis Hall, Berkeley, CA 94720-1710, USA
e-mail: mosalam@berkeley.edu

P. Gardoni (ed.), *Risk and Reliability Analysis: Theory and Applications*,
Springer Series in Reliability Engineering, DOI 10.1007/978-3-319-52425-2_22

1 Introduction

Holistic building design is a complex process because there are several sources of uncertainty, the number of stakeholders is high, and the lifecycle of a building is long. It has been recently recognized that design for resilience is to design for sustainability to reduce the environmental impacts and societal consequences of post-hazard repairs (Wei et al. 2016). Conversely, design for sustainability is to design for resiliency to prevent that the unlikely extreme events may impact the fairness inter- and intra-generational of the urban communities. Consequently, a framework is needed for the decision-making of the most suitable holistic building design (Bocchini et al. 2014). It is crucial to develop an integrated methodical framework as a Decision Support Tool (DST) for the optimal decision amongst alternatives subjected to uncertainty and incomplete information.

In a decision-making process, the first step is the choice of suitable Decision Variables (DVs) expressed in terms of the direct interest of various stakeholders to define the global performance of the system. Together with the DVs, the decision-maker explores several design alternatives and/or actions through the building lifecycle. Subsequently, making use of the DST, the optimal alternative may be determined with general consensus from the stakeholders.

The optimal choice takes into account multiple conflicting criteria by making use of Multi Criteria Decision-Making (MCDM) methods, such as the Multi-Attribute Utility Theory (MAUT) (Keeney and Raiffa 1993). An important challenge of MAUT for sustainable design stems from the different sources of uncertainty, which in turn imply uncertainty in the decision. To this aim, the objective of this chaper is to develop a full probabilistic formulation of MAUT, whose focus is the definition of a DST for a sustainable and resilient building design. In this regard, the main task is modeling the joint probability distribution of the DVs in real-world engineering systems. We adopt the Performance-Based Engineering (PBE) methodology, which is extensively used as a probabilistic approach for evaluating system performance measures meaningful to various stakeholders, e.g. monetary losses, downtime, and casualties (Pinto et al. 2012). PBE approach links in a natural way the building design to the desired performances. For this reason, from PBE emerge principles of resilient design and sustainable design as well. Thus, PBE represents a simple and effective tool for holistic building design.

The joint adoption of MAUT with PBE gives rise to the extended framework PBE-MAUT. The joint dependencies among the DVs are modeled through multivariate probabilistic models, e.g. the Nataf model (Liu and Der Kiureghian 1986) or the probabilistic model of Distributions with Independent Components (DIC), recently developed in (Alibrandi and Mosalam 2017a).

The second step in a decision-making process is the determination of the optimal probability distribution of the DVs for different design options. In PBE-MAUT, the final outcome is the probability distribution of the multi-attribute utility function of each alternative, defined as a random variable U. The full distribution of the utility function gives the most comprehensive information about the utility of the design

alternative. To rank the alternatives, the most widely used metric in engineering is the expected utility (Von Neumann and Morgenstern 1944). However, according to Haimes (Haimes 2004), the expected utility does not distinguish between events of high probabilities and low consequences and events of low probabilities and high consequences. Actually, researchers have found that the choice of the decision makers have some discrepancies with respect to the expected utility of the decision variable. To this aim, some improvements of the expected utility theory have been proposed: in (Cha and Ellingwood 2013) risk-averse utility functions based on the individual risk perceptions are adopted, in (Gardoni et al. 2016) the Life-Cycle Cost Analysis is developed through the Life Profitability Method, so the optimal decisions are based on a more complete cost model. Several researchers have proposed the adoption of risk measures applied to the DVs (Artzner et al. 1999; Rockafellar 2007; Rockafellar and Royset 2015). In this chapter, risk measures, e.g. expected value, quantiles, and superquantiles, are applied to the utility variables. This formulation allows to include the risk perception of the decision maker when a complete description of the decision variable is not available.

In the literature, it is however recognized that risk-averse utility functions should not substitute a proper modeling of the consequences, such that a rational decision-making can be made risk-neutral with a good understanding of the consequences. This is here accomplished by determining the distributions of the utilities through the First-Order Reliability Method (FORM), which gives a good tradeoff between accuracy and efficiency; moreover the knowledge of the design point allows to define significant realizations of the DVs corresponding to chosen degrees of risk. The FORM results can effectively guide the decision-maker to make a rational choice of the optimal design.

The approach is formulated using the Bayesian Network (BN) (Nielsen and Jensen 2009) which is a probabilistic model that facilitate efficient graphical representation of the dependence among random variables. An important advantage of the BN is its capacity in predicting probabilistic updating when new information is acquired, e.g. through a network of sensors or from observations after inspection. Another advantage of the BN is transparent modeling, allowing its adoption by users with limited background in probabilistic or reliability analysis. BN can also model time-dependent uncertain parameters easily (Straub 2009; Straub and Der Kiureghian 2010a, b). In the proposed computational framework, the Dynamic Bayesian Networks (DBNs) are used to model stochastic processes of all the quantities of interest, including the time-dependent utility functions. This allows a transparent lifecycle modeling of the involved time-dependent uncertainties and a clear description of the dynamic evolution of the optimal decision.

The proposed PBE-MAUT represents a powerful tool for an extended multi-objective system of management and design. It involves analyses of climate, energy, sustainability, and lifecycle cost in addition to hazard, structural, damage, and loss included in the original PBE. After describing the main features of the framework, PBE-MAUT is applied to an office of CREATE Building in Singapore,

which underlines the main strengths of the proposed framework as an effective DST for holistic building design.

2 Multi Criteria Decision-Making Under Uncertainty

2.1 MAUT

Decision-making problems involving conflicting criteria fall in the broad class of the Multi-Criteria Decision Analysis (MCDA). In this context, a powerful tool is given by the MAUT (Keeney and Raiffa 1993) where each alternative receives a score through the definition of suitable overall utility functions defined in terms of the chosen criteria. The general procedure for MAUT consists of: (*i*) selection and definition of criteria and design alternatives, (*ii*) selection of weights, and (*iii*) ranking of the alternatives through the utility functions.

In a decision-making model, the *Requirements* are the most general standpoints, e.g. Functional, Social, Environmental, and Economical (San-José Lombera and Garrucho Aprea 2010; Pons and Aguado 2012), which may be unfolded in several *Criteria* or *Attributes* (e.g. lifecycle cost), where each criterion may involve several *Indicators* or *Decision Variables* (DVs), e.g. energy expenditure and economic losses. Typically, there are several criteria to consider and generally some of them may be inevitably conflicting. The first step in the decision-making problem is to identify from the criteria a set of n indicators (or DVs) $c_1, c_2, \ldots, c_n$ collected in the vector c. The next step is to define a finite set of m design alternatives, i.e. $a = \left\{ a^{(1)} \quad a^{(2)} \quad \ldots \quad a^{(m)} \right\}$. In general, each alternative i depends on all indicators, i.e. $a^{(i)} = a^{(i)}(c_1, c_2, \ldots, c_n)$.

The alternatives in MAUT are ranked through the utility function, a value-measuring function that converts the values of the DVs to scores representing the degree of preference of the decision-maker within the decision model. For each design alternative, a utility function $U^{(i)} = U\left(c_1^{(i)}, c_2^{(i)}, \ldots, c_n^{(i)}\right)$ is defined such that the most and least beneficial options have utilities $U_{max}^{(i)} = 1$ and $U_{min}^{(i)} = 0$, respectively. Other options have utility scores between these limits, which are higher when the performance of a given alternative is better. The utility function $U(c)$ is expressed as a combination of single attribute utility functions $U_j(c_j)$ of only one DV where the relative importance is defined by weights w_j, $0 \le w_j \le 1$, $\sum_{j=1}^{n} w_j = 1$, of the different attributes. Several methods for assigning the weights are discussed in (Wang et al. 2009). A simple model of aggregating the attributes is the *linear model*:

$$U(c_1, c_2, \ldots, c_n) = \sum_{j=1}^{n} w_j U_j(c_j) \tag{1}$$

The additive rule in Eq. (1) is generally valid if the effects of the interaction between indicators are negligible. A simple single-attribute utility function is *linear* as follows:

$$U_j(c_j) = \begin{cases} 1.0 & c_j \le c_{j,min} \\ (c_{j,max} - c_j)/(c_{j,max} - c_{j,min}) & c_{j,min} < c_j < c_{j,max} \\ 0.0 & c_j \ge c_{j,max} \end{cases} \quad (2)$$

where $c_{j,min}$ and $c_{j,max}$ are respectively the most and least beneficial values of the indicator. The shape of the utility functions may contain information about the risk attitude of the decision-maker (Keeney and Raiffa 1993; Winston 2003). The *linear* utility is representative of a risk-neutral attitude. A concave utility function is said to be risk-averse because it shows the tendency of the decision-maker to a conservative behavior. Risk-seeking attitudes are represented by convex utility functions, see Fig. 1.

Rational decision-makers may adopt a linear risk-neutral U considering consequence models, as discussed below. In deterministic MAUT, the optimal decision corresponds to the maximum utility, i.e. $U^{(opt)} = U\left(c_1^{(opt)}, c_2^{(opt)}, \ldots, c_n^{(opt)}\right) = max\left\{U^{(1)}, U^{(2)}, \ldots, U^{(m)}\right\}$.

2.2 Probabilistic MAUT

From Eq. (1), it is possible to score the design alternatives and to determine their ranking. However, in real-world applications, the indicators c_j and the elicitation of

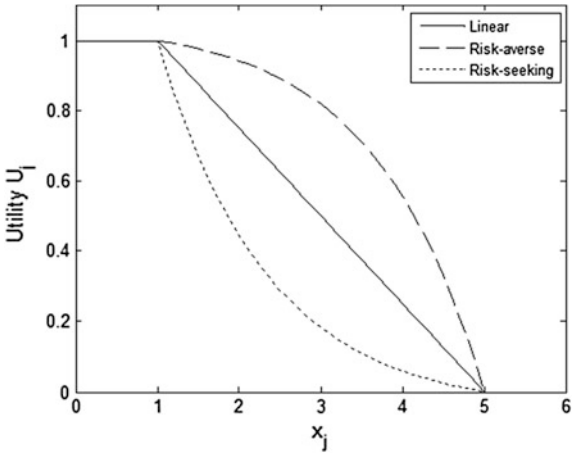

Fig. 1 Comparison between linear, risk-averse, and risk-seeking single-attribute utility functions

the utility functions contain various sources of uncertainty. In the following, it is assumed that only the indicators c_j are uncertain and modeled through random variables of known distributions. Thus, the utility function of the *i*th alternative $U^{(i)} = U\left(c^{(i)}\right)$ is a random variable since $c^{(i)}$ is a vector of random variables and depends on the corresponding joint Probability Density Function (PDF), $f_c^{(i)} = f_c\left(c^{(i)}\right)$, of the indicators $c^{(i)}$, which can be determined from the PBE approach, as described below. Since $U^{(i)}$ is a random variable, it is completely defined by its Cumulative Distribution Function (CDF), which can be evaluated through the structural reliability theory by introducing a limit state function $G\left(\xi, c^{(i)}\right) = U\left(c^{(i)}\right) - \xi$, where $F_U^{(i)}(\xi) = Prob\left[G\left(\xi, c^{(i)}\right) \le 0\right]$, i.e.

$$F_U^{(i)}(\xi) = Prob\left[U\left(c^{(i)}\right) \le \xi\right] = \int_{\{G(\xi, c^{(i)}) \le 0\}} f_c^{(i)}(c)dc \tag{3}$$

The general framework of probabilistic MAUT is shown in Fig. 2.

The knowledge of the CDF fully defines the utility of the *i*th alternative, since its Probability Of Exceeding (POE) $P_U^{(i)}(\xi) = Prob\left[U\left(c^{(i)}\right) \ge \xi\right]$, is equal to the complementary CDF, i.e. $P_U^{(i)}(\xi) = 1 - F_U^{(i)}(\xi)$, while the PDF may be determined as

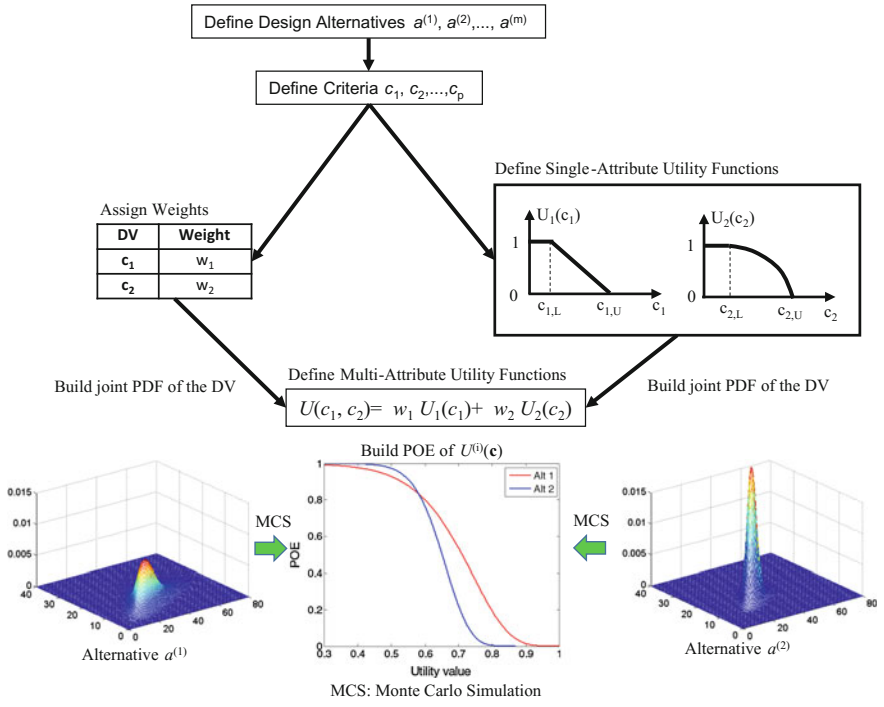

Fig. 2 Schematic of the probabilistic MAUT

$f_U^{(i)}(\xi) = \partial F_U^{(i)} / \partial \xi$. To rank the alternatives, a metric is necessary, where several measures can be determined from the POE (Rockafellar and Royset 2015; Haukaas 2013). A well-founded measure to rank the alternatives is the expected utility (Von Neumann and Morgenstern 1944), coinciding with the expected value of the utility variables $U^{(i)}$:

$$\overline{U}^{(i)} = E\left[U\left(c^{(i)}\right)\right] = \int \xi f_U^{(i)}(\xi) d\xi = \int U^{(i)}(c) f_c^{(i)}(c) dc \tag{4}$$

2.3 Expected Utility and Risk Measures for a Single Criterion

The expected utility, Eq. (4), is a commonly used metric in decision theory. However, some violations of the axiomatic basis of the expected utility model are well-documented (Ditlevsen 2003; Maes and Faber 2007). The expected utility presumes that the decision-maker behaves rationally. However, the concept of human rationality may not be valid in high-uncertainty situations. The prospect theory (Kahneman and Tversky 1979; Tversky and Kahneman 1992) is an alternative to the expected utility theory, and it has been applied to study the risk averseness in engineering applications (Cha and Ellingwood 2012, 2013). Different from expected utility theory, in the prospect theory, the risk perception is incorporated into the formulation of the utility functions. However, in literature it is recognized that a proper modeling of the consequences through an accurate probabilistic model should not be substituted by a risk-averse decision model. This is the approach followed in (Gardoni et al. 2016) where the expected lifecycle cost is described through a more complete financial information.

Assume that two different alternatives $c^{(1)}$ and $c^{(2)}$ for a given criterion c are given by the PDFs $f_C^{(1)}(c)$ and $f_C^{(2)}(c)$, respectively. The distribution $f_C^{(1)}(c)$ is lognormal with parameters $\mu = -ln(2)/2$ and $\sigma^2 = ln(2)$, i.e. with mean $E\left[C^{(1)}\right] = 1$ and variance $Var\left[C^{(1)}\right] = 1$. The distribution $f_C^{(2)}(c)$ is a Kernel Density from a superposition of three lognormal distributions (Alibrandi and Ricciardi 2008), $f_C^{(2)}(c) = \sum_{i=1}^{3} p_i f_i^{LN}(c; c_i, h)$ with centers $c_1 = 0.5$, $c_2 = 0.8$ and $c_3 = 4$, bandwidth $h = 1/5$, and weights $p_1 = 0.9$, $p_2 = 0$ and $p_3 = 0.1$. Thus, the mean and variance of this alternative are $E\left[C^{(2)}\right] = 4/5$ and $Var\left[C^{(2)}\right] = 1$, respectively. The two distributions are presented in Fig. 3.

Assume the criterion c is the total cost (initial construction + lifecycle) of a building. The rationale behind the expected value of the utility is maximizing the resources over the lifecycle time amongst many decisions. A design with the smallest average cost would be best on average. Since $E\left[C^{(2)}\right] < E\left[C^{(1)}\right]$, the second design alternative is preferred. However, from Fig. 3a, it is seen that the first alternative is

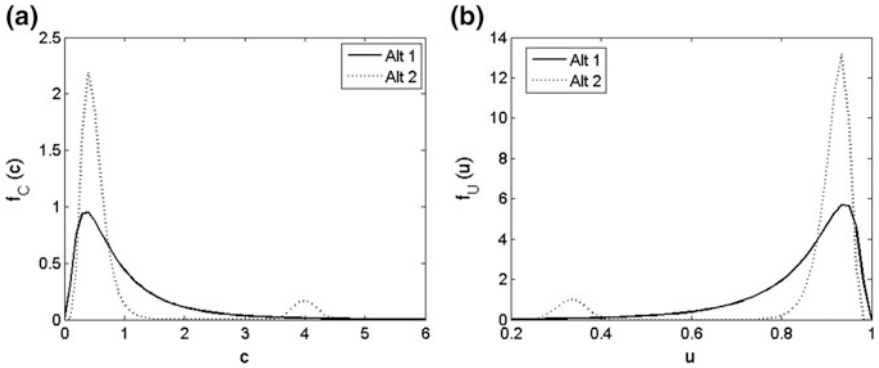

Fig. 3 Distributions corresponding to two alternatives for a chosen criterion. **a** PDF of the alternatives, **b** PDF of the utilities

safer with respect to *high-consequence* events. Suppose the decision-maker cannot afford some socio-economic costs above the threshold $c \geq 3.5$, then the decision-maker would be inclined to choose the first design alternative. Moreover, in the context of sustainability, the criterion could not be the economic cost only, but also environmental responsibility, then the decision-maker may want to avoid the second alternative where an unlikely event with high consequences may occur.

If an accurate modeling of the consequences is developed and described by the PDFs of the cost of the two alternatives, a linear utility function, Eq. (2), may be adopted, i.e. $U(c) = (c_{max} - c)/c_{max}$. It is noted that the utility function is described as a random variable $U = U(c)$ subjected to the preference of the decision-maker and the randomness of the uncertain criterion. These two issues are well-defined and kept distinct by the functional relationship given by U and distribution $f_C(c)$. Accordingly, the distribution of the utility incorporates the randomness of the criterion and the risk aversion of the decision-maker, i.e. $f_U(u) = f_C(c)/|J(c)|$ where $J(c) = dU/dc$ is the Jacobian of the transformation. The distribution of the utilities for this example are shown in Fig. 3b. Assuming $c_{max} = 6$, the expected utility for the two alternatives is $\overline{U}^{(1)} = 0.839$ and $\overline{U}^{(2)} = 0.867$. Thus, a decision-maker following the expected utility theory would state that the best alternative is the second. It is noted that, in presence of a linear utility function, the minimization of the expected cost is equivalent to the maximization of the expected utility.

Suppose that the decision-maker implements his/her risk-aversion through a nonlinear utility function, e.g. $U(c) = 1 - (c/c_{max})^{\gamma}$ where $U(0) = 1$, $U(c_{max}) = 0$, while γ gives the degree of risk-aversion. Figure 3a represents the nonlinear utility functions for different values of γ and Fig. 4b shows the corresponding expected utilities of the two alternatives.

The application of the expected utility theory determines the second alternative as the optimal one. Moreover, an increase in the degree of risk-averseness increases the preference of the second alternative. The example shows that in some cases the adoption of risk-averse functions may give misleading results. Conversely, as

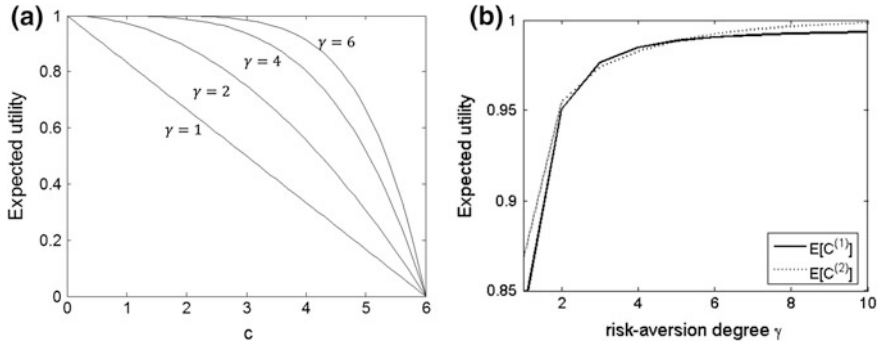

Fig. 4 Decision-making of the two alternatives in Fig. 3a considering risk-aversion. **a** Nonlinear utility function for different degrees of risk-averseness, **b** corresponding expected utilities

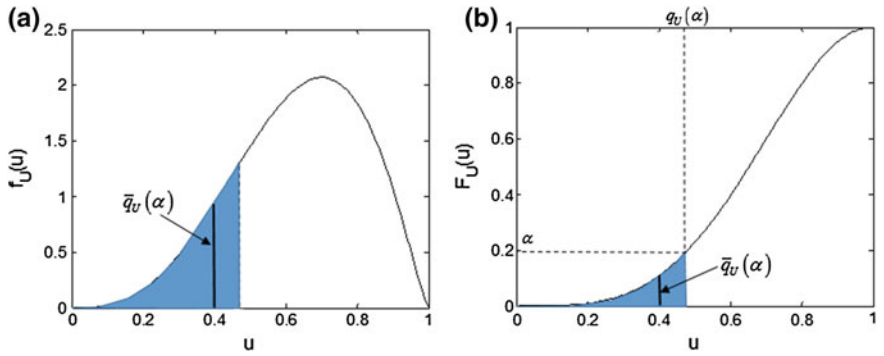

Fig. 5 Schematic of the superquantile

suggested in (Gardoni et al. 2016), a complete model of the consequences with risk-neutral attitude should be applied, when available. In such cases, to take into account the risk-aversion towards the extreme events, risk measures may be adopted to the utility. Largely adopted risk measures are α-quantile $\xi \equiv q_U(\alpha) = F_U^{-1}(\alpha)$, refer to Eq. (3), or α-superquantile, an expected conditional value of the random variable u, i.e.

$$\overline{q}_U(\alpha) = E[U|0 \le u \le \xi] = \frac{\int_0^{\xi} \xi' f_U(\xi') d\xi'}{\int_0^{\xi} f_U(\xi') d\xi'} = \frac{1}{\alpha} \int_0^{\alpha} q_U(\alpha') d\alpha' \tag{5}$$

The superquantile is an average of quantiles for probability levels $0 < \alpha' < \alpha$, Fig. 5.

Note that for $\alpha = 1$, $\overline{q}_U(1) = \overline{U}$, while the left tail of $f_U(u)$ (corresponding to extreme events with low utility) is defined for low values of α. Thus, the superquantile may describe all properties of the whole distribution. Moreover, it has useful mathematical properties, like coherency and regularity. In this example,

the expected utility is obtained from Eq. (5) for $\alpha = 1$, i.e. $\overline{q}_U^{(1)}(1) \equiv \overline{U}^{(1)} = 0.839$ and $\overline{q}_U^{(2)}(1) \equiv \overline{U}^{(2)} = 0.867$. On the other hand, the risk towards extreme events may be considered by choosing $\alpha = 0.10$ in Eq. (5) to give $\overline{q}_U^{(1)}(0.10) = 0.514 > \overline{q}_U^{(2)}(0.10) = 0.409$, and the first alternative is preferred.

2.4 Decision Analysis Using Target

This link between utilities and probabilities is well recognized in literature. The expected utility model itself can be entirely reformulated in the context of probability (Castagnoli and Li Calzi 1996; Bordley and LiCalzi 2000). The expected utility is a linear functional over the probability distribution associated with an alternative/decision where $U(c)$ is bounded and monotonic and possesses all the properties of a CDF if $U(c)$ is increasing or POE if $U(c)$ is decreasing. Consequently, the utility function can be interpreted as a probability distribution of an uncertain target T stochastically independent from the alternatives. In engineering problems, most criteria have decreasing utility functions, so $U(c)$ represents the POE of the target:

$$U(c) = Prob[T > c] = 1 - F_T(c) \tag{6}$$

where $F_T(c) = Prob[T \leq c]$. It is noted that the expected utility can be defined as a classical reliability problem:

$$\begin{aligned} \overline{U}^{(i)} &= \int U(c) f_C^{(i)}(c) dc = \int Prob\left[T \geq c'\right] f_C^{(i)}\left(c'\right) dc' = Prob\left[T \geq c^{(i)}\right] \\ &= \int_{\{c^{(i)} - T \leq 0\}} f_T(\tau) f_C^{(i)}(c) d\tau dc \end{aligned} \tag{7}$$

where $f_T(\tau)$ is the PDF of the uncertain target expressing the modeling of the uncertainty of the decision-maker about his target. The concept of utility function can then be replaced by the notion of target, which is easier to understand. Moreover, the target-based model allows to easily describe some known risk-averse nonlinear utility functions. For example, Fig. 6 shows the linear utility function described as a target uniformly distributed over the consequences between $c_{min} = 0$ and $c_{max} = 6$. In (Cha and Ellingwood 2013) the risk perception of the losses is modelled through some risk-averse utility functions. It is easy to check that they correspond to a target with exponential distributions presented in Fig. 7. As expected, these PDFs give greater weight to the highest consequences as a function of the parameter $\gamma > 0$ representing the degree of risk aversion.

In Eq. (7), the model uncertainties related to the utility function(s) can be addressed as parameter uncertainties of the distributions modeling the target(s).

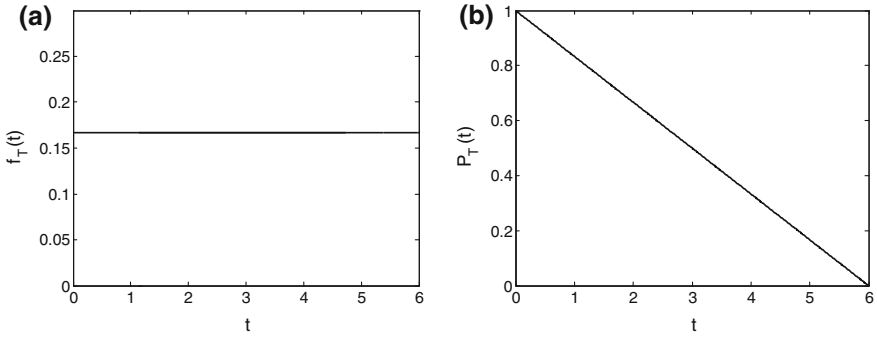

Fig. 6 Linear utility expressed through the target. **a** PDF, **b** POE

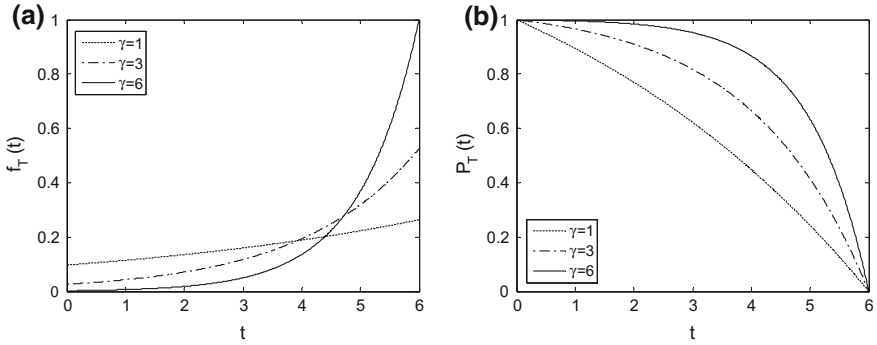

Fig. 7 Risk-averse utility function expressed through the target. **a** PDF, **b** POE

Assume that the decision-maker has a target T between two bounds, c_{min} and c_{max}. According to the principle of Maximum Entropy, the least biased distribution with the given information is the uniform. This shows that in absence of further information, a rational decision-maker is risk-neutral. Moreover, the application of the MaxEnt principle may be adopted to determine utility values when only partial information is available about the decision maker's preferences. Consequently, updating subjective utilities through Bayesian analysis can be advantageous and straightforward.

3 Evaluation of the Distribution of the Utility Functions

The multi-attribute utility function $U^{(i)} = U\left(c^{(i)}\right)$ is a function of random variables, which also makes it a random variable itself. Our focus herein is on a *multi-criteria*

decision-making, such that $U^{(i)}$ takes into account several joint criteria, typically conflicting, and whose consequences (direct and indirect) can go beyond economic issues. However, in Eq. (1) the contributions of several criteria are combined into a single random variable, while for a rational decision it would be useful to know the values of the most critical realization of the decision variables, for a chosen degree of risk-aversion. This can be obtained by applying the FORM to $U^{(i)}$, as described below. The evaluation of the distribution of the utilities, Eq. (3), can be performed using structural reliability theory. The most robust procedure for this purpose is the Monte Carlo Simulation (MCS) (Ditlevsen and Madsen 1996; Melchers 1999), which is however computationally demanding.

A good tradeoff between accuracy and efficiency is provided by the FORM. After probabilistic transformation towards the standard normal space u, Eq. (3) becomes:

$$F_U^{(i)}(\xi) = Prob\left[U^{(i)}(u) \le \xi\right] = \int\limits_{\{g_i(\xi,u)\le 0\}} \varphi_n(u)\, du \tag{8}$$

where $\varphi_n(u)$ is n variate PDF of the normal standard distribution, while $g_i(\xi,u) = U^{(i)}(u) - \xi$ is the limit state function in the normal standard space corresponding to the ith alternative. The design point $u_i^*(\xi)$ is the most likely realization of the random variables giving rise to the event $[g_i(\xi,u)\le 0] \equiv \left[U^{(i)}(u)\le\xi\right]$, i.e. the point closest to the origin of the standard normal space of the limit state surface $g_i(\xi,u)=0$ and obtained as the solution of an optimization problem:

$$u_i^*(\xi) = argmin\{\|u\| : g_i(\xi,u)=0\} \tag{9}$$

The reliability index is defined as the distance to the design point from the origin of the standard normal space $\beta_i(\xi) = \left\|u_i^*(\xi)\right\|$. Thus, FORM gives an approximation of the distribution $F_U^{(i)}(\xi) = \Phi[-\beta_i(\xi)]$, where Φ is CDF of the normal standard distribution, to that defined by Eq. (3) and it is accurate enough for most cases of practical interest. If this is not the case, the recently proposed Secant Hyperplane Method (Alibrandi et al. 2016; Alibrandi and Mosalam 2017b) can be used.

Typically, a decision-maker desires to choose the best alternative having some information about the consequences of the choices. This may be obtained easily by noting that

$$\beta_i(\xi) = \Phi^{-1}\left[1 - F_U^{(i)}(\xi)\right] = \Phi^{-1}(1-\alpha) \tag{10}$$

Through an algorithm of inverse reliability (Der Kiureghian et al. 1994) for a chosen $\beta=\beta_0$, corresponding to probability $\alpha_0 = \Phi(-\beta_0)$ of the distribution of the utility function, the threshold $\xi_0^{(i)}$ of $U^{(i)}$ is determined such that $\beta_i\left(\xi_0^{(i)}\right) = \beta_0$. Once $\xi_0^{(i)}$ is evaluated, the corresponding limit state function $g_i\left(\xi_0^{(i)}, u\right) = U^{(i)}(u) - \xi_0^{(i)}$ is

defined, and the design point $u_{0i}^{*} = u_i^{*}\left(\xi_0^{(i)}\right)$ together with its mapping in the original space $c_{0i}^{*} = c_i^{*}\left(\xi_0^{(i)}\right)$ are found. Thus, each alternative is defined by a single deterministic value c_{0i}^{*} for chosen quantile. The alternatives can also be ranked through a deterministic MAUT by applying Eq. (1) to the design points, i.e. $U^{(i)} = U\left(c_{0i}^{*}\right)$.

The application of the classical MAUT to the design points corresponding to different quantiles allows to choose not only the best design alternative, but also gives information for the most critical realization of the indicators for different degrees of risk. In this way, the decision-maker can select, consciously, the best alternative, taking into account all consequences of all scenarios, including the worst ones. A detailed numerical application is presented in (Mosalam et al. 2016)

4 Joint Distribution of the Uncertain Parameters

A key point in the determination of the distributions of the utility functions is represented by the evaluation from the joint PDF $f_c^{(i)}(c)$ of the indicators, Eq. (3). It is underlined that especially the tails of the utility functions are sensitive to the distributions of the input parameters $c_1, c_2, \ldots, c_n$, which therefore have to be modeled as accurately as possible, given the available information. In most cases, the criteria derive from p basic random variables $x_1, x_2, \ldots, x_p$, i.e. $c_j = c_j\left(x_1, x_2, \ldots, x_p\right)$. In some cases, the decision variables may coincide with the basic variables (e.g. $c_1 \equiv x_1$, $c_2 \equiv x_2$, …), but, in general, it is expected that they differ. This implies that the utility functions are a function of the basic variables $U^{(i)} = U\left[c\left(x^{(i)}\right)\right] = U\left(x^{(i)}\right)$. The relationships from the basic variables $x^{(i)}$ to the DVs $c^{(i)}$ may be determined through the classical PBE approach, or the unified reliability framework, below described.

4.1 PBE Approach

The Pacific Earthquake Engineering Research (PEER) Center developed a robust PBE methodology focused on earthquake engineering (PBEE), which is based on explicit determination of system performance measures meaningful to various stakeholders such as monetary losses, downtime, and casualties based on probabilistic assessment (Günay and Mosalam 2013). The PEER PBEE methodology consists of four successive analyses: hazard, structural, damage, and loss. The methodology focuses on the probabilistic calculation of meaningful system performance measures considering the involved uncertainties in an integrated manner. PBE can be one of the solutions to estimate the performance corresponding to each DV, not only structural losses, but also other criteria such as construction and

maintenance costs, CO_2 emission during the construction and operation phases, and energy expenditure.

The distributions of the DVs can be estimated by adopting a novel *extension* of the PBE methodology considering the e*nergy efficiency* and *sustainability* in addition to structural safety (Gunay and Mosalam 2012). Accordingly, structural safety, environmental responsibility, and human comfort constitute the objectives of an extended multi-objective framework where analyses involving climate, energy, sustainability, and lifecycle cost are included in addition to the hazard, structural, damage, and loss analyses of the original PBEE method.

The adoption of the PBE methodology (Cornell and Krawinkler 2000) has several advantages: (*i*) it is based on the total probability theorem, which requires elementary knowledge of probabilistic concepts and thus easily adopted and interpreted in practice, (*ii*) it is already applied for the evaluation of the safety of the structures subjected to seismic hazard by practicing engineers, the extension to different hazards and DVs is straightforward, and (*iii*) the different stages of the analysis can be performed by separate groups of multi-disciplinary researchers.

4.2 Unified Reliability Approach

The PBE approach can also be defined through a unified reliability approach (Haukaas 2008) where the input quantities are directly modeled through random variables and stochastic processes using p basic random variables $x_1, x_2, \ldots, x_p$ collected in vector x. The decision variables $c_1, c_2, \ldots, c_n$ expressing resiliency and sustainability decision criteria in such case are expressed directly in terms of x. In the most general case the input quantities may be defined in terms of stochastic processes or random fields

$$X(t,r,x) = s_0(t,r)x_0 + \sum_k s_k^c(t,r)x_k^c + s_k^s(t,r)x_k^s = s(t,r)\cdot x \tag{11}$$

where x is a vector of basic random variables, $r = \{\, x \quad y \quad z \,\}^T$ is a vector defining the spatial location, while $s(t,r)$ is a vector of suitable deterministic shape functions. In the case of Gaussian processes, typically x represents a vector of normal standard random variables. Through calls to a solver used as a black-box, the DVs may be defined as stochastic processes

$$DV_j(t,r,x) = a_{j,0}(t,r)x_0 + \sum_k a_{j,k}^c(t,r)x_k^c + a_{j,k}^s(t,r)x_k^s = a_j(t,r)\cdot x \tag{12}$$

If PBE-MAUT is developed through the unified reliability approach, all probabilistic models for each alternative are unified into one reliability analysis (Haukaas 2008; Alibrandi and Mosalam 2015a). It allows explicit account of *all*

uncertainties, e.g. those in material properties or epistemic ones, and to model all the quantities of interest as stochastic processes or random fields.

4.3 Probability Distributions

If only a small size of data is available, the marginal distributions can be modeled using known parametric distribution, e.g. Normal, Lognormal, or Weibull, with parameters determined through the "method of the moments" or "method of maximum likelihood". A statistical test to accept or reject the probability model is usually adopted. However, for an assigned physical quantity, in presence of a small size of data, it is not possible to statistically justify a specific single distribution. An effective tool for this purpose is represented by the "method of the maximum entropy" (Jaynes 1957; Kapur and Kesavan 1992) giving the least biased distribution with respect to the available information. In this regard, a kernel density estimation based on the maximum entropy principle, which adopts generalized moments including power and fractional ones, is recently proposed in (Alibrandi and Mosalam 2017c). The method, called GKDMEM, may be considered an effective approach for evaluating the optimal distributions of the criteria $c_1, c_2, \ldots, c_n$, and can also elicit the utility functions in terms of preferences of the decision-maker.

In some cases, the scarcity of data may prevent the definition of a reliable probability distribution, in terms of PDF and/or its parameters. In such cases, suitable distributions based on engineering judgment and/or expert opinion may be adopted. If new information becomes available, it will be used to update the probability distributions of the uncertainties through Bayes' updating rule. Knowing the marginal distributions of the DVs and their correlations, the modeling of the joint dependencies can be effectively developed by the Nataf model (Liu and Der Kiureghian 1986). It is noted that if in the decision-making model the focus is about the modeling of joint extreme events, the approximation given by Nataf could be inadequate. In such cases, one can adopt DIC, a multivariate probabilistic model developed in (Alibrandi and Mosalam 2016)

5 Bayesian Networks for Sustainable and Resilient Building Design

The BNs are graphical probabilistic models that facilitate efficient representation of the dependence among random variables. They are based on the Bayes' rule and the Bayesian inference, such that the network is updated in real-time when new information (e.g. from a network of sensors) is acquired. BNs can also be effectively used in "what-if" analyses, i.e. to analyze the behavior of the system if a

given event should occur. The BNs have a transparent modeling, and they can be adopted by users with limited background in probabilistic or reliability analysis.

Following (Straub and Der Kiureghian 2010a, b) the BNs are combined with structural reliability methods, where the conditional probabilities are given by the methods of the structural reliability theory. The Influence Diagram is a BN with the addition of decision and utility nodes, where the optimal alternative is based on the principle of maximum expected utility (Von Neumann and Morgenstern 1944). This approach has been recently followed in (Bensi et al. 2009) for post-earthquake risk-assessment. Here, the BNs are applied to the evaluation of sustainable and resilient building design. Moreover, following the general framework of PBE-MAUT, the distribution of the utility functions is directly modeled as a node of the BN, while the metric (e.g. expected utility, quantiles or superquantiles) is determined as a derived quantity. In the proposed framework, starting from the design criteria and alternatives chosen in PBE-MAUT, the BN model is constructed, where all the conditional probabilities are determined through the computational tools of structural reliability. The distributions of the utility functions are updated in real-time when new information over the uncertain parameters is available, or when a specific alternative is chosen.

Figure 8 shows that the classical PBEE approach (where the input is the seismic hazard) can be incorporated inside PBE-MAUT and analyzed by the BN modeling. Here, four *DV*s have been chosen: $c_1 \equiv$ *Loss* L, $c_2 \equiv$ *Fatalities* (*Fat*), $c_3 \equiv$ *Downtime* (*Dt*), and $c_4 \equiv$ *Injuries* (*In*) with the utility function expressed as $U = U(c_1, c_2, c_3, c_4)$. The links from $PR \equiv$ *Price Rate*, $DM \equiv$ *Damage Measure*, and $C \equiv$ *Collapse* to $L \equiv$ *Loss* indicate that the distribution of L is conditioned on *PR, DM*, and *C*. In the BN terminology, L is a child of *PR*, *DM*, and *C*, which are the parents of L. BN has the assumption of conditional independence, i.e. any node depends only on its parent node and it is conditionally independent of any unlinked nodes. Figure 8 also shows the node U_m giving a superquantile of the utility.

For sustainability, the corresponding BN is shown in Fig. 9, where *CV* is the *Climate Variable*, *EM* is the *Energy Measure*, while two *DV*s have been chosen: $c_1 \equiv CO_2$ and $c_2 \equiv EE$, while $U = U(c_1, c_2)$. Figure 10 shows the integrated model taking into account seismic risk and sustainability. It is noted that the DM affects both seismic loss L as well as CO_2 because of post-seismic repair.

The procedure may be extended to multiple hazards and sustainability criteria. An example is shown in Fig. 11 where the structural safety is detected through the criteria $c_1 \equiv$ *Loss* L and $c_2 \equiv$ *Injuries/Fatalities*. It is assumed that the system may be subjected to three different potential natural hazards: Earthquake, Flood, and Haze. Two different failure modes are assumed and it is conjectured that the second failure mode can trigger the fire hazard. Further decision criteria may be: human comfort in the facility, energy efficiency (expressed through the Energy Expenditure *EE*) and the environmental responsibility (expressed through CO_2 emission).

The BN can also manage lifecycle analyses easily. For example, the time-dependent cost due to damage and its corresponding utility function for different alternatives and scenarios can be determined (Alibrandi and Mosalam 2015b). Accordingly, it is possible to determine the optimal decision after t years.

Fig. 8 BN for seismic risk

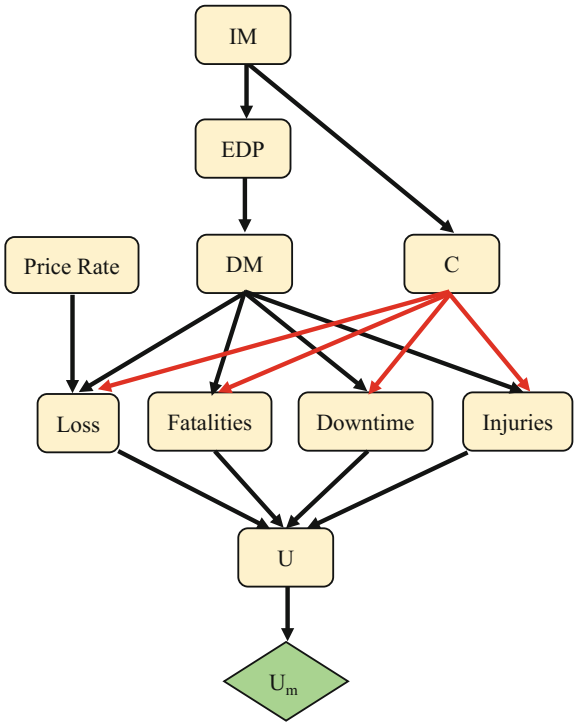

Fig. 9 BN for sustainability

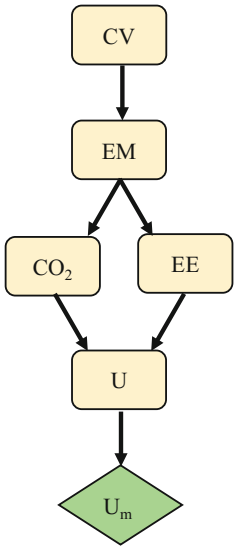

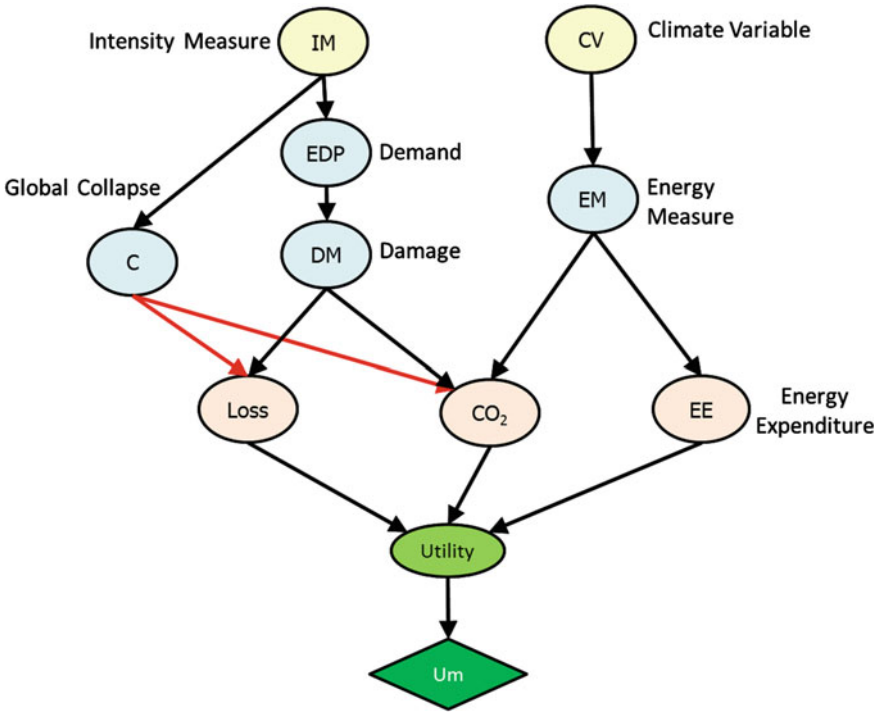

Fig. 10 BN for integrated framework including seismic risk and sustainability

This implies that holistic design, including resiliency and sustainability, may be well managed by the proposed framework. The resiliency may be defined in terms of the functionality $Q(t)$ (Bocchini et al. 2014; Bruneau et al. 2003)

$$R_L = \int_{t_0}^{t_r} [100 - Q(t)]dt \tag{13}$$

where R_L is loss of resilience experience by the system, t_0 is the instant when the extreme event occurs, t_0 is the time instant when the fully functionality is restored, see also Fig. 12.

In the BN model of Fig. 13, the lifecycle holistic analysis of a system subjected to a hazard can be analyzed. The *DV*s are the *Construction Cost* $c_1 \equiv CC$, the *Economic Losses* $c_2(t) \equiv L(t)$, the environmental impact represented by CO_2 emission, i.e $c_3(t) \equiv CO_2(t)$, and the functionality of the system $c_4(t) \equiv Q(t)$. This model can analyze several stochastic processes, including the Damage Measure $DM(t)$, and the utility function $U(t)$. The model can incorporate the degradation of the material. Moreover, it is assumed that, at each year, the decision-maker can choose to develop a plan of maintenance and repair. This will affect not only the economic losses $L(t)$, but also the sustainability $CO_2(t)$ because of the carbon

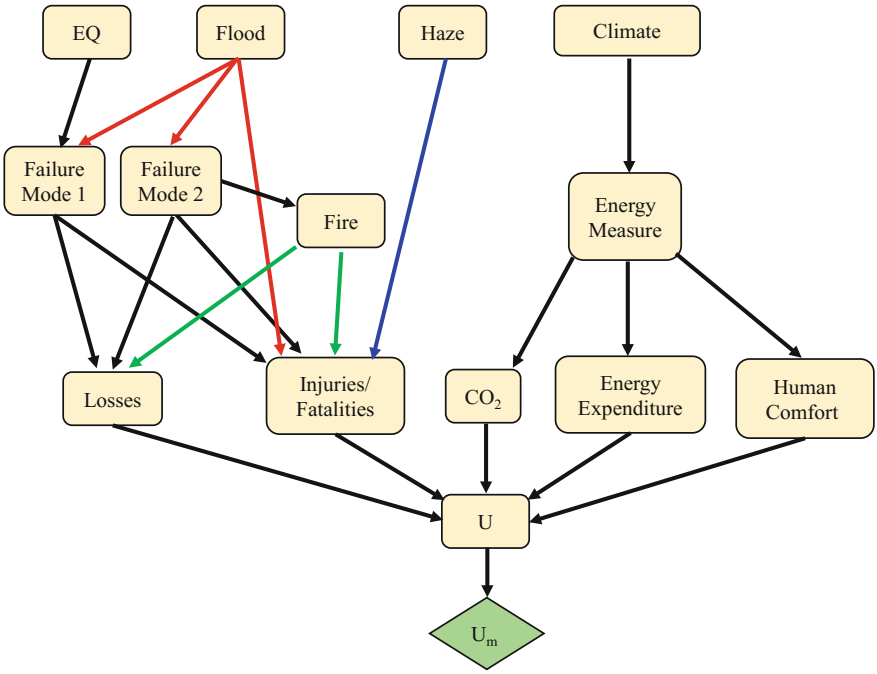

Fig. 11 BN for integrated framework including sustainability and multiple hazards

Fig. 12 Loss of resiliency

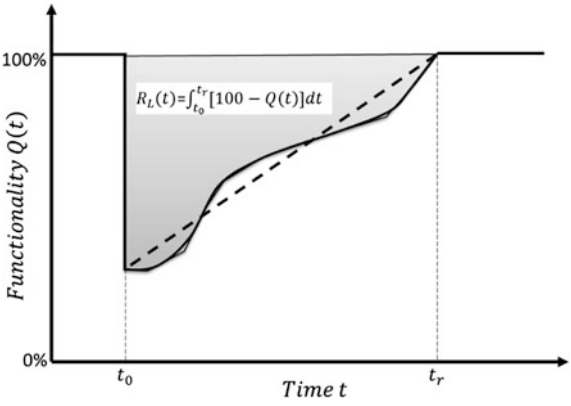

emission due to post-hazard repair, and the resilience through the functionality $Q(t)$. The example shows the strict relationships between sustainability and resilience. The lifecycle actions of the decision-maker will affect the results of the utility function after t years, and accordingly the optimal decision. The conditional probabilities of the BN model may be defined through the classical PBE methodology or through the tools of stochastic dynamic analysis. For the evaluation of the

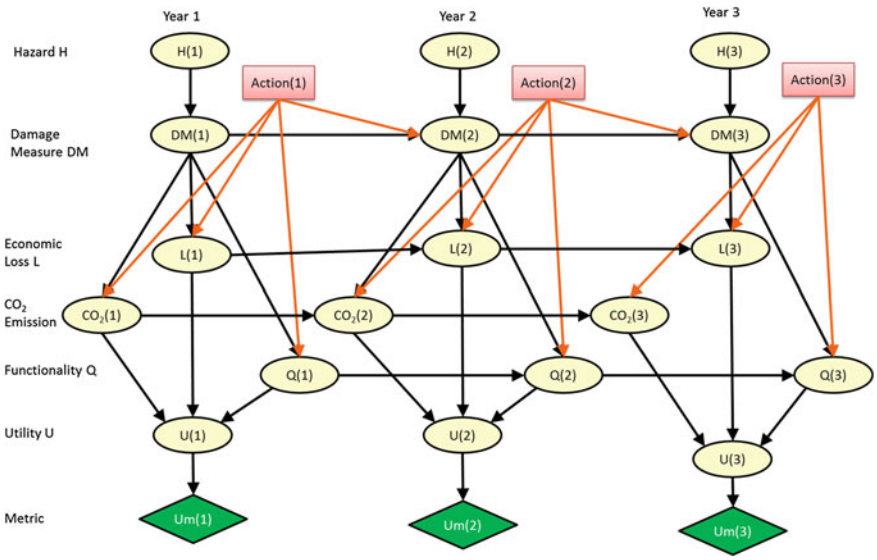

Fig. 13 BN for lifecycle holistic analysis

distributions, including their tails, statistical methods based on the Maximum Entropy principle (Jaynes 1957; Kapur and Kesavan 1992; Alibrandi and Mosalam 2016) or stochastic equivalent linearization methods (Alibrandi and Mosalam 2016; Fujimura and Der Kiureghian 2007; Garrè and Der Kiureghian 2010; Alibrandi and Koh 2017) may be adopted because of their effective computational cost.

Moreover, the BN can easily manage Bayesian updating, refer to Fig. 14. Through a network of sensors, information in real time about Energy Consumption *EC* is determined. The Bayesian updating may be developed also over the shape of the utility function(s) (represented in figure by the risk-aversion parameter γ) and the weights of the alternatives. This feature is attractive since there is an increasing interest in smart cities connecting human, physical and cyber elements. This can be achieved transparently using a BN-based unified framework.

It has been underlined that a significant source of uncertainty is related to the utility function, which is defined through subjective utilities expressing the preferences of the decision-maker. Moreover, the utilities can be modeled as probability distributions of subjective preferences of the decision-maker. Consequently, in a sustainable building design, the decision-maker can update, using Bayes' rule and/or MaxEnt method, not only objective probabilities related to experimental data but also subjective utilities together with their weights. This is very important especially in modern society, where technological innovation and novel challenges may change the analysis of the consequences day by day. It is difficult for a decision-maker to describe utility functions capturing food shortage as a result of drought, pollution or an extreme event (e.g. failure of a nuclear power plant near the ocean) if no one has previously studied this phenomenon. Therefore, it is believed

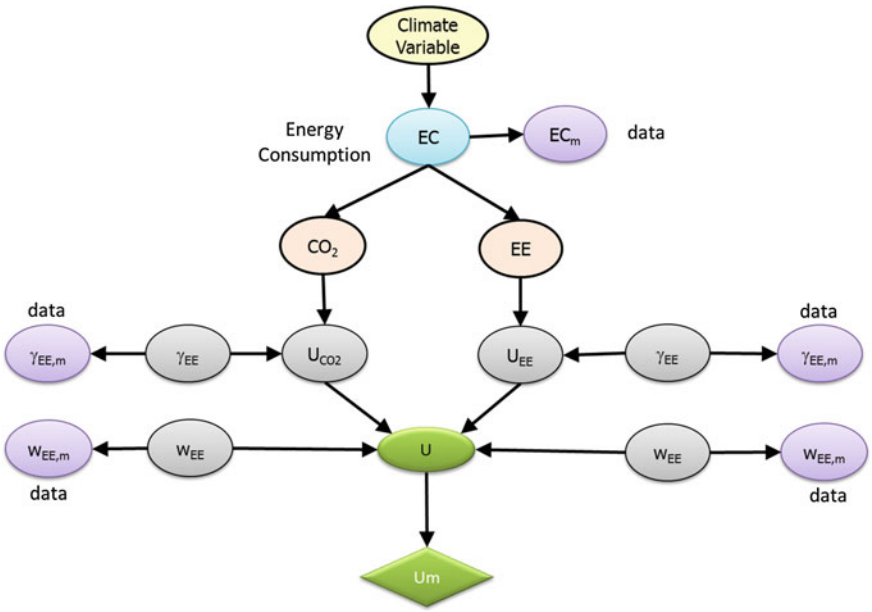

Fig. 14 BN for sustainability under Bayesian updating

that the Bayesian updating of the utility and weights is important for the decision-making process and it can be managed in a straightforward manner using the BNs.

6 Lifecycle Sustainability Analysis of Sinberbest Office Space in the Create Building, Singapore

As an example, a sustainability lifecycle analysis is considered for an office space located in the SinBerBEST of the 11th floor of the CREATE Building, Singapore, shown in Fig. 15.

6.1 Decision Criteria

In the SinBerBEST (Singapore Berkeley Building Efficiency and Sustainability in the Tropics) office, economic and environmental requirements are considered for the lifecycle analysis. We consider as indicators $c_1 \equiv CO_2$ *emission*, the *Energy*

Expenditure $c_2 \equiv EE$, and $c_3 \equiv IC$ is the *Initial Cost* of the adopted energy systems. It is assumed that the weights chosen by the decision-maker for these criteria are $w_1 \equiv w_{CO2} = 0.4$, $w_2 \equiv w_{EE} = 0.35$, and $w_3 \equiv w_{IC} = 0.25$. This implies that the decision-maker prefers to maximize the energy efficiency and the environmental sustainability during the lifecycle.

Fig. 15 Office at CREATE building, 11th floor

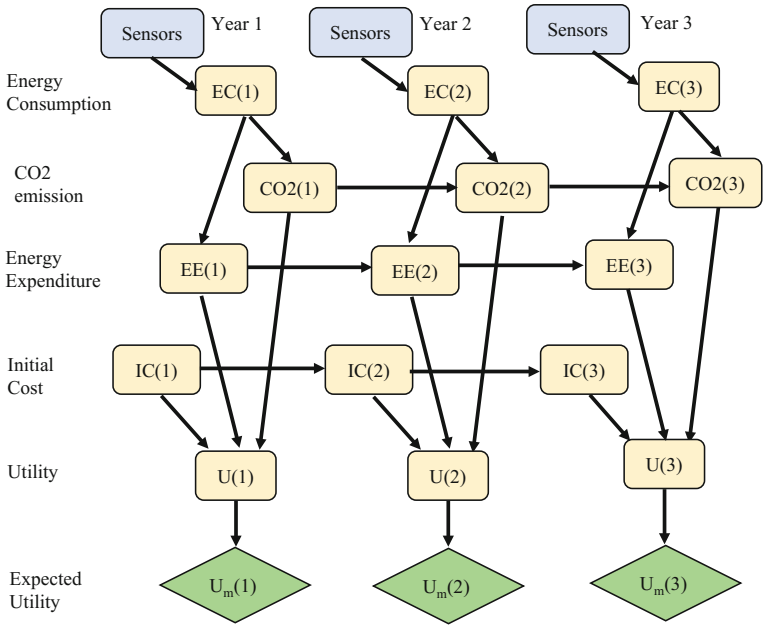

Fig. 16 BN model of the lifecycle sustainable design of the SinBerBEST office

6.2 Definition of the Alternatives and BN Model for Lifecycle Analysis

Two different energy plans have been considered as alternative sustainability designs, namely "*Plan 1: Electricity + PV panels*" and "*Plan 2: Electricity only*", where PV stands for Photo Voltaic. The two alternatives are studied through a lifecycle analysis developed through the BN model in Fig. 16.

6.3 PBE-MAUT

In the lifecycle analysis, all the criteria, including the Energy Consumption $EC(t)$, are modeled through stochastic processes. This because the EC varies during the hours of the day, as well as in the different days of the year. The data are collected from the Process Information (PI) system, which is a real-time data application with a highly efficient time-series database developed by OSIsoft. Currently, only the data of nine months of 2015 are available, Fig. 17. It is assumed that the probabilistic modeling of $EC(t)$ is representative of each year during the lifecycle analysis. The PI system is coupled with the developed software for the Decision Support Tool (DST). This implies that when new information is available, the probabilistic modeling of $EC(t)$ is updated in real-time together with the BN model underlying the decision-making process. In the analysis it is assumed that the parameters of the distribution are deterministic, but they are updated when new information is available from the PI system. In Fig. 18 the distributions of $EC(t)$ after collecting data for one month (August 2015) and nine months (from August 2015 to April 2016) are shown.

It is assumed that the PV panels necessary to cover the energy consumption have a cost of 2,110 $S and a lifecycle of 25 years. The lifecycle of the office is assumed equal to 50 years.

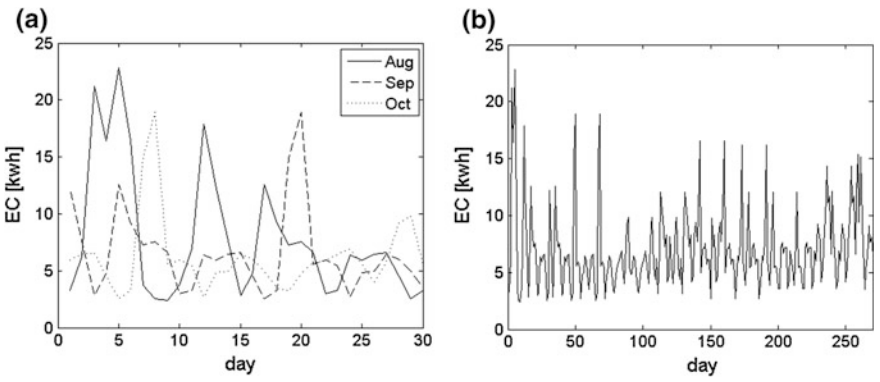

Fig. 17 Energy consumption in the SinBerBEST office during (**a**) typical month and (**b**) the year

For the PBE-MAUT, the linear single-attribute utility functions, Eq. (2), have been used. For $U_{CO_2}(t, co_2)$, $U_{EE}(t, ee)$, and $U_{IC}(t, ic)$, the maximum and minimum utility are achieved for $co_{2,min} = 0$ ton, $ee_{min} = ic_{min} = 0$ \$S and $co_{2,max} = 80$ ton, $ee_{max} = 25,000$ \$S, and $ic_{max} = 5,000$ \$S.

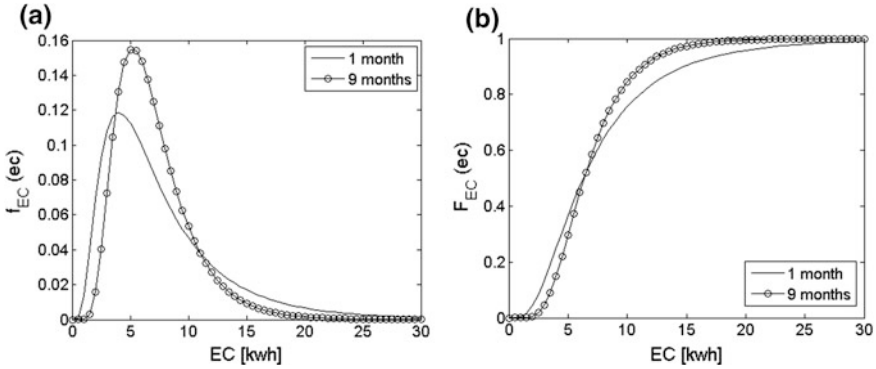

Fig. 18 Distribution of daily energy consumption in SinBerBEST office, data collected after one (August 2015) and nine months: **a** PDF and **b** CDF

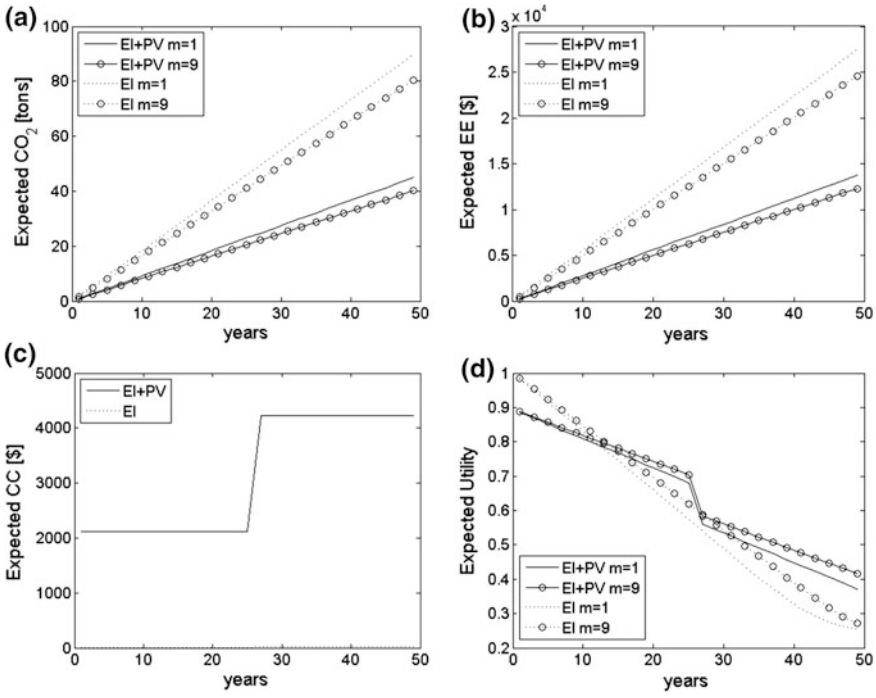

Fig. 19 Expected values of the criteria, collecting data for m = 1 and m = 9 months: **a** CO_2, **b** EE, **c** CC, and **d** utility functions

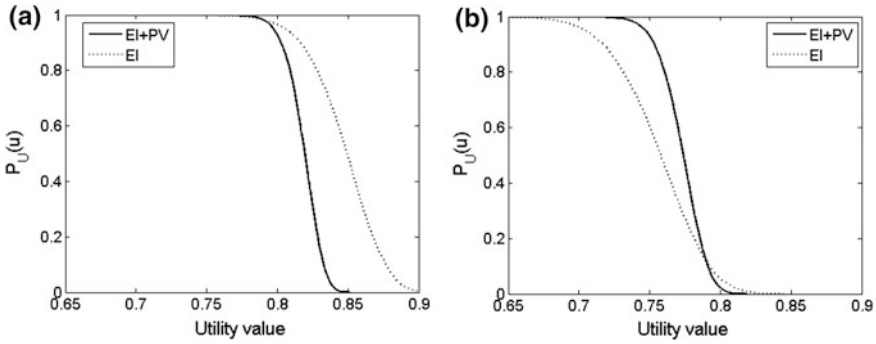

Fig. 20 Utility distribution of the two alternatives at **a** $t = 10$ years and **b** $t = 16$ years

In Fig. 19, the expected values of the criteria and the expected utilities are presented. It is shown that during the lifecycle, as expected, the hybrid system "*Electricity+PV panels*" is more effective in terms of $CO_2(t)$ emissions and $EE(t)$. However, after 25 years, the replacement of the PV panels implies a utility reduction due to the installation cost. Also, the figures clearly show that when new data are available the optimal decision is updated in real time. An advantage of the proposed approach is that the time-dependent distributions of the utility functions can be determined; this allows to determine any needed metric, and not only the expected utility. In Fig. 20, we represent the utility functions at $t_1 = 10$ years and $t_2 = 16$ years. It is shown that a change in the optimum alternative is realized in this short time window.

7 Concluding Remarks

For sustainable and resilient building design, the evaluation of the best decision is challenging because the number of stakeholders is large, there are several sources of uncertainty in the construction process, and the lifecycle of a building is long. Only a holistic approach, which considers all the current and future components, typically conflicting with each other, can identify a suitable decision. To achieve this holistic objective, an effective tool, termed PBE-MAUT, is presented. This tool is an extended framework which integrates the Multi Attribute Utility Theory (MAUT) with the Performance-Based Engineering (PBE) approach and methods of reliability theory.

In the developed framework, the quantification of uncertainties can be achieved through the classical PBE approach based on the evaluation of conditional probabilities or the unified reliability approach. The application of FORM to the utility

functions allows to obtaining information for the most critical realizations of the indicators, which gives the decision-maker a closer insight toward the direct and follow-up consequences of the design alternatives and/or actions during the lifecycle. PBE-MAUT can be described within the broad framework of the BN models, which conveniently allow the lifecycle analysis of a system, including the modeling of the degradation of the materials, as well as analysis of the consequences for strategies of maintenance and repair. The proposed Decision Support Tool (DST) has a very broad range of applications. For example, it can be applied for lifecycle analysis of a sustainable and resilient system under multiple natural hazards with comprehensive consideration of uncertainties, or to check different sustainable technologies (Muin et al. 2015), e.g. façade system for given climate conditions. The proposed DST can represent the main engine of a *Holistic Design Platform* (HDP) under uncertainty integrating several tasks of the construction process, e.g. structural and architectural design, performance building simulation, construction management, etc. It is of interest to observe that the HDP allows, through a unified framework, the integration of physical, cyber, and human elements to produce a smart building. For this reason, it can have significant implications for the development of smart cities and interdependent infrastructural systems, where issues of sustainability and resilience are of great importance. To this aim, ongoing research is devoted to the integration of the DST with the game theory and agent based modelling.

Acknowledgements The presented research is funded by the Republic of Singapore's National Research Foundation through a grant to the Berkeley Education Alliance for Research in Singapore (BEARS) for Singapore-Berkeley Building Efficiency and Sustainability in the Tropics (SinBerBEST) Program. BEARS has been established by the University of California, Berkeley as a center for intellectual excellence in research and education in Singapore. The authors thank Dr. S. Günay and Prof. P. Gardoni for their reviews of earlier versions of the manuscript and for their valuable suggestions.

References

Alibrandi U, Koh CG (2017) Stochastic dynamic analysis of floating production systems using the first order reliability method and the secant hyperplane method. Ocean Eng

Alibrandi U, Mosalam KM (2015a) FORM for probabilistic sustainable building design. In: Symposium on reliabality engineering systems (SRES 2015)

Alibrandi U, Mosalam KM (2015b) Lifecycle optimal design using Performance Based Engineering. In: Second international conference on performance-based and lifecycle structural engineering (PLSE 2015)

Alibrandi U, Mosalam KM (2017a) A multivariate distribution model using independent components. J R Stat Soc Ser C (Applied Stat (submitted)

Alibrandi U, Mosalam KM (2017b) Equivalent linearization methods for nonlinear stochastic dynamic analysis using linear response surfaces. J Eng Mech

Alibrandi U, Mosalam KM (2017c) The Kernel density maximum entropy with generalized moments applied to seismic fragilties. Int J Numer Methods Eng (submitted)

Alibrandi U, Ricciardi G (2008) Efficient evaluation of the pdf of a random variable through the kernel density maximum entropy approach. Int J Numer Methods Eng 75:1511–1548. doi:10.1002/nme.2300

Alibrandi U, Ma C, Koh CG (2016) Secant hyperplane method for structural reliability analysis. J Eng Mech. doi:10.1061/(ASCE)EM.1943-7889.0001024

Artzner P, Delbaen F, EBER Société Générale J, David Heath P (1999) Coherent measures of risk. Math Finan 9:203–228. doi: 10.1111/1467-9965.00068

Bensi MT, Kiureghian a. Der, Straub D (2009) A Bayesian network framework for post-earthquake infrastructure system performance assessment. In: TCLEE 2009 Lifeline Earthq Eng Multihazard Environ:1096–1107

Bocchini P, Asce M, Frangopol DM et al (2014) Resilience and sustainability of civil infrastructure : toward a unified approach. J Infrastruct Syst 20:1–16. doi:10.1061/(ASCE)IS.1943-555X.0000177

Bordley R, LiCalzi M (2000) Decision analysis using targets instead of utility functions. Decis Econ Financ 23:53–74. doi:10.1007/s102030050005

Bruneau M, Chang SE, Eguchi RT et al (2003) A framework to quantitatively assess and enhance the seismic resilience of communities. Earthq Spectra 19:733–752. doi:10.1193/1.1623497

Castagnoli E, Li Calzi M (1996) Expected utility without utility. Theory Decis 41:281–301

Cha EJ, Ellingwood BR (2012) Risk-averse decision-making for civil infrastructure exposed to low-probability, high-consequence events. Reliab Eng Syst Saf 104:27–35. doi:10.1016/j.ress.2012.04.002

Cha EJ, Ellingwood BR (2013) Seismic risk mitigation of building structures: the role of risk aversion. Struct Saf 40:11–19. doi:10.1016/j.strusafe.2012.06.004

Cornell CA, Krawinkler H (2000) Progress and Challenges in Seismic Performance Assessment. PEER Cent News 3:1–4

Der Kiureghian A, Zhang Y, Li CC (1994) Inverse Reliability problem. J Eng Mech 120:1154–1159

Ditlevsen O (2003) Decision modeling and acceptance criteria. Struct Saf 25:165–191. doi:10.1016/S0167-4730(02)00048-6

Ditlevsen O, Madsen HO (1996) Structural reliability methods

Fujimura K, Der Kiureghian A (2007) Tail-equivalent linearization method for nonlinear random vibration. Probabilistic Eng Mech 22:63–76. doi:10.1016/j.probengmech.2006.08.001

Gardoni P, Guevara-Lopez F, Contento A (2016) The life profitability method (LPM): a financial approach to engineering decisions. Struct Saf 63:11–20

Garrè L, Der Kiureghian A (2010) Tail-equivalent linearization method in frequency domain and application to marine structures. Mar Struct 23:322–338. doi:10.1016/j.marstruc.2010.07.006

Gunay M, Mosalam KM (2012) PEER performance-based earthquake engineering methodogy: revisited and extended to sustainable design. In: 10th international congress on advances in civil engineering

Günay S, Mosalam KM (2013) PEER performance-based earthquake engineering methodology, revisited. J Earthq Eng 17:829–858. doi:10.1080/13632469.2013.787377

Haimes Y (2004) Risk modeling, assessment, and management

Haukaas T (2008) Unified reliability and design optimization for earthquake engineering. Probab Eng Mech 23:471–481. doi:10.1016/j.probengmech.2007.10.008

Haukaas T (2013) Probabilistic models, methods, and decisions in earthquake engineering. In: Safety, reliability, risk and life-cycle performance of structures and infrastructures—Proceedings of 11th international conference on structural safety and reliability, ICOSSAR 2013, pp 47–66

Jaynes ET (1957) Information theory and statistical mechanics. Phys Rev 106:181–218. doi: 10.1103/PhysRev.106.620

Kahneman D, Tversky A (1979) Prospect theory: an analysis of decision under risk. Econometrica 47:263–292. doi:10.2307/1914185

Kapur J, Kesavan H (1992) Entropy optimization principles with applications. Academic Press, San Diego, NY

Keeney R, Raiffa H (1993) Decisions with multiple objectives–preferences and value tradeoffs. Behav Sci. doi:10.1002/bs.3830390206

Liu PL, Der Kiureghian A (1986) Multivariate distribution models with prescribed marginals and covariances. Probab Eng Mech 1:105–112. doi:10.1016/0266-8920(86)90033-0

Maes MA, Faber MH (2007) Preferences utility and risk perception in engineering decision making. Int J Risk Assess Manag 7:807–827. doi:10.1504/IJRAM.2007.014661

Melchers RE (1999) Structural reliability, analysis and prediction. New York

Mosalam KM, Alibrandi U, Lee H, Armengou J (2016) Performance-based engineering for holistic building design. Struct Saf (submitted

Muin S, Gunay S, Mosalam KM (2015) Decision Making of Innovative Building Facade use in Singapore. In: Proceedings of the second international conference on performance-based and lifecycle structural engineering

Nielsen TD, Jensen FV (2009) Bayesian network and decision graph. Springer Sci Bus Media. doi:10.1007/978-0-387-68282-2

Pinto P, Bazzurro P, Elnashai A et al (2012) Probabilistic performance-based seismic design. Technical Report

Pons O, Aguado A (2012) Integrated value model for sustainable assessment applied to technologies used to build schools in Catalonia, Spain. Build Environ 53:49–58. doi:10.1016/j.buildenv.2012.01.007

Rockafellar RT (2007) Coherent approaches to risk in optimization under uncertainty. INFORMS Tutorials Oper Res 38–61. doi: 10.1287/educ.1073.0032

Rockafellar RT, Royset JO (2015) Engineering decisions under risk averseness. ASCE-ASME J Risk Uncertain Eng Syst Part A Civ Eng 1:4015003. doi:10.1061/AJRUA6.0000816

San-José Lombera J-T, Garrucho Aprea I (2010) A system approach to the environmental analysis of industrial buildings. Build Environ 45:673–683. doi:10.1016/j.buildenv.2009.08.012

Straub D (2009) Stochastic modeling of deterioration processes through dynamic Bayesian networks. J Eng Mech 135:1089–1099. doi:10.1061/(ASCE)EM.1943-7889.0000024

Straub D, Der Kiureghian A (2010a) Bayesian network enhanced with structural reliability methods: methodology. J Eng Mech 136:1248–1258

Straub D, Der Kiureghian A (2010b) Bayesian network enhanced with structural reliability methods: application. J Eng Mech 136:1259–1270. doi:10.1061/(ASCE)EM.1943-7889.0000170

Tversky A, Kahneman D (1992) Advances in prospect theory: cumulative representation of uncertainty. J Risk Uncertain 5:297–323. doi:10.1007/BF00122574

Von Neumann J, Morgenstern O (1944) Theory of games and economic behavior, vol 625. Princeton University Press. doi: 10.1177/1468795X06065810

Wang JJ, Jing YY, Zhang CF, Zhao JH (2009) Review on multi-criteria decision analysis aid in sustainable energy decision-making. Renew Sustain Energy Rev 13:2263–2278. doi:10.1016/j.rser.2009.06.021

Wei H, Shohet IM, Skibniewski M et al (2016) Assessing the lifecycle sustainability costs and benefits of seismic mitigations designs for buildings Title. J Archit Eng 22

Winston WL (2003) Operations research: applications and algorithms. Comput Sci Commun Dict. doi:10.1007/SpringerReference_20294

Innovative Derivatives to Drive Investment in Earthquake Protection Technologies

Yuji Takahashi

Abstract We propose derivatives that compensate for the preparation cost to a building owner unless a specified earthquake occurs. By purchasing the derivatives, the building owner should pay for the earthquake protection only when the specified earthquake occurs. Otherwise the additional preparation cost will be covered by the derivative counterparty. In exchange for the coverage, the building owner is required to deposit a principal, which is lost when the earthquake happens. The proposed derivatives are expected to result in the efficient promotion of earthquake protection technologies in seismic regions. This chapter presents a scheme to swap the cash flow with a regular catastrophe bond. The price of the proposed derivatives is the ratio of the notional amount to the compensation given the earthquake does not take place. The pricing is formulated based on credit default swap (CDS) pricing. We present a numerical example using an actual cat bond, where up-to-date seismological models are introduced into pricing.

Keywords Earthquake protection · Derivatives · Cat bond · CDS pricing · Seismological model

1 Introduction

Large earthquakes have been causing serious economic damages and killing many people in seismically active regions. About 10% of all earthquakes over the world occur in Japan, while the country occupies only 0.3% in terms of land area (NLIORJ

This chapter was submitted to the Applied Financial Project of Master of Financial Engineering, Haas School of Business, University of California at Berkeley, and won the Gifford Fong Associate Prize.

Y. Takahashi (✉)
Asset Risk Management Department, MetLife Insurance K.K, Tokyo, Japan
e-mail: yuji.takahashi.yt@gmail.com

P. Gardoni (ed.), *Risk and Reliability Analysis: Theory and Applications*,
Springer Series in Reliability Engineering, DOI 10.1007/978-3-319-52425-2_23

2003). The latest catastrophe event was the Kobe earthquake in 1995, which results in 6,435 fatalities and economic loss of about $ 100 billion (estimated by the Cabinet office of Japan: COJ). Also after that, several damaging earthquakes, e.g., the Northern Miyagi earthquake in 2003, the Niigata Chuetsu earthquake in 2004, and the Fukuoka western off-shore earthquake in 2005, entailed significant damages.

The San Francisco Bay Region is also at high risk. Earthquakes are forecasted by the US Geological Survey, (USGS 2003), and by the Headquarters for Earthquake Research Promotion (HERP 2005) which provides government forecasted earthquakes in Japan, in both cases based on cutting-edge seismological models. HERP (2005) identified more than three hundred seismic sources and evaluated their location, magnitude and probabilities, some major ones of which are listed in Table 1. By comparing to San Francisco Bay Region (USGS 2003), larger earthquakes are forecasted to happen in greater probabilities.

The COJ organized a working group to estimate future economic losses and the numbers of fatalities incurred by the major earthquakes, which are also shown in Table 1. The Tokai, Tonankai, and Nankai earthquakes are expected to have large magnitude and cover a large portion in geographically-central part of Japan. It is notable that the monetary loss for the South Kanto earthquake is larger than those for the Tokai, Tonankai, and Nankai earthquakes despite its magnitude is smaller (7.2). This is because the South Kanto earthquake is considered to take place just beneath the Tokyo region, which is the most urbanized area involving huge potential exposure. No matter which earthquake happens, the losses are significant relative to Japan's CDP of about $4.5 trillion and population of about 120 million.

In order to prepare for catastrophe events, physical technologies have been developed by structural engineers. Not only traditional strengthening, but also more advanced technologies such as vibration energy-dissipation dampers and base isolation systems are demonstrated to mitigate earthquake damages on buildings. Now these technologies are fully commercialized, and building owners seem to perceive them to be effective in protecting their properties and lives.

However, in reality, the penetration of protection technologies is very slow even in the seismic regions where building owners consider their earthquake risks. The government and earthquake researchers started to investigate and list some reasons why people do not employ such excellent protection technologies. One of them is the construction cost, which is approximately estimated to be additional 2–10% for new buildings and 5–30% for existing ones.

Table 1 Earthquake probability and estimated loss (HERP 2005 and COJ)

Name	Magnitude	30- year probability	Economic loss ($ billion)	# of fatalities
Kobe (reference)	7.3	Occurred in 1995	100	6,435
South Kanto	7.2	72%	1,120	11,000
Tokai	8.0	86%	370	9,200
Tonankai	8.1	60%	570	17,800
Nankai	8.4	50%		

Takahashi (2006) pointed out that many building owners do not invest in the protection, even though they well understand their effectiveness, because they think "the investment should be successful if earthquake hits me in the future. But waste of money if there is not earthquake". This means that the building owners who invested in protections must expose themselves to the "risk that earthquake does not occur". Indeed the investment will be a sunk cost unless the protection gets no opportunity to work.

So as to solve the above problem, Takahashi (2006) proposed derivatives that pay when pre-specified earthquakes do not occur. This study demonstrated that the security is formed by swapping the payoff with that of regular earthquake derivatives, which pay in case of earthquake occurrences. The derivatives were priced based on insurance mathematics. From practical viewpoints, however, the proposed derivatives should have maturity of 5 to 30 years while regular earthquake derivatives are annual contracts. This inconsistency is problematic because the originator must maintain the sales quantity of regular earthquake derivatives in order to balance the cash flow for both sides.

This study proposes a new scheme utilizing a cat (catastrophe) bond to balance the cash flows from both entities over time. Normally the maturities of cat bonds range from 1 to 10 years (MMC Securities 2007), which matches that of the proposed derivatives. Section 2 describes the basic scheme of the new product. Section 3 presents pricing formulas, and Sect. 4 shows a numerical example using a cat bond actually issued in Japan in 1997 (Misani 1999).

2 Basic Scheme

This chapter proposes derivatives that continue to pay coupons, which compensate for the additional cost for protection, to a building owner until a pre-specified earthquake occurs (if any) or maturity. This security is realized by combining the default leg (or insurer leg) of a cat bond because their payoffs are opposite and can be swapped. Section 2.1 overviews conventional cat bonds, and Sects. 2.2 and 2.3 presents the basic scheme and price of the newly proposed derivatives, respectively.

2.1 General View of Regular Cat Bond

Many references about cat bond are available, e.g., Geman (1999), Misani (1999), Swiss Re (2003), and GAO (2003). A cat bond is an Alternative Risk Transfer (ART) instrument, which uses techniques other than traditional insurance and reinsurance to provide risk bearing entities with coverage or protection. The ART market grew out of a series of insurance crises in the 1970s through 1990s, when rising rates and the difficulty of obtaining sufficient amounts of coverage in some commercial insurance lines drove purchasers of traditional coverage to seek more

robust ways to buy protection. Most of these techniques permit investors in the capital markets to take a more direct role in providing insurance and reinsurance protection, so ART brings about a convergence of insurance and financial markets.

Key sectors of the Alternative Risk Transfer marketplace include cat bonds, reinsurance sidecars, the use of captive insurance companies, financial reinsurance, finite risk insurance, contingent capital, captive insurers and reinsurers, dual trigger insurance, industry loss warranties and weather derivatives. Among them, risk securitization including catastrophe bonds and reinsurance sidecars is the major sector of ART activity.

Cat bonds are risk linked securities that transfer a specified set of risks from the sponsor to the investors. They are used by insurers as an alternative method to traditional catastrophe reinsurance.

Traditionally, in order for insurers to pass on some of their risks, they would typically purchase catastrophe insurance and pass the risk on to reinsurers. Cat bonds provide insurers an alternative method to minimize the risk and pass on the risk to investors instead. The insurer would act as a sponsor of the cat bond. The insurer works closely with an investment bank to structure the specific features of the bond. Cat bonds are generally issued by special purpose entities in Bermuda. Key participants of cat bonds are specialized catastrophe-oriented funds and asset managers.

Similar to that of a regular bond with floating rates, cat bond pays regular coupons with a LIBOR plus anywhere from 3% to 20%. A different feature of the cat bond is that it has a trigger condition. If the trigger condition is not met, the cat bond behaves like a regular bond. On the other hand, if the trigger condition is met, the principal initially paid by the investor is forgiven and the sponsor would use the money to pay claims.

- **Indemnity**: the cat bond is triggered by the issuer's actual losses and the sponsor is indemnified.
- **Modeled loss**: The cat bond is triggered when the modeled losses are above a certain threshold determined by the catastrophe modeling software.
- **Indexed to industry loss**: The cat bond is triggered when the total loss of the insurance industry reaches a certain threshold.
- **Parametric**: The bond is triggered based on the index of natural hazard.

Investors are interested in investing in cat bonds for two main reasons. First, cat bonds have higher interest rates than comparably rated corporate instruments if they are not triggered. Secondly, cat bonds help investors achieve diversification because their return is uncorrelated with the return on other investments in fixed income or in equities. Key participants of cat bonds are specialized catastrophe-oriented funds and asset managers.

Cat bonds are rated by agencies such as S&P, Moody's and Fitch. Cat bonds are generally rated below investment grades (B and BB). The probability of default due to a catastrophic event (earthquake or hurricane) triggering the loss of capital is the key rating criteria. Catastrophe models are used to determine this probability.

2.2 New Derivatives to Promote Earthquake Protection

Figure 1 illustrates the simplified scheme of the derivatives we propose in this chapter. Suppose that someone buys a house for \$300 K, and invests \$25 K in an earthquake protection system, e.g., conventional strengthening, dampers and base-isolation. The total amount, \$325 K, is paid. Simultaneously, the owner makes a deposit, say \$25 K × α (coverage ratio), in the SPV (Special Purpose Vehicle).

The building owner then receives coupons, which consists of premiums from an insurer and LIBOR on the deposit, until a pre-specified earthquake event takes place, or the bond matures (Fig. 1a). As shown in Fig. 1b, if a specified earthquake occurs before the maturity, the notional deposited by the building owner, \$25 K × α, will be immediately paid to the insurer, and the contract will terminate. The insurer then covers the payout to its policy holders damaged by the earthquake. The building owner must lose the deposit of \$25 K × α, but he/she should realize that the protection saved his/her life and property and the investment decision to protect the house against the earthquake risk was the right decision.

Until the earthquake happens, the initial investment in the protection will be compensated by the coupon payments, and if the bond matures before any earthquake event, the deposit of \$25 K × α is also returned to the home owner (Fig. 1c).

The above example assumed that the house owner pays the construction cost, \$325 K, and the deposit, \$25 K × α, by cash. However, in reality, many building owners use mortgages for most if not all of their home purchase cost. The use of a mortgage is not essential to this scheme, but it will make the financing of the SPV deposit even easier for the homeowner. Figure 2 explains the scheme as a realistic example.

The house owner pays the mortgage for construction and deposit, (\$12.7 K + \$1.1 K + \$1.1αK)/2, semiannually for 30 years. The lender pays \$325 K to the builder for the construction, and a notional of \$25 K × α to the SPV at the beginning. The building owners can receive the coupons, which covers part of or whole mortgage payments for the protection of \$1.1 K per year, until earthquakes occur.

If an earthquake occurs, the notional is moved to the insurer and the contract terminates as seen in Fig. 2b. After this event, the building owner must continue to pay the mortgage without receiving the coupon. But again, the owner should be willing to give the notional because the protection protected his/her property and life, and he/she can realize that the investment was correct.

Figure 2c suggests that if there is no earthquake before the maturity, the notional of \$25 K × α is redeemed to the building owner.

The above example assumed a digital payoff, i.e., \$0 or \$25 K × α, for simplicity. In practice, the amount of payoff (LGD: Loss Given Default) can be determined as a function of the magnitude of the earthquake event, as portrayed in Fig. 3. If earthquake of magnitude greater than the attachment point, M_a, does not occur, the whole notional is returned to the building owner, i.e., LGD = 0.

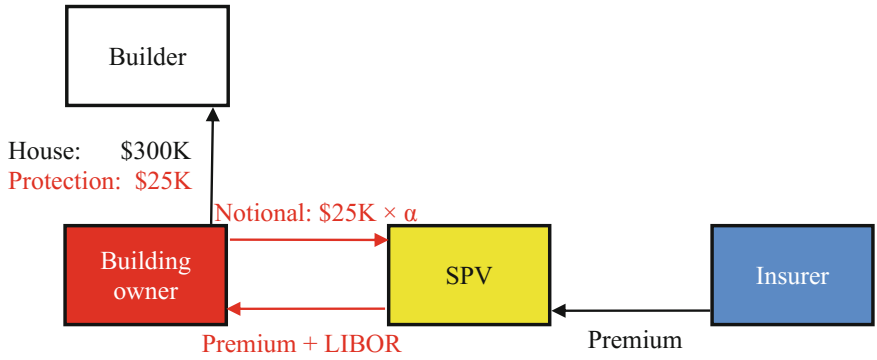

(a) At the beginning and until earthquake occurs

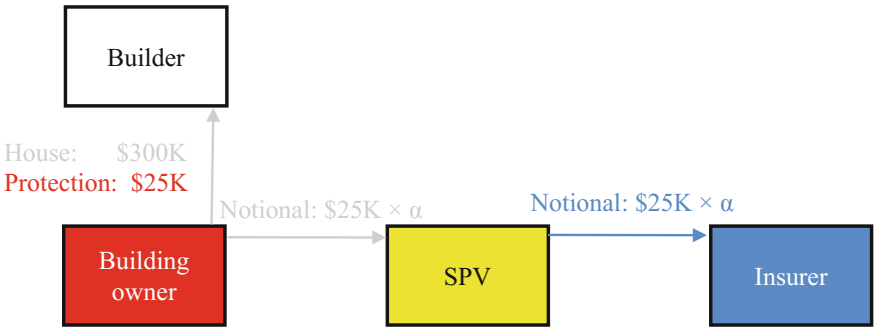

(b) If earthquake occurs before maturity

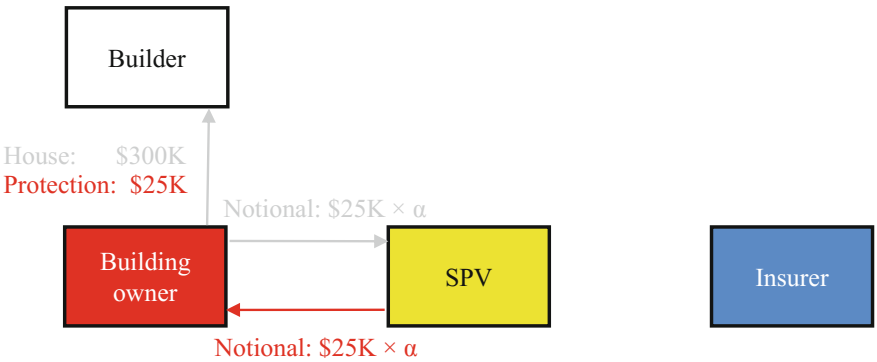

(c) If there is no earthquake before maturity

Fig. 1 Basic scheme of proposed derivatives (without using mortgage)

Otherwise it is paid to the insurer, but the amount depends on the magnitude. In case of an earthquake of magnitude greater than the detachment point, M_d, LGD = 1.0.

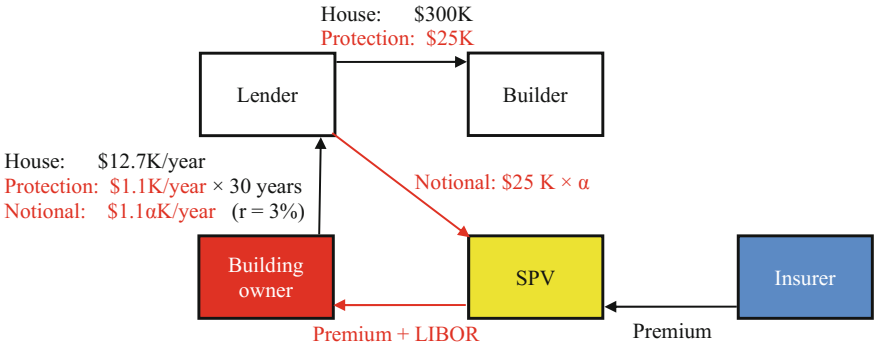

(a) At the beginning and until earthquake occurs

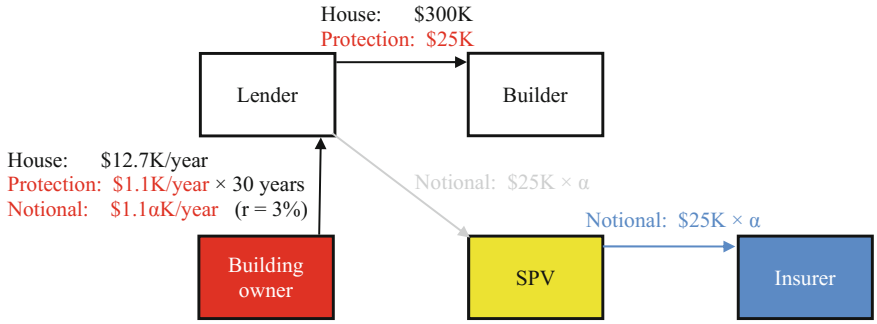

(b) If earthquake occurs before maturity

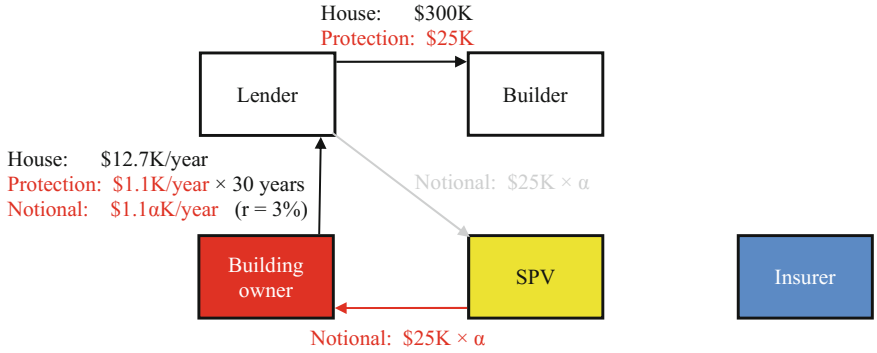

(c) If there is no earthquake before maturity

Fig. 2 Basic scheme of proposed derivatives (using mortgage)

The insurer receives more the larger the earthquake. This is a common feature of many current cat bonds. On the other hand, the owner loses more as a larger earthquake happens. This is appropriate since he/she will receive greater protection, in saving his/her life and property, the larger the earthquake.

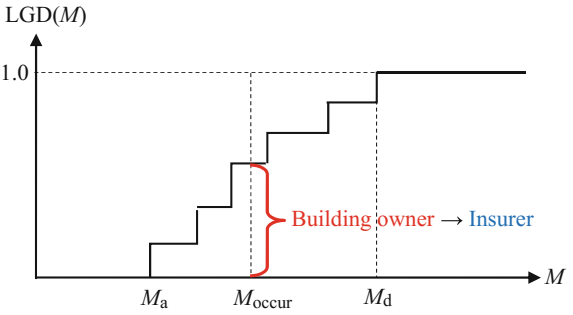

Fig. 3 Magnitude-dependent loss given default to building owner

Figures 1 and 2, for simplicity, assume a direct contract between the SPV and building owner. Nonetheless, it may not be practical because a large number of building owners should be collected and pooled in order to balance the payoff amount. The products can be distributed by the builder or lender, where the premium and redemption are paid to the building owners through either of the two entities. The incentive for builders and lenders is that they can increase their lending amounts or construction business by utilizing the derivatives as a sales tool.

2.3 Derivatives Price

The proposed security involves two prices for the insurer leg and for the building owner leg. The first one is the premium paid from the insurer to the owner through SPV, as illustrated in Figs. 1 and 2. This premium can be priced by putting risk premium on the annual expected loss (Geman 1999), or following CDS (Credit Default Pricing) pricing (Lando 2004).

The second price is the notional amount that the building owner is required to deposit in the SPV relative to the compensation amount (sum of the present values of spread payments), α in Figs. 1 and 2, until the maturity given an earthquake does not occur. For example, if this ratio is computed to be 1.5, a deposit of $37.5 K is required when the owner intends to cover a protection cost of $25 K. Section 3 formulates those prices, and Sect. 4 provides numerical examples.

3 Pricing Formula

In practice of cat bond pricing, the annual expected loss without discounting, E[L], is taken as a proxy to determine the market spread (Misani 1999; Lane 2006). We will compute risk-neutral spread as well, so it is formulated here.

By considering the scheme presented in Figs. 1 and 2, we can see that the payoff of the proposed derivatives is similar to that of a CDS. The difference is that a CDS

does not require notional up front, and a premium leg pays only when default occurs. On the other hand, a principal is deposited in the SPV in the proposed derivatives in order to eliminate credit risk of building owners. However, this does not make any difference in terms of pricing because the interest on the deposit, LIBOR, is paid to the building owner. Thus we can apply CDS pricing to our case.

By referring to Lando (2004), the present value to the insurer leg is formulated as

$$V_{Insurer} = E_0^Q\left[e^{-\int_0^\tau r(s)ds} \cdot LGD(M) \cdot N \cdot 1_{\{\tau<T\}}\right] \tag{3.1}$$

where $r(s)$ is a risk-free rate, LGD(M) is a magnitude-dependent loss given default, N is a notional, τ is the time when an earthquake occurs, and $1_{\{\tau<T\}}$ is an indicator function which is equal to one if earthquake occurs and zero if no earthquake happens before its maturity, T. Similarly, the value for the building owner leg is expressed as

$$V_{Owner} = E_0^Q\left[\sum_{i=1}^{n_\Delta} e^{-\int_0^{t_i} r(s)ds} \cdot s_{RN} \cdot \Delta \cdot N \cdot 1_{\{\tau<t_i\}} + e^{-\int_0^\tau r(s)ds} \cdot s_{RN} \cdot (\tau - t_i) \cdot N \cdot 1_{\{t_i<\tau<t_{i+1}\}}\right] \tag{3.2}$$

where n_Δ is the number of coupon payments to the owner, s_{RN} is a risk-neutral (physical) spread over LIBOR, Δ is a time interval between two successive coupon payments. The first term in the expectation accounts for the sum of present values of risk-neutral spreads, and the second term denotes an accrued spread. By equating the values of both parties, we obtain

$$s_{RN} = \frac{E_0^Q[e^{-\int_0^\tau r(s)ds} \cdot LGD(M) \cdot 1_{\{\tau<T\}}]}{E_0^Q[\sum_{i=1}^{n_\Delta} e^{-\int_0^{t_i} r(s)ds} \cdot \Delta \cdot 1_{\{\tau<t_i\}} + e^{-\int_0^\tau r(s)ds} \cdot (\tau - t_i) \cdot 1_{\{t_i<\tau<t_{i+1}\}}]}. \tag{3.3}$$

Note that N disappeared. It is very difficult to obtain closed-form solutions for the numerator and denominator because it is the first passage problem among multiple potential earthquakes. Furthermore we will use not only the Poisson model but also time-dependent probabilistic models for earthquake occurrences (see Sect. 4). Therefore we will compute the numerator and denominator by performing Monte Carlo simulations.

Market spread, s_{market}, is determined by multiplying a risk-neutral spread given by Eq. (3.3) by a multiplier by considering risk- and ambiguous-aversion of investors. The compensation for the building owner given earthquake does not occur, C, is the sum of the present values of spreads up to maturity, i.e.,

$$C = \sum_{i=1}^{T/\Delta} e^{-\int_0^{t_i} r(s)ds} \cdot s_{market} \cdot \Delta \cdot N. \tag{3.4}$$

By solving Eq. (3.4) for *N/C*, we obtain

$$\frac{N}{C} = \frac{\text{Deposit}}{\sum PV[\text{spread}|\text{no earthquake}]} = \frac{1}{s_{market} \cdot \Delta \cdot \sum_{i=1}^{T/\Delta} e^{-\int_0^{t_i} r(s)ds}}. \tag{3.5}$$

N/C represents how much the building owner have to make deposit relative to the coverage given no earthquake (equivalent to α in Figs. 1 and 2). For example, $N = \$50$ K if the owner wants to cover \$25 K and if $N/C = 2.0$. Figure 4 plots the relationship between s_{market} and *N/C*, assuming $r_f = 1.5\%$ and $\Delta = 0.5$ year.

We can see *N/C* is inversely proportional to s_{market}. This means that the owner is required more deposit as the market spread becomes smaller. Note that the smaller spread results from a smaller probability of earthquake, i.e., a larger probability that

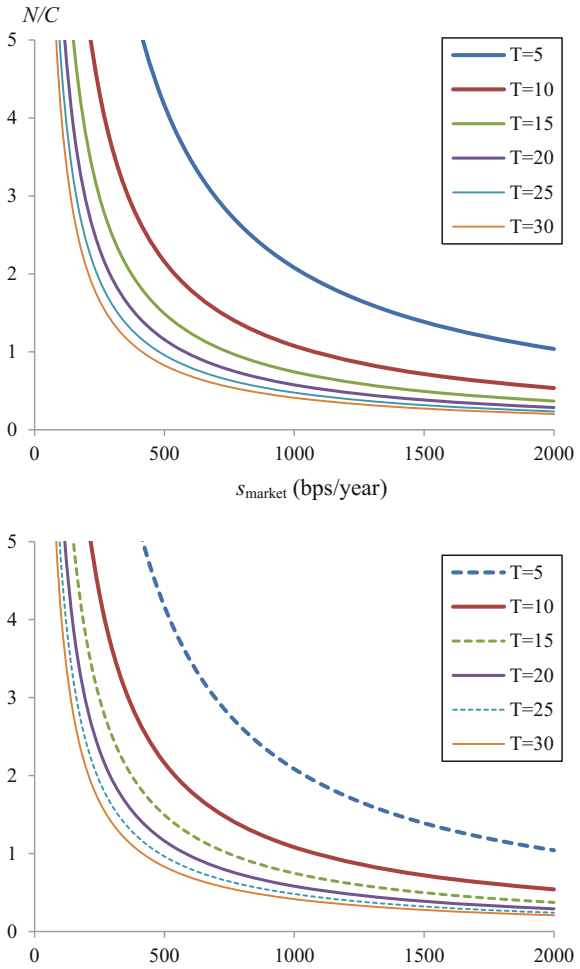

Fig. 4 Ratio of deposit to coverage versus market spread of cat bond ($r_f = 1.5\%$ and $\Delta = 0.5$ year). (Color figure online)

the deposit is redeemed to the owner. This implies the tradeoff between the amount of deposit and the earthquake probability (or default probability). In general, probabilities of large earthquakes are small, e.g., 10% in 10 years, meaning the building owners are repaid in high probabilities, 90% in 10 years, although they have to make considerable amounts of deposits.

Also *N/C* becomes smaller as *T* gets longer. This is simply understood: the probability of earthquake rises with length of time, i.e., the probability that the owner is redeemed declines as time window is extended.

4 Case Study

This section presents numerical examples of the security proposed in Sect. 2. We utilize a cat bond that was actually issued in Japan in 1997 because we can benchmark our pricing. Section 4.1 outlines the cat bond, and Sect. 4.2 describes the probabilistic models of earthquake occurrences. Our pricing of the cat bond is benchmarked with the actual one in Sect. 4.3. Section 4.4 prices the notional amount that the building owner is required in the proposed derivatives.

4.1 An Actual Cat Bond

At least ten earthquake-related bonds have been issued in Japan since the first one in 1997 (MMC Securities 2007). This section deals with the first cat bond issued by Parametric Re (Misani 1999). In order to securitize the insurance risk of $100 million underwritten by Tokio Marine, Parametric Re was established on November 3 in 1997 based on the insurance law of Cayman Islands. The 10-year cat bonds would mature November 19 in 2007, and consist of the following two tranches.

- Note: paying LIBOR + 430 basis points. The notional of $80 million is not protected.
- Unit: paying LIBOR + 206 basis points. The notional of $20 million is protected.

In the worst case, investors of the note lose all their principal while those of the unit lose 50%. This means the cat bond covers $90-million reinsurance of Tokio Marine.

If an earthquake with magnitude of 7.1 or greater occurs within the inner grid shown in Fig. 5, the investors would lose. The inner grid covered large cities with huge exposures such as Tokyo and Yokohama. The payoff depends on the earthquake magnitude, and is listed in Table 2. Similarly, the unit deprives the investors of the notional if an earthquake of 7.3 or greater happens inside the outer grid

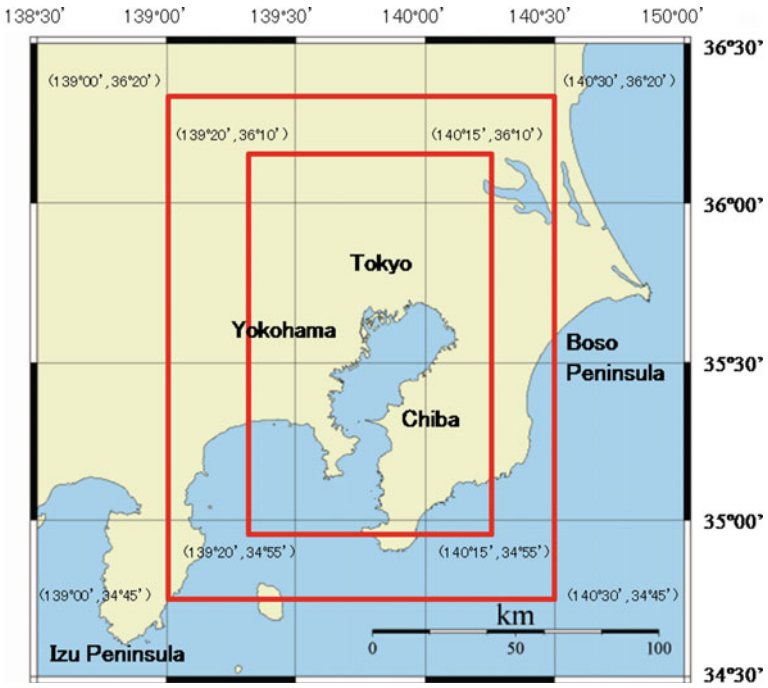

Fig. 5 Grids for cat bond

Table 2 Investors' loss versus earthquake magnitude (from Misani 1999)

Magnitude	Loss to principal	
	Note (Inner grid) (%)	Unit (Outer grid excluding inner grid) (%)
≥ 7.1	25	0
≥ 7.2	40	0
≥ 7.3	55	25
≥ 7.4	70	44
≥ 7.5	85	63
≥ 7.6	100	81
≥ 7.7	100	100

(excluding the inner grid). But the loss is calculated as the ratios in the third column in Table 2 times the worst loss of 50%.

The trigger, which would determine the payoff, was specified as the magnitude reported by the Japan Meteorological Agency (JMA). This was the first cat bond whose trigger was a physical measurement (as described in the previous section, others were triggered by actual insurance loss or model loss, which are ambiguous for investors). Investors favored this feature because physical measurements enable them to compute the payoffs objectively and rapidly. On the other hand, Tokio

Marine took the basis risk, i.e., the amount of the payoffs from the cat bonds would not match that of the insurance payments to its clients once an earthquake takes place.

Figure 6 illustrates the simplified issuance scheme of the cat bond. Parametric Re issued the cat bonds as an SPV (Specific Purpose Vehicle), which is established to eliminate the credit risk of bond issuer (insurance company). Tokio Marine made a reinsurance contract of $90 million with Swiss Re. Tokio Marines was to pay fixed rate, i.e., the reinsurance cost would be fixed during the 10 years. Parametric Re entered into interest swap, paying fixed rate and receiving floating rate, with Swiss Re Financial Products. This enabled Parametric Re to pay floating rate to the investors while receiving fixed rate from Swiss Re.

EQE International, which was a leading firm in risk management of natural hazards, constructed a risk model of the cat bond. By collecting past earthquake

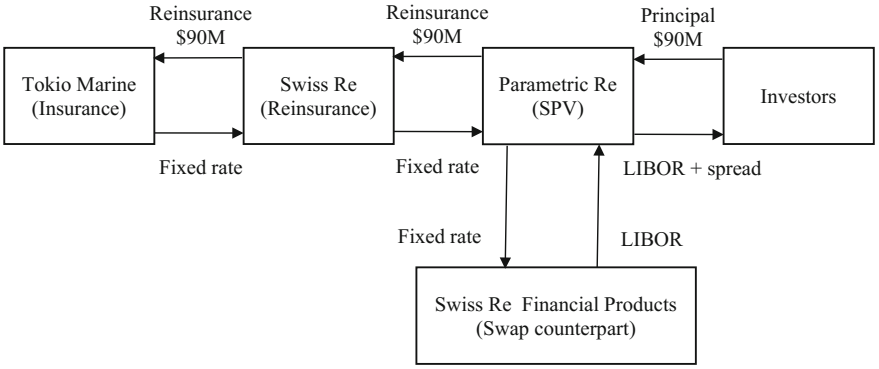

Fig. 6 Transaction scheme of the cat bond (simplified from Misani 1999)

Table 3 Risk evaluation of cat bond (from Misani 1999)

Magnitude	Note				Unit			
	Cum. Prob. (%)	Prob. (%)	Loss (%)	$E[L_m]$ (%)	Cum. Prob. (%)	Prob. (%)	Loss (%)	$E[L_m]$ (%)
≥ 7.1	0.64	0.12	25	0.03	0.37	0.00	0	0.00
≥ 7.2	0.52	0.09	40	0.04	0.37	0.00	0	0.00
≥ 7.3	0.43	0.07	55	0.04	0.37	0.07	25	0.02
≥ 7.4	0.36	0.06	70	0.04	0.30	0.06	44	0.03
≥ 7.5	0.30	0.05	85	0.04	0.24	0.04	63	0.03
≥ 7.6	0.25	0.04	100	0.04	0.20	0.04	81	0.03
≥ 7.7	0.21	0.21	100	0.21	0.16	0.16	100	0.16
			$E[L]$ =	44 bps			$E[L]$ =	26 bps
		Market spread =		430 bps		Market spread =		206 bps

data and introducing the latest seismological knowledge, EQE International estimated the probability of earthquakes within the specified grids (see Table 3). The expected losses of the note and unit were 0.44% and 0.26%, respectively. According to this evaluation, Moody's rated the note and unit as Ba2 and Baa3, and Duff and Phelp's rated BB and BBB-.

The spreads for the note and unit were priced to be 430 basis points and 206 basis points, respectively (Table 3). These spreads were higher by 2% than those of the same rated corporate bonds issued around the same time.

4.2 Earthquake Models

Based on the up-to-date seismological knowledge, USGS (2003) and HERP (2005) constructed earthquake models around San Francisco Bay Region and Japan, respectively. HERP identified more than three hundred seismic sources, among which Table 4 lists ones around the grids of the benchmark cat bond. We utilize the cutting-edge seismic models developed by HERP (2005) in our derivatives pricing.

Table 4 contains magnitude, M_{JMA}, mean return period, T, aperiodicity, α, and the time elapsed since the last earthquake, t_0. HERP prepared mean and conservative parameters for the BPT (Brownian Passage Time) model (Matthews et al. 2002), and the latter gives higher probabilities. The horizontal-plane projections of the seismic sources are mapped in Figs. 7, 8 and 9.

As shown in Table 2, the cat bond pays only when an earthquake of magnitude of 7.1 or greater occurs. Thus we exclude the earthquakes with magnitude smaller than 7.1, i.e., Isehara, Miura peninsula main Takeyama, and Miura peninsula south, and consider the earthquakes highlighted in Table 4 in the following analysis.

For the Poison model in Monte Carlo simulations, we generate a uniform random variable at each time increment, dt. If this number is smaller than the

Table 4 Seismic sources around Tokyo (HERP 2005 as of January 2006)

#	Name	Active fault/ Plate boundary	M_{JMA}	Prob. (30 years)	Prob. model	T (years)		α	t_0 (years)	
						mean	conservative		mean	conservative
01	Kamogawa Teichi	Active fault	7.2	0.38%	Poisson	7900	7900	--	--	--
02	Kanto Heiya Hokuseien	Active fault	8.0	0%	BPT	21500	13000	0.24	4350	6200
03	Hirai-Kushibiki	Active fault	7.1	0.43%	Poisson	7000	7000	--	--	--
04	Tachikawa	Active fault	7.4	1.3%	BPT	12500	10000	0.24	16500	20000
05	Isehara	Active fault	7.0	0%	BPT	5000	4000	0.24	956	1606
06	Kannawa-Kozu-Matsusda	Active fault	7.5	4.2%	BPT	1050	800	0.24	781	906
07	Miura peninsula main Kinugasa-Kitatake	Active fault	7.2	0.0047%	BPT	3400	1900	0.24	1406	1506
08	Miura peninsula main Takeyama	Active fault	6.9	8.4%	BPT	1750	1600	0.24	2103	2300
09	Miura peninsula south	Active fault	7.0	1.9%	Poisson	1600	1600	--	--	--
10	Taisho-type Kanto	Plate boundary	7.9	0.065%	BPT	219.7	219.7	0.21	82.3	82.3
11	South Kanto	Plate boundary	6.7-7.2	72%	Poisson	23.8	23.8	--	--	--

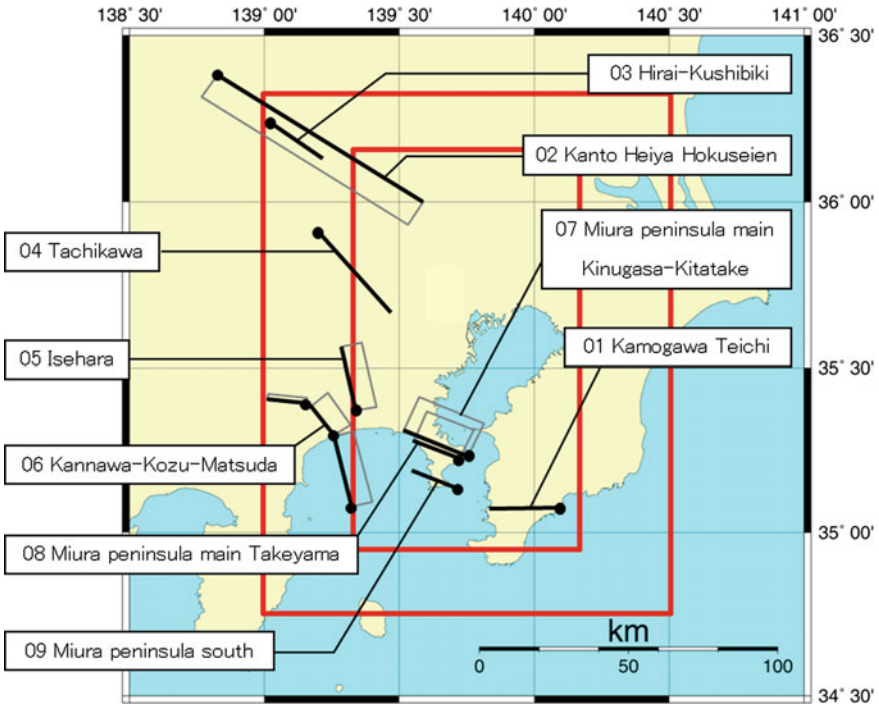

Fig. 7 Active faults around grids

probability that the event occur during *dt*, computed by Eq. (4.1), an earthquake is considered to happen.

$$F(dt) = 1 - exp(-\mu \cdot dt) \tag{4.1}$$

where μ is a mean occurrence rate per unit time (= 1/*T*). The BPT model is a closed-form probability density function of time intervals for the Brownian Relaxation Oscillator (BRO). The BRO regards stress accumulation in a seismic source as the arithmetic Brownian motion which is given by

$$x(t + dt) = x(t) + \mu \cdot dt + \alpha\sqrt{\mu \cdot dt} \cdot z(t) \tag{4.2}$$

where $x(t)$ is a stress level at time t and $z(t)$ is a standard normal random variable. The BRO is immediately relaxed (reset to be zero) when it hits the threshold, $x(t) = 1.0$, the immediate relaxation accounts for an earthquake. The fact that there has been no earthquake since the last event (between $t = -t_0$ and $t = 0$) requires to cull out cycles which breach the following inequality in a Monte Carlo simulation.

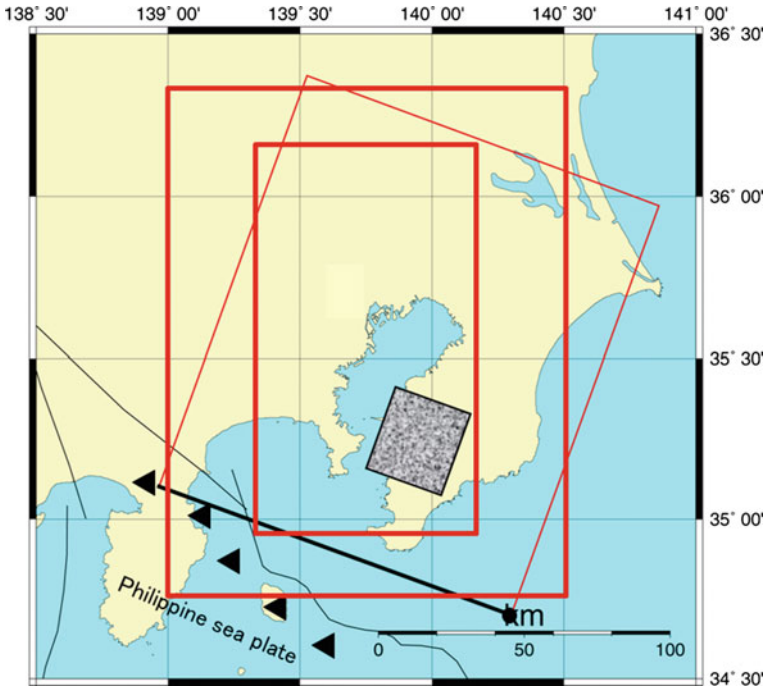

Fig. 8 Seismic source and fault plane of South Kanto earthquake

$$x(t) < 1.0 \qquad \forall -t_0 < t < 0 \tag{4.3}$$

where $t = 0$ is set to be the starting time of derivatives contract. Figure 10 displays one sample path of the BRO for the Taisho-type earthquake with $\mu = 1/219.7$ (per year), $\alpha = 0.21$, and $t_0 = 82.3$ (year). This figure demonstrates that the earthquake occurs once about 220 years, and about five times in thousand years. The time interval is random because of the arithmetic Brownian stress accumulations.

The benchmark cat bond pays only when the epicenter of an earthquake falls in either grid. An epicenter is the horizontal-plane projection of a hypocenter, which is the point where the fault rupture starts. As seen in Figs. 7, 8 and 9, only part of some seismic sources falls into the grids, and the fractions are presented in Table 5.

It is very difficult to predict the location of epicenter or hypocenter even by the most advanced seismological knowledge, and HERP (2005) assumes that it is uniformly distributed within a fault rupture plane. We follow this assumption in Monte Carlo simulations to compute the numerator and denominator in Eq. (3.3). For example, the inner-grid cat bond pays in a probability of 50% even if the Tachikawa earthquake happens.

The seismic sources mechanically interact with each other through underground structures. For example, the stress distribution around a seismic source changes and its earthquake probability rises/drops just after a neighboring earthquake occurs.

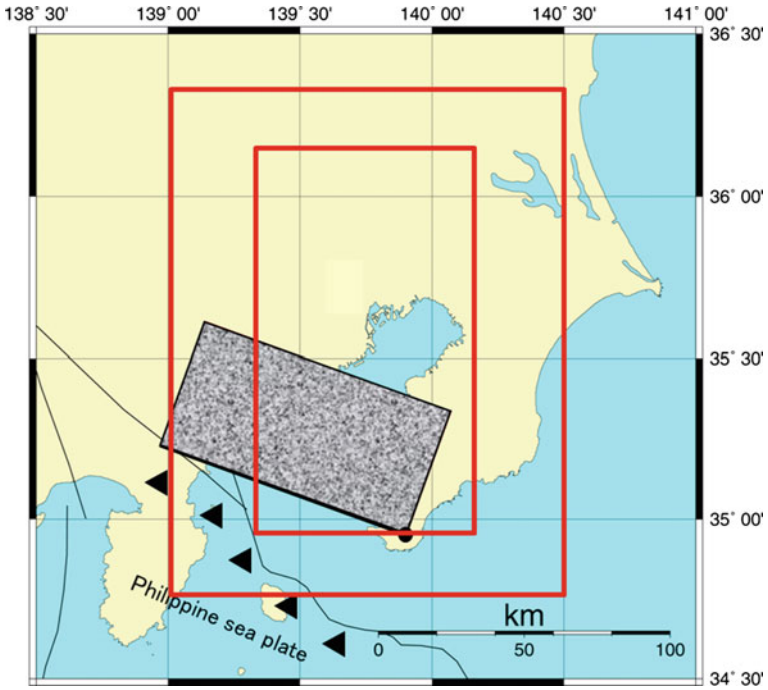

Fig. 9 Fault plane of Taisho-type Kanto earthquake

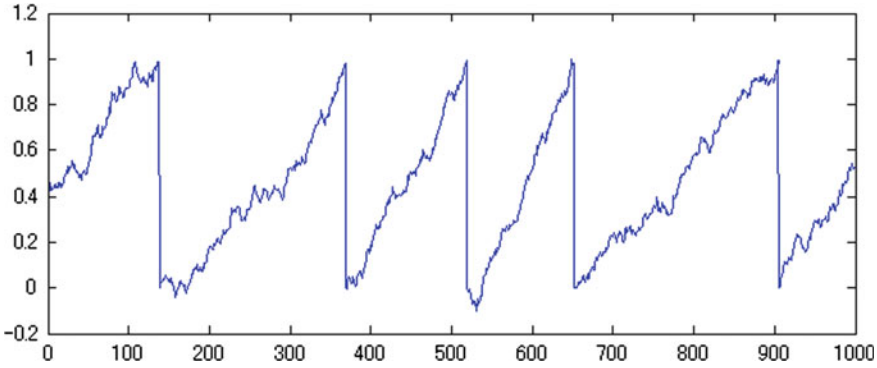

Fig. 10 A sample path of Brownian Relaxation Oscillator ($\mu = 1/219.7$, $\alpha = 0.21$, and $t_0 = 82.3$)

Unlike USGS (2003), HERP (2005) does not take into account the mechanical interaction yet and assumes the activities of seismic sources are independent of each other. We follow this assumption.

Table 5 Fraction of seismic source falling into cat bond grids

#	Name	Inner grid	Outer grid
01	Kamogawa Teichi	1.000	1.000
02	Kanto Heiya Hokuseien	0.355	0.774
03	Hirai-Kushibiki	0.000	1.000
04	Tachikawa	0.500	1.000
05	Isehara	0.250	1.000
06	Kannawa-Kozu-Matsusda	0.000	1.000
07	Miura peninsula main Kinugasa-Kitatake	1.000	1.000
08	Miura peninsula main Takeyama	1.000	1.000
09	Miura peninsula south	1.000	1.000
10	Taisho-type Kanto	0.521	0.910
11	South Kanto	0.714	0.998

4.3 Benchmarking

By using the seismological models presented in Sect. 4.2, we computed the annual expected loss, $E[L]$, and risk-neutral spread, s_{RN}, of the benchmark cat bond. The latter is calculated by Eq. (3.3), where the numerator and denominator are evaluated by Monte Carlo simulations with 100,000 cycles in each case. Time increment, dt, is set to be 0.01 year.

The annual expected loss of the cat bond, $E[L]$, is time-dependent because we are using not only the Poisson model but also the BRO model. We can also calculate the "averaged" annual expected loss ex post by assuming the process follows the Poisson model. First we compute the probability mass function of LGD during the maturity of 10 years, $F(10)$. By substituting $F(10)$ into Eq. (4.6), the "averaged" annual probability, $F(1)$, is evaluated.

$$F(T) = 1 - e^{-T/\mu} \tag{4.4}$$

$$F(1) = 1 - e^{-1/\mu} \tag{4.5}$$

$$F(1) = 1 - \{1 - F(T)\}^{1/T} \tag{4.6}$$

The "averaged" annual expected loss is the average of LGD weighted by the "averaged" annual probability, $F(1, \mathrm{LGD})$.

$$E[L] = \sum_{all\ LGD} F(1, LGD) \cdot LGD \tag{4.7}$$

Table 6 compares our estimations to the benchmark given by Geman (1999). Our mean model gives the numbers comparable to the benchmark, and our conservative model gives lager values, especially, for the outer-grid bond.

Table 6 Annual expected loss and spread (in bps) (starting time of November 1997)

Grid	Benchmark (Geman 1999)		Mean model		Conservative model	
	$E[L]$	s_{market}	Averaged $E[L]$	s_{RN}	Averaged $E[L]$	s_{RN}
Inner	44.00	430	32.25	33.15	49.99	52.11
Outer	26.00	206	30.23	32.78	99.00	112.01

Table 7 Annual expected loss, spread (in bps), and required notional (starting time of January 2010)

Grid	Conservative model		s_{market} (hypothetical)	*N/C*
	$E[L]$	s_{RN}		
Inner	50.43	52.63	250	4.32
Outer	102.05	115.62	500	2.16

To be sure, we are using a very different model from the benchmark (the seismological model for the actual pricing is not opened to the public). This is because the actual pricing was done before the cat bond issue in 1997 and we are using newer models developed by HERP (2005), including the BPT models first appeared in seismology in 1999. Nevertheless our results are comparable to the benchmark.

We can confirm that s_{RN} is slightly larger than $E[L]$ in each case. This is mainly because the former considers the time value of future payoffs whereas the latter does not.

4.4 Pricing

Now we price the proposed derivatives by supposing it will be issued in 2010, which is 13 years after the benchmark cat bond. We performed the same Monte Carlo simulations as those shown in Sect. 4.3 except for the values of t_0, starting times since the last earthquakes.

Table 7 presents the results for the conservative model. By comparing Tables 7 to 6, it is found that $E[L]$ and s_{RN} become slightly greater. This is because a BRO is more likely hit the threshold as the longer time elapses since the previous earthquakes.

Lane (2006) indicated that the ratio of s_{market} to $E[L]$ comes about five recently. Thus we hypothesize s_{maket} as 250 bps for the inner grid and 500 bps for the outer grid. By substituting these numbers along with $T = 10$ years, $\Delta = 0.5$ years, and $r_{\text{f}} = 1.5\%$ into Eq. (3.5), we obtained *N/C* of 4.32 and 2.16, respectively.

Figure 11 illustrates the outer-grid case, where the building owner is required to deposit \$54 K (= \$25 × 2.16) when he/she wants to cover the protection cost of \$25 K. Instead he/she can receive annual coupons (500 bps + LIBOR) × \$54 K until an earthquake of 7.3 or greater (if any) or maturity. Unless such an earthquake

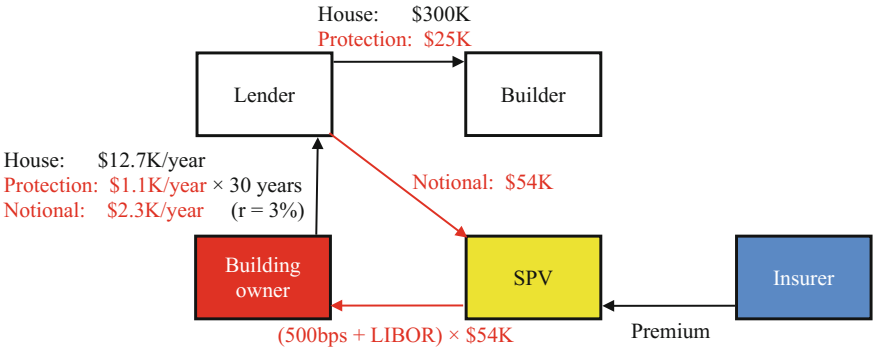

(a) At the beginning and until earthquake occurs

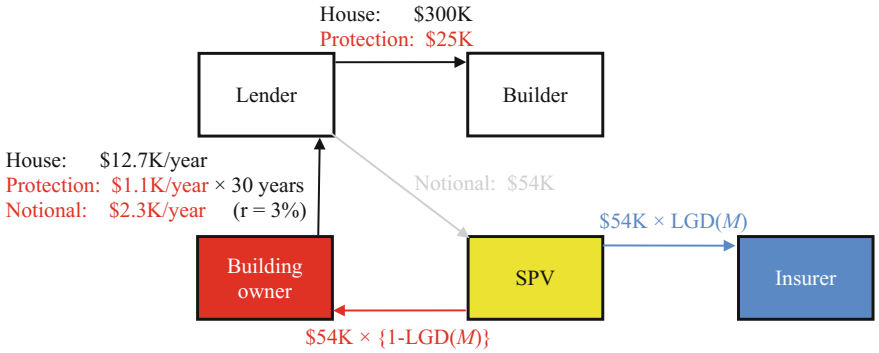

(b) If earthquake of magnitude M occurs before maturity of 10 years

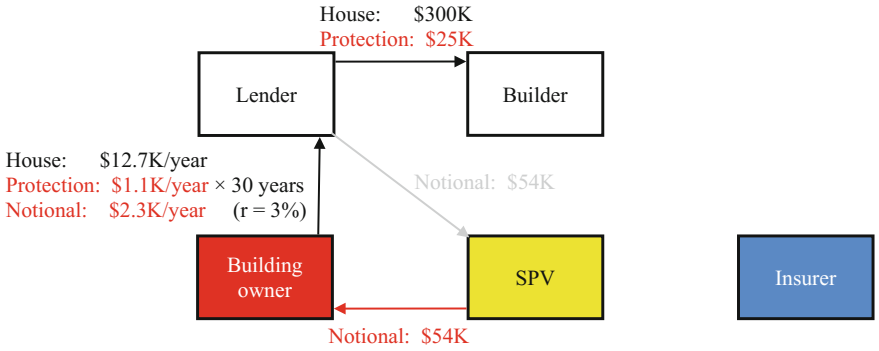

(c) If there is no earthquake before maturity of 10 years

Fig. 11 Numerical example for outer grid (using mortgage)

occurs for 10 years, the principal of $54 K will be redeemed to the owner. If such an earthquake occurs, the notional is slit to the building owner and the insurer depending on its magnitude.

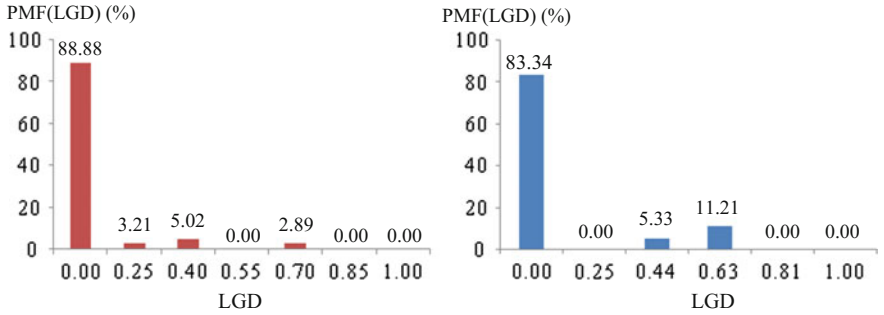

Fig. 12 Probability mass function of loss to building owners (within 10 years)

Figure 12 is the probability mass function of the LGD for the building owner during the contract period of 10 years. For the outer grid, he/she can receive all coupons and the principal of \$54 K in a probability of 83.34%. He/she loses \$24 K (0.44 × \$54 K) in 5.33% and \$34 K (0.63 × \$54 K) in 11.21%. On the other hand, the owner has to make a larger deposit of \$180 K (= \$25 × 4.32) for the inner grid in return for a higher redemption probability of 88.88%.

This exemplifies the tradeoff between the default probability and the amount of the notional. The deposit amount relative to the compensation (*N/C*) is larger in seismically safe regions because the redemption probability (or no earthquake probability) is larger. In contrary, the deposit is smaller in seismically active regions because the redemption probability is smaller.

5 Conclusions

This chapter presented derivatives to spur the penetration of physical earthquake-protection technologies, especially in seismically active regions. This contract pays coupons to a building owner until a pre-determined earthquake takes place (if any) or maturity. The coupons cover the owner's investment in the protection in case of no earthquake. This security is constructed by swapping the payoff with the insurer leg of a regular cat bond because their payoffs are the mirror image of each other. In order to pay to the insure leg when earthquake occurs, the building owner deposits a principal.

There are two steps to price the proposed security. The first step is the spread of an ordinary cat bond. In addition to a conventional pricing based on annual expected loss, this chapter demonstrated that our case can utilize CDS pricing. Needless to say, the greater the default (or earthquake risk) is, the greater a spread is. The second step is to determine the notional amount deposited by the building owner relative to the amount he/she wants to cover if there is no earthquake. We clarified the tradeoff between the default (earthquake) probability and the notional

amount required: the notional amount is greater as the probability that earthquake does not occur, which result in the full coverage and redemption to the building owner, the higher.

A numerical example dealing with an actual cat bond was presented. The payoff of the cat bond under consideration is determined by magnitude of earthquakes, an objective physical measurement. We introduced the up-to-date seismological models, i.e., Poisson and Brownian Relaxation Oscillator, and parameters developed by Japanese seismologists into cat bond pricing. Based on market spread, inferred by putting market risk premium over the evaluated annual expected loss or risk-neutral spread of the cat bond, we estimate the notional amount for the building owner. We numerically confirmed the tradeoff between the notional amount and earthquake probability. This means that the notional requirement is smaller in more dangerous places.

Let's look at the potential markets in Japan. The total amount of housing and building starts was about $240 billion in the fiscal year of 2007 according to the Ministry of Land, Infrastructure, and Transportation (MLIT 2008). The earthquake protection markets are estimated to be about $4.8–$24 billion provided that an additional cost ranges from 2% to 10% relative to the total amount of a new construction. The market for remodeling of existing housings and buildings was about $14 billion in the fiscal year of 2005 (MLIT 2007). The protection markets are estimated to be about $0.7–$4.2 billion by assuming an earthquake protection costs 5–30% in remodeling. The total markets of earthquake protections for new and existing buildings are estimated to be $5.5–$28.2 billion, which will remarkably contribute to Japan's GDP of 4.5 trillion.

The derivatives security proposed in this chapter plays several roles. First it expands earthquake reinsurance capacity like regular cat bonds. Second it increases the business of construction industry because they can sell their physical technologies more. The emphasis is that the derivatives are applicable not only to constructions of new buildings but also to seismic upgrades of existing ones. Third lenders also increase their mortgage amount to building owners. Finally the products enable not only to mitigate economic loss but also to save human lives, by fueling penetration of physical earthquake-protection technologies. This is the essential difference from conventional earthquake insurances. They transfer loss from one to others, but do not reduce loss at all from the macroscopic perspective. Nor do they save human lives. But our derivatives can do both.

References

Cabinet Office of Japan (COJ) Earthquake loss estimations, (in Japanese)

Geman H (1999) Insurance-linked securities, Insurance and weather derivatives, pp 155–166, Risk Books

Headquarters for Earthquake Research Promotion (HERP) (2005) Part 1: Explanation for probabilistic seismic hazard map, National Seismic Hazard Map for Japan, (in Japanese)

Lando D (2004) 8.4 Pricing the default swap, Credit Risk Modeling, Princeton University Press, pp 206–208
Lane M (2006) Over the top, but not off the boil. Trade Notes, Lane Financial L.L.C
Matthews MV, Ellsworth WL, Reasenberg PA (2002) A Brownian model for recurrent earthquakes. Bull Seismol Soc Am 92:2233–2250
Ministry of Land, Infrastructure, and Transportation (MLIT) (2008) Statistics for Building Construction Starts in 2007
Ministry of Land, Infrastructure, and Transportation (MLIT) (2007) Survey on Building Remodeling Markets in 2005
Misani N (1999) Chapter 2 cat bond, Risk management between insurance and finance: New instruments for the management of pure risks: catastrophe bonds, insurance derivatives, contingent capital, risk fusion, EGEA, pp 27–90
MMC Securities (2007) The Catastrophe Bond Market at Year-End 2006
Non-Life Insurance Rating Organization of Japan (NLIROJ) (2003) Earthquake Insurance in Japan
Swiss Re (2003) The picture of ART, sigma, No.1
Takahashi Y (2006) Financial technology to promote earthquake preparation, Journal of Structural and Construction Engineering, Vol 602, pp 95–102, Architectural Institute of Japan (in Japanese)
United States General Accounting Office (GAO) (2003) Catastrophe insurance risks: status of efforts to securitize natural catastrophe and terrorism risk, GAO-03-1033
U.S. Geological Survey (USGS) (2003) Earthquake probabilities for the San Francisco Bay Region: 2002-2031, USGS Open-File Report 03-214

Erratum to: Model Checking After Bayesian Inference

Matteo Pozzi and Daniele Zonta

Erratum to:
Chapter "Model Checking After Bayesian Inference" in:
P. Gardoni (ed.), *Risk and Reliability Analysis: Theory and Applications*, Springer Series in Reliability Engineering,
https://doi.org/10.1007/978-3-319-52425-2_14

The original version of the book was inadvertently published with the incorrect affiliation "Pittsburgh, UK", which has been now corrected as "Pittsburgh, USA" for author "Matteo Pozzi" in chapter "Model Checking After Bayesian Inference".

The updated online version of this chapter can be found at
https://doi.org/10.1007/978-3-319-52425-2_14

P. Gardoni (ed.), *Risk and Reliability Analysis: Theory and Applications*,
Springer Series in Reliability Engineering, https://doi.org/10.1007/978-3-319-52425-2_24